Metasomatism in Oceanic and Continental Lithospheric Mantle

Edited by
M. Coltorti and M. Grégoire

Geological Society
Special Publication 293

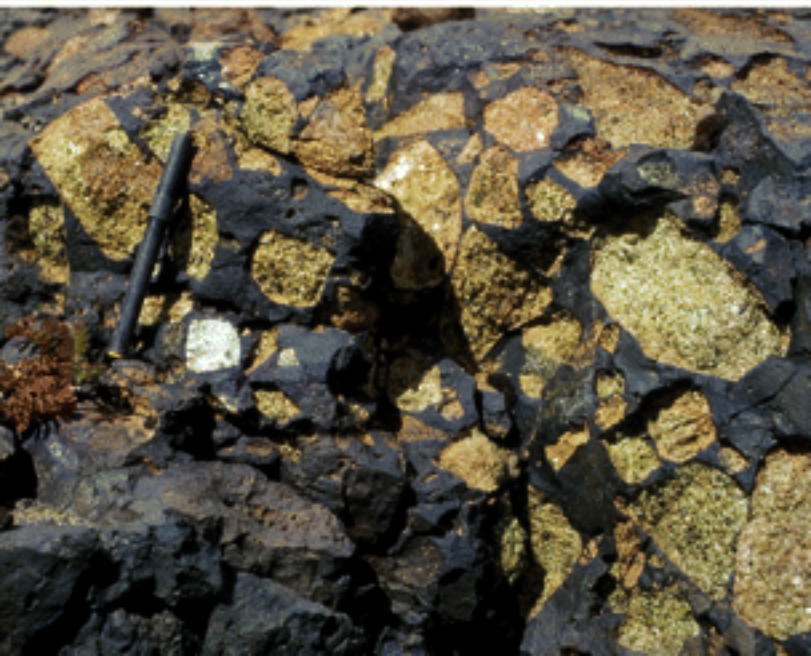

Metasomatism in Oceanic and Continental Lithospheric Mantle

Geological Society books refereeing procedures

The Society makes every effort to ensure that the scientific and production quality of its books matches that of its journals. Since 1997, all book proposals have been refereed by specialist reviewers as well as by the Society's Books Editorial Committee. If the referees identify weaknesses in the proposal, these must be addressed before the proposal is accepted.

Once the book is accepted, the Society Book Editors ensure that the volume editors follow strict guidelines on refereeing and quality control. We insist that individual papers can only be accepted after satisfactory review by two independent referees. The questions on the review forms are similar to those for *Journal of the Geological Society*. The referees' forms and comments must be available to the Society's Book Editors on request.

Although many of the books result from meetings, the editors are expected to commission papers that were not presented at the meeting to ensure that the book provides a balanced coverage of the subject. Being accepted for presentation at the meeting does not guarantee inclusion in the book.

More information about submitting a proposal and producing a book for the Society can be found on its web site: www.geolsoc.org.uk.

It is recommended that reference to all or part of this book should be made in one of the following ways:

COLTORTI, M. & GRÉGOIRE, M. (eds) 2008. *Metasomatism in Oceanic and Continental Lithospheric Mantle*. Geological Society, London, Special Publications, **293**.

SEGHEDI, I., NTAFLOS, T. & PÉCSKAY, Z. 2008. The Gătaia Pleistocene lamproite: a new occurrence at the southeastern edge of the Pannonian Basin, Romania. *In*: COLTORTI, M. & GRÉGOIRE, M. (eds) *Metasomatism in Oceanic and Continental Lithospheric Mantle*. Geological Society, London, Special Publications, **293**, 83–100.

GEOLOGICAL SOCIETY SPECIAL PUBLICATION NO. 293

Metasomatism in Oceanic and Continental Lithospheric Mantle

EDITED BY

M. COLTORTI
Università degli Studi di Ferrara, Italy

and

M. GREGOIRE
Université Toulouse III, France

2008
Published by
The Geological Society
London

THE GEOLOGICAL SOCIETY

The Geological Society of London (GSL) was founded in 1807. It is the oldest national geological society in the world and the largest in Europe. It was incorporated under Royal Charter in 1825 and is Registered Charity 210161.

The Society is the UK national learned and professional society for geology with a worldwide Fellowship (FGS) of over 9000. The Society has the power to confer Chartered status on suitably qualified Fellows, and about 2000 of the Fellowship carry the title (CGeol). Chartered Geologists may also obtain the equivalent European title, European Geologist (EurGeol). One fifth of the Society's fellowship resides outside the UK. To find out more about the Society, log on to www.geolsoc.org.uk.

The Geological Society Publishing House (Bath, UK) produces the Society's international journals and books, and acts as European distributor for selected publications of the American Association of Petroleum Geologists (AAPG), the Indonesian Petroleum Association (IPA), the Geological Society of America (GSA), the Society for Sedimentary Geology (SEPM) and the Geologists' Association (GA). Joint marketing agreements ensure that GSL Fellows may purchase these societies' publications at a discount. The Society's online bookshop (accessible from www.geolsoc.org.uk) offers secure book purchasing with your credit or debit card.

To find out about joining the Society and benefiting from substantial discounts on publications of GSL and other societies worldwide, consult www.geolsoc.org.uk, or contact the Fellowship Department at: The Geological Society, Burlington House, Piccadilly, London W1J 0BG: Tel. +44 (0)20 7434 9944; Fax +44 (0)20 7439 8975; E-mail: enquiries@geolsoc.org.uk.

For information about the Society's meetings, consult *Events* on www.geolsoc.org.uk. To find out more about the Society's Corporate Affiliates Scheme, write to enquiries@geolsoc.org.uk.

Published by The Geological Society from:
The Geological Society Publishing House, Unit 7, Brassmill Enterprise Centre, Brassmill Lane, Bath BA1 3JN, UK

(*Orders*: Tel. +44 (0)1225 445046, Fax +44 (0)1225 442836)
Online bookshop: www.geolsoc.org.uk/bookshop

British Library Cataloguing in Publication Data

A catalogue record for this book is available from the British Library.

ISBN 978-1-86239-242-7

Typeset by Techset Composition Ltd., Salisbury, UK

Printed by Cromwell Press, Trowbridge, UK

Distributors

North America
For trade and institutional orders:
The Geological Society, c/o AIDC, 82 Winter Sport Lane, Williston, VT 05495, USA
Orders: Tel +1 800-972-9892
Fax +1 802-864-7626
Email gsl.orders@aidcvt.com

For individual and corporate orders:
AAPG Bookstore, PO Box 979, Tulsa, OK 74101-0979, USA
Orders: Tel +1 918-584-2555
Fax +1 918-560-2652
Email bookstore@aapg.org
Website http://bookstore.aapg.org

India
Affiliated East-West Press Private Ltd, Marketing Division, G-1/16 Ansari Road, Darya Ganj, New Delhi 110 002, India
Orders: Tel +91 11 2327-9113/2326-4180
Fax +91 11 2326-0538
Email affiliat@vsnl.com

Contents

Metasomatism in oceanic and continental lithospheric mantle: introduction

M. COLTORTI[1] & M. GRÉGOIRE[2]

[1]*Department of Earth Sciences, University of Ferrara, via Saragat 1, 44100 Ferrara, Italy (e-mail: clt@unife.it)*

[2]*Laboratoire Dynamique Terrestre et Planétaire, UMR-CNRS 5562, Observatoire Midi-Pyrénées, 31400, Toulouse, France*

In the foreword of the volume *Mantle Metasomatism* by Menzies & Hawkesworth (1987), Boettcher stated that the concept of mantle metasomatism has been of immense heuristic value for Earth scientists. At that time, metasomatism was still strongly related to allochemical metamorphism, where chemical composition of the rock is changed by the additional or removal of material. However, the concept of modal or patent (where a new phase is petrographically evident) and cryptic (where chemical enrichment is not accompanied by the presence of a newly formed phase) metasomatism had already been introduced by the pioneering works of Harte (1983), Menzies (1983) and Dawson (1984).

Outstanding progress has characterized the past two decades, and the processes and agents of metasomatism are now much better understood, in part as a result of the significant advancements of *in situ* microanalytical techniques such as secondary ionization mass spectrometry (SIMS) and laser ablation-inductively coupled plasma-mass spectrometry (LA-ICP-MS). The *in situ* analyses substantially deepened knowledge of intermineral and solid–liquid partitioning coefficients as well as identifying the geochemical features of metasomatizing agents recorded by secondary paragenesis, (namely, clinopyroxenes, amphiboles and glasses), which are the main acceptors of trace elements within the mantle.

Glasses were initially interpreted as the product of host basalt infiltration and their petrological importance was disregarded. During the 1990s, the importance of identifying the geochemical features of the metasomatizing agents was properly highlighted and the study of glasses represented an important improvement in the understanding of metasomatic processes. Irrespective of their origin as products of (1) reaction (Coltorti *et al.* 2000), (2) *in situ* melting (Chazot *et al.* 1996; Yaxley *et al.* 1997), (3) decompressional melting (Francis, 1976; Gamble & Kyle, 1987) or (4) partial melting (Draper & Green, 1997), the glasses' geochemical features can be a valuable clue to the nature of the metasomatizing agent. However, glasses are usually small and more difficult to analyse with the less time-consuming but larger-spot LA-ICP-MS. For this reason, at the beginning of this century, attention has been drawn back to minerals, such as clinopyroxene, amphibole and/or phlogopite (e.g. Grégoire *et al.* 2000; Moine *et al.* 2001; Coltorti *et al.* 2007*a*). Another revolution is on the horizon because of the introduction of LA-ICP-MS-MC (LA-ICP-MS with multi-collector) and a new generation of femtolasers associated with ICP-MS which, with their increased sensitivity and enhanced performances, will allow the development of both *in situ* isotopic analyses and trace element analyses in orthopyroxene and olivine. LA-ICP-MS-MC will permit pinpointing of single ages and geochemical signatures instead of an average obtained by mineral separates, whereas femtolaser-ICP-MS will allow the study of more refractory rocks, such as harzburgites and dunites (which very rarely contain clinopyroxene and/or amphibole and/or glass) and other orthopyroxene-rich metasomatic parageneses, which are rather abundant in mantle wedges (e.g. Smith *et al.* 1999; Grégoire *et al.* 2001; McInnes *et al.* 2001; Ishimaru *et al.* 2007).

Most of the 14 papers in the present volume mainly rely on *in situ* major and trace element analyses of clinopyroxene and amphiboles, with the aim of identifying the nature of the metasomatizing agents affecting different portions of the lithospheric mantle. Some very basic concepts are at the core of these papers. Metasomatism is a process that enriches the lithosphere. Thus the lithosphere had previously been depleted by one or more partial melting episodes. As a consequence, metasomatism is the last event to be recorded by minerals, and it would be hidden or even completely erased by any melting process. Assuming that these logical connections are true at low melt–rock interaction, which can be practically considered synonymous with metasomatism, they are not valid for high melt–rock interaction, where percolation and impregnation can be responsible for both depletion

From: COLTORTI, M. & GRÉGOIRE, M. (eds) *Metasomatism in Oceanic and Continental Lithospheric Mantle.* Geological Society, London, Special Publications, **293**, 1–9.
DOI: 10.1144/SP293.1 0305-8719/08/$15.00

and enrichment processes (see the work of Piccardo on several ophiolitic bodies of the Alpine–Apennine system). The increase of fluid/rock ratios also implies a drift in the metasomatizing agent's composition from highly SiO_2-undersaturated, volatile- and alkali-rich silicate magmas (including CO_2-rich or even carbonatite melts) towards SiO_2-saturated and even SiO_2-oversaturated magmas. In parallel, the tectonic framework will change from intraplate, where SiO_2-undersaturated magmas are more abundant, to suprasubduction and mid-ocean ridge settings, where SiO_2-saturated and -oversaturated magmas predominate. The effects of these different interactions are presented in this volume, and they were studied on both continental and oceanic lithosphere, including the transition between the two that occurs when an ocean starts to open.

The transition between continental and oceanic lithosphere

Piccardo presents a comprehensive review of petrological, field and age relationships of several peridotite and ophiolite bodies of the Alpine–Apennine system. The continental lithosphere here results from the accretion of several masses of the convective asthenospheric mantle, which occurred from Proterozoic to Permian times. Lithosphere extension caused adiabatic upwelling and decompression melting, resulting in large-volume production of mid-ocean ridge basalt (MORB)-like magmas, which percolated and impregnated the continental lithospheric mantle. The continental lithosphere was progressively heated and asthenospherized until complete failure of continental crust occurred and mantle was exhumed at the sea floor. From this study it appears that the separation between continental and oceanic mantle lithosphere is not straightforward. Continental lithosphere can be progressively transformed into oceanic through impregnation, and oceanic lithosphere can be accreted at the base of the continental lithosphere. These facts have some relevance when the provenance and the nature of both depleted and enriched components are described in mantle xenoliths from continental and oceanic settings, as well as the occurrence of pieces of continental lithosphere found as xenoliths in ocean island basalts (Bonadiman *et al.* 2005, 2006; O'Reilly *et al.* 2006). Moreover, the simple paradigm that depleted rocks record a partial melting event is questioned (see also Bodinier 2007), especially when the dimensions of the outcrop (as for xenoliths) do not permit a thorough investigation of the field relationships. The need for more sophisticated geochemical tools capable of distinguishing between harzburgites produced by reaction with a melt and those produced by a 'simple' partial melting episode is envisaged. Melt–rock impregnation casts doubts on the barometric significance of the aluminous phase; impregnated plagioclase peridotites that were previously reasonably interpreted as having formed at low pressure can in fact coexist with reactive spinel peridotite.

Metasomatism in subduction-related environments and post-collisional orogens

The study of mantle xenoliths is limited by their small dimensions compared with Alpine or ophiolitic peridotite, but they have the exclusive advantage of a very rapid (in geological terms) ascent (from a few hours to several days), which allows the preservation of the textural features formed at mantle depth. Therefore, geochemical studies can be applied to different generations of minerals, which in turn can be related to various metasomatic events. Most probably the concept of mantle metasomatism itself could not have been developed without xenoliths. Unfortunately, xenoliths are rarely brought to the surface by calc-alkaline *sensu lato* lavas, thus our knowledge of the mantle wedge above subduction zones is still limited. A vigorous debate is currently developing on the nature of the fluids migrating into this portion of the mantle, as well as on the different residential times of the subduction signature in mantle wedges.

Ishimaru & Arai studied one of the few occurrences of this type of xenoliths, from Avacha volcano (Kamchatka), contributing to knowledge of the petrological features of the fluids migrating into mantle wedges. The Avacha peridotites have experienced metasomatism to various extents, with the formation of metasomatic orthopyroxene replacing primary olivine, by the infiltration of slab-derived, sulphur-bearing, SiO_2-rich fluids. Secondary metasomatic minerals are also constituted by clinopyroxene, Cr-rich (in some cases Al-rich) spinels and tremolite to Mg-hornblende and edenite. This paper, which is complementary to that of Ishimaru *et al.* (2007), focuses particularly on the amphibole, which can be considered a key mineral for a better understanding of the geochemical signature of metasomatizing agents in subduction environments. In the Avacha peridotites, amphiboles appear particularly depleted in TiO_2 and Nb, supporting the idea that fluids from the slab are already depleted in these elements. The large mass of trace element data on amphibole provided by these two papers was also used by Coltorti *et al.* (2007*a*) to propose a geochemical separation, based on high field strength element (HFSE) contents, between amphiboles formed in

subduction settings and those formed in intraplate environments. This geochemical tool has already been used to identify relics of subduction events recorded in xenoliths entrapped in alkaline, intraplate settings (Beccaluva *et al.* 2004; Coltorti *et al.* 2007*b*).

The paper by **Ntaflos *et al.*** focuses on anhydrous spinel peridotite xenoliths enclosed in the Late Miocene olivine melanephelinites of the Viliga River Volcanic Field (NE Russia), just a few hundred kilometres north of the previous occurrence. These strongly alkaline lavas overlie a massive sequence of plutonic and effusive calc-alkaline rocks, and indicate that subduction processes took place in this region from Early to Late Cretaceous times. Ntaflos *et al.* propose that the mantle xenoliths derived from Pacific asthenospheric mantle and not from the Asian mantle wedge, which should have been affected by the subduction fluids. They also demonstrate that the xenoliths were not affected by metasomatic processes. The clinopyroxene REE modelling indicates that the fertile peridotites experienced 2 – 9% batch melting whereas the most depleted peridotites experienced 15% batch melting. Similar results were derived from the olivine and whole-rock FeO and MgO modelling. A magmatic refertilization of a depleted lithospheric mantle wedge is excluded as a possible reason for the fertility of the Viliga peridotites because neither whole-rock chemistry nor clinopyroxene trace elements provide evidence for metasomatism. In addition, the low $^{87}Sr/^{86}Sr$ ratios and the high, partly higher than mid-ocean ridge basalt (MORB), $^{143}Nd/^{144}Nd$ ratios point to an asthenospheric origin. The model that Ntaflos *et al.* propose to explain the origin of the Viliga peridotites is a 'piecemeal' breakup of the subducted palaeo-Pacific plate, which allowed the Pacific asthenospheric mantle to intrude the mantle wedge through a slab window. Subsequently, olivine melanephelinites that were generated at deeper levels sampled this part of asthenospheric mantle on their way to the surface. The absence of any evidence for subduction-related metasomatism implies that the asthenospheric upwelling occurred when subduction was no longer active. This observation makes it also unlikely that subduction-metasomatized domains were preserved within the mantle at that time, thus giving some clues about the mode and time of material recycling above a subduction zone.

The paper by **Seghedi *et al.*** is the first report of a new occurrence of lamproite in a region where this rock type was previously unknown. These rocks are of great interest for understanding the genesis of ultrapotassic rocks in general, for defining the nature of the metasomatizing agents of the subcontinental lithospheric mantle, and for clarifying the geodynamic evolution of the central–eastern European basin and orogen. The area where the Gătaia lamproite occurs is remarkable: the southernmost margin of the Pannonian Basin, where lithosphere thickness steeply increases southwards and eastwards, representing a transition between the Carpathian and the Serbo-Macedonian domains. The mantle source of this magma could have been influenced by several subduction events both beneath the Tisza–Dacia block and the Serbo-Macedonian Massif (Kovàcs *et al*. 2007). Prelević *et al.* (2007) inferred a two-stage metasomatism, the first being subduction-related whereas the second is linked to alkaline silicate metasomatism for similar lamproitic rocks in the Serbian domain, a few tens of kilometres to the south. Both stages of the metasomatism impinged upon a very refractory lithosphere, produced in a suprasubduction environment. The first slab-related metasomatism is not recognized for the Gataia lamproite. Based on trace element and isotopic data, **Seghedi *et al.*** exclude the presence of any subduction-related metasomatism and infer that only alkaline metasomatism can be recognized. The paper is a valuable contribution to a long-standing debate, and represents a stimulus for the discussion on the petrological evolution of the source of these very peculiar rocks (Conticelli *et al.* 2007; Prelević *et al.* 2007).

Metasomatism in continental intraplate and rifting settings

The processes and nature of metasomatizing agents in intraplate settings are much better understood than are those in subduction environments. A consensus exists on the way to distinguish between alkaline silicate (both Na- and K-rich) and carbonatite melts, considered to be by far the most important metasomatizing agents in intraplate lithospheric mantle. On the other hand, a major debate is currently developing on the possibility of relating the various metasomatic signatures, which may be recorded in mantle xenoliths from the same locality, to a single metasomatic event through an infiltration–reaction process (Bodinier *et al.* 2004; Xu & Bodinier 2004). The increasing availability of dating on mantle material (Pearson *et al.* 2007) will hopefully permit, in the near future, linkages between geological processes recorded in the upper and lower crust and depletion and enrichment processes observed within the mantle. In this framework, the distinction between a single metasomatic event or multiple events will be crucial.

Most of the papers presented in this section of the book deal with this aspect, although the question is clearly far from being solved.

The first question posed by **Orejana & Vilaseca** about alkaline metasomatism is its relationship with the host lavas; another important point to address when dealing with this topic. They present a complete dataset (major and trace element, and Nd–Sr isotopic compositions) of highly altered anhydrous and hydrated (amphibole- and phlogopite-bearing) pyroxenites hosted in Permian lamprophyric dykes. The occurrence of amphibole and phlogopite with major element composition similar to those found in peridotites affected by mantle metasomatism and also very different, particularly regarding Mg-number, Cr and Ti contents, from those found in cumulitic pyroxenites, leads **Orejana & Vilaseca** to think that these phases resulted from a reaction with an infiltrating melt after the pyroxenites were formed. The metasomatic processes seem to be heterogeneous, as the xenoliths show three different trace element signatures in minerals: (1) light rare earth element (LREE)-enriched clinopyroxenes with HFSE negative anomalies in primitive mantle-normalized spidergrams; (2) clinopyroxenes and amphiboles with high incompatible trace element contents (large ion lithophile elements (LILE); HFSE and REE); (3) relatively REE- and HFSE-poor clinopyroxenes and amphiboles. These metasomatic characteristics support three different metasomatic agents: carbonatites, silicate magmas and hydrous fluids or melts. **Orejana & Vilaseca** propose that these agents are all derived from the progressive differentiation of a single CO_2–H_2O-rich highly alkaline agent, genetically related to the Spanish Central System Permian alkaline lamprophyric dykes. In this respect there should be a genetic relationship between the metasomatizing agents and the host lavas, as inferred in many other occurrences of intraplate metasomatism (Wulff-Pedersen *et al.* 1999; Beccaluva *et al.* 2001; Coltorti *et al.* 2004), but the reactions, as supported by high Mg-number of the secondary phases and their growing time with respect to the velocity of ascent, have to have occurred at mantle depths some time before the xenoliths were entrapped (Beccaluva *et al.* 2001; Coltorti *et al.* 2004).

The second, and even more relevant, point is the interpretation of the different geochemical signatures recorded by the metasomatic phases (namely, clinopyroxene, amphibole and phlogopite). Could they be interpreted as the result of a single metasomatic event or could they be the result of several episodes of metasomatism? This is, at the moment, an open debate. Coltorti *et al.* (2007*a*, *b*), for example, interpreted the low HFSE abundances and the relative negative anomalies in the chondrite-normalized diagram for amphibole as a signature for subduction-related metasomatism and, using a well-studied example of vein and disseminated amphibole from Kerguelen, demonstrated that the infiltration and reaction from a large vein into the peridotite matrix is not able to vary significantly the Zr/Nb ratios (Coltorti *et al.* 2007*b*). On the other hand, based on the study of Bodinier *et al.* (2004) and Xu & Bodinier (2004), **Orejana & Vilaseca** inferred that this depletion could be related to the differentiation of a single magma, which will be enriched in H_2O and CO_2. In this way, the different geochemical signatures recorded by the secondary phases can be ascribed to a single geochemical process instead of to different geological processes.

Galan *et al.* deal with similar questions in their examination of the geochemical features of clinopyroxenes, amphiboles and phlogopites in mantle xenoliths from Neogene–Quaternary alkaline mafic lavas from Catalonia (NE Spain). Their study provides evidence to show that the subcontinental lithospheric mantle beneath this area is mostly made of protogranular anhydrous spinel lherzolites and harzburgites, with minor pyroxenites, and subordinate porphyroclastic and equigranular peridotites. A melt depletion event (up to 30% partial melting), related to mantle decompression and probably starting within the garnet lherzolite field, affected the peridotites. Evidence for subsequent metasomatism is widespread in harzburgites, but also occurs in some lherzolites. Two types of cryptic metasomatism, one related to carbonatite melts and the other to alkaline silicate melts, are distinguished. Evidence of modal metasomatism is rare and is restricted to the formation of amphibole or phlogopite. This modal metasomatism could be linked to either kind of cryptic metasomatism. The carbonatite metasomatism is more widespread than the silicate Fe–Ti-rich melt type. The latter could be compared with that observed in the nearby Pyrenean peridotite massifs, adjacent to the intrusions of Cretaceous alkaline magmas. Catalonia pyroxenite xenoliths are interpreted as cumulates from these alkali basalts. In this case the two or three different metasomatic agents are considered independent and not derived by a single fluid differentiating while infiltrating into the peridotite matrix. However, the question of Nb-depleted carbonatite still arises. Could this melt be a derivative of a unique alkaline silicate melt after differentiation through a reactive chromatographic process with early crystallization of amphibole and phlogopite $\pm$ Ti-oxides? However, the very limited modal amount of these phases, none of which is particularly enriched in this element, limits the applicability of the model and again gives rise to the question of whether this HFSE depletion, particularly regarding Nb, could be a sign of a previous, tectonically different and independent metasomatism (Coltorti *et al.* 2007*a*, *b*).

The paper by **Demény *et al.*** reports mineral chemistry, D/H and oxygen isotope ratios for

amphibole, biotite, pyroxene and feldspar from gabbroic plutons and amphibole xenoliths or xenocrysts in younger basalts of La Palma, following an analogous study on Fuerteventura (Demény *et al.* 2004). **Demény *et al.*** use the data reported here to support their earlier interpretation that the H–O isotopic signature derived from a deep mantle source. This conclusion would be very important for our understanding of mantle stable isotope systematics, although some difficulties may arise in clearly discriminating between shallow differentiation processes and those occurring at mantle depth. This approach is contributing to the current debate regarding mantle plumes, whose existence is under heavy criticism (Foulger *et al.* 2005). The H and O isotope compositions of amphibole, biotite, pyroxene and feldspar separates from the Basal Complex gabbros, as well as amphibole xenocrysts and amphibololite xenoliths in basalts seem to be devoid of any metasomatic influence (–90‰ and 5.1‰, respectively, relative to V-SMOW), and are very similar to those found for Fuerteventura. According to **Demény *et al.*** the most plausible explanation for the low $\delta^{18}O$ value is the presence of subducted ocean crust in the mantle plume source, whereas the low δD values could be related to volatiles ascending from deep in the Earth. Thus stable isotope data could provide a potentially powerful tool to support not only the existence of mantle plumes but also the presence of recycled (via subduction and deep mantle circulation) oceanic crust in the source of ocean-island basalt (OIB) magmatism (see also Thirlwall *et al.* 2006, who found similarly low $\delta^{18}O$ for some Icelandic basalts). Eventually this paper may also contribute to the estimation of the role and abundance of pyroxenites in the genesis of basaltic magmas (see also Sobolev *et al.* 2005).

Touron *et al.* present major and trace element stable and radiogenic isotope analyses of minerals from two localities within the Devés Volcanic District (French Massif Central). Anhydrous spinel lherzolites characterize mantle xenoliths from Mt. Briançon, whereas at Marais de Limagne, amphibole-bearing (with sporadic presence of phlogopite) lherzolites and harzburgites are also present. The metasomatic agent can be modelled as a sub-alkaline TiO_2, Th- and U-rich fluid or melt. Associated with negative anomalies in HFSE in chondrite-normalized spidergrams, such chemical characteristics are compatible with a carbonate-rich silicate melt or fluid as the metasomatic agent. Nevertheless, the occurrence of two geochemical signatures in amphibole, even within a single sample, may suggest a multistage metasomatism. Previous studies attributed the amphibole origin to an enriched mantle component, possibly related to the Variscan subduction in the Massif Central (Deloule *et al.* 1991; Lenoir *et al.* 2000). The isotopic compositions of Sr and Nd of clinopyroxene and amphibole indicate that the metasomatic fluid or melt derived from mixing between a depleted mantle (DM)-type, deeply recycled component and the European asthenospheric reservoir (Granet *et al.* 1995).

The metasomatism of the upper mantle beneath the Hyblean Plateau (Sicily) is the purpose of the first paper by **Perinelli *et al.*** They propose a two-stage evolutionary history for Hyblean anhydrous spinel lherzolites and harzburgites: (1) a slight to moderate (6–13%) partial melting event, which, using Re–Os *in situ* isotopic determinations (Sapienza *et al.* 2006), was estimated to have occurred at a minimum Palaeoproterozoic–Archaean age; (2) a cryptic metasomatism event that introduced LREE, Sr, HFSE, V and Ti into the 'barren' peridotite, probably lasting from Carboniferous times to the present day, which is supported by the Sm–Nd isotopic study (Tonarini *et al.* 1996) and by the widespread presence of glassy veins. The latter metasomatizing episode was caused by a hawaiitic melt and, according to **Perinelli *et al.***, is related to the presence of the glassy veins, and is not considered relevant on a regional scale. The metasomatizing melt determined oxidation of the upper mantle, increasing its redox state to above the fayalite–magnetite–quartz buffer (FMQ). Melt–peridotite interaction episodes are generally related to metasomatic re-equilibration with a siliceous melt similar to the Upper Miocene host basalt, again posing the question of the relationships between metasomatism and magmatism: the former probably representing a precursor to the latter. Some peculiar spoon-shaped clinopyroxene trace element patterns are explained as chromatographic effects of the melt flowing into a conduit and variably metasomatizing the surrounding country rocks. The Hyblean peridotites were equilibrated in the spinel peridotite stability field. P–T estimates are consistent with the data obtained previously on pyroxenite xenoliths, suggesting a highly perturbed palaeo-geotherm, probably, related to the numerous magmatic intrusions at the crust–mantle boundary and responsible for the metasomatic event(s) recorded by peridotites.

Ismail *et al.* present an original occurrence of spinel ± amphibole-bearing mantle xenoliths from the Neogene–Quaternary volcanic province of Jabel El Arab (southern Syria). This locality, together with many others in the region, is difficult to access and the study contributes to the knowledge of the lithosphere of the Dead Sea rift zone, at the boundary between the African and Arabian plates. The great majority of xenoliths are harzburgites, with a few lherzolites and wehrlites. Based on clinopyroxene trace element contents, three groups of

harzburgites are distinguished, showing a complex evolutionary history that involves polybaric partial melting (from garnet to spinel stability fields) at various degrees (<20%), followed by various metasomatic episodes. Some Group II harzburgite mineralogical and geochemical compositions indicate a near re-equilibration with a silicate melt at a relatively high melt/rock ratio, which increased the incompatible trace element abundances but did not significantly affect major element compositions. Some of the Group III harzburgites have mineralogical and geochemical compositions indicative of metasomatism by small silicate- or carbonate-rich melt fractions, resulting in selective major and trace element enrichments in the clinopyroxenes (high LREE/HREE ratio coupled with low HFSE). The carbonate-rich melt is not considered a mantle-derived carbonatite but the result of progressive reactions and crystallizations of an original volatile-bearing silicate melt with the residual peridotites. These metasomatic events were responsible for the presence of amphibole, as well as for the enrichment observed in the clinopyroxenes. The widespread presence of glassy patches filled with secondary cpx + ol + sp in both anhydrous and hydrous xenoliths provides evidence for the percolation of small silicate melt fractions shortly before eruption. These melts did not originate by *in situ* partial melting of amphibole but were derived from partial melting of amphibole in the nearby lithospheric mantle and subsequent fractional crystallization of clinopyroxene, olivine and spinel in reaction zones. Whether the different types of metasomatism could all be contemporaneous and derivatives of the same original silicate melt source or whether the lithospheric mantle was affected by different metasomatic media at different times, also considering that volcanism in southern Syria has been continuous since Miocene, remains an open and highly debatable question.

Based on the study of the Gharyan peridotite xenoliths from NW Libya, **Beccaluva *et al.*** assess the role of HIMU metasomatic components in the African lithospheric mantle. The mantle spinel lherzolite xenoliths from the Gharyan volcanic field represent slightly to moderately depleted mantle material likely to have resulted from extraction of basic melts during pre-Palaeozoic times. Subsequent metasomatic effects are evidenced by the widespread pyrometamorphic textures represented by reaction patches. Trace element analyses of both bulk rocks and constituent pyroxenes show variable enrichments in incompatible elements possibly caused by interaction with Na-alkali silicate basic melts similar to those from north African volcanic districts. Most clinopyroxene separates from the Gharyan xenoliths show Sr–Nd–Pb isotope compositions that indicate a prevalent HIMU metasomatic signature. A coherent Sr–Nd–Pb signature approaching DM is recorded by a single sample relatively unaffected by metasomatic reactions, whereas some other samples characterized by Sr–Nd ratios approaching DM, but with a Pb isotope HIMU affinity, may be attributable to higher mobility of Pb relative to Sr and Nd during metasomatism. **Beccaluva *et al.*** conclude that the Na–alkali silicate agent(s), characterized by a clear HIMU signature, affected, to a variable extent, a depleted lithospheric mantle section (DM). This prevalent HIMU fingerprint compares favourably with the geochemical features of alkaline basic lavas and associated mantle xenoliths from other volcanic districts of northern Africa, suggesting a common sub-lithospheric metasomatic agent across the region.

The second paper by **Perinelli *et al.*** develops an experimental approach aimed at reproducing the effect of metasomatism induced by alkaline magma on upper mantle of Northern Victoria Land (Antarctica). This is one of the few attempts to experimentally model this process; it also had the aim of constraining the P–T–X conditions suitable for the formation of amphibole. The model is developed using a natural nephelinite magma (variably doped with H_2O and TiO_2) sandwiched between natural anhydrous peridotite and pyroxenite matrixes in analogy to what has been observed in mantle xenoliths from Antarctica (Coltorti *et al.* 2004; Perinelli *et al.* 2006). These experiments are difficult to perform for many reasons, one of which is the differential temperature gradient that exists when basaltic magmas intrude a peridotite host. This condition cannot be simulated in a small capsule, and the nephelinite has to be pre-heated and pre-quenched. During the reaction, if the conditions to form amphibole are to be created, the temperature cannot be too high (amphibole is not stable above 1100 °C at 1.5–2 GPa, Niida & Green 1999), which means that the nephelinite is not completely melted and the composition of the infiltrating melts would be different from that of the starting material (i.e. the nephelinite). **Perinelli *et al.*** show that, in experiments on nephelinite–lherzolite and nephelinite–pyroxenite assemblages, considerable chemical modifications are observed in both lherzolitic and pyroxenitic portions of the charges, suggesting that metasomatic reactions developed during the experiments. Clinopyroxene composition changes from diopside to high-Mg–Cr–(Na) augite and omphacite in lherzolite and to low-Mg and high-Ti–Al–Fe–Na augite in pyroxenite. The observed Ti increase in natural clinopyroxenes is fairly well matched by crystals formed in pyroxenite, whereas even the use of Ti-doped nephelinite caused a negligible Ti increase in clinopyroxene of lherzolite. Spinels (in lherzolite) and

olivines (in pyroxenite) were compositionally modified by metasomatic melts: Cr-number increases and Mg-number decreases in spinel, and forsterite decreases in olivine. Synthetic glasses that fit better with natural melts are produced by runs at $T < 1250\ ^{\circ}C$ in nephelinite–wehrlite experiments and at $T = 1250\ ^{\circ}C$ and 1.5 GPa in the nephelinite–lherzolite experiment.

Pre-Mesozoic metasomatism in continental intraplate settings

The paper by **Bonadiman *et al.***, based on major and trace element and Nd–Sr–Hf isotopic (both on whole rock and separate clinopyroxenes) compositions, demonstrates that the Scottish lithospheric mantle beneath Rinibar and Streap has been affected by Palaeozoic kimberlite or carbonatite and subduction-related metasomatic events. Rinibar mantle xenoliths show two different metasomatic styles, one carbonatitic and one kimberlite-like, both derived from the same source. This is supported by the similarity of Sr and Nd isotopic ratios at 550 ± 50 Ma. This age can be related to the opening of the Iapetus Ocean following the break-up of the Rodinia supercontinent. Late Proterozoic–Early Phanerozoic carbonatite magmatism is also recognized within Scotland. Moreover, the genesis of the coherent suite of megacrysts from the Scottish Permo-Carboniferous high-alkaline lavas involved carbonatitic melt fractions. The emplacement of very small fraction partial melts (and related mantle metasomatism) in relation to the rifting and drifting of the Iapetus Ocean could be compared with the opening of the Atlantic Ocean, where Early to Late Cretaceous kimberlite and alkaline–carbonatite complexes are found on both sides of the ocean in Brazil and Angola. At 500 Ma the tectonic regime changed from divergent to convergent. It may have been during this convergent stage (*c*. 400 Ma) that the metasomatism affecting the Streap lithospheric mantle occurred. The various terranes that now constitute Scotland in fact came into conjunction at the end of Caledonian Orogeny, and were certainly contiguous by 416 Ma. Clinopyroxenes from this locality show trace element contents that can be explained by slab-related metasomatic fluids, and based on Nd–Sr and Hf isotopes a substantial amount of sediments (*c*. 10%) is necessary to explain the isotopic features of these samples. The Rinibar clinopyroxenes record no subduction-related imprint. This could imply that either the northeasternmost portion of the Highland Terrane lithospheric mantle was unaffected by the Caledonian subduction or, alternatively, that the subduction-related metasomatism recorded in the Streap mantle may have been older, and occured when the two lithospheric blocks were far apart.

Finally, the study of **Ashchepkov *et al.*** proposes to use monomineral thermobarometry to reconstruct mantle sections beneath Yakutian kimberlite pipes (Siberia, Russia). They demonstrate that their methods offer the possibility to determine the general features of the lithological stratigraphy of mantle columns. They also propose that mantle sections containing large amounts of eclogites have, as a rule, peridotites with hybrid features, and sometimes metasomatites and anatexic pyroxenites. For them, a layered mantle structure is characteristic beneath most kimberlite pipes and is probably related to the periodicity of superplume activity in the Precambrian. Finally, they argue that the largest diamondiferous pipes exhibit the specific structural features of their underlying mantle columns; that is, the presence of dunite horizons, subadiabatic temperature gradients, and large amounts of pyroxenites.

The authors are deeply grateful to N. Arndt, D. Bell, M. Benoit, S. Cebria, G. Chazot, S. Conticelli, J.-Y. Cottin, G. Ceuleneer, L. Dallai, J.-M. Dautria, G. Delpech, G. Dobosi, H. Downes, S. Duggen, S. Foley, C. Garrido, J.-P. Liegois, M. Menzies, A. Montanini, E.-R. Neumann, P. Nimis, G. Ranalli, C. Shaw, C. Szabò, M. Thirlwall, M. Toplis and G. Yaxley for their suggestions and comments, which greatly improved the overall quality of the volume.

References

BECCALUVA, L., BONADIMAN, C., COLTORTI, M., SALVINI, L. & SIENA, F. 2001. Depletion events, nature of metasomatizing agent and timing of enrichment processes in lithospheric mantle xenoliths from the Veneto Volcanic Province. *Journal of Petrology*, **42**, 173–187.

BECCALUVA, L., BIANCHINI, G., BONADIMAN, C., SIENA, F. & VACCARO, C. 2004. Coexisting anorogenic and subduction-related metasomatism in mantle xenoliths from the Betic Cordillera (southern Spain). *Lithos*, **75**, 67–87.

BODINIER, J.-L. 2007. Rejuvenation of lithospheric mantle by thermal erosion and refertilization: case studies in Ronda and Lherz orogenic peridotites. *In*: *EGU General Assembly, Vienna, 15–20 April 2007, Abstracts CD*.

BODINIER, J.-L., MENZIES, M. A., SHIMIZU, N., FREY, F. A. & MCPHERSON, E. 2004. Silicate, hydrous and carbonate metasomatism at Lherz, France: contemporaneous derivatives of silicate melt–harzburgite reaction. *Journal of Petrology*, **45**, 299–320.

BONADIMAN, C., BECCALUVA, L., COLTORTI, M. & SIENA, F. 2005. Kimberlite-like Metasomatism and 'garnet signature' in spinel-peridotite xenoliths from Sal, Cape Verde archipelago: relics of a subcontinental mantle domain within the Atlantic oceanic lithosphere? *Journal of Petrology*, **46**, 2465–2493.

BONADIMAN, C., COLTORTI, M., SIENA, F., O'REILLY, S. Y., GRIFFIN, W. L. & PEARSON, N. J. 2006. Archean to Proterozoic depletion in Cape Verde lithospheric mantle. *In*: *16th Goldschmidt Conf, 27 August–1 September 2006, Abstract CD.*

CHAZOT, G., MENZIES, M. A. & HARTE, B. 1996. Silicate glasses in spinel lherzolites from Yemen: origin and chemical compositions. *Chemical Geology*, **134**, 159–179.

COLTORTI, M., BECCALUVA, L., BONADIMAN, C., SALVINI, L. & SIENA, F. 2000. Glasses in mantle xenoliths as geochemical indicators of metasomatic agents. *Earth and Planetary Science Letters*, **183**, 303–320.

COLTORTI, M., BECCALUVA, L., BONADIMAN, C., FACCINI, B., NTAFLOS, T. & SIENA, F. 2004. Amphibole genesis via metasomatic reaction with clinopyroxene in mantle xenoliths from Victoria Land, Antarctica. *Lithos*, **75**, 115–139.

COLTORTI, M., BONADIMAN, C., FACCINI, B., GRÉGOIRE, M., O'REILLY, S. Y & POWELL, W. 2007*a*. Amphibole from suprasubduction and intraplate litospheric mantle. *Lithos*; doi: 10.1016/j.lithos.2007.05.009.

COLTORTI, M., BONADIMAN, C., FACCINI, B., NTAFLOS, T. & SIENA, F. 2007*b*. Slab melt and intraplate metasomatims in Kapfenstein mantle xenoliths (Styria Basin, Austria). *Lithos*, **94**, 66–89.

CONTICELLI, S., GUARNIERI, L., MATTEI, M. *ET AL.* 2007. Potassic and ultrapotassic magmatism in the Western Mediterranean Basin and insights on its geodynamic significance—1: evidence from Pb, Nd, and Sr isotopes and trace elements data on lamproite, shoshonites and calc-alkalic associations from Tuscany, Murcia–Almeria, Corsica, and Western Alps. *In*: *European Mantle Workshop, Ferrara, 29–31 August 2007, Abstracts CD*.

DAWSON, J. B. 1984. Contrasting types of mantle metasomatism? *In*: KORNPROBST, J. (ed.) *Kimberlites II; the Mantle and Crust–Mantle Relationships*. Elsevier, Amsterdam, 289–294.

DELOULE, E., ALBARÈDE, F. & SHEPPARD, S. M. F. 1991. Hydrogen isotope heterogeneities in the mantle from ion probe analyses of amphiboles from ultramafic rocks. *Earth and Planetary Science Letters*, **105**, 543–553.

DEMÉNY, A., VENNEMANN, T. W., HEGNER, E. *ET AL.* 2004. H, O, Sr, Nd and Pb isotopic evidence for recycled oceanic crust in the Transitional Volcanic Group of Fuerteventura, Canary Islands, Spain. *Chemical Geology*, **205**, 37–54.

DRAPER, D. S. & GREEN, T. H. 1997. *P–T* phase relations of silicic, alkaline, aluminous mantle xenolith glasses under anhydrous and C–O–H fluid-saturated conditions. *Journal of Petrology*, **38**, 1187–1224.

FOULGER, G. R., NATLAND, J. H., PRESNALL, D. C. & ANDERSON, D. L. (eds) 2005. *Plates, Plumes and Paradigms*. Geological Society of America, Special Papers, **388**.

FRANCIS, D. M. 1976. The origin of amphibole in lherzolite xenoliths from Nunivak island, Alaska. *Journal of Petrology*, **17**, 357–378.

GAMBLE, J. A. & KYLE, P. R. 1987. The origin of glass and amphibole in spinel-wehrlite xenoliths from Foster Crater, McMurdo volcanic group, Antarctica. *Journal of Petrology*, **28**, 755–779.

GRANET, M., WILSON, M. & ACHAUER, U. 1995. Imagine a mantle plume beneath the French Massif Central. *Earth and Planetary Science Letters*, **136**, 281–296.

GRÉGOIRE, M., MOINE, B. N., O'REILLY, S. Y., COTTIN, J. Y. & GIRET, A. 2000. Trace element residence and partitioning in mantle xenoliths metasomatized by high alkaline silicate and carbonate-rich melts (Kerguelen Islands, Indian Ocean). *Journal of Petrology*, **41**, 477–509.

GRÉGOIRE, M., MCINNES, B. I. A. & O'REILLY, S. Y. 2001. Hydrous metasomatism of oceanic sub-arc mantle, Lihir, Papua New Guinea, Part 2. Trace element characteristics of slab-derived fluids. *Lithos*, **59**, 91–108.

HARTE, B. 1983. Mantle peridotites and processes—the kimberlite sample. *In*: HAWKESWORTH, C. J. & NORRY, M. J. (eds) *Continental Basalts and Mantle Xenoliths*. Shiva, Natwich, 46–91.

ISHIMARU, S., ARAI, S., ISHIDA, Y., SHIRASAKA, M. & OKRUGIN, V. M. 2007. Melting and multi-stage metasomatism in the mantle wedge beneath a frontal arc inferred from highly depleted peridotite xenoliths from the Avacha volcano, southern Kamchatka. *Journal of Petrology*, **48**, doi:10.1093/petrology/egl065.

KOVÀCS, I., CSONTOS, L., SZABÓ, C., BALI, E., FALUS, G., BENEDEK, K. & ZAJACZ, Z. 2007. Paleogene–early Miocene igneous rocks and geodynamics of the Alpine–Carpathian–Pannonian–Dinaric region: An integrated approach. *In*: BECCALUVA, L., BIANCHINI, G. & WILSON, M. (eds) *Cenozoic Volcanism in the Mediterranean Area*. Geological Society of America, Special Papers, **418**, 93–112.

LENOIR, X., GARRIDO, C. J., BODINIER, J.-L. & DAUTRIA, J.-M. 2000. Contrasting lithospheric mantle domains beneath the Massif Central (France) revealed by geochemistry of peridotite xenoliths. *Earth and Planetary Science Letters*, **181**, 359–375.

MCINNES, B. I. A., GRÉGOIRE, M., BINNS, R. A., HERZIG, P. M. & HANNINGTON, M. D. 2001. Hydrous metasomatism of oceanic sub-arc mantle, Lihir, Papua New Guinea: Petrology and geochemistry of fluid-metasomatised mantle wedge xenoliths. *Earth and Planetary Science Letters*, **188**, 169–183.

MENZIES, M. A. 1983. Mantle ultramafic xenoliths in alkaline magmas: evidence for mantle heterogeneity modified by magmatic activity. *In*: HAWKESWORTH, C. J. & NORRY, M. J. (eds) *Continental Basalts and Mantle Xenoliths*. Shiva, Nantwich, 92–110.

MENZIES, M. A. & HAWKESWORTH, C. J. 1987. *Mantle Metasomatism*. Academic Press, London.

MOINE, B. N., GRÉGOIRE, M., O'REILLY, S. Y., SHEPPARD, S. M. F. & COTTIN, J. Y. 2001. High field strength element (HFSE) fractionation in the upper mantle: evidence from amphibole-rich composite mantle xenoliths from the Kerguelen Islands (Indian Ocean). *Journal of Petrology*, **42**, 2145–2167.

NIIDA, K. & GREEN, D. H. 1999. Stability and chemical composition of pargasitic amphibole in MORB

pyrolite under upper mantle conditions. *Contributions to Mineralogy and Petrology*, **135**, 18–40.

O'REILLY, S. Y., ZHANG, M., GRIFFIN, W. L., BEGG, G. & HIRONSKY, J. 2006. Ancient lithosphere domains in ocean basins are key geochemical 'reservoirs'. *In*: *16th Goldschmidt Conference, 27 August–1 September 2006, Melbourne, Australia, Abstracts CD*.

PEARSON, N., O'REILLY, S., GRIFFIN, W., ALARD, O. & BELOUSOVA, E. 2007. Linking crustal and mantle events using *in-situ* U–Pb, Lu–Hf and Re–Os isotope analysis. *In*: *European Mantle Workshop, Ferrara, 29–31 August 2007, Abstracts CD*.

PERINELLI, C., ARMIENTI, P. & DALLAI, L. 2006. Geochemical and O-isotope constraints on the evolution of lithospheric mantle in the Ross Sea rift area (Antarctica). *Contributions to Mineralogy and Petrology*, **151**, 245–266.

PRELEVIĆ, D., FOLEY, S. F. & CVETKOVIĆ, V. 2007. A review of petrogenesis of Mediterranean Tertiary lamproites: a perspective from the Serbian ultrapotassic province. *In*: BECCALUVA, L., BIANCHINI, G. & WILSON, M. (eds) *Cenozoic Volcanism in the Mediterranean Area*. Geological Society of America, Special Papers, **418**, 113–130.

SAPIENZA, G., GRIFFIN, W. L., O'REILLY, S. Y. & MORTEN, L. 2006. Crustal zircons and mantle sulfides: Archean to Triassic events in the lithosphere beneath south-eastern Sicily. *Lithos*, **96**, 503–523.

SMITH, D., RITER, J. C. A. & MERTZMAN, S. A. 1999. Water–rock interactions, orthopyroxene growth, and Si-enrichment in the mantle: evidence in xenoliths from the Colorado Plateau, southwestern United States. *Earth and Planetary Science Letters*, **167**, 45–54.

SOBOLEV, A. V., HOFMANN, A. W., SOBOLEV, S. & NIKOGOSIAN, I. K. 2005. An olivine-free mantle source of Hawaiian shield basalts. *Nature*, **434**, 590–597.

THIRLWALL, M. F., GEE, M. A. M., LOWRY, D., MATTEY, D. P., MURTON, B. J. & TAYLOR, R. N. 2006. Low $\delta^{18}O$ in the Icelandic mantle and its origins: evidence from Reykjanes Ridge and Icelandic lavas. *Geochimica et Cosmochimica Acta*, **70**, 993–1019.

TONARINI, S., D'ORAZIO, M., ARMIENTI, P., INNOCENTI, F. & SCRIBANO, V. 1996. Geochemical features of Eastern Sicily lithosphere as probed by Hyblean xenoliths and lavas. *European Journal of Mineralogy*, **5**, 1153–1174.

WULFF-PEDERSEN, E., NEUMANN, E.-R., VANNUCCI, R., BOTTAZZI, P. & OTTOLINI, L. 1999. Silicic melts produced by reaction between peridotite and infiltrating basaltic melts: ion probe data on glass and minerals in veined xenoliths from La Palma, Canary Islands. *Contributions to Mineralogy and Petrology*, **137**, 59–82.

XU, Y. G. & BODINIER, J.-L. 2004. Contrasting enrichments in high- and low-temperature mantle xenoliths from Nushan, eastern China: results of a single metasomatic event during lithospheric accretion. *Journal of Petrology*, **45**, 321–341.

YAXLEY, G. M., KAMENETSKY, V., GREEN, D. H. & FALLOON, T. J. 1997. Glasses in mantle xenoliths from Western Victoria, Australia, and their relevance to mantle processes. *Earth and Planetary Science Letters*, **148**, 433–446.

The Jurassic Ligurian Tethys, a fossil ultraslow-spreading ocean: the mantle perspective

G. B. PICCARDO

Dipartimento per lo Studio del Territorio e delle sue Risorse, University of Genova, Corso Europa 26, I-16132, Genova, Italy (e-mail: piccardo@dipteris.unige.it)

Abstract: Alpine–Apennine ophiolites derive from the Jurassic Ligurian Tethys oceanic basin formed by lithosphere extension and failure in the pre-Triassic Europe–Adria system. The basin was floored by mantle peridotites and was characterized by along-axis alternation of avolcanic and volcanic segments. Lithosphere extension and thinning caused asthenosphere adiabatic upwelling and decompressional melting. Mid-ocean ridge basalt (MORB)-type melts diffusely percolated through and reacted with the overlying lithospheric peridotites, which were strongly modified, both depleted (harzburgites and dunites) and enriched (plagioclase peridotites), by melt–peridotite interaction and melt refertilization. The stratigraphic–structural features (mantle at the sea floor and alternation of avolcanic and volcanic segments) coupled with petrological features (presence of alkaline melts and strongly heterogeneous, melt-modified peridotites) allow us to interpret *the Ligurian Tethys as a Jurassic analogue of modern ultraslow-spreading oceans*. The Liguria Mode for the inception of an oceanic basin consists of: (1) *the rifting (continental) stage*, dominated by extension of continental lithosphere and tectonic exhumation of lithospheric mantle; (2) *the drifting (transition) stage*, characterized by melt-related processes (i.e. inception of asthenosphere partial melting and MORB melt percolation through the overlying mantle lithosphere); (3) *the spreading (oceanic) stage*, characterized by failure of the continental crust, sea-floor exposure of mantle peridotites and discontinuous MORB extrusion.

The Ligurian Tethys basin separated the Europe and Adria plates during Late Jurassic–Cretaceous times. Opening of the Ligurian Tethys was kinematically related to pre-Jurassic rifting and Late Jurassic spreading in the central Atlantic and was a consequence of the passive extension of the Europe–Adria continental lithosphere (Fig. 1). Segments of the oceanic lithosphere of the Jurassic basin form large ophiolite bodies in the orogenic system of the Western–Central Alps (Platta, Malenco, Pennidic Units, Lanzo, Chenaillet, Erro–Tobbio), the Northern Apennines (Internal and External Liguride Units, Tuscany) and Corsica (Monte Maggiore).

Palinspastic reconstructions suggest that the Ligurian Tethys did not reach the size of modern oceans (Winterer & Bosellini 1981): oceanic accretion in the Ligurian Tethys started in the Middle Jurassic and continued for *c*. 25 Ma. Age data indicate a narrow time span between the end of divergence and the onset of convergence and subduction. In the Alpine realm, plate convergence leading to subduction of the oceanic lithosphere probably started in the Late Cretaceous. The subduction zone had a SW–NE trend, with the Europe plate underthrusting the Adria plate, and it was most probably intracontinental in the northernmost Alpine sector, and progressively intra-oceanic towards the Ligurian sector (Dal Piaz 1993, and references therein).

The Ligurian Tethys was completely closed in the Early Tertiary, when segments of its oceanic lithosphere were emplaced as west-vergent thrust units in the Alps and east-vergent thrust units in the Apennines. Depending on their stratigraphic, structural and metamorphic characteristics, the various ophiolitic sequences of the Western Alps (WA)–Northern Apennines (NA) have been ascribed to different palaeogeographical settings in the Jurassic–Cretaceous Ligurian Tethys (Fig. 2). Accordingly, the Lanzo and Voltri ophiolite massifs of the Western and Ligurian Alps, which bear clear records of eclogite-facies recrystallization and underwent LT–HP subductive evolution were located west of the subduction zone and are considered parts of the Europe plate. The ophiolite-bearing Liguride Units of the Northern Apennines, which escaped subduction and underwent low-grade orogenic metamorphism, were located east of the subduction zone and are considered part of the Adria plate (Piccardo & Vissers 2007, and references therein).

Since the early 1970s it has been recognized that: (1) Ligurian ophiolitic mantle peridotites are, dominantly, rather fertile, cpx-rich lherzolites (e.g. Bezzi & Piccardo 1971; Nicolas & Jackson 1972); (2) both gabbroic intrusive rocks and basaltic volcanites in Ligurian ophiolites have mid-ocean ridge basalt (MORB) affinity (e.g. Beccaluva *et al.* 1980; Serri 1980). The most relevant lithostratigraphic features of these ophiolites is that serpentinized mantle peridotites underlie both basaltic lava flows and oceanic sediments, whereas sheeted dyke

From: COLTORTI, M. & GRÉGOIRE, M. (eds) *Metasomatism in Oceanic and Continental Lithospheric Mantle.* Geological Society, London, Special Publications, **293**, 11–34.
DOI: 10.1144/SP293.2 0305-8719/08/$15.00

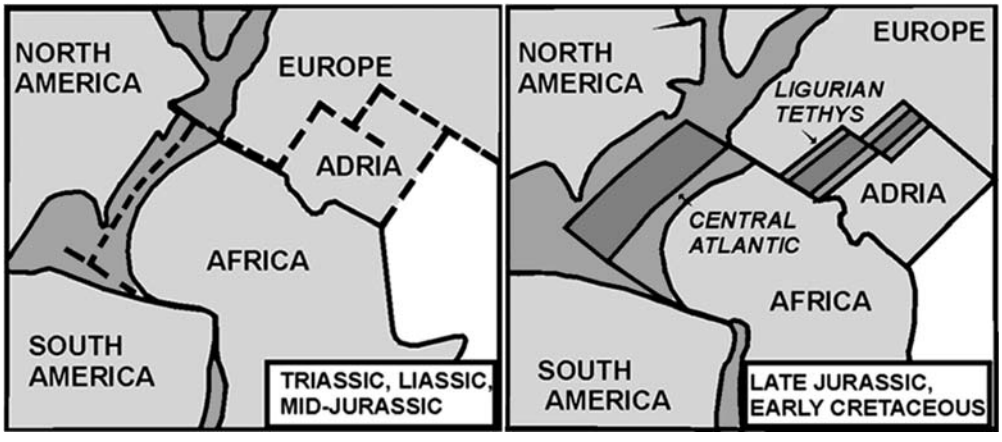

Fig. 1. Mesozoic evolution of central Atlantic and Ligurian Tethys basins, from continental rifting to ocean formation (redrawn and modified after Lemoine *et al.* 1987).

complexes and gabbroic Layer 3 are completely lacking. Kilometre-size gabbroic bodies are solely present as intrusions into mantle rocks. Thus, a general consensus exists on the interpretation that the Ligurian Tethys basin was floored by a peridotite basement (Decandia & Elter 1969; Bezzi & Piccardo 1971; Piccardo 1976; Lemoine *et al.* 1987; Abbate *et al.* 1994).

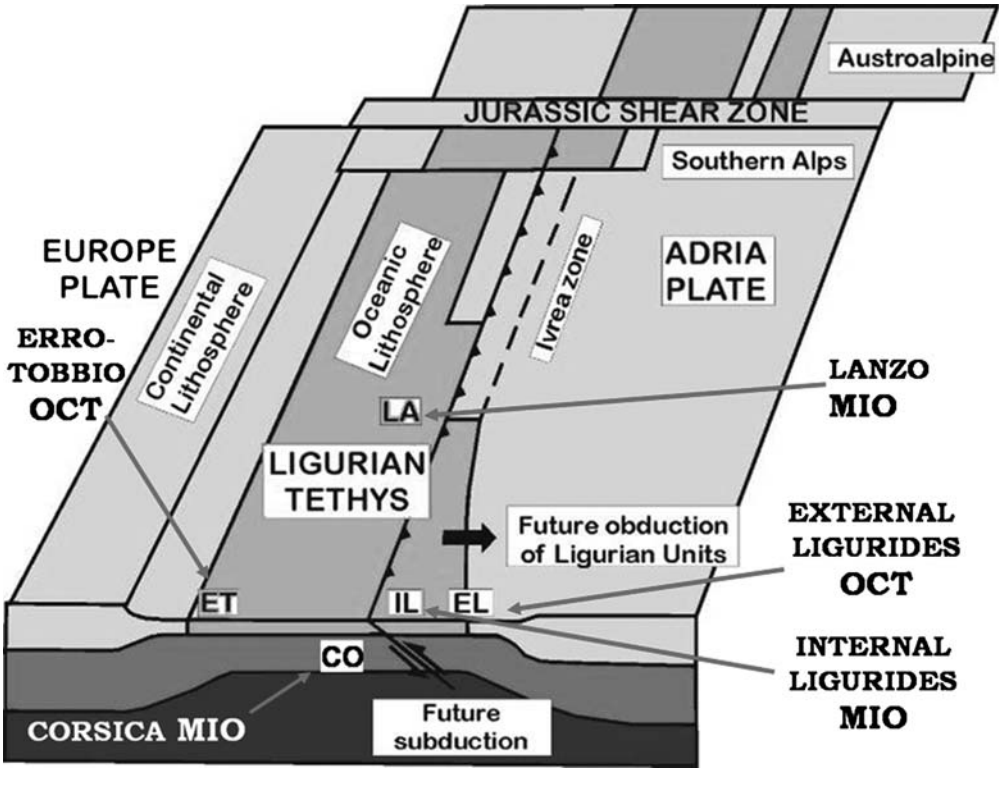

Fig. 2. Generalized palaeogeographical restoration of the Ligurian Tethys, with location of the main ophiolite sequences at ocean–continent transition (OCT) and more internal oceanic (MIO) settings (redrawn and modified after Dal Piaz 1993).

On the basis of stratigraphic and structural features, the Liguride Units have been divided into two main groups: the Internal (IL) and the External (EL) Ligurides. The IL Units have been referred to more internal settings of the basin and consist of serpentinized mantle peridotites, usually covered by ophicarbonate breccias (ophicalcite) and intruded by gabbroic bodies. Ultramafic and gabbroic rocks are locally covered by MORB-type basaltic flows and oceanic sediments (radiolarian cherts, Calpionella Limestones and Palombini Shales) (Abbate *et al.* 1994, and references therein). The EL Units have been referred to more pericontinental settings of the Adria block and two domains have been distinguished (Marroni *et al.* 2002, and references therein): (1) the Western EL Domain, characterized by ophiolite olistoliths (MORB-type basalts and mantle peridotites) in the Basal Complex associated with continental mafic or felsic granulites and granitoids; this domain has been considered as an ocean–continent transition zone; (2) the Eastern EL Domain, characterized by units with Austro-Sudalpine or Insubrian affinity, and lacking ophiolites; this domain has been interpreted as the westernmost zone of the thinned Adria continental margin.

Structural, petrological and geochemical data on mantle peridotites deriving from different settings of the Ligurian Tethys basin have shown their extreme compositional heterogeneity (e.g. Piccardo 1976, 2003; Beccaluva & Piccardo 1978; Ernst & Piccardo 1979; Beccaluva *et al.* 1984; Rampone *et al.* 1995, 1996, 1998; Piccardo *et al.* 2004; 2007*a*; Müntener & Piccardo 2006) and have revealed that they were exhumed from the sub-continental lithospheric mantle to the sea floor of the basin by means of kilometre-scale extensional shear zones (e.g. Drury *et al.* 1990; Vissers *et al.* 1991; Hoogerduijn Strating *et al.* 1993; Montanini *et al.* 2006; Piccardo & Vissers 2007).

This paper aims to: (1) review present knowledge on the most relevant field, structural and compositional characteristics of mantle rocks that were exposed at the sea floor of the Ligurian Tethys basin; (2) document the close relationships between petrology and geodynamic setting of the various peridotite massifs; (3) provide evidence for the close similarity of the ancient Ligurian Tethys and modern ultraslow-spreading oceans; (4) discuss the geodynamic evolution of the Jurassic Ligurian Tethys, on the basis of the structural–compositional evolution recorded in the mantle peridotites. The discussion is based on field, structural, petrological and geochemical data for ophiolitic peridotite massifs from the Western Alps and Northern Apennines in NW Italy, which preserve mantle structures and compositions, although some of them were involved in the Alpine subduction.

Peridotite petrology and geodynamic setting

The considered ophiolitic peridotites derive from both ocean–continent transition (OCT) zones and more internal oceanic (MIO) settings of the ancient Ligurian Tethys basin. Mantle peridotites occur as: (1) kilometre-scale olistoliths, in close association with MORB pillow lava flows and continental crust material within the structural units deriving from the OCT zones of the Adria margin (e.g. the External Ligurides); (2) the basement of MORB lava flows and oceanic sediments in the ophiolite sequences from the MIO settings (e.g. the Internal Ligurides) (Abbate *et al.* 1994; Marroni *et al.* 2002; and references therein). The majority of the NA Internal Liguride Units and of the WA Pennidic Units, which presumably derived from the MIO settings of the basin, consist of serpentinized mantle peridotites, associated with volcanic rocks (or meta-volcanic rocks in the WA; i.e. greenschist or eclogitic metabasites) showing MORB affinity and oceanic sediments (or meta-sediments in the WA; i.e. calc-schists or schistes lustreés). these sequences preserve the original oceanic stratigraphy which indicates the presence of both:

(1) ***avolcanic sequences***, showing direct mantle exposure at the sea floor, without interposed basalts, below the sedimentary cover; (2) ***volcanic sequences***, showing a basaltic cover interposed on top of serpentinized mantle peridotites. In the following, the terms avolcanic and volcanic are used to indicate the absence or presence of volcanic rocks in the oceanic sequence, instead of amagmatic and magmatic.

Recent mantle studies on ophiolitic peridotites from the Ligurian Tethys (e.g. Piccardo *et al.* 2004, and references therein) indicate the abundance of records of melt percolation and impregnation in peridotites even deriving from avolcanic sequences, suggesting that *melt was in the system* even without sea-floor emplacement of volcanic rocks. Accordingly, the terms *amagmatic* and *magmatic* are solely used when referring to previous papers, where these terms were used to indicate avolcanic and volcanic ridge segments in present-day ultraslow-spreading ridges (e.g. Michael *et al.* 2003).

The sub-continental lithospheric peridotites from OCT settings

Mantle peridotites from OCT settings (Platta, Malenco, Northern Lanzo massif, part of Erro–Tobbio (ET) and some bodies in the External Ligurides) are rather fertile lherzolites, showing (1) high contents (10–15% by volume) of clinopyroxene

with relatively high Na and Al contents (Fig. 3a), (2) Ti-pargasite-bearing spinel-facies assemblage, (3) widespread spinel (and garnet) pyroxenite bands and locally phlogopite-hornblendite dykes, and (4) bulk-rock compositions consistent with melting residua after low degrees of partial melting; accordingly, they plot along the melting trends calculated by Niu (1997) (Fig. 3b).

Microstructural–paragenetic features indicate that they were uplifted from garnet-peridotite facies and were equilibrated at spinel-facies conditions (at T in the range 900–1100 °C), on an average continental geotherm (Müntener *et al.* 2004; Piccardo *et al.* 2004, 2007*a*; Montanini *et al.* 2006; Piccardo & Vissers 2007; and references therein).

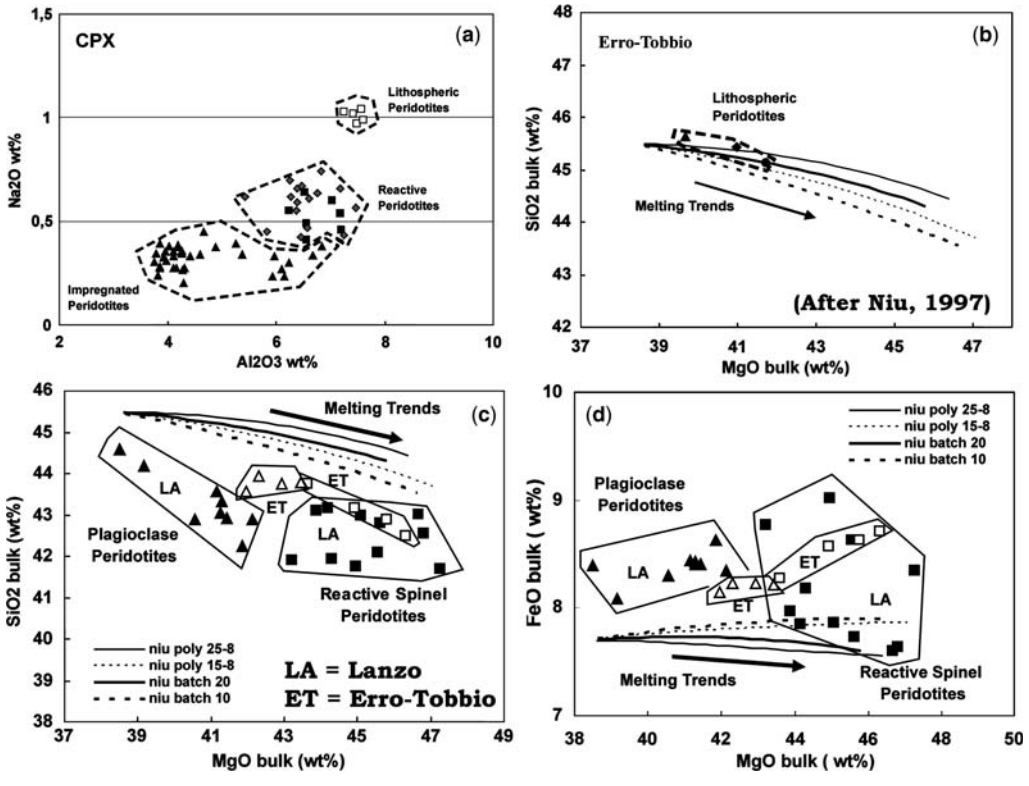

Fig. 3. Bulk-rock characteristics of the various types of mantle peridotites from the Erro–Tobbio and South Lanzo massifs (data from Piccardo & Vissers 2007; Piccardo *et al.* 2007*a*). (**a**) Na_2O v. Al_2O_3 wt% of clinopyroxenes from (1) sub-continental lithospheric peridotites, (2) reactive spinel peridotites and (3) impregnated plagioclase peridotites. Clinopyroxenes in (1) maintain relatively high Na and La contents, whereas Na significantly decreases in (2) and Na + Al strongly decrease in (3), as a result of equilibrium crystallization with plagioclase (data from Piccardo *et al.* 2007*a*). (**b**) Bulk-rock SiO_2 v. MgO wt% contents of sub-continental lithospheric peridotites from the Erro–Tobbio massif. Mantle melting trends calculated by Niu (1997) are also reported. The representative points of the Erro–Tobbio lithospheric peridotite samples plot along the melting trends, suggesting their origin as refractory residua after variable degrees of partial melting (data from Piccardo & Vissers 2007). (**c**) Bulk-rock SiO_2 v. MgO wt% contents of reactive spinel peridotites and impregnated plagioclase peridotites from the Erro–Tobbio and South Lanzo massifs. Melting trends are reported from Niu (1997). Legend: niu poly 25-8 and niu poly 15-8 are trends related to fractional melting in the range of 2.5–0.8 and 1.5–0.8 GPa, respectively; niu batch 10 and niu batch 20 are the trends related to batch melting at constant P (i.e) 1 and 2 GPa, respectively). The representative points of the Erro–Tobbio and South Lanzo peridotites plot at significantly lower SiO_2 contents, at corresponding MgO contents, than melting trends indicating that these rocks underwent significant 'undersaturation', i.e. replacement of mantle pyroxenes by olivine during reactive melt–peridotite interaction (data from Piccardo & Vissers 2007; Piccardo *et al.* 2007*a*). (**d**) Bulk-rock FeO v. MgO wt% contents of reactive spinel peridotites and impregnated plagioclase peridotites from the Erro–Tobbio and South Lanzo massifs. Melting trends are reported from Niu (1997). Legend as in (**c**). The representative points of the Erro–Tobbio and South Lanzo peridotites plot at significantly higher FeO contents, at corresponding MgO contents than melting trends (data from Piccardo & Vissers 2007; Piccardo *et al.* 2007*a*).

Some EL (OCT) lherzolites gave Nd model ages of 1.9–1.7 Ga (assuming a CHUR mantle source) (Rampone *et al.* 1995), which have been considered ages of isolation from the convective mantle and accretion to the thermal lithosphere. On the basis of Nd and Sr isotopic ratios of separated cpx, the northern body of the Lanzo Massif has been considered by Bodinier *et al.* (1991) as a section of sub-continental mantle lithosphere that became isolated from the convective mantle 400–700 Ma ago. These lines of evidence support the interpretation that OCT peridotites derive from the sub-continental lithospheric mantle of the Europe–Adria system and that the different bodies were accreted to the sub-continental lithosphere at different times.

Generally, the complete textural and compositional equilibration at spinel-facies conditions of many OCT peridotite masses has been interpreted as the annealing recrystallization of pristine mantle protoliths from the asthenosphere at conditions compatible with a mean sub-continental geotherm, after isolation from the convective mantle. Accordingly, they have been considered to represent the stage of accretion to the thermal lithosphere and incorporation into the mantle lithosphere (Piccardo 1976; Rampone *et al.* 1995; Piccardo *et al.* 2004; Piccardo & Vissers 2007). For the Erro–Tobbio body, all the petrological features pre-existing the sp-facies annealing recrystallization (i.e. partial melting, melt intrusion (formation of pyroxenite bands) and plastic deformation) have been referred to a previous asthenospheric stage of evolution (Piccardo & Vissers 2007, and references therein).

Sub-continental lithospheric peridotites show composite subsolidus decompressional evolutions under lithospheric thermal conditions (i.e. lithospheric evolution). Sub-continental peridotites from Erro-Tobbio and some External Liguride masses show that sp-facies equilibrium granular structures and pyroxenite banding are strongly deformed along kilometre-scale extensional shear zones, where the syntectonic metamorphic assemblage of the tectonite–mylonite bands varies from spinel- to plagioclase- to amphibole-(chlorite)-peridotite facies assemblages, and was followed by formation of serpentinite mylonites. This has been interpreted (e.g. Drury *et al.* 1990; Vissers *et al.* 1991; Hoogerduijn Strating *et al.* 1993; Piccardo & Vissers 2007) as evidence that the sub-continental lithospheric mantle was progressively exhumed towards the sea floor of the basin during lithospheric extension, and that the extensional shear zones accommodated most of the exhumation and thinning of the sub-continental mantle lithosphere.

Recently, the exhumation history of a garnet pyroxenite-bearing mantle section (hereafter referred to as the Mt. Prinzera body) from the External Liguride, deriving from deep levels (garnet facies) of the sub-continental lithosphere, has been investigated by Montanini *et al.* (2006). The exhumation was accomplished in two separate steps. The first step has been referred to Late Palaeozoic continental extension, whereas the second step (i.e. the low-pressure portion of the exhumation), including formation of plagioclase mylonitic shear zones, was related to the Mesozoic (Triassic to Jurassic) rifting that led to continental breakup (Montanini *et al.* 2006). In fact, Lu–Hf isochrons gave a minimum age of 220 $\pm$ 13 Ma for the development of plagioclase-facies mylonites (Montanini *et al.* 2006), suggesting that the Mt. Prinzera lherzolites underwent subsolidus decompressional evolution starting from Triassic times as a consequence of lithospheric extension. In the Mt. Prinzera peridotite, the anhydrous ductile evolution is overprinted by different episodes of deformation under hydrous conditions: the Sm–Nd isochron on Mg-hornblende-bearing veins gave an age of 186.0 $\pm$ 1.5 Ma, which has been interpreted as a maximum time estimate for the onset of mantle hydration (Montanini *et al.* 2006). The retrograde evolution from plagioclase- to amphibole-facies conditions in the Mt. Prinzera peridotite was almost coeval with the intrusion of MORB gabbros in other sectors of the External Liguride mantle section (Sm–Nd isochron ages of 179 $\pm$ 9 Ma, Tribuzio *et al.* 2004).

Additional informations on the decompressional evolution of the lithospheric mantle in the Ligurian Tethys realm derives from the Malenco peridotite in the Central Alps (Trommsdorff *et al.* 1993; Müntener & Hermann 2001, and references therein), which was equilibrated at high mantle levels in Late Palaeozoic times. This peridotite underwent decompression, as indicated by the development of hydrated shear zones (tremolite–chlorite peridotite mylonites), starting at about 225 Ma ($^{40}Ar/^{39}Ar$ amphibole age determinations), which has been related to the onset of rifting of the lithosphere leading to continental breakup. Accordingly, extensional evolution in the shallow mantle (i.e. Malenco) was almost coeval with extension and thinning in the deeper spinel-facies lithospheric mantle (i.e. Mt. Prinzera).

On the basis of available data on the OCT peridotites, it can be speculated that in pre-Triassic times the different mantle sections were at different levels (i.e. P–T conditions) in the sub-continental lithospheric mantle of the Europe–Adria realm, but they underwent decompressional exhumation together starting from Middle to Late Triassic times, as a consequence of lithospheric extension.

The heterogeneous peridotites from MIO settings

The peridotites from MIO settings show extreme compositional heterogeneity, varying from fertile

spinel lherzolites to depleted spinel harzburgites and dunites to plagioclase-enriched peridotites (Piccardo *et al.* 2004). Fertile spinel lherzolites show structural and compositional features similar to those of OCT peridotites, whereas the majority of mantle peridotites (i.e. depleted spinel harzburgites–dunites and plagioclase-enriched peridotites) have structural and compositional characteristics suggesting melt–peridotite interaction processes (Piccardo *et al.* 2004, 2007*a*; Piccardo & Vissers 2007, and references therein).

The different rock-types show clear mutual relationships in the field: pristine fertile spinel lherzolites, still preserved in places as decametre- to hectometre-sized remnants, are transformed to granular rocks recording melt–peridotite interaction processes. These 'reacted' peridotites retain widespread textural–compositional relics of the lithospheric protoliths (i.e. phantoms of pyroxenite banding, where pyroxenes are corroded and replaced by new olivine, sp trains left after dissolution of pyroxenes of pre-existing pyroxenite bands, opx + sp clusters recording spinel-facies breakdown of precursor garnet, etc.) (see Piccardo *et al.* 2004, 2007*a*; Piccardo & Vissers 2007, and references therein).

Some Internal Liguride peridotites gave a Nd model age of about 275 Ma (Rampone *et al.* 1996), which has been interpreted as the age of Permian partial melting and accretion to the thermal lithosphere. Comparable Nd model ages have been obtained from the Platta peridotites in the Central Alps (Müntener *et al.* 2004). These peridotites are considered as representing mantle sections that were partially melted during Permian extension-related mantle melting and magma production in the Alpine realm (e.g. Dal Piaz 1993, and references therein) and were accreted to the thermal lithosphere prior to and independently from the Jurassic evolution. IL MORB gabbroic intrusive rocks yielded Sm–Nd isochron ages of 164 Ma. The Nd isotope composition recalculated to 164 Ma for IL gabbroic and peridotitic rocks give $\varepsilon_{Nd} = 8.6$ and $\varepsilon_{Nd} = 11.9–14.8$, respectively; this isotopic contrast has been interpreted by Rampone *et al.* (1998) as evidence of the lack of a genetic crust–mantle link between IL residual mantle and IL MORB magmatism. Tribuzio *et al.* (2004) have recently argued against the geochronological meaning of Nd model ages provided by these MIO peridotites on the basis of close isotopic similarities to abyssal peridotites from modern oceans (Salter & Dick 2002).

Geochronological data on melt percolation in MIO peridotites are available for some Monte Maggiore (Corsica) impregnated plagioclase peridotites (Rampone & Piccardo 2003) which gave Sm–Nd cpx–plg isochron ages of 155 ± 6 Ma. Some plagioclase peridotites from the Mt. Nero body of the External Liguride units yielded Sm–Nd cpx–plg isochron ages of $(163–165) \pm 20$ Ma that have been interpreted by Rampone *et al.* (1995) to date the exhumation of the External Liguride mantle to plagioclase-facies conditions. Field and microstructural–geochemical features show that the Mt. Nero peridotites are plagioclase-enriched impregnated peridotites (Müntener & Piccardo 2003; Piccardo *et al.* 2004, 2006; Poggi *et al.* 2005) formed by melt–peridotite interaction. It is thus plausible, as recently proposed by Montanini *et al.* (2006), that the ages reported by Rampone *et al.* (1995) record a stage of MORB melt – peridotite interaction and impregnation in the External Liguride mantle.

On the basis of these data, it can be speculated that MORB melt percolation and impregnation in MIO peridotites occurred in Jurassic times.

Melt interaction processes in MIO peridotites

Pristine spinel lherzolite protoliths (sub-continental lithospheric spinel peridotites) are transformed to different types of granular rocks, both spinel and plagioclase peridotites, which show structural and compositional features suggesting melt–peridotite interaction. These 'modified' peridotites cropping out in MIO settings are hereafter referred to as *reactive*, *impregnated* and *replacive peridotites*, on the basis of their field, structural and compositional features (see below).

Field observations indicate that (Piccardo *et al.* 2004, 2006, 2007*a*): (1) pristine sub-continental spinel peridotites are transformed to reactive depleted spinel peridotites (harzburgites and dunites); (2) subcontinental and reactive spinel peridotites are transformed to impregnated plagioclase peridotites; (3) impregnated plagioclase peridotites are cut by and replaced by spinel peridotites (harzburgites and dunites).

Bulk-rock compositions of reactive and impregnated peridotites from South Lanzo and Erro–Tobbio indicate that they are commonly characterized by significant lower SiO_2, and higher FeO, than refractory residua calculated by Niu (1997), at similar MgO contents (Fig. 3c and d). Accordingly, neither reactive nor impregnated peridotites correspond to refractory residua after any kind of partial melting, as modelled by Niu (1997).

Reactive spinel peridotites. These crop out in kilometre-scale areas and usually have granular textures and variable grain size. They consist of two main rock-types: (1) coarse granular, clinopyroxene-bearing spinel harzburgites which replace the pristine foliated sub-continental spinel

peridotites; (2) granular, orthopyroxene-bearing spinel dunites which cut, in the form of metre-wide bands and decametre-wide bodies, the former coarse granular spinel harzburgites.

Spinel harzburgites show peculiar microstructures: (1) unstrained olivine coronas partly replacing corroded, deformed and exsolved pyroxene porphyroclasts; these are indicative of pyroxene-dissolving- and olivine-forming processes caused by peridotite interaction with diffusely percolating pyroxene (−silica)-undersaturated melts of deeper origin; (2) interstitial formation of new pyroxenes; this is indicative of incipient crystallization of the percolating melts which attained pyroxene(−silica) saturation during the reactive percolation.

Reactive spinel peridotites are strongly depleted in pyroxenes and enriched in olivine. They have highly variable clinopyroxene (from 1 to 12%), significantly low orthopyroxene (<15%) and high olivine (up to 92%) modal contents. They show a significant decoupling between bulk and mineral major and trace element compositions. According to their bulk-rock MgO contents, they should correspond to refractory residua after 15–25% of partial melting of a fertile mantle source (according to modelling of Niu 1997), whereas clinopyroxene rare earth element (REE) contents and patterns indicate that the equilibrium melts were MORB-type melt increments formed by low degrees (1–5%) of fractional melting of spinel-facies depleted mantle (DM) asthenospheric sources. This decoupling indicates that partial melting was not the process responsible for their formation (Piccardo & Vissers 2007; Piccardo *et al.* 2007*a*).

In the Erro–Tobbio Massif, clinopyroxenes from reactive peridotites showing highly variable clinopyroxene modal contents (1–12%) have closely similar trace element contents (Fig. 4a); this suggests that the different samples were variably depleted in clinopyroxene by melt reactive percolation but were equilibrated with the same percolating melt. Model calculations indicate that the percolating melt was closely similar to a single melt increment produced by 4% fractional melting of a spinel-facies depleted MORB mantle (DMM) asthenospheric source (Fig. 4b).

In the Lanzo Massif, clinopyroxenes from reactive peridotites show strongly variable trace element contents and REE patterns (Fig. 4c). In some cases (e.g. sample LAS3), they show REE patterns closely similar to those of clinopyroxenes equilibrated with a single melt increment produced by 5% fractional melting of a spinel-facies DMM asthenospheric source. In one case (sample LAF17), they show strongly humped REE patterns with significant light REE (LREE) and heavy REE (HREE) fractionations, with a maximum at Eu (at about $10 \times$ C1); model calculations suggest that the percolating melt was closely similar to a single melt increment produced by 5% fractional melting of a garnet-facies DMM asthenospheric source (Fig. 4e). In other cases, they show depleted sinusoidal REE patterns, which are indicative of the presence of transient geochemical gradients in the equilibrium melts during melt–peridotite interaction (see Piccardo *et al.* 2007*a*, for a more detailed discussion).

Structural and compositional features of these peridotites preclude their interpretation as refractory residua after partial melting and indicate that they were formed by melt–peridotite interaction processes. The trace element composition of their clinopyroxenes documents both (1) the presence of significant chemical exchanges between the migrating melts and the ambient peridotite during diffuse and reactive porous flow melt percolation, and (2) the nature of the percolating melts, corresponding to MORB-type melt increments formed by rather low degrees (1–5%) of fractional melting of (garnet)–spinel-facies DM asthenospheric mantle sources.

Impregnated plagioclase peridotites. These rocks crop out over kilometre-scale areas and form at the expense of both lithospheric and reactive spinel peridotites. In the field their most distinctive feature is the significant enrichment of plagioclase, which frequently reaches 15% by volume. They are composed of a deformed and corroded spinel-facies mantle assemblage (the mantle porphyroclasts) and an unstrained interstitial igneous assemblage of plagioclase and pyroxenes. Characteristic microstructures are the replacement of mantle olivine by orthopyroxene and, in some cases, of clinopyroxenes by orthopyroxene + plagioclase aggregates, and the formation of plagioclase and pyroxenes as single crystals or millimetre-sized gabbroic aggregates. These microstructures suggest that pristine spinel peridotite underwent interaction with and interstitial crystallization of percolating melts (Piccardo *et al.* 2004, 2007*a;* Piccardo & Vissers 2007).

Accordingly, plagioclase peridotites are hybrid rocks representing mixtures of mantle peridotites plus variable percentages of melt-derived microgabbroic material. Their bulk-rock compositions are enriched in fusible components and are more 'fertile' than sp-peridotites, sometimes exceeding primitive mantle (PM) estimates (by Hofmann 1988) (Fig. 5a). The bulk-rock composition of the plagioclase peridotites defines a trend of increasing SiO_2, Al_2O_3 and CaO and decreasing MgO, which starts from the field delimited by the reactive spinel peridotite compositions and points to 'gabbroic' samples (i.e. former peridotites with plagioclase contents higher than 10% by

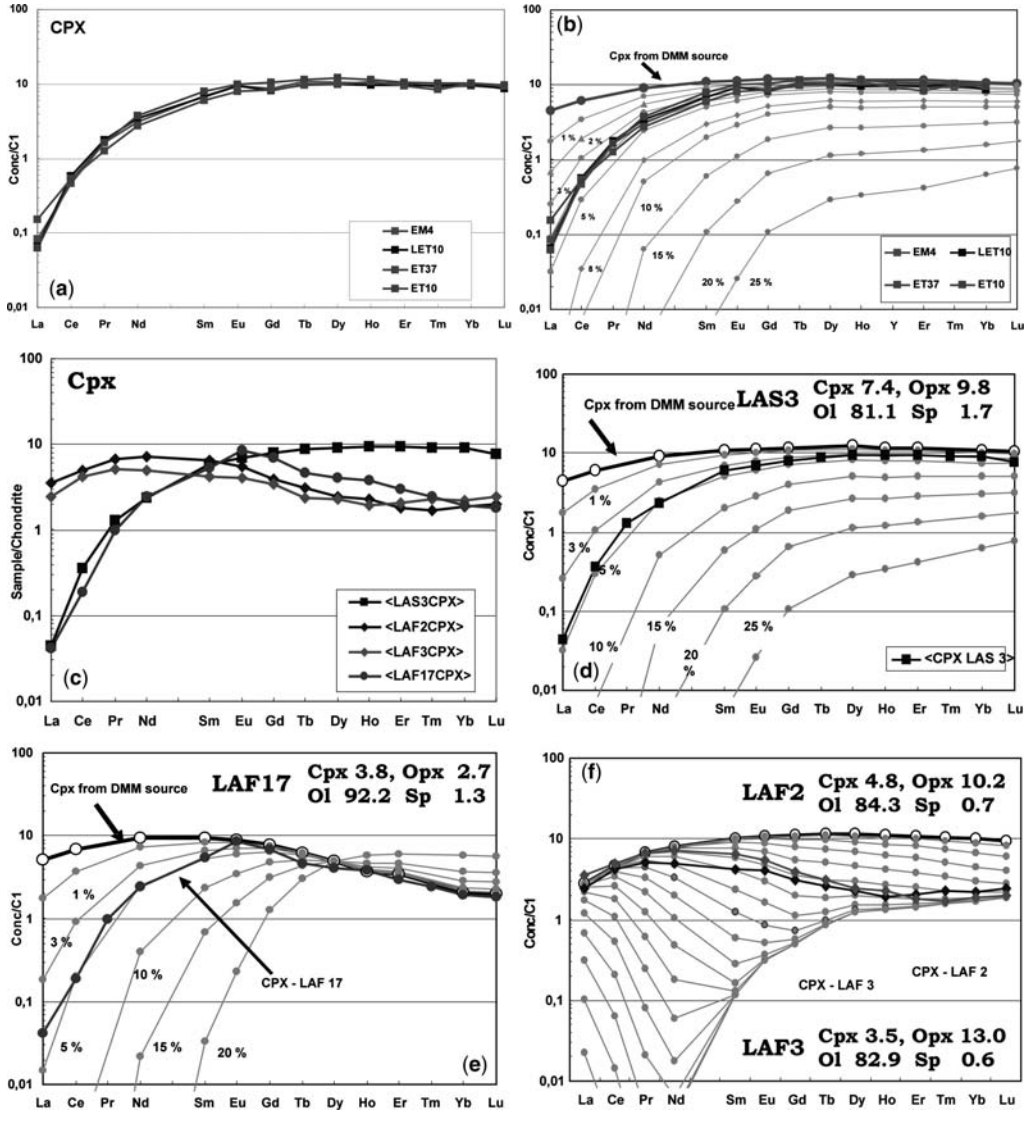

Fig. 4. REE patterns of clinopyroxenes from Erro–Tobbio and South Lanzo reactive spinel peridotites (data from Piccardo & Vissers 2007; Piccardo *et al.* 2007*a*). (**a**) REE patterns of clinopyroxenes from Erro–Tobbio reactive spinel peridotites. (**b**) The REE patterns of clinopyroxenes from Erro–Tobbio reactive spinel peridotites are plotted together with REE patterns of clinopyroxenes obtained after 1 – 25% of fractional melting following the melting model of Johnson *et al*. (1990), using cpx/liquid K_D of Hart & Dunn (1993), starting from the mantle source of Ionov *et al.* (2002). REE patterns of Erro–Tobbio clinopyroxenes are almost coincident with REE patterns of clinopyroxenes in equilibrium with liquids after about 4% fractional melting of a spinel-facies asthenospheric mantle source (data from Piccardo & Vissers 2007). (**c**) REE patterns of clinopyroxenes from South Lanzo reactive spinel peridotites. (Note the strong heterogeneity of the spectra) (data from Piccardo *et al.* 2007*a*). (**d**) The REE patterns of average clinopyroxene of sample LAS3 from South Lanzo reactive spinel peridotites (note the strongly pyroxene-depleted, olivine-enriched modal composition) are plotted together with REE patterns of clinopyroxenes obtained after 1 – 25% of fractional melting following the melting model of Johnson (1990), using cpx/liquid K_D of Hart & Dunn (1993), starting from the mantle source of Ionov *et al.* (2002). REE patterns of these clinopyroxenes are almost coincident with REE patterns of clinopyroxenes in equilibrium with liquids after about 5% fractional melting of a spinel-facies asthenospheric mantle source (data from Piccardo *et al.* 2007*a*). (**e**) The REE patterns of average clinopyroxene of sample LAF17 from South Lanzo reactive spinel peridotites (note the strongly pyroxene-depleted, olivine-enriched modal composition) are plotted together with the REE patterns

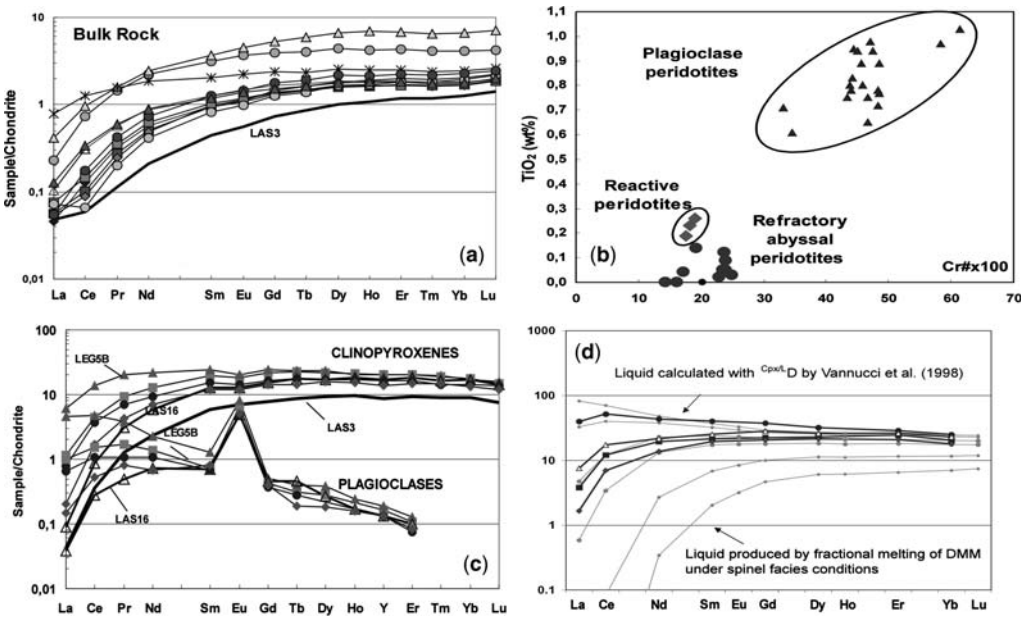

Fig. 5. Bulk-rock and mineral major and trace element compositions of impregnated plagioclase peridotites from the South Lanzo massif (data from Piccardo *et al.* 2007*a*). (**a**) Bulk-rock REE patterns. The bulk-rock REE pattern of the reactive spinel peridotite LAS3 is also reported for comparison. A significant LREE fractionation is always present, and HREE reach concentrations higher (>3 times C1) than the estimated composition of primitive mantle. (**b**) TiO_2 v. Cr-number in spinels from impregnated plagioclase peridotites from the South Lanzo massif. Compositions of oceanic refractory peridotites are also reported for comparison (data from Piccardo *et al.* 2007*a*). (Note the relatively very high Ti contents of spinels, closely similar to Ti in spinel in equilibrium with MORB (Dick & Bullen 1984).) (**c**) C1 normalized REE patterns of clinopyroxenes and plagioclase from the impregnated plagioclase peridotites of South Lanzo. Note that clinopyroxenes and plagioclase show strong variation of LREE fractionation and, particularly plagioclase REE patterns, show variation from negative to positive LREE fractionation. The C1 normalized REE pattern of clinopyroxene from the reactive spinel harzburgite LAS3 is also reported for comparison. Note that clinopyroxenes from the impregnated plagioclase peridotites are significantly enriched in REE. (**d**) The liquids in equilibrium with the clinopyroxenes from representative impregnated plagioclase harzburgites have been calculated using the $^{cpx/liquid}D$ proposed by Vannucci *et al.* (1998) for silica-saturated basaltic system. Their calculated REE patterns are plotted against the REE patterns of fractional melting liquids calculated by a fractional melting model of a spine-facies DM mantle source. It can be inferred that impregnated peridotites were percolated by fractional melt increments produced by 1–6% fractional melting of a spinel-facies DM mantle source (see Piccardo *et al.* 1997*a*, for more discussion).

volume). Spinels in plagioclase peridotites have high Ti contents (TiO_2 in the range 0.6–1.0 wt%), similar to spinels in equilibrium with MORB (Dick & Bullen 1984) (Fig. 5b). Moreover, their mantle and magmatic pyroxenes are enriched in REE, high field strength elements (HFSE) and Sc with respect to those of the reactive spinel peridotites and to those in equilibrium with MORB (Fig. 5c).

Fig. 4. (*Continued*) of garnet-facies residual clinopyroxenes calculated using the garnet peridotite melt modes from Walter (1998). REE patterns of these clinopyroxenes are almost coincident with REE patterns of clinopyroxenes in equilibrium with liquids after about 5% fractional melting of a garnet-facies asthenospheric mantle source (data from Piccardo *et al.* 2007*a*). (**f**) The REE patterns of average clinopyroxenes of samples LAF2 and LAF3 from South Lanzo reactive spinel peridotites (note the strongly pyroxene-depleted, olivine-enriched modal compositions) are plotted together with REE abundance in clinopyroxenes modelled by numerical simulation (Plate Model, Vernieéres *et al.* 1997) of reactive porous flow of melts into a depleted peridotite (see Piccardo *et al.* 2007*a*, for a more detailed discussion of the modelling). The simulation results show that the REE fractionation of clinopyroxenes LAF2 and LAF3 can be result from transient geochemical gradients induced by the reactive migration of melt increments by 0.5% fractional melting of a spinel-facies DMM source (data from Piccardo *et al.* 2007*a*).

Bulk-rock major element composition and mineral chemistry are not strictly correlated as would be expected in the case of simple partial melting. Conversely, a significant correlation is apparent between the major and trace elements of plagioclase and interstitial clinopyroxene (e.g. the striking correlation between REE fractionation and albite content in plagioclase) (Fig. 5c). Therefore, it has been inferred (Piccardo *et al.* 2007*a*) that the composition of these rocks was fully reset by the percolating melts. REE patterns and fractionation of melts calculated to be in equilibrium with the magmatic clinopyroxenes, using K_d appropriate for silica-saturated systems (Vannucci *et al.* 1998), indicate that percolating liquids were single melt increments with MORB affinity generated by 1–6% fractional melting of spinel-facies DM asthenospheric sources (Piccardo *et al.* 2004, 2007*a*; Piccardo & Vissers 2007).

The widespread replacement of kinked mantle olivine by newly formed orthopyroxene and the abundant orthopyroxene crystallization in gabbro–noritic patches indicate that the parental melts of the plagioclase-bearing mineral assemblages were silica-saturated. Silica-saturated melts have been interpreted as either the last melt fractions produced by low-pressure partial melting of depleted peridotites underneath mid-ocean ridges (e.g. Dijkstra *et al.* 2001, 2003) or the product of progressive pyroxenes(–silica) saturation of melts percolating through mantle peridotite by reactive porous flow as a result of mineralogical reactions involving the assimilation of mantle pyroxenes and segregation of olivine (Kelemen *et al.* 1995*a*, *b*). Several lines of evidence (see Piccardo *et al.* 2007*a*, for a more detailed discussion) suggest that the silica-saturated composition of melts that formed the impregnated plagioclase peridotites was attained during open-system, reactive (pyroxene-dissolving, olivine-precipitating) migration through the lithospheric mantle.

The presence of plagioclase as isolated crystals and within the gabbroic mineral aggregates, and as a product of mineral reactions, suggests that melt percolation and melt refertilization occurred at plagioclase-facies conditions. Melt impregnation at plagioclase-facies conditions developed on pristine spinel peridotites that underwent melt reactive percolation at relatively deeper, sp-facies conditions. This indicates that lithospheric mantle underwent multiple episodes of melt–peridotite interactions during progressive exhumation towards shallow levels in the lithosphere.

Replacive spinel peridotites. These rocks are mostly spinel harzburgites and dunites and crop out in the form of decimetre - to metre-scale bands concordant with the main foliation of the host plagioclase peridotite, and decametre-scale bodies of dunites discordant to the plagioclase peridotite foliation and to the concordant bands of replacive spinel peridotites (Piccardo *et al.* 2004). Replacive spinel harzburgites show microstructures that indicate early pyroxene-dissolving, olivine-forming melt–rock interaction processes. In the South Lanzo body, replacive harzburgites and dunites sporadically contain single crystals or veins of new clinopyroxene, up to a few centimetres in diameter and poikilitic on olivine. Centimetre-scale euhedral clinopyroxenes and fuzzy pyroxenite and gabbroic dykelets occasionally occur in the centre of the dunite bands. Moreover, thin, centimetre-scale gabbroic or gabbro–noritic dykelets cut across dunites and the surrounding peridotites. Peridotites are cut by metre-wide gabbroic dykes, displaying sharp contacts and chilled margins to the host peridotite (Piccardo *et al.* 2007*a*).

Spinels in replacive dunites have exceptionally high Ti contents (TiO_2 up to >1.0 wt%), similar to spinels from MORB (Dick & Bullen 1984). Interstitial and megacrystic clinopyroxenes in South Lanzo replacive harzburgites and dunites have variable compositions, showing both depleted to strongly depleted incompatible trace element composition and MORB *sensu lato* signatures.

It has been inferred that focused melt–peridotite interaction within the harzburgite–dunite channels was capable of producing 'refractory' harzburgitic peridotites with 'depleted' geochemical compositions (see Piccardo *et al.* 2007*a*, for a more detailed discussion). The extensive modification of the ascending melt recorded by 'depleted' replacive harzburgites can be reasonably ascribed to the early stages of 'opening' of the migration pathways and/or of lateral 'growth' of the channels. It has been argued by Piccardo *et al.* (2007*a*) that, within such bands, channelled melt migration had a transient character, too short to allow the attainment of chemical equilibration with the injected melt of MORB *sensu lato* composition (see next section).

The clinopyroxene composition of both concordant and discordant replacive spinel harzburgites and dunites from South Lanzo indicates that they attained chemical equilibrium with liquids varying in composition from normal MORB (N-MORB) to slightly large ion lithophile element (LILE)-enriched MORB (Piccardo *et al.* 2007*a*) (Fig. 6a). This evidence indicates that replacive channels were exploited by MORB *sensu lato* melts to migrate toward shallow crustal levels. Relatively LILE-enriched clinopyroxene compositions ubiquitously characterize the later clinopyroxene megacrysts forming veins in both concordant and discordant dunite bodies, as well as the cumulus clinopyroxenes in gabbroic dykelets and dykes. The systematic increase in LILE concentration, documented in the

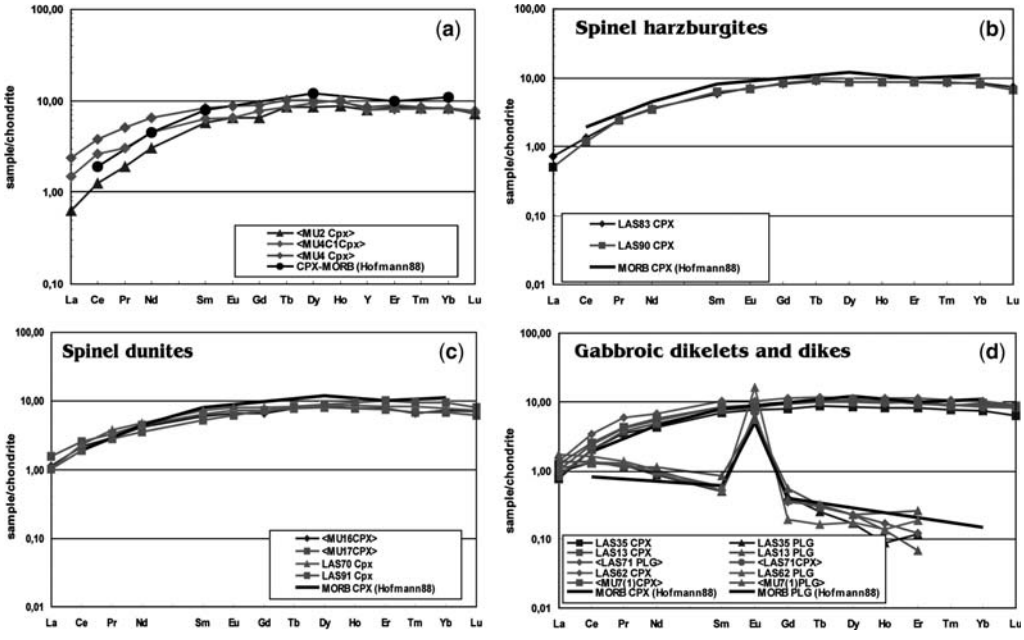

Fig. 6. REE patterns of clinopyroxenes and plagioclase in replacive spinel harzburgites and dunites, and gabbroic dykelets and dykes, from the South Lanzo massif (data from Piccardo *et al.* 2007*a*). REE patterns are closely similar to slightly LREE-enriched with respect to corresponding mineral in equilibrium with MORB melts. Trends of REE patterns of clinopyroxene and plagioclase calculated in equilibrium with MORB of Hofmann (1988) are reported for comparison.

clinopyroxenes from the earlier concordant harzburgite and dunite bands to the later clinopyroxene megacrysts in dunites, and clinopyroxene in gabbro dykelets and dykes (Fig. 6d), is consistent with the change of the geochemical affinity of the ascending asthenospheric melts, from N-MORB to transitional MORB (T-MORB).

Available data from the Mt. Nero (EL) and Lanzo massifs suggest that replacive harzburgite channels were, in places, preferential paths for upward migration of melts showing alkaline affinity (Piccardo *et al.* 2006, 2007*b*). The Mt. Nero impregnated plagioclase peridotites are locally replaced by metre-wide bands of clinopyroxene-bearing spinel harzburgites (Piccardo *et al.* 2006). Interstitial clinopyroxenes in refractory harzburgites crystallized from the melts migrating within these replacive channels. They have significantly high LREE contents and show convex-upward REE patterns, with a maximum in the region Sm–Eu, at more than 10 times C1, and significant negative HREE (Sm_N/Yb_N *c.* 2; Yb_N *c.* 5.4) and LREE fractionations (La_N/Sm_N in the range 0.33–0.40; $La_N = 3.5–4.4$) (Fig. 7a). Moreover, they, have relatively high $HFSE^{(4+,5+)}$, except for Ti. Calculated equilibrium liquids show significantly LREE/HREE fractionated REE patterns ($La_N/Yb_N = 5–6.5$), and high LREE concentrations ($La_N = 65–80$) (Fig. 7b). These trace element concentrations and fractionations are consistent with liquids with alkaline affinity. In the North Lanzo massif (Piccardo *et al.* 2007*b*) metre- to decametre-wide bands of coarse granular, clinopyroxene-bearing replacive harzburgites cut through impregnated plagioclase-rich lherzolites. Interstitial magmatic clinopyroxenes from the replacive harzburgites show significantly high LREE contents and negative LREE–HREE fractionation (Fig. 7c). Calculated equilibrium liquids show marked LREE/HREE fractionation ($La_N/Yb_N > 11$), and high LREE concentrations (La_N up to 140); REE patterns of the equilibrium liquids are closely similar to those of alkaline basalts (Fig. 7d).

Bodinier *et al.* (1991) studied a refractory cpx-poor spinel lherzolite (sample L212) forming 'a poorly defined layer of unknown extension within the plagioclase lherzolites' of the Central Lanzo body, which has been interpreted by Piccardo *et al.* (2007*a*) as a late spinel harzburgite band replacing pre-existing MORB-impregnated plagioclase peridotites. Cpx from sample L212 'has a similar LREE contents to the plagioclase lherzolites from the same area, but shows an increasing depletion towards the HREE (Ce_N/Yb_N higher than unity)' (Bodinier *et al.* 1991) (Fig. 7E).

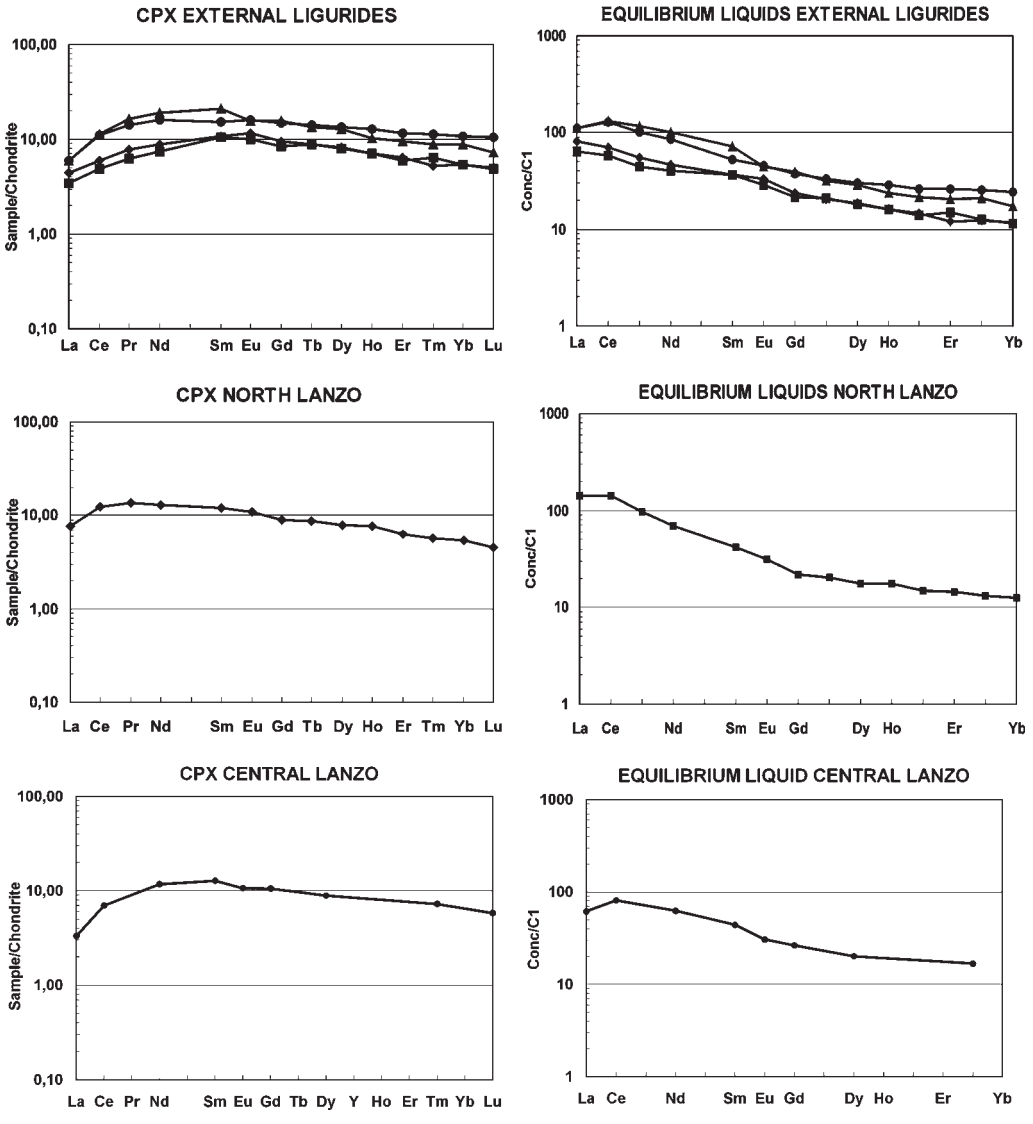

Fig. 7. REE patterns of clinopyroxenes from Mt. Nero and North Lanzo replacive spinel harzburgites (data from Piccardo *et al.* 2006, 2007*b*), and Central Lanzo refractory harzburgites (data from Bodinier *et al.* 1991) and the calculated equilibrium liquids (clinopyroxene/liquid partition coefficients from Ionov *et al.* 2002). (**a, b**) Interstitial magmatic clinopyroxenes in Mt. Nero harzburgite channels show high LREE contents and convex-upward REE patterns, with a maximum in the region Sm–Eu, at more than 10 times C1, and negative HREE (Sm_N/Yb_N *c*. 2; Yb_N *c*. 5.4) and LREE fractionations (La_N/Sm_N in the range 0.33–0.40; $La_N = 3.5–4.4$). Calculated equilibrium liquids have significant LREE/HREE fractionation ($La_N/Yb_N = 5–6.5$), and high LREE concentrations ($La_N = 65–80$). (**c, d**) Interstitial magmatic clinopyroxene in the North Lanzo replacive harzburgite has, similarly, significantly high LREE contents and negative LREE–HREE fractionation Calculated equilibrium liquid shows marked LREE/HREE fractionation ($La_N/Yb_N > 11$), and high LREE concentrations (La_N up to 140), closely similar to those of alkaline basalts. (**e, f**) Clinopyroxene from the Central Lanzo refractory cpx-poor spinel lherzolite L212 of Bodinier *et al.* (1991) and calculated equilibrium liquid.

According to Bodinier *et al.* (1991), These refractory peridotites have undergone a single-stage process that is responsible for both their residua character and their high LREE/HREE ratio, and that might be the percolation of melts resulting from an olivine-forming reaction between the percolating magma and the host peridotites. L212 clinopyroxene has significantly high $^{87}Sr/^{86}Sr$ ratios (>0.70453) and low $^{143}Nd/^{144}Nd$ ratios (<0.512796) ($\varepsilon_{Sr} = +3.4$, $\varepsilon_{Nd} = +0.9$) and plots close to CHUR values: it is characterized by much higher Sr and lower Nd isotopic ratios than the host plagioclase peridotites. This indicates, according to Bodinier *et al.* (1991), that the host refractory peridotite has been percolated by magma unrelated to the massif and that this magma was clearly of deeper asthenospheric origin showing 'plume-type' signature. The calculated equilibrium liquid shows an REE pattern closely similar to that of the alkaline liquids in equilibrium with clinopyroxenes from the North Lanzo replacive spinel harzburgite bands (Fig. 7f).

Accordingly, melts with alkaline affinity were present during the evolution of the Ligurian Tethys system. Field evidence suggests that these melts did not ascend *preceding* MORB melt percolation but migrated upwards during the last stages of focused melt migration *following* diffuse melt percolation and impregnation by fractional melts with MORB affinity (Piccardo *et al.* 2006, 2007*b*). It has been suggested (Piccardo *et al.* 2007*c*) that alkaline liquids may have been produced by partial melting of garnet-pyroxenite-bearing lithospheric mantle sections that were tectonically detached by delamination and founded in the upwelling melting asthenosphere during lithosphere extension and continental rifting. In this scenario, MORB melts formed by melting of DM asthenosphere may have migrated earlier than the alkaline melts formed by melting garnet pyroxenites. This process can be responsible for both the formation of alkaline liquids (Piccardo *et al.* 2006, 2007*b*) and the garnet signature of the subsequent MORB gabbroic intrusions and basaltic extrusions (Montanini & Tribuzio 2007) (see below).

The oceanic peridotites from MIO settings

Depleted spinel peridotites from the Monte Maggiore (Corsica) massif yielded Sm–Nd model ages of 164 ± 14 Ma; they have been interpreted by Rampone *et al.* (2005) as refractory residua after Jurassic oceanic partial melting. Following this interpretation, these peridotites could represent refractory peridotites that originated during formation of the Jurassic Ligurian Tethys.

Moreover, impregnated plagioclase peridotites and MORB gabbro dykes from the same massif yielded Sm–Nd cpx–plg isochron ages of 155 ± 6 Ma (Rampone & Piccardo 2003) and 162 ± 10 Ma (Rampone *et al.* 2005), respectively. It can be speculated that, at least at Monte Maggiore, asthenosphere partial melting, MORB melt percolation and MORB melt intrusion were closely related and can be referred to the same asthenosphere melting stage during the formation of the Jurassic Ligurian Tethys. According to Rampone *et al.* (2005) the Monte Maggiore peridotite–gabbro association provides evidence that a 'mature' oceanic stage, showing melt–refractory residua relationships between gabbros and peridotites, has been attained in the Jurassic Ligurian Tethys ocean.

Summary

Spinel lherzolites from OCT settings derive from the sub-continental lithospheric mantle of the Europe–Adria system. They were isolated from the convective asthenosphere and accreted to the sub-continental thermal lithosphere starting from Proterozoic times. They underwent subsolidus decompressional evolution, starting from Triassic times, during passive extension of the continental lithosphere of the Europe–Adria system.

The majority of peridotites from MIO settings derive from pristine peridotites from the pre-Triassic sub-continental mantle lithosphere, which were transformed to melt-modified peridotites by interaction with MORB-type melts and were intruded by MORB melts during Jurassic times. In the case of Monte Maggiore (Corsica), depleted spinel peridotites could represent refractory residua after asthenosphere partial melting during the Jurassic ocean formation.

The melt-modified peridotites from MIO settings consist of: (1) *reactive spinel peridotites* formed by interaction of pristine sub-continental lithospheric peridotites with silica-undersaturated MORB-type melt increments; (2) *plagioclase-enriched peridotites* formed by impregnation–refertilization of pristine spinel peridotites by silica-saturated melt increments with MORB affinity, which attained silica saturation during reactive percolation in the lithospheric mantle column prior to reaching the impregnation level; (3) *replacive spinel peridotites* (harzburgites and dunites) formed by focused and reactive migration of aggregated MORB melts. Harzburgite–dunite channels were exploited for shallow-level delivery of aggregate MORB and, more rarely, alkaline liquids.

In the case of Monte Maggiore, MIO refractory peridotites could represent residual mantle after Jurassic asthenosphere partial melting, which

was accreted to the thermal lithosphere during Jurassic times.

Comparison with modern ultraslow-spreading oceans

Where the oceanic stratigraphy is preserved, as for the majority of the Ligurian ophiolite sequences from MIO settings, field and structural evidence indicates that the oceanic settings of provenance were characterized by: (1) mantle exposure at the sea floor; (2) both avolcanic and volcanic segments; (3) the lack of sheeted dyke complexes and gabbroic Layer 3.

In present-day oceanic basins the direct exposure at the sea floor of crust-free mantle lithosphere is more common than previously recognized (Dick *et al*. 1984, 2006; Cannat 1993, 1996; Cannat *et al.* 1997; Bonatti *et al.* 2001; Michael *et al.* 2003): it has been suggested that nearly half of the global mid-ocean ridge system is made of mantle peridotites (Dick *et al*. 2003). Recent investigations of the South-West Indian Ridge and Arctic Ridge have revealed an ultraslow-spreading class of ocean ridge that is characterized by intermittent volcanism and continuous emplacement of mantle to the sea floor over large regions, whereas the spreading rate is lower than *c*. 20 mm a^{-1} (Dick *et al.* 2003, and references or therein).

A distinctive characteristic of ultraslow-spreading ridges (e.g. the Gakkel Ridge and the Lena Trough) is the relative abundance of mildly enriched or even alkaline basalts (Muhe *et al.* 1997; Dick *et al.* 2003; Michael *et al.* 2003; Nauret *et al.* 2005, 2006), enriched in LREE and other incompatible elements and showing alkaline and/or isotopically enriched signatures. Their origin from melting of garnet eclogite or veined mantle has been suggested (e.g. Nauret *et al.* 2004, 2005; Snow *et al.* 2006).

Magmatic rocks from the Ligurian Tethys (gabbros and basalts) are mostly derived from MORB melts. In fact, the trace element compositions of computed liquids in equilibrium with clinopyroxene, $^{87}Sr/^{86}Sr$ and $^{143}Nd/^{144}Nd$ ratios of whole rocks and mineral separates, and initial ε_{Nd} values (8.6–8.7) of Internal Liguride ophiolitic gabbros are consistent with typical MORB compositions (Rampone *et al.* 1998; Tribuzio *et al.* 2004*a*). The basaltic rocks show an overall tholeiitic composition and MORB affinity (Beccaluva *et al.* 1984; Marroni *et al.* 1998; Rampone *et al.* 1998, and references therein), as confirmed by their fairly homogeneous $^{143}Nd/^{144}Nd$ ratios, ranging from 0.51305 to 0.51310 (Rampone *et al.* 1998). Montanini & Tribuzio (2007) found that the Ligurian ophiolitic gabbros and basalts show peculiar trace element fingerprints (i.e., Zr enrichment, relatively high Sm/Yb ratios and anomalous composition of the less radiogenic Nd isotope) indicating a garnet signature which can be explained by low degree melting of a mixed source of spinel peridotite with small amounts of garnet pyroxenite.

Available data from the Lanzo and Mt. Nero massifs indicate that melts showing enriched and even alkaline affinity were present in the Ligurian Tethys. In particular, replacive spinel harzburgite bands cutting and replacing impregnated plagioclase peridotites in North and Central Lanzo and at Mt. Nero have clinopyroxenes showing trace element concentration and REE patterns consistent with clinopyroxenes in equilibrium with liquids with alkaline affinity (Piccardo *et al.* 2006, 2007*b*).

Another characteristic of the ultraslow-spreading ridges is the strong compositional variability of the exposed abyssal peridotites. Concerning, in particular, Gakkel Ridge, Hellebrand *et al.* (2006*a*, *b*) recognized that at the magma-poor region at 3–20°E different domains are characterized by rock types showing large compositional variations: (1) modally fertile lherzolites, showing local heterogeneity (dunites); (2) lherzolites, cpx-poor harzburgites, dunites (depleted and enriched samples within the single dredge); (3) virtually cpx-free harzburgites and dunites. Hellebrand *et al.* (2006) suggested that: (1) this evidence indicates both low degrees of regional partial melting and reactive melt transport; (2) the extreme depletion of cpx-free harzburgites and dunites may be the result of large-scale reaction with percolating melts; (3) the reactive melt transport is superimposed on the near-fractional 'background' melting and must have been restricted to focused melt transport channels and confined infiltration zones. Interestingly, interstitial clinopyroxene in highly depleted harzburgites is LREE enriched: this was explained by Hellebrand *et al.* (2006*a, b*) as a result of diffuse and pervasive percolation of low-degree melts from a garnet peridotite (pyroxenite) source. This is closely similar to some replacive depleted harzburgite bands from the Ligurian Tethys, which contain LREE-enriched to alkaline clinopyroxenes (see above). Plagioclase peridotites are widespread at Gakkel Ridge; von der Handt *et al.* (2006) have recently proposed that plagioclase peridotites on Gakkel Ridge formed by impregnation of transient depleted melts at low pressure. This is closely similar to the impregnated plagioclase peridotites from the Ligurian Tethys (see above). Accordingly, the presence of peridotites both depleted and enriched by melt migration and melt–peridotite interaction is a characteristic feature of ultraslow-spreading ridges.

Recently, Shimizu *et al.* (2006) stressed that geochemical studies of abyssal peridotites show that large local-scale (single-dredge to hand-specimen scales)

variations in isotopic composition, modal abundance and trace element content of clinopyroxene are produced by melt–rock reaction during melt migration in the mantle (e.g. Warren *et al.* 2006) and are distinct characteristics of ultraslow-spreading ridge peridotites. According to Shimizu *et al.* (2006), these geochemical characteristics are useful to identify ancient ultraslow-spreading ridge peridotites among 'orogenic lherzolite massifs'. On the basis of initial Nd and Sr isotopic characteristics, the large variations of modal clinopyroxene and of trace element contents in clinopyroxene over a sampling scale length of 150 m, and the ample evidence for chromatographic melt–rock reaction in the presence of garnet, Shimizu *et al.* (2006) proposed that the Horoman peridotite massif (Hokkaido, Japan) could represent abyssal peridotite beneath the Palaeo-Pacific ridge when its spreading rate was ultraslow.

Recent investigations on ophiolitic peridotites from the Ligurian Tethys have shown the presence and abundance of melt-modified peridotites, with strong compositional heterogeneity on a metre-scale distance, characterized by strong modal variation and trace element contents of clinopyroxene. These variations have been related to the effects of widespread percolation, interaction and impregnation of pristine sub-continental lithospheric peridotites with percolating melts during inception of the Ligurian Tethys basin (Piccardo *et al.* 2004, 2007*a*, and references therein).

Accordingly, stratigraphic–structural features (i.e. mantle at the sea floor and alternation of avolcanic and volcanic segments), coupled with the petrological features of magmas (i.e.the presence of mildly enriched or alkaline melts) and peridotites (i.e. extreme compositional heterogeneity related to melt percolation and melt–peridotite interaction processes) are in favour of the interpretation of the Ligurian Tethys as a Jurassic analogue of modern ultraslow-spreading ridges (Piccardo 2006).

The geodynamic evolution of the Ligurian Tethys basin

The mantle perspective

Ophiolitic peridotites from the Jurassic Ligurian Tethys show records of composite histories of tectonic–metamorphic and melt-related events preceding their exposure at the sea floor of the basin. The extensional evolution of the mantle lithosphere leading to opening of the Ligurian Tethys most probably started during Triassic times and was dominated by two main processes (Piccardo & Vissers 2007): (1) ***the subsolidus evolution***, characterized by deformation and recrystallization events leading to the progressive upwelling during lithosphere extension and thinning; (2) ***the melt-related evolution***, characterized by melt–peridotite interaction processes induced by the reactive percolation through the extending mantle lithosphere of MORB-type melts.

Field and structural evidence indicates that (1) deformation associated with lithospheric extension and thinning, forming kilometre-scale shear zones in the mantle lithosphere, was partially overprinted by structural and compositional changes induced by melt–rock interaction, and (2) decompressional partial melting of the underlying asthenospheric mantle was induced by lithosphere extension and thinning. Accordingly, deformation and melt percolation in the mantle lithosphere were closely related and mutually dependent.

Mantle processes and geodynamic evolution

The Triassic lithosphere extension caused subsolidus exhumation of the sub-continental lithospheric mantle, by means of hectometre- to kilometre-scale shear zones, which led to the sea-floor exposure of the sub-continental lithospheric mantle during Jurassic times. Extension started presumably during the Triassic (estimated at 220 Ma in EL mantle for the subsolidus decompressional transition from spinel- to plagioclase-facies assemblages: Montanini *et al.* 2006). Structural and petrological investigations on the Erro–Tobbio (ET) peridotite (e.g. Ernst & Piccardo 1979; Piccardo *et al.* 1990) have shown that pristine spinel peridotites from the sub-continental lithosphere underwent localized deformation starting from spinel-facies conditions. Detailed studies (Drury *et al.* 1990; Vissers *et al.* 1991; Hoogerduijn Strating *et al.* 1993) have shown that they are transected by five generations of shear zone structures forming porphyroclastic spinel-bearing peridotite tectonites, plagioclase-, hornblende- and chlorite-bearing peridotite mylonites, and serpentinite mylonites. The shear zone structures developed at progressively lower P and T conditions (Hoogerduijn Strating *et al.* 1993). The P–T path obtained for the ET peridotite is indicative of subsolidus uplift, from deeper levels (i.e. spinel-facies conditions) of the sub-continental lithospheric mantle towards the ocean floor (Hoogerduijn Strating *et al.* 1993). Discrete gabbro bodies and dykes with MORB affinity (Piccardo 1984; Hoogerduijn Strating *et al.* 1993; Borghini *et al.* 2007) intruded the ET peridotite after melt percolation and plagioclase-facies deformation and prior to serpentinization of the ambient peridotite at oceanic conditions (Piccardo & Vissers 2007).

Lithosphere extension and thinning induced almost adiabatic upwelling of the underlying

asthenosphere and its partial melting on decompression (Piccardo & Vissers 2007; Piccardo *et al.* 2007*a*, *b*, and references therein). Information on the minimum age of partial melting inception in the Ligurian Tethys realm derives from the intrusion ages (i.e. about 180 Ma) of the oldest MORB-type gabbros that were intruded in the extending mantle lithosphere of the ocean–continent transition (Tribuzio *et al.* 2004; Rampone *et al.* 2005). These ages suggest that asthenosphere partial melting under decompression started most probably during Late Triassic–Early Jurassic times. Preliminary data on the Finero gabbroic complex in the Western Alps, however, indicate the MORB affinity of parental melts and an intrusion age of about 230 Ma (Peressini *et al.* 2004), suggesting that asthenosphere decompressional melting should have started, at least locally, in Middle to Late Triassic times.

Asthenospheric MORB-type melts migrated upwards by diffuse porous flow and percolated through the extending sub-continental mantle lithosphere (Piccardo *et al.* 2004, 2007*a*; Piccardo & Vissers 2007). Asthenospheric melts reacted with the mantle lithosphere and with the deformed rocks of the extensional shear zones, thus indicating that inception of asthenosphere partial melting and MORB percolation occurred during lithosphere extension and thinning (Piccardo & Vissers 2007). The upwelling hot asthenosphere caused heating of the extending mantle lithosphere (Piccardo *et al.* 2007*a*) whereas the upward migration of the asthenospheric melts produced the compositional modification (both depletion and enrichment) of the extending lithospheric mantle, which underwent thermo-chemical erosion (i.e. it was 'asthenospherized'; Bodinier & Godard 2003; Piccardo 2003; Piccardo *et al.* 2004, 2007*a*; Müntener *et al.* 2005). Available data and interpretations (see the previous section) indicate that melt percolation–impregnation in MIO peridotites (i.e. Monte Maggiore, Corsica, and Mt. Nero, External Ligurides) occurred during the Middle Jurassic, very close in time to MORB gabbroic intrusion into MIO peridotites.

Asthenosphere partial melting formed Jurassic refractory peridotites, coeval and cogenetic with the Jurassic MORB melts. These refractory peridotites were accreted to the thermal lithosphere and were percolated by new batches of MORB melts that formed in the underlying melting asthenosphere. Continuing extension caused complete failure of the continental crust and sea-floor exposure of: (1) pristine subcontinental lithospheric mantle; (2) melt-modified subcontinental mantle; (3) finally, Jurassic refractory residual mantle.

The above evidence contradicts previous inferences that the tectonic exhumation of the External Ligurides and Erro–Tobbio sub-continental mantle was completely unrelated to mantle melting and melt production (Rampone *et al.* 2005) and, moreover, that the magmatic activity to weaken the strong lithosphere was absent during thinning and exhumation of the mantle lithosphere of the basin (Lavier & Manatschal 2006).

Transition from whole-lithosphere extension to oceanic spreading

Field and structural data clearly suggest that the recognized melt-related events occurred during lithospheric extension. According to Piccardo & Vissers (2007), this evidence supports the idea that the various melt-related processes were related to the same melting cycle of the asthenosphere, connected to the continuing geodynamic evolution of the Europe–Adria system, leading to Jurassic ocean opening.

On the basis of the available radiometric ages on gabbroic rocks with MORB affinity intruded into the ophiolitic mantle, the evidence that MORB intrusion was preceded by percolation and impregnation by fractional melts with MORB affinity, and the palaeogeographical distribution of the peridotite massifs (see Piccardo & Vissers 2007, and references therein), a comprehensive scenario for the transition from lithospheric rifting to oceanic drifting and opening can be proposed (Fig. 8).

Sm–Nd mineral isochron ages indicate very similar intrusion ages of gabbroic rocks from the OCT zones of both the European and the Adria margins: 180 ± 14 Ma for the ET gabbros (Rampone *et al.* 2005) and 179 ± 9 Ma for in the EL gabbros (Tribuzio *et al.* 2004). Younger ages (170 ± 13 and 173 ± 4.8 Ma) are yielded by gabbros from the more internal units of Tuscany (Tribuzio *et al.* 2004), whereas MORB gabbroic intrusions in Internal Ligurides and Monte Maggiore peridotites show very similar intrusion ages: 165 ± 14 Ma for the former (Rampone *et al.* 1998) and 162 ± 10 Ma for the latter (Rampone *et al.* 2005). These data indicate that magmatic processes were distributed in a broadly symmetrical way (Piccardo & Vissers 2007): slightly older (Early–Middle Jurassic; about 180 Ma) in the OCT settings of both the Europe and Adria palaeomargins, and slightly younger (Middle Jurassic; about 164 Ma) in the MIO settings of the basin. Gabbroic bodies intruded mantle peridotites before exposure at the sea floor and failure of the continental crust (the synrift OCT gabbros of Tribuzio *et al.* 2004).

Complete failure of the continental lithosphere occurred, most probably, at 165 Ma, according to the age of the older pelagic sediments of the Ligurian Tethys (Bathonian–Callovian) (De Wever &

Caby 1981; Marcucci & Passerini 1991). Volcanism, although discontinuous and strongly reduced, associated with chert deposition and in the absence of remnants of continental crust material, has been confined to the latest stage of oceanic evolution (Late Jurassic, 156–150 Ma; Piccardo *et al.* 2006, and references therein). The volcanic rocks from the Ligurian Tethys overlie sections of older sub-continental mantle that contain MORB gabbroic intrusions slightly older (164 Ma) than MORB volcanism (Piccardo *et al.* 2004, and references therein). Rifting and drifting in the Ligurian Tethys were significantly avolcanic, but not amagmatic, similar to the situation described at ultraslow-spreading oceanic settings (i.e. Gakkel Ridge, Arctic Ocean, and Southwest Indian Ridge; Muller *et al.* 1999; Cannat *et al.* 2003, 2005; Dick *et al.* 2003; Michael *et al.* 2003; Sauter *et al.* 2004, and references therein).

Available structural and petrological data on the rift evolution of the mantle lithosphere of the Europe–Adria system show that the lithospheric mantle was significantly percolated and modified by MORB melts from the underlying DM asthenosphere during extension and thinning (e.g. Drury *et al.* 1990; Vissers *et al.* 1991; Hoogerduijn Strating *et al.* 1993; Müntener & Piccardo 2003; Piccardo 2003; Piccardo *et al.* 2004). The presence and abundance of melt-modified peridotites along the axial zone of the future oceanic basin (Piccardo *et al.* 2004, 2007*a*), and the evidence that lithospheric mantle underwent asthenospherization (thermo-mechanical and thermo-chemical erosion) prior to oceanic opening strongly suggest that melt percolation and asthenosphere–lithosphere interaction should have played an important role in the transition from lithosphere extension to ocean opening.

Recently, Ranalli *et al.* (2007) explored the thermal and rheological consequences of thermo-mechanical erosion of the lithosphere during lithosphere extension and asthenosphere–lithosphere interaction by modelling the temperature and rheological properties of the thinned lithosphere as a function of thickness of the asthenospherized lithospheric mantle and time since asthenospherization. Those workers proposed that thermo-mechanical erosion of the lithospheric mantle, related to lithosphere–asthenosphere interaction, can be an important factor in a geologically rapid decrease in total lithospheric strength. This softening could lead to whole-lithosphere failure and consequently to transition from continental extension to oceanic spreading. Corti *et al.* (2007) used analogue models to investigate extension of sub-continental mantle lithosphere weakened by percolating asthenospheric melts. Model results suggest that mantle percolation by asthenospheric melts is able to promote strong localized thinning of the sub-continental lithosphere, provided that a significant thickness of the lithospheric mantle is weakened by migrating melts within a narrow zone. Model results support the hypothesis that mantle percolation by asthenospheric melts is a controlling factor in the transition from distributed continental deformation to localized oceanic spreading.

Conceptual models for the tectonic evolution of magma-poor rifted margins have been proposed (e.g. Whitmarsh *et al.* 2001; Manatschal 2004; Lavier & Manatschal 2006), on the basis of sequential modes of lithosphere extension from pure shear to simple shear to sea-floor spreading, which are mainly based on geophysical or geological observations on the conjugate margins of the present-day West Iberia–Newfoundland in the Atlantic and the ancient Europe–Adria in the Alps. Lavier & Manatschal (2006) distinguished three evolution stages: (1) the stretching mode, characterized by distributed listric normal faulting cutting through the brittle upper crust and soling out at mid-crustal levels; (2) the thinning mode, characterized by the occurrence of crustal-scale shear zones thinning the crust to less than 10 km; (3) the exhumation mode, characterized by downward-concave faults that generate fault offsets more than 10 km, and exhumation of the serpentinized sub-continental mantle at the sea floor. Two processes have been invoked by Lavier & Manatschal (2006) to weaken the lithosphere and to explain the evolution of rifting: attenuation of the middle crust in the initial stage of rifting, and serpentinization of the mantle lithosphere during the last exhumation phase. Those workers suggested that mid-crustal weakening and serpentinization allow for thinning and exhumation of an originally strong mantle, and that these two processes represent key mechanisms allowing continental break-up in a strong lithosphere *in the absence of magmatic activity to weaken the lithosphere* (Lavier & Manatschal 2006).

Although great attention has been dedicated by Lavier & Manatschal (2006) to the behaviour of the crust, little attention has been given to the behaviour of the upper mantle, both lithospheric and asthenospheric, during the various stages of lithosphere attenuation. In particular, serpentinization alone seems highly inadequate to accommodate extension, thinning and failure of the sub-continental lithosphere, starting from at least spinel-facies conditions.

Available data from WA–NA ophiolitic peridotites document that during the pre-oceanic rifting stages of the basin: (1) lithosphere extension caused extensional deformation and tectonic–metamorphic evolution of the subcontinental mantle lithosphere,

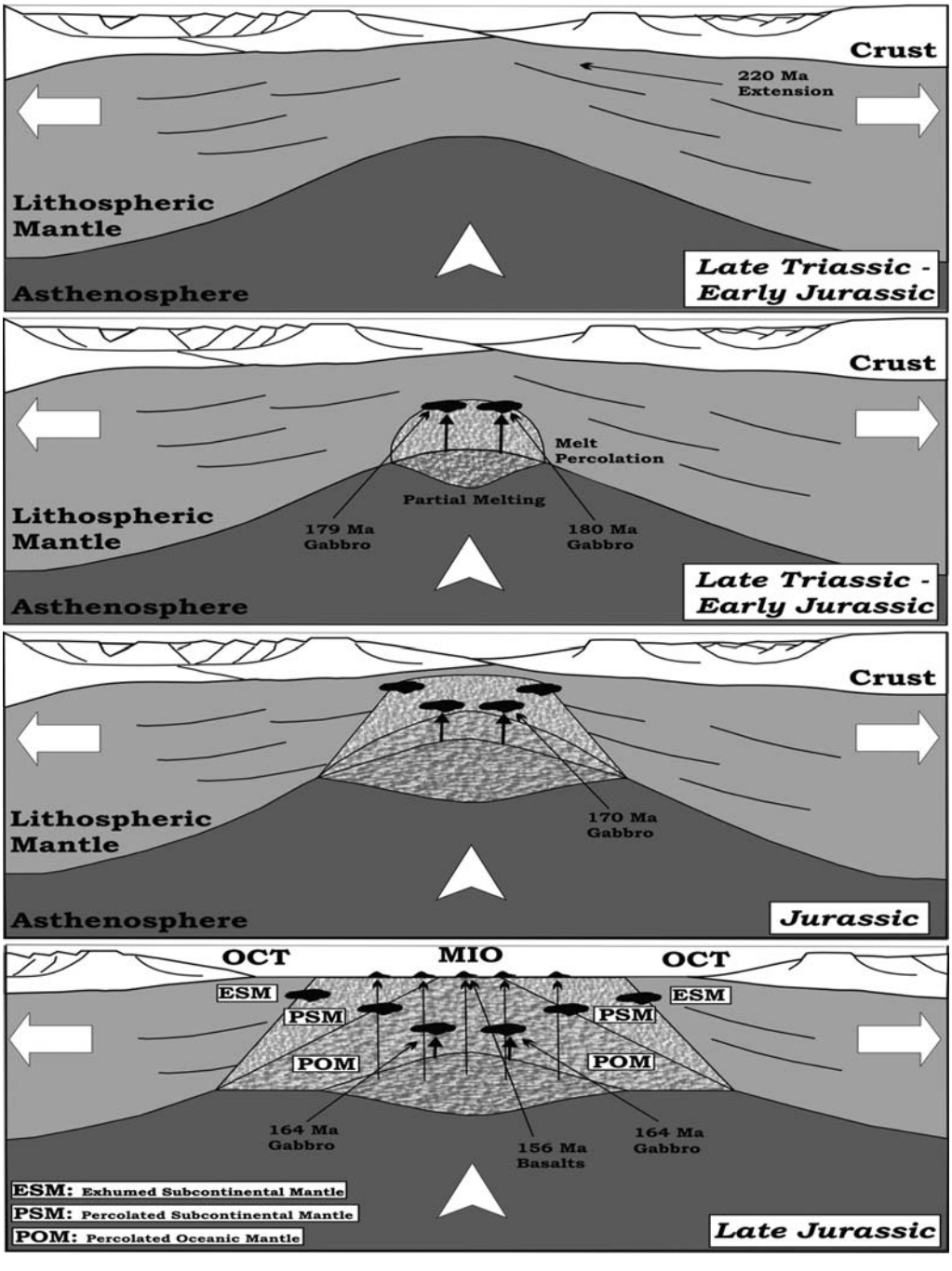

Fig. 8. Formation of the ultraslow-spreading ocean of the Ligurian Tethys (**a**) **The rifting (sub-continental) stage**, dominated by extension of continental lithosphere and tectonic exhumation of lithospheric mantle; lithosphere extension, which presumably started during the Triassic (already active at 220 Ma in the EL mantle, Montanini *et al.* 2006), caused subsolidus exhumation of the sub-continental lithospheric mantle, by means of kilometre-scale shear zones (e.g. Drury *et al.* 1990; Vissers *et al.* 1991; Hoogerduijn Strating *et al.* 1993). (**b**) **The drifting (transition) stage**, characterized by melt-related processes; that is, inception of partial melting of the asthenosphere and melt percolation through, and melt intrusion within the overlying lithospheric mantle. Lithosphere extension and thinning

starting from spinel-facies conditions, with formation of tectonite–mylonite shear zones (e.g. Drury *et al.* 1990; Vissers *et al.* 1991; Hoogerduijn Strating *et al.* 1993; Montanini *et al.* 2006; Piccardo & Vissers 2007), which have been considered relevant to lithosphere thinning and to subsolidus exhumation of the lithospheric mantle; (2) lithosphere extension and thinning caused adiabatic upwelling and decompressional melting of the underlying asthenosphere; the asthenospheric melts migrated via diffuse porous flow through the extending mantle lithosphere (Piccardo *et al.* 2004, 2007*a*); (3) deformation and melt-related processes in the mantle lithosphere were interdependent and mutually enhancing during lithosphere exhumation (Piccardo & Vissers 2007); (4) heating by asthenosphere upwelling and reactive percolation of asthenospheric melts through the mantle lithosphere caused diffuse structural, compositional and rheological modification of the mantle lithosphere, leading to its thermo-chemical and thermo-mechanical erosion; this has been considered relevant to weaken the mantle lithosphere and to enhance the transition from distributed continental deformation to localized oceanic spreading (Müntener & Piccardo 2003; Piccardo 2003; Piccardo *et al.* 2004; Corti *et al.* 2007; Ranalli *et al.* 2007).

It can, accordingly, be recognized that the interplay between deformation, melt percolation and compositional–rheological modification (thermo-chemical and thermo-mechanical erosion) of the mantle lithosphere had a fundamental role in weakening the extending lithosphere and was a controlling factor in the transition from distributed continental deformation to localized oceanic spreading.

A conceptual model for the inception of an ultraslow-spreading ocean: the Liguria Mode

The present knowledge on the petrology and palaeogeographical setting of mantle peridotites from the Ligurian Tethys allows us to present a conceptual model, the **Liguria Mode**, for the inception and evolution of an oceanic basin whose formation was dominated by the passive extension of the continental lithosphere (Fig. 8) (Piccardo 2006).

The following stages can be envisaged.

(1) ***The rifting (continental) stage***, which is dominated by extension and thinning of continental lithosphere and tectonic exhumation of sub-continental lithospheric mantle via kilometre-scale extensional shear zones.

(2) ***The drifting (transition) stage***, which is characterized by progressive thinning of the continental lithosphere and by concomitant melt-related processes. Lithosphere extension and thinning induce adiabatic upwelling and decompressional partial melting of the asthenosphere. MORB-type fractional melts percolate through the overlying sub-continental lithospheric mantle along the axial zone of the future oceanic basin, and modify large areas of the extending sub-continental mantle. Refractory peridotites, residual of asthenosphere partial melting and cogenetic with the MORB melts are formed and accreted to the thermal lithosphere after MORB-type melt extraction.

(3) ***The spreading (oceanic) stage***, which is characterized by complete failure of the continental crust, and direct exposure at the sea floor of mantle peridotites; these may be sub-continental peridotites (at OCT settings), melt-modified sub-continental

Fig. 8. (*Continued*) induced almost adiabatic upwelling of the underlying asthenosphere and its partial melting on decompression (Piccardo & Vissers 2007; Piccardo *et al.* 2007*a*). Asthenospheric melts percolated through, and reacted with the mantle lithosphere and with the deformed rocks of the extensional shear zones, thus indicating that inception of asthenosphere partial melting and MORB percolation occurred during lithosphere extension and thinning (Piccardo & Vissers 2007). Available ages of MORB gabbroic intrusion (179–180 Ma for the oldest MORB gabbros in OCT peridotites (Tribuzio *et al.* 2004; Rampone *et al.* 2005)) indicate that asthenosphere partial melting started most probably not later than Late Triassic–Early Jurassic times. (**c**) **The drifting (transition) stage**, characterized by: (1) melt-related processes; that is, partial melting of the asthenosphere and melt percolation through, and melt intrusion within the overlying lithospheric mantle; (2) formation of melt-modified peridotites, both depleted (harzburgite–dunite) and enriched (plagioclase peridotite); (3) accretion of 'oceanic' refractory residua after asthenosphere partial melting, coeval and cogenetic with the Jurassic MORB melts, to the thick thermal lithosphere. It must be recalled that during the last stages of focused melt percolation within harzburgite–dunite channels, enriched and alkaline melts migrated from deeper levels and/or different mantle sources than previous MORB-type melts. (**d**) **the spreading (oceanic) stage**, characterized by the complete failure of the continental crust and the 'modified' sub-continental lithospheric mantle. Oceanic peridotites (i.e. the refractory residua after Jurassic partial melting) were later exposed at the sea floor along the axial zone of the basin. These refractory peridotites were accreted to the thermal lithosphere after MORB melt extraction, were percolated by newly formed MORB melts from the underlying melting asthenosphere (percolated oceanic mantle) and were exposed at the sea floor of the basin. MORB magmas sporadically reached the sea floor, were extruded above mantle peridotites, and formed volcanic segments along the axis of the basin.

peridotites, or refractory residual peridotites after oceanic partial melting (at MIO settings).

Lithosphere extension and thinning of the mantle lithosphere are accommodated by lithosphere-scale extensional shear zones and induce asthenosphere adiabatic upwelling and decompressional melting. Mantle lithosphere is weakened by heating from upwelling asthenosphere and diffuse percolation of asthenospheric melts. The thermo-mechanical erosion of the mantle lithosphere facilitates the transition from distributed lithosphere deformation to localized oceanic spreading.

Conclusion

The following steps have been envisaged during the progressive exhumation of Ligurian peridotites from the sub-continental mantle lithosphere to the sea floor.

(1) Mantle protoliths of the Ligurian ophiolitic peridotites were accreted to the thermal lithosphere and underwent complete equilibrium recrystallization at sub-continental lithospheric conditions after isolation from the convecting asthenosphere.

(2) The various peridotite masses were originally located in the mantle lithosphere at different structural levels; that is, at different depths and/or at different positions with respect to the future passive continental margins and to the axial zone of the embryonic basin. Accordingly, mantle sections located closer to the continent (i.e. future OCT peridotites) or at shallower levels (closer to the crust) should have escaped the melt-related events and evolved along a complete subsolidus path (the *cold exhumation* of Muntener & Piccardo 2003). Conversely, peridotite masses from more axial settings (i.e. future MIO peridotites) underwent a more composite evolution, characterized by both tectonic–metamorphic and melt-related processes, and were asthenospherized (the *hot exhumation* of Muntener & Piccardo 2003).

(3) Along the axial zone of the rifting system, mantle asthenosphere underwent near-adiabatic upwelling and partial melting under decompression, and formed single melt fractions with MORB affinity. MORB-type melt–fractions migrated by reactive porous flow through the overlying, extending mantle lithosphere; melt–peridotite interaction formed melt-modified peridotites.

(4) After diffuse percolation–impregnation of axial sub-continental lithospheric peridotites, further melt upwelling occurred within focused harzburgite–dunite channels. Generally these channels were used by upward migration of aggregated MORB melts; locally they were exploited by enriched to alkaline melts, most probably deriving from mantle sources deeper than and/or different from the DM asthenospheric sources of previous MORB-type melts.

(5) Axial melt-modified peridotites were progressively uplifted to more cold, brittle and hydrous conditions, associated with hydrous fluid migration, and localized amphibole peridotite and chlorite peridotite mylonites were formed, which accommodated the later stages of exhumation towards the sea floor. Diffuse serpentinization occurred along serpentinite mylonite shear zones, which was preceded or followed by MORB intrusion in dykes. Finally, complete failure of the continental crust allowed sub-continental peridotites, melt-modified peridotites and refractory residual peridotites to be exposed at the sea floor, where they were discontinuously covered by MORB.

Across-axis variation of mantle petrology indicates the three stages of evolution of the basin (Fig. 8): (1) exhumed subcontinental mantle characterizes the OCT zones, representing the *rifting stage*; (2) percolated subcontinental mantle mostly characterizes the more external MIO settings, representing the *transitional drifting stage*, where significant lithosphere attenuation was accompanied by asthenosphere partial melting and lithosphere melt percolation, preceding the complete failure of continental crust; (3) percolated oceanic mantle, cogenetic with the Jurassic MORB melts, possibly characterizes some more internal MIO settings, representing the *oceanic spreading stage*, when refractory residua after Jurassic partial melting were emplaced at the sea floor, after complete failure of the continental crust and the modified sub-continental mantle lithosphere.

The Italian MIUR (Ministero dell'Istruzione, dell'Universita e della Ricerca) (PRIN-COFIN2005: 'Lithosphere evolution induced by migration of mantle-derived melts at different geodynamic settings') and the University of Genova are acknowledged for financial support. The participants at the Peridotite Workshop 2005 (Lanzo, 27–30, September 2005) and the Polar Ridges Meeting and Workshop 2006 (Sestri Levante, 19–22, September 2006) are acknowledged for the stimulating and inspiring discussions during the meetings and the field trips. An earlier version of the manuscript was reviewed by A. Montanini and G. Ranalli; their comments and suggestions significantly improved the paper and their work is gratefully acknowledged. Discussions with and suggestions by A. Zanetti and R. Vannucci are acknowledged. Special thanks are due to M. Piccardo and A. Pruzzo for technical support. This paper is dedicated to the memory of Franca Cimmino.

References

ABBATE, E., BORTOLOTTI, V., PASSERINI, P., PRINCIPI, G. & TREVES, B. 1994. Oceanisation processes and sedimentary evolution of the Northern Apennine

ophiolite suite: a discussion. *Memorie della Societá Geologica Italiana*, **48**, 117–136.

BECCALUVA, L. & PICCARDO, G. B. 1978. Petrology of the Northern Apennine ophiolites and their significance in the Western Mediterranean area. *In*: CLOSS, H., ROEDER, D. & SCHMIDT, K. (eds) *Alps, Apennines, Hellenides*. Inter-Union Commission on Geodynamics Scientific Report, **38**, 243–254.

BECCALUVA, L., PICCARDO, G. B. & SERRI, G. 1980. Petrology of the Northern Apennine ophiolites and comparison with other Tethyan ophiolites. *In*: PANAYIOTOU, A. (ed.) *Ophiolites*, Geological Survey Department, Nicosia, 314–331.

BECCALUVA, L., MACCIOTTA, G., PICCARDO, G. B. & ZEDA, O. 1984. Petrology of lherzolitic rocks from the Northern Apennine ophiolites. *Lithos*, **17**, 299–316.

BEZZI, A. & PICCARDO, G. B. 1971. Structural features of the Ligurian ophiolites: petrologic evidence for the 'oceanic' floor of northern Apennines geosyncline. *Memorie della Societa Gelogica Italiana*, **10**, 53–63.

BODINIER, J. L. & GODARD, M. 2003. Orogenic, ophiolitic, and abyssal peridotites. *In*: *Treatise on Geochemistry*, Volume 2. Elsevier, Amsterdam, 103–170.

BODINIER, J. L., MENZIES, M. A. & THIRLWALL, M. F. 1991. Continental to oceanic mantle transition—REE and Sr–Nd isotopic geochemistry of the Lanzo Lherzolite Massif. *Journal of Petrology, Special Lherzolite Issue*, 191–210.

BONATTI, E., BRUNELLI, D., FABRETTI, P., LIGI, M., PORTARO, R. A. & SEYLER, M. 2001. Steady-state creation of crust-free lithosphere at cold spot in mid-ocean ridges. *Geology*, **29**, 979–982.

BORGHINI, G., RAMPONE, E., CRISPINI, L., DE FERRARI, R. & GODARD, M. 2007. Origin and emplacement of ultramafic–mafic intrusions in the Erro–Tobbio mantle peridotite (Ligurian Alps, Italy). *Lithos*, **94**, 210–229.

CANNAT, M. 1993. Emplacement of mantle rocks in the sea-floor at mid-ocean ridges. *Journal of Geophysical Research*, **98**, 4162–4172.

CANNAT, M. 1996. How thick is the magmatic crust at slow spreading oceanic ridges? *Journal of Geophysical Research*, **101**, 2847–2857.

CANNAT, M., CHATIN, F., WHITECHURCH, H. & CEULENEER, G. 1997. Gabbroic rocks trapped in the upper mantle at mid-ocean ridge. *In*: KARSOM, J. A., CANNAT, M., MILLER, D. J. & ELTON, D. (eds) *Proceeding of the Ocean Drilling Program, Scientific Results*, **153**, Ocean Drilling Program, College Station, TX, 243–264.

CANNAT, M., ROMMEVAUX-JESTIN, C. & FUJIMOTO, H. 2003. Melt supply variations to a magma-poor ultra-slow spreading ridge (Southwest Indian Ridge 61° to 69°E). *Geochemistry Geophysics, Geosystems*, **4**, 9104.

CANNAT, M., SAUTER, D., ESCARTIN, J., MENDEL, V., RUELLAN, E. & OKINO, K. 2005. A-volcanic seafloor generation at a melt-poor ultraslow-spreading ridge: Southwest India Ridge 61°–67°E. *Geophysical Research Abstracts*, **7**, abstract number 09159.

CORTI, G., BONINI, M., INNOCENTI, F., MANETTI, P., PICCARDO, G. B. & RANALLI, G. 2007. Experimental models of extension of continental lithosphere weakened by percolation of asthenospheric melts. *Journal of Geodynamics*, **43**, 465–483.

DAL PIAZ, G. V. 1993. Evolution of Austro-Alpine and Upper Pennidic basement in the North-Western Alps from Variscan convergence to post-Variscan extension. *In*: VON RAUMER, J. F. & NEUBAUER, F. (eds) *Pre-Mesozoic Geology in the Alps*. Springer, New York, 327–344.

DECANDIA, F. A. & ELTER, P. 1969. Riflessioni sul problema delle ofioliti nell'Appennino Settentrionale (nota preliminare). *Atti della Società Toscana di Scienze Naturali*, **75**, 1–9.

DE WEVER, P. & CABY, R. 1981. Datation de la base des Schistes Lustrés postophiolitiques (Oxfordien Supérieur–Kimmeridgien Moyen) dan les alpes Cottien (Saint-Vera, France). *Comptes Rendus de l'Académie des Sciences*, **292**, 467–472.

DICK, H. J. B. & BULLEN, T. 1984. Chromian spinel as a petrogenetic indicator in abyssal and alpine-type peridotites and spatially associated lavas. *Contributions to Mineralogy and Petrology*, **86**, 54–76.

DICK, H. J. B., FISHER, R. L. & BRYAN, W. B. 1984. Mineralogical variability of the upper mantle along mid-ocean ridges. *Earth and Planetary Science Letters*, **69**, 88–106.

DICK, H. J. B., LIN, J. & SCHOUTEN, H. 2003. An ultraslow-spreading class of ocean ridge. *Nature*, **426**, 405–412.

DICK, H. J., STANDISH, J. & SNOW, J. 2006. Ultraslow spreading ridges. *Ofioliti*, **31**, 232.

DIJKSTRA, A. H., DRURY, M. & VISSERS, R. L. M. 2001. Structural petrology of plagioclase peridotites in the West Othis Mountains (Greece): melt impregnation in mantle lithosphere. *Journal of Petrology*, **42**, 5–24.

DIJKSTRA, A. H., BARTH, M. G., DRURY, M. R., MASON, P. R. D. & VISSERS, R. L. M. 2003. Diffuse porous melt flow and melt–rock reaction in the mantle lithosphere at a slow-spreading ridge: A structural petrology and LA-ICP-MS study of the Othris Peridotite Massif (Greece). *Geochemistry, Geophysics, Geosystems*, doi:2001GC000278.

DRURY, M. R., HOOGERDUIJN STRATING, E. H. & VISSERS, R. L. M. 1990. Shear zone structures and microstructures in mantle peridotites from the Voltri Massif, Ligurian Alps, NW Italy. *Geologie en Mijnbouw*, **69**, 3–17.

ERNST, W. G. & PICCARDO, G. B. 1979. Petrogenesis of some Ligurian peridotites: I. Mineral and bulk rock chemistry. *Geochimica et Cosmochimica Acta*, **43**, 219–237.

HELLEBRAND, E., SNOW, J. E., DICK, H. J. B. & VON DER HANDT, A. 2006*a*. Inherited depletion in the oceanic mantle inferred from peridotite composition and distribution along Gakkel Ridge. *Ofioliti*, **31**, 235.

HELLEBRAND, E., SNOW, J. E., DICK, H. J. B. & VON DER HANDT, A. 2006*b*. Inherited depletion in the oceanic mantle: peridotite composition and distribution along Gakkel Ridges. *EOS Transactions, American Geophysical Union*, **87**, Fall Meeting Supplement, abstract, T104A-011.

HOFMANN, W. A. 1988. Chemical differentiation of Earth: the relationship between mantle, continental crust and oceanic crust. *Earth and Planetary Science Letters*, **90**, 297–314.

HOOGERDUIJN STRATING, E. H., RAMPONE, E., PICCARDO, G. B., DRURY, M. R. & VISSERS, R. L. M. 1993. Subsolidus emplacement of mantle peridotites during incipient oceanic rifting and opening of the Mesozoic Tethys (Voltri Massif, NW Italy). *Journal of Petrology*, **34**, 901–927.

IONOV, D. A., BODINIER, J. L., MUKASA, S. B. & ZANETTI, A., 2002. Mechanisms and sources of mantle metasomatism: major and trace element conditions of peridotite xenoliths from Spitzbergen in the context of numerical modelling. *Journal of Petrology*, **43**, 2261–2278.

KELEMEN, P. B., WHITEHEAD, J. A., AHARONOV, E. & JORDAHL, K. A. 1995*a*. Experiments on flow focusing in soluble porous media, with applications to melt extraction from the mantle. *Journal of Geophysical Research*, **100**, 475–496.

KELEMEN, P. B., SHIMIZU, N. & SALTERS, V. J. M. 1995*b*. Extraction of mid-ocean-ridge basalt from the upwelling mantle by focused flow of melt in dunite channels. *Nature*, **375**, 747–753.

LAVIER, L. L. & MANATSCHAL, G. 2006. A mechanism to thin the continental lithosphere at magma-poor margins. *Nature*, **440**, 324–328.

LEMOINE, M., TRICART, P. & BOILLOT, G. 1987. Ultramafic and gabbroic ocean floor of the Ligurian Tethys (Alps, Corsica, Apennines): in search of a genetic model. *Geology*, **15**, 622–625.

MANATSCHAL, G. 2004. New models for evolution of magma-poor rifted margins based on a review of data and concepts from West Iberia and the Alps. *International Journal of Earth Science*, **93**, 432–466.

MARCUCCI, M. & PASSERINI, P. 1991. Radiolarian-bearing siliceous sediments in the Mesozoic of the Northern and Central Apennines. *Ofioliti*, **16**, 121–126.

MARRONI, M., MOLLI, G., MONTANINI, A. & TRIBUZIO, R. 1998. The association of continental crust rock with ophiolites in the Northern Apennine (Italy): implication for the continent-ocean transition in the Western Tethys. *Tectonophysics*, **292**, 43–66.

MARRONI, M., MOLLI, G., MONTANINI, A., OTTRIA, G., PANDOLFI, L. & TRIBUZIO, R. 2002. The External Ligurian units (Northern Apennine, Italy): from rifting to convergence of a fossil ocean-continent transition zone. *Ofioliti*, **27**, 119–131.

MICHAEL, P. J., LANGMUIR, C. H., DICK, H. J. B. *ET AL.* 2003. Magmatic and amagmatic seafloor generation at the ultraslow-spreading Gakkel ridge, Arctic Ocean. *Nature*, **423**, 956–961.

MONTANINI, A. & TRIBUZIO, R. 2007. Petrogenesis of basalts and gabbros from an ancient continent–ocean transition (External Liguride ophiolites, Northern Italy): implications for a pyroxenite-derived component. *In*: *FIST Geoitalia 2007, Sessione T14, Abstract Volume*, 58.

MONTANINI, A., TRIBUZIO, R. & ANCZKIEWICZ, R. 2006. Exhumation history of a garnet pyroxenite-bearing mantle section from a continent–ocean transition (Northern Apennine ophiolites, Italy). *Journal of Petrology*, **47**, 1943–1971.

MUHE, R. K., BOHRMANN, H., GARBE-SCHONBERG, D. & KASSENS, H. 1997. E-MORB glasses from Gakkel Ridge (Arctic Ocean) at 87°N: evidence for the Earth's most northerly volcanic activity. *Earth and Planetary Science Letters*, **152**, 1–9.

MULLER, M. R., MINSHULL, T. A. & WHITE, R. S. 1999. Segmentation and melt supply at the Southwest Indian Ridge. *Geology*, **27**, 867–870.

MÜNTENER, O. & HERMANN, J. 2001. The role of lower crust and continental upper mantle during formation of nonvolcanic passive margins: evidence from the Alps. *In*: WILSON, R. C. L., WHITMARSH, R. B., TAYLOR, B. & FROITZHEIM, N. (eds) *Non-volcanic Rifting of Continental Margins: a Comparison of Evidence from Land and Sea.* Geological Society, London, Special Publications, **187**, 267–288.

MÜNTENER, O. & PICCARDO, G. B. 2003. Melt migration in ophiolites: the message from Alpine-Apennine peridotites and implications for embryonic ocean basins. *In*: DILEK, Y. & ROBINSON, P. T. (eds) *Ophiolites in Earth History*. Geological Society, London, Special Publications, **218**, 69–89.

MÜNTENER, O. & PICCARDO, G. B. 2006. Remnants of ocean–continent transition, (ultra-) slow spreading oceanic crust and oceanic core complexes preserved in the Alps of NW Italy and SE France: an analogue to Polar systems? *In*: *Polar Ridge Meeting and Workshop 2006, Field Guide to the Post-conference Field Trip*, 1–45.

MÜNTENER, O., PETTKE, T., DESMURS, L., MEIER, M. & SCHALTEGGER, U. 2004. Refertilization of mantle peridotites in embryonic ocean basins: trace element and Nd isotopic evidence and implications for crust–mantle relationships. *Earth and Planetary Science Letters*, **221**, 293–308.

MÜNTENER, O., PICCARDO, G. B., POLINO, R. & ZANETTI, A. 2005. Revisiting the Lanzo peridotite (NW-Italy): 'asthenospherization' of ancient mantle lithosphere. *Ofioliti*, **30**, 111–124.

NAURET, F., SNOW, J. E., HELLEBRAND, E., VON DER HANDT, A., FEIG, S. T., GAO, Y. & JOVANOVIC, Z. 2004. Lena Trough Basalts: Low degree garnet melting signatures. *EOS Transactions American Geophysical Union*, **85**, Fall Meeting Supplement, T12A–07.

NAURET, F., SNOW, J. F., HELLEBRAND, E., VON DER HANDT, A., GAO, Y., FEIG, S. & JOVANOVIC, Z. 2005. Mid ocean rift alkali basalts from Arctic Lena Trough. *EGU Conference*, Vienna, EGU05–A07843.

NAURET, F., WEIS, D. & SNOW, J. E. 2006. Isotope geochemistry of Lena Trough. *Ofioliti*, **31**, 241–242.

NICOLAS, A. & JACKSON, E. D. 1972. Répartition en deux provinces des peridotites des chaines alpines longéant la Méditerranée: implications géotectoniques. *Schweizerische Mineralogische und Petrographische Mitteilungen*, **52**, 479–495.

NIU, Y. 1997. Mantle melting and mantle extraction processes beneath ocean ridges: evidence from abyssal peridotites. *Journal of Petrology*, **38**, 1047–1074.

PERESSINI, G., MAZZUCCHELLI, M., RIVALENTI, G. & HOFFMANN, A. W. 2004. Triassic emplacement of the external Gabbro Unit of the Finero mafic complex: U–Pb SHRIMP zircon age and their implication for the Ivrea–Verbano zone, Western Italian Alps. *Geophysical Research Abstracts*, **6**, abstract number 05072.

PICCARDO, G. B. 1976. Petrologia del massiccio lherzolitico di Suvero (La Spezia). *Ofioliti*, **1**, 279–317.

PICCARDO, G. B. 1984. Le ofioliti metamorfiche del Gruppo di Voltri, Alpi Liguri: caratteri primari ed interpretazione geodinamica. *Memorie della Societá Geologica Italiana*, **28**, 95–114.

PICCARDO, G. B. 2003. Mantle processes during ocean formation: petrologic records in peridotites from the Alpine-Apennine ophiolites. *Episodes*, **26**, 193–200.

PICCARDO, G. B. 2006. The pre–oceanic evolution of the Jurassic Ligurian Tethys: a fossil slow/ultra-slow spreading ocean: the mantle perspective. *EOS Transactions, American Geophysical Union*, Fall Meeting Supplement, abstract.

PICCARDO, G. B. & VISSERS, R. L. M. 2007. The pre-oceanic evolution of the Erro–Tobbio peridotite (Voltri Massif—Ligurian Alps, Italy). *Journal of Geodynamics* **43**, 417–449.

PICCARDO, G. B., RAMPONE, E. & VANNUCCI, R. 1990. Upper mantle evolution during continental rifting and ocean formation: evidence from peridotite bodies of the Western Alpine–Northern Apennine system. *Mémories De la Sociéte Géologique de France*, **156**, 323–333.

PICCARDO, G. B., MÜNTENER, O., ZANETTI, A. & PETTKE, T. 2004. Ophiolitic peridotites of the Alpine–Apennine system: mantle processes and geodynamic relevance. *International Geology Review*, **46**, 1119–1159.

PICCARDO, G. B., POGGI, E. & ZANETTI, A. 2006. Melt diffuse refertilization and focused migration in lithospheric mantle of a fossile rifted margin: the Mt. Nero peridotite (External Ligurides, Italy). *EOS Transactions American Geophysical Union,* **87**, Fall Meeting Supplement, Abstract, T104A-07.

PICCARDO, G. B., ZANETTI, A. & MÜNTENER, O. 2007*a*. Melt/peridotite interaction in the Lanzo South peridotite: field, textural and geochemical evidence. *Lithos*, **94**, 181–209.

PICCARDO, G. B., ZANETTI, A., PRUZZO, A. & PADOVANO, M. 2007*b*. The North Lanzo peridotite body (NW-Italy): lithospheric mantle percolated by MORB and alkaline melts. *Periodico di Mineralogia*, in press.

PICCARDO, G. B., RANALLI, G. & VISSERS, R. L. M. 2007*c*. The geodynamic evolution of the Jurassic Ligurian Tethys viewed from a mantle perspective. *Bollettino della Societá Geologica Italiana, Special Volume*, in press.

POGGI, E., PICCARDO, G. B. & ZANETTI, A. 2005. Melt percolation and impregnation in peridotites from a fossil rifted margin: evidence from the Mt. Nero peridotite (External Ligurides, Northern Apennine, Italy). *Geophysical Research Abstracts*, **7**, abstract numbers 00464.

RAMPONE, E. & PICCARDO, G. B. 2003. Melt impregnation in the oceanic lithosphere mantle: insights from the Monte Maggiore (Corse, France) ophiolitic peridotites. *In*: *FIST, GeoItalia 2003 Riassunti*, Sessione 6, 253–255.

RAMPONE, E., HOFMANN, A. W., PICCARDO, G. B., VANNUCCI, R., BOTTAZZI, P. & OTTOLINI, L. 1995. Petrology, mineral and isotope geochemistry of the External Liguride peridotites (Northern Apennine, Italy). *Journal of Petrology*, **36**, 81–105.

RAMPONE, E., HOFMANN, A. W., PICCARDO, G. B., VANNUCCI, R., BOTTAZZI, P. & OTTOLINI, L. 1996. Trace element and isotope geochemistry of depleted peridotites from an N-MORB type ophiolite (Internal Liguride, N. Italy). *Contributions to Mineralogy and Petrology*, **123**, 61–76.

RAMPONE, E., HOFMANN, A. W. & RACZEK, I. 1998. Isotopic contrasts within the Internal Liguride ophiolite (N. Italy): the lack of a genetic mantle–crust link. *Earth and Planetary Science Letters*, **163**, 175–189.

RAMPONE, E., PICCARDO, G. B., ROMAIRONE, A., RACZEK, L., ABOUCHAMI, W. & HOFMANN, A. W. 2005. Mantle–crust relations in embryonic slow-spreading ocean basins: insights from the Ligurian and Corsican ophiolites. *Geophysical Research Abstracts*, **7**, abstract numbers 07883.

RANALLI, G., PICCARDO, G. B. & CORONA-CHAVEZ, P. 2007. Softening of the subcontinental lithospheric mantle by asthenosphere melts and the continental extension/oceanic spreading transition. *Journal of Geodynamics* **43**, 450–464.

SALTER, V. J. M. & DICK, H. J. B. 2002. Mineralogy of the mid-ocean-ridge basalt source from neodymium isotopic composition of abyssal peridotites. *Nature*, **418**, 68–72.

SAUTER, D., MENDEL, V. & ROMMEVAUX-JESTIN, C. 2004. Focused magmatism versus amagmatic spreading along the ultra-slow spreading Southwest Indian Ridge: Evidence from TOBI side scan sonar imagery. Geochemistry Geophysics Geosystems, **5**, 738.

SERRI, G. 1980. Chemistry and petrology of gabbroic complexes from the Northern Apennines ophiolites. *In*: PANAYIOTOU, A. (ed.) *Ophiolites*. Geological Survey Department, Nicosia, 296–313.

SHIMIZU, N., WARREN, J. M., FREY, F. A. & TAKAZAWA, E. 2006. The Horoman peridotite Massif: an example of ancient ultraslow-spreading ridge abyssal peridotites? *EOS Transactions American Geophysical Union*, **87**, Fall Meeting Supplement, Abstract, T104A-08.

SNOW, J. E., NAURET, F., HELLEBRAND, E. & VON DER HANDT, A. 2006. Direct evidence for vein melting from Arctic MORB and peridotite. T104A-05.

TRIBUZIO, R., THIRLWALL, M. F. & VANNUCCI, R. 2004. Origin of the gabbro–peridotite association from the Northern Apennine ophiolites (Italy). *Journal of Petrology*, **45**, 1109–1124.

TROMMSDORFF, V., PICCARDO, G. B. & MONTRASIO, A. 1993. From magmatism, trough metamorphism to sea-floor emplacement of sub-continental Adria lithosphere during pre-Alpine rifting (Malenco, Italy). *Schweizerische Mineralogische and Petrographische Mitteilungen*, **73**, 191–203.

VANNUCCI, R., BOTTAZZI, P., WULFF-PEDERSEN, E. & NEUMANN, E.-R. 1998. Partitioning of REE, Y, Sr, Zr and Ti between clinopyroxene and silicate melts in the mantle under La Palma (Canary Islands): implications for the nature of the metasomatic agents. *Earth and Planetary Science Letters*, **158**, 39–51.

VERNIÈRES, L., GODARD, M. & BODINIER, J. L. 1997. A plate model for the simulation of trace element fractionation during partial melting and magma transport in the Earth's upper mantle. *Journal of Geophysical Research*, **102**, 24771–24784.

VISSERS, R. L. M., DRURY, M. R., HOOGERDUIJN STRATING, E. H. & VAN DER WAL, D. 1991. Shear zones in the upper mantle: a case study in an Alpine lherzolite massif. *Geology*, **19**, 990–993.

VON DER HANDT, A., SNOW, J. E. & HELLEBRAND, E. 2006. A quantitative assessment of melt origin versus subsolidus formation of plagioclase in Gakkel Ridge peridotites. *Ofioliti*, **31**, 248–249.

WALTER, M. J. 1998. Melting of garnet peridotite and the origin of komatiite and depleted lithosphere. *Journal of Petrology*, **39**, 29–60.

WARREN, J. M., SHIMIZU, N., DICK, H. J., SAKAGUCHI, C. & NAKAMURA, E. 2006. *EOS Transactions*, American Geophysical Union, **87**, Fall Meeting Supplement, Abstract, T104A-12.

WHITMARSH, R. B., MANATSCHAL, G. & MINSHULL, T. A. 2001. Evolution of magma-poor continental margins from rifting to sea-floor spreading. *Nature*, **413**, 150–154.

WINTERER, E. L. & BOSELLINI, A. 1981. Subsidence and sedimentation on the Jurassic passive continental margin, Southern Alps, Italy. *AAPG. Bulletin*, **63**, 394–421.

Calcic amphiboles in peridotite xenoliths from Avacha volcano, Kamchatka, and their implications for metasomatic conditions in the mantle wedge

S. ISHIMARU & S. ARAI

Department of Earth Sciences, Kanazawa University, Kakuma, Kanazawa 920-1192, Japan (e-mail: jaja@earth.s.kanazawa-u.ac.jp)

Abstract: Highly metasomatized parts of peridotite xenoliths from Avacha volcano, Kamchatka, Russia, characteristically contain calcic amphiboles, especially tremolites. They are rich in metasomatic pyroxenes with high Mg-number (= Mg/(Mg + Fe) atomic ratio), up to 0.94–0.98, and contain Cr-poor aluminous spinels. They have the spinel lherzolite mineral assemblage and equilibrium temperatures of 900–1000 °C or higher, beyond the stability field of tremolite. The tremolite was therefore retrogressively formed after the peak of high-temperature metasomatism. The high-Mg-number, low-alkali environment facilitates the formation of tremolite instead of Al-rich calcic amphiboles. A sulphur-bearing silicic melt derived from a slab is a probable agent involved in the metasomatism. High fO_2 recorded in the highly metasomatized peridotites is consistent with this process. This type of metasomatism can produce high-Mg-number peridotites and pyroxenites with low-Cr-number spinel within the mantle wedge where the Mg-number of silicates is positively correlated with the Cr-number of spinel in ambient peridotites.

Calcium-rich amphiboles are important accessory minerals in upper mantle peridotites; they occur either as residual phases after hydrous partial melting (e.g. Ozawa 1988) or as metasomatic phases precipitated from aqueous agents (e.g. Arai 1986). Tremolites and other calcic amphiboles are especially common in abyssal peridotites and ophiolitic or solid intrusive peridotites, their chemical compositions being variable depending on alteration, metamorphic and metasomatic conditions (e.g. Evans 1982). The calcic amphiboles have a two-fold importance in the upper mantle. They play a significant role in storing various incompatible trace elements in the upper mantle (e.g. Dawson & Smith 1982). Many elements can be incorporated in the calcic amphiboles, which are therefore a subtle indicator of chemical environment of the upper mantle. The calcic amphiboles are changeable in chemistry, especially in Al and alkali contents, depending on equilibrium temperatures in the peridotite–H_2O system (e.g. Evans 1982). Tremolitic amphiboles gradually change to pargasitic amphiboles; that is, the Al and alkali contents increase, with an increase of temperature in the hydrous peridotite system (Evans 1982). Tremolites, except some sodic tremolites (Aoki *et al.* 1972; Smith 1979), have been very rarely reported from peridotite xenoliths because of their derivation beyond the stability field of calcic tremolites. As far as we know, tremolites have been reported only in peridotite xenoliths only from Lihir, Papua New Guinea (Franz *et al.* 2002). Geochemical characteristics of the tremolites, however, have not been clearly described yet.

We describe various calcic amphiboles, from tremolites to pargasites or edenites, in peridotite xenoliths from Avacha volcano, which are metasomatized to various degrees (Arai *et al.* 2003). Avacha volcano constitutes the volcanic front of the Kamchatka arc (e.g. Tatsumi *et al.* 1994), and the peridotite xenoliths can provide us with direct information on mantle materials and processes beneath the volcanic front. Peridotite xenoliths derived from the mantle wedge beneath the volcanic front are not available elsewhere, except Iraya volcano, in the Philippines (see Arai *et al.* 2007). The volcanic front is the locus where magma production rates are the highest in arcs (e.g. Sugimura *et al.* 1963), which suggests the existence of a large amount of high-degree mantle restite at depth. The mantle metasomatism as a result of dehydration of subducted materials (e.g. Tatsumi 1986) is expected to be most prominent beneath the volcanic front. The amphiboles in the Avacha peridotite xenoliths are a good indicator of physical–chemical conditions of melting and metasomatism of the mantle wedge just beneath the volcanic front.

Geological background

Avacha volcano is a stratovolcano, located on the frontal volcanic chain (= volcanic front) of the southern Kamchatka arc (Tatsumi *et al.* 1994),

From: COLTORTI, M. & GRÉGOIRE, M. (eds) *Metasomatism in Oceanic and Continental Lithospheric Mantle.* Geological Society, London, Special Publications, **293**, 35–55.
DOI: 10.1144/SP293.3 0305-8719/08/$15.00

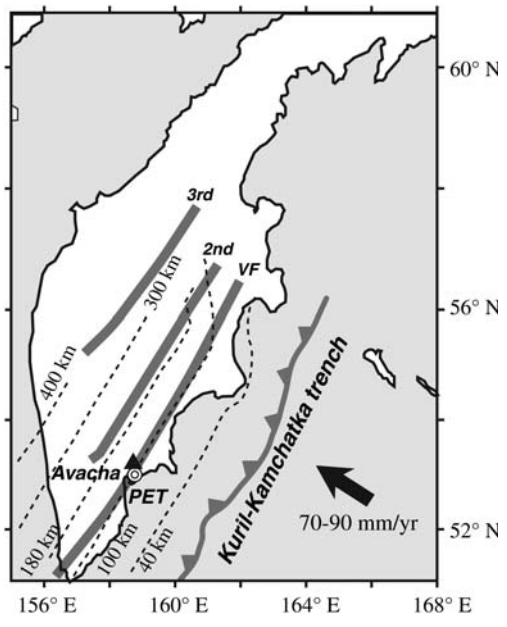

Fig. 1. Schematic map of the Kamchatka arc region, modified from Ishimaru *et al.* (2007, fig. 1). The contours of the Wadati–Benioff zone are adopted from Gorbatov *et al.* (1997), and the three volcanic chains are from Tatsumi *et al.* (1994). PET, Petropavlovsk-Kamchatsky, the capital city of Kamchatka. Subduction speed of the Pacific plate is 70–90 mm a^{-1} (Minster *et al.* 1974). Bold lines, labelled VF, 2nd and 3rd, represent the volcanic chains defined by Tatsumi *et al.* (1994), and are the volcanic front, second volcanic chain and third volcanic chain, respectively.

and the depth to the subducting slab is 120 km there (Gorbatov *et al.* 1997) (Fig. 1). Beneath the southern Kamchatka arc, the old and cold Pacific plate has subducted at relatively rapid rates (70–90 mm a^{-1}) (Minster *et al.* 1974) (Fig. 1). Volcanic activity started in the late Pleistocene, and all the effusive rocks have a calc-alkaline affinity. The activity is subdivided into two stages, IAv and IIAv, on the basis of eruption ages and chemical compositions (Braitseva *et al.* 1998). Mantle peridotite xenoliths are enclosed by IAv low-K andesitic to basaltic andesitic tephra and pyroclastic flows, and banded pumices can be observed in the layers containing peridotite xenoliths.

Petrographical features

Modal proportions of minerals were determined for the peridotite xenoliths by the point-counting method, taking 2000–4000 points per thin section (28 mm × 48 mm). Almost all of the Avacha peridotite xenoliths are spinel harzburgites, containing small amounts of clinopyroxene (<2 vol%), and we found subordinate olivine clinopyroxenites, olivine orthopyroxenites, and dunites (Arai *et al.* 2003; Ishimaru *et al.* 2007). The peridotite xenoliths have been metasomatized to various extents by hydrous SiO_2-rich melts or fluids (Arai *et al.* 2003; Ishimaru *et al.* 2007). There is a grain-size variety of minerals from >1 cm to 10 μm (Arai *et al.* 2003) (Figs 2 and 3). Fine-grained peridotite xenoliths have been also reported from Iraya volcano, Luzon arc, Philippines (e.g. Arai *et al.* 1996, 2004). Arai *et al.* (1996) defined the fine-grained peridotites, containing >10 vol% fine-grained minerals, as 'F-type peridotites' and the other peridotites, formed by coarse-grained minerals, as 'C-type peridotites'. We will follow this usage in the following sections. The F-type peridotites occupy *c.* 15% of all collected peridotite xenoliths from Avacha volcano, although they are much more predominant in the xenoliths suite from the Iraya volcano, Philippines (almost 90% of the total). There is no difference in constituent minerals between the C-type and F-type peridotites from Avacha volcano, although we could not determine the modal compositions of the F-type peridotites because of extremely fine grain sizes of their minerals.

C-type peridotites are composed of olivine, orthopyroxene, minor amounts of clinopyroxene and amphiboles, and small amounts of metasomatic minerals (orthopyroxenes, clinopyroxene and amphiboles) are common. We found metasomatic amphiboles, associated with metasomatic orthopyroxenes in C-type peridotites, although some amphiboles are possibly primary because of their coarse size and lack of association with the other metasomatic minerals (Fig. 3a and b) (Ishimaru *et al.* 2007). Phlogopite is absent except in one metasomatized C-type harzburgite (Ishimaru *et al.* 2007). Avacha peridotites also have hornblendite selvages surrounding xenoliths, but almost all of them are not related to the amphiboles of the inner part of peridotites (Arai *et al.* 2003; Ishimaru *et al.* 2007).

We found Al-poor calcic amphiboles, tremolites and Al-poor magnesio-hornblendes (after Leake *et al.* 1997), in two F-type peridotites (samples 672 and 166) as well as in a metasomatically formed orthopyroxene-rich vein crosscutting a C-type peridotite (sample 530). We describe each xenolith in detail below.

Highly metasomatized F-type peridotite; sample 672

This sample is composed of fine minerals (Fig. 2a and b), and some chromian spinels are fragmented and stretched. The grain-size distribution is

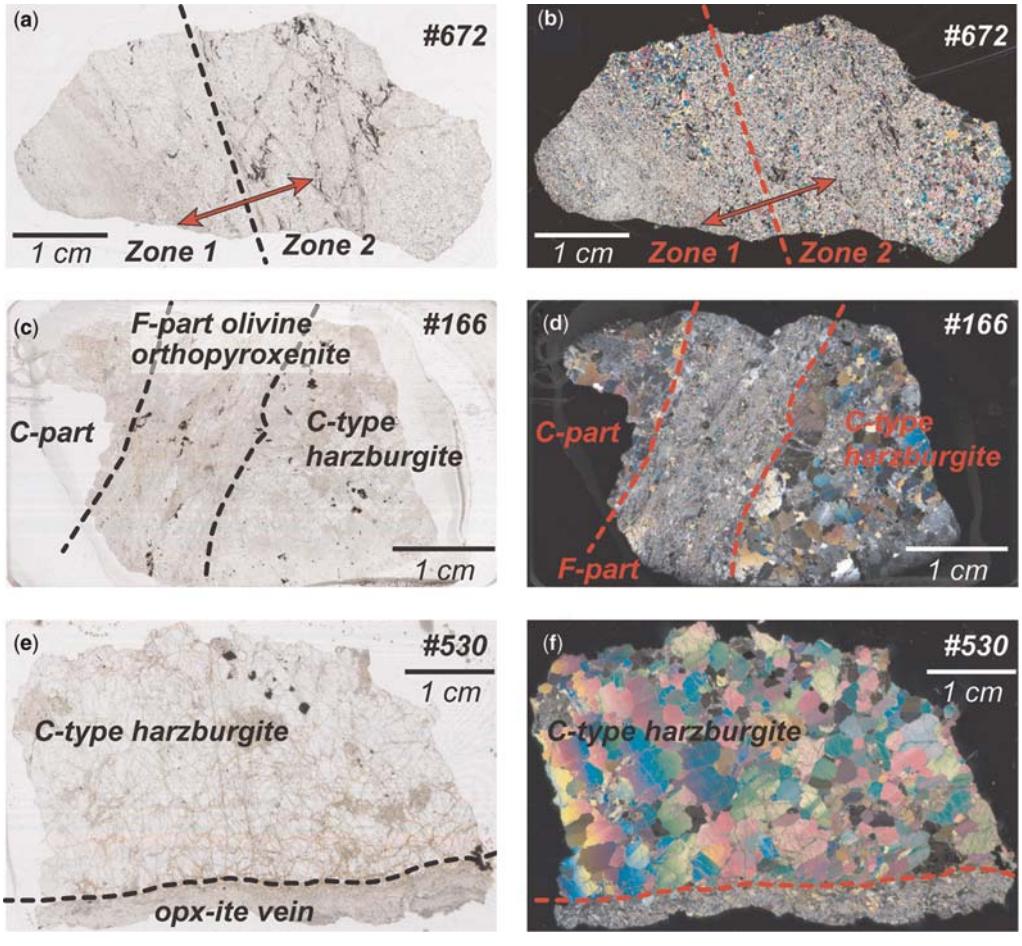

Fig. 2. Scanned images of thin sections. (**a**) plane-polarized light (PPL) image of F-type spinel peridotite (sample 672). The extremely fine grain sizes of minerals and the fluid trails of stretched chromian spinel aggregates (black) should be noted. The thin-section area is divided into two portions (Zones 1 and 2) in terms of chemistry. (**b**) Cross-polarized light (XPL) image of (a). (**c**) PPL image of a xenolith composed of coarse-grained (C-type) and fine-grained (F-type) peridotites (sample 166). (**d**) XPL image of (c). (**e**) PPL image of C-type spinel harzburgite with an orthopyroxenite (opx-ite) vein (sample 530). (**f**) XPL image of (e).

heterogeneous; some parts are composed of relatively coarse minerals (*c*. 0.5 mm), and other parts of fine minerals (<10 μm) (Fig. 2b). Modal proportions of minerals are also highly variable, from websteritic to dunitic lithologies, and we divided this sample into two zones on the basis of their major-element mineral chemistry (Fig. 2a and b). Details of mineral chemistries will be described in the 'Major-element compositions of minerals' section.

Zone 1 is composed of fine grains (up to 0.5 mm, but mostly less than 0.1 mm across) of clinopyroxene, orthopyroxene, chromian spinel, amphiboles, and minor amounts of olivine, and shows a mosaic texture (Fig. 3c). Clinopyroxene is the most dominant phase in this zone, and orthopyroxene and amphiboles could be observed interstitial to clinopyroxenes. The modal proportions of minerals are highly variable from websterite through lherzolite and/or wehrlite to dunite, and amounts of olivine seem to increase toward Zone 2. There are no exsolution lamellae in pyroxenes (Fig. 3c). Some grains of tremolite were discovered in this zone. Chromian spinels are coarser than other minerals, and form fragmented and elongated aggregates, although disseminated fine spinel grains are also observed in this zone (Fig. 3c and d). Backscattered electron images of chromian spinels strongly suggest that they are composed of two phases: the darker phase surrounds or cuts the brighter phase with sharp boundaries (Fig. 3d).

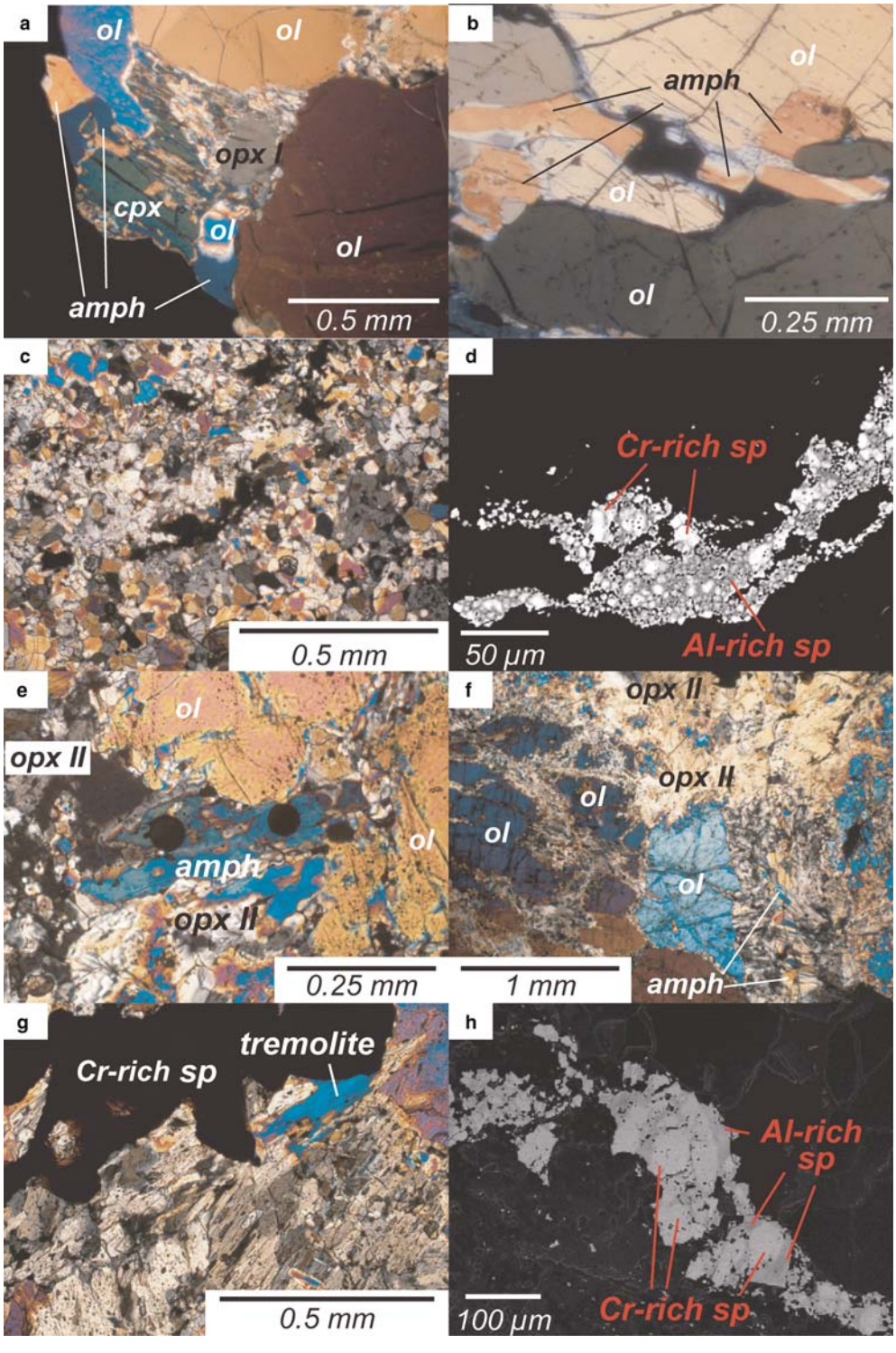

Fig. 3. (*Continued*)

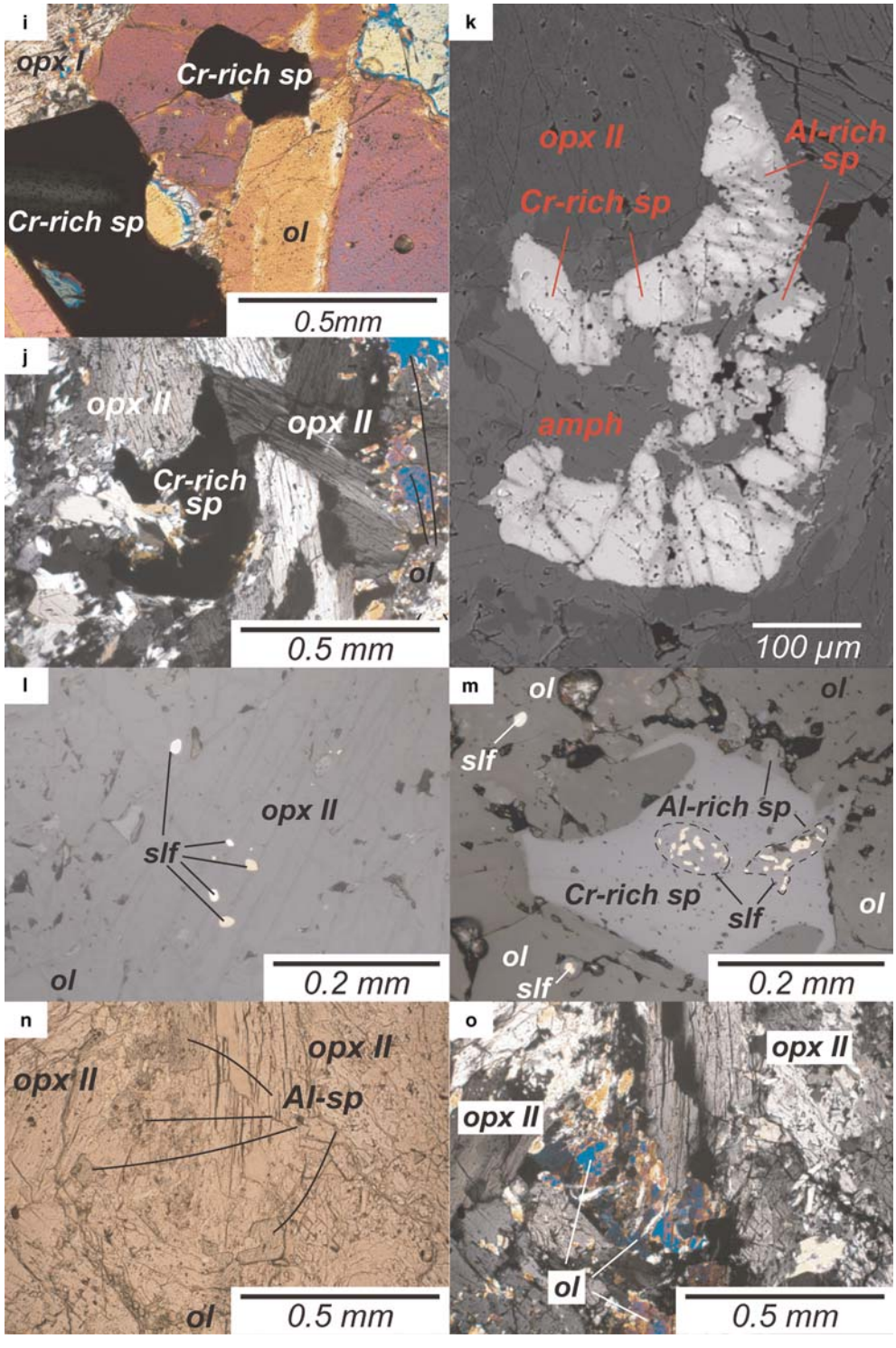

Fig. 3. (*Continued*)

In Zone 2, minerals are almost the same as in Zone 1 except for the absence of calcic amphiboles in the former. Minerals are coarser in Zone 2 than in Zone 1, and there are some metasomatic veins, composed of metasomatic orthopyroxenes replacing olivine with or without clinopyroxenes (Fig. 2a and b). The metasomatic orthopyroxenes sometimes show radial aggregation replacing olivine, and are the same as those typically observed in the metasomatized C-type peridotites (Arai *et al.* 2003; Ishimaru *et al.* 2007). Chromian spinels form irregular trails, and their modal amounts are higher in Zone 2 than in Zone 1 (Fig. 2a). Some olivine grains are kinked, but neither kinking nor exsolution was observed in pyroxenes.

Composite xenolith of C-type and F-type peridotites; sample 166

This sample is composed of coarse-grained and fine-grained parts (C-part and F-part, respectively) with high amounts of secondary orthopyroxenes forming radial aggregates (Fig. 2c and d). There are several metasomatic orthopyroxenite veins cutting older textures (Fig. 3f), and the amphiboles were precipitated at the centre of some orthopyroxenite veins (Fig. 3f).

The C-part is spinel harzburgite that contains coarse orthopyroxene grains with minor amounts of clinopyroxene and amphiboles, and some of the grains are more than 1 mm across (Fig. 2c). Olivines are kinked and some contain subgrains, which are almost equal in size (around 0.2 mm). Chromian spinels are opaque and have subhedral shapes. Almost all primary orthopyroxenes are recrystallized along their margins, and some contain exsolution lamellae of clinopyroxene. Clinopyroxenes are free from exsolution lamellae and kinking. Amphiboles are frequently associated with metasomatic orthopyroxenes (see Fig. 3e–g). Several grains of tremolite and Al-poor magnesio-hornblende are observed (Fig. 3e and g), and we found Al-poor magnesio-hornblende (tremolitic hornblende) at the rim of edenite (Table 1; Fig. 3e).

The F-part is almost olivine orthopyroxenite, containing some amounts of clinopyroxene and amphibole, and the olivine varies in size from 1.0 mm to less than 0.1 mm (Fig. 3f). Olivine-rich zones form islands in the F-part olivine orthopyroxenite, being elongated almost parallel to the direction of boundaries between the C-part and F-part (Fig. 2d). Almost all orthopyroxene grains are possibly of metasomatic origin; they form radial aggregates or are recrystallized (Fig. 3f). The orthopyroxene is coarser than olivine, and has neither exsolution lamellae nor kinking. Some orthopyroxenes clearly formed at the expense of relatively coarse olivine (Fig. 3f). Chromian spinels are opaque and some grains are fragmented and stretched (Fig. 2c). Some spinels in the F-part of this sample have peculiar zoning (Fig. 3h), such as the chromian spinel in sample 672 (Fig. 3d), observed by backscattered electron imaging. The darker part partly surrounds the brighter part (Fig. 3h).

C-type peridotite with an orthopyroxenite vein; sample 530

This sample is basically a coarse-grained and slightly metasomatized peridotite, with a thick

Fig. 3. Photomicrographs of Avacha peridotite xenoliths. All are transmitted XPL images, except (d), (h) and (k), which are backscattered electron images of chromian spinel with unusual zoning, (n), which is a transmitted PPL image, and (l) and (m), which are reflected PPL images. ol, olivine; opx I, primary orthopyroxene; opx II, metasomatic orthopyroxene; cpx, clinopyroxene; amph, hornblende; sp, spinel; slf, sulphides. (**a**) Discrete primary amphibole in C-type spinel harzburgite (sample 200). (**b**) Primary amphibole in C-type spinel harzburgite (sample 200). (**c**) Fine-grained websteritic mineral assemblages in Zone 1 of F-type peridotite (sample 672). The minerals are mainly orthopyroxene, clinopyroxene and amphiboles with minor olivine, and chromian spinel is elongated (see (d)). (**d**) Backscattered electron image of chromian spinel, observed at the centre of (c). Spinel has brighter and darker parts, corresponding to Cr-rich and Al-rich zones respectively. (**e**) Relatively coarse hornblende grain in C-type part of sample 166. Two black spots were made by laser shot in *in situ* trace-element analysis. The optical zoning of hornblende, where the rim (greenish) has lower Al_2O_3 content than the core (bluish), should be noted. (**f**) Transition zone between C-type and F-type parts in sample 166. Coarse olivine grains are partly replaced by metasomatic orthopyroxene, sometimes forming a vein, and by metasomatic hornblende (at centre right). (**g**) Tremolite associated with chromian spinel in F-type part of sample 166. (**h**) Backscattered electron image of chromian spinel with unusual zoning in F-type part of sample 166. (**i**) Harzburgite zone of sample 530 with opaque subhedral chromian spinel. (**j**) Anhedral chromian spinel with optical inhomogeneity in orthopyroxene vein of sample 530. (**k**) Backscattered electron image of chromian spinel in the centre of (j). Brighter and darker parts correspond to Cr-rich and Al-rich zone, respectively. The Al-rich zone containing fluid inclusions has cut the Cr-rich spinel as veinlets. (**l**) Globular sulphide blebs in secondary orthopyroxenes of the orthopyroxenite vein of sample 530. (**m**) Sulphide blebs associated with spinels, especially aluminous ones, in the orthopyroxenite vein of sample 530. (**n**) Aluminous spinel in the orthopyroxene vein of sample 530. The spinels are pale green in colour and are closely associated with olivines. (**o**) XPL image of (n).

orthopyroxenite vein (*c*. 5 mm) (Fig. 2e and f). The peridotite part is spinel harzburgite, composed of olivine, orthopyroxene, chromian spinel, and minor amounts of clinopyroxene and hornblende, which varies from edenite to magnesio-hornblende (Leake *et al.* 1997). Olivines and orthopyroxenes are kinked (Figs 2f and 3i). Some orthopyroxenes have exsolution lamellae of clinopyroxene, and are recrystallized. Chromian spinels are opaque and have subhedral shapes (Fig. 3i).

At the boundary zone between the orthopyroxenite vein and spinel harzburgite host, there are numerous sulphide globules (Fig. 3l and m), and the wall olivine is replaced by metasomatic orthopyroxenes (Fig. 3j). The orthopyroxenite vein is composed of orthopyroxene, amphiboles, clinopyroxene, spinels, and minor amounts of olivine and sulphide. All silicate minerals are kinked in this orthopyroxenite vein, and the orthopyroxenes sometimes form radial aggregates. We found two kinds of spinel, opaque and pale green, in thin section (Fig. 3j, n and o). The opaque spinel is chromian and the green spinel is aluminous spinel, which is formed around the chromian spinel or embedded in olivine as inclusion (Fig. 3j, k and m–o). Chromian spinels, especially the parts with darker backscattered image, rarely contain many sulphide globules (Fig. 3m). Olivines are fine and frequently replaced by metasomatic orthopyroxenes, and are frequently dusty because of the inclusions of fine green spinel and fluids (Fig. 3n and o). Clinopyroxenes are usually small and exhibit long prismatic shapes intergrown with orthopyroxene. Amphiboles have prismatic shapes and sometimes have cleavage planes crossing at 120°. There are some tremolite and Al-poor magnesio-hornblende grains in this orthopyroxenite vein.

Mineral chemistry

Analytical methods

We used an electron microprobe JXA8800 (JEOL) at the Center for Cooperative Research of Kanazawa University for major-element analyses of minerals. Analytical conditions were 20 kV accelerating voltage, 20 nA probe current and 3 μm probe diameter for ordinary analyses, and 15 kV accelerating voltage, 20 nA probe current and focused probe diameter of <1 μm for analysis of minerals in the specific samples (672, 166 and 530). Ferrous and ferric iron contents in chromian spinel were determined by calculation, based on spinel stoichiometry. Trace-element concentrations in minerals were determined by laser ablation inductively coupled plasma mass spectrometry (LA-ICP-MS), using a GeoLas Q-Plus, MicroLas LA system coupled with an Agilent 7500s, Yokogawa Analytical Systems ICP-MS system. The laser-spot diameter was 50 μm for clinopyroxenes and amphiboles, and 100 μm for orthopyroxenes. The energy of laser ablation was 5 Hz and 8 J cm^{-2}. The NIST 612 standard glass was used for calibration with Si as an internal standard. Details of the analytical methods have been described by Ishida *et al.* (2004) and Morishita *et al.* (2005).

Major-element compositions of minerals

Summary for C-type and F-type peridotites. The peridotite xenoliths from Avacha volcano, Kamchatka, are depleted in basaltic components (Arai *et al.* 2003). Fo contents of the C-type olivine vary slightly from one sample to another (Fo = 90.5–92.0), but there is no obvious intragrain chemical zonation (Arai *et al*. 2003) (Fig. 4). Chemical variations of chromian spinels are not very large (Fig. 5); Mg-number (=Mg/(Mg + Fe^{2+}) atomic ratio) and Cr-number (=Cr/(Cr + Al) atomic ratio) vary from 0.53 to 0.71 and from 0.52 to 0.74, respectively. There are chemical variations in major elements of orthopyroxenes, between primary and metasomatic ones (Arai *et al.* 2003; Ishimaru *et al.* 2007), but Mg-numbers (=Mg/(Mg + Fe) atomic ratios) of orthopyroxenes (Fig. 6) are almost the same as or slightly higher (0.90–0.93) than those of coexisting olivines. Major-element concentrations of clinopyroxenes show similar depletion, being low in TiO_2, Al_2O_3 and Na_2O and high in MgO (see Fig. 7). Amphiboles in C-type peridotites are variable in chemistry from pargasite through edenite to magnesio-hornblende, and have relatively high Mg-numbers (0.89–0.92). We identified primary amphiboles in C-type peridotites from Avacha volcano, and the primary hornblendes have slightly higher contents of Al_2O_3 and TiO_2, on average, than the metasomatic ones (see Table 1; Fig. 8).

Chemical features of F-type peridotite vary from one sample to another from relatively FeO*-rich to MgO-rich; the range of Fo content of olivine in F-type peridotites is 90.8–93.3 (Fig. 4). There are wide variations in major-element concentrations of chromian spinel in F-type peridotites, and the Cr-numbers and Mg-numbers differ from sample to sample (0.18–0.84 and 0.57–0.81, respectively) (Fig. 5). Pyroxenes in F-type peridotites have similar chemical features to those observed in C-type peridotites, and the orthopyroxenes are especially similar in chemistry to the metasomatic ones in C-type peridotites. Sulphide globules are sometimes observed and are identified as monosulphide solid solution (MSS) with Fe:Ni atomic ratios of around 2 : 1.

Table 1. *Representative microprobe analyses of amphiboles in C-type peridotites (samples 200 and 227) and tremolite-bearing peridotite xenoliths (samples 672, 166 and 530) from Avacha volcano, Kamchatka*

Sample no:	200		227	672								
	C-type harzburgite		in opx vein	Zone 1 (websterite–lherzolite–wehrlite–dunite part)								
Point:	7-1	11-1	5-1	1-1	1-2	1-3	3-4	5-1	6-1	9-1	32-1	34-1
Amph-type:	edenite	edenite	edenite	tremolite	mg-hb	mg-hb	mg-hb	tremolite	mg-hb	tremolite	tremolite	edenite
SiO_2	46.7	47.2	48.1	54.2	48.1	47.6	51.6	56.2	50.6	56.3	56.6	47.8
TiO_2	0.32	0.55	0.05	0.02	0.09	0.06	0.04	0.02	0.05	0.03	0.00	0.13
$Al2O_3$	11.8	11.2	10.6	4.10	10.1	9.87	7.19	3.83	9.00	2.64	3.58	11.4
$Cr2O_3$	0.59	1.58	0.14	1.13	2.29	2.07	1.44	0.29	0.86	0.43	0.31	1.16
FeO*	3.8	3.82	3.49	1.09	1.52	1.50	1.35	1.33	2.00	1.92	1.41	2.94
MnO	0.04	0.07	0.05	0.03	0.05	0.03	0.05		0.02	0.03		0.03
MgO	19.5	19.4	19.8	22.5	20.4	20.2	21.5	23.5	21.4	22.8	23.7	19.7
CaO	11.9	11.2	11.9	12.1	12.1	11.6	12.1	12.7	12.1	11.5	12.5	12.4
Na_2O	2.34	2.25	2.24	0.79	1.67	1.77	1.26	0.73	1.61	0.54	0.76	2.04
K_2O	0.23	0.20	0.23	0.14	0.40	0.33	0.22	0.05	0.18	0.06	0.06	0.26
NiO	0.12	0.10	0.15	0.16	0.17	0.15	0.16	0.12	0.06	0.13	0.12	0.13
Total	97.4	97.6	96.8	96.2	97.0	95.2	97.0	98.8	97.9	96.4	99.1	98.0
Mg-no.	0.901	0.900	0.910	0.974	0.960	0.960	0.966	0.969	0.950	0.955	0.968	0.923
Cations (O = 23)												
Si	6.596	6.643	6.796	7.535	6.761	6.799	7.178	7.600	6.991	7.780	7.633	6.671
Ti	0.034	0.058	0.005	0.002	0.009	0.006	0.004	0.002	0.005	0.003	0.000	0.014
Al	1.954	1.860	1.770	0.673	1.674	1.660	1.178	0.610	1.466	0.429	0.568	1.876
Cr	0.066	0.176	0.016	0.124	0.254	0.234	0.158	0.031	0.094	0.047	0.033	0.128
Fe*	0.451	0.450	0.412	0.126	0.178	0.179	0.156	0.150	0.232	0.222	0.159	0.343
Mn	0.005	0.009	0.006	0.004	0.006	0.004	0.006	0.000	0.002	0.004	0.000	0.003
Mg	4.099	4.068	4.162	4.670	4.278	4.301	4.456	4.736	4.403	4.696	4.748	4.103
Ca	1.800	1.683	1.795	1.795	1.821	1.775	1.806	1.837	1.794	1.708	1.808	1.862
Na	0.639	0.613	0.612	0.212	0.455	0.490	0.341	0.192	0.431	0.144	0.197	0.551
K	0.042	0.036	0.041	0.024	0.072	0.060	0.038	0.009	0.032	0.011	0.011	0.046
Ni	0.014	0.011	0.017	0.017	0.019	0.017	0.018	0.013	0.007	0.015	0.013	0.014
Total	15.701	15.606	15.632	15.183	15.529	15.524	15.339	15.178	15.456	15.057	15.170	15.612
ol Mg-no.†	0.911	0.911	*0.921*	*0.963*	*0.963*	*0.963*	0.960	0.960	0.948	0.933	0.954	0.936
sp Cr-no.‡	–	–	–	0.505	0.505	0.505	0.593	–	0.299	0.737	–	–
sp Cr-no.§										0.545		

*Total iron given as FeO.
†Mg-number of co-existing olivine within 1mm distance; italic values are for orthopyroxene when olivine is absent.
‡High Cr-numbers of two co-existing zoned spinels within 1mm distance.
§Low Cr-numbers of two co-existing zoned spinels within 1mm distance.

Highly metasomatized F-type peridotite; sample 672. As described above, we divided sample 672 into two zones based on mineral composition; major-element chemical variations of minerals are wide in Zone 1 and relatively narrow in Zone 2 (see Figs 4 and 5). In Zone 1, minerals show a wide range of extremely high Mg-numbers (Figs 4–7). Both clinopyroxenes and orthopyroxenes have the highest Mg-number (up to 0.98 and up to 0.97, respectively) in the area most distant from the boundary of Zones 1 and 2, which is websterite in lithology. Olivines have low NiO contents (as low as 0.3 wt%) in Zone 1 relative to the olivine–mantle array (Takahashi 1986), and show a negative correlation between the NiO and Fo contents (from 0.31 wt% at Fo_{95} to 0.43 wt% at Fo_{92}). We found peculiar chemical zonation in chromian spinels coexisting with the high-Mg-number pyroxenes (see Fig. 3b). The lighter core has higher Cr-number (*c.* 0.63) than the darker rim (*c.* 0.49), whereas the calculated Fe^{3+} contents are the same. The chromian spinels have higher Mg-numbers in Zone 1 than in Zone 2 at given Cr-numbers (Fig. 5), and fine spinels have lower Cr-numbers and higher Mg-numbers than relatively coarse ones even within Zone 1. Orthopyroxenes in Zone 1 have

166						530					
C-type harzburgite			F-part olivine orthopyroxenite			peridotite part		orthopyroxenite vein			
3-1-1_core edenite	3-1-2_rim mg-hb	5-1 tremolite	6-1 edenite	10-1 edenite	10-2 edenite	3-1-1_core mg-hb	3-1-2_rim edenite	5-2 tremolite	5-3 edenite	8-2-1 tremolite	8-2-2 mg-hb
48.4	53.3	55.0	46.4	49.0	48.5	50.8	48.9	55.4	47.1	56.6	51.5
0.06	0.01	0.00	0.14	0.14	0.17	0.10	0.14	0.04	0.12	0.00	0.06
9.38	4.98	3.36	12.3	9.95	10.4	7.54	8.71	4.55	12.75	2.18	7.53
1.23	0.72	0.73	0.01	0.00	0.01	1.73	1.85	0.01	0.04	0.06	0.07
3.39	2.74	2.59	3.86	4.64	4.33	3.17	3.37	2.10	2.80	1.91	2.49
0.05	0.03	0.03	0.06	0.16	0.15	0.03	0.05	0.06	0.03	0.00	0.01
20.3	22.1	22.6	19.8	20.7	20.4	20.8	20.2	22.6	19.9	23.4	21.3
12.2	12.0	12.2	11.7	10.8	11.2	12.3	12.0	12.6	12.7	12.2	12.4
2.07	1.31	0.95	2.48	2.17	2.09	1.87	2.01	0.71	1.83	0.43	1.17
0.23	0.12	0.05	0.20	0.12	0.12	0.03	0.18	0.15	0.20	0.06	0.20
0.13	0.10	0.09	0.15	0.14	0.17	0.10	0.10	0.12	0.10	0.10	0.10
97.4	97.4	97.7	97.0	97.7	97.5	98.4	97.5	98.4	97.6	97.0	96.8
0.914	0.935	0.940	0.901	0.888	0.894	0.921	0.914	0.951	0.927	0.956	0.939
6.818	7.398	7.587	6.561	6.856	6.803	7.051	6.878	7.548	6.584	7.784	7.180
0.007	0.001	0.000	0.015	0.015	0.018	0.011	0.015	0.004	0.012	0.000	0.006
1.557	0.814	0.546	2.054	1.640	1.721	1.232	1.444	0.729	2.100	0.353	1.238
0.137	0.079	0.079	0.001	0.000	0.001	0.189	0.206	0.001	0.004	0.006	0.008
0.399	0.318	0.298	0.456	0.543	0.507	0.367	0.396	0.239	0.327	0.219	0.290
0.006	0.004	0.004	0.007	0.019	0.018	0.004	0.006	0.007	0.004	0.000	0.001
4.252	4.557	4.648	4.161	4.304	4.260	4.286	4.221	4.593	4.142	4.799	4.435
1.834	1.787	1.798	1.767	1.611	1.676	1.822	1.813	1.843	1.902	1.800	1.846
0.565	0.352	0.255	0.680	0.588	0.567	0.504	0.549	0.188	0.495	0.114	0.316
0.042	0.021	0.009	0.035	0.021	0.022	0.005	0.033	0.026	0.036	0.010	0.035
0.014	0.011	0.010	0.017	0.016	0.019	0.011	0.011	0.013	0.012	0.011	0.012
15.631	15.341	15.232	15.755	15.614	15.612	15.482	15.572	15.191	15.617	15.098	15.367
0.919	0.919	0.917	0.926	0.920	0.920	0.909	0.909	0.940	0.940	*0.937*	*0.937*
–	–	0.654	–	–	–	–	–	0.000	0.000	–	–

wide variations in Mg-number (0.93–0.97), but with constant Al_2O_3 and CaO. The major-element chemical variations of orthopyroxene are almost the same for Zones 1 and 2, except for the lower Mg-numbers in Zone 2 than in Zone 1 (Fig. 6). Olivines in Zone 2 have almost the same NiO content as low as the lowest-Fo olivine in Zone 1 (0.36–0.43 wt%). Clinopyroxenes have low TiO_2 (mostly <0.05 wt%) and Na_2O (0.01–0.16 wt%) contents, and are noticeably high in Al_2O_3 (up to 2.8 wt%) for their high Mg-numbers (0.95) (Fig. 7). All the amphiboles examined are calcic amphiboles (Leake *et al.* 1997), but are variable from edenite to tremolite (Leake *et al.* 1997) (Table 1). The Fe-numbers (Fe-number $=$ 1 $-$ Mg-number) of amphiboles are correlated positively with alkaline contents (Na + K) and Al, and negatively with Si (Fig. 8a–c). TiO_2 contents in amphiboles are low (<0.15 wt%) (Fig. 8d). We can see positive correlations for Fe-number between amphiboles and coexisting olivine or clinopyroxene (Fig. 8e and f).

Composite xenolith of C-type and F-type peridotites; sample 166. Minerals have higher Mg-numbers in C-type olivine orthopyroxenite than in C-type harzburgite, and the chemical variations of olivine and spinel are not large within each part (Figs 4 and 5). Minerals in C-type harzburgite have the same chemical variations as in ordinary C-type peridotites (Figs 4 and 5). NiO contents of olivine in both C-type harzburgite and F-type olivine orthopyroxenite are varied, exhibiting a negative correlation with the Fo content (from 0.30 wt% at Fo_{93} to 0.48 wt% at Fo_{91}). Some chromian spinels in F-type olivine orthopyroxenite have the same chemical zoning as observed in sample 672 (see Fig. 3d and h), and the compositional gap is also almost the same as in sample 672; the darker zone

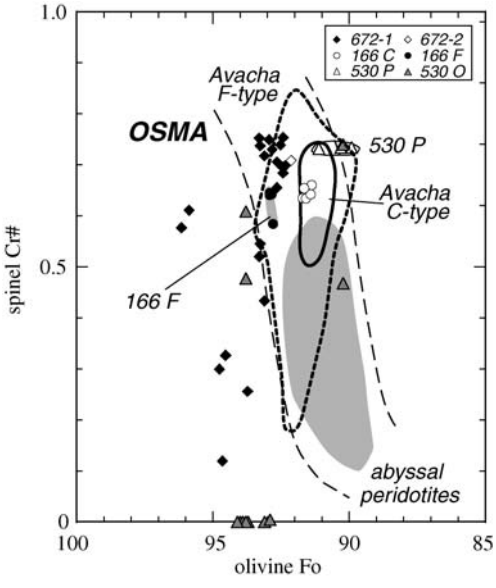

Fig. 4. Relationships between Fo contents of olivine and Cr/(Cr + Al) ratios (=Cr-number) of chromian spinel in tremolite-bearing peridotite xenoliths (samples 672, 166 and 530) from Avacha volcano, Kamchatka. OSMA, olivine–spinel-mantle array as a residual trend of spinel peridotites (Arai 1994). Shaded area represents abyssal peridotites (Arai 1994). Bold continuous line and bold dashed line show the chemical variations of C-type and F-type peridotites from Avacha, respectively. It should be noted that some olivines coexist with low-Cr-number spinels. 672-1 and 672-2 are Zone 1 and Zone 2, respectively, of sample 672; 166 C and 166 F are the C-type part spinel harzburgite and the F-type part olivine orthopyroxenite, respectively, of sample 166; 530 P and 530 O are the spinel harzburgite part and orthopyroxenite vein, respectively, of sample 530.

has lower Cr-number and higher Mg-number (0.36 and 0.75) than the brighter zone (0.64 and 0.66). However, there is no obvious chemical zoning in spinels in the C-type part of the xenolith.

All amphiboles are calcic, and vary from pargasite to tremolite (Leake *et al.* 1997) (Fig. 8a and b). One edenite in the C-type part has an Al-poor magnesio-hornblende rim (Fig. 3 g), and Al_2O_3 and alkali ($Na_2O + K_2O$) contents decrease from 9.4 to 5.0 wt% and from 2.3 to 1.4 wt%, respectively, and Mg-numbers increase from 0.91 to 0.94, from the core to rim (Table 1). All the amphiboles in the F-type part are edenite, and the Al_2O_3 contents are higher than those in the C-type part, varying only from 10.0 to 13.1 wt% (Table 1). Amphiboles have lower Fe-number and Si contents in the C-type than in the F-type part (Fig. 8).

C-type peridotite with an orthopyroxenite vein; sample 530. Fo contents of olivine in the harzburgite part are lower (90.3–91.2) than in ordinary C-type peridotites, but are rather high (up to 94.1) in the orthopyroxenite vein (Fig. 4). Some olivines in the orthopyroxenite vein have low NiO contents (down to 0.17 wt%) with high Fo contents (up to 94), and the low-NiO olivines are closely associated with the Al-spinels (see Fig. 3n and o). The Cr-number of spinel in the harzburgite part is high (0.73), and is equivalent to the highest Cr-number of spinels in ordinary C-type peridotites (Figs 4 and 5). It is noteworthy that there are Al-spinels almost free of Cr_2O_3 (<0.4 wt%) in the orthopyroxenite vein (Fig. 3n and o). We could find chromian spinels also in the orthopyroxene vein, and some of them are rimmed and veined by Al-rich spinels (Fig. 3j, k and m). The Al-rich spinels surrounding chromian spinel have lower Cr-number and higher Mg-number (0.32–0.41 and 0.75–0.78, respectively) than the core (0.61–0.65 and 0.67–0.68) (see Fig. 3 k and m). The Mg-number range of orthopyroxenes is almost the same as that of olivines (0.90–0.92) both in the harzburgite part and orthopyroxenite vein, and the Mg-numbers are higher in the orthopyroxenite vein than in the harzburgite part. The Al_2O_3 contents of orthopyroxene are higher in the orthopyroxenite vein than in the harzburgite part (Fig. 6), although those of clinopyroxene are almost the same in both parts (Fig. 7). The variations of CaO content in orthopyroxenes and Na_2O contents of clinopyroxene are also the same for the orthopyroxenite vein and harzburgite part (Figs 6 and 7), although the Mg-numbers are higher in the orthopyroxenite vein than in the harzburgite part.

Amphiboles in the harzburgite part vary from edenite to magnesio-hornblende, and the TiO_2 contents are low (<0.15 wt%) (Fig. 8d). On the other hand, amphiboles in the orthopyroxenite vein are highly varied from pargasite to tremolite (Fig. 8a). The tremolites (or Al-poor magnesio-hornblende) and edenite sometimes coexist within a few millimetres. The Fe-numbers of amphiboles are correlated positively with Al or alkali (Na + K) contents, and negatively with Si contents in the orthopyroxenite vein (Fig. 8). The TiO_2 contents and Fe-numbers are also low (<0.15 wt% and 0.05–0.09, respectively) in these amphiboles (Fig. 8d).

Trace-element concentrations in minerals

We determined trace-element concentrations of metasomatic minerals (i.e. orthopyroxenes, clinopyroxenes and amphiboles) in the tremolite- (or Al-poor magnesio-hornblende)-bearing samples (166 and 530). REE patterns of clinopyroxenes are slightly enriched in light REE (LREE) relative to middle REE (MREE) (Fig. 9a). Trace-element

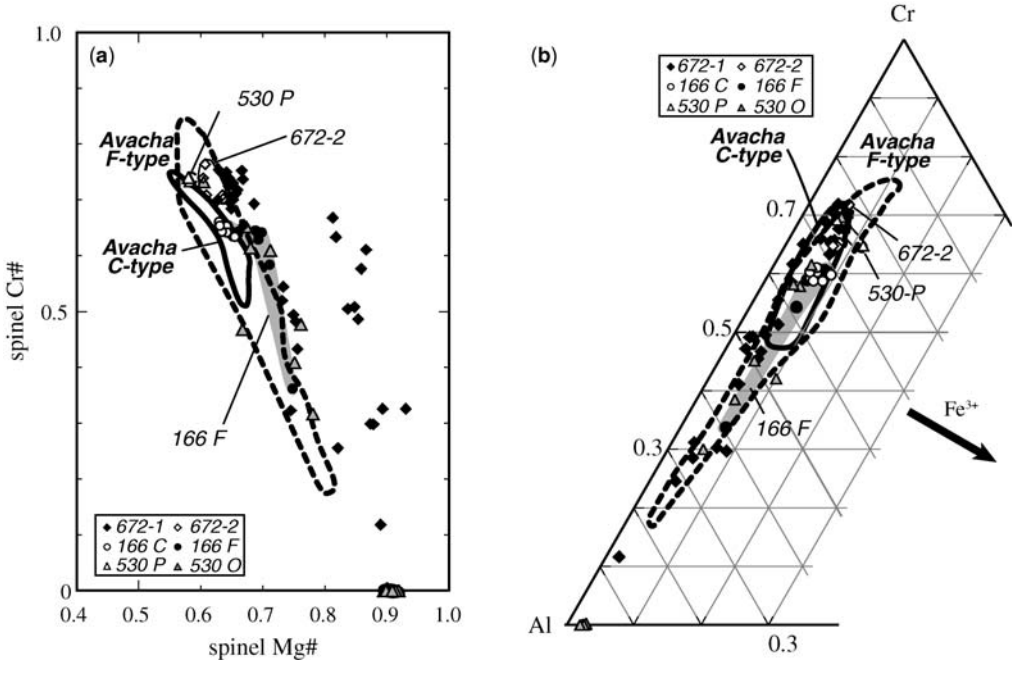

Fig. 5. Chemical variations of spinels in tremolite-bearing peridotite xenoliths (samples 672, 166 and 530) from Avacha volcano, Kamchatka. (**a**) Relationships between the Mg-number (= $Mg/(Mg + Fe^{2+})$) and Cr-number (=$Cr/(Cr + Al)$) of spinels. (**b**) Cr–Al–Fe^{3+} cation ratios of spinels. Bold continuous line and bold dashed line show the chemical variations of C-type and F-type peridotites from Avacha, respectively. It should be noted that some of the spinels examined have higher Mg-number and lower Cr-number than spinels in both C-type and F-type peridotites from Avacha. Abbreviations are as in Figure 4.

patterns of clinopyroxenes demonstrate positive spikes at Sr and Pb relative to neighbouring elements (Fig. 9b). $(La/Yb)_N$ (subscript N indicating normalization to primitive mantle values of McDonough & Sun 1995) and $(Sm/Yb)_N$ ratios of clinopyroxene are 0.49–0.53 and 0.16–0.22, respectively. The Nd/Yb ratio of clinopyroxenes in tremolite-bearing samples is rather high (0.61–0.67), reflecting relatively low Yb content (0.24–0.27 ppm) (Table 2). Orthopyroxenes are also enriched in heavy REE (HREE), and their REE patterns are flat from LREE from MREE (Fig. 9c). Trace-element patterns of orthopyroxenes have negative spikes at Sr for the F-type part of sample 166, but a weak positive Sr spike in the orthopyroxenite vein in sample 530 (Fig. 9d). Amphiboles in sample 166 are LREE-enriched, and their REE patterns have a positive anomaly at Eu (Fig. 9e). The amphiboles have lower concentrations of REE in the C-type than in the F-type part, and tremolite and Al-poor magnesio-hornblende have lower concentrations than other amphiboles in the F-type part (Fig. 9e). The REE patterns of amphiboles in the orthopyroxenite vein of sample 530 are almost identical to each other, showing LREE- and HREE-enriched patterns with positive spikes at Eu (Fig. 9g). The REE concentrations of amphiboles in sample 530 are almost the same as those of tremolite and Al-poor magnesio-hornblende in the F-type part of sample 166 (Fig. 9e and g). The trace-element patterns of amphiboles in sample 166 have positive spikes at Ba and U and negative spikes at Nb, Pb and Ti relative to neighbouring elements (Fig. 9f), although those of sample 530 have positive spikes at Pb and Sr (Fig. 9h). All the REE and trace-element patterns and their abundances in these metasomatic minerals from tremolite-bearing samples are similar to those from the metasomatic vein in a highly metasomatized sample 227, which is edenite-bearing, but free of tremolite (Fig. 9) (see Ishimaru *et al.* 2007).

Equilibrium conditions and thermometry

We estimated equilibrium temperatures by using the two-pyroxene geothermometer of Wells (1977), and found that they vary even within a single sample. The estimated equilibrium temperatures of Avacha peridotite xenoliths, both

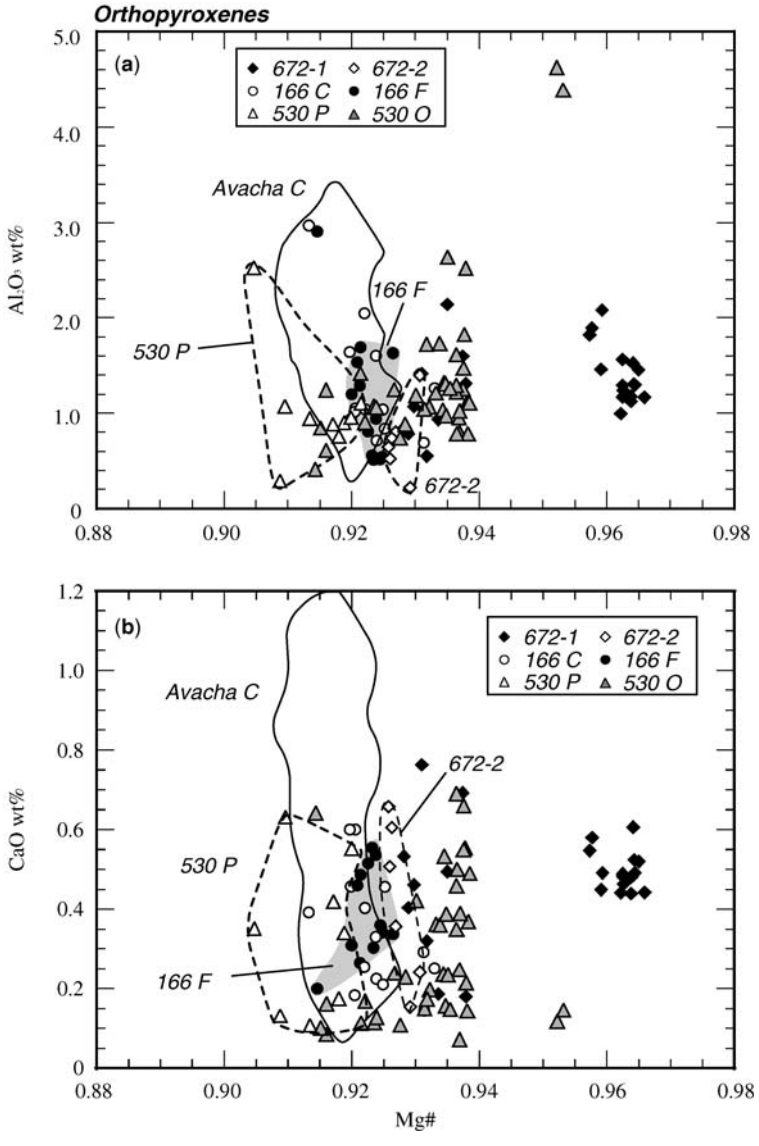

Fig. 6. Major-element chemical variations in orthopyroxenes of tremolite-bearing peridotite xenoliths (samples 672, 166 and 530) from Avacha volcano, Kamchatka. (**a**) Mg-number v. Al_2O_3 wt%. (**b**) Mg-number v. CaO wt%. Avacha C, distributions of clinopyroxene in C-type peridotites from Avacha volcano, Kamchatka. It should be noted that the orthopyroxenes in the examined samples have higher Mg-number on average than the primary ones in C-type peridotites from Avacha. Abbreviations are as in Figure 4.

metasomatized and unmetasomatized, vary from 850 to 1100 °C, and there is no appreciable difference between them (Arai *et al.* 2003; Ishimaru *et al.* 2007). The equilibrium temperatures in the tremolite-bearing samples are varied: they vary from 831 to 1081 °C in Zone 1 and from 886 to 953 °C in Zone 2 of sample 672, from 927 to 950 °C in the F-type part and from 886 to 958 °C in the C-type part of sample 166, and from 881 to 977 °C in the peridotite zone and from 798 to 971 °C in the orthopyroxenite vein of the sample.

The orthopyroxenite vein within sample 530 has the mineral assemblage olivine + orthopyroxene + clinopyroxene + spinel, where the silicates are highly magnesian (Figs 4, 6 and 7) and spinel is Cr-free (Figs 4 and 5). The xenolith was definitely derived from the spinel lherzolite stability field of the $CaO–MgO–Al_2O_3–SiO_2$ system (e.g. Kushiro

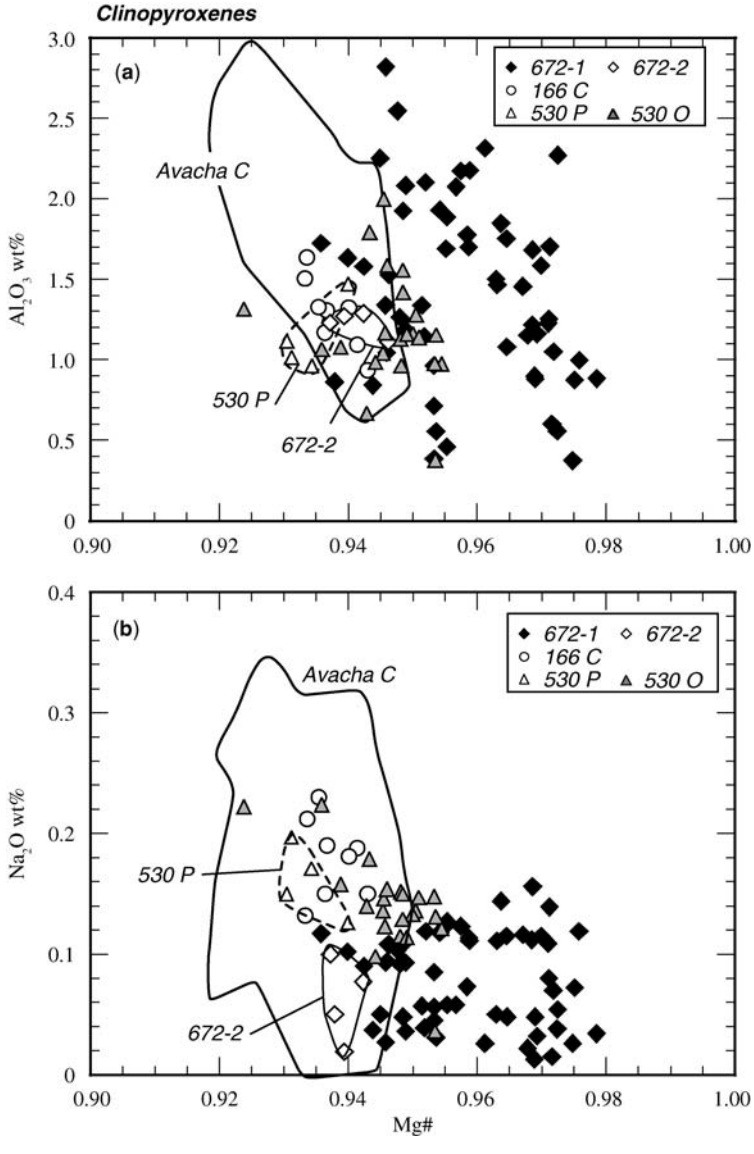

Fig. 7. Major-element chemical variations in clinopyroxenes in tremolite-bearing peridotite xenoliths (samples 672, 166 and 530) from Avacha volcano, Kamchatka. (**a**) Mg-number v. Al_2O_3 wt%. (**b**) Mg-number v. Na_2O wt%. Avacha C, distributions of clinopyroxene in C-type peridotites from Avacha volcano, Kamchatka. It should be noted that some clinopyroxenes are high in Mg-number relative to primary ones in C-type peridotites from Avacha. Abbreviations are as in Figure 4.

& Yoder 1966), and the equilibrium pressure is, therefore, 0.8–104 GPa if the temperature is around 1000 °C. Arai *et al.* (2003) referred to the spinel lherzolite stability field for a highly metasomatized fine-grained peridotite that contains a low-Cr-number (< 0.2) spinel, and the derivation depth might be shallower than 60 km. We calculated the redox state of the tremolite-bearing peridotite xenoliths from Avacha by using the oxygen barometer of Ballhaus *et al.* (1990, 1991). The calculated oxygen fugacities of tremolite-bearing peridotite xenoliths (samples 672, 166 and 530) assuming $P = 1.5$ GPa vary from -0.19 to $+1.35$ ($\Delta\log(fO_2)_{FMQ}$, where FMQ is the fayalite–magnetite–quartz buffer), and this range is almost the same as in primary peridotites ($\Delta\log(fO_2)_{FMQ} = -0.2$ to $+1.2$). The tremolite-bearing samples (672, 166 and 530) do not show high oxygen fugacity relative to

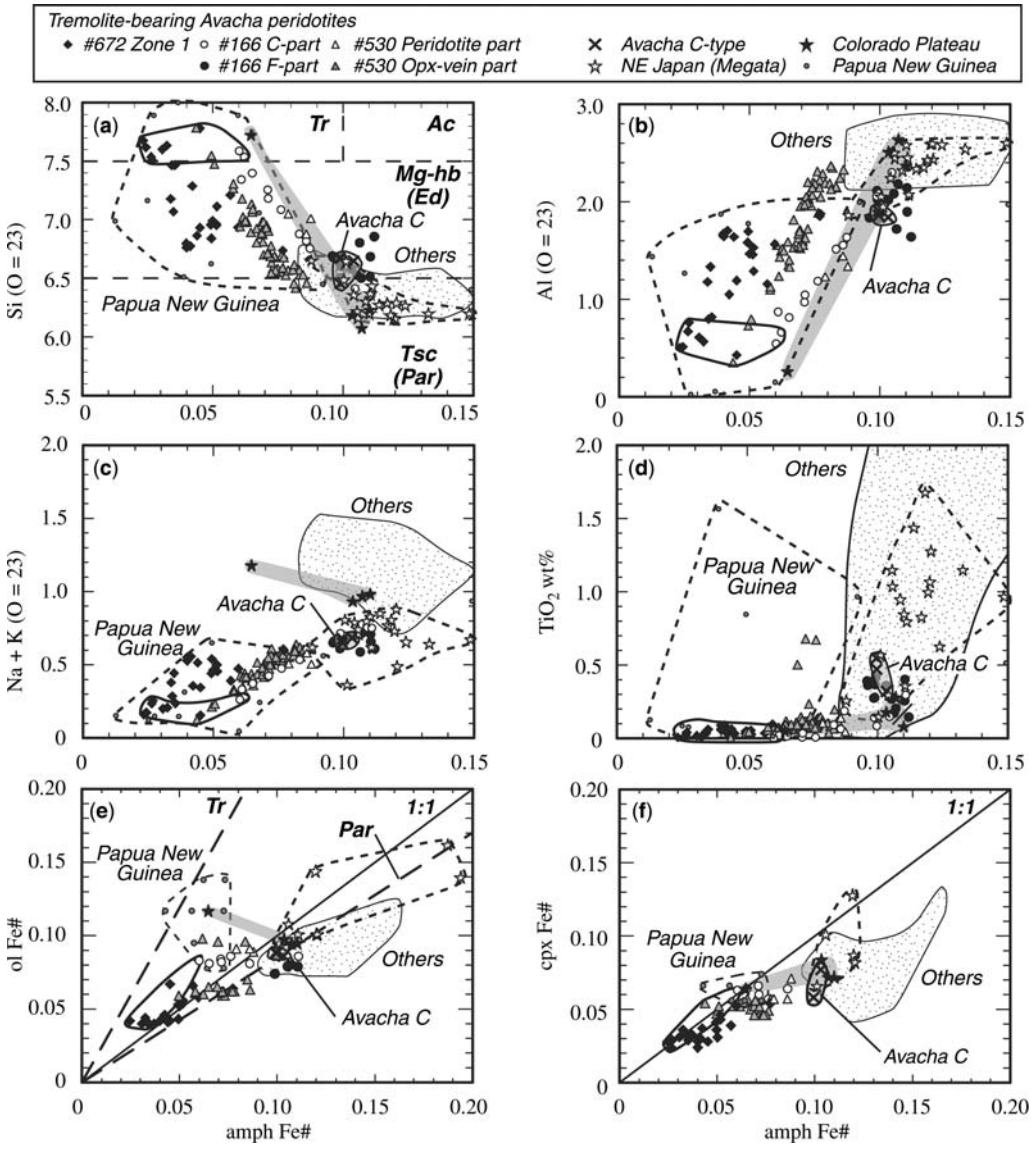

Fig. 8. Relationships between Fe-number (= Fe/(Fe + Mg) = 1 − Mg-number) of Ca-amphiboles in tremolite-bearing peridotite xenoliths (samples 672, 166 and 530) from Avacha volcano, Kamchatka and other chemical parameters. (**a**) Number of Si atoms per formula unit (p.f.u.) in Ca-amphiboles. Tr, tremolite; Ac, actinolite; Mg-hb, magnesio-hornblende; Ed, edenite; Tsc, tschermakite; Par, pargasite. Nomenclature is after Leake *et al*. (1997), and abbreviations in parentheses are for (Na +K) > 0.5 p.f.u. (**b**) Number of Al atoms (p.f.u.) in Ca-amphiboles. (**c**) Number of (Na +K) atoms (p.f.u.) in Ca-amphiboles. (**d**) TiO_2 contents of Ca-amphiboles. (**e**) Fe-number of olivines. Two dashed lines, labelled Tr and Par, indicate Mg–Fe distributions between olivine and tremolite and pargasite, respectively, in mantle-derived peridotites summarized by Evans (1982). (**f**) Fe-number of amphiboles v. Fe-number of clinopyroxenes. 'Avacha C' shows the field for primary amphiboles in C-type peridotites from Avacha. Distributions of amphiboles of the Colorado Plateau (Aoki *et al*. 1972; Smith 1979; Smith *et al*. 1999), Papua New Guinea (McInnes *et al.* 2001; Franz *et al.* 2002) and NE Japan (Megata volcano) (Aoki & Shiba 1973; Arai 1986; Abe *et al.* 1992, 1995) are shown for comparison. Dotted areas show the field for amphiboles from other arc-related areas: Nunivak (Francis 1976), Mexico (Blatter & Carmichael 1998), Patagonia (Gorring & Kay 2000; Laurora *et al.* 2001; Rivalenti *et al.* 2004*a*,*b*; Bjerg *et al.* 2005), and the Pannonian Basin (Szabó & Taylor 1994; Szabó *et al.* 1995; Vaselli *et al.* 1995; Zanetti *et al.* 1995). Continuous lines show the compositional field for tremolites from the Avacha peridotite xenoliths.

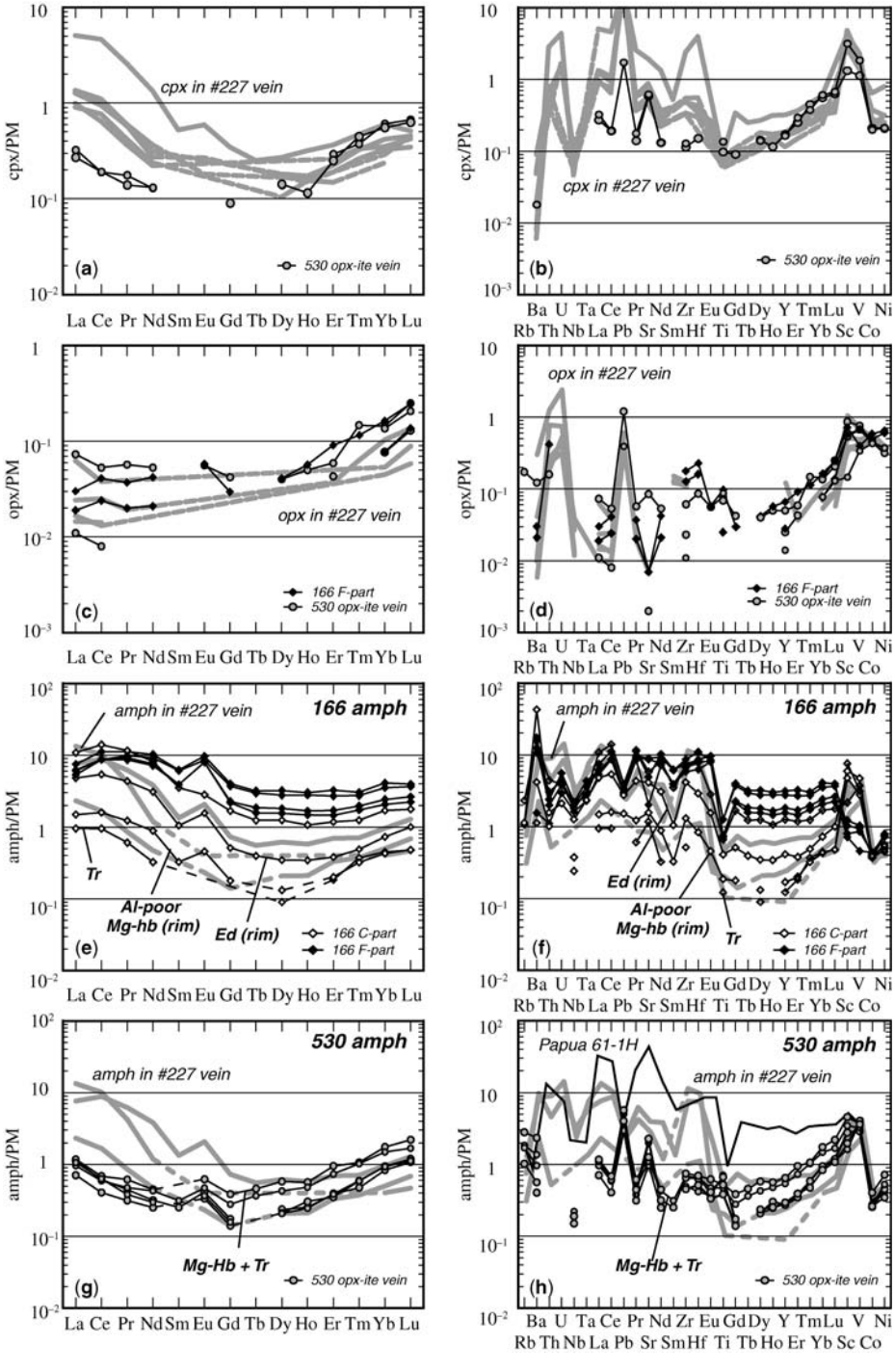

Fig. 9. Primitive mantle (PM)-normalized (McDonough & Sun 1995) REE and trace-element patterns of clinopyroxenes (**a**, **b**), orthopyroxenes (**c**, **d**) and amphiboles (**e**–**h**). Wide grey lines indicate the patterns of minerals in an orthopyroxenite vein of a highly metasomatized C-type spinel harzburgite xenolith (sample 227) from Avacha volcano, Kamchatka (see Ishimaru *et al.* 2007). Papua 61-1H is a pattern of metasomatic amphibole from Papua New Guinea (Grégoire *et al.* 2001). Abbreviations are as in Figure 8.

Table 2. *Minor- and trace-element concentrations (ppm) of minerals (clinopyroxenes, orthopyroxenes and amphiboles) determined by LA-ICP-MS in tremolite-bearing peridotite xenoliths (samples 166 and 530) from Avacha volcano, Kamchatka*

Sample no:	166									
	C-type harzburgite				F-type olivine orthopyroxenite					
Point: Mineral:	3-1-1_core edenite	3-1-2_rim mg-hb	3-2 pargesite	5-1 tremolite	6-1 edenite	6-2 edenite	10-1 edenite	10-2 edenite	6-1 opx	10-1 opx
Li	0.814	0.748	1.30	*D.L.*	1.01	1.00	1.32	1.05	0.618	0.668
B	17.3	17.9	119	16.5	9.76	9.03	13.2	17.8	7.36	8.86
Sc	97.3	77.4	35.1	124	19.8	16.7	11.6	13.1	9.27	11.6
Ti	496	226	802	147	872	1526	913	1529	29.6	117
V	388	229	306	257	85.4	78.2	37.5	70.6	55.6	32.4
Cr	8194	6389	1787	9084	341	37.4	63.9	30.1	381	41.8
Co	41.5	38.6	39.6	42.4	40.0	42.8	46.5	45.3	52.4	61.7
Ni	1053	950	1111	886	1420	1559	1432	1488	1176	1270
Rb	0.684	*D.L.*	1.397	*D.L.*	0.483	0.645	*D.L.*	0.470	*D.L.*	*D.L.*
Sr	82.6	31.3	116	23.5	173	178	40.3	98.7	0.142	0.130
Y	1.78	0.730	5.43	0.528	6.74	11.9	7.89	13.5	0.121	0.283
Zr	43.6	13.8	69.7	5.44	72.8	90.9	61.8	78.4	1.33	1.86
Nb	0.836	0.247	1.19	0.160	1.32	1.46	1.07	1.33	*D.L.*	*D.L.*
Ba	284	27.7	104	7.46	82.4	115	10.3	70.8	0.138	0.195
La	3.12	0.965	7.05	0.618	4.02	3.95	3.47	4.84	0.012	0.019
Ce	9.07	2.67	23.5	1.59	14.7	14.5	14.5	18.8	0.041	0.069
Pr	1.11	0.312	2.96	0.154	2.34	2.49	2.18	2.85	0.005	0.009
Nd	3.85	1.11	10.2	0.406	9.52	11.5	8.96	12.8	0.026	0.053
Sm	0.428	0.133	1.43	*D.L.*	1.58	2.48	1.58	2.54	*D.L.*	*D.L.*
Eu	0.240	0.070	0.436	*D.L.*	1.23	1.31	1.23	1.49	*D.L.*	0.009
Gd	0.278	0.097	0.912	*D.L.*	1.19	2.02	1.24	2.18	*D.L.*	0.016
Tb	0.039	*D.L.*	0.123	*D.L.*	0.157	0.293	0.183	0.316	*D.L.*	*D.L.*
Dy	0.234	0.089	0.839	0.061	1.05	1.87	1.22	2.18	*D.L.*	0.028
Ho	0.051	*D.L.*	0.160	*D.L.*	0.219	0.416	0.249	0.451	*D.L.*	0.009
Er	0.167	0.088	0.519	0.081	0.638	1.19	0.750	1.43	*D.L.*	0.040
Tm	0.033	0.022	0.085	0.025	0.118	0.186	0.134	0.207	*D.L.*	0.007
Yb	0.323	0.190	0.749	0.198	0.915	1.56	1.07	1.81	0.034	0.072
Lu	0.068	0.033	0.120	0.032	0.151	0.248	0.178	0.268	0.009	0.017
Hf	0.828	0.237	2.23	*D.L.*	2.27	3.12	1.77	2.42	0.045	0.064
Ta	0.088	*D.L.*	0.115	*D.L.*	0.133	0.161	0.085	0.103	*D.L.*	*D.L.*
Pb	0.414	0.229	0.589	*D.L.*	0.499	0.501	0.437	0.459	*D.L.*	*D.L.*
Th	0.126	0.081	0.353	*D.L.*	0.158	0.191	0.089	0.243	0.033	*D.L.*
U	0.043	*D.L.*	0.080	*D.L.*	0.077	0.113	0.060	0.089	*D.L.*	*D.L.*

D. L., Below detection limit.

the primary peridotite xenoliths from Avacha, although they are distinctly more oxidized than the abyssal peridotites ($\Delta\log(fO_2)_{FMQ} = -2.5$ to $+0.5$; Bryndzia & Wood, 1990).

Discussion

Chemical characteristics of calcic amphiboles from Avacha

Calcic amphiboles in peridotite xenoliths have been reported from numerous localities irrespective of tectonic settings, and they vary in chemistry from tremolite to kaersutite (e.g. Dawson & Smith 1982). Figure 8 compares the calcic amphiboles in the Avacha peridotite xenoliths (samples 672, 166 and 530) with those in other peridotite xenoliths from arc and related settings. Primary amphiboles in C-type peridotite xenoliths from Avacha have almost the same compositions as those in peridotite xenoliths from Megata volcano, NE Japan (Fig. 8). The calcic amphiboles in the tremolite-bearing peridotite xenoliths (samples 672, 166 and 530) from Avacha volcano have lower Fe-numbers and Si contents than those from other localities except Papua New Guinea and the Colorado Plateau (Fig. 8). Tremolite-bearing peridotite xenoliths have been reported also from these localities (Papua New Guinea, Franz *et al.* 2002; Colorado Plateau, Smith 1979). The calcic amphiboles of Avacha tremolite-bearing peridotite xenoliths have almost

530									
Orthopyroxenite vein									
1-2 cpx	4-2 cpx	3-1 opx	4-2 opx	10-1 opx	1-1 edenite	2-1 edenite	7-1 mg-hb	8-1 mg-hb	8-2 tr + mg-hb
1.11	1.01	0.682	0.932	0.946	1.52	1.57	1.05	1.18	1.47
12.3	9.52	9.27	18.0	25.9	12.7	11.1	8.60	14.5	42.8
50.5	21.3	2.37	8.74	14.0	26.4	32.0	45.1	56.2	74.3
162	117	105	82.9	94.6	855	810	463	570	629
150	91.7	27.9	54.9	62.1	321	331	239	270	298
688	193	*D.L.*	249	254	43.3	22.3	402	510	890
20.7	21.9	45.1	46.0	47.5	29.2	27.5	26.9	28.8	42.7
410	405	730	621	723	841	682	887	1,037	1,410
D.L.	*D.L.*	*D.L.*	*D.L.*	0.103	1.11	1.69	0.615	1.02	0.522
12.2	11.6	*D.L.*	0.049	1.69	40.1	45.4	19.6	22.1	25.2
0.702	0.733	0.061	0.107	0.214	1.23	1.27	1.18	2.34	2.80
1.35	1.19	0.116	0.245	0.638	5.19	6.84	4.77	7.25	7.86
D.L.	*D.L.*	*D.L.*	*D.L.*	0.009	0.135	0.153	0.099	0.145	0.126
0.116	*D.L.*	*D.L.*	*D.L.*	0.805	9.07	15.5	3.73	6.39	2.68
0.209	0.175	*D.L.*	0.007	0.047	0.688	0.726	0.459	0.624	0.761
0.318	0.319	*D.L.*	0.013	0.089	1.06	1.04	0.684	0.990	1.15
0.045	0.035	*D.L.*	*D.L.*	0.015	0.097	0.113	0.080	0.121	0.157
0.163	0.164	*D.L.*	*D.L.*	0.066	0.374	0.398	0.313	0.539	0.560
D.L.	*D.L.*	*D.L.*	*D.L.*	*D.L.*	*D.L.*	0.103	*D.L.*	0.127	0.115
D.L.	*D.L.*	*D.L.*	*D.L.*	0.009	0.056	0.064	0.052	0.073	0.096
D.L.	0.049	*D.L.*	*D.L.*	0.023	0.085	0.095	0.076	0.152	0.210
D.L.	*D.L.*	*D.L.*	*D.L.*	*D.L.*	*D.L.*	*D.L.*	*D.L.*	0.036	0.046
0.093	0.095	*D.L.*	*D.L.*	0.027	0.140	0.160	0.141	0.289	0.391
D.L.	0.017	*D.L.*	*D.L.*	0.007	0.037	0.038	0.045	0.072	0.084
0.127	0.110	*D.L.*	0.019	0.026	0.169	0.172	0.154	0.322	0.417
0.025	0.030	*D.L.*	*D.L.*	0.010	0.040	0.032	0.040	0.070	0.072
0.266	0.244	0.034	0.060	0.063	0.411	0.370	0.416	0.655	0.773
0.045	0.042	0.009	0.014	0.017	0.076	0.073	0.080	0.113	0.149
D.L.	*D.L.*	*D.L.*	*D.L.*	0.024	0.118	0.180	0.146	0.185	0.198
D.L.	*D.L.*	*D.L.*	*D.L.*	*D.L.*	*D.L.*	*D.L.*	*D.L.*	*D.L.*	*D.L.*
0.256	*D.L.*	*D.L.*	*D.L.*	0.180	0.759	0.857	0.438	0.446	0.604
D.L.	*D.L.*	*D.L.*	*D.L.*	0.013	*D.L.*	*D.L.*	*D.L.*	*D.L.*	*D.L.*
D.L.	*D.L.*	*D.L.*	*D.L.*	*D.L.*	*D.L.*	*D.L.*	*D.L.*	*D.L.*	*D.L.*

the same chemical compositions as those of Papuan xenoliths (Fig. 8), except for Mg–Fe partitioning with olivine and clinopyroxene (Fig. 8e and f). Some of the tremolites from Papua New Guinea and the Colorado Plateau show the Mg–Fe partitioning with olivine almost equivalent to the low-temperature pairs in ordinary solid intrusive peridotites (Fig. 8e; Evans 1982). In contrast to this, the tremolite–olivine pairs from the Avacha xenoliths show apparent partition coefficients closer to unity, suggesting higher equilibration temperatures, than the Papuan pairs on average (Fig. 8e).

The tremolites and other Al-poor amphiboles exhibit lower REE contents than Al-rich ones (edenites and pargasites) in the Avacha peridotites (Fig. 9), suggesting a systematic variation of REE contents of the metasomatic agents involved. It is noteworthy that a calcic amphibole from a Papuan peridotite xenolith (No. 61-1H; Gregoire *et al.* 2001) is very similar to Al-rich amphiboles in sample 166 from Avacha (Fig. 9f), indicating a similarity in chemical signature of metasomatic agents between the two localities.

Genesis of calcic amphiboles in the Avacha peridotites

The C-type peridotite xenoliths from Avacha have been metasomatized to various extents by SiO_2-rich aqueous fluids (and melt), related to the subducting slab (Arai *et al.* 2003; Ishimaru *et al.* 2007). The F-type peridotite xenoliths have also undergone metasomatism, and metasomatic

orthopyroxenes replacing olivine are observed extensively (Arai *et al.* 2003). The calcic amphiboles, especially tremolites, described in this paper, were found only in highly metasomatized parts of the peridotite xenoliths (samples 672, 166 and 530) from Avacha volcano (see Fig. 3 g). A relatively low-temperature condition is indispensable for tremolite formation in the upper mantle. The upper stability limit of tremolite is 830 °C at 1 GPa and 850 °C at 2 GPa (Boyd 1959), or is lower than 800 °C at these pressures in association with olivine (e.g. Jenkins 1983). The tremolites in Papuan peridotite xenoliths are metasomatic and were observed in the core of plagioclase in metasomatized plagioclase lherzolite, and have low equilibrium temperatures (720–780 °C) (Franz *et al.* 2002). On the other hand, the tremolites from the Colorado Plateau peridotite xenolith have high Na_2O contents (up to 3.8 wt%), and were interpreted as the result of reaction of spinel, clinopyroxene and an aqueous fluid at low temperature (below 700 °C) (Smith 1979). In contrast, two-pyroxene equilibrium temperatures recorded in the tremolite-bearing Avacha peridotite xenoliths are higher than the stability limits; some highly metasomatized peridotites including Zone 1 of sample 672 have equilibrium temperatures higher than 1000 °C. This may indicate a type of 'retrogressive' formation of the tremolites within the Avacha peridotites after the main stage of high-temperature metasomatism.

The other important point for the tremolite formation in the Avacha peridotites is the bulk chemistry. The tremolite-bearing part of the Avacha peridotites is characterized by very high Mg-numbers of its minerals (Figs 4–8). Alkali contents are very low, but CaO and SiO_2 contents are high because these rocks are rich in pyroxenes and amphiboles (e.g. Fig. 3c, e–l, n and o). Interestingly, the Cr-number of spinel is very low (Figs 4 and 5) even though Mg-numbers of silicates are high. High-Mg-number, low-alkali bulk compositions may facilitate the formation of tremolitic amphiboles. With a deficiency of alkalis, tremolite exhibits very limited solid solution toward tschermakite even in association with aluminous spinel and orthopyroxene as in the case of Avacha samples (e.g. sample 530; Figs 3 k, n and 4) (Jenkins 1988). With a decrease of Mg-number natural tremolites show an increase tschermakite molecules (Cao *et al.* 1986).

Implications for mantle-wedge processes beneath a volcanic front

The intense metasomatism of peridotite xenoliths from Avacha volcano, Kamchatka, may be representative of active metasomatism of the mantle wedge beneath the volcanic front by fluids (or melts) released from the subducting slab (Arai *et al.* 2003; Ishimaru *et al.* 2007). The prominent mantle metasomatism recorded by peridotite xenoliths from Lihir volcano, Papua New Guinea (Grégoire *et al.* 2001; McInnes *et al.* 2001; Franz *et al.* 2002) and Iyara volcano, Philippines (Vidal *et al.* 1989; Maury *et al.* 1992; Arai *et al.* 2004) has exactly the same situation. The metasomatized peridotites from Avacha are rich in metasomatic pyroxenes formed at the expense of olivine, indicating metasomatic addition of silica (pyroxenes). The predominance of clinopyroxene over orthopyroxene in association with calcic amphiboles in sample 672 may also indicate addition of calcium. The metasomatic agent should have been rich in aluminium, because Cr-free Al-rich spinel was precipitated with metasomatic silicates (Fig. 3n and o) or Al-rich spinel overgrew fragmented chromian spinel (Fig. 3d, h and k). Relatively low alkali contents of calcic amphiboles (Fig. 8c) and the near absence of phlogopite indicate low alkali contents of the metasomatic agent involved. The drastic increase of Mg-number in the metasomatized peridotite possibly indicates subtraction of iron during the metasomatism.

A sulphur-bearing silicic melt (e.g. Métrich *et al.* 1999) is the most suitable candidate for such a metasomatic agent. It can extract Fe or Ni from olivine to leave the high-Mg-number, or low-Ni olivine, and precipitate pyroxenes at the expense of olivine. Sporadic globular MSS (Fig. 3l and m), which is commonly observed in metasomatized peridotites from Avacha (Arai *et al.* 2003), is a precipitate from the interacted melt. Extraction or precipitation of Fe-rich sulphide at the expense of fayalite component may raise fO_2 through the reaction $Fe_2SiO_4 + 0.5S_2 = FeS + FeSiO_3 + 0.5O_2$ (Gaetani & Grove 1999). The overall high fO_2 in the metasomatized peridotites from Avacha (Arai *et al.* 2003; Ishimaru *et al.* 2007) is consistent with this interpretation (see de Hoog *et al.* 2001). Sulphur possibly plays an important role in controlling the redox state of magmas and their source within the mantle wedge (e.g. Hattori *et al.* 2002; de Hoog *et al.* 2004). Deficiency of alkalis may require early-stage precipitation of phlogopites and amphiboles; for example, just above the slab (e.g. Tatsumi 1986). The silicic melt probably had almost the same chemical characteristics as those of the metasomatized peridotite xenoliths from Lihir, Papua New Guinea because of the similarity between metasomatic minerals in the Avacha peridotites and Papua New Guinean peridotites (Fig. 9), where the metasomatic agent was considered to be slab-derived fluids (Grégoire *et al.* 2001; Franz *et al.* 2002).

This type of metasomatism can produce metasomatic peridotites or pyroxenites with aluminous spinels within the upper mantle (Fig. 4). The Mg-number of silicates is expected to be covariant with the Cr-number of spinel through upper mantle processes. However, some highly magnesian peridotites and pyroxenites have highly aluminous spinels, or aluminous spinel rocks are observed associated with magnesian peridotites (e.g. Rajesh *et al.* 2004). The nature of the agent to form high-Mg-number, low-Cr-number ultramafic rocks has not been clear to date, but slab-derived melts are one of the possible candidates (e.g. Franz & Wirth 2000).

Summary and conclusions

(1) Avacha peridotite xenoliths contain tremolite grains in highly metasomatized zones, composed of metasomatic orthopyroxene, clinopyroxene and chromian spinel (rarely aluminous spinel) and minor amounts of olivine and sulphide. The two-pyroxene thermometer of Wells (1977) yields temperatures of mostly 900–1000 °C but rarely >1000 °C, beyond the stability limit of tremolite. This indicates retrogressive formation of tremolite after the thermal peak of high-temperature metasomatism.

(2) The tremolite-bearing part is characterized by high Mg-number and high pyroxene (silica) contents, suggesting removal of iron and addition of silica on metasomatism. The metasomatism added CaO but not alkalis. The tremolites were produced in the high-Mg-number and low-alkali environment at high temperatures relative to those in peridotite xenoliths from Papua New Guinea and the Colorado Plateau.

(3) The metasomatic agent is slab-derived sulphur-bearing silicic melt, which is common within the mantle wedge. This allows subtraction of iron from olivine with precipitation of pyroxenes and amphiboles. This interpretation is consistent with the overall high fO_2 of metasomatized peridotites from Avacha.

(4) This metasomatism can produce high-Mg-number peridotites and pyroxenites with low-Cr-number spinels within the upper mantle where the Mg-number of silicates is covariant with the Cr-number of spinel.

The samples used in this paper were mainly collected by K. Kadoshima and A. Koyanagi in field research in 2000. The ICP-MS system was installed in the course of research of the 21st-Century COE project 'Environmental Monitoring and Prediction of Long- and Short-Term Dynamics of Pan-Japan Sea Area: Construction of Monitoring Network and Assessment of Human Effects' led by K. Hayakawa, Kanazawa University. Y. Ishida assisted us in LA-ICP-MS analysis. K. Tazaki helped us to use the electron microprobe at the Center for Cooperative Research, Kanazawa University, and T. Morishita, J. Uesugi and Y. Shimizu assisted us in microprobe analysis. We are grateful to S. Duggen and Cs. Szabó for their critical comments and to M. Coltorti for his editorial handling.

References

ABE, N., ARAI, S. & SAEKI, Y. 1992. Hydration processes in the arc mantle; petrology of the Megata peridotite xenoliths, the Northeast Japan arc. *Journal of Mineralogy, Petrology and Economic Geology*, **87**, 305–317 [in Japanese with English abstract].

ABE, N., ARAI, S. & NINOMIYA, A. 1995. Peridotite xenoliths and essential ejecta from the Ninomegata crater, the Northeastern Japan arc. *Journal of Mineralogy, Petrology and Economic Geology*, **90**, 41–49 [in Japanese with English abstract].

AOKI, K. & SHIBA, I. 1973. Pargasites in lherzolite and websterite inclusions from Itinome-gata, Japan. *Journal of the Japanese Association of Mineralogists, Petrologists and Economic Geologists*, **68**, 303–310.

AOKI, K., FODER, R. V., KEIL, K. & DOWTY, E. 1972. Tremolite with high richterite-molecule content in kimberlite from Buell Park, Arizona. *American Mineralogist*, **57**, 1889–1893.

ARAI, S. 1986. K/Na variation in phlogopite and amphibole of upper mantle peridotites due to fractionation of the metasomatizing fluids. *Journal of Geology*, **94**, 436–444.

ARAI, S. 1994. Characterization of spinel peridotites by olivine–spinel compositional relationships: review and interpretation. *Chemical Geology*, **113**, 191–204.

ARAI, S., KIDA, M., ABE, N., NINOMIYA, A. & YUMUL, G. P., JR 1996. Classification of peridotite xenoliths in calc-alkaline andesite from Iraya volcano, Batan Island, the Philippines, and its genetical implications. *Science Reports of Kanazawa University*, **41**, 25–45.

ARAI, S., ISHIMARU, S. & OKRUGIN, V. M. 2003. Metasomatized harzburgite xenoliths from Avacha volcano as fragments of mantle wedge of the Kamchatka arc: Implication for the metasomatic agent. *Island Arc*, **12**, 233–246.

ARAI, S., TAKADA, S., MICHIBAYASHI, K. & KIDA, M. 2004. Petrology of peridotite xenoliths from Iraya volcano, Philippines, and its implication for dynamic mantle-wedge processes. *Journal of Petrology*, **45**, 369–389.

ARAI, S., ABE, N. & ISHIMARU, S. 2007. Mantle peridotites from the Western Pacific. *Gondwana Research*, **11**, 180–199.

BALLHAUS, C., BERRY, R. F. & GREEN, D. H. 1990. Oxygen fugacity controls in the Earth's upper mantle. *Nature*, **348**, 437–440.

BALLHAUS, C., BERRY, R. F. & GREEN, D. H. 1991. High pressure experimental calibration of the olivine–orthopyroxene–spinel oxygen geobarometer: implications for the oxidation state of the upper mantle. *Contributions to Mineralogy and Petrology*, **107**, 27–40.

BJERG, E. A., NTAFLOS, T., KURAT, G., DOBOSI, G. & LABUDÍA, C. H. 2005. The upper mantle beneath

Patagonia, Argentina, documented by xenoliths from alkali basalts. *Journal of South American Earth Sciences*, **18**, 125–145.

BLATTER, D. L. & CARMICHAEL, I. S. E. 1998. Hornblende peridotite xenoliths from central Mexico reveal the highly oxidized nature of subarc upper mantle. *Geology*, **26**, 1035–1038.

BOYD, F. R. 1959. Hydrothermal investigations of amphiboles. *In*: ABELSON, P. H. (ed.) *Researches in Geochemistry*. Wiley, New York, 377–396.

BRAITSEVA, O. A., BAZANOVA, L. I., MELEKESTSEV, I. V. & SULERZHITSKIY, L. D. 1998. Large Holocene eruptions of Avacha volcano, Kamchatka (7200–3500 ^{14}C years B.P.). *Volcanology and Seismology*, **20**, 1–27.

BRYNDZIA, L. T. & WOOD, B. J. 1990. Oxygen thermobarometry of abyssal spinel peridotites: the redox state and C–O–H volatile composition of the Earth's suboceanic upper mantle. *American Journal of Science*, **290**, 1093–1116.

CAO, R.-I., ROSS, C. & ERNST, W. G. 1986. Experimental studies to 10 kb of the bulk composition tremolite$_{50}$ – tschermakite$_{50}$ + excess H_2O. *Contributions to Mineralogy and Petrology*, **93**, 160–167.

DAWSON, J. B. & SMITH, J. V. 1982. Upper-mantle amphiboles: a review. *Mineralogical Magazine*, **45**, 35–46.

DE HOOG, J. C. M., MASON, P. R. D. & VAN BERGEN, M. J. 2001. Sulfur and chalcophile elements in subduction zones: constraints from a laser ablation ICP-MS study of melt inclusions from Galunggung Volcano, Indonesia. *Geochimica et Cosmochimica Acta*, **65**, 129–146.

DE HOOG, J. C. M., HATTORI, K. H. & HOBLITT, R. P. 2004. Oxidized sulfur-rich mafic magma at Mount Pinatubo, Philippines. *Contributions to Mineralogy and Petrology*, **146**, 750–761.

EVANS, B. W. 1982. Amphiboles in metamorphosed ultramafic rocks. *In*: VEBLEN, D. R. & RIBBE, P. H. (eds) *Amphiboles: Petrology and Experimental Phase Relations*. Mineralogical Society of America, Reviews in Mineralogy, **9B**, 98–113.

FRANCIS, D. M. 1976. The origin of amphibole in lherzolite xenoliths from Nunivak Island, Alaska. *Journal of Petrology*, **17**, 357–378.

FRANZ, L. & WIRTH, R. 2000. Spinel inclusions in olivine of peridotite xenoliths from TUBAF seamount (Bismarck Archipelago/Papua New Guinea): evidence for the thermal and tectonic evolution of the oceanic lithosphere. *Contributions to Mineralogy and Petrology*, **140**, 283–295.

FRANZ, L., BECKER, K.-P., KRAMER, W. & HERZIG, P. M. 2002. Metasomatic mantle xenoliths from the Bismarck microplate (Papua New Guinea)—Thermal evolution, geochemistry and extent of slab-induced metasomatism. *Journal of Petrology*, **43**, 315–343.

GAETANI, G. A. & GROVE, T. L. 1999. Wetting of mantle olivine by sulfide melt: implications for Re/Os ratios in mantle peridotite and late-stage core formation. *Earth and Planetary Science Letters*, **169**, 147–163.

GORBATOV, A., KOSTOGLODOV, V., SUÁREZ, G. & GORDEEV, E. 1997. Seismicity and structure of the Kamchatka subduction zone. *Journal of Geophysical Research*, **102**, 17883–17898.

GORRING, M. L. & KAY, S. M. 2000. Carbonatite metasomatized peridotite xenoliths from southern Patagonia: implications for lithospheric processes and Neogene plateau magmatism. *Contributions to Mineralogy and Petrology*, **140**, 55–72.

GRÉGOIRE, M., MCINNES, B. I. A. & O'REILLY, S. Y. 2001. Hydrous metasomatism of oceanic sub-arc mantle, Lihir, Papua New Guinea Part 2. Trace element characteristics of slab-derived fluids. *Lithos*, **59**, 91–108.

HATTORI, K., ARAI, S. & CLARKE, B. 2002. Selenium, tellurium, arsenic and antimony contents in primary mantle sulphides. *Canadian Mineralogist*, **40**, 637–650.

ISHIDA, Y., MORISHITA, T., ARAI, S. & SHIRASAKA, M. 2004. Simultaneous *in-situ* multi-element analysis of minerals on thin section using LA-ICP-MS. *Science Report of Kanazawa University*, **48**, 31–42.

ISHIMARU, S., ARAI, S., ISHIDA, Y., SHIRASAKA, M. & OKRUGIN, V. M. 2007. Melting and multi-stage metasomatism in the mantle wedge beneath a frontal arc inferred fron highly depleted peridotite xenoliths from the Avacha volcano, southern Kamchatka. *Journal of Petrology*, **48**, 395–433.

JENKINS, D. M. 1983. Stability and composition relations of calcic amphiboles in ultramafic rocks. *Contributions to Mineralogy and Petrology*, **83**, 375–384.

JENKINS, D. M. 1988. Experimental study of the join tremolite–tschermakite: a reinvestingaion. *Contributions to Mineralogy and Petrology*, **99**, 392–400.

KUSHIRO, I. & YODER, H. S. 1966. Anorthite–forsterite and anorthite–enstatite reactions and their bearing on the basalt–eclogite transformation. *Journal of Petrology*, **7**, 337–362.

LAURORA, A., MAZZUCCHELLI, M., RIVALENTI, G., VANNUCCI, R., ZANETTI, A., BARBIERI, M. A. & CINGOLANI, C. A. 2001. Metasomatism and melting in carbonated peridotite xenoliths from the mantle wedge: the Gobernador Gregores case (Southern Patagonia). *Journal of Petrology*, **42**, 69–87.

LEAKE, B. E., WOOLLEY, A. R., ARPS, C. E. S., *ET AL.* 1997. Nomenclature of amphiboles. Report of the subcommittee on amphiboles of the International Mineralogical Association Commission on new minerals and mineral names. *European Journal of Mineralogy*, **9**, 623–651.

MAURY, R. C., DEFANT, M. J. & JORON, J.-L. 1992. Metasomatism of the sub-arc mantle inferred from trace elements in Philippine xenoliths. *Nature*, **360**, 661–663.

MCDONOUGH, W. F. & SUN, S.-S. 1995. The composition of the Earth. *Chemical Geology*, **120**, 223–253.

MCINNES, B. I. A., GRÉGOIRE, M., BINNS, R. A., HERZIG, P. M. & HANNINGTON, M. D. 2001. Hydrous metasomatism of oceanic sub-arc mantle, Lihir, Papua New Guinea: petrology and geochemistry of fluid-metasomatised mantle xenoliths. *Earth and Planetary Science Letters*, **188**, 169–183.

MÉTRICH, N., SCHIANO, P., CLOCCHIATTI, R. & MAURY, R. C. 1999. Transfer of sulfur in subduction settings: an example from Batan Island (Luzon volcanic arc, Philippines). *Earth and Planetary Science Letters*, **167**, 1–14.

MINSTER, J. B., JORDAN, T. H., MOLNAR, P. & HAINES, E. 1974. Numerical modelling of instantaneous plate tectonics. *Geophysical Journal*, **36**, 541–576.

MORISHITA, T., ISHIDA, Y., ARAI, S. & SHIRASAKA, M. 2005. Determination of multiple trace element compositions in thin (<30 μm) layers of NIST SRM 614 and 616 using laser ablation-inductively coupled plasma-mass spectrometry (LA-ICP-MS). *Geostandards and Geoanalytical Research*, **29**, 107–122.

OZAWA, K. 1988. Ultramafic tectonite of the Miyamori ophiolitic complex in the Kitakami Mountains, Northeast Japan: hydrous upper mantle in an island arc. *Contributions to Mineralogy and Petrology*, **99**, 159–175.

RAJESH, V. J., ARIMA, M. & SANTOSH, M. 2004. Dunite, glimmerite and spinellite in Achankovil Shear Zone, South India: highly potassic CO_2-rich melt influx along an intra-continental shear zone. *Gondwana Research*, **7**, 961–974.

RIVALENTI, G., MAZZUCCHELLI, M., LAURORA, A., CIUFFI, S. I. A., ZANETTI, A., VANNUCCI, R. & CINGOLANI, C. A. 2004*a*. The backarc mantle lithosphere in Patagonia, South America. *Journal of South American Earth Sciences*, **17**, 121–152.

RIVALENTI, G., ZANETTI, A., MAZZUCCHELLI, M., VANNUCCI, R. & CINGOLANI, C. A. 2004*b*. Equivocal carbonatite markers in the mantle xenoliths of the Patagonia backarc: the Gobernador Gregores case (Santa Cruz Province, Argentina). *Contributions to Mineralogy and Petrology*, **147**, 647–670.

SMITH, D. 1979. Hydrous minerals and carbonates in peridotite inclusions from the Green Knobs and Buell Park kimberlitic diatremes on the Colorado Plateau. *In*: BOYD, F. R. & MEYER, H. O. A. (eds) *The Mantle Sample: Inclusions in Kimberlites and Other Volcanics*. American Geophysical Union, Washington, DC, 345–356.

SMITH, D., RITER, J. C. A. & MERTZMAN, S. A. 1999. Erratum to 'Water–rock interactions, orthopyroxene growth, and Si-enrichment in the mantle: evidence in xenoliths from the Colorado Plateau, southern United States'. *Earth and Planetary Science Letters*, **167**, 347–356.

SUGIMURA, A., MATSUDA, T. K., CHINZEI, K. & NAKAMURA, K. 1963. Quantitative distribution of late Cenozoic volcanic materials in Japan. *Bulletin Volcanologique*, **26**, 125–140.

SZABÓ, CS. & TAYLOR, L. A. 1994. Mantle petrology and geochemistry beneath the Nógrád–Gömör Volcanic Field, Carpathian–Pannonian Region. *International Geology Review*, **36**, 328–358.

SZABÓ, CS., VASELLI, O., VANNUCCI, R., BOTTAZZI, P., OTTOLINI, L., CORADOSSI, N. & KUBOVICS, I. 1995. Ultramafic xenoliths from the Little Hungarian Plain (Western Hungary): a petrologic and geochemical study. *Acta Vulcanologica*, **7**, 249–263.

TAKAHASHI, E. 1986. Origin of basaltic magmas—implications from peridotite melting experiments and an olivine fractionation model. *Bulletin of Volcanological Society of Japan*, **30**, S17–40 [in Japanese with English abstract].

TATSUMI, Y. 1986. Formation of the volcanic front in subduction zones. *Geophysical Research Letters*, **13**, 717–720.

TATSUMI, Y., FURUKAWA, Y., KOGISO, T., YAMANAKA, Y., YOKOYAMA, T. & FEDETOV, S. A. 1994. A third volcanic chain in Kamchatka: thermal anomaly at transform/convergence plate boundary. *Geophysical Research Letters*, **21**, 537–540.

VASELLI, O., DOWNES, H., THIRLWALL, M. *ET AL.* 1995. Ultramafic xenoliths in Plio-Pleistocene alkali basalts from the Eastern Transylvanian basin: depleted mantle enriched by vein metasomatism. *Journal of Petrology*, **36**, 23–53.

VIDAL, P., DUPUY, C., MAURY, R. & RICHARD, M. 1989. Mantle metasomatism above subduction zones: trace-element and radiogenic isotope characteristics of peridotite xenoliths from Batan Island (Philippines). *Geology*, **17**, 1115–1118.

WELLS, P. R. A. 1977. Pyroxene thermometry in simple and complex systems. *Contributions to Mineralogy and Petrology*, **62**, 129–139.

ZANETTI, A., VANNUCCI, R., OBERTI, R. & DOBOSI, G. 1995. Trace-element composition and crystal-chemistry of mantle amphiboles from the Carpatho-Pannonian region. *Acta Volcanologica*, **7**, 265–276.

Asthenospheric signature in fertile spinel lherzolites from the Viliga Volcanic Field in NE Russia

T. NTAFLOS[1], C. TSCHEGG[1], M. COLTORTI[2], V. V. AKININ[3] & J. KOSLER[4]

[1]*Department of Lithospheric Sciences, University of Vienna, Vienna, Austria (e-mail: theodoros.ntaflos@univie.ac.at)*

[2]*Department of Earth Sciences, University of Ferrara, 44100 Ferrara, Italy*

[3]*North East Interdisciplinary Scientific Research Institute, Magadan, Russia*

[4]*Department of Earth Science, University of Bergen, Bergen, Norway*

Abstract: Mantle xenolith bearing olivine melanephelinites from the Okhotsk sector of the Okhotsk–Chukotka Volcanic Belt (OCVB), northeastern Russia, occur as small isolated volcanoes emplaced within massive late Early to Late Cretaceous subduction-related calc-alkaline rocks. The xenoliths are typical medium- to fine-grained anhydrous mainly spinel lherzolites that are strongly to weakly foliated with intensive to minor recrystallization to equigranular texture. The primitive mantle normalized whole-rock REE have flat patterns or patterns with slightly elevated light REE (LREE) ($(La/Yb)_N = 0.48–1.38$). The REE in clinopyroxenes have systematically decreasing normalized abundances from Sm to La, implying that the LREE enrichments in the whole-rock REE patterns are attributed to circulation of minor intergranular fluids or melts. Equilibration temperatures and pressures calculated for the Viliga samples are in the range of 1050–1160 °C and 15–21 kbar, respectively. Ca diffusion rates in olivine reveal a rapid transport to the surface (2–6 days) of these peridotites. Model calculations have shown that the fertile lherzolites can be produced by 2–9% batch melting, whereas the depleted peridotites require 15% batch melting of a primitive source. The cessation of the interaction between the palaeo-Pacific plate and the NE Russian margin at *c*. 87 Ma apparently caused a 'piecemeal' collapse of the former followed by intrusion and ascent of olivine melanephelinitic magma, which entrained xenoliths from the asthenospheric mantle of the subducted plate during the Pliocene through the generated window(s). Moreover, clinopyroxenes that have low $^{87}Sr/^{86}Sr$ and high $^{143}Nd/^{144}Nd$ and plot in and above the mid-ocean ridge basalt (MORB) field are consistent with an upwelling asthenospheric mantle through the window(s) created by the 'piecemeal' collapse of the palaeo-Pacific plate.

Mantle xenoliths in alkali basalts emplaced in massive subduction-related calc-alkaline rocks are important rocks, as they could provide information about the nature of the lithospheric mantle wedge and the geochemical and metasomatic processes that occur in such tectonic settings. Fluids released from sediments of a downgoing subduction slab could cause modal metasomatism in the lithospheric mantle wedge, forming hydrous phases such as amphibole and phlogopite (Peacock 1993). Migration of melts produced by melting of a downgoing subduction slab can also affect the lithospheric mantle wedge, causing cryptic metasomatism, as has been demonstrated by Kilian & Stern (2002) for the Cerro Fraile mantle xenoliths in southernmost Patagonia and by Kepezhinskas *et al.* (1996) for the Valovayam Volcanic Field in the northern segment of Kamchatka arc xenoliths.

The mantle xenoliths from the Viliga River volcanic field in the northern Okhotsk region, NE Siberia (Fig. 1), are hosted by olivine melanephelinites and basanites and occur at two localities (Kananyga River and Aliki River areas) on top of calc-alkaline rocks up to 1550 m above sea level, which are related to the subduction of the palaeo-Pacific slab (Zonenshain *et al.* 1990). The age of the undersaturated lavas ranges from 10.7 to 7 Ma (Akinin 1997, 2005; Apt *et al.* 1998). A limited number of mantle xenoliths from the region have been studied by Akinin *et al.* (1997) and Apt *et al.* (1998). Here we present a summary of the petrology, mineralogy and geochemistry of the ultramafic xenoliths from both localities and discuss the implications of these data with respect to the subduction slab and mantle wedge processes.

Geological settings

The Okhotsk–Chukotka belt consists to a large degree of coeval Cretaceous and early Tertiary volcanic and plutonic rocks that occur along the

From: COLTORTI, M. & GRÉGOIRE, M. (eds) *Metasomatism in Oceanic and Continental Lithospheric Mantle.* Geological Society, London, Special Publications, **293**, 57–81.
DOI: 10.1144/SP293.4 0305-8719/08/$15.00

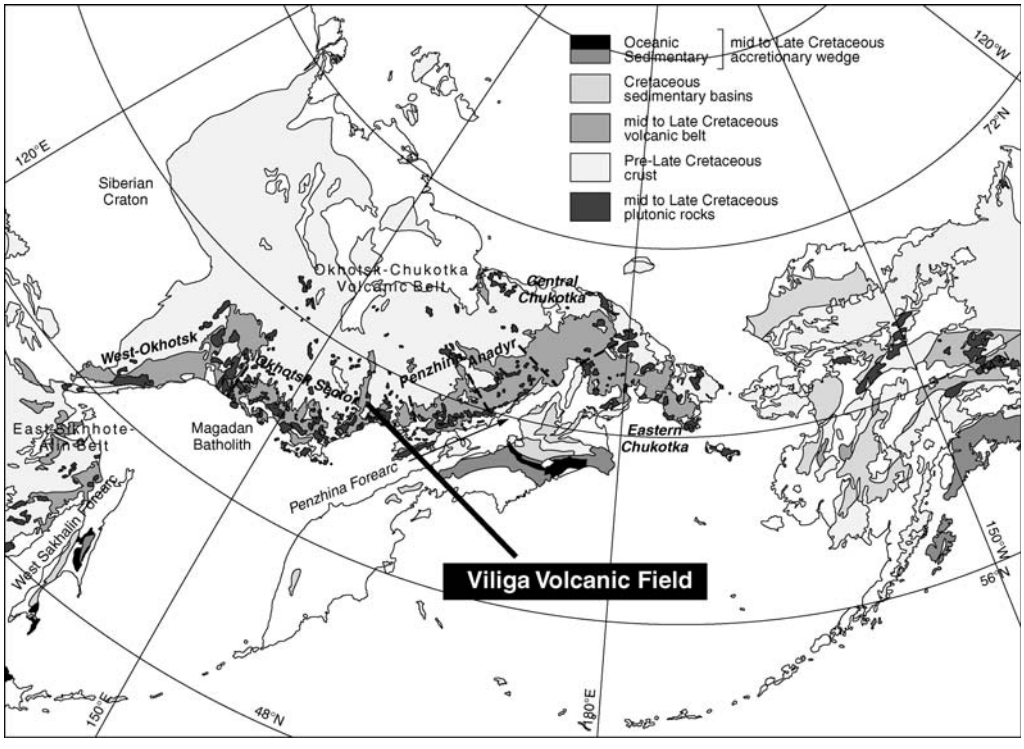

Fig. 1. Location map showing the Okhotsk–Chukotka Volcanic Belt divided into six sectors: the West Okhotsk, Okhotsk, Penzhina, Anadyr, Central Chukotka and Eastern Chukotka sectors. The Viliga Volcanic Field with xenolith-bearing olivine melanephelinites is located in the Okhotsk sector (adapted and modified from Hourigan & Akinin 2004).

continental margin in NE Russian. These igneous-arc-related rocks form a widespread Andean-style magmatic arc sequence that occurs for about 3500 km along the entire length of the belt from the Chukotka Peninsula in the north to the Uda River in the southwestern Okhotsk region (Zonenshain *et al.* 1990; Hourigan & Akinin 2004). The rocks of the Okhotsk–Chukotka Volcanic Belt (OCVB) are Early Cretaceous and Late Cretaceous, or locally Palaeocene, gently dipping basalts, andesitic basalts, andesites, dacites, rhyolites, tuffs, and rare beds of nonmarine clastic rocks with conglomerates and sandstones in the base (Nokleberg *et al.* 1998). On the basis of their lithological similarities within specific geographical regions the belt has been divided into seven sectors. From NE to SW these are the Eastern Chukotka flank zone, the Central Chukotka sector, the Anadyr sector, the Penzhina sector, the Okhotsk sector and the Western Okhotsk flank zone. The duration of the magmatic activity in the Okhotsk–Chukotka volcanic belt is still debated but generally it has been estimated to range from middle Albian to Campanian time (Hourigan & Akinin 2004, and references therein).

Distributed along the OCVB are Pliocene or Pleistocene mantle xenolith bearing olivine melanephelinites and basanites. The Viliga xenolith-bearing olivine melanephelinites and basanites are located in the Okhotsk sector (Fig. 1) and were intruded into Cretaceous subduction-related calc-alkaline rocks. However, only two out of five outcrops are xenolith bearing: one (VL1) in the Kananyga River and the other (VL5) in the Aliki River about 40 km NE from the Kananyga River.

Analytical techniques

Electron microprobe analyses of major minerals were carried out with a Cameca SX 100 electron microprobe at the University of Vienna, Department of Lithospheric Sciences. All analyses were made against mineral standards by utilizing wavelength-dispersive spectrometers; acceleration voltage and beam current were 15 kV and 20 nA, respectively, and standard correction procedures were applied. For Ca analyses in olivine an acceleration voltage of 20 kV and a beam current of 80 nA

were used. As primary standard we used pure wollastonite, and as secondary standard the San Carlos olivine. The secondary standard is a fragment of the gem-quality single crystal San Carlos olivine (sample SC/KA), which was used by Köhler & Brey (1990) for calibrating the Ca exchange between olivine and clinopyroxene, used as a geobarometer. The mean Ca content determined for this fragment is 524 ppm and the analytical error is *c*. 1%. A detailed description of the determination of the Ca content of the SC/KA has been given by Köhler & Brey (1990). Counting time was 100 s on peak position and on each background position. To control the accuracy and reproducibility of Ca analyses along a profile through the olivine in contact with clinopyroxene, every 15th analysis were performed on the SC/KA olivine. For example, the SC/KA in the sample VL1-7 were measured 12 times. The average Ca content was 537.5 ppm with $\chi^2 = 0.0949$. The Ca content was then normalized to the reference value of 524 ppm and this factor was used to correct the Ca contents of the analyses.

Major and trace element analyses were carried out by X-ray fluorescence (XRF) Spectrometry (Philips 2400 system). Th, U and REE were analysed by inductively coupled plasma-mass spectrometry (ICP-MS) (ELAN 6100 system) at the University of Vienna, Department of Lithospheric Sciences. Clinopyroxene preparation and Sr and Nd isotopic analytical work were also performed at the Laboratory of Geochronology, Department of Lithospheric Sciences, University of Vienna, using the analytical procedure described by Thoni & Miller (2004), and determination of the Sr and Nd isotopes was carried out by thermal ionization mass spectrometry (TIMS), using a ThermoFinnigan Triton TI system. Xenolith modal proportions were calculated using two methods. First we used an automatic point counter with 2000 points per thin section to acquire the modal phase proportions; second, we calculated the modal distribution using the mass balance of bulk-rock (XRF) and mineral analyses (electron microprobe analysis; EMPA). A comparison of the results from the two methods is given in Table 1.

Trace element contents of minerals were analysed by laser ablation (LA) ICP-MS at the University of Bergen, Norway (VG Elemental Plasma Quad 3 system). The laser system was used in pulse mode with a frequency of 10 Hz and energy of about 0.1–0.15 mJ per pulse. The laser beam was 20 μm wide. The spots for analysis were selected under optical microscope. The NIST 610 and 612 glasses were used as the external standard and the CaO content in minerals was used as the internal standard for yield calculations. Typical detection limits are in the range of 20–40 ppb for REE, Sr, Zr, Hf and Y; 200 ppb for V and Sc; and 4–6 ppm for Co, Cu and Zn.

Results

Petrography

The xenoliths from both localities (Kananyga River and Aliki River) are variable in size and consist mostly of spinel lherzolites. The largest xenoliths have a diameter of up to 90 cm but they are strongly oxidized and therefore have not been sampled. The common size of the sampled xenoliths varies between 10 and 25 cm in diameter. Also, augite megacrysts up to 5 cm in size were found as inclusions in the basalts. From our collection we selected 14 samples that were large enough able to provide representative whole-rock analyses and large thin sections. With the exception of one sample, VL1-35 (Fig 2a), which has equigranular texture, all the samples have protogranular textures, are fine-grained and exhibit evidence of deformation (foliation and alignment of elongate spinel grains; Fig. 2b). In same cases, clinopyroxene shows typical spongy rims attributed to the reaction with fluids or melts that caused its partial breakdown. The spongy rims show intergrowths of a second generation clinopyroxene (cpx2) and glass. The thickness of these spongy rims is variable and occasionally if clinopyroxene is small the primary clinopyroxene (cpx) exists, if at all, only in the core of the grain. The petrographic features and the modal composition of the studied samples are given in Table 1.

Mineral chemistry

Olivine

Microprobe analyses of olivine are given in Table 2. With an exception of sample VL5-3, which has Fo 87.9, all the samples have Fo values that vary from 89.6 to 90.5. CaO abundances from routine EPMA analyses show minor variations around 0.1 wt%. However, in the detailed Ca profiles used for pressure calculations and 'geospeedometry' the CaO content in the rims rises to 0.32 wt%. MnO and NiO abundances range from 0.11 to 0.17 and from 0.33 to 0.40, respectively.

Orthopyroxene

Orthopyroxene microprobe analyses are given in Table 3. All orthopyroxenes in the Viliga xenoliths are relative Al-rich (4.7–6.1% Al_2O_3). Within individual samples orthopyroxenes are homogeneous and there are virtually no compositional differences

Table 1. *Modal composition using mass balance and point-counting methods of the Viliga peridotites with short petrographic description*

Sample	Modal composition								Petrographic description*
	Olivine		Orthopyroxene		Clinopyroxene		Spinel		
	MB	PC	MB	PC	MB	PC	MB	*PC*	
VL1-1	72.6	55.8	19.7	34.9	6.9	13.2	0.8	2.2	cpx coexisting with opx; sp vermicularly intergrown with opx
VL1-2	47.9	47.9	29.7	32.9	19.9	24.7	2.5	3.9	numerous larger cpx aggregates; sp mainly vermicularly intergrown with opx: 'holly leaf' outline
VL1-3	61.4	57.3	25.8	29.5	11.5	13.8	1.3	2.1	reacted cpx rims caused by host infiltration; vermicularly grown sp: 'holly leaf' outline
VL1-7	53.4	27.7	28.4	49.2	16.3	12.5	1.8	2.2	strongly fractured coexisting cpx and opx phases; sp vermicularly intergrown with opx: 'holly leaf' outline
VL1-8	60.2	64.8	24.9	40.4	12.6	15.6	2.1	1.7	partly fractured opx + cpx; sp vermicularly intergrown with opx; inclusions of ol, cpx and opx in sp
VL1-9	63.6	58.3	22.0	34.2	12.8	8.9	1.6	2.1	reacted cpx rims along cracks; sp vermicularly intergrown with opx: 'holly leaf' outline
VL1-12	57.6	54.4	24.6	32.3	16.0	12.2	1.8	1.9	large primary ol grains recrystallized to fine-grained ol aggregates; sp randomly interstitial and vermicularly intergrown with opx
VL1-19	56.9	55.1	23.0	27.9	18.0	15.9	2.1	2.0	aggregates with cpx, opx and sp; sp randomly interstitial but also vermicularly intergrown with opx: 'holly leaf' outline
VL1-26	59.4	49.2	21.0	34.4	18.7	15.8	2.0	2.9	phlogopite bearing; opx with inclusions of ol; sp vermicularly intergrown with opx
VL1-34	61.0	58.3	22.1	20.7	15.1	19.4	1.8	2.3	strongly reacted cpx rims along cracks; sp vermicularly intergrown with opx: 'holly leaf' outline
VL1-35	60.1	63.6	24.0	35.9	13.9	12.5	1.7	2.8	slightly altered paragenesis; strongly reacted cpx rims caused by host infiltration, interstitially and vermicularly grown sp
VL5-3	60.4		21.5		16.0		1.6		strongly reacted cpx and sp; melt pockets with glass and secondary cpx; zoned sp
VL5-12	56.9		26.2		15.2		1.7		strongly fractured and reacted cpx; sp zoned and interstitially but also vermicularly grown: 'holly leaf' outline
VL5-15	57.3		25.8		14.9		1.8		strongly fractured and reacted cpx; sp zoned and vermicularly intergrown with opx: 'holly leaf' outline

*All samples with kink-banded olivine and protogranular texture, except sample VL1-35, which has equigranular texture.
MB, mass balance method; PC, point-counting method.

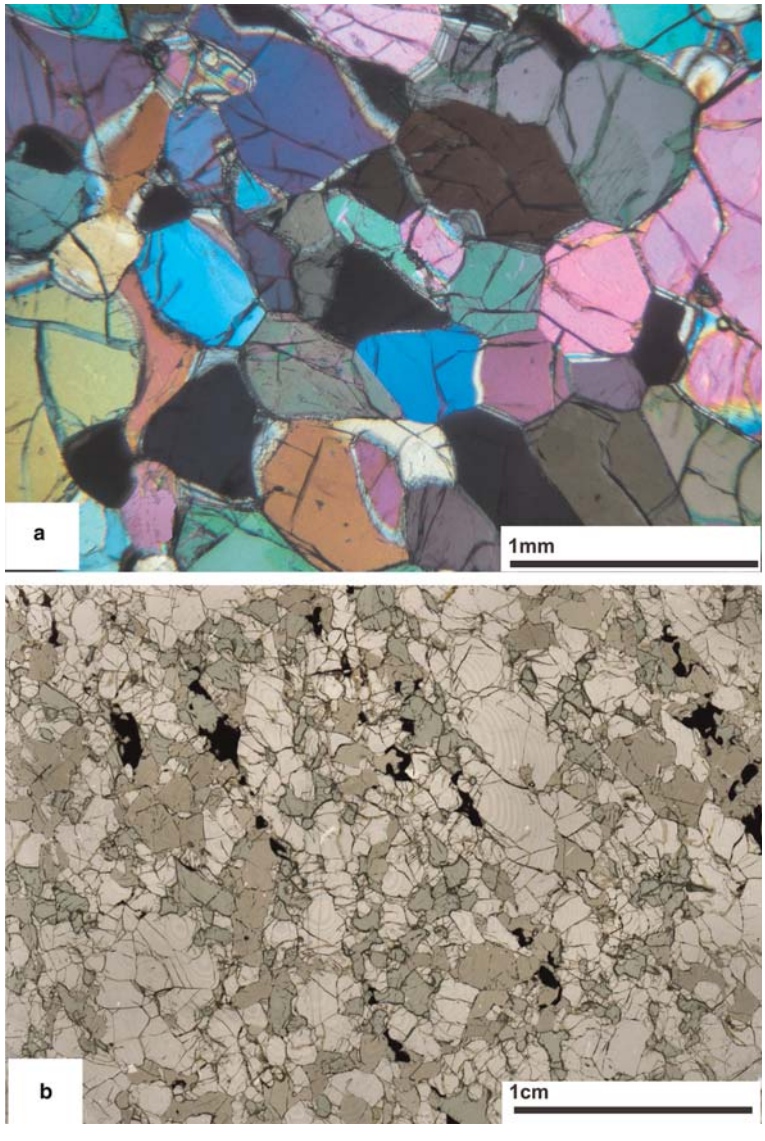

Fig. 2. Photomicrographs of Viliga lherzolite xenoliths. (**a**) well-equilibrated equigranular texture, sample VL1-35 (crossed Nicols); (**b**) fine-grained protogranular texture with well-aligned and elongated spinels (plane-polarized light). Most samples are exceptional fresh.

between core and rim. As for olivine, sample VL5-3 has the lowest mg-number (0.88). In all other samples mg-number varies from 0.90 to 0.91. CaO abundances range between 0.85 and 1.12 wt%, within the range typical for orthopyroxenes in the spinel peridotite field.

Clinopyroxene

Clinopyroxene microprobe analyses are given in Table 4. According to their composition and texture, two kinds of clinopyroxene have been identified: primary clinopyroxene (cpx1) and secondary clinopyroxene (cpx2). Secondary clinopyroxene occurs mainly in the spongy rims of the primary clinopyroxene. These rims consist of glass and cpx2 and are the result of partial breakdown of the cpx1 as a result of reaction with intergranular circulation of host basalt fluids or melts. Primary clinopyroxenes are diopsides, which are remarkably homogeneous within the individual samples. The Al_2O_3 content varies

Table 2. *Representative olivine microprobe analyses (wt%)*

Sample:	VL1-1	VL1-2	VL1-3	VL1-7	VL1-8	VL1-9	VL1-12	VL1-19	VL1-26	VL1-34	VL1-35	VL5-3	VL5-6	VL5-12	VL5-13	VL5-15
SiO_2	41.2	40.6	40.2	40.5	41.2	41.0	41.1	40.8	41.3	40.6	40.7	40.6	39.8	41.1	40.6	41.0
FeO	9.4	10.4	9.2	9.7	9.5	9.8	10.1	10.1	9.9	10.1	10.0	11.8	9.7	9.9	9.7	9.9
MnO	0.15	0.16	0.11	0.12	0.16	0.14	0.14	0.16	0.14	0.14	0.12	0.17	0.15	0.17	0.15	0.14
NiO	0.34	0.40	0.38	0.33	0.36	0.33	0.35	0.35	0.29	0.35	0.36	0.37	0.39	0.33	0.34	0.37
MgO	50.3	49.7	50.5	47.3	50.6	49.8	49.0	49.1	49.7	48.8	49.6	48.0	49.0	49.4	49.0	49.5
CaO	0.10	0.08	0.09	0.09	0.08	0.09	0.12	0.11	0.08	0.08	0.05	0.05	0.09	0.05	0.09	0.08
Total	101.5	101.4	100.5	98.1	101.9	101.3	100.9	100.6	101.4	100.1	100.9	101.1	99.2	101.1	100.1	101.1
Mg-no.	90.52	89.52	90.76	89.72	90.48	90.02	89.65	89.61	89.98	89.63	89.86	87.85	90.03	89.93	89.99	89.95

Total iron is shown as FeO. mg-number = 100 × (molar MgO/(MgO + FeO)).

Table 3. *Representative orthopyroxene microprobe analyses (wt%)*

Sample:	VL1-1	VL1-2	VL1-3	VL1-7	VL1-8	VL1-9	VL1-12	VL1-19	VL1-26	VL1-34	VL1-35	VL5-3	VL5-6	VL5-12	VL5-13	VL5-15
SiO_2	55.1	54.7	53.4	53.7	54.9	54.4	54.3	53.9	54.4	53.8	55.2	54.5	53.1	55.0	53.5	54.5
TiO_2	0.06	0.19	0.10	0.15	0.12	0.12	0.18	0.20	0.16	0.20	0.14	0.10	0.16	0.20	0.18	0.17
Al_2O_3	4.7	5.5	5.2	6.1	5.2	5.3	5.7	5.9	5.6	5.5	4.7	5.5	6.0	5.3	5.7	5.9
Cr_2O_3	0.54	0.33	0.50	0.43	0.50	0.50	0.43	0.41	0.38	0.38	0.34	0.42	0.47	0.45	0.51	0.47
FeO	6.0	6.4	5.9	6.3	6.0	6.2	6.4	6.3	6.3	6.4	6.3	7.3	6.0	6.2	6.1	6.3
MnO	0.10	0.13	0.11	0.16	0.12	0.13	0.15	0.15	0.14	0.16	0.14	0.17	0.12	0.15	0.15	0.13
NiO	0.08	0.11	0.07	0.11	0.12	0.10	0.10	0.07	0.10	0.12	0.11	0.06	0.12	0.09	0.13	0.08
MgO	33.3	33.1	33.2	32.4	33.5	32.9	32.2	32.1	32.5	32.1	33.3	31.6	31.9	32.7	32.3	32.4
CaO	0.98	0.85	0.95	1.09	0.88	0.92	0.95	1.03	0.90	0.92	0.71	0.84	1.12	0.83	1.11	1.08
Na_2O	0.14	0.18	0.13	0.22	0.15	0.14	0.16	0.19	0.13	0.21	0.14	0.22	0.21	0.14	0.23	0.16
Total	101.0	101.4	99.4	100.6	101.4	100.7	100.5	100.3	101.4	99.7	101.1	100.69	99.3	101.13	99.9	101.19
Mg-no.	90.89	90.25	90.97	90.21	90.87	90.45	90.04	90.08	90.13	89.94	90.42	88.46	90.39	90.33	90.42	90.17

Total iron is shown as FeO. mg-number $= 100 \times$ (molar MgO/(MgO + FeO)).

Table 4. *Representative clinopyroxene microprobe analyses (wt%)*

Sample:	VL1-1	VL1-2	VL1-3	VL1-7	VL1-8	VL1-9	VL1-12	VL1-19	VL1-26	VL1-34	VL1-35	VL5-3	VL5-6	VL5-12	VL5-13	VL5-15
SiO_2	52.1	51.6	50.5	51.4	51.9	51.9	51.4	51.2	51.7	50.9	51.8	52.0	50.3	51.6	51.1	52.1
TiO_2	0.27	0.71	0.44	0.52	0.47	0.45	0.69	0.63	0.56	0.62	0.61	0.65	0.61	0.72	0.55	0.55
Al_2O_3	6.0	7.9	6.9	7.9	7.2	7.2	7.9	8.1	7.8	7.7	7.4	8.1	7.9	7.8	7.6	7.8
Cr_2O_3	1.04	0.66	0.93	0.83	0.91	0.93	0.80	0.78	0.80	0.77	0.78	0.78	0.82	0.80	0.81	0.87
FeO	2.9	3.2	2.7	3.3	3.0	3.0	3.1	3.1	3.2	3.1	2.9	3.6	3.2	3.0	3.4	3.3
MnO	0.09	0.12	0.08	0.11	0.11	0.12	0.11	0.11	0.10	0.08	0.10	0.09	0.14	0.09	0.14	0.12
NiO	0.01	0.04	0.07	0.02	0.07	0.05	0.05	0.05	0.05	0.05	0.07	0.04	0.09	0.04	0.03	0.05
MgO	16.3	15.5	16.2	16.2	15.7	15.8	15.7	15.6	15.5	15.5	15.2	14.6	15.8	15.5	15.8	16.0
CaO	20.4	19.4	20.0	18.3	19.5	19.6	19.2	18.7	19.1	19.2	19.8	18.3	18.1	18.9	18.6	18.6
Na_2O	1.49	2.11	1.62	1.85	1.84	1.94	2.00	2.02	1.99	2.06	2.22	2.35	2.05	1.82	2.09	1.62
Total	100.7	101.2	99.6	100.5	100.8	100.9	101.1	100.3	100.9	99.9	100.9	100.4	99.1	100.3	100.2	100.9
Mg-no.	90.95	89.77	91.44	89.76	90.32	90.29	89.91	89.84	89.75	89.90	90.43	87.90	89.69	90.23	89.28	89.73

Total iron is shown as FeO. mg-number $= 100 \times$ (molar MgO/(MgO + FeO)).

from 6.0 to 8.1 wt%, with an overall good positive correlation with Al_2O_3 in orthopyroxene. The Al_2O_3 and Na_2O contents in cpx2 are lower than those of cpx1, whereas the opposite is true for MgO and CaO contents (Fig. 3a and b). The Na_2O and Al_2O_3 abundances in the cpx2 are up to 70% and 35% respectively lower than in cpx1, indicating their strong partitioning into the melt. The MgO and CaO contents of cpx2 are in respect to the primary ones about 15% higher than those of cpx1. This indicates that MgO and CaO after the breakdown of the primary clinopyroxene are preferially incorporated into cpx2 and not into the glass.

Spinel

Spinel microprobe analyses are given in Table 5. The most Cr-rich spinels with cr-number = 0.21 were found in the most depleted sample, VL1-1. All other samples have cr-numbers ranging from 0.08 to 0.15. The mg-number varies between 0.76 and 0.79, with the exception of sample VL5-5, which has mg-number = 0.71. The Cr-number of spinel and the forsterite Fo content in olivine, which are sensitive indicators of the degree of depletion in mantle peridotite, are positively correlated (not shown).

Whole-rock major element chemistry

Fourteen representative whole-rock major and trace element analyses from the Viliga xenolith suite are given in Table 6. The whole-rock major element composition of the peridotites corresponds to that of fertile to moderately depleted spinel lherzolites (Al_2O_3, CaO and MgO contents vary in the range of 2.8–4.7, 2.7–4.1 and 36.7–40.7 wt%, respectively). An exception is sample VL1-1, which is a strongly depleted spinel lherzolite (Al_2O_3 1.74 wt%, CaO 1.65 wt% and MgO 43.5 wt%). The Viliga xenoliths form negative linear trends on plots of CaO, Al_2O_3, TiO_2 and Na_2O v. MgO (Fig. 4), similar to those that have been observed in many other mantle xenolith suites worldwide (Ionov *et al.* 1993). Sample VL1-2 has higher Al_2O_3 and CaO abundances than the primitive mantle (McDonough & Sun 1995). Its unusual high cpx modal composition (Table 1), which could point to an anomalous local cpx enrichment, seems to be the reason for the elevated Al_2O_3 and CaO contents above primitive mantle. The Ca/Al ratios show a positive correlation with MgO and generally increase from 1.08 to 1.24.

Whole-rock REE chemistry

Whole-rock REE analyses are given in Table 6 and shown in Figure 5. In Figure 5a, the sample that is most depleted in major elements, sample VL1-1 (Al_2O_3 and CaO 1.74 and 1.65 wt%, respectively) is also the most depleted in REE ($Lu_N = 0.5$). The less depleted samples have Lu_N values that range from 1.4 to 2.3 (Fig. 5b). The degree of depletion indicated by the chondrite-normalized REE patterns shows that a group of samples is enriched in light rare earth elements (LREE) and has $(La/Sm)_N$

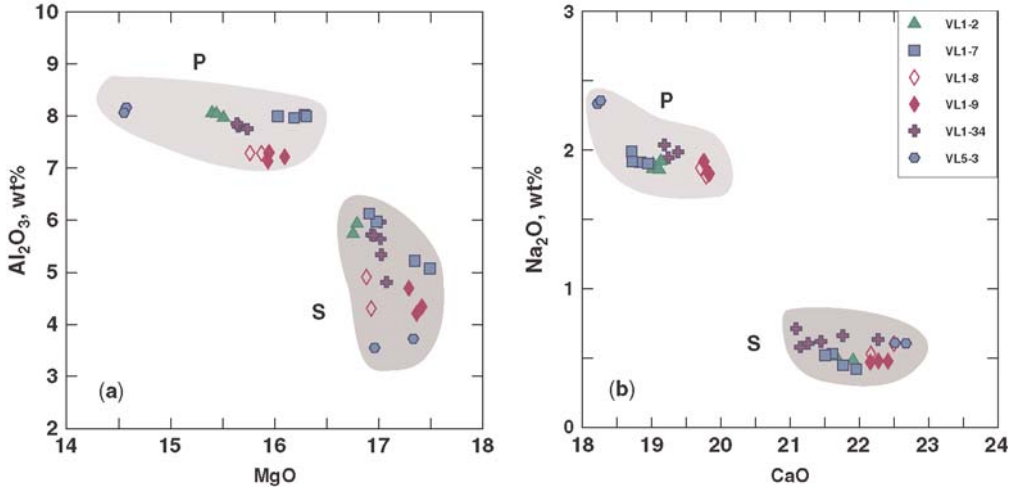

Fig. 3. Variation diagrams of MgO v. Al_2O_3 and CaO v. Na_2O in clinopyroxenes from Viliga xenoliths. P, primary clinopyroxene (cpx1); S, secondary clinopyroxene (cpx2), formed after reaction of cpx1 with intergranular fluids or melts.

Table 5. *Representative spinel microprobe analyses (wt%)*

Sample:	VL1-1	VL1-2	VL1-3	VL1-7	VL1-8	VL1-9	VL1-12	VL1-19	VL1-26	VL1-34	VL1-35	VL5-3	VL5-6	VL5-12	VL5-13	VL5-15
SiO_2	0.06	0.05	0.07	0.09	0.06	0.06	0.07	0.08	0.08	0.06	0.06	0.07	0.08	0.04	0.09	0.09
TiO_2	0.09	0.19	0.16	0.18	0.17	0.17	0.21	0.21	0.17	0.15	0.18	0.11	0.21	0.20	0.20	0.19
Al_2O_3	51.6	60.6	54.9	58.4	55.9	56.0	58.4	58.8	59.2	58.0	58.3	55.1	57.0	58.2	56.5	58.2
Cr_2O_3	15.9	7.5	12.4	9.2	11.2	11.6	9.0	8.5	8.8	9.5	9.4	11.5	9.8	9.5	10.4	9.5
FeO	8.9	8.7	8.3	9.0	7.8	8.3	8.0	8.1	8.4	8.4	9.0	11.6	9.0	8.8	9.1	9.1
Fe_2O_3	3.2	2.3	2.0	1.8	3.2	2.8	2.7	2.5	2.5	2.5	1.64	2.36	1.88	2.04	1.97	1.97
MnO	0.04	0.07	0.07	0.07	0.09	0.10	0.08	0.09	0.12	0.07	0.07	0.08	0.07	0.06	0.09	0.10
NiO	0.31	0.36	0.37	0.35	0.37	0.33	0.36	0.33	0.36	0.34	0.34	0.40	0.43	0.40	0.38	0.31
MgO	20.4	21.7	20.8	21.0	21.5	21.3	21.7	21.6	21.6	21.4	21.0	18.8	20.6	21.1	20.6	21.0
Total	100.3	101.2	98.8	100.0	100.0	100.2	100.3	100.0	101.0	100.2	99.9	99.7	98.9	100.0	99.1	100.2
mg-no.	75.61	78.24	78.59	77.89	78.29	77.93	78.68	78.85	78.41	78.14	78.14	70.97	77.50	78.00	77.14	77.59
cr-no.	20.65	8.31	15.12	10.58	13.46	13.89	10.33	9.72	9.91	10.93	10.82	13.95	11.55	10.91	12.35	10.93

mg-number $= 100 \times$ (molar $MgO/(MgO + FeO)$); cr-number $= 100 \times$ (molar $Cr_2O_3/(Cr_2O_3 + Al_2O_3)$).

Table 6. *Whole-rock major and trace element abundances in Viliga peridotites*

Sample:	VL1-1	VL1-2	VL1-3	VL1-7	VL1-8	VL1-9	VL1-12	VL1-19	VL1-26	VL1-34	VL1-35	VL5-3	VL5-12	VL5-15
XRF analyses (wt%)														
SiO_2	43.5	45.3	44.2	45.2	44.4	44.5	45.0	44.6	44.8	44.5	44.6	44.6	45.6	45.3
TiO_2	0.04	0.18	0.09	0.14	0.11	0.10	0.16	0.17	0.14	0.13	0.12	0.18	0.16	0.15
Al_2O_3	1.74	4.7	2.8	4.0	3.4	3.0	3.7	4.0	4.0	3.5	3.3	3.5	3.7	3.9
FeO	8.3	8.0	7.7	8.0	7.9	8.2	8.3	8.2	8.2	8.4	8.3	9.6	8.0	8.0
MnO	0.13	0.13	0.12	0.13	0.13	0.13	0.13	0.13	0.13	0.13	0.13	0.16	0.13	0.13
MgO	43.5	36.7	41.5	38.5	40.5	40.7	38.8	38.3	38.7	39.8	40.0	38.4	39.4	39.5
CaO	1.65	4.1	2.6	3.3	2.7	2.7	3.4	3.7	3.3	3.2	2.9	3.2	3.1	3.1
Na_2O	0.09	0.34	0.17	0.28	0.27	0.21	0.29	0.33	0.27	0.26	0.27	0.44	0.27	0.30
K_2O	0.01	0.00	0.01	0.01	0.02	0.01	0.02	0.02	0.01	0.00	0.01	0.38	0.07	0.13
P_2O_5	0.01	0.01	0.01	0.02	0.02	0.01	0.02	0.02	0.02	0.01	0.01	0.03	0.02	0.03
Total	98.9	99.4	99.4	99.5	99.5	99.6	99.7	99.4	99.5	99.9	99.6	100.4	100.5	100.5
mg-no.	90.37	89.14	90.53	89.58	90.12	89.82	89.33	89.31	89.40	89.46	89.56	87.69	89.76	89.75
XRF analyses (ppm)														
Nb	3.2	3.0	3.4	3.2	3.2	3.2	3.4	3.4	3.3	3.2	3.3	1.6	1.2	1.7
Zr	2.8	8.3	4.4	6.4	5.7	5.2	7.9	8.0	7.5	6.2	6.3	4.7	5.2	4.4
Sr	4.0	17.3	6.5	12.4	11.1	10.0	16.5	16.9	14.7	10.9	11.0	61.8	29.1	29.6
Ga	1.8	3.6	2.1	3.2	2.7	2.4	2.8	3.0	3.1	2.5	2.5	2.7	3.5	2.4
Zn	37.5	41.1	38.0	40.2	42.1	38.7	39.5	42.3	40.5	39.5	39.4	87.5	58.3	61.1
Cu	12.5	24.9	21.1	37.8	22.6	17.5	26.3	30.0	27.0	22.3	30.5	8.2	36.7	33.9
Ni	2087	1718	1987	1990	2051	1895	1858	1960	1856	1870	1952	1591	1846	1833
Co	99	87	93	90	97	91	90	94	92	93	94	109	109	107
Cr	2140	2438	2400	2622	2794	2127	2143	2389	2298	2130	2165	2123	2208	2352
V	35	73	48	64	57	49	61	68	62	54	57	74	71	77
ICP-MS analyses (ppm)														
Sc	6.438	11.122	9.753	12.473	31.718	9.074	28.612	27.089	23.743	8.971	7.750	16.899	16.351	16.520
Y	0.493	2.527	1.165	1.829	2.350	1.627	2.825	3.096	2.710	1.885	1.616	3.769	3.775	3.337
La	0.142	0.220	0.204	0.220	0.370	0.196	0.401	0.379	0.362	0.203	0.205	1.136	0.697	0.464
Ce	0.285	0.681	0.412	0.551	0.831	0.460	0.991	0.977	0.907	0.521	0.604	2.933	1.625	1.057
Pr	0.025	0.112	0.050	0.081	0.114	0.067	0.149	0.158	0.135	0.083	0.079	0.426	0.221	0.168
Nd	0.125	0.627	0.265	0.437	0.571	0.349	0.768	0.824	0.685	0.460	0.417	1.858	1.079	0.843
Sm	0.043	0.255	0.103	0.215	0.206	0.142	0.298	0.307	0.253	0.200	0.159	0.466	0.358	0.297
Eu	0.017	0.106	0.041	0.106	0.087	0.059	0.127	0.128	0.107	0.088	0.065	0.195	0.147	0.124
Gd	0.063	0.402	0.168	0.274	0.299	0.231	0.418	0.456	0.389	0.293	0.262	0.595	0.512	0.433
Tb	0.009	0.073	0.031	0.050	0.055	0.042	0.077	0.086	0.073	0.056	0.046	0.100	0.093	0.079

(*Continued*)

Table 6. Continued

Sample:	VL1-1	VL1-2	VL1-3	VL1-7	VL1-8	VL1-9	VL1-12	VL1-19	VL1-26	VL1-34	VL1-35	VL5-3	VL5-12	VL5-15
Dy	0.081	0.500	0.229	0.351	0.390	0.308	0.517	0.564	0.492	0.380	0.320	0.612	0.597	0.535
Ho	0.018	0.111	0.052	0.080	0.089	0.069	0.118	0.127	0.113	0.085	0.072	0.130	0.128	0.116
Er	0.063	0.336	0.161	0.245	0.286	0.213	0.355	0.383	0.343	0.252	0.223	0.388	0.396	0.350
Tm	0.009	0.050	0.023	0.037	0.044	0.030	0.053	0.055	0.052	0.038	0.032	0.053	0.057	0.051
Yb	0.074	0.328	0.166	0.250	0.308	0.215	0.360	0.383	0.355	0.262	0.221	0.370	0.395	0.341
Lu	0.012	0.049	0.024	0.038	0.049	0.033	0.054	0.059	0.057	0.039	0.033	0.056	0.060	0.054
Th	0.250	0.501	0.278	0.366	0.443	0.285	0.352	0.315	0.314	0.284	0.238	0.009	0.064	0.003
La/Yb	1.9	0.7	1.2	0.9	1.2	0.9	1.1	1.0	1.0	0.8	0.9	3.1	1.8	1.4
La/Sm	3.3	0.9	2.0	1.0	1.8	1.4	1.3	1.2	1.4	1.0	1.3	2.4	1.9	1.6
Tb/Yb	1.0	1.4	1.3	1.4	1.2	1.4	1.5	1.5	1.4	1.5	1.4	1.9	1.6	1.6

Total iron is shown as FeO. mg-number $= 100 \times$ (molar MgO/(MgO + FeO)).

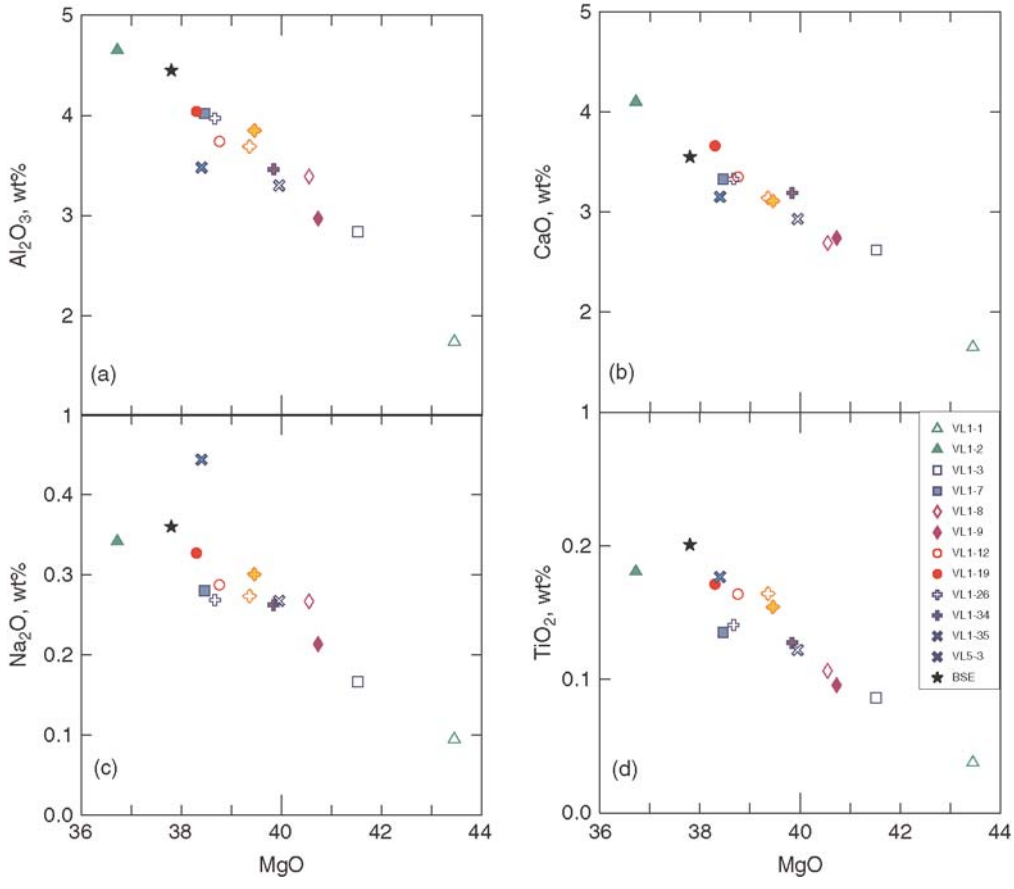

Fig. 4. Whole-rock variation diagrams of MgO v. Al_2O_3, CaO, Na_2O and TiO_2 indicate the fertile character of the Viliga peridotites. The filled star indicates Bulk Silicate Earth after McDonough & Sun (1995).

ratio ranging from 1.16 to 2.13 (Fig. 5a) whereas REE patterns from the other samples show minor to almost no LREE enrichment (Fig. 5b). All samples except VL5-3 have $(Sm/Lu)_N$ ratios that range between 0.60 and 0.99, suggesting that the middle REE (MREE) and heavy REE (HREE) in the Viliga xenoliths have not been affected by metasomatic processes. Sample VL5-3, in contrast, has been massively affected by metasomatic processes, as indicated by the high $(Sm/Lu)_N$ value (1.39) and the 'spongy' clinopyroxenes.

Clinopyroxene trace elements

Clinopyroxene LA-ICP-MS trace element analyses from 13 samples are given in Table 7. HREE and Y correlate positively with Ti (Fig. 6), indicating melt depletion processes. Similarly, the increase of LREE with increasing Sr contents that plot exclusively in the melt depletion area in Figure 7 supports the above observations about melt extraction and precludes metasomatic processes. In the chondrite-normalized diagram (Fig. 8) the REE patterns show a slight depletion of LREE with respect to HREE $[(La/Sm)_N$ 0.23–0.60]. The HREE abundances show a minor but systematic decrease from Tb to Lu. Typically, the $(Tb/Lu)_N$ ratios vary from 1.07 to 1.34, with exception of sample VL1-1, which has $(Tb/Lu)_N = 0.75$. On the primitive mantle normalized diagram the high field strength elements (HFSE) Ti and Zr are depleted relative to adjacent REE. The Ti/Ti* ratios vary from 0.50 to 0.69 and the Zr/Zr* ratios vary from 0.49 to 0.96 (Ti and Zr are primitive mantle normalized whereas $Ti^* = (Eu_N + Gd_N)/2$ and $Zr^* = (Nd_N + Sm_N)/2$), indicating that the Ti anomaly is larger than that of Zr (Fig. 9). As expected, the most pronounced negative Ti and Zr anomalies were found in the most

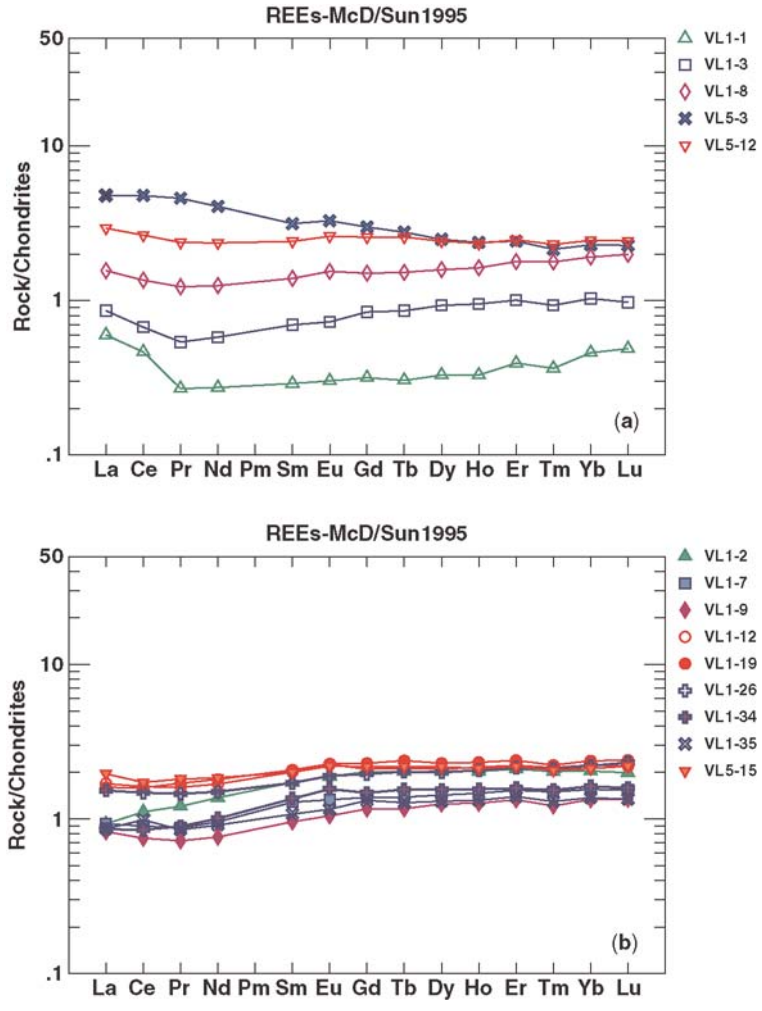

Fig. 5. Whole-rock chondrite-normalized (McDonough & Sun 1995) REE abundances: (**a**) LREE-enriched peridotites; (**b**) slightly LREE-enriched peridotites.

depleted sample, VL1-1 ($Ti/Ti^* = 0.50$ and $Zr/Zr^* = 0.49$). Incompatible elements such as Nb, Ta, U, Th, Ba and Rb are strongly depleted, with the exception of the VL1-26 sample, which has values around unity in the primitive mantle normalized diagram (Fig. 9).

Clinopyroxene Sr and Nd radiogenic isotopes

The Sr and Nd isotopic compositions of four clinopyroxenes from the Viliga xenoliths are given in Table 8 and plotted in Figure 10. Samples VL1-26 and VL3-15 have the lowest $^{87}Sr/^{86}Sr$ (0.702128 and 0.702357, respectively) and plot in the depleted MORB mantle (DMM) end-member field of Zindler & Hart (1986) whereas samples VL1-1 and VL1-3 have the highest $^{143}Nd/^{144}Nd$ (0.513581 and 0.513622, respectively), which plot above the DMM field, and have slightly more radiogenic $^{87}Sr/^{86}Sr$ (0.702838 and 0.703261, respectively) than samples VL1-26 and VL3-15. The clinopyroxene Nd data do not correlate with major element compositions, as the samples with the highest $^{143}Nd/^{144}Nd$ are the most depleted whereas Sr data correlate with major element compositions, with depleted samples having higher $^{87}Sr/^{86}Sr$ and fertile samples having lower $^{87}Sr/^{86}Sr$.

Table 7. *LA-ICP-MS analyses of clinopyroxenes (ppm)*

Sample:	VL1-1	VL1-2	VL1-3	VL1-7	VL1-8	VL1-9	VL1-12	VL1-19	VL1-26	VL1-34	VL1-35	VL5-13	VL5-6
Sc	54.3	52.2	51.5	44.8	52.5	53.5	52.0	49.8	55.6	54.9	53.6	46.0	45.0
V	221	247	223	216	240	226	222	209	198	206	229	215	220
Co	23.7	23.8	23.7	25.5	24.2	23.4	23.8	22.0	19.7	20.8	20.8	25.5	25.9
Cu	1.64	2.43	1.62	1.80	2.60	8.09	1.91	1.71	1.68	1.77	1.88	1.63	2.25
Zn	11.8	12.0	12.1	14.0	12.6	12.1	12.7	11.1	9.5	9.7	9.9	14.0	14.2
Rb	0.062		0.040	0.010	0.028				0.061	0.012		0.021	0.011
Sr	32.5	86.2	34.8	71.1	76.7	62.4	87.5	81.4	94.3	73.8	82.3	75.8	69.0
Y	8.85	17.1	14.1	14.3	13.8	14.4	18.1	17.6	18.5	18.5	17.0	15.4	15.4
Zr	6.29	31.6	14.2	23.1	21.7	20.5	34.1	32.4	41.1	30.7	30.0	26.5	25.6
Nb	0.377	0.160	0.202	0.338	0.299	0.117	0.322	0.305	0.761	0.186	0.219	0.197	0.279
Ba	0.053	0.034	-	0.239	0.310	0.316		0.018		0.031	0.020	0.170	0.124
La	0.520	1.038	0.426	0.938	1.004	0.661	1.169	1.182	1.739	0.912	1.038	0.887	0.814
Ce	1.628	4.395	1.819	3.715	3.864	2.805	4.660	4.360	5.385	3.425	4.395	3.950	3.625
Pr	0.274	0.793	0.396	0.692	0.682	0.557	0.871	0.842	0.979	0.702	0.793	0.752	0.707
Nd	1.328	4.847	2.641	4.081	3.845	3.147	5.122	4.900	4.820	4.280	4.040	4.477	4.280
Sm	0.580	1.764	1.290	1.520	1.445	1.250	1.906	1.813	1.980	1.725	1.711	1.560	1.745
Eu	0.255	0.716	0.489	0.645	0.585	0.546	0.785	0.740	0.768	0.728	0.716	0.686	0.696
Gd	0.977	2.511	1.888	2.272	2.032	2.054	2.702	2.635	2.705	2.790	2.511	2.514	2.355
Tb	0.196	0.445	0.366	0.408	0.357	0.368	0.485	0.482	0.493	0.497	0.445	0.451	0.424
Dy	1.443	3.075	2.545	2.751	2.420	2.566	3.290	3.235	3.410	3.253	3.075	2.992	2.855
Ho	0.344	0.695	0.571	0.632	0.540	0.572	0.707	0.697	0.743	0.702	0.695	0.669	0.622
Er	1.030	2.065	1.659	1.761	1.521	1.629	2.060	2.023	2.239	2.067	2.065	1.851	1.880
Tm	0.164	0.313	0.254	0.274	0.242	0.241	0.295	0.312	0.343	0.326	0.313	0.283	0.274
Yb	1.091	2.025	1.650	1.790	1.627	1.570	1.870	2.020	2.235	2.040	2.025	1.778	1.787
Lu	0.164	0.318	0.248	0.269	0.251	0.222	0.285	0.293	0.332	0.307	0.318	0.254	0.263
Hf	0.145	1.014	0.519	0.719	0.658	0.577	1.096	0.971	1.152	0.950	0.897	0.765	0.804
Ta	0.033	0.013	0.011	0.017	0.028		0.037	0.021	0.045	0.014	0.018	0.017	0.017
Pb	0.048	0.063	0.048	0.133	0.057	0.082	0.060	0.029	0.047	0.063	0.512	0.123	0.065
Th	0.023	0.010	0.048	0.020	0.030	0.008	0.025	0.027	0.085	0.010	0.010	0.013	0.013
U	0.012	0.006	0.004	0.010	0.008	0.008	0.006	0.006	0.020	0.004	0.004	0.005	0.006

Each analysis is the average of two cpx grains; empty entries indicate failed determination.

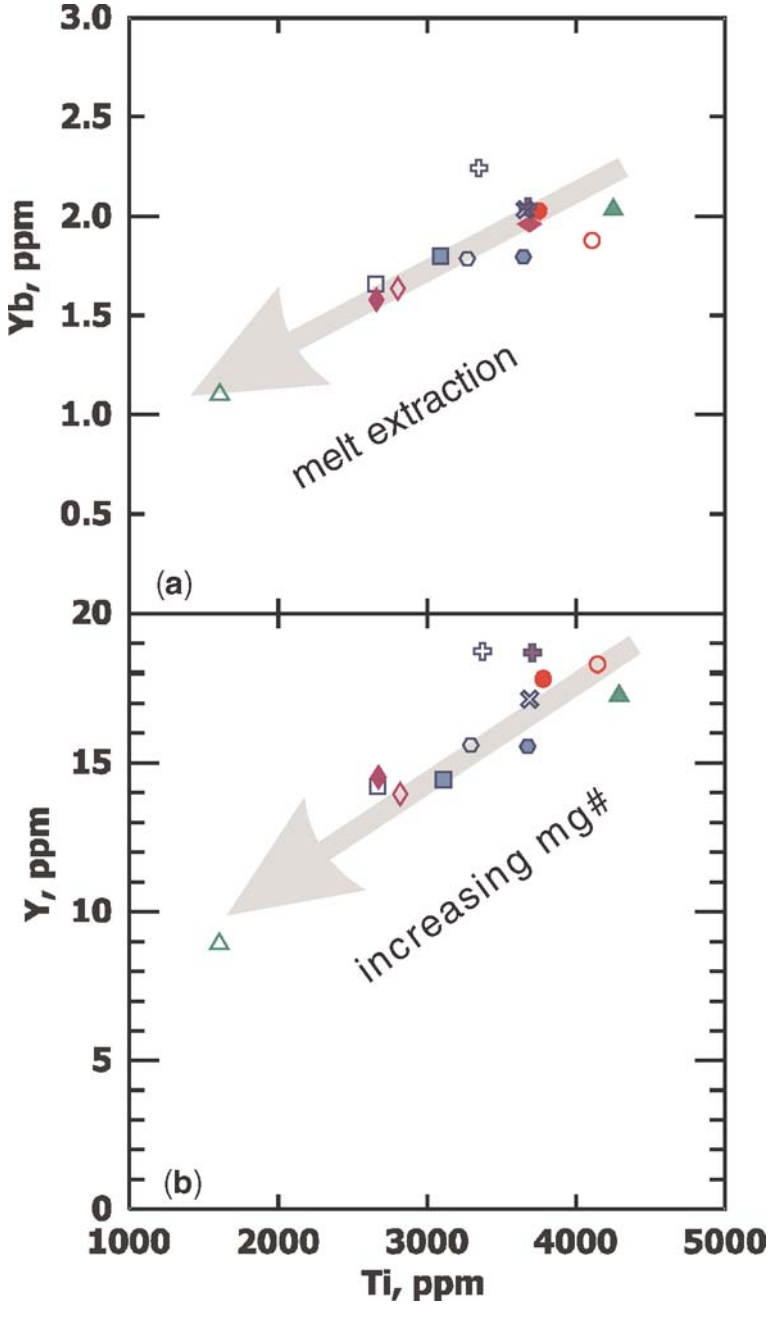

Fig. 6. Variation plots of Ti v. Yb and Y in clinopyroxenes. The arrow in both diagrams indicates increasing degree of partial melting (adapted from Norman 1998). Symbols are as in Figure 4.

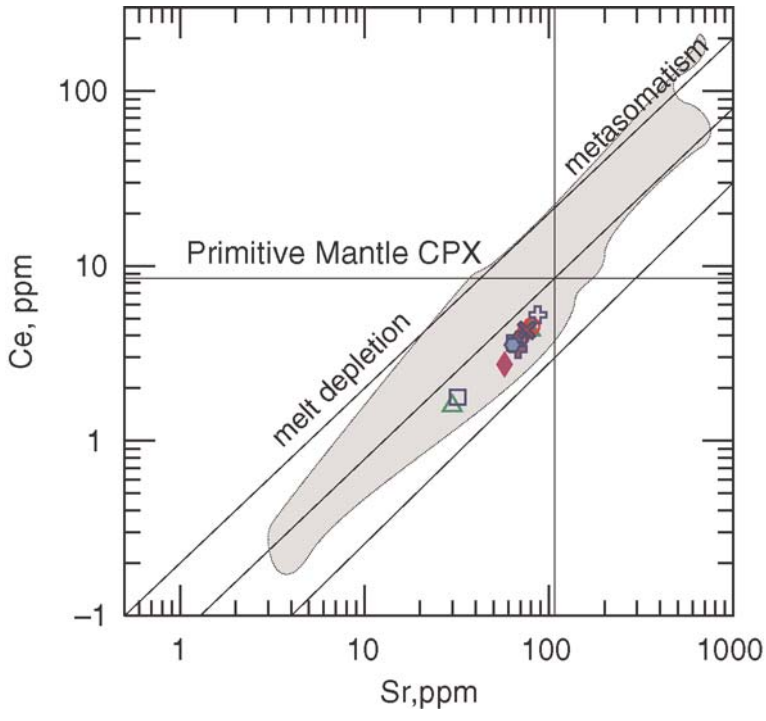

Fig. 7. Sr v. Ce diagram showing that clinopyroxenes from Viliga plot in the melt depletion field. Fine grey line indicates field for samples from China, Kerguelen, Australia and Mexico–western USA after Norman (2001) and references therein. Symbols are as in Figure 4.

Discussion

P–T *conditions*

Because the constituent minerals are not zoned and clinopyroxenes do not have exsolution lamellae, average microprobe analyses can be used for equilibrium temperature calculations. As a geobarometer for peridotites equilibrated in the spinel peridotite field we used the Ca exchange between olivine and clinopyroxene (Köhler & Brey 1990). The application of this barometer depends first on

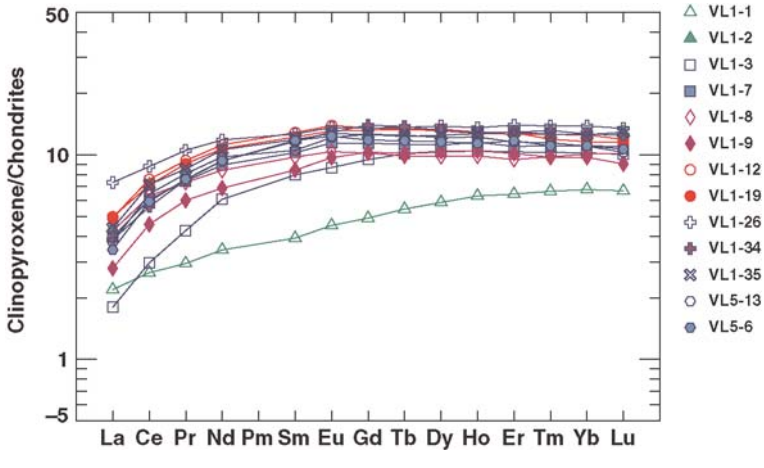

Fig. 8. Chondrite-normalized (McDonough & Sun 1995) abundance patterns of clinopyroxene obtained by LA-ICP-MS on Viliga peridotites.

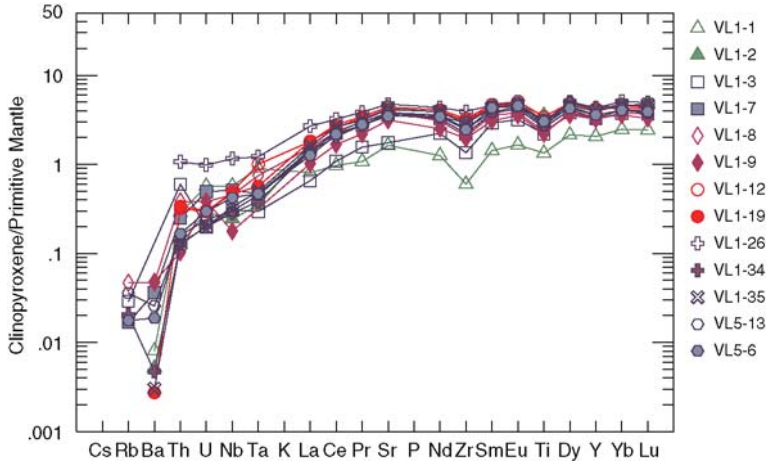

Fig. 9. Primitive mantle normalized (McDonough & Sun 1995) multi-element abundance patterns of clinopyroxene obtained by LA-ICP-MS on Viliga peridotites.

the accuracy and precision of the Ca content in olivine coexisting with clinopyroxene. The low Ca concentrations in olivine were estimated with high accuracy and precision using the analytical conditions described above. To avoid the phase boundary fluorescence effect (PBF), coexisting olivine and clinopyroxene from five samples were separated under a binocular microscope and were then polished. It turned out that two of the samples did not represent the outermost rims that should be in contact with coexisting clinopyroxenes and from two of the other samples it appears that a few microns of the outermost rim are missing. Coexisting olivine and clinopyroxene were separated under the microscope in a double-polished thin section of 150 μm thickness of sample VL1-7. The reliability of this barometer is strongly dependent also on the accuracy of the temperature estimation. The use of the two-pyroxene thermometer after Brey & Köhler (1990), in which the experimental data are the same as used for the Ca-ol–cpx barometer, provides internal consistency and minimizes the error on the temperature estimation. Following the advice given by Köhler & Brey (1990), we used an iterative procedure to simultaneously calculate pressure and temperature. The results are given in Table 9. Only five samples were used for this calculation. The estimated pressures range from 15.2 to 21.3 kbar and temperatures from 1032 to 1166 °C. Pressure estimates have to be interpreted with caution, as Ca solubility in olivine is strongly temperature dependent and its diffusion is much faster in olivine than in clinopyroxene. Because the estimated temperatures are within the range in which the barometer is calibrated (900–1400 °C) and because all minerals, with exception of the outermost rim in olivine that has elevated Ca contents, are not zoned the estimated pressures reveal that

Table 8. *Clinopyroxene Sr- and Nd-isotopic ratios for Vilga and Hannuoba, eastern China xenoliths*

Sample	Rb (ppm)	Sr (ppm)	$^{87}Rb/^{86}Sr$	$^{87}Sr/^{86}Sr$	Sm (ppm)	Nd (ppm)	$^{147}Sm/^{144}Nd$	$^{143}Nd/^{144}Nd$
VL1-1 CPX	0.06	32.5	0.005	0.702838	0.58	1.32	0.27	0.513581
VL1-3 CPX	0.04	34.8	0.003	0.703261	1.29	2.64	0.31	0.513622
VL1-26 CPX	0.06	69.9	0.002	0.702128	1.98	4.8	0.25	0.513326
VL5-13 CPX	0.02	75.8	0.001	0.702357	1.71	4.04	0.26	0.513234
DM1-4				0.702215				0.513585
DM1-9				0.702156				0.513483
MHP79/4-cpx				0.702286				0.513329
441-1				0.702131				0.514806

DM1-4 and DM1-9 from Song & Frey (1989), MHP79/4-cpx from Rudnick *et al.* (2004) and 44-1 from Apt *et al.* (1998).

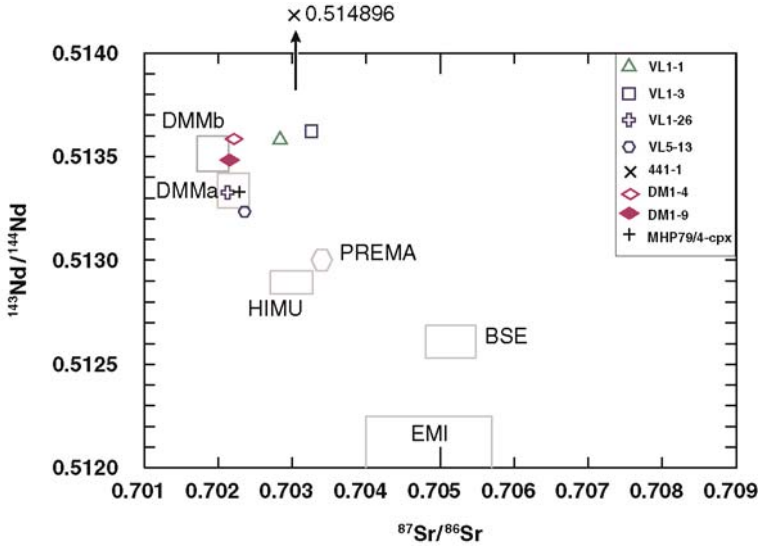

Fig. 10. $^{143}Nd/^{144}Nd$ v. $^{87}Sr/^{86}Sr$ for clinopyroxenes from four Viliga peridotites. Plus sign and diamonds indicate clinopyroxenes from Hannuoba xenoliths (Song & Frey 1989; Rudnick *et al.* 2004). Sample 441-1 is clinopyroxene from Viliga (Apt *et al.* 1998). Fields after Zindler & Hart (1986).

the peridotites equilibrated at different depths beneath Viliga. For the other samples the temperature calculations were performed at 15 kbar pressure, which, according to calculated pressures, should represent a minimum value for that region. For comparison, the temperatures estimated using the Wells (1977) two-pyroxene thermometer are also given. Temperatures estimated using the Brey & Köhler (1990) thermometer are systematically 40–91 °C higher than those estimated using the Wells (1977) thermometer. The uncertainities on the pressure estimates are in the range of ±2.7 kbar (Köhler & Brey 1990).

The advantage of the ol–cpx *in situ* separation is that the detailed Ca core–rim profiles in olivine provide PBF-free Ca diffusion profiles (Fig. 11). The characteristic Ca diffusion profiles in olivine with the elevated Ca content in the rims is attributed

Table 9. *Equilibration temperatures and pressures for Viliga peridotites*

Sample	*T* (°C) (WELLS)[1]	*T* (°C) (BK)[2]	*P* (kbar) (KB)[3]
VL1-1	981	1047	19
VL1-2	960	1032	
VL1-3	965	1032	15
VL1-7	1067	1166	20.6
VL1-8	989	1058	
VL1-9	972	1063	18.6
VL1-12	990	1080	21.3
VL1-19	1014	1092	
VL1-26	994	1071	
VL1-34	966	1029	
VL1-35	904	956	
VL5-3	988	1075	
VL5-6	1029	1083	
VL5-12	1026	1070	
VL5-13	1004	1057	
VL5-16	1079	1119	

Temperature estimates assuming a pressure of 15 kbar, after [1]Wells (1977); [2]Brey & Köhler (1990); pressure estimates after [3]Köhler & Brey (1990).

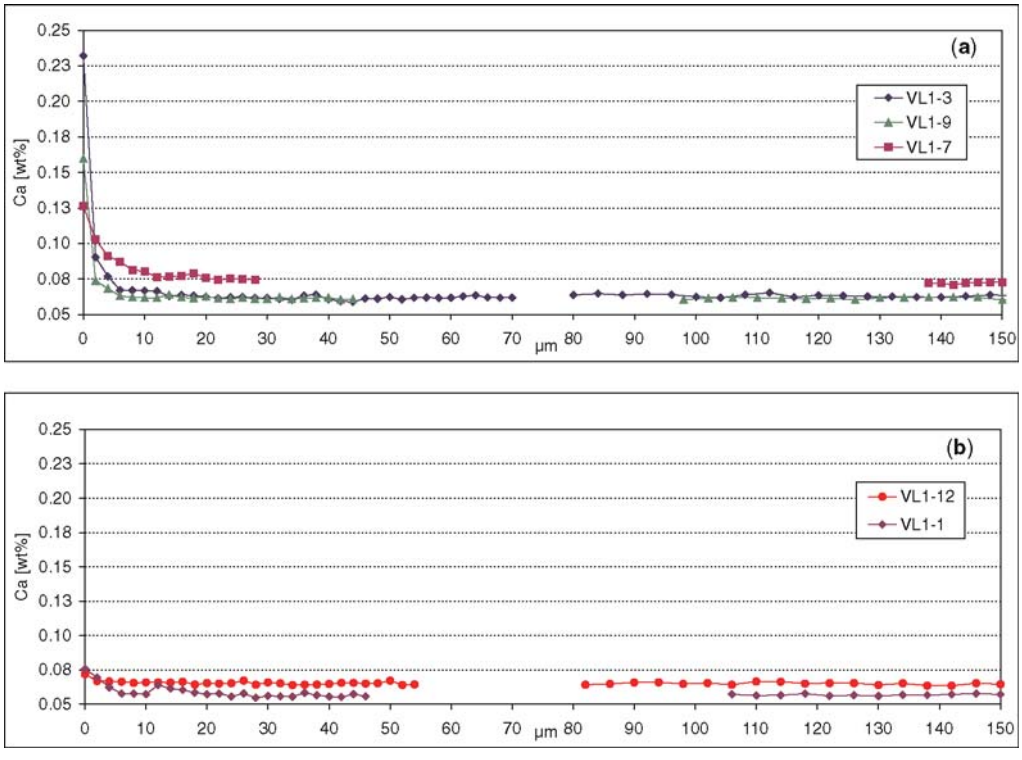

Fig. 11. Detailed Ca profiles in olivine (distance from grain rims). (**a**) *In situ* separation in thick section from coexisting clinopyroxene in thick section (VL1-7) and hand-picked olivine under the microscope coexisting with clinopyroxene. (**b**) Hand-picked olivine in which the very outermost margin is not present.

to the temperature increase caused by the incorporation of the peridotites into host basalts and their transport to the surface (Köhler & Brey 1990). The most representative Ca profile in olivine can be considered that of sample VL1-7, in which, because of the *in situ* ol–cpx separation, the Ca content at the outermost rim in contact with clinopyroxene is not affected by PBF effects and corresponds to the real Ca concentration. The Ca diffusion profiles in olivine grains as demonstrated by Kil & Wendlandt (2004) for upper mantle under the Rio Grande Rift could reveal the thermal history of the xenoliths and provide information about local thermal perturbation caused by the intrusion of host magma in the lithosphere prior to xenolith incorporation. In the Viliga peridotites the thermal history as derived from the Ca diffusion profiles in olivine grains does not support complex processes. It is rather a single event apparently related to their entrainment in the host magma and transport. Changes in the P–T conditions before this event (the last heating stage) were insignificant because minerals are not zoned and appear to be in chemical and textural equilibration. This event, according to the calculations, was short. Using the 1D diffusion model of Lasaga (1998), we estimated the duration of the heating event applying the equation

$$T_{1/2} = (X_{1/2})^2/2D$$

where $T_{1/2}$ is the time necessary to reach half of the equilibration concentration at a distance $X_{1/2}$ from the rim and the diffusion coefficient for Ca in olivine $D = 3.18 \times 10^{-12}$ cm^2 s^{-1} at $fO_2 = 10^{-8}$ bar and $T = 1200$ °C (Jurewicz & Watson 1988). The estimated duration of heating varies between 1 and 6 days. There is a remarkably good positive correlation between pressure of equilibration (depth) and heating time or transport duration in days inferred from the above calculations (Fig. 12).

Metasomatic events

The most striking characteristic of the Viliga spinel peridotites is the absence of metasomatism, either cryptic or modal. The phlogopite found in sample VL1-26 does not appear to affect significantly the bulk LREE; compared with the HREE they are

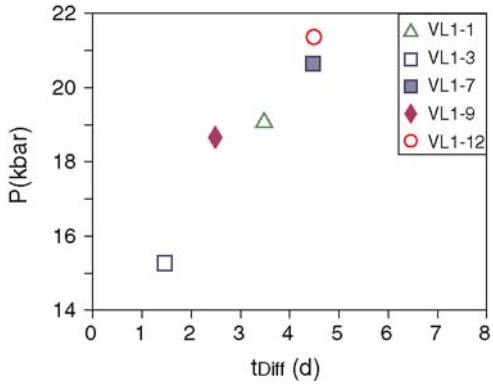

Fig. 12. Ca diffusion rates in days v. pressure (depth).

slightly elevated, suggesting that only a few isolated grains should be present in this sample. The depletion of LREE relative to the HREE and the high Nd- and low Sr-isotopic ratios in clinopyroxene from this sample provide evidence against cryptic metasomatism.

Whereas a number of samples are to variable degree enriched in LREE relative to HREE, the REE in clinopyroxenes are, without exception, all depleted in LREE relative to HREE. The clinopyroxene REE patterns preclude cryptic metasomatism and the absence of hydrous phases precludes modal metasomatism. Therefore the elevated LREE contents are ascribed to the infiltration of host basalt fluids or melts. In fact, the spongy clinopyroxenes are also related to this event, as the clinopyroxenes close to the xenolith–host basalt interface are more affected than those located far from the interface.

The melting processes

The geochemical data (major, trace element and mineral compositions) of Viliga peridotites represent residues after variable degrees of partial melting of a primitive mantle. The degree of melting of the Viliga spinel peridotites calculated on the basis of bulk FeO and MgO contents and constituent olivine (Frey *et al.* 1985) ranges from 2 to 16%, whereas the majority of the calculations, apart from those for the most depleted samples, indicate melt extractions between 2 and 9%. These calculations are in good agreement with those made using the REE in clinopyroxenes (Norman 1998), which show that clinopyroxenes represent the residues after 3–15% batch melting of a primitive mantle (Fig 13a and b). All samples, again with the exception of samples VL1-1 and VL1-3, which are the most depleted (*c*. 15% extraction of basaltic components), have experienced degrees of melting in the range of *c*. 3–7%. Considering that the estimated P–T conditions and the variations in degree of partial melting do not correlate, we assume that the samples are not related to a stratified Earth mantle. The relatively good agreement between the two different approaches used to calculate the degrees of melting and the absence of metasomatic events together provide arguments against the possibility that the fertile Viliga lherzolites represent refertilization of previously depleted rocks. On the assumption that refertilization took place, LREE enrichment in the clinopyroxenes should be observed. However, the clinopyroxenes have $(La/Yb)_N < 1$ and thus have not been affected by any magmatic refertilization. This ratio can be maintained if the ascending melt intrudes into a cold environment, making reaction with the residual clinopyroxene difficult. Subsequent cooling of the liquid would result in crystallization of minerals that correspond to the melt composition (Gannoun *et al.* 2004). Such possibilities can be precluded for the Viliga spinel lherzolites because, first, a magmatic refertilization would change the bulk chemistry of the samples, which would decisively affect the calculated degrees of partial melting based on the bulk FeO and MgO contents, and, second, the temperatures are high enough that possible reaction of a melt with the residual clinopyroxenes would not be avoided. Considering the above arguments and taking into account the depleted nature of the Nd–Sr isotopic ratios in clinopyroxenes (they plot in the DMM field; Fig. 10), the spinel lherzolite xenoliths do not support a complex history beneath Viliga but rather a simple evolution.

Clinopyroxenes from 'dry' peridotites with Sr and Nd isotopic compositions that cover the MORB field have been described by Jagoutz *et al.* (1980), Menzies (1983), Stosch *et al.* (1986), Song & Frey (1989), Ionov *et al.* (1992), Kempton *et al.* (1999), Xu *et al.* (2003) and Rudnick *et al.* (2004). Two of the Viliga clinopyroxene Sr–Nd isotopic ratios plot in the upper part of the MORB field and the other two (VL-1 and VL-3) have Nd-isotopic ratios higher than those of MORB. Amongst other analyses from the same area, Apt *et al.* (1998) also reported a single analysis of clinopyroxene with even higher Nd-isotopic ratios (sample 441-1, $^{143}Nd/^{144}Nd = 0.514896$) and $^{87}Sr/^{86}Sr = 0.702131$, which is similar to sample VL1-26 described here. Their analyses were performed at the Rice University, Houston, with a Finnigan MAT-262 system. Nd-isotopic ratios higher than those of MORB have also been reported by Song & Frey (1989) and Rudnick *et al.* (2004) for the Hannuoba xenoliths in

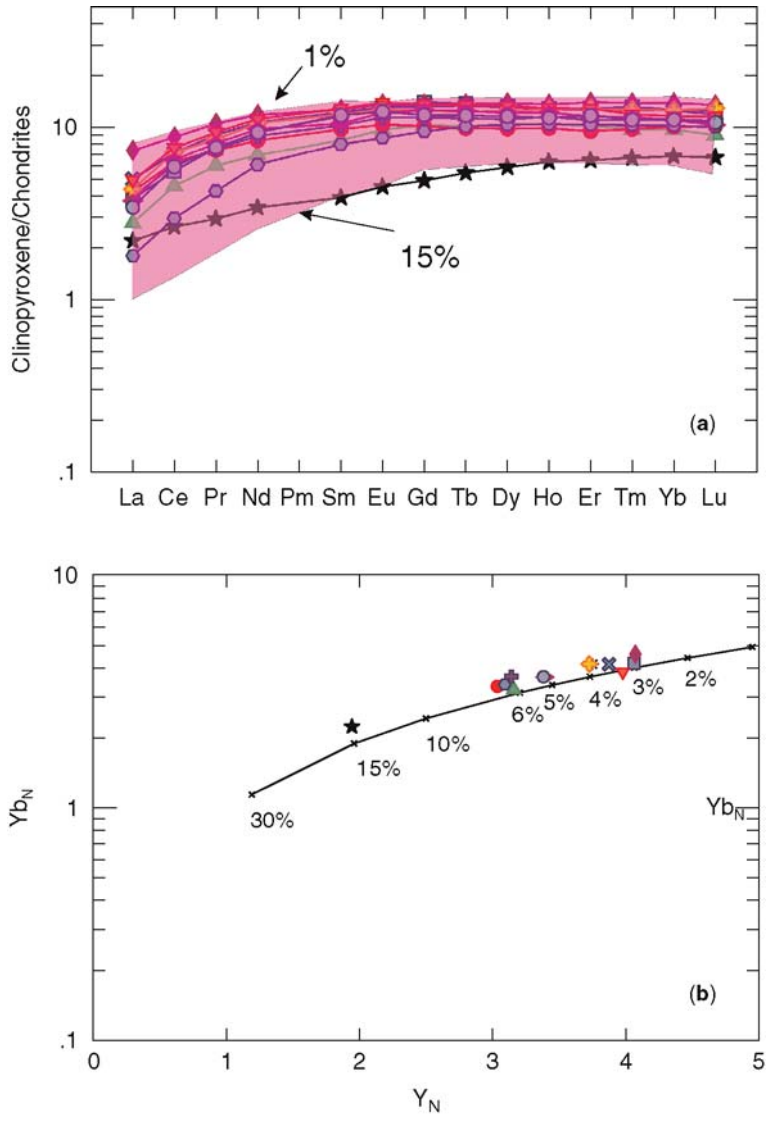

Fig. 13. Model calculations for clinopyroxene REE. (**a**) Chondrite-normalized REE abundance patterns of clinopyroxenes from Viliga and of predicted residual clinopyroxenes from batch melting model calculations (shaded area). (**b**) Predicted batch melting model trend with primitive mantle normalized Y and Yb. The Viliga data fit the trend very well. Normalization values after McDonough & Sun (1995). Symbols are as in Figure 4.

Eastern China, and by Xu *et al.* (2003) for the Huinan xenoliths in NE China. Song & Frey (1989) suggested that the high $^{147}Nd/^{144}Nd$ and low $^{87}Sr/^{86}Sr$ indicate long-term parent–daughter depletion and represent a Proterozoic lithospheric mantle. Elevated $^{147}Nd/^{144}/Nd$ values (higher than those of MORB) in orogenic peridotites have been interpreted as having asthenospheric origin (Bodinier & Godard 2004). However, to our knowledge, basalts with such a Nd-isotopic signature have not yet been found on Earth. Thus the question arises of whether such extreme Nd-isotopic ratios in mantle clinopyroxenes, plotting well off the mantle array, may form a unique group.

Calculation of model Nd ages for the Viliga peridotites reveals major depletion events of a Bulk Earth composition at 2–3 Ga. Alternatively, they could be derived from an already depleted source, such as a source from which MORB has been extracted. It appears that the second possibility does not apply, as the Viliga peridotites are, in general, fertile spinel lherzolites.

Geodynamic implication

The Viliga xenolith-bearing olivine melanephelinites and basanites are located in the Okhotsk sector (Fig. 1) and were intruded into Late Cretaceous calc-alkaline rocks that are related to the subduction of the palaeo-Pacific oceanic plate. Subduction-related calc-alkaline rocks with ages younger than the late Cretaceous have not be found in this region. The prevailing explanation for waning of the calc-alkaline magmatism is the cessation of the subduction process. Recently, Hourigan & Akinin (2004) suggested that the Okhotsk–Chukotka volcanic belt was never a high-standing arc sequence like the modern Andes, as the volcanic rocks are flat-lying and no major shortening deformation has been observed. Furthermore, shallowing of the downgoing plate could be account for by the observed continent-ward migration of the axis of arc magmatism with time.

The Viliga xenoliths belong to this subduction-related tectonic setting. However, it appears that these xenoliths do not represent parts of the usually metasomatized mantle wedge, as no hydrous phases are present and the LREE depletion in clinopyroxenes precludes cryptic metasomatism. In addition, the low Sr- and high Nd-isotopic values and the inferred model ages point to a single melting process before at least 2 Ga, whereas the continental crust above the mantle wedge in Viliga, as far it is known, is of Palaeozoic to early Mesozoic age (Nokleberg *et al.* 1998). Even if the subcontinental lithospheric mantle were the residue after crustal extraction and now represents a 'fossil' asthenosphere, it is unlikely that it could escape the influence of metasomatic fluids or melts related to the downgoing subduction slab. Therefore, the xenoliths are not intimately related to the subduction process.

The proposed model for the origin of the Viliga spinel lherzolites is illustrated in Figure 14. During the time between the cessation of the subduction at *c*. 87 Ma (Hourigan & Akinin 2004) and the volcanic activity that brought the xenoliths to the surface at *c*. 10.7–7 Ma (Akinin *et al.* 1997, 2005), the slab experienced a 'piecemeal' breakup, which allowed an upwelling asthenospheric mantle through the window(s) between the slab pieces. Subsequently, olivine melanephelinites that were generated at deeper levels (Apt *et al.* 1998) sampled the spinel lherzolites from the asthenospheric mantle, on their way to the surface. Xenoliths from the lithospheric mantle could also have been entrained in the host magma. The absence of such xenoliths is regarded as a sampling problem.

The possibility that the Viliga xenoliths are samples from the lithospheric part of the subducted slab seems to be unrealistic because, first, the peridotites are fertile and, second, as can be inferred from the calculated P–T conditions, the maximum depth from which the xenoliths were entrained in the host magma is *c*. 70 km and the part closest to the trench, the so-called volcanic front, is consistently located *c*. 110 km above the subducting slab (Tatsumi & Eggins 1995).

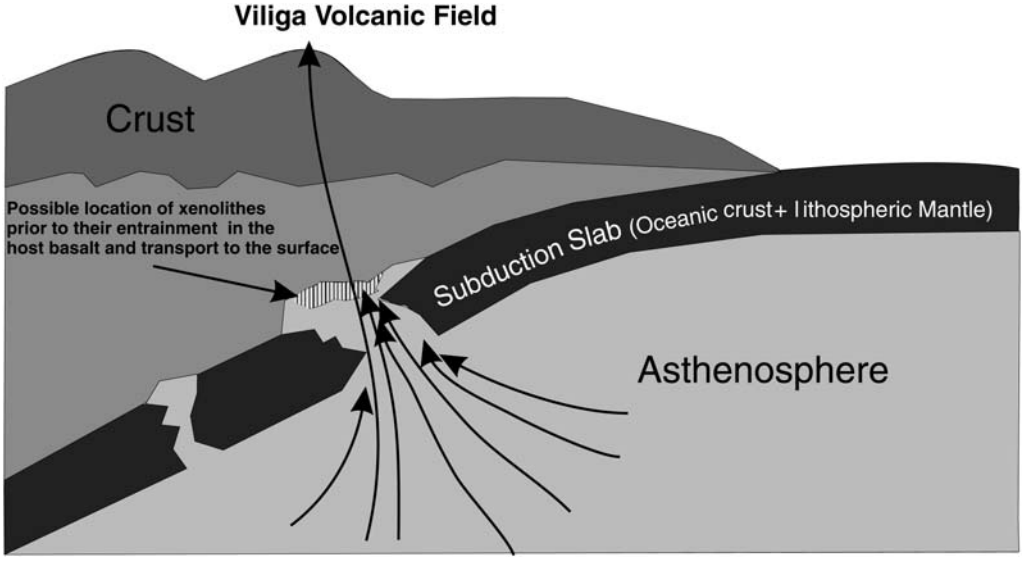

Fig. 14. Schematic representation of the 'piecemeal' breakup of the palaeo-Pacific plate followed by asthenospheric mantle upwelling to which Viliga xenoliths belong. Arrows show olivine melanephelinitic lavas of late Miocene age that brought the xenoliths to the surface.

Conclusions

Anhydrous spinel peridotites in olivine melanephelinites from the Viliga River Volcanic Field are located within subduction-related massive calc-alkaline rocks. Their source is believed to be the asthenospheric mantle and not the suprasubducted lithospheric mantle. Constituent minerals are homogeneous and no compositional variations in terms of major and minor elements have been observed. The estimated equilibrium pressures range from 15.2 to 21.3 kbar and temperatures from 1032 to 1166 °C.

The xenoliths have not been affected by metasomatic processes. Thin intergranular films of fluids or melts from the host basalt can account for the elevated whole-rock LREE abundances, as the downward clinopyroxene REE patterns preclude cryptic metasomatism. The clinopyroxene REE modelling indicates that the fertile peridotites experienced 2–9% batch melting whereas the most depleted peridotites experienced 15% batch melting. Similar results were derived from the olivine and whole-rock FeO and MgO modelling.

A magmatic refertilization of a depleted mantle wedge lithosphere can be excluded as a possible reason for the fertility of the Viliga peridotites because neither whole-rock chemistry nor clinopyroxene trace elements provide evidence for metasomatism. In addition, the low $^{87}Sr/^{86}Sr$ and the high, partly higher than MORB, $^{143}Nd/^{144}Nd$ point to an asthenospheric origin.

A possible model explaining the origin of the Viliga peridotites is a 'piecemeal' breakup of the subducted palaeo-Pacific plate, which allowed an upwelling asthenospheric mantle to intrude in the evolved window(s) between the slab pieces. Subsequently, olivine melanephelinites that were generated at deeper levels (Apt *et al.* 1998) sampled the spinel lherzolites from the asthenospheric mantle on their way to the surface.

This work was supported by UNESCO grant IGCP-430 to T.N. We are grateful to M. Gelman and V. Leonova, from NEISRI, Russia, for field assistance and logistical support. We gratefully acknowledge O. Wronska for the clinopyroxene separation and M. Thöni for Sr and Nd isotope analyses, from the Department of Lithospheric Sciences, University of Vienna. We thank I. Ryabchikov, IGEM, Russia for informal review. The reviews of G. Dobosi and G. Yaxley greatly improved the manuscript.

References

AKININ, V. V., APT, Y. E., ASHCHEPKOV, I. V. & LYAPUNOV, S. M. 1997. The geochemistry of abyssal xenoliths from melanephelinites of northeast Russia. *Transactions (Doklady) of the Russian Academy of Sciences/Earth Science Sections*, **335**, 752–756.

AKININ, V. V., MILLER, E. L. & LAYER, P. 2005. Late Cretaceous modification of deep continental crust in the NE Paleo Pacific: additional evidence from Viliga lower crust xenoliths. *EOS Transactions, American Geophysical Union*, **86**, Fall Meeting Supplement, P, Abstract V51D-1516.

APT, Y. E., AKININ, V. V. & WRIGHT, J. E. 1998. Sr, Nd and Pb isotopes in Neogene melanephelinites and deep-seated xenoliths from northeast Russia. *Geochemistry International*, **36**, 24–33.

BODINIER, J.-L. & GODARD, M. 2004. Orogenic, Ophiolitic, and Abyssal Peridotites. *In*: CARLSON, R. W. (ed.) *The Mantle and Core*, *Volume 2*. Elsevier, Amsterdam, 103–170.

BREY, G. P. & KÖHLER, T. 1990. Geothermobarometry in four-phase lherzolites II. New thermobarometers, and practical assessment of existing thermobarometers. *Journal of Petrology*, **31**, 1353–1378.

FREY, F. A., SUEN, J. C. & STOCKMAN, H. W. 1985. The Ronda high temperature peridotite: geochemistry and petrogenesis. *Geochimica et Cosmochimica Acta*, **49**, 2469–2491.

GANNOUN, A., BURTON, K. W., THOMAS, L. E., PARKINSON, I. J., VAN CALSTEREN, P. & SCHIANO, P. 2004. Osmium isotope heterogeneity in the constituent phases of mid-ocean ridge basalts. *Science*, **303**, 70–72.

HOURIGAN, J. K. & AKININ, V. V. 2004. Tectonic and chronostratigraphic implications of new $^{40}Ar/^{39}Ar$ geochronology and geochemistry of the Arman and Maltan–Ola volcanic fields, Okhotsk–Chukotka volcanic belt, northeastern Russia. *Geological Society of America Bulletin*, **116**, 637–654.

IONOV, D. A., KRAMM, U. & STOSCH, H. G. 1992. Evolution of the upper mantle beneath the southern Baikal rift zone: an Sr–Nd isotope study of xenoliths from the Bartoy volcanoes. *Contributions to Mineralogy and Petrology*, **111**, 235–247.

IONOV, D. A., ASHCHEPKOV, I. V., STOSCH, H.-G., WITT-EICKSCHEN, G. & SECK, H. A. 1993. Garnet peridotite xenoliths from the Vitim volcanic field, Baikal region: the nature of the garnet–spinel peridotite transition zone in the continental mantle. *Journal of Petrology*, **34**, 1141–1175.

JAGOUTZ, E., CARLSON, R. W. & LUGMAIR, G. W. 1980. Equilibrated Nd–unequilibrated Sr isotopes in mantle xenoliths. *Nature*, **286**, 708–710.

JUREWICZ, A. J. G. & WATSON, E. B. 1988. Cations in olivine, Part 2: Diffusion in olivine xenocrysts, with applications to petrology and mineral physics. *Contributions to Mineralogy and Petrology*, **99**, 186–201.

KEMPTON, P. D., HAWKESWORTH, C. J., LOPEZ-ESCOBAR, L., PEARSON, D. G. & WARE, A. G. 1999. Spinel ± garnet lherzolite xenoliths from Pali Aike, Part 2: trace element and isotopic evidence on the evolution of lithospheric mantle beneath southern Patagonia. *In*: GURNEY, J. J., GURNEY, J. L., PASCOE, M. D. & RICHARDSON, S. H. (eds) *Proceedings of the 7th International Kimberlite Conference.* Red Roof Design, Cape Town, 415–428.

KEPEZHINSKAS, P., DEFANT, M. J. & DRUMMOND, M. S. 1996. Progressive enrichment of island arc mantle by melt–peridotite interaction inferred from

Kamchatka xenoliths. *Geochimica et Cosmochimica Acta*, **60**, 1217–1229.

KIL, Y. & WENDLANDT, R. F. 2004. Pressure and temperature evolution of upper mantle under the Rio Grande Rift. *Contributions to Mineralogy and Petrology*, **148**, 265–280.

KILIAN, R. & STERN, C. R. 2002. Constraints on the interaction between slab melts and the mantle wedge from adakitic glass in peridotite xenoliths. *European Journal of Mineralogy*, **14**, 25–36.

KÖHLER, T. & BREY, G. P. 1990. Calcium exchange between olivine and clinopyroxene calibrated as a geothermobarometer for natural peridotites from 2 to 60 kb with applications. *Geochimica et Cosmochimica Acta*, **54**, 2375–2388.

LASAGA, A. C. 1998. *Kinetic Theory in the Earth Sciences*. Princeton University Press, Princeton, NJ.

MCDONOUGH, W. F. & SUN, S.-s. 1995. The composition of the Earth. *Chemical Geology*, **120**, 223–253.

MENZIES, M. 1983. Mantle ultramafic xenoliths in alkaline magmas: Evidence for mantle heterogeneity modified by magmatic activity. *In*: HAWKESWORTH, C. J. & NORRY, M. J. (eds) *Continental Basalts and Mantle Xenoliths.* Shiva, Nantwich, 92–110.

NOKLEBERG, W. J., PARFENOV, L. M., MONGER, J. W. H., *ET AL*. 1998. Phanerozoic tectonic evolution of the Circum-North Pacific. *US Geological Survey, Open-File Report*, **98–0754**.

NORMAN, M. D. 1998. Melting and metasomatism in the continental lithosphere: laser ablation ICPMS analysis of minerals in spinel lherzolites from eastern Australia. *Contributions to Mineralogy and Petrology*, **130**, 240–255.

NORMAN, M. D. 2001. Applications of laser ablation ICPMS to the trace element geochemistry of basaltic magmas and mantle evolution. *In*: SYLVESTER, P. (ed.) *Laser-Ablation-ICPMS in the Earth Sciences; Principles and Applications*. Mineralogical Association of Canada, Short Course Series, **29**, 163–184.

PEACOCK, S. M. 1993. Large-scale hydration of the lithosphere above subducting slabs. *Chemical Geology*, **108**, 49–59.

RUDNICK, R. L., GAO, S., LING, W.-l., LIU, Y.-s. & MCDONOUGH, W. F. 2004. Petrology and geochemistry of spinel peridotite xenoliths from Hannuoba and Qixia, North China craton. *Lithos*, **77**, 609–637.

SONG, Y. & FREY, F. A. 1989. Geochemistry of peridotite xenoliths in basalts from Hannuoba, Eastern China: Implications for subcontinental mantle heterogeneity. *Geochimica et Cosmochimica Acta*, **53**, 97–113.

STOSCH, H.-G., LUGMAIR, G. W. & KOVALENKO, V. I. 1986. Spinel peridotite xenoliths from the Tariat Depression, Mongolia. II: Geochemistry and Nd and Sr isotopic composition and their implications for the evolution of the subcontinental lithosphere. *Geochimica et Cosmochimica Acta*, **50**, 2601–2614.

TATSUMI, Y. & EGGINS, S. 1995. *Subduction Zone Magmatism.* Blackwell Science, Cambridge, MA.

THONI, M. & MILLER, C. 2004. Ordovician metapegmatite garnet (N-W Otztal basement, Tyrol, Eastern Alps): preservation of magmatic garnet chemistry and Sm–Nd age during mylonitization. *Chemical Geology*, **209**, 1–26.

WELLS, P. R. A. 1977. Pyroxene thermometry in simple and complex systems. *Contributions to Mineralogy and Petrology*, **62**, 129–139.

XU, Y.-G., MENZIES, M. A., THIRLWALL, M. F., HUANG, X.-L., LIU, Y. & CHEN, X.-M. 2003. 'Reactive' harzburgites from Huinan, NE China: products of the lithosphere–asthenosphere interaction during lithospheric thinning? *Geochimica et Cosmochimica Acta*, **67**, 487.

ZINDLER, A. & HART, S. R. 1986. Chemical geodynamics. *Earth and Planetary Science Letters*, **14**, 493–571.

ZONENSHAIN, L. P., KUZMIN, M. I., NATAPOV, L. M. & PAGE, B. M. 1990. *Geology of the USSR: A plate-tectonic synthesis*. American Geophysical Union, Geodynamics Series, **21**.

The Gătaia Pleistocene lamproite: a new occurrence at the southeastern edge of the Pannonian Basin, Romania

I. SEGHEDI[1], T. NTAFLOS[2] & Z. PÉCSKAY[3]

[1]*Institute of Geodynamics, 19–21, str. Jean-Luis Calderon, 020032 Bucharest, Romania (e-mail: seghedi@ns.igr.ro)*

[2]*Department of Geological Sciences, University of Vienna-Geozentrum, Althanstr. 14, 1090 Vienna, Austria*

[3]*Institute of Nuclear Research of the Hungarian Academy of Sciences, PO Box 51, Bem ter 18/c, H-4001 Debrecen, Hungary*

Abstract: The petrological identity of the lamproite occurrence situated *c*. 5 km south of Gătaia (Banat, western Romania), until now considered to be an alkali basalt, has been revealed by exploration drilling. This drilling programme pierced a slightly vesicular lava flow inside the Şumiga hill (198 m above sea level), revealing a sequence of vesicular lava intercalated with fallout scoria deposits. The isolated lamproite volcano, dated at 1.32 ± 0.06 Ma (whole-rock K/Ar method), is situated at the southeastern margin of the Pannonian Basin and at the western margin of the South Carpathians, along an important NE–SW fault system. The lamproite magma erupted through flat-lying Miocene sedimentary rocks, which overlie older crystalline basement that experienced intense lithospheric deformation and orogeny during Cretaceous times. The lamproite is associated with contemporaneous volcanic activity that lies 50–150 km to the NNE, along the South Transylvanian fault system (Lucareţ alkali basalts, Uroiu shoshonites); these rocks, however, are not consanguineous, and derive from different mantle sources. There are, however, similarities to Oligocene lamproites from Serbia (Bogovina), generated on similar basement. The lamproite is fresh and has a slightly porphyritic texture with phenocrysts of high-Mg olivine and microphenocrysts of euhedral leucite in a glassy matrix. The matrix also contains microcrysts of olivine, armalcolite, apatite, sanidine, low Al-diopside, fluorine-bearing titanium phlogopite, fluorine-bearing amphibole and accessory chrome spinels. Ba-sulphate aggregates fill small vesicles. Very rare clots of corroded Al-phlogopite surrounded by secondary spinels are enclosed by leucite aggregates, suggesting formation during an earlier event. Major and trace element geochemistry and Sr and Nd isotopes show that the rock is a typical lamproite, close to the compositions of Leucite Hills and Gaussberg lamproites. The source for the Gătaia lamproite was probably a garnet harzburgite lithospheric mantle, metasomatized by alkaline mafic melts, most probably active at the Cretaceous–Palaeogene boundary. Metasomatism by alkaline melts is indicated by high abundances of incompatible trace elements, such as Ba, Sr, Rb and Zr. The Gătaia lamproite probably had a limited available source volume for melting that reflects the ambient thermal regime in the typical post-collisional tectonic setting active during Late Neogene to Quaternary time. Emplacement of this lamproite was probably a result of surface uplift and erosion at the base of the lithosphere, marking the collapse of the Alpine orogen.

Pliocene–Pleistocene ultrapotassic magmatic activity is uncommon in the Carpathian–Pannonian region and the only example described so far is an olivine leucitite from Bar, in the Pannonian Basin (Harangi *et al.* 1995), dated at 2.17 Ma (Pécskay *et al.* 1995*a*). Its mineral assemblage consists of olivine, clinopyroxene and phlogopite as phenocryst phases combined with groundmass leucite, with a bulk-rock composition of 50.38 wt% SiO_2 and 7.77 wt% MgO (Harangi *et al.* 1995). The new lamproite occurrence described here was until now considered to be an alkali basalt (Mateescu 1937; Drăgulescu *et al.* 1968). This lamproite was revealed by a private exploration drilling programme in the summit of the volcano, which passed through *c*. 2 m of soil and *c*. 4 m of oxidized and weathered scoria-like clinker before intercepting a slightly vesicular lava flow *c*. 10 m thick.

Ultrapotassic rocks of Tertiary–Quaternary age occur in several localities in the Alpine–Mediterranean region and are mostly considered to be of orogenic type (Mitchell & Bergman 1991). Ultrapotassic rocks occur in Spain (Venturelli *et al.* 1984*a*, 1988, 1991; Benito *et al.* 1999; Turner *et al.* 1999), Italy (Venturelli *et al.* 1984*b*; Peccerillo 1985, 1990, 1995, 1998; Conticelli & Peccerillo 1992; Conticelli *et al.* 1992, 2002; Conticelli 1998), Turkey (Çoban & Flower 2007),

From: COLTORTI, M. & GRÉGOIRE, M. (eds) *Metasomatism in Oceanic and Continental Lithospheric Mantle.* Geological Society, London, Special Publications, **293**, 83–100.
DOI: 10.1144/SP293.5 0305-8719/08/$15.00

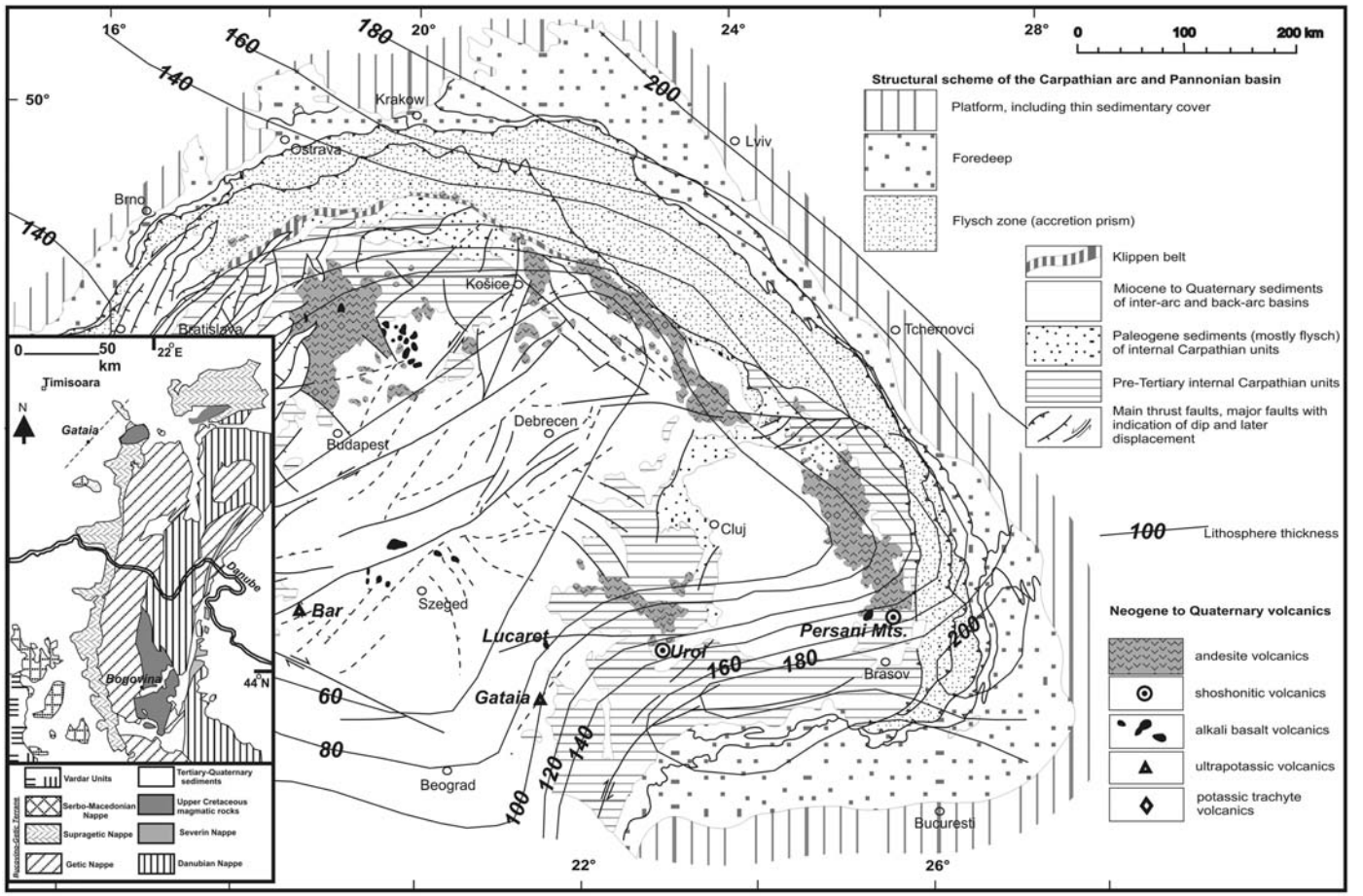

Fig. 1. Distribution of the Gătaia lamproite in the context of Miocene–Quaternary magmatism in the Carpathian–Pannonian region (map is a simplified version of the map of Pécskay *et al*. 2006). The inset show the western South Carpathians nappe stack, the Upper Cretaceous magmatic rocks and Gătaia (Romania) and Bogovina (Serbia) occurrences, simplified after Kräutner (1997). Lithosphere thickness is according to Lenkey (1999) and references therein.

the Alps (Venturelli *et al.* 1984*b*) and the Balkan Peninsula (Prelević *et al*. 2001, 2005, 2007; Yanev *et al*. 2003; Altherr *et al.* 2004) although, according to the classification of Mitchell & Bergman (1991), few of them are true lamproites.

In this paper, we present electron microprobe data for the Gătaia lamproitic mineral phases and glass, which are all fresh (an exceptional situation for this rock-type), major and trace element, and strontium and neodymium isotope data that are relevant to the interpretation of the petrogenesis of this special magma. We discuss the issue of the mantle source for the Gătaia lamproite by comparing it with lamproitic rocks of similar age worldwide, including those of Oligocene age from Serbia (emplaced on a similar basement), and with local calc-alkaline, alkali basaltic, potassic and ultrapotassic rocks from the Carpathian–Pannonian region. We argue that the Gătaia lamproite derives from lithospheric mantle connected with the Tisia terrane, which reveals enrichment, via alkaline mafic melts, similar to the source of other anorogenic lamproites.

Geological setting

The Gătaia lamproite occurrence is situated *c*. 5 km south of Gătaia (Banat) (Fig. 1). It forms a lava flow within the Şumiga hill (198 m above sea level (a.s.l.)), which comprises a lava cone with a base of *c*. 2 km diameter, apparently composed of a succession of lava flows, 10–20 m thick, intercalated with less abundant highly vesicular scoria fall deposits (mostly intensely weathered). The isolated Gătaia volcano is situated at the southeastern margin of the Pannonian Basin and at the western margin of the South Carpathians terrane (Fig. 1), along a regionally important NE–SW fault system. The latter has not been mapped until now, although it parallels older Mesozoic tectonic features and formed as a result of Miocene tectonic uplift (e.g. Iancu *et al.* 2005) (Fig. 1). The lamproite melts have been erupted onto relatively undeformed flat-lying Pleistocene terrace deposits and Miocene sedimentary rocks at the margin of the Pannonian Basin. The Miocene succession overlies older crystalline basement made up of Supragetic Units, which record the intense lithospheric deformation and orogeny during Cretaceous times (e.g. Săndulescu 1984; Iancu *et al.* 2005) (Fig. 1). The Gătaia (Şumiga hill) lamproite represents a short-lived magmatic episode, contemporaneous with volcanic activity recorded by alkali basalts in Lucareţ and shoshonites in Uroiu (e.g. Pécskay *et al.* 1995*b*; Seghedi *et al.* 2004*a*) that lie 50–150 km to the NNE, along the South Transylvanian fault system (Săndulescu 1988; Kräutner 1997) (Fig. 1). Although contemporaneous, these groups of rocks are not consanguineous and are inferred to be derived from a different mantle source (or sources) (e.g. Seghedi *et al.* 2004*a*, *b*).

Petrography

The Gătaia lamproite is dark grey, fine-grained and slightly porphyritic (Fig. 2a). It contains high-Mg olivine (30–35 vol %) and microphenocrysts of euhedral leucite (35–40 vol %) in a glassy groundmass. The groundmass forms 25–35 vol % of the rock and encloses microcrysts of olivine, armalcolite, apatite, sanidine, low Al-diopside, fluorine-bearing titanium phlogopite and fluorine-bearing richterite. Cr-spinels occur as accessories (included in olivine and rarely in the groundmass) along with very rare titanomagnetite. Very rare clots of corroded Al-phlogopite, surrounded by secondary spinels (56.7 wt% Al_2O_3), are enclosed by leucite aggregates. Ba-sulphate aggregates fill small vesicles and represent the final mineral phase. Rare inclusions of fused sedimentary rocks (*c*. 5 mm long) have also been found, and are sometimes surrounded by spotted fine hyalophane aggregates.

Analytical methods and age

The analysed samples are petrographically fresh and show no evidence of hydrothermal alteration. For whole-rock K/Ar measurements (Debrecen laboratory) the rock samples were crushed and sieved to separate the 250–100 μm fraction for Ar analysis. Argon was extracted from the sample by RF fusion in a Mo crucible, in a previously baked stainless steel vacuum system. ^{38}Ar spike was added from a gas pipette and the evolved gases were cleaned using Ti and SAES getters and liquid nitrogen traps, respectively. Cleaned argon was transported directly into the mass spectrometer and Ar isotope ratio was measured in the static mode, using a 15 cm radius magnetic sector type mass spectrometer. To determine potassium content pulverized samples (0.1 g) were digested in HF with addition of sulphuric and perchloric acids. The digested sample was dissolved in 100 ml 0.25 mol $^{-1}$ HCl. After a subsequent fivefold dilution 100 ppm Na and 100 ppm Li were added as a buffer and Li internal standard. K concentrations were measured by a digitized flame photometer (Corning 480 type).

The interlaboratory standards Asia 1/65, LP-6, HD-B1, and GL-O combined with atmospheric Ar were used to control the measurements. Details of the instruments, applied methods, and calibration results have been published by Balogh (1985). The rock was dated by the K/Ar method (K% = 8.191; ^{40}Ar rad % = 33.3; ^{40}Ar rad

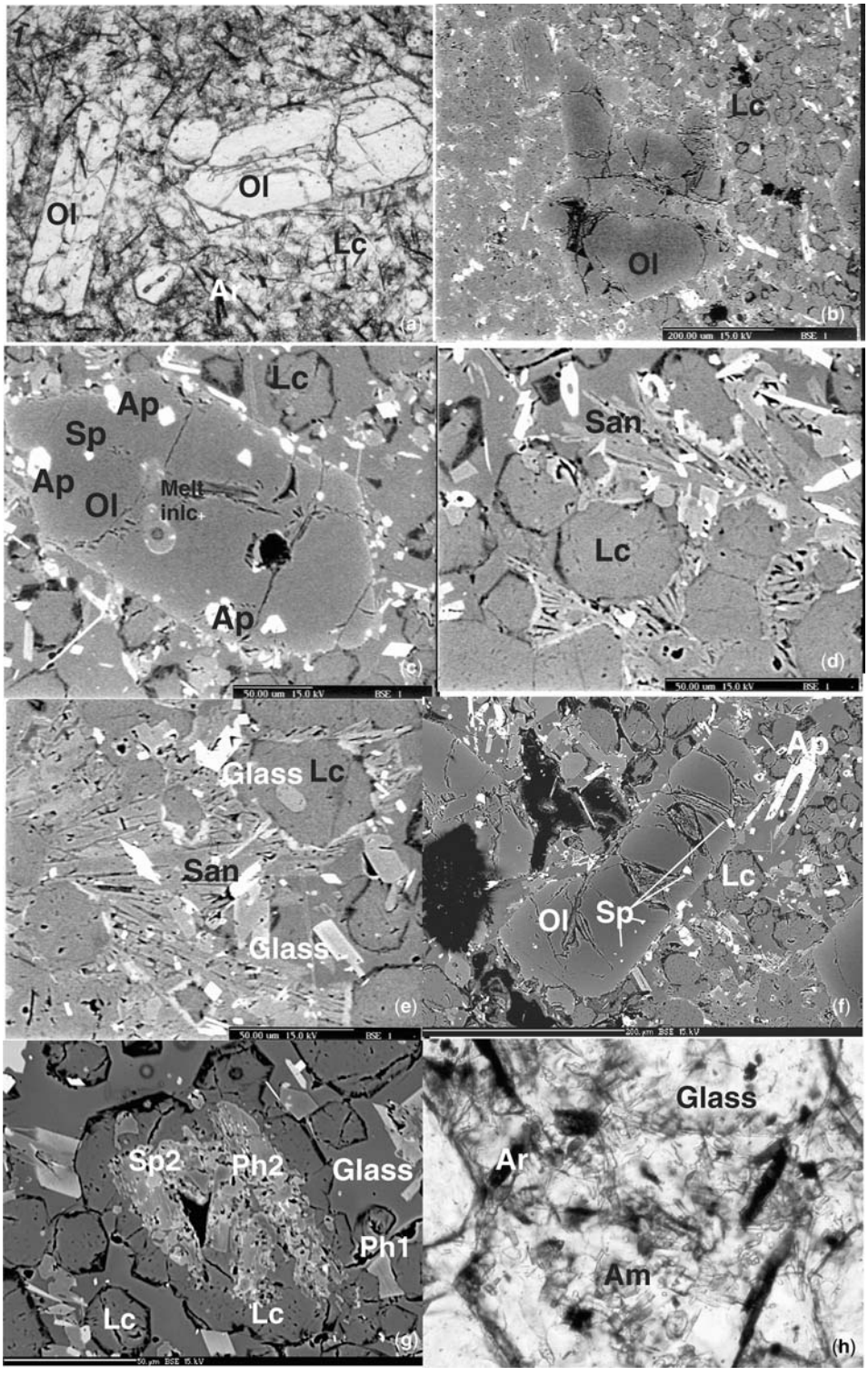

Fig. 2. (*Continued*).

(cm^3 STP g^{-1}) $\times$ 10^{-7} = 4.207] at 1.32 $\pm$ 0.06 Ma, corresponding to the Pleistocene interval.

Minerals were analysed on a CAMECA SX100 microprobe at the Department of Lithospheric Science, University of Vienna, using ZAF correction procedures. Counting times at the peak position for Na and F were 10 s and for all other elements were 20 s. Operating conditions were 10 kV and 10 nA for Na and F and for all other elements 15 kV and 20 nA, and natural minerals were used as standards. A 5 μm defocused beam was used for analysing feldspar glass and leucite.

Major and trace element analyses were carried out using X-ray fluorescence (XRF) techniques (Philips 2400). Th, U and REE were analysed by inductively coupled plasma-mass spectrometry (ICP-MS) (ELAN 6100) at the Department of Lithospheric Sciences, University of Vienna. Sr and Nd isotopic analytical work was performed at the Laboratory of Geochronology, Department of Lithospheric Sciences, University of Vienna, using the analytical procedure described by Thoni & Miller (2004), and determination of Sr and Nd isotope ratios was carried out by thermal ionization mass spectrometry (TIMS) a Thermo Finnigan Triton TI system.

Mineral chemistry

Olivine

Multiple generations of olivine are recognized (Table 1). The largest crystals (up to 1 cm) form widespread phenocrysts, now largely corroded and kinked. These large olivines have a magnesian core (94–91 Fo) rich in NiO that grades into a magnesium-depleted rim (Fig. 2a and b). The high-Fo olivine cores are also rich in P_2O_5 (Table 1, sample 8.1p). Smaller groundmass olivine is iron-enriched (84–80 Fo), euhedral and of similar composition to the rims of the phenocrysts. In addition, several generations of chrome spinels and apatite and various silicate–melt inclusions (*c*. 50 μm) are present inside the olivine, some of which are rich in apatite (Fig. 2c).

Leucite

Leucite is an important component of the rock, forming euhedral to subhedral crystals (0.2–1 mm) or aggregates (Table 1; Fig. 2d and e). The crystals are sometimes weakly anisotropic and complexly twined. They rarely enclose poikilitic high-Al phlogopites. The contact between leucite crystals and glassy groundmass is marked by a dark rim, suggesting a compositional change with a slight increase in SiO_2 (1–2.5%) and a decrease in K_2O (2–2.5%). A tendency to higher Al_2O_3 (*c*. 3%) paired with lower K_2O (*c*. 3.5%) reveals the decomposition of leucite into sanidine (Fig. 2e).

Sanidine

Sanidine is mostly present as late-stage rosette-like crystals replacing the glassy matrix and leucite (evident in compositional transitions at the margins of leucite; see above; Fig. 2e and f). This relationship suggests a high-temperature devitrification as the glass became saturated (Table 1). Besides this polycrystalline sanidine, which has high Ba content, we have found rare high-Ti sanidine included in the groundmass olivine (Table 1). The high-Ti sanidine suggests that at a certain level of silica saturation during late-stage crystallization, the melt may have crystallized primary sanidine and olivine; we suppose that in the following stages of crystallization the large-volume production of armalcolite consumed all available Fe and Ti and suppressed further generation of sanidine as a primary mineral.

Spinels

Primary spinels are common minerals in Gătaia lamproite (Table 1). Rare secondary spinels are also

Fig. 2. (*Continued*) (**a**) Photomicrograph (plane-polarized light) of slightly porphyritic lava flow of Gătaia lamproite showing olivine (Ol) phenocrysts, leucite (Lc) microcrysts and armalcolite (Ar) needles in a brownish vitreous glass, which includes many other minerals. Field of view 2.2 cm. (**b**) Back-scattered electron image showing a large subhedral corroded and kinked olivine (Ol), embedded in a mass of leucite (Lc), glass and other minerals. (**c**) Back-scattered electron image showing a euhedral crystal of olivine (Ol) full of melt and apatite (Ap) inclusions. (**d**) Back-scattered electron image showing euhedral leucite (Lc) crystals, with a dark rim at the contact with the glass, surrounded by sanidine (San) that grows in the glass. (**e**) Back-scattered electron image showing euhedral to subhedral crystals of leucite (Lc), one with glass inclusion surrounded by rosette-like crystals of sanidine (San) replacing the glassy matrix and leucite. (**f**) Back-scattered electron image showing a line of spinel (Sp) inclusions in an olivine crystal (Ol), and a hollow apatite (Ap) in the glass. (**g**) Back-scattered electron image showing a relict of high-Al phlogopite (Ph2) microcrystals trapped in leucite (Lc) aggregate and surrounded by secondary spinels (Sp2). In the glass there is a late-stage phlogopite crystal (Ph1). (**h**) Photomicrograph (plane-polarized light) showing tiny crystals of amphibole (Am) in the glass. Field of view 0.9 cm.

Table 1. *Representative microprobe analyses of the mineral phases in the Gătaia lamproite*

Mineral		SiO_2	TiO_2	Al_2O_3	V_2O_3	Cr_2O_3	Fe_2O_3*	FeO†	MnO	NiO	ZnO	MgO	CaO	Na_2O	K_2O	P_2O_5	BaO	ZrO_2	F	Total	Fo	Cr-no.	Mg-no.
Olivine	core	41.3				0.05		6.3	0.12	0.74		51.6	0.11			0.07				100.29	92.9		
	rim	39.9				0.06		12.9	0.27	0.33		46.1	0.2							99.76	85.4		
	mph	38.0				<0.02		17.2	0.29	0.16		42.7	0.34							98.74	81.5		
Spinel	sp-g	0.10	13.37	0.41	0.50	34.3	8.2	37.6	0.57	0.17	0.29	3.4								98.93		80.5	13.9
	sp-i	0.06	5.77	2.15	0.16	49.6	8.4	25.4	0.36	0.15	0.23	7.4								99.75		81.6	34.5
	sp-s	0.31	1.39	57.7	<0.02	0.22	6.4	18.6	0.1	0.17	<0.02	15.7								100.58		0.24	60.1
Phlogopite	Phl-m	43.6	7.7	8.4				7.8	0.03	0.04		18.7	0.1	0.71	9.5				3.6	100.21			
	Phl-r	35.9	9.4	17.3				7.8	0.04	0.06		16.9	0.07	0.22	9.3				2.8	99.79			
Leucite		58.4	0.31	21.8				1.01				0.26	0.02	0.49	18.5					100.72			
Clinopyroxene		52.7	1.71	0.41		0.42		4.3	0.13			17.9	22.0	0.32						99.89			
Amphibole		55.6	5.5	2.31			<0.02	5.8	0.09	0.02		16.3	5.5	4.1	3.7				1.94	100.86			
		53.5	5.8	0.67			2.27	3.7	0.11	0.02		18.4	5.9	4.3	3.7				2.05	100.42			
Armalcolite		0.3	69.1	0.30		0.47		21.2	0.17	0.04		7.2	0.13		0.24					99.18			
Sanidine		64.8	0.43	15.3				2.5				0.56		0.97	14.8		0.75			100.11			
		61.1	1.57	17.9				1.4				1.83		0.1	15.6					99.57			
Glass		68.0	2.7	10.1				3.7	0.03			1.05	0.07	2.5	7.1	0.21		0.25		95.66			
		61.2	2.8	16.5				1.6	0.03			1.45	1.29	1.31	9.8					95.98			
Hyalophane		42.6	0.49	24.2				0.21				0.02	<0.02	0.49	4.8		27.6			100.4			
		38.6	0.41	28.2				2.5				1.56	0.03	0.52	4.9		22.1			98.77			
Apatite		SiO_2	CaO	SrO	P_2O_5	La_2O_3	Ce_2O_3	F		Total													
		0.65	54.6	0.71	40.6	0.19	0.4	3.6		100.71													

*Fe_2O_3 estimated by stoichiometric normalization.
†Fe total as FeO if Fe_2O_3 not given.
All the analyses represent the average of 2–4 measured points. mph, microphenocryst; lack of value indicates not analysed; sp-g, spinel in groundmass; sp-i, spinel inclusions in olivine; sp-s, secondary spinel; Phl-m, matrix phlogopite; Phl-r, relict phlogopite; Cr-number=mol($Cr/Cr + Al + Fe^{3+}$) × 100; Mg-number=mol($Mg/Mg + Fe$) × 100.

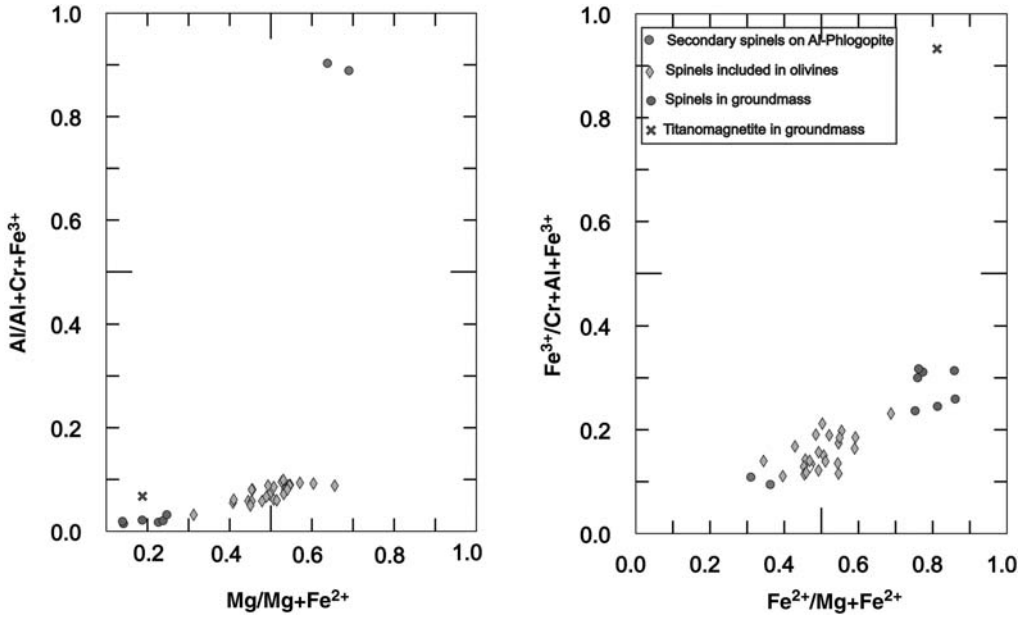

Fig. 3. Variation of $Al/(Al + Cr + Fe^{3+})$ v. $Mg/(Mg + Fe^{2+})$ and $Fe^{3+}/(Cr + Al + Fe^{3+})$ v. $Fe^{2+}/(Mg + Fe^{2+})$ of various spinels in Gătaia lamproite.

present. The primary spinels occur as small euhedral crystals (*c*. 100 μm) included in olivine and, in the groundmass, as chromites. Secondary spinels are Al-rich and are included in leucite, and are interpreted to derive from breakdown of unstable Al-phlogopite (earlier phlogopite) (Figs 2g and 3). Jaques & Foley (1985) found similar pleonaste spinels in West Kimberley lamproite and considered that they formed by reaction from leucite.

The primary spinels fall in group 2 of Mitchell & Bergman (1991). There is a continuous compositional trend showing decreasing Al and Mg with increasing Cr and Fe. The earlier crystals show lower $Cr/(Cr + Al)$ ratios (88), which correlate with high-Fo (93) olivine. A single titaniferous magnetite in the groundmass may represent the end of this trend, or may be of another, unknown, origin (Fig. 3). The chromites show variable Mg- and Cr-number (100 atomic $Cr/(Cr + Al)$), between 5 and 58 and between 88 and 98, respectively, and an increasing trend of TiO_2 content (from 2 to 12.19%) along with decreasing Al_2O_3 (from 4.3 to 0.3%).

Phlogopite

Phlogopite (Table 1) is present as microphenocrysts in the groundmass, and as relict high-Al and Ti-rich (7.8–10.6 wt%) microcrysts trapped in leucite (Fig. 2g). High-Al phlogopites show lower SiO_2 and Na_2O, and slightly lower MgO and F, relative to groundmass phlogopites. The aluminous mica, however, has a high TiO_2 content (7.9–9.3%), similar to that of phlogopite phenocrysts from the Leucite Hills (Mitchell & Bergman 1991). However, their TiO_2 content is similar to that of phlogopite in the matrix (Fig. 2h), which has compositions typical of those in the groundmass of lamproites (e.g. Mitchell & Bergman 1991). High-Al phlogopites are not in equilibrium with the host lava, as evidenced by their marginal breakdown and formation of secondary spinel. They have been found in many lamproites and are considered to be high-pressure cognate phases that form via polybaric fractionation, leading to Al deficiency and hence peralkalinity of the residual liquid (Mitchell & Bergman 1991).

Amphibole

Amphibole is rare and forms small crystals (5–10 μm) in the matrix (Table 1, Fig. 2h), as one of the latest crystallizing phases. Amphiboles are typically richterites, a characteristic species for lamproitic magmas, with similar compositions to Leucite Hills, Smoky Butte, West Kimberley or Spanish lamproites (e.g. Wagner & Velde 1986; Mitchell & Bergman 1991). They show variable FeO (2.2–5.8 wt%) and MgO (16.3–19.5 wt%) composition and rather constant F content (1.9–2.1 wt%).

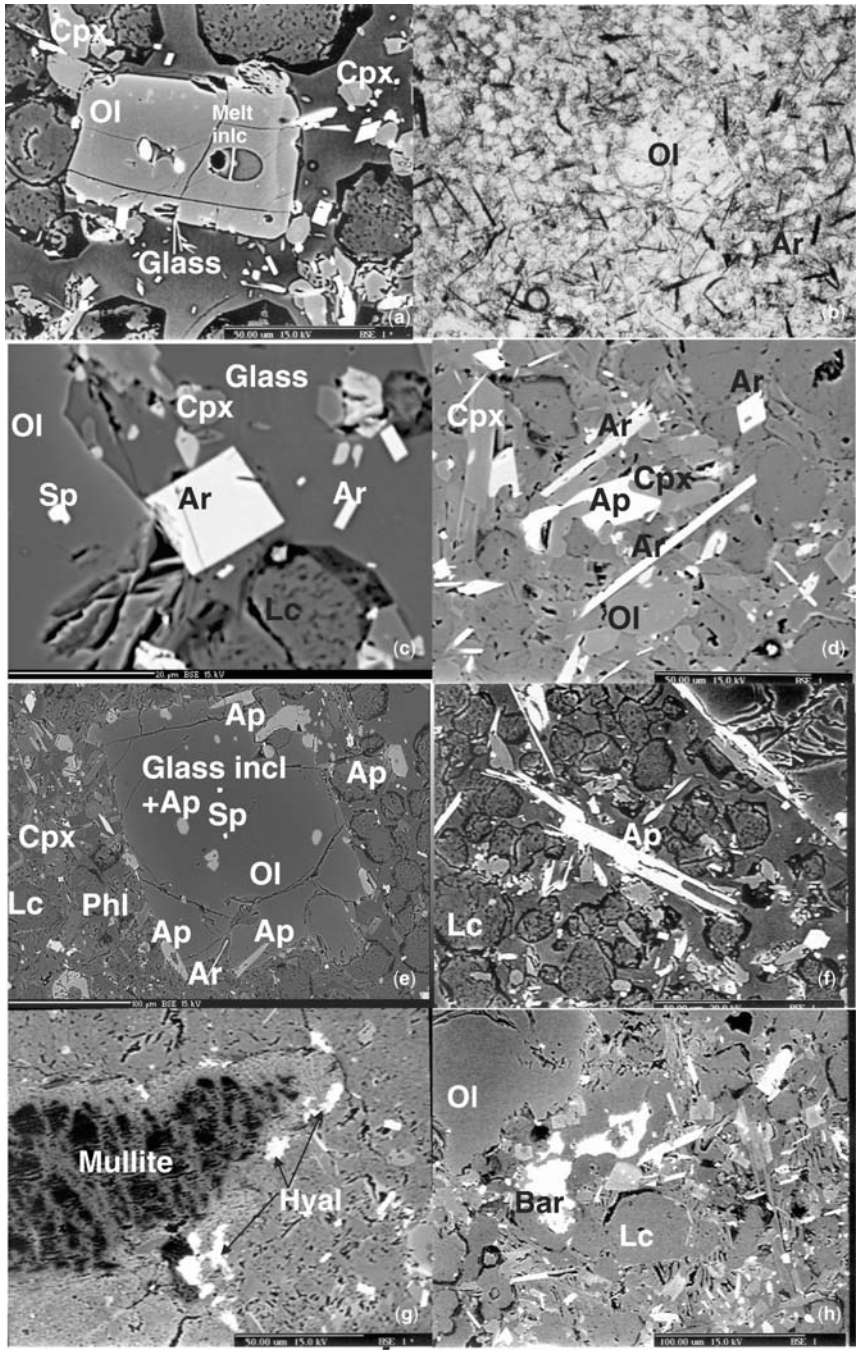

Fig. 4. (**a**) Back-scattered electron image showing clinopyroxene (Cpx) generated as late crystals in the glass, surrounded by olivine (Ol) with apatite (Ap) and a melt inclusion, leucite (lc) and other minerals. (**b**) Photomicrograph (plane-polarized light) showing olivine (Ol), leucite (Lc) and armalcolite (Ar), as opaque needles in the glassy groundmass. Field of view 2.0 cm. (**c**) Back-scattered electron image showing a rhombic section of an armalcolite crystal (Ar), which grew in the glassy groundmass and is surrounded also by spinels (Sp), clinopyroxene (Cpx) and leucite (Lc). (**d**) Back-scattered electron image showing relationships of the late-stage minerals generated in the Gătaia lamproite: clinopyroxene (Cpx), armalcolite (Ar), olivine (Ol), surrounded by leucite crystals (Lc). (**e**) Back-scattered

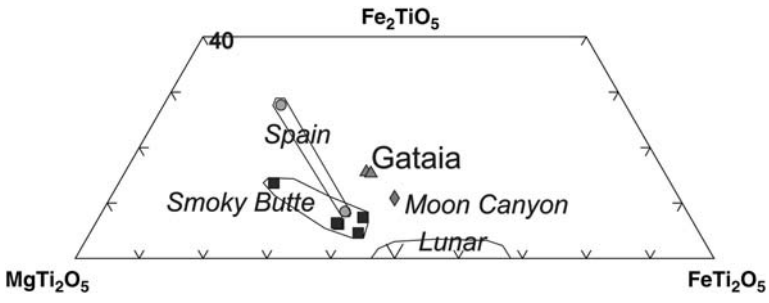

Fig. 5. $MgTi_2O_5$–Fe_2TiO_5–$FeTi_2O_5$ ternary diagram showing the composition of Gătaia armalcolites. Smoky Butte, Spain, Moon Canyon and lunar armalcolite from Velde (1975), Mitchell & Bergman (1991) and references therein.

Clinopyroxene

Clinopyroxene forms small euhedral crystals in the matrix (10–20 μm) and also forms a late crystallizing phase (Table 1, Fig. 4a). Its composition shows low Al_2O_3 contents, which are typical of lamproitic compositions, and they have a formula of En_{50-49} $Fe_{7-5}Wo_{44-43}$.

Armalcolite

Armalcolite is a late phase in the crystallization sequence and occurs as elongate euhedral or skeletal crystals (0.2–1.2 mm) that are equally distributed in the groundmass (Fig. 4b and c), which show a purplish tint in thin section and a weak birefringence (Fig. 4d). Its formula is very similar to armalcolite reported worldwide (Fig. 5). High Mg/Fe ratios (around unity) suggest generation at high temperature (e.g. Velde 1975); on the other hand, the skeletal crystal shape suggests fast growth during low-*P* quenching of the lamproite magma. This paper gives the first description of this mineral in the Carpathian–Pannonian region.

Apatite

Apatite is a widespread mineral formed during all stages of crystallization, and is *c*. 10–500 μm in length. It is included in olivine (in phenocrysts, early generated olivine (Fo_{90-92}) and the last generated olivine (Fo_{80-78})), as well as in the groundmass glass, where the largest skeletal crystals are found (up to 1 mm) (Fig. 4e). Many of these crystals show a hollow core (Fig. 4f). The apatites are fluor-type, having a fluorine content ranging from 2.6% to 3.7% (and to 4.5%, although these compositions do not fit the stoichiometric formulae) (Table 1). The early apatites, sometimes recrystallized in the olivine melt inclusions, have lower fluorine contents (2.6–4.1%) relative to the groundmass apatites (4.2–4.5%) and show small differences in all other components (P_2O_5 39.8–41.1%; Ce_2O_3 0.31–0.41%; La_2O_3 0.11–0.21%; SrO 0.56–0.80%). This composition corresponds to 'apatite B' of O'Reilly & Griffin (2000), which suggests its crystallization from magmas within the carbonate–silicate compositional spectrum, which favour high abundances of light rare earth elements (LREE), Y and Sr contents of the rock.

Glass

The rock has a glassy groundmass, whose composition is SiO_2-rich and fairly homogeneous (Table 1), which gains a *c*. 2% increase in SiO_2 by recalculation to 100 wt% on a CO_2-free basis. We have not found alteration processes; however, we have observed that devitrification and recrystallization of the glass, as well as leucite, took place and generated sanidine. Fresh glass should be the result of a liquid line of descent resulting from fractionation of the lamproitic magma. We have also measured the glass included in several olivine crystals (Table 1), which shows higher Al_2O_3 and

Fig. 4. (*Continued*) electron image showing various locations of apatite (Ap) generated in the Gătaia lamproite: together with melt glass inclusion in olivine (Ol), as a single grain inclusion in olivine, as a late-stage inclusion in glass of the rock. Also, late-stage minerals such as clinopyroxene (Cpx) or phlogopite (Ph) can be seen, together with the prevalent leucite (Lc) crystals. (**f**scattered electron image showing hollow-cored apatite (Ap) that grew in the glassy groundmass, surrounded by leucite (Lc) crystals. (**g**) Back-scattered electron image showing anhedral hyalophane at the contact of a small fused argillaceous inclusion (now mullite) in the Gătaia lamproite. (**h**) Back-scattered electron image showing irregular voids in the Gătaia lamproite, filled with barite (Bar). The image also shows olivine (Ol), leucite (Lc), and other minerals.

K_2O but lower SiO_2 relative to the groundmass glass. There is a negligible difference between the whole-rock and glass K_2O composition, which suggests that differentiation resulted in SiO_2 enrichment.

Table 2. *Whole-rock major (%) and trace element (ppm) contents, including REE analyses and $^{87}Sr/^{86}Sr$ and $^{143}Nd/^{144}Nd$ isotope values for the Gătaia lamproite in comparison with those for the Bar leucitite (from Harangi* et al. *1995)*

Sample	Gătaia	Bar
(wt%)		
SiO_2	52.74	50.38
TiO_2	2.99	2.31
Al_2O_3	9.34	15.27
Fe_2O_3*	6.7	7.1
MgO	11.73	7.77
MnO	0.09	0.11
CaO	3.43	5.99
Na_2O	1.27	2.97
K_2O	8.67	6.4
P_2O_5	2.15	0.88
LOI	0.46	0.82
Total	99.57	99.18
mg-no.	75.7	70.3
K_2O/Na_2O	6.84	2.15
(ppm)		
Ni	478	154
Cr	539	242
Co	39	na
V	162	183
Sc	14	16.9
Cu	53	na
Zn	99	na
Rb	205	161
Ba	2750	2414
Th	16.3	17.8
Nb	68	57
Pb	11	na
Sr	868	1140
Zr	1243	604
Y	21.54	20
La	125	84
Ce	258	152
Nd	121	75
Sm	15	10.2
Eu	3.7	2.87
Gd	10.9	na
Dy	5.13	na
Er	2.01	na
Tb	1.2	0.82
Yb	1.29	1.14
Lu	0.17	na
$^{87}Sr/^{86}Sr$	0.705713 ± 5	0.70503
$^{143}Nd/^{144}Nd$	0.512572 ± 4	0.512592

*Fe total as Fe_2O_3.
LOI, loss on ignition; na, not analysed.

Hyalophane and barite

Hyalophane is a rare secondary mineral (Table 1) and was generated as a consequence of high-temperature contact reaction processes that fused a small argillaceous fragment enclosed in the magma and transformed it to mullite (Fig. 4g). The contact processes suggest a high-Ba environment, also attested to by the late-stage barite generation (Fig. 4h), which appears as the last generated mineral.

Geochemistry and classification

A lamproite attribute of the rock is given by its relatively low contents of Al_2O_3 (9.34 wt%) and CaO (3.43 wt%) in combination with high abundances of Rb (205 ppm), Ba (2750 ppm), Sr (868 ppm) and Zr (1243 ppm), as well as La (134 ppm) and Ce (253 ppm) (e.g. Mitchell & Bergman 1991) (Table 2). The major and trace element geochemistry confirms that the rock is a typical lamproite, close to Leucite Hills and Gaussberg lamproite compositions (Fig. 6). It is characterized by high Mg-number (75.7), high abundances of Ni (478 ppm) and Cr (539 ppm), as well as high primary K_2O contents (8.67 wt%) and K_2O/Na_2O ratios (6.84).

Primitive mantle-normalized incompatible element diagrams show the strongly enriched nature of the Gătaia rocks (Fig. 7). The normalized patterns range from several times primitive mantle for heavy REE (HREE), Ti and Y, to several hundred times for large ion lithophile elements (LILE), such as Ba, Rb, U, K, Pb and Sr, or LREE such as La, Ce and Nd. The trace element patterns are distinguished by a slight negative Nb anomaly, as compared with Serbian, Spanish or Italian lamproites, which show accentuated Nb and Ti anomalies, despite the generally high contents of these elements (Table 2 and Fig. 7). The rocks also have positive Zr anomalies.

In Figure 7 primitive mantle-normalized incompatible element diagrams compare ultrapotassic rocks from Serbia (Bogovina, 30 Ma old; see inset of Fig. 1), closest spatially to the studied area (Fig. 7a) and various rock-types of a similar age in the Carpathian–Pannonian region (Fig. 7b). Serbian lamproites show different patterns with stronger negative anomalies of Nb and Ti in contrast to Gătaia compositions, with the exception of the Bogovina sample (BO-138) (Prelević *et al.* 2004), which, other than an accentuated Pb anomaly, shows similar patterns to the Gătaia sample. The Bogovina lamproite was generated on a terrane basement similar to that of Gătaia (the East Serbian composite terrane corresponds to

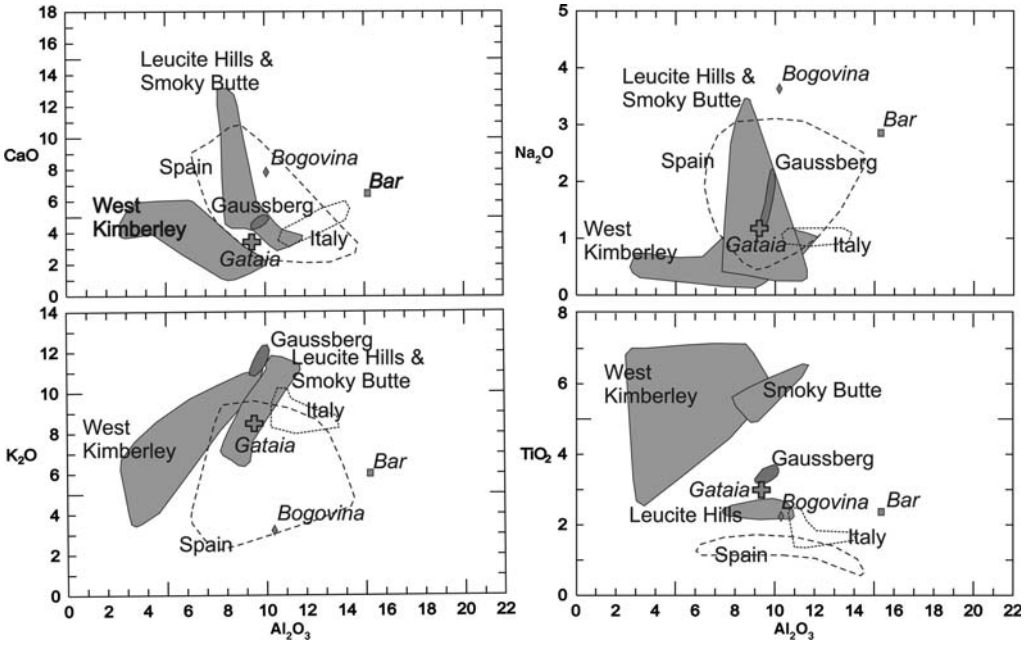

Fig. 6. CaO, K_2O, Na_2O and TiO_2 v. Al_2O_3 for Gătaia lamproite in comparison with lamproites from West Kimberley in Australia, Leucite Hills in Wyoming, Smoky Butte in Montana, Gaussberg in East Antarctica, Italy and Spain. Also, Bar and Bogovina samples are shown. Data sources: West Kimberley, Jaques *et al.* (1984, 1986), and Nixon *et al.* (1984) and Gaussberg, Sheraton & Cundari (1980); Leucite Hills, Kuehner *et al.* (1981), Barton & Hamilton (1982), Mitchell & Bergman (1991) and Mitchell (1995); Smoky Butte, Wagner & Velde (1986) and Mitchell *et al.* (1987); Spain, Nixon *et al.* (1984), Venturelli *et al.* (1984*a*), Wagner & Velde (1986), Toscani *et al.* (1995) and Salvioli-Mariani & Venturelli (1996); Italy, Conticelli & Peccerillo (1992); Bogovina, Prelević *et al.* (2005); Bar, Harangi *et al.* (1995).

the Getic nappe system; see Kräutner 1997; Iancu *et al.* 2005), although about 30 Ma earlier (Prelević *et al.* 2005). As regards the contemporaneous rocks in the Carpathian–Pannonian region, only the Bar rocks (2.2 Ma) show similar patterns to those of Gătaia; all the other contemporaneous calc-alkaline (La Gruiu in Perşani Mts, 1.16 Ma), alkaline (Uroiu shoshonite, 1.64 Ma) and alkali basaltic (Lucareţ, 2.4 Ma; Sărata-Perşani Mts, 1.5 Ma) have larger negative anomalies of Nb, Rb and Ce, Pb and Sr. Depletions of Nb relative to Ba and La, as well as high ratios of Ba/La,

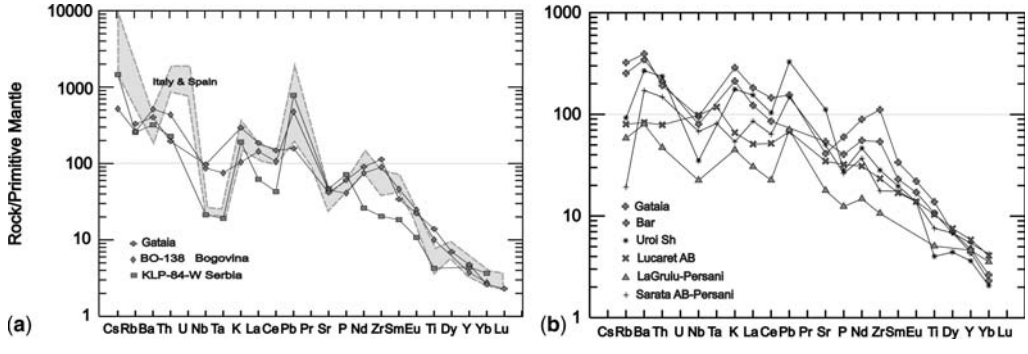

Fig. 7. Primitive mantle-normalized element diagrams for mafic alkalic rocks and selected calc-alkaline basalts in Serbia (**a**) and the Carpathian–Pannonian region (**b**) in comparison with Gătaia lamproite, using the normalizing coefficient of Sun & McDonough (1989). Data sources as in Figure 6, Mason *et al*. (1996), Downes *et al*. (1995*a*) and Seghedi *et al.* (2004*a*).

suggest a genetic relationship for these other rocks with a subduction-related metasomatic event (e.g. Tatsumi & Eggins 1995).

REE abundances (Table 2) of the Gătaia rock are similar to those of other olivine lamproites (Mitchell & Bergman 1991, and references therein; Prelević *et al.* 2007), as well to the Bar ultrapotassic rock (Harangi *et al.* 1995). $^{87}Sr/^{86}Sr$ v. $^{143}Nd/^{144}Nd$ ratios (Fig. 8) of the Gătaia sample plot in the upper corner of the enriched quadrant of the diagram, along with the Bar ultrapotassic rock, suggesting that it is one of the least isotopically enriched ultrapotassic rocks known in the world. The Bogovina lamproite, which shows a geochemical resemblance to the Gătaia rock but with higher $^{87}Sr/^{86}Sr$ and lower $^{143}Nd/^{144}Nd$, plots toward the more enriched crustal field (Prelević *et al.* 2005).

Discussion

Magma evolution

The mineral chemistry (olivine trend to lower Mg-number; Cr and Ni contents), spinels, glass and whole-rock compositions indicate that fractionation processes occurred during the ascent of magma to the surface. The presence of clots of corroded Al-phlogopite (17.25 wt% Al_2O_3), surrounded by secondary spinels (56.7 wt% Al_2O_3) enclosed by leucite aggregates, suggests formation during an earlier event, as high-pressure phases (Mitchell & Bergman 1991). Fractionation of phlogopite and olivine would result in an increase in SiO_2 content, decreasing MgO, Ni and Cr contents, and a slight increase in FeO and P_2O_5. $^{87}Sr/^{86}Sr$ and $^{143}Nd/^{144}Nd$ isotopic ratios (0.70571 and 0.51257, respectively), are closer to asthenosphere-derived melts relative to other lamproites; however, primary mantle-like $^{87}Sr/^{86}Sr$ and $^{143}Nd/^{144}Nd$ values may be achieved by a depleted lithospheric mantle source via metasomatism. Compared with other lamproites in the Mediterranean and Carpathian–Pannonian area (Harangi *et al.* 1995; Prelević *et al.* 2007, and references therein), Gătaia has a composition closest to the Bar leucitite, which was attributed to a phlogopite-bearing mantle source (Harangi *et al.* 1995). Such a source is consistent with lithosphere-metasomatic enrichment, implying alkaline melt percolation distinct from subduction-related metasomatism involved in generation of orogenic lamproites (e.g. Prelević *et al.* 2007).

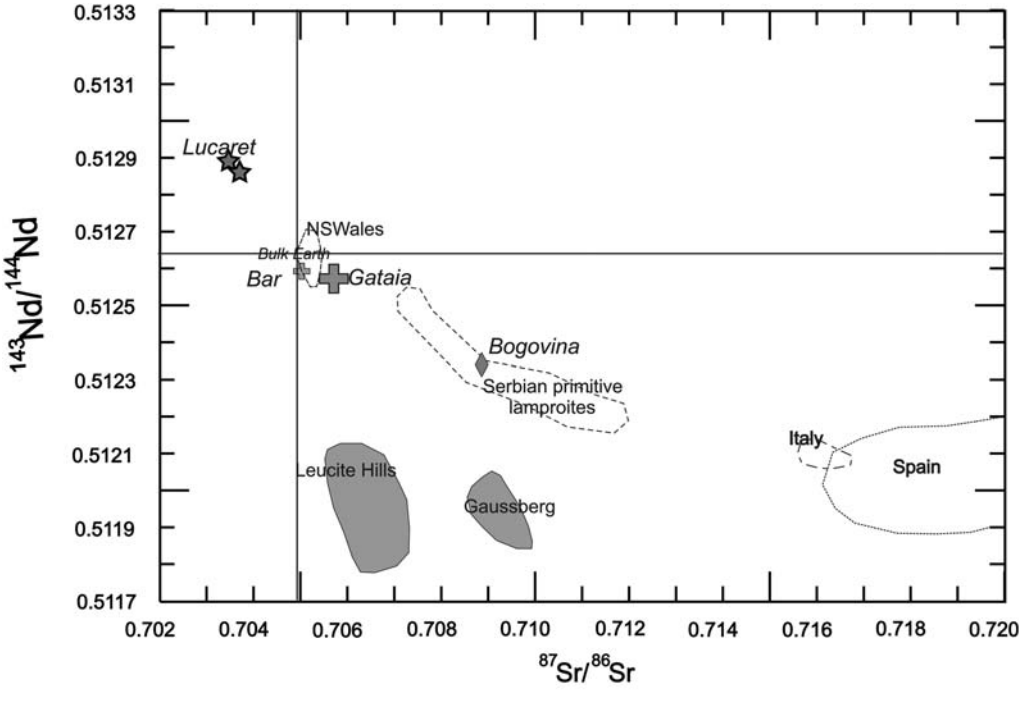

Fig. 8. $^{87}Sr/^{86}Sr$ v. $^{143}Nd/^{144}Nd$ variation for Gătaia and Bar, as well as Lucareţ alkali basalts, in comparison with Leucite Hills, Gaussberg, Serbian, Spanish, Italian and New South Wales lamproites. Data sources are as in Figure 6.

Mantle source

Fertility evidence. The idiomorphic tabular shape of the earlier-generated olivines (even deformed and corroded) (Fig. 2b) and their homogeneous compositional trend, which shows rim compositions consistent with that of euhedral small olivines growing in the groundmass, indicate that they represent phenocrysts that reached equilibrium with the magma. The cores of these early olivines have Fo contents up to 93 and host spinel inclusions with high Cr-number (*c*. 90), which decrease toward their margins to Fo_{78-82} (olivine) and Cr_{88} (spinel). This unusual composition is also known in other lamproites (e.g. Venturelli *et al.* 1984*a*; Mitchell & Bergman 1991; Prelević *et al.* 2005), as well as in komatiites (e.g. Arndt *et al.* 1977), and appears to conflict with their high SiO_2. A normal peridotite mantle source and/or high-temperature melting is not appropriate for the early olivines and Cr-spinels, which instead indicate a refractory, depleted peridotite as one component of the mantle source (Foley & Venturelli 1989; Arai 1994; Prelević *et al.* 2005). The olivine–spinel pairs from Gătaia plot in the most refractory part of the olivine–spinel mantle array of Arai (1994) (Fig. 9). Experimental studies failed to establish multiphase saturation in all peridotite minerals on the liquidi of ultrapotassic rocks (e.g. Foley *et al.* 1986).

However, to produce lamproite magma, in addition to depleted peridotitic mantle it is necessary to add a second component that contains high abundances of incompatible elements and would reduce the solidus temperature of the source mantle. Such situations have already been mooted in the literature (Foley 1992; Mitchell 1995) in the 'vein + wall-rock melting' model, which proposes that lamproites are the products of melting of refractory mantle intersected by phlogopite- and clinopyroxene-bearing veins. According to the 'vein + wall-rock' model, vein assemblages consisting principally of non-peridotitic K-rich ultramafic lithology melt at lower temperatures than the surrounding peridotite, and the resulting alkaline melt infiltrates and 'dissolves' the peridotite.

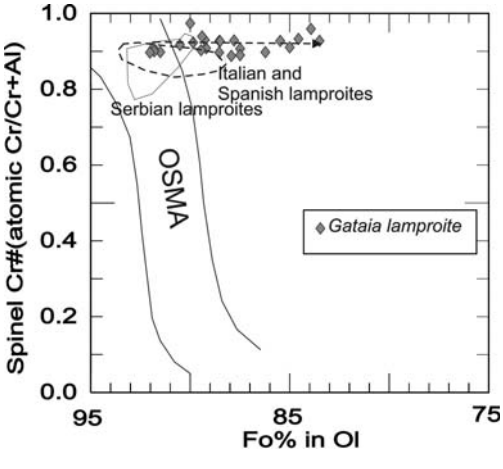

Fig. 9. Distribution of olivine–spinel pairs from the Gătaia lamproite on the olivine Fo v. spinel Cr-number diagram, showing the olivine–spinel mantle array (OSMA) defined by Arai (1994).

Geochemical evidence. Higher Rb/Sr and Rb/Ba ratios for the Gătaia lamproite, relative to most basalts, including mid-ocean ridge basalts (MORB) and ocean island basalts (OIB), reveal an enrichment of Rb relative to Ba and Sr, indicating partial melting of a similar source to that deduced for other lamproites, as can be seen in Figure 10. The plot reflects a style of enrichment analogous to anorogenic lamproites (e.g. West Kimberley), and different from orogenic ones, which show an increasing trend in Rb/Sr ratios (e.g. SE Spain, Italy or other orogenic lamproites) (Fig. 10). According to Figure 10 the source of the Gătaia lamproite is closer to phlogopite-bearing peridotites (e.g. Erlank *et al.* 1987). Melting of phlogopite veins in a harzburgitic substrate may explain the fact that the Gătaia lamproite has very a low CaO/Al_2O_3 ratio (0.36) and low CaO (3.43 wt%) and Sc contents (14 ppm). In addition, liquidus and near-liquidus studies on various lamproite compositions (e.g. Edgar & Vukadinovic 1992) have suggested that the Gătaia lamproitic magma may have formed by partial melting of a phlogopite-bearing mantle source.

Mineralogical evidence. If the hypothesis that two mantle sources with significant differences in mineralogy and chemical composition contributed to the generation of the Gătaia rock is accepted, it is not appropriate to apply any simple trace element modelling. Recently Prelević *et al.* (2005) discussed the mineralogy of the source for Serbian lamproites, using trace element behaviour, without setting quantitative constraints on the melting degree and source mineralogy. Zr was used as marker for vein + wall-rock melting, as it is incompatible, not being included in any important mineral within the rock, even the most enriched ones, as is the case for the Gătaia lamproite. Relatively constant Zr/Nb ratios for the Gătaia (20) and Bogovina (18) rocks indicate that the depletion of Nb was not controlled by a residual mineral in the source, implying that the Ti–Nb depletion could be a feature of the metasomatic agent.

High thermal stability of F-apatite, as compared with OH-apatite, would have a greater buffering

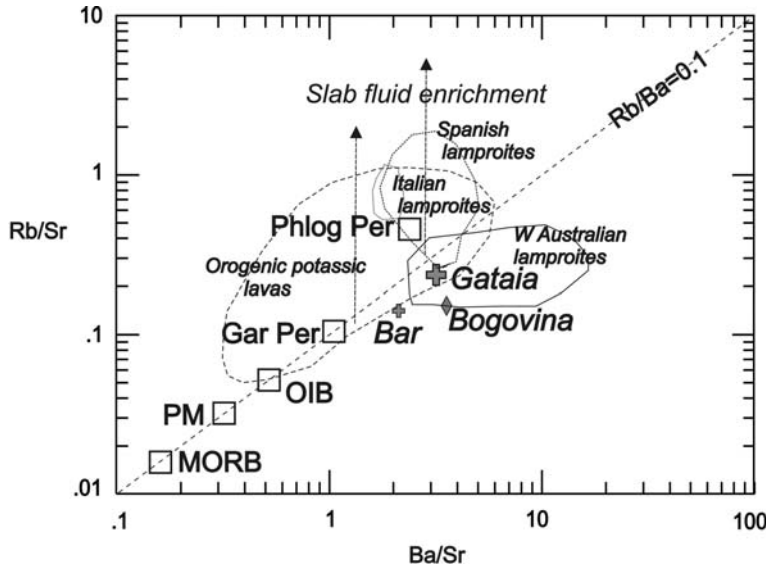

Fig. 10. Ba/Sr v. Rb/Sr ratios in various igneous compositions, such as MORB (Pearce 1983), OIB and PM (primitive mantle) (Sun & McDonough 1989) and garnet peridotites (Gar Per; Erlank *et al.* 1987). Results show a trend with narrow limits of 0·03 and 0·1 for the Rb/Ba ratio; the ultrapotassic lavas from phlogopite peridotite xenoliths (Erlank *et al.* 1987), from SE Spain (Venturelli *et al.* 1984*a*), Central Italy (Conticelli & Peccerillo 1992) and Western Australian lamproites (Mitchell & Bergman 1991), and from Gătaia lamproite and Bar leucitite, are characterized by an enrichment of Rb relative to Ba and Sr.

effect, offering a reasonable explanation for enrichment of F in the groundmass apatites. This study agree with other studies that at least F, and probably P, entered solid rather than liquid phases (e.g. Vukadinovic & Edgar 1993), as the result of partial melting of an F- and P-rich lithospheric mantle source. On the other hand, the high phosphorus content of the source suggested by early generated apatites, often recrystallized in the olivine melt inclusions where they show lower fluorine content (2.6–4.1%) and higher calculated OH compared with the groundmass apatites (4.2–4.5%), indicate both F and P buffering effects of phlogopite and apatite. Ba is also strongly incompatible in the Gătaia rock, as well as in the extremely Ba-enriched (*c.* 3000 ppm) lamproite from Bogovina (Serbia), which may be a result of melting of a Ba-rich phase in the mantle. However, Ba-type minerals were generated only as the latest phases in the Gătaia lamproite, as sanidine, barite or, rarely, as thermal contact minerals (hyalophane).

Regional comparative remarks and melting processes. The Gătaia samples show some geochemical similarities to Bogovina samples; that is, similar patterns in mantle-normalized trace element variation diagrams (Fig. 7), with less pronounced Ti and Nb troughs and no Eu trough, with the exception of high Pb (a crustal signature) and high isotopic Sr for Bogovina analyses. Prelević *et al.* (2005) interpreted the chemistry of Bogovina lamproites in terms of multiple metasomatic enrichment of the lithospheric mantle source. First, a subduction-related metasomatic event of Mesozoic age took place; this was followed by a second event, as a result of melt percolation related to the Palaeocene–Eocene alkaline basaltic magmatic episode. The latter is also recorded in mantle xenoliths near Bogovina (Cvetković *et al.* 2004; Prelević *et al.* 2005) and in the Poiana Ruscă Mountains near Gătaia (Downes *et al.* 1995*b*). This younger metasomatic event would cause the deflection of the isotopic signature towards HIMU (Prelević *et al.* 2005) and enrichment in TiO_2, Nb and Eu. We suggest that ultrapotassic magmatism in Bar, Gătaia and Bogovina belongs to a source that records only a metasomatic overprint of alkaline mafic melts. The evidence presented here is not consistent with metasomatism related to subduction, nor does it argue for the multiple metasomatic enrichment model of Prelević *et al.* (2005). The higher $^{87}Sr/^{86}Sr$ of the Bogovina sample simply suggests crustal assimilation processes during its generation (with deflection of Sr and Nd isotopic ratios), sufficient to explain the chemical and isotopic similarities between this rock and the Pannonian Basin ultrapotassic rocks (with low $^{87}Sr/^{86}Sr$).

In spite of the age differences between them, the chemistry of the rocks at Bogovina, Gătaia and Bar indicate a common lithosphere, in accordance with the geotectonic model envisaged by Csontos *et al.* (2002), which assigns them to the Tisia (Tisza) terrane. The isolated occurrence of Gătaia lamproite suggests a limited source volume available for melting, which we ascribe to the ambient thermal regime in a typical post-collisional tectonic setting, during the Late Neogene to Quaternary tectonic evolution, which indicates surface uplift and erosion that marks the collapse of the Alpine orogen (e.g. Iancu *et al.* 2005). The suggested depth for the base of the lithosphere (e.g. Lenkey 1999, and references therein), envisaged as the source area for the Gătaia lamproite, lies at 80–110 km (Fig. 1), and is in agreement with experimental studies that suggest deep melting of a harzburgitic-type mantle for this type of magma (Foley *et al.* 1986; Sato *et al.* 1997; Elkins-Tanton & Grove 2003). The Bar ultrapotassic rock, belonging to the same Tisia terrane basement, indicates a shallower depth to the base of lithosphere (<60 km), consistent with a phlogopite lherzolite source (Harangi *et al.* 1995) (see Fig. 1).

Conclusions

According to its mineralogical and petrological composition, the Pleistocene Gătaia rock is similar to the other known lamproites in the world. The Gătaia lamproite was generated via low-degree partial melting of a garnet harzburgite source that records a metasomatic overprint via alkaline mafic melts (not metasomatism via subduction), probably active at the Cretaceous–Palaeogene boundary (Downes *et al.* 1995*b*; Cvetković *et al.* 2004). The Sr and Nd isotopic data reveal that the Gătaia lamproite, along with the Bar ultrapotassic rock, is one of the most unenriched ultrapotassic rocks known; this is probably related to the invoked metasomatic processes. We concur with the 'vein + wall-rock' model (Foley 1992; Mitchell 1995) in which vein assemblages of ultramafic mineralogy (rich in phlogopite, F, P and Ba) began to melt at lower temperatures than the surrounding refractory peridotite. The resulting alkaline melt infiltrated and 'dissolved' the peridotite. Further ascent of the lamproitic magma toward the surface implies polybaric fractionation, which was controlled by the buffering effect of both F and P, as phlogopite and apatite. This study attests to the similar composition of the lithosphere involved in genesis of both the Gătaia rock and the neighbouring ultrapotassic rocks (at Bogovina and Bar), consistent with geotectonic models that envisage their affiliation to the Tisia (Tisza) terrane (e.g. Csontos *et al.* 2002). However, the Gătaia rocks derive from a greater depth (>100 km) relative to those from Bar (<60 km), and did not experience assimilation processes, as suggested by the evolution of Bogovina magmas (suggesting a different geotectonic setting during the Oligocene, which favoured assimilation processes). The trigger for melting in the case of the Gătaia lamproite was probably related to the Late Neogene to Quaternary surface uplift and erosion of the South Carpathians that marked the lithospheric collapse of the Alpine orogen.

This work was made possible by the availability of a core-sample of an exploration drill that pierced a lava flow of Gătaia volcano, which was offered to I.S. by the geologist I. Lopătiță. The probe and geochemical data have been supported by a bilateral agreement between Romanian and Austrian Academies, which are both acknowledged. We express our gratitude for this agreement to G. Kurat. The Institute of Geodynamics of the Romanian Academy is also acknowledged. We are grateful to M. McClintock for the first English review. We thank H. Downes for her advice. We thank S. Conticelli for their constructive reviews.

References

ALTHERR, R., MEYER, H.-P., HOLL, A., VOLKER, F., ALIBERT, C., MCCULLOCH, M. T. & MAJER, V. 2004. Geochemical and Sr–Nd–Pb isotopic characteristics of Late Cenozoic leucite lamproites from the East European Alpine belt (Macedonia and Yugoslavia). *Contributions to Mineralogy and Petrology*, **147**, 58–73.

ANDERSON, A. T., BUNCH, T. E., CAMERON, E. N. *ET AL*. 1970. Armalcolite: a new mineral from the Apollo II samples. *Proceedings of the Apollo 11 Lunar Science Conference, Geochimica et Cosmochimica Acta, Supplement*, **I**, 55–63.

ARAI, S. 1994. Compositional variation of olivine–chromian spinel in Mg-rich magmas as a guide to their residual spinel peridotites. *Journal of Volcanology and Geothermal Research*, **59**, 279–293.

ARNDT, N. T., NALDRETT, A. J. & PYKE, D. R. 1977. Komatiitic and iron-rich tholeiitic lavas of Munro Township, Northeast Ontario. *Journal of Petrology*, **18**, 319–369.

BALOGH, K. 1985. K–Ar dating of Neogene volcanic activity in Hungary. Experimental technique, experiences and methods of chronological studies. *ATOMKI Reports*, **D/1**, 277–288.

BARTON, M. & HAMILTON, D. L. 1982. Water-undersaturated melting experiments bearing upon the origin of potassium rich magmas. *Mineralogical Magazine*, **45**, 267–278.

BENITO, R., LOPEZ-RUIZ, J., CEBRIA, J. M., HERTOGEN, J., DOBLAS, M., OYARZUN, R. & DEMAIFFE, D. 1999. Sr and O isotope constraints on source and crustal contamination in the high-K calc-alkaline and shoshonitic Neogene volcanic rocks of SE Spain. *Lithos*, **46**, 773–802.

ÇOBAN, H. & FLOWER, M. F. J. 2007. Mineral phase compositions in silica-undersaturated 'leucite' lamproites from the Bucak area, Isparta, SW Turkey. *Lithos*, **89**, 275–299.

CONTICELLI, S. 1998. The effect of crustal contamination on ultrapotassic magmas with lamproitic affinity: mineralogical, geochemical and isotope data from the Torre Alfina lavas and xenoliths, Central Italy. *Chemical Geology*, **149**, 51–81.

CONTICELLI, S. & PECCERILLO, A. 1992. Petrology and geochemistry of potassic and ultrapotassic volcanism in central Italy: petrogenesis and inferences on the evolution of the mantle sources. *Lithos*, **28**, 221–240.

CONTICELLI, S., MANETTI, P. & MENICHETTI, S. 1992. Mineralogy, geochemistry and Sr-isotopes in orendites from South Tuscany, Italy; constraints on their genesis and evolution. *European Journal of Mineralogy*, **4**, 1359–1375.

CONTICELLI, S., D'ANTONIO, M., PINARELLI, L. & CIVETTA, L. 2002. Source contamination and mantle heterogeneity in the genesis of Italian potassic and ultrapotassic volcanic rocks: Sr–Nd–Pb isotope data from Roman Province and Southern Tuscany. *Mineralogy and Petrology*, **74**, 189–222.

CSONTOS, L., MÁRTON, E., WORUM, G. & BENKOVICS, I. 2002. Geodynamics of SW-Pannonian inselbergs (Mecsek and Villany Mts., SW Hungary): inference from complex structural analysis. *In*: CLOETINGH, S. A. P. L., HORVÁTH, F., BADA, G. & LANKREIJER, A. C. (eds) *Neotectonics and Surface Processes: the Pannonian Basin and Alpine/Carpathian System*. European Geophysical Union, Stephan Müller Special Publication Series, **3**, 1–19.

CVETKOVIĆ, V., DOWNES, H., PRELEVIĆ, D., JOVANOVIĆ, M. & LAZAROV, M. 2004. Characteristics of the lithospheric mantle beneath East Serbia inferred from ultramafic xenoliths in Paleogene basanites. *Contributions to Mineralogy and Petrology*, **148**, 335–357.

DOWNES, H., SEGHEDI, I., SZAKÁCS, A. *ET AL*. 1995*a*. Petrology and geochemistry of the late Tertiary/Quaternary mafic alkaline volcanism in Romania. *Lithos*, **35**, 65–81.

DOWNES, H., VASELLI, O., SEGHEDI, I. *ET AL*. 1995*b*. Geochemistry of the Late Cretaceous–early Tertiary magmatism in Poiana Ruscă (Romania). *Acta Volcanologica*, **7**, 209–219.

DRĂGULESCU, A., HINCULOV, L. & MIHĂILĂ, N. 1968. *Geological map of Romania, scale 1:200 000*. Sheet 24, Timişoara. Geological Institute of Romania, Bucharest.

EDGAR, A. D. & VUKADINOVIC, D. 1992. Implications of experimental petrology to the evolution of ultrapotassic rocks. *Lithos*, **28**, 205–220.

ELKINS-TANTON, L. T. & GROVE, T. L. 2003. Evidence for deep melting of hydrous metasomatized mantle: Pliocene high-potassium magmas from the Sierra Nevadas. *Journal of Geophysical Research*, **108**, 2350, doi:10. 1029/2002JB002168.

ERLANK, A. J., WATERS, F. G., HAWKESWORTH, C. J., HAGGERTY, S. E., ALLSOPP, H. L., RICKARD, R. S. & MENZIES, M. 1987. Evidence for mantle metasomatism in peridotite nodules from the Kimberley pipes, South Africa. *In*: MENZIES, M. & HAWKESWORTH, C. J. (eds) *Mantle Metasomatism*. Academic Press, London, 221–311.

FOLEY, S. F. 1992. Vein-plus-wall-rock melting mechanisms in the lithosphere and the origin of potassic alkaline magmas. *Lithos*, **28**, 435–453.

FOLEY, S. F. & VENTURELLI, G. 1989. High K_2O rocks with high MgO, high SiO_2 affinities. *In*: CRAWFORD, A. J. (ed.) *Boninites and Related Rocks*. Unwin Hyman, London, 72–88.

FOLEY, S. F., TAYLOR, W. R. & GREEN, D. H. 1986. The role of fluorine and oxygen fugacity in the genesis of the ultrapotassic rocks. *Contributions to Mineralogy and Petrology*, **94**, 183–192.

HARANGI, S., WILSON, M. & TONARINI, S. 1995. Petrogenesis of Neogene potassic volcanic rocks in the Pannonian Basin. *Acta Vulcanologica*, **7**, 125–134.

IANCU, V., BERZA, T., SEGHEDI, A., GHEUCA, I. & HANN, H. H. 2005. Alpine polyphase tectonometamorphic evolution of the South Carpathians: A new overview. *Tectonophysics*, **410**, 337–365.

JAQUES, A. L. & FOLEY, S. F. 1985. The origin of Al-rich spinel inclusions in leucite from the leucite lamproites of Western Australia. *American Mineralogist*, **70**, 1143–1150.

JAQUES, A. L., LEWIS, J. D., SMITH, C. B., GREGORY, G. P., FERGUSON, J., CHAPPELL, B. W. & MCCULLOCH, M. T. 1984. The diamond-bearing ultrapotassic (lamproitic) rocks of the West Kimberley region, Western Australia. *In*: KORNPROBST, J. (ed.) *Kimberlites I: Kimberlites and Related Rocks*. Elsevier, Amsterdam, 225–254.

JAQUES, A. L., LEWIS, J. D. & SMITH, C. B. 1986. The kimberlites and lamproites of Western Australia. *Geological Survey of Western Australia Bulletin*, **132**, 1–268.

KRÄUTNER, H. G. 1997. Alpine and pre-alpine terranes in the Romanian Carpathians and Apuseni Mts. *Annales Géologiques Pays Hélléniques*, lère Série **XXVII**, 331–400.

KUEHNER, S. M., EDGAR, A. D. & ARIMA, M. 1981. Petrogenesis of the ultrapotassic rocks from the Leucite Hills, Wyoming. *American Mineralogist*, **66**, 663–677.

LENKEY, L. 1999. *Geothermics of the Pannonian basin and its bearing on the tectonics of basin evolution*. PhD thesis, Vrije Universiteit Amsterdam.

MASON, P., DOWNES, H., THIRLWALL, M. F., SEGHEDI, I., SZAKÁCS, A., LOWRY, D. & MATTEY, D. 1996. Crustal assimilation as a major petrogenetic process in the East Carpathian Neogene and Quaternary continental margin arc, Romania. *Journal of Petrology*, **37**, 927–959.

MATEESCU, Ş. 1937. Vulcanismul cuaternar din partea de nord-vest a Banatului. *Revista Muzeului de Geologie şi Mineralogie a Universitaţii din Cluj*, **VI**, 72–97.

MITCHELL, R. H. 1995. Melting experiments on a sanidine phlogopite lamproite at 4–7 GPa and their bearing on the sources of lamproitic magmas. *Journal of Petrology*, **36**, 1455–1474.

MITCHELL, R. H. & BERGMAN, S. C. 1991. *Petrology of Lamproites*. Plenum, New York.

MITCHELL, R. H., PLATT, R. G. & DOWNEY, M. 1987. Petrology of lamproites from Smoky Butte, Montana. *Journal of Petrology*, **28**, 645–677.

NIXON, P. H., THIRLWALL, M. F., BUCKLEY, F. & DAVIES, C. J. 1984. Spanish and western Australian lamproites: aspects of whole rock chemistry. *In*: KORNPROBST, J. (ed.) *Kimberlites I: Kimberlites and Related Rocks*. Elsevier, Amsterdam, 285–296.

O'REILLY, S. Y. & GRIFFIN, W. L. 2000. Apatite in the mantle: implication for metasomatic processes and high heat production in Phanerozoic mantle. *Lithos*, **53**, 217–232.

PEARCE, J. A. 1983. Role of the sub-continental lithosphere in magma genesis at active continental margins. *In*: HAWKESWORTH, C. J. & NORRY, M. J. (eds) *Continental Basalts and Mantle Xenoliths*. Shiva, Nantwich, 230–249.

PECCERILLO, A. 1985. Roman comagmatic province (central Italy); evidence for subduction-related magma genesis. *Geology*, **13**, 103–106.

PECCERILLO, A. 1990. On the origin of the Italian potassic magmas—comments. *Chemical Geology*, **85**, 183–196.

PECCERILLO, A. 1995. Mafic calc-alkaline to ultrapotassic magmas in central–southern Italy; constraints on evolutionary processes and implications for source composition and conditions of magma generation. *In*: CORDANI, U. G. & SVISERO, D. P. (eds) *Proceedings of the Symposium on the Physics and the Chemistry of the Upper Mantle*. Academia Brasileira de Ciencias, Rio de Janeiro, 171–189.

PECCERILLO, A. 1998. Relationships between ultrapotassic and carbonate-rich volcanic rocks in central Italy: petrogenetic and geodynamic implications. *Lithos*, **43**, 267–279.

PÉCSKAY, Z., LEXA, J., SZAKÁCS, A. *ET AL*. 1995*a*. Space and time distribution of Neogene – Quaternary volcanism in the Carpatho-Pannonian Region. *Acta Volcanologica*, **7**, 15–29.

PÉCSKAY, Z., EDELSTEIN, O., SEGHEDI, I., SZAKÁCS, A., KOVACS, M., CRIHAN, M. & BERNAD, A. 1995*b*. K–Ar datings of the Neogene–Quaternary calc-alkaline volcanic rocks in Romania. *Acta Volcanologica*, **7**, 53–63.

PÉCSKAY, Z., LEXA, J., SZAKÁCS, A. *ET AL*. 2006. Geochronology of Neogene–Quaternary magmatism in the Carpathian arc and Intra-Carpathian area: a review. *Geologica Carpathica*, **57**, 511–530.

PRELEVIĆ, D., CVETKOVIĆ, V., FOLEY, S. F., JOVANOVIĆ, M. & MELZER, S. 2001. Tertiary ultrapotassic–potassic rocks from Serbia, Yugoslavia. *Acta Vulcanologica*, **13**, 101–115.

PRELEVIĆ, D., FOLEY, S. F., CVETKOVIĆ, V. & ROMER, R. L. 2004. Origin of minette by mixing of lamproite and dacite magmas in Veliki Majdan, Serbia. *Journal of Petrology*, **45**, 759–792.

PRELEVIĆ, D., FOLEY, S. F., ROMER, R. L., CVETKOVIĆ, V. & DOWNES, H. 2005. Tertiary ultrapotassic volcanism in serbia: constraints on petrogenesis and mantle source characteristics. *Journal of Petrology*, **46**, 1443–1487.

PRELEVIĆ, D., FOLEY, S. F., ROMER, R. L. & CVETKOVIĆ, V. 2007. A review of petrogenesis of Mediterranean Tertiary lamproites: a perspective from the Serbian ultrapotassic province. *In*: WILSON, M., BECCALUVA, L. & BIANCHINI, G. (eds) *Cenozoic Volcanism in the Mediterranean Area.* Geological Society of America, Special Papers, **418**, 113–127.

SALVIOLI-MARIANI, E. & VENTURELLI, G. 1996. Temperature of crystallization and evolution of the Jumilla and Cancarix lamproites (SE Spain) as suggested by melt and solid inclusions in minerals. *European Journal of Mineralogy*, **8**, 1027–1039.

SĂNDULESCU, M. 1984. *Geotectonica României*. Tehnică, Bucharest.

SĂNDULESCU, M., 1988. Cenozoic tectonic history of the Carpathians. *In*: ROYDEN, L. H. & HORVATH, F. (eds) *The Pannonian Basin: a Study in Basin Evolution*. American Association of Petroleum Geologists, Memoirs, **45**, 17–25.

SATO, K., KATSURA, T. & ITO, E. 1997. Phase relations of natural phlogopite with and without enstatite up to 8 GPa: Implication for mantle metasomatism. *Earth and Planetary Science Letters*, **146**, 511–526.

SEGHEDI, I., DOWNES, H., SZAKÁCS, A. *ET AL*. 2004*a*. Neogene–Quaternary magmatism and geodynamics in the Carpathian–Pannonian region: a synthesis. *Lithos*, **72**, 117–146.

SEGHEDI, I., DOWNES, H., VASELLI, O., SZAKÁCS, A., BALOGH, K. & PÉCSKAY, Z. 2004*b*. Post-collisional Tertiary–Quaternary mafic alkalic magmatism in the Carpathian–Pannonian region: a review. *Tectonophysics*, **393**, 43–62.

SHERATON, J. W. & CUNDARI, A. 1980. Leucitites from Gaussberg, East Antarctica. *Contributions to Mineralogy and Petrology*, **71**, 417–427.

SUN, S.-S & MCDONOUGH, W. F. 1989. Chemical and isotopic systematics of oceanic basalts: implications for mantle compositions and processes. *In*: SAUNDERS, A. D. & NORRY, M. J. (eds) *Magmatism in the Ocean Basins*. Geological Society, London, Special Publications, **42**, 313–345.

TATSUMI, Y. & EGGINS, S. 1995. *Subduction Zone Magmatism*. Blackwell Science, Cambridge, MA.

THONI, M. & MILLER, C. 2004. Ordovician metapegmatite garnet (N-W Otztal basement, Tyrol, Eastern Alps): preservation of magmatic garnet chemistry and Sm–Nd age during mylonitization. *Chemical Geology*, **209**, 1–26.

TOSCANI, L., CONTINI, S. & FERRARINI, M. 1995. Lamproitic rocks from Cabezo Negro de Zeneta: brown micas as a record of magma mixing. *Mineralogy and Petrology*, **55**, 281–292.

TURNER, S., PLATT, J. P., GEORGE, R. M. M., KELLEY, S. P., PEARSON, D. G. & NOWELL, G. M. 1999. Magmatism associated with orogenic collapse of the Betic–Alboran domain, SE Spain. *Journal of Petrology*, **40**, 1011–1036.

VELDE, D. 1975. Armalcolite–Ti-phlogopite–diopside–analcite-bearing lamproites from Smoky Butte, Garfield County, Montana. *American Mineralogist*, **60**, 566–573.

VENTURELLI, G., CAPEDRI, S., BATTISTINI, G. D., CRAWFORD, A., KOGARKO, L. & CELESTINI, S. 1984*a*. The ultrapotassic rocks from southeastern Spain. *Lithos*, **17**, 37–54.

VENTURELLI, G., THORPE, R., PIAZ, G. D., MORO, A. D. & POTTS, P. 1984*b*. Petrogenesis of calc-alkaline, shoshonitic and associated ultrapotassic Oligocene

volcanic rocks from the Northwestern Alps, Italy. *Contributions to Mineralogy and Petrology*, **86**, 209–220.

VENTURELLI, G., MARIANI, E. S., FOLEY, S. F., CAPEDRI, S. & CRAWFORD, A. J. 1988. Petrogenesis and conditions of crystallization of Spanish lamproitic rocks. *Canadian Mineralogist*, **26**, 67–79.

VENTURELLI, G., CAPEDRI, S., BARBIERI, M., TOSCANI, L., MARIANI, E. S. & ZERBI, M. 1991. The Jumilla lamproite revisited—a petrological oddity. *European Journal of Mineralogy*, **3**, 123–145.

VUKADINOVIC, D. & EDGAR, A. D. 1993. Phase relations in the phlogopite–apatite system at 20 kbar; implications for the role of fluorine in mantle melting. *Contributions to Mineralogy and Petrology*, **114**, 247–254.

WAGNER, C. & VELDE, D. 1986. The mineralogy of K-richterite-bearing lamproites. *American Mineralogist*, **71**, 17–37.

YANEV, Y., BOEV, B., DOGLIONI, C., INNOCENTI, F., MANETTI, P. & LEPITKOVA, S. 2003. Neogene ultrapotassic–potassic volcanic association in the Vardar zone (Macedonia). *Comptes Rendus de l'Académie Bulgare des Sciences*, **56**, 53–58.

Heterogeneous metasomatism in cumulate xenoliths from the Spanish Central System: implications for percolative fractional crystallization of lamprophyric melts

D. OREJANA & C. VILLASECA

Department of Petrology and Geochemistry, Complutense University of Madrid, Madrid 28040, Spain (e-mail: dorejana@geo.ucm.es)

Abstract: The alkaline lamprophyres and diabases from the Spanish Central System carry a heterogeneous suite of xenoliths including a group of highly altered ultramafic pyroxenites that contain Cr–Mg-rich high-*T* hydrous minerals (Ti-phlogopite and pargasitic to kaersutitic amphibole), indicative of modal metasomatism. The trace element mineral compositions of these xenoliths show three patterns: type A xenoliths, with light rare earth element enriched clinopyroxenes with high field strength element (HFSE) negative anomalies; type B xenoliths, with clinopyroxenes and amphiboles with high incompatible trace element contents (large ion lithophile elements (LILE), HFSE and REE); type C xenoliths, with relatively REE- and HFSE-poor clinopyroxenes and amphiboles. These metasomatic signatures suggest the involvement of three different metasomatic agents: carbonate, silicate and hydrous fluids or melts, respectively. These agents could have been derived from the progressive differentiation of a CO_2–H_2O-rich highly alkaline magma, genetically related to the Late Permian alkaline magmatism. Because of the original sub-alkaline nature of the pyroxenite xenoliths, they might have been formed originally as pyroxene-rich cumulates associated with underplated Hercynian calc-alkaline basic magmas. Metasomatism as a result of the infiltration of alkaline magmas within these cumulates might explain the relatively high radiogenic Nd composition of the altered ultramafic xenoliths.

Ultramafic xenoliths carried by mantle-derived alkaline volcanic and subvolcanic magmas sometimes include pyroxenitic types, which are much less abundant than typical mantle lithologies (peridotites). Several possible origins have been proposed for pyroxenite xenoliths: (1) cumulates or segregations from mantle-derived magmas introduced as dykes or veins within the lithospheric mantle (e.g. Frey & Prinz 1978; Downes 2001); (2) cumulates crystallized within deep magma chambers near the upper mantle–lower crust boundary, associated with underplating of mafic magmas (e.g. Féménias *et al.* 2003); (3) restites produced during melting and genetically associated with overlying orogenic batholiths (Ducea & Saleeby 1998); (4) remnants of oceanic crust, subducted into the asthenosphere and then streaked out by mantle convection until they were incorporated into the lithosphere (Allègre & Turcotte 1986). Moreover, some pyroxenites have been subjected to a later enrichment process (Garrido & Bodinier 1999; Litasov *et al.* 2000; Xu 2002).

The Upper Permian alkaline lamprophyres and diabases from the Spanish Central System (SCS) carry a heterogeneous xenolith suite, including lower crustal granulites (Villaseca *et al.* 1999) and ultramafic pyroxenites and hornblendites (Orejana *et al.* 2006). Some types of pyroxenites have never been studied because of their scarcity and alteration. These altered pyroxenites show a relict high-*T* paragenesis composed of clinopyroxene, amphibole and phlogopite, pointing to the involvement of a metasomatic transformation at depth.

The nature of the metasomatizing agents in enrichment processes can be broadly divided into three categories: (1) silicate melts (e.g. Ionov *et al.* 2002*a*; Witt-Eickschen *et al.* 2003); (2) carbonate or carbonatitic melts and/or fluids (e.g. Ionov 1998; Yaxley *et al.* 1998; Xu *et al.* 2003); (3) hydrous fluids (e.g. Johnson *et al.* 1996).

The presence of multiple types of geochemical patterns in a single suite of ultramafic xenoliths is relatively common and sometimes has led to the conclusion that various genetically unrelated liquids were involved (Grégoire *et al.* 2003; Witt-Eickschen *et al.* 2003), whereas, in other cases, it has been interpreted as being derived from different metasomatic agents genetically related to a single original melt by percolative fractional crystallization (Litasov *et al.* 2000; Ionov *et al.* 2002*a*; Xu & Bodinier 2004). The widely accepted porous melt flow model (Navon & Stolper 1987) predicts the possibility of generation of volatile-rich (H_2O–CO_2) melts or fluids from a single volatile-rich magma (Downes 2001; Xu & Bodinier 2004) as a result of a continuous reaction with the rock matrix. These low-viscosity agents

From: COLTORTI, M. & GRÉGOIRE, M. (eds) *Metasomatism in Oceanic and Continental Lithospheric Mantle.* Geological Society, London, Special Publications, **293**, 101–120.
DOI: 10.1144/SP293.6 0305-8719/08/$15.00

are capable of producing a strong interaction with the wall rock.

This paper focuses on the petrography and the major and trace element mineral composition of the altered pyroxenite SCS xenoliths, with the intention of constraining their origin, and discusses the interaction with metasomatic agents and their relationship with the host alkaline basic magmas at different emplacement levels.

Geological background

The SCS is a plutonic–metamorphic terrane composed of several Hercynian granitic intrusions, emplaced into Neoproterozoic metasediments and Palaeozoic orthogneisses (Fig. 1). This basement is crosscut by several post-orogenic dyke swarms with contrasting geochemical affinities: calc-alkaline, shoshonitic, alkaline and tholeiitic (Villaseca *et al.* 2004). The alkaline suite can be divided in two groups: (1) basic to ultrabasic lamprophyres (camptonites) and diabases; (2) red monzo-syenitic porphyries. Geochronological data on this alkaline magmatism yield an age of intrusion in the range 252–264 Ma (264 Ma, Ar–Ar in amphibole, Perini *et al.* 2004; Scarrow *et al.* 2006; or 252 Ma, U–Pb in zircon, Fernández-Suárez *et al.* 2006).

The SCS alkaline magmatism occurred in an anorogenic setting during the initial stages of North Atlantic opening. Orogenic Hercynian metamorphism in the area reached its peak at around 330 Ma and afterwards experienced a marked retrograde cooling path associated with moderate uplift (Escuder Viruete *et al.* 1998). During these post-orogenic conditions, voluminous granitic and calc-alkaline magmas intruded these crustal levels, promoting important local contact metamorphism. At 70 Ma after the regional metamorphism, during Late Permian times, lamprophyre dyke swarms were emplaced at very shallow and cool levels, although this did not result in contact metamorphism because of the small volume of magma. These uplifted crustal blocks into which the lamprophyres were intruded have not experienced burial since Early Mesozoic times, as revealed by fission-track data (Bruijne & Andriessen 2000). Moreover, a significant hydrothermal imprint is not observed in either the lamprophyre dykes or the plutono-metamorphic wall rocks, suggesting long-term stable crustal conditions after the alkaline magmatism. Therefore, the significant degree of alteration shown by the studied pyroxenite xenoliths suggests a genetic relationship with the host lamprophyric melt as discussed below.

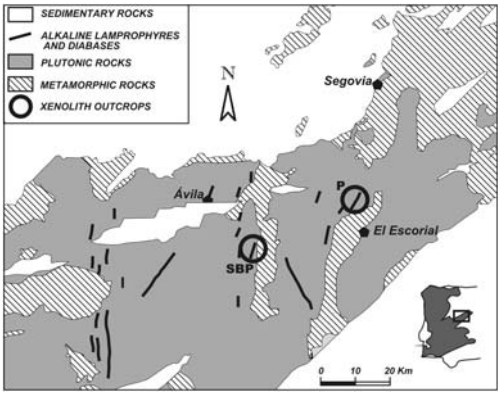

Fig. 1. Sketch map of the Spanish Central System showing the location of the Permian alkaline lamprophyres and diabases, and the outcrops of the altered ultramafic xenoliths (P, Peguerinos; SBP, San Bartolomé de Pinares).

The SCS alkaline lamprophyres and diabases carry a wide variety of xenolithic material, comprising wall-rock fragments (granites and gneises), lower crustal xenoliths (granulites *sensu lato*) and mafic to ultramafic pyroxene-rich cumulates from the upper mantle–lower crust boundary. This last group of xenoliths has been divided, in previous studies, in four subgroups according to their petrographic characteristics (Orejana *et al.* 2006): (1) highly altered xenoliths; (2) spinel pyroxenites; (3) hydrated clinopyroxenites; (4) magmatic amphibole-rich clinopyroxenites and hornblendites.

Type 2 spinel pyroxenites and type 4 hornblendites are generally larger in size and more abundant than the other ultramafic xenoliths (Orejana *et al.* 2006). They have been interpreted as magmatic cumulates or segregates crystallized at the upper mantle–lower crust boundary. The amphibole-rich type 4 xenoliths show magmatic textures, and have been interpreted as crystallizing from the alkaline melts (Orejana *et al.* 2006). In contrast, type 2 xenoliths display a granoblastic texture and, occasionally, also contain orthopyroxene (e.g. websterite 102131). Thus, they have been interpreted as being related to earlier magmatic events associated with underplating of calc-alkaline basic magmas at the base of the crust (Orejana *et al.* 2006).

Types 1 and 3 ultramafic xenoliths of Orejana *et al.* (2006) show a variable amount of high-*T* hydrated phases (amphibole and phlogopite). Nevertheless, their crystalloblastic fabric and modal mineral composition differentiate them from the clearly igneous-textured type 4 xenoliths (also rich in amphibole or phlogopite). Their scarcity and small size represent major hindrances to their study, especially when considering their whole-rock and isotope geochemistry.

Nevertheless, in this paper we present a general petrographic and geochemical characterization of these enclaves, mainly focusing on major and trace element mineral composition, although whole-rock geochemical analyses and Sr–Nd isotope determinations have been carried out on two samples.

Analytical methods

The major element mineral composition has been analysed at the Centro de Microscopía Electrónica 'Luis Bru' (Complutense University of Madrid) using a Jeol JZA-8900 M electron microprobe with four wavelength-dispersive spectrometers. Analytical conditions were an accelerating voltage of 15 kV and an electron beam current of 20 nA, with a beam diameter of 5 μm. Elements were counted for 10 s on the peak and 5 s on each background position. Corrections were made using the ZAF method.

We have determined *in situ* the concentrations of 27 trace elements (rare earth elements (REE), Ba, Rb, Th, U, Nb, Ta, Pb, Sr, Zr, Hf, Y, V, Cr and Ni) in clinopyroxene, amphibole and phlogopite, on >130 μm thick polished sections by laser ablation inductively coupled plasma mass spectrometry (LA-ICP-MS) at the University of Bristol using a VG Elemental PlasmaQuad 3 ICP-MS system coupled to a VG LaserProbe II (266 nm frequency-quadrupled Nd–YAG laser). The counting time for one analysis was typically 100 s (40 s measuring gas blank to establish the background and 60 s for the remainder of the analysis). The diameter of laser beam was around 20 μm. The NIST 610 and 612 glass standards were used to calibrate relative element sensitivities for the analyses of the silicate minerals. Each analysis was normalized to Ca using concentrations determined by electron microprobe.

The whole-rock major and trace element composition of two xenoliths was analysed at the CNRS-CRPG Nancy. The samples were melted using $LiBO_2$ and dissolved with HNO_3. Solutions were analysed by inductively coupled plasma atomic emission spectrometry (ICP-AES) for major elements, whereas trace elements were determined by ICP-MS. Uncertainties in major elements are bracketed between 1 and 3%, except for MnO (5–10%) and P_2O_5 (>10%). Carignan *et al.* (2001) have evaluated the precision of Nancy ICP-MS analyses at low concentration levels from repeated analyses of the international standards BR, DR-N, UB-N, AN-G and GH. The precision for Rb, Sr, Zr, Y, V, Hf and most of the REE are in the range 1–5%, whereas they range from 5 to 10% for the other trace elements, including Tm. More information on the procedure, precision and accuracy of Nancy ICP-MS analyses has been given by Carignan *et al.* (2001).

Sr–Nd isotopic analyses of two xenoliths were carried out at the CAI de Geocronología y Geoquímica Isotópica of the Complutense University of Madrid, using an automated VG Sector 54 multicollector thermal ionization mass spectrometer with data acquired in multidynamic mode. Isotopic ratios of Sr and Nd were measured on a subset of whole-rock powders. The analytical procedures used in this laboratory have been described elsewhere (Reyes *et al.* 1997). Repeated analysis of NBS 987 gave $^{87}Sr/^{86}Sr = 0.710249 \pm 30$ (2σ, $n = 15$) and for the JM Nd standard $^{143}Nd/^{144}Nd = 0.511809 \pm 20$ (2σ, $n = 13$). The 2σ error on ε(Nd) calculation is ± 0.4. An estimated age of 265 Ma was used for calculating initial isotopic ratios.

Petrography of xenoliths

Although the altered pyroxenite xenolith suite has been previously classified into two types, the similarity of their petrography (high degree of alteration and the common presence of high-temperature hydrated minerals), suggests that they all form a heterogeneous, genetically related group. Thus, for the sake of simplicity, we shall refer to them hereafter as altered ultramafic SCS xenoliths.

These altered ultramafic SCS xenoliths have been sampled at two outcrops: Peguerinos (P) and San Bartolomé de Pinares (SBP) (Fig. 1). They are small in size, never exceeding 2.7 cm, and are irregular to semi-rounded in shape. Their modal composition is summarized in Table 1.

SCS altered pyroxenite xenoliths are composed of variable amounts of two mineral parageneses: (1) a granoblastic high-*T* assemblage of clinopyroxene, amphibole, phlogopite and spinel; (2) a later, volatile-rich alteration assemblage of chlorite group and talc minerals that pseudomorph granoblastic crystals. The texture of the altered ultramafic SCS xenoliths is fine-grained, equigranular and granoblastic, showing typical triple junctions indicative of solid-state equilibration. This high-*T* crystalloblastic fabric is preserved irrespective of the degree of secondary alteration.

Mineral heterogeneity might be related to the small size of these xenoliths, giving rise to a wide range of modal composition. Moreover, the lack of olivine suggests a cumulate origin instead of representing mantle fragments. Primary high-*T* minerals are restricted to uncoloured clinopyroxene, pargasitic to kaersutitic amphibole, Ti-phlogopite and brown spinel (Table 1). Clinopyroxene modal

Table 1. *Modal analyses of SCS altered xenoliths*

Sample:	104394	104546B	105776	105787	103656-1	103656-2	103657B-1	103657B-2	103657B-3	104534A	104535	104540A	105788
Locality:	P	P	P	SBP	SBP	SBP	SBP	SBP	SBP	SBP	SBP	SBP	SBP
Type:	A	B	A	C	B	B	B	B	B	B	B	B	B
Cpx	9.5	18.2	10.5	16.4	2.6	58.2	35.0	21.9	9.6	74.3	41.4	80.9	9.3
Amph		3.0		1.7	1.3		16.0			5.4	3		10.8
Phl					0.7		12.0						3.2
Sp	2.7	3.0	3.0	3.1					0.9		6.1		
Sulph.	1.8	3.0							89.5	20.3	49.5	19.1	76.7
Sec.min.	86.0	72.8	86.5	78.8	95.4	41.8	37.0	78.1	0.9×0.45	0.3×0.3	0.3×0.6	0.3×0.7	0.8×1.1
Size (cm)	1.5×0.3	0.6×0.5	2.3×0.6	0.7×1	0.5×0.6	0.7×0.3	0.2×0.2	1.1×0.6					

P, Peguerinos; SBP, San Bartolomé de Pinares. Sec.min., secondary minerals.

proportion ranges from 2.6 to 81%. Spinel, amphibole and phlogopite are not always all present in these xenoliths. Although spinel is regularly disseminated when it appears, amphibole and phlogopite are more dispersed. Neither mineral zoning nor pyroxene exsolution lamellae have been observed in these high-*T* minerals.

These pyroxenite xenoliths have secondary minerals in variable proportions from 19 to 95%. These alteration phases are mainly talc and chlorite group minerals, pale brownish chlorite being the most common. Unaltered orthopyroxene has never been observed in these xenoliths. Olivine pseudomorphs are unlikely because the presence of this mineral in the original paragenesis is very limited according to their normative composition as deduced from whole-rock chemistry: *Ol* does not exceed 9%, whereas *Hy* ranges from 80 to 99% (see Table 4). The normative compositions of analysed samples plot within the field of orthopyroxenite in the ultramafic rocks classification diagram, pointing to orthopyroxene as the main original mafic phase (now pseudomorphed) in the modal composition of these xenoliths. In summary, normative and modal compositions point to a wide range of altered pyroxenites probably including orthopyroxenites and websterites.

The mineral chemistry of chlorite pseudomorphs also supports the interpretation that orthopyroxene was the main primary mineral of these pyroxenite xenoliths. When comparing the chemical composition of the abundant chloritized pseudomorphs with secondary chlorite from the partial replacement of orthopyroxene from the websterite sample 102131 (type 2 xenoliths of Orejana *et al.* 2006) we notice the good overlap of the two compositional fields (Fig. 2). Furthermore, the pale brownish colour and the good cleavage of both chlorite crystals reinforce the suggestion that they belong to the same chlorite type. The wide chemical composition shown by these chlorites suggests complex chemical substitution processes towards talc end-member compositions (Fig. 2). Talc and occasional Fe-sulphide are other secondary mineral phases.

Mineral chemistry

According to mineral chemistry, we have classified the altered xenoliths into three sub-types by their trace element contents (mainly light rare earth elements (LREE) in clinopyroxene and amphibole): type A xenoliths, with Sr–LREE-enriched clinopyroxene and lacking high-*T* hydrous phases (amphibole or phlogopite); type B xenoliths, with LREE-enriched clinopyroxene and amphibole; and type C xenoliths, with REE-poor clinopyroxene and amphibole.

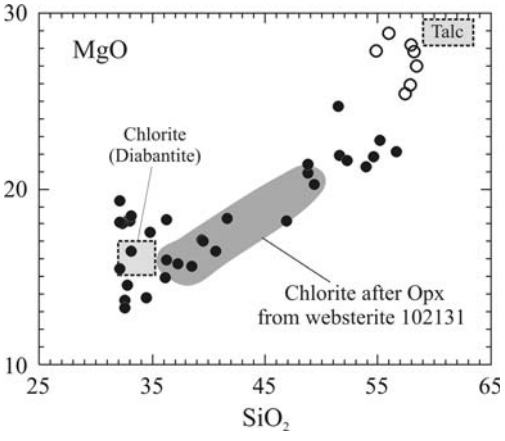

Fig. 2. Major element contents of secondary alteration minerals of the ultramafic SCS xenoliths (●, brownish chlorite ○, talc). Talc and chlorite (diabantite) compositional fields taken from data summarized by Deer *et al.* (1976).

Major elements

Clinopyroxene is diopside and augite with a heterogeneous major and trace element composition (Tables 2 and 3). Al_2O_3, TiO_2 and Na_2O may reach high concentrations: 4.2–7.7 wt%, 0.3–1.4 wt% and 0.41–1.75 wt%, respectively. Nevertheless, the heterogeneity shown by the major element composition highlights the large compositional ranges shown by clinopyroxenes from type B xenoliths (Fig. 3). This latter group has Mg-number values ranging from 0.78 to 0.93, whereas types A and C are restricted to Mg-number = 0.89–0.93 and are generally homogeneous with respect to major element composition, except for Na (Fig. 3).

Amphibole is absent in type A xenoliths (Table 1). Similar to what is observed for clinopyroxene, amphibole major and trace element composition is heterogeneous for type B xenoliths (Fig. 3). On the whole, they are Ti–Al-rich pargasites or kaersutites (TiO_2: 1.9–5.1 wt%; Al_2O_3: 12.9–15.7 wt%), with Na_2O in the range 2.2–3.3 wt%, K_2O from 0.71 to 1.84 wt% and high Mg-number (0.73–0.89), which overlaps the values for clinopyroxene (Table 2). Type C amphiboles do not differ significantly in their major element composition from type B (Fig. 3), but have higher Cr contents (7436–7845 ppm, compared with 2004–3236 ppm for type B; Table 3).

Phlogopite is present only in type B xenoliths (Table 1). Its major element composition is homogeneous, with Mg-number ranging from 0.82 to 0.86, overlapping the values for clinopyroxene and amphibole (Table 2). They typically have high TiO_2 (2.46–5.14 wt%), Cr_2O_3 (0.42–1.11 wt%) and Al_2O_3 (15.6–16.8 wt%) contents (Fig. 3). This composition contrasts with the lower Mg-number and Cr contents, and higher Ti concentrations of phlogopites from the SCS hornblenditic xenoliths, which have been interpreted as magmatic segregates genetically linked to the host alkaline melts (Orejana *et al.* 2006), and also with phlogopites from typical cumulate xenoliths (Fig. 3); but it is very similar to that of phlogopites from metasomatic ultramafic xenoliths, such as those reported by Shaw (2004). Because of the scarcity and small size of phlogopite from the altered ultramafic SCS xenoliths, we could not analyse their trace element composition.

Spinel is present in the three altered ultramafic SCS xenolith types. It is always Al–Cr-rich and Ti-poor, with Cr_2O_3 ranging from 4.8 to 14.3 wt%, Al_2O_3 from 49.7 to 63.5 wt%, TiO_2 <0.22 wt% and Mg-number from 0.69 to 0.79 (Table 2). Nevertheless, spinel from type B xenoliths shows the lowest Cr_2O_3 and highest Al_2O_3 concentrations (4.8 and 63.5 wt%, respectively). Spinel of type A and C xenoliths displays the same narrow compositional range: 11.3–14.3 wt% for Cr_2O_3 and 49.7–55.9 wt% for Al_2O_3.

Trace elements

Clinopyroxene trace element characteristics emphasize the existence of three types of altered ultramafic xenoliths (Fig. 4a). Clinopyroxenes from type A xenoliths display the most LREE-enriched patterns, which may reach 100 times chondrite values, whereas heavy REE (HREE) tend to converge to concentrations shown by clinopyroxenes from the other two xenolith types. This LREE enrichment is also accompanied by high contents of Sr (208–230 ppm), but low values for Zr (22–26 ppm) and Nb (0.12–0.24 ppm) (Table 3). Accordingly, their primitive mantle-normalized trace element pattern is distinctive, with strong negative anomalies at Zr-Hf and Nb-Ta, and at Ba and Ti (Fig. 4b). Type B clinopyroxenes are also enriched in LREE, but with lower concentrations than type A. Moreover, they yield convex-upwards chondrite-normalized REE patterns with the peak position between Ce and Nd, which is characteristic of clinopyroxenes formed as deep cumulates crystallized from basic alkaline magmas (Irving & Frey 1984) (Fig. 4a). Nevertheless, the LREE concentrations of type B clinopyroxenes are significantly higher than those shown by Irving & Frey (1984). The primitive mantle-normalized trace element pattern of these clinopyroxenes is very similar to that of type A, but concentrations of Zr (32.1–72.5 ppm), Hf

Table 2. *Major element composition and* P–T *estimates of representative high-*T *minerals from the SCS altered ultramafic xenoliths*

Type:	Clinopyroxene					Amphibole					Phlogopite			Spinel		
	A	B	B	B	C	B	B	B	C	C	B	B	B	A	B	C
Sample:	104394 13	104546B 25	104534A 33	104535 26	105787 45	104546B 23	105788 33	104535 24	105787 46	105787 47	103656-1 36	103657B-1 4	105788 40	104394 5	104546B 22	105787 43
SiO_2	51.28	50.27	50.92	50.42	50.58	41.68	40.77	41.21	41.26	42.21	37.48	36.93	37.47	0.03	0.06	0.07
TiO_2	0.48	0.79	0.82	0.54	0.31	4.25	4.32	2.87	1.98	2.05	2.46	4.92	3.40	0.13	0.16	0.12
Al_2O_3	5.83	7.46	7.26	5.63	5.99	15.34	14.24	13.19	14.57	14.99	15.75	15.81	16.76	55.91	63.47	53.09
FeO^T	2.44	3.23	6.45	6.89	2.90	3.60	6.63	9.25	4.26	4.08	7.26	7.41	5.98	11.33	4.79	13.01
Cr_2O_3*	0.79	0.35	0.19	0.42	0.87	–	–	–	–	–	1.11	0.76	0.69	10.94	10.29	13.13
MnO	0.09	0.07	0.05	0.10	0.04	0.13	0.07	0.08	0.04	0.00	0.04	0.03	0.07	0.08	0.08	0.07
MgO	16.02	15.48	13.68	13.73	15.24	16.33	14.38	13.60	16.99	17.22	20.03	18.69	19.93	20.51	21.33	20.61
CaO	22.98	20.33	19.41	20.08	20.87	10.94	11.51	10.75	10.50	11.11	0.02	0.03	0.06	0.00	0.00	0.00
Na_2O	0.95	1.02	1.27	1.55	1.59	3.09	2.49	3.18	3.08	3.09	1.22	0.87	0.64	0.00	0.00	0.00
K_2O	0.00	0.00	0.00	0.00	0.00	1.04	1.71	0.74	1.12	1.05	8.84	9.08	9.15	0.00	0.00	0.01
Total	100.86	99.00	100.05	99.36	98.39	96.40	96.12	94.87	93.80	95.80	94.21	94.53	94.15	98.93	100.18	100.11
Mg-no.	0.92	0.89	0.83	0.78	0.90	0.89	0.79	0.72	0.88	0.88	0.83	0.82	0.86	0.77	0.79	0.74
Cations calculated on the basis of 6 O for clinopyroxene; 24 (O, OH, F) for amphibole; 24 (O, OH, F, Cl) for phlogopite; 32 O for spinel																
Si	1.837	1.835	1.837	1.856	1.853	6.854	7.491	6.395	6.196	6.062	5.720	5.620	5.680	0.010	0.010	0.010
Ti	0.013	0.022	0.039	0.015	0.008	0.526	0.597	0.335	0.224	0.221	0.280	0.560	0.390	0.020	0.020	0.020
Al	0.246	0.321	0.213	0.245	0.259	2.970	3.081	2.410	2.577	2.535	2.830	2.835	2.990	13.820	15.030	13.190
Fe	0.073	0.099	0.170	0.212	0.088	0.495	1.019	1.200	0.535	0.490	0.930	0.940	0.760	1.880	0.760	2.170
Cr	0.022	0.010	0.010	0.012	0.025	0.075	0.059	0.074	0.151	0.143	0.130	0.090	0.080	1.920	1.730	2.320
Mn	0.003	0.002	0.002	0.003	0.001	0.018	0.011	0.011	0.005	0.000	0.010	0.000	0.010	0.010	0.010	0.010
Mg	0.856	0.842	0.836	0.754	0.832	4.003	3.939	3.146	3.804	3.687	4.560	4.240	4.500	6.420	6.390	6.480
Ca	0.882	0.795	0.844	0.792	0.819	1.927	2.266	1.787	1.690	1.709	0.000	0.000	0.010	0.000	0.000	0.000
Na	0.066	0.072	0.048	0.111	0.113	0.985	0.887	0.957	0.897	0.861	0.360	0.260	0.190	0.000	0.000	0.000
K	0.000	0.000	0.001	0.000	0.000	0.218	0.401	0.146	0.215	0.192	1.720	1.760	1.770	0.000	0.000	0.000
ΣCations	3.998	3.998	4.000	4.000	3.998	18.071	19.751	16.461	16.294	15.900	16.540	16.305	16.380	24.080	23.950	24.200
T (°C)†	896	1049	1092	1078	988	1004	1009	966	937	938						
P (kbar)†	6.7	9.9	10.7	7.6	10.2											

*Cr contents in amphibole have been determined by LA-ICP-MS (see Table 3).
†T estimations calculated using single pyroxene and Al–Ti in amphibole thermometers of Mercier (1980) and Otten (1984), respectively. P estimations calculated using the barometer of Nimis & Ulmer (1998).

Table 3. *Trace element composition of representative clinopyroxenes and amphiboles from SCS altered ultramafic xenoliths*

	Clinopyroxene									Amphibole							
Type:	A	A	A	B	B	B	C	C	C	B	B	B	B	B	C	C	C
Sample:	104394	104394	104394	104546B	104535	104534A	105787	105787	105787	104546B	104546B	104534A	104534A	104534A	105787	105787	105787
	12	21	51	41	33	41	10	7	9	31	33	22	23	24	1	2	3
Ba	0.84	1.37	2.42	1.57	0.92	3.92	2.60	2.17	bd	172	178	236	247	228	79.7	82.1	84.3
Rb	bd	bd	1.65	bd	0.67	0.43	0.65	0.47	bd	4.84	5.12	6.01	6.03	6.20	5.69	5.97	6.33
Sr	230	212	215	95.3	107.6	101.2	44.8	44.0	40.9	278	208	474	488	504	120	120	117
Pb	na	na	na	na	na	na	0.46	0.16	0.17	na	na	na	na	na	0.29	0.45	0.43
Th	0.06	0.10	0.08	0.31	0.24	0.14	bd	bd	0.06	0.20	0.33	0.15	0.16	0.19	bd	bd	bd
U	bd	bd	0.03	0.09	0.08	0.05	bd	bd	bd	0.05	0.11	0.03	0.05	0.04	bd	bd	bd
Zr	24.5	24.8	25.9	38.4	70.5	56.2	17.5	16.7	16.4	66.7	73.2	52.6	51.8	52.6	16.8	18.0	15.6
Nb	0.10	0.17	0.13	1.56	0.27	0.59	0.16	bd	0.11	78.4	53.2	43.1	45.3	45.2	1.35	1.23	1.36
Y	16.8	15.5	14.9	19.9	24.4	18.6	16.7	15.5	15.1	21.7	21.8	21.7	22.7	21.8	17.3	18.2	17.8
V	254	246	251	286	623	709	344	320	319	440	450	909	944	905	501	545	543
Ni	393	404	386	315	116	74	432	286	325	605	596	129	149	129	na	na	na
Cr	5215	4948	5020	2046	2892	1745	5239	4687	5310	3124	3236	2087	2182	2118	7436	7845	7721
Ta	0.01	0.04	0.02	0.09	0.07	0.11	0.05	bd	bd	2.73	1.61	1.83	1.90	1.83	0.07	0.10	bd
Hf	0.89	0.89	1.16	1.50	2.41	1.61	0.88	0.88	0.75	1.51	1.56	1.46	1.34	1.41	0.95	0.83	0.62
La	20.71	20.76	20.43	6.73	9.05	6.88	2.35	2.24	2.11	10.10	12.00	9.94	10.29	10.35	3.14	3.02	3.32
Ce	70.19	69.42	70.24	22.41	28.93	21.65	6.61	6.27	6.37	30.73	35.51	27.40	27.48	27.49	8.41	8.98	9.10
Pr	10.64	10.14	10.23	3.73	4.15	3.22	1.05	0.90	0.99	4.71	4.74	4.04	4.14	4.25	1.29	1.40	1.27
Nd	46.37	49.40	44.52	18.45	19.25	15.56	5.81	5.42	5.63	21.61	24.53	19.82	20.19	19.78	7.03	6.86	7.19
Sm	8.61	8.91	8.29	5.64	5.50	3.61	1.84	1.81	2.07	5.89	5.61	5.08	5.55	5.07	2.59	2.21	2.45
Eu	2.14	2.15	2.18	1.75	1.79	1.42	0.71	0.66	0.65	2.04	1.90	1.78	1.94	2.04	0.89	0.80	0.75
Gd	5.74	5.11	5.48	4.99	4.84	3.47	2.58	1.92	2.46	5.50	5.61	4.56	4.31	4.64	2.43	2.81	2.77
Tb	0.80	0.72	0.75	0.72	0.90	0.58	0.43	0.39	0.42	0.89	0.78	0.71	0.72	0.70	0.45	0.54	0.56
Dy	3.60	3.36	3.60	4.81	5.16	4.02	3.25	2.67	2.76	4.30	4.14	4.17	4.29	4.66	3.21	2.97	2.88
Ho	0.68	0.57	0.66	0.97	1.06	0.71	0.67	0.58	0.56	0.91	0.88	0.88	0.97	0.92	0.56	0.75	0.69
Er	1.86	1.72	1.67	2.20	2.71	2.00	1.98	1.70	1.55	2.18	2.25	2.18	2.45	2.22	1.76	1.98	2.00
Tm	0.27	0.22	0.20	0.27	0.39	0.25	0.30	0.29	0.24	0.26	0.33	0.33	0.32	0.32	0.27	0.30	0.22
Yb	1.44	1.43	1.38	2.00	2.52	1.80	1.83	1.74	1.95	2.11	1.56	2.16	2.54	1.86	1.57	2.37	1.61
Lu	0.18	0.20	0.17	0.26	0.39	0.27	0.26	0.26	0.24	0.22	0.28	0.31	0.31	0.28	0.29	0.24	0.22
LREE	156.52	158.63	153.71	56.96	66.88	50.92	17.65	16.64	17.17	73.05	82.39	66.28	67.65	66.94	22.47	22.48	23.32
HREE	14.56	13.34	13.91	16.21	17.96	13.10	11.30	9.54	10.17	16.36	15.84	15.30	15.90	15.59	10.54	11.95	10.95
REE	173.22	174.12	169.80	74.92	86.63	65.44	29.66	26.84	27.99	91.45	100.13	83.36	85.49	84.57	33.90	35.23	35.02

na, not analysed; bd, below detection limit.

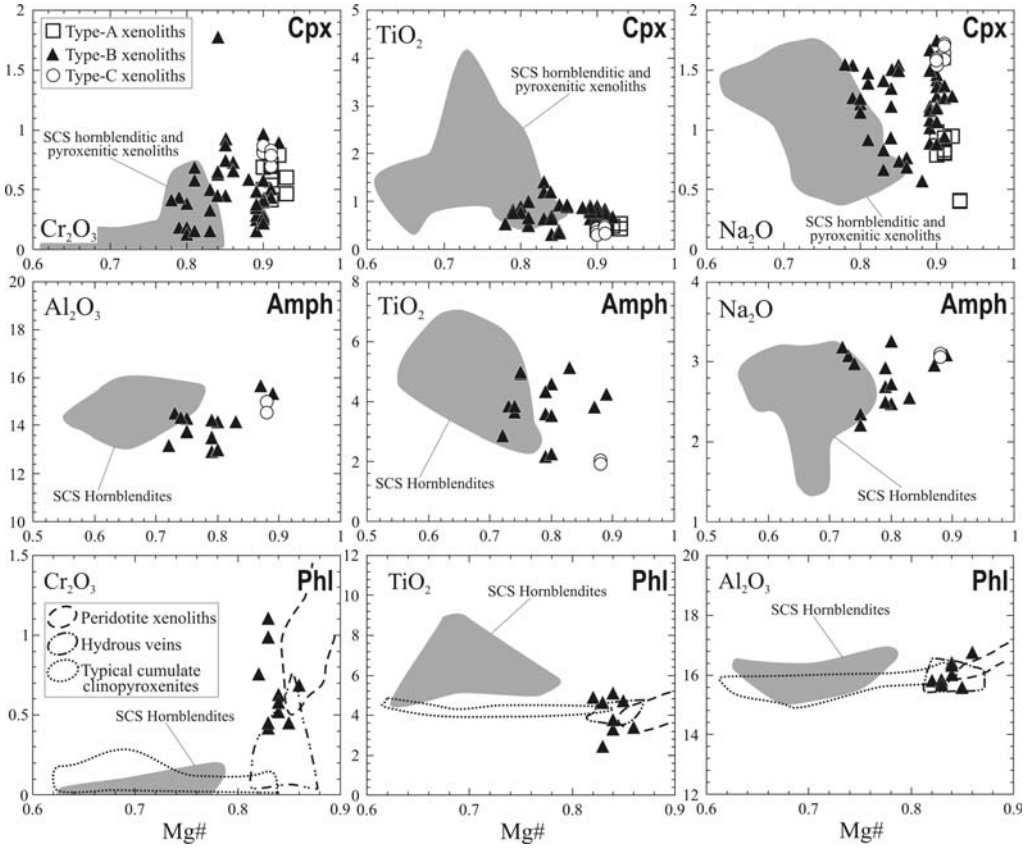

Fig. 3. Major element composition of clinopyroxene, amphibole and phlogopite from the altered ultramafic SCS xenoliths. Mineral composition of the SCS Sp-pyroxenites and hornblendites taken from Orejana *et al.* (2006). Fields of phlogopites from peridotites, hydrous veins and typical clinopyroxenites after Shaw (2004).

(1.14–2.75 ppm), Nb (0.14–1.55 ppm) and Ta (0.02–0.17 ppm) are clearly higher, whereas the converse applies to Sr (92.9–111.8 ppm) (Fig. 4b). Type B clinopyroxenes are also distinguished by their lower Cr concentration (1630–3080 ppm) when compared with type A and C clinopyroxenes (4158–5310 ppm) (Table 3). Finally, type C clinopyroxenes have generally lower trace element concentrations (Sr 40.9–44.1 ppm; Zr 15.7–18.2 ppm; Nb 01–0.6 ppm; LREE 16.6–17.7 ppm), with their maximum difference being the almost flat chondrite-normalized REE patterns (Fig. 4a).

Amphibole trace element compositions reproduce the chondrite- and primitive mantle-normalized patterns of clinopyroxenes in each xenolith, showing marked heterogeneity (Table 3). Type B amphiboles are characteristically LREE enriched and show a convex-upwards REE pattern, with La abundances *c*. 40 times chondrite values (Fig. 4c). This composition is similar to that of amphiboles interpreted as deep cumulates crystallized from alkaline basic melts (Irving & Frey 1984), although being LREE enriched. The primitive mantle-normalized trace element pattern of amphiboles from type B xenoliths is characterized by Ba and Nb–Ta positive peaks and U–Th and Zr–Hf negative anomalies (Fig. 4d). These patterns contrast markedly with that of amphiboles from type C xenoliths, which show general low trace element concentrations; REE have flat patterns, similar to that for clinopyroxene from these xenoliths, and primitive mantle spidergrams are characterized by the presence of high field strength elemet (HFSE) (Nb–Ta and Zr–Hf) negative anomalies (Fig. 4d).

Whole-rock geochemistry

Major and trace element composition

It has been possible to analyse only two altered ultramafic SCS xenoliths for whole-rock geochemistry.

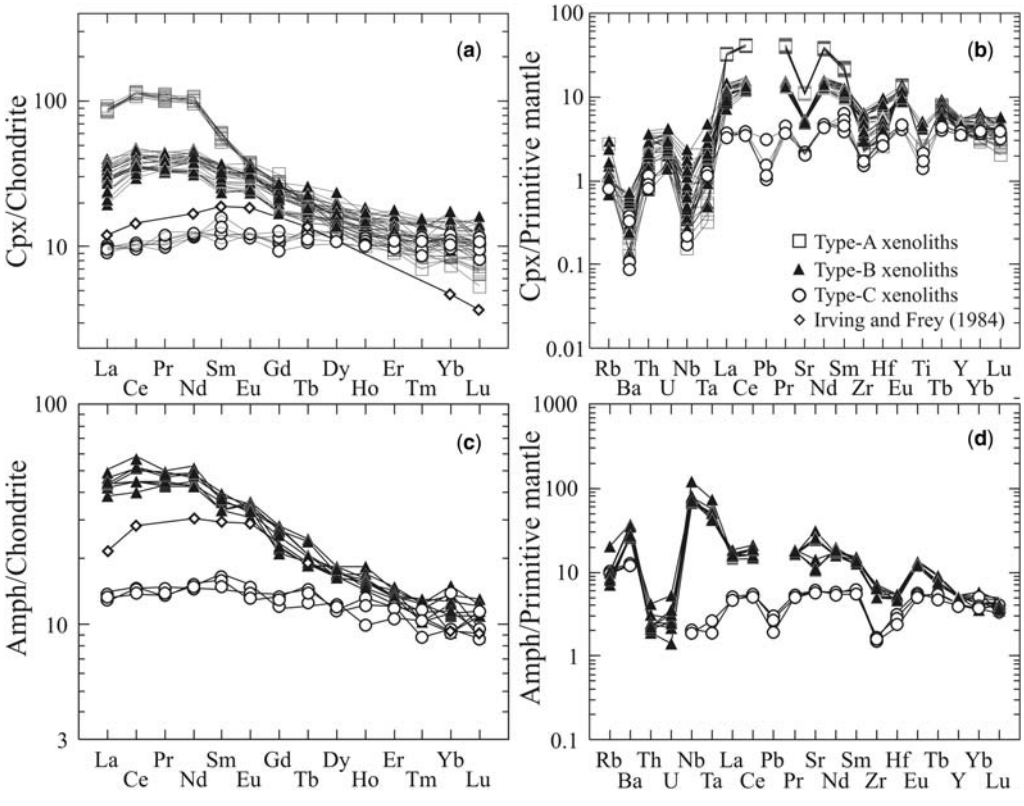

Fig. 4. (**a**) Chondrite-normalized and (**b**) primitive mantle-normalized trace element composition of clinopyroxenes from the altered ultramafic SCS xenoliths. (**c**) Chondrite-normalized and (**d**) primitive mantle-normalized trace element composition of amphiboles from the altered ultramafic SCS xenoliths. Data for other SCS xenoliths are taken from Orejana *et al.* (2006). ◇, averaged REE composition of deep cumulates from basaltic magmas, taken from Irving & Frey (1984). Chondrite and primitive mantle values are taken, respectively, from Sun & McDonough (1989) and McDonough & Sun (1995).

These two samples correspond to type A and C xenoliths. Nevertheless, major and trace element composition, as well as isotopic ratios, are necessarily influenced by their high degree of alteration (Table 1): 86.5 vol% in sample 105776 (type A xenoliths) and 78.8 vol% in sample 105787 (type C xenoliths), and their high loss on ignition (LOI) values (close to 10 wt%), so that these results should be interpreted with caution.

The major element composition of these xenoliths is characterized by low contents of TiO_2 (<0.2 wt%), CaO (<4 wt%), Na_2O (<0.47 wt%) and K_2O (<0.13 wt%), and relatively high concentrations of SiO_2 (48–50 wt%) and MgO (23–24 wt%) (Table 4). The high proportion of secondary talc in the analysed samples could explain the Si–Mg-rich nature of these altered xenoliths (Mg-number values vary from 0.81 to 0.84). The low CaO content is likely to be related to the scarcity of modal clinopyroxene (10–17%).

Both xenoliths have a homogeneous major element composition, different from those of most of the cumulate pyroxenites and hornblendites of Orejana *et al.* (2006), although they plot close to the websterite xenolith 102131 (Fig. 5). It is important to note the similarity between major element contents of the analysed altered xenoliths and the orthopyroxene composition (taken from the above-mentioned websterite 102131) (Fig. 5). The whole-rock composition of analysed pyroxenites yields high normative *Hy* for both samples (Table 4), indicating the predominance of orthopyroxene in the original modal composition of the xenoliths.

Altered ultramafic SCS xenoliths have variable trace element contents. Sample 105776 (type A) has higher REE–LILE–HFSE contents compared with sample 105787 (type C) (Table 4). On the whole, both pyroxenites show low concentrations, although some incompatible elements display moderate (Rb, K and LREE), or even high contents

Table 4. *Whole-rock geochemistry of SCS altered ultramafic xenoliths (major elements, trace elements, Sr–Nd isotope ratios and CIPW normative composition)**

	Sample				
	105776	105787		105776	105787
SiO_2	49.67	48.32	Ba	30.1	203
TiO_2	0.2	0.1	Rb	6.61	4.07
Al_2O_3	4.09	4.43	Cs	8.96	4.15
$Fe_2O_3^{\dagger}$	11.02	9.08	Sr	58.8	58.5
MnO	0.03	0.07	Pb	1.93	bd
MgO	23.07	23.85	Th	0.18	0.02
CaO	2.21	4	U	0.12	0.02
Na_2O	0.19	0.47	Zr	14.5	3.30
K_2O	0.12	0.13	Nb	2.07	0.23
P_2O_5	0.07	0	Y	7.21	3.74
LOI	9.51	9.75	V	89.4	91.1
Total	100.18	100.2	Ni	1910	2117
Mg-no.	0.81	0.84	Cr	2948	3043
			Ta	0.15	0.02
Q	2.9	0.0	Hf	0.44	0.14
Or	0.8	0.9	La	7.09	2.45
Ab	1.8	4.4	Ce	10.22	5.91
An	11.1	10.7	Pr	1.39	0.74
Ne	0.0	0.0	Nd	5.94	2.93
Lc	0.0	0.0	Sm	1.40	0.65
Di	0.6	9.1	Eu	0.50	0.23
Hy	79.8	66.0	Gd	1.41	0.66
Ol	0.0	6.7	Tb	0.24	0.11
Mt	2.4	2.0	Dy	1.37	0.67
Il	0.4	0.2	Ho	0.26	0.14
Ap	0.2	0.0	Er	0.73	0.38
End-members			Tm	0.11	0.06
Ol	0.0	8.2	Yb	0.70	0.35
Hy	99.3	80.7	Lu	0.11	0.06
Dy	0.7	11.1			
Sr–Nd isotopic ratios					
$^{87}Rb/^{86}Sr$	0.32	0.2	$^{147}Sm/^{144}Nd$	0.1426	0.1341
$^{87}Sr/^{86}Sr \pm 2\sigma$	0.707811 ± 47	0.707800 ± 05	$^{143}Nd/^{144}Nd \pm 2\sigma$	0.512597 ± 06	0.512585 ± 06
$^{87}Sr/^{86}Sr_{265Ma}$	0.70658	0.70704	$\varepsilon(Nd)_{265\ Ma}$	1.03	1.08

*Normative composition has been calculated considering that Fe_2O_3 represents 15% of total Fe.
†Total Fe is represented as Fe_2O_3.
bd, below detection limit.

(Ba in sample 105787, 203 ppm). The chondrite-normalized REE pattern is flat for HREE and increasingly fractionated from middle REE (MREE) to LREE, and is subparallel for the two samples (Fig. 6a). The primitive mantle-normalized trace element patterns display clear negative anomalies for HFSE (Th, Nb–Ta, Zr–Hf and Ti), but they are significantly more marked in sample 105787 (type C) than in sample 105776 (type A) (Fig. 6b). In this latter xenolith, whole-rock trace element geochemistry is dominated by clinopyroxene composition, and the normalized patterns mimic those of this mineral, with negative anomalies at the HFSE. A similar pattern occurs for sample 105787, where the presence of a HFSE-poor amphibole adds to the HFSE-poor nature of clinopyroxene, although it results in the increased Ba concentration of this xenolith.

Sr–Nd isotope composition

The initial Sr and Nd isotopic ratios of the analysed altered ultramafic SCS xenoliths have $(^{87}Sr/^{86}Sr)_0$

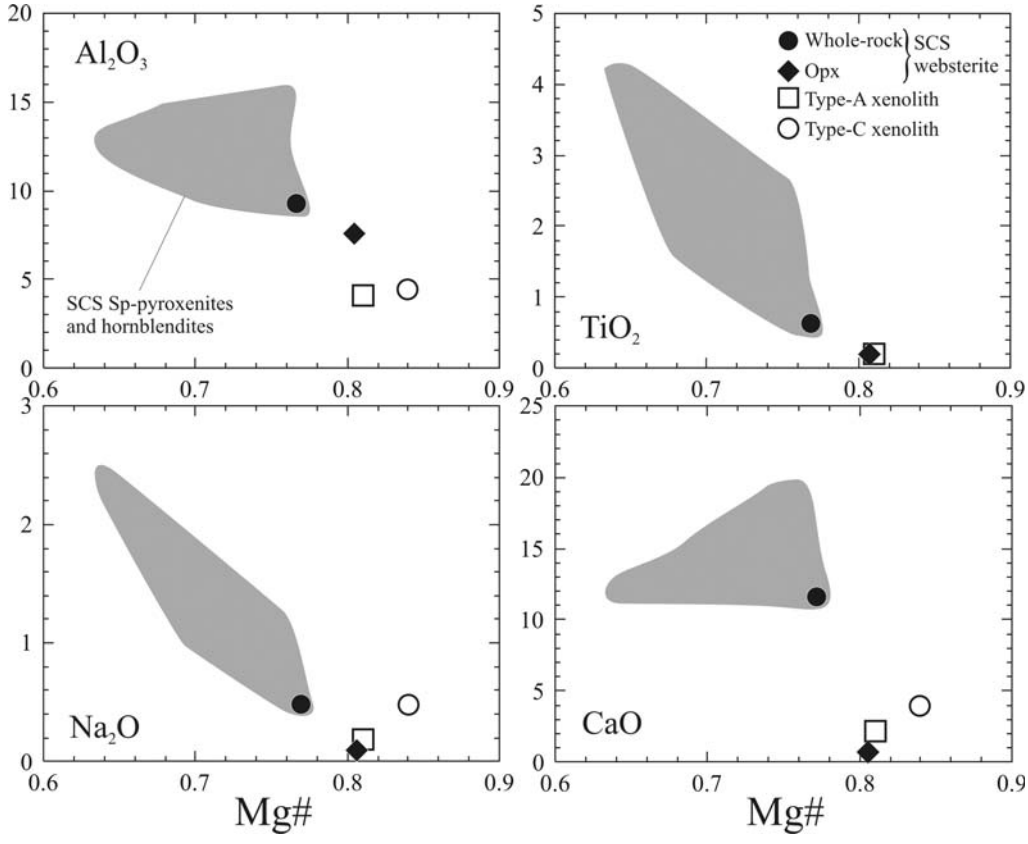

Fig. 5. Major element whole-rock composition of the altered ultramafic SCS xenoliths. Fields of other ultramafic SCS xenoliths (Sp-pyroxenites and hornblendites) and whole-rock and orthopyroxene composition of the websterite 102131 are taken from Orejana *et al.* (2006).

from 0.70658 to 0.70704 and εNd *c.* +1 (Table 4). The Sr isotopic composition of the host dykes is markedly different from that of the altered xenoliths, but radiogenic Nd values resemble those of the isotopically enriched lamprophyre dykes, and also those of the more radiogenic subalkaline SCS pyroxenites (Fig. 7). This composition falls outside the mantle array, because of the relative

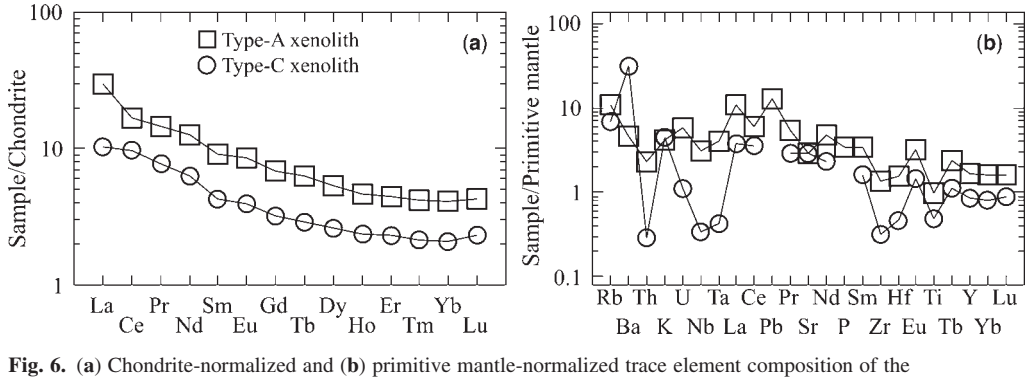

Fig. 6. (**a**) Chondrite-normalized and (**b**) primitive mantle-normalized trace element composition of the altered ultramafic SCS xenoliths. Normalizing values for chondrite and primitive mantle from Sun & McDonough (1989) and McDonough & Sun (1995), respectively.

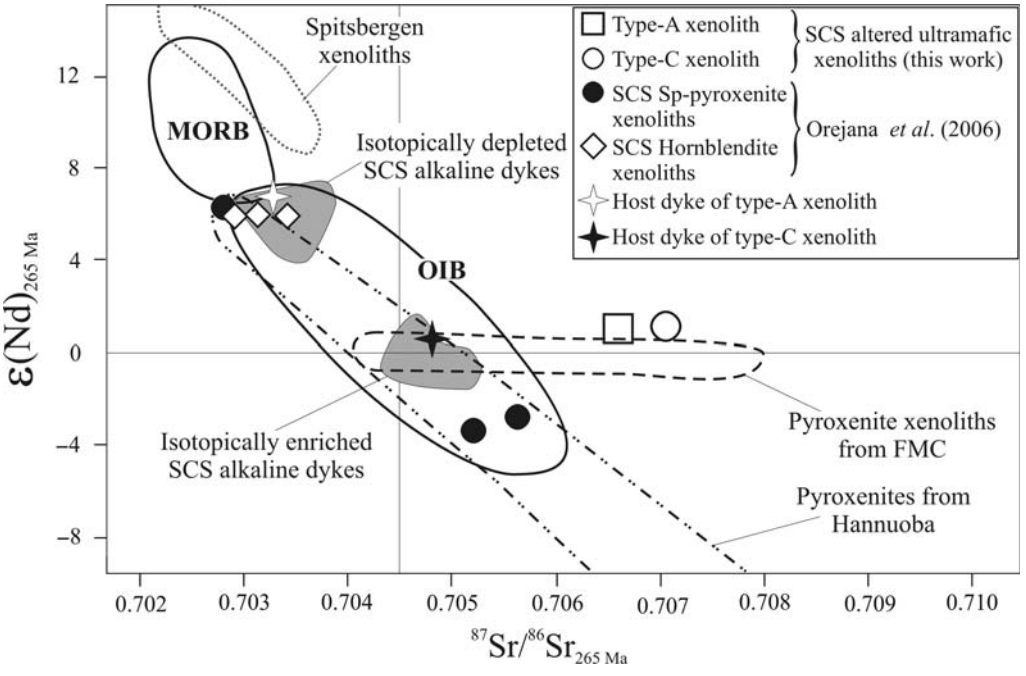

Fig. 7. Sr–Nd isotopic composition of altered xenoliths (calculated at 265 Ma), in comparison with isotopic ratios of the SCS alkaline magmatism (Villaseca *et al.* 2004), SCS cumulate pyroxenites (Orejana *et al.* 2006) and pyroxenite xenoliths from the FMC (Downes & Dupuy 1987), Spitsbergen (Ionov *et al.* 2002*b*) and Hannuoba (Xu 2002). MORB and OIB fields are after Wilson (1989).

radiogenic Sr, whereas εNd values are similar to BSE (Bulk Silicate Earth) values. Similar deviations from the mantle array have been described in mantle xenoliths from Spitsbergen (Ionov *et al.* 2002*b*) and the French Massif Central (FMC) (Downes & Dupuy 1987) (Fig. 7), and have been interpreted as a consequence of percolative porous melt flow metasomatism and an enrichment event caused by EMI-like magmas, respectively. This high $^{87}Sr/^{86}Sr$ trend of the altered SCS xenoliths contrasts with that displayed by pyroxenite xenoliths from Hannuoba (towards both higher Sr and lower Nd radiogenic ratios), which might represent the involvement of fluids derived from subduction or from a delaminated lower crust (Xu 2002).

Discussion

The origin of secondary alteration

The presence of chlorite and talc in these xenoliths suggests re-equilibration in a volatile-rich environment, probably interacting with a $H_2O–CO_2$-rich fluid. The selective alteration, which mainly affects the primary orthopyroxene of the xenolith, is also reproduced in the host lamprophyre where clinopyroxene, amphibole or phlogopite phenocrysts are well preserved, whereas olivine is totally pseudomorphed by talc. The common presence of carbonate-rich and chlorite-rich ocelli in the lamprophyres suggests significant volatile exsolution by the ultrabasic magma at subvolcanic emplacement levels. Thus, it is possible that a selective low-*P* alteration of suspended solids (xenoliths, phenocrysts) occurred during lamprophyric magma devolatilization. Chlorite group minerals in ultramafic assemblages can appear at high temperatures under low-pressure conditions (<1 kbar), in the range of 850–900 °C (Pawley 2003). Talc could appear slightly later, at around 800 °C (Pawley & Wood 1995). This estimate of relatively high-temperature alteration is close to, or overlaps, the solidus condition for volatile-rich lamprophyric magmas (Esperança & Holloway 1987). Volatiles exsolved from the lamprophyric melt react with suspended solids (xenoliths, phenocrysts) and promote the alteration of a restricted mineral phase assemblage (i.e. orthopyroxene in pyroxenites, garnet in granulite xenoliths and olivine in lamprophyres). The restricted alteration of pyroxenite xenoliths (not related to vein or fracture filling) and olivine

in lamprophyres could continue to late-stage or subsolidus conditions. The subsolidus autometasomatic alteration of primary minerals in lamprophyres as a result of their high volatile content has been frequently described (Rock 1991). Petrographic features also do not suggest external hydrothermal invasive alteration, in agreement with the anorogenic setting of this alkaline magmatism. Devolatilization of the lamprophyric magma is the only possible agent to alter the incorporated xenoliths close to or at the shallow level of emplacement.

Nature of the metasomatic agents

The presence of high-*P* and high-*T* metasomatism within the altered SCS pyroxenite xenoliths can be recognized in the formation of new minerals (mainly Mg–Cr-rich amphibole and phlogopite) and in the modification of the incompatible trace element composition of the clinopyroxene (and more specifically LREE enrichment and variable HFSE depletion). The major element composition of studied amphibole and phlogopite is very similar to that shown by equivalent phases interpreted as the products of metasomatism within mantle xenoliths (Ionov *et al.* 1997). Amphiboles are essentially Ti–Cr-pargasites (less commonly kaersutites) and micas are titanian phlogopites. In all samples the Mg-number values of amphibole and mica are very close to those of coexisting clinopyroxene (Table 2), indicating that the minerals are close to chemical equilibrium. Type A and C altered SCS xenoliths show a homogeneous mineral composition, with Mg-number in the narrow range 0.88–0.93 for both amphibole and clinopyroxene. Greater heterogeneity in major element mineral chemistry is shown by type B xenoliths, but they also display similar Mg-number for their constituent minerals (0.78–0.92 for clinopyroxene, 0.72–0.89 for amphibole and 0.82–0.86 for phlogopite).

The most significant differences between the altered SCS xenoliths are mainly restricted to trace element mineral compositions. Type A xenoliths do not show hydrous high-T minerals (amphibole or phlogopite) indicative of modal metasomatism, but clinopyroxene displays highly LREE-enriched chondrite-normalized patterns (Fig. 4a), with high $(La/Yb)_N$ ratios ranging from 7.8 to 11.6 (Fig. 8). Moreover, strong negative HFSE (Nb–Ta, Zr–Hf and Ti) anomalies and high concentrations of Sr may be recognized (Fig. 4b). These characteristics indicate the involvement of cryptic metasomatism, which is analogous to similar enrichment in peridotite xenoliths from basalts (e.g. Frey & Prinz 1978; Kempton 1987; Kempton *et al.* 1999).

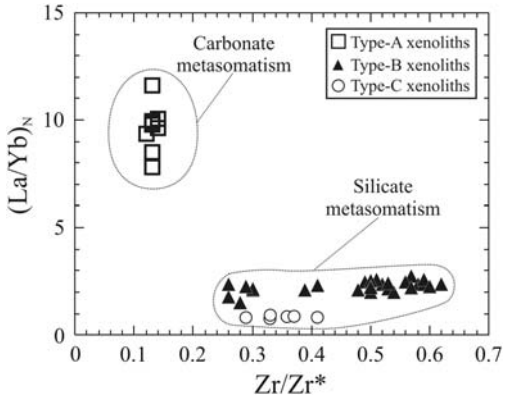

Fig. 8. $(La/Yb)_N$ v. Zr anomaly ($Zr/Zr^* = Zr_N/(Eu_N + ((Sm_N - Eu_N)/2))$) for clinopyroxene from the altered ultramafic SCS xenoliths.

Strong enrichments in LREE have been related to silicate and carbonate melts (Downes 2001; Ionov *et al.* 2002*a*; Xu 2002; Xu *et al.* 2003). Experimental studies on carbonate metasomatism have concluded that carbonatite melts may carry high concentrations of LILE, REE, U and Th, but they are characterized by low HFSE contents (Green & Wallace 1988). This HFSE depletion leads to the formation of clinopyroxene with deep troughs at Ta–(Nb), Zr–Hf and Ti, if a carbonate melt acts as the metasomatic agent (e.g. Ionov 1998; Yaxley *et al.* 1998). The above premises coincide with the $(La/Yb)_N$ and Zr/Zr^* values, which have been used to distinguish between clinopyroxenes associated with carbonate and silicate metasomatism (Fig. 8). We have calculated the composition of melts in equilibrium with type A clinopyroxenes using the cpx/carbonatite partition coefficients of the compilation of Klemme *et al.* (1995). The results represent liquids with a composition very similar to the average composition of calciocarbonatites (Woolley & Kempe 1989) or to that of selected Kola carbonatites (Downes *et al.* 2005) (Fig. 9a), suggesting that a carbonate-rich melt was likely to have been responsible for the cryptic metasomatism in type A xenoliths.

Type B xenoliths contain clinopyroxene and amphibole with convex-upwards chondrite-normalized REE patterns, resembling those of deep-seated cumulates from basaltic magmas (Irving & Frey 1984), but they are markedly more LREE-rich, with the peak position normally located at Ce (Fig. 4a). Amphibole is characteristically enriched in Nb–Ta and Ti (Fig. 4d), which is typical of Mg–Cr-rich metasomatic amphiboles crystallized in veins within the mantle from highly alkaline basic melts (Downes 2001; Witt-Eickschen *et al.*

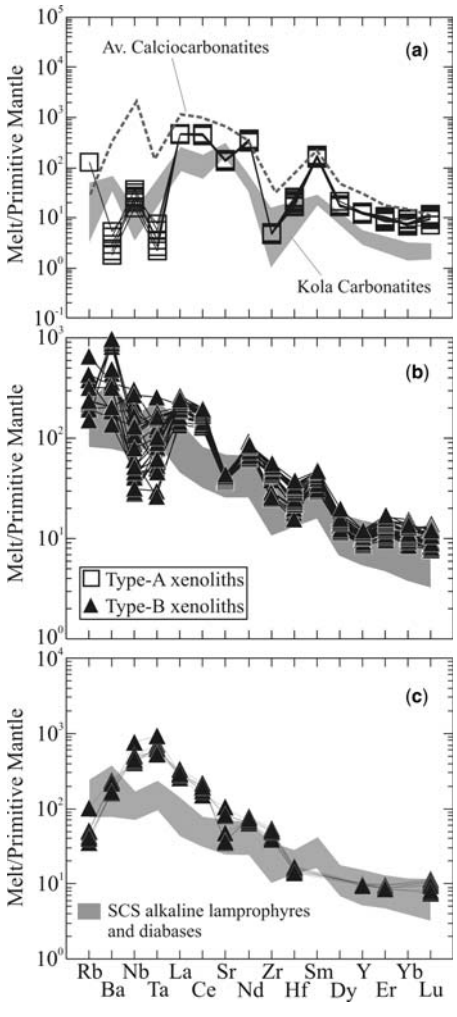

Fig. 9. (**a**) Trace element composition of melts in equilibrium with clinopyroxenes from type A altered xenoliths, associated with carbonate melts. Data calculated using cpx/carbonatite melt partition coefficients (Klemme *et al.* 1995). (**b**) Trace element composition of melts in equilibrium with clinopyroxenes from type B altered xenoliths, associated with the SCS alkaline magmas. Data calculated using cpx/basaltic melt partition coefficients (Hart & Dunn 1993), except for Rb (Foley *et al.* 1996) and Ta (averaged value determined at $P = 1.0$ GPa by Skulski *et al.* 1994). (**c**) Trace element composition of melts in equilibrium with amphiboles from type B altered xenoliths, associated with the SCS alkaline magmas. Data calculated using amph/silicate melt partition coefficients of LaTourrette *et al.* (1995). Average composition of calciocarbonatites taken from Woolley & Kempe (1989). Compositional field of selected Kola carbonatites taken from Downes *et al.* (2005). SCS alkaline dykes range taken from Villaseca *et al.* (2004). Normalizing values for primitive mantle from McDonough & Sun (1995).

2003). Phlogopite is also typically Cr–Mg-rich, displaying higher Mg-number (0.82–0.86) and lower TiO_2 contents (<5 wt%) than those expected for micas formed from evolved basic melts as pyroxenitic xenoliths (Mg-number *c*. 0.65–0.75 and TiO_2 *c*. 6–9 wt%; Ionov *et al.* 1997; Shaw 2004), whereas Cr and Mg concentrations resemble those of metasomatic micas crystallized in veins within the upper mantle (Fig. 3). Trace element signatures of clinopyroxene and amphibole from type B xenoliths point clearly to a metasomatic origin associated with an alkaline silicate melt (modal metasomatism). Using the experimental cpx/silicate melt partition coefficients of Hart & Dunn (1993), except for Rb (Foley *et al.* 1996) and Ta (averaged value determined at $P = 1.0$ GPa by Skulski *et al.* 1994), and the amph/silicate melt partition coefficients of LaTourrette *et al.* (1995), we have calculated the hypothetical trace element composition of melts in equilibrium with both minerals from this type of xenolith, which is represented in Figure 9b and c. The primitive mantle-normalized trace element pattern of estimated melts broadly overlaps the compositional range corresponding to the SCS Permian alkaline lamprophyres and diabases, only showing slightly higher concentrations of Nb, Ta, La and Ce for estimates made using $D^{\mathrm{amph/melt}}$. This similarity suggests that the metasomatic agent responsible for the crystallization of amphibole and the modification of the clinopyroxene trace element composition from type B xenoliths might be genetically related to the SCS Permian alkaline magmatism.

The third distinctive geochemical signature described in the altered ultramafic SCS xenoliths corresponds to clinopyroxene and amphibole from type C xenoliths, which display similar flat REE patterns and strong HFSE depletions. This latter aspect contrasts significantly with the primitive mantle-normalized trace element patterns of amphiboles from type B and C xenoliths: the former gives rise to strong positive Nb–Ta anomalies, whereas type C amphiboles show negative Nb–Ta anomalies (Fig. 4d). In contrast, the HFSE depletions in clinopyroxenes from type A and C xenoliths (Fig. 4b) represent analogous behaviour indicative of high incompatibility of these elements in both metasomatizing agents, and, in general terms, this characteristic has been ascribed to reaction with H_2O–CO_2-rich melts (e.g. Downes 2001; Ionov *et al.* 2002a; Xu & Bodinier 2004).

Single or multiple enrichment events?

The heterogeneous trace element mineral chemistry of the altered SCS xenoliths can be explained by advocating two possibilities: (1) that different,

genetically unrelated metasomatic agents have operated within the upper mantle–lower crust boundary below the SCS, giving rise to three contrasting trace element patterns; or (2) that a single melt has affected the wall-rock after fractionating to produce three different (but genetically linked) metasomatic agents. In any case, the composition of melts in equilibrium with type B xenoliths strongly supports metasomatism being caused by highly alkaline magmas similar to the SCS Late Permian alkaline magmatism, which is the only alkaline magmatic event recorded in central Spain.

There are numerous cases where heterogeneous trace element enrichment signatures within mantle xenoliths have been interpreted as being controlled by a unique metasomatic agent, as a result of a differentiation process (e.g. Grégoire *et al.* 2000; Xu & Bodinier 2004). Opposite to modal metasomatism within the wall-rock, restricted to zones adjacent to vein conduits, a 'diffuse' metasomatism has been proposed, corresponding to migrations of melts that percolate along grain boundaries in a solid matrix (i.e. porous flow; e.g. Xu & Bodinier 2004). The metasomatic agent is generally a small melt fraction rich in volatiles. Such melts, because of their low viscosity and low dihedral wetting angles, such as occur for carbonatitic melts, can escape their source regions at melt fractions as low as 0.1%, percolating through the rock matrix because of the formation of interconnected grain-edge networks (e.g. Minarik 1998; Witt-Eickschen *et al.* 2003). This characteristic makes these magmas very effective as mobile metasomatic agents in the lithospheric mantle (Navon & Stolper 1987; Green & Wallace 1988; Yaxley *et al.* 1998). Reactive porous flow metasomatism has been used to explain the variable LREE enrichment in clinopyroxene with almost constant HREE (Bedini *et al.* 1997; Vernières *et al.* 1997; Ionov *et al.* 2002*a*). Moreover, a direct relationship between the style of metasomatism and the distance from its source has been observed in peridotite massifs (e.g. Bodinier *et al.* 1990), and ascribed to a single metasomatic event involving a progressively differentiated melt solidifying down a thermal gradient. Nevertheless, the general equilibrium conditions attained by minerals in the altered SCS xenoliths, as demonstrated by similar Mg-number values and the absence of strongly fractionated LREE ratios, such as La/Ce, La/Pr or La/Nd, suggest that source composition dominated the metasomatic process over fractionation mechanisms (chromatographic effect), so that the rock acquired strong chemical fingerprints of the metasomatic agents.

We propose that metasomatism within the altered ultramafic SCS xenoliths represents the involvement of a single parental melt. The estimated trace element composition of melts in equilibrium with type B xenoliths (associated with silicate melt metasomatism) suggests that this agent was similar to the Permian alkaline magmatism. Clinopyroxene and amphibole from type B xenoliths show chemical characteristics similar to those of metasomatic phases crystallized in veins. Nevertheless, a differentiation process must have occurred while alkaline melts percolated through the wall-rock, to produce type A–C geochemical signatures. Crystallization of amphibole and phlogopite in vein conduits and in the wall-rock may result in a significant decrease in water and Nb–Ta contents in the residual melts. Taking into account the high H_2O and CO_2 contents characteristic of these alkaline melts, a decrease in water in the percolating fluid or melt would favour the formation of a carbonate-rich fraction responsible for the anhydrous transformation of type A xenoliths, probably at a greater distance from the magma source. Reaction of a carbonate melt with the wall-rock would result in a continuous exhaustion of its silicate component and an increasing proportion of the carbonate component in its composition (Mattielli *et al.* 1999), because carbonates are not stable in the shallow mantle at moderate to high temperatures (Dalton & Wood 1993).

Formation of type C clinopyroxene and amphibole may be interpreted within this theoretical model. The differences shown by type B and type C amphiboles in their trace element composition (e.g. Zr–Nb concentrations) are very similar to those described for vein and disseminated amphiboles within metasomatized mantle xenoliths (Ionov *et al.* 1997; Fig. 10). Whereas convex-upwards REE patterns in type B xenoliths could be ascribed to silicate melt crystallization in veins, the flat REE patterns and the negative HFSE anomalies of

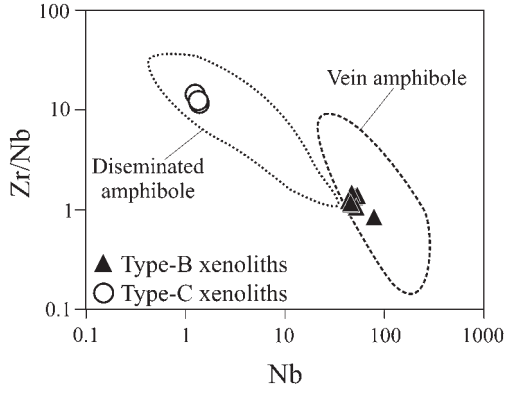

Fig. 10. Zr/Nb v. Nb for amphiboles from the altered ultramafic SCS xenoliths. Fields for disseminated and vein amphibole are taken from Ionov *et al.* (1997).

amphibole from type C xenoliths resemble trace element contents of disseminated amphibole. Transition from the convex-shaped REE pattern to the LREE-depleted pattern for vein and disseminated amphiboles, respectively, has been documented in several studies (Downes *et al.* 1995; Vaselli *et al.* 1995; Zanetti *et al.* 1996). The above differences in trace element composition between metasomatic amphiboles have been explained by the lower solubility of HFSE in aqueous fluids when compared with silicate melts (Ionov & Hofmann 1995), in accordance with the widely accepted model of mantle metasomatism involving expulsion of fluids from a network of veins filled with crystallizing basaltic melts (Wilshire 1987; O'Reilly *et al.* 1991). Thus, it is likely that percolation of the H_2O–CO_2-rich metasomatic agent, before total exhaustion of water, would have given rise to crystallization of a HFSE-poor amphibole in type C xenoliths.

Nature of the pyroxenite protolith

Although the whole-rock geochemistry of type B xenoliths has not been determined, the similarities in petrography (granoblastic texture, high degree and type of alteration, modal composition), and in major element mineral composition, when compared with the other altered xenoliths, suggest that they all are probably related to similar protoliths. The modal abundance of pseudomorphed orthopyroxene, as stated above, combined with their Opx-rich normative composition (Table 4) and the negative Nb–Ta (immobile elements) anomaly in multi-element normalized plots shown by the pyroxenites are in clearly contrast to the host alkaline magma chemistry. Subsequently, pyroxenite parental melts show a sub-alkaline affinity. Their granoblastic texture indicates solid-state equilibration before being trapped by ascending alkaline magmas.

P–T estimates on mineral equilibria in ultramafic xenoliths give metamorphic conditions close to mantle–crust boundary levels (Orejana *et al.* 2006). This is in agreement with estimated conditions for accompanying granulite xenoliths (Villaseca *et al.* 1999). Moreover, recent estimates on pyroxene-bearing charnockite xenoliths also yield *P–T* conditions that rarely indicate significant mantle depths, taking into account an estimated average crustal thickness of 35km (see Villaseca *et al.* 1999, and references therein). *P–T* estimates in the studied altered pyroxenites using single-cpx thermometry (Mercier 1980), Ti-in-amphibole thermometry (Otten 1984) and cpx barometry (Nimis & Ulmer 1998) give values that are mostly in the range of 935–1075 °C and 7.6–10.2 kbar (Table 2), overlapping previously published data on SCS xenolith suites. The lack of clear mantle-derived (i.e. peridotite) xenoliths in the lamprophyres also argues for a non-mantle provenance of these rocks. Thus, pyroxenite xenoliths could represent ultramafic igneous bodies recrystallized during granulite-facies conditions at the base of the SCS continental crust.

Prior to entrainment of the alkaline magmatism, three intrusive suites of calc-alkaline basic rocks have been identified within the SCS (Villaseca *et al.* 2004): (1) gabbros to quartz diorites emplaced in small massifs (Gb1), coeval with the granitic Hercynian batholith; (2) medium-K calc-alkaline dyke swarms (Gb2); (3) shoshonitic dyke swarms (Gb3). Gb1 rocks were intruded between 345 and 310Ma (Bea *et al.* 1999), whereas Gb2 and Gb3 represent a post-collisional, late-stage magmatism emplaced no earlier than 295Ma (Galindo *et al.* 1994). Thus, the origin of the protolith of the altered SCS xenoliths might be associated with crystallization of ultramafic pyroxene-rich cumulates from these basic sub-alkaline magmas at the lower crust–upper mantle boundary, in the context of an underplating event, as has been proposed for other Permian pyroxenitic xenoliths from the French Massif Central (Féménias *et al.* 2003).

The Sr–Nd isotopic ratios (calculated at 265Ma) of the two analysed samples (type A and C xenoliths) give rise to a homogeneous εNd *c.* +1, but relatively variable radiogenic Sr isotopic ratios (Fig. 11). A wide range of $^{87}Sr/^{86}Sr$ ratios in ultramafic xenoliths accompanied by little variation of the εNd value has been explained by interaction with oceanic waters associated with a lithospheric component affected by subduction (e.g. Downes *et al.* 1992; Rosenbaum *et al.* 1997; Downes 2001; Xu 2002). Nevertheless, the SCS represents the innermost part of the Hercynian Belt, precluding the possibility of an oceanic subducted component in this region. Moreover, the primary mineral chemistry of the altered SCS xenoliths strongly suggests that metasomatism was caused by the infiltration of alkaline magmas genetically related to the host Permian alkaline dykes. Superimposed upon this there is also a later strong alteration process caused by the devolatilization of the lamprophyric magma.

The relatively enriched Sr isotopic signature might represent an enriched composition in the source, probably linked to the Gb2 or Gb3 sub-alkaline basic magmas mentioned above, as they show a similar Sr isotopic composition to that of the altered xenoliths. The relatively high εNd value of the altered xenoliths points to the isotopically depleted SCS alkaline dykes as the main metasomatic melt via the two processes indicated above. We have tested this possibility by applying a simple mixing model that considers the averaged composition of the SCS depleted lamprophyres and

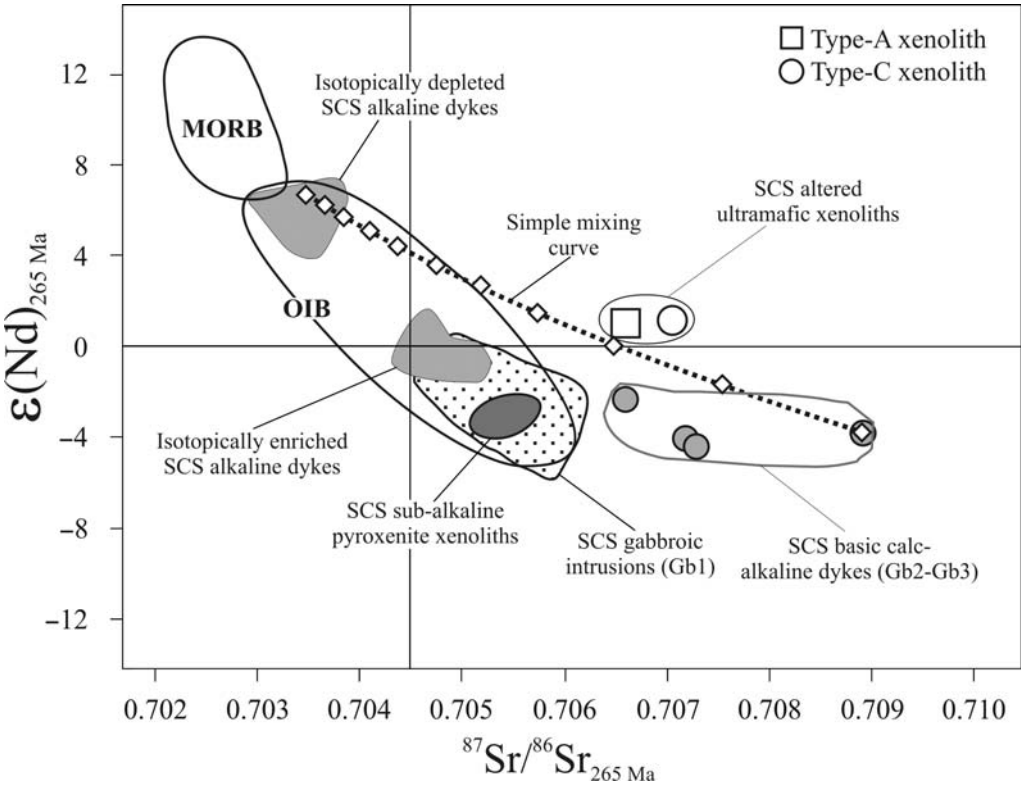

Fig. 11. Comparison of Sr–Nd isotopic ratios of the altered SCS xenoliths with respect to different SCS magmatic rocks. Composition of alkaline and sub-alkaline (Gb1–Gb2–Gb3) intrusions after Villaseca *et al.* (2004), calculated at 265 Ma. SCS sub-alkaline pyroxenitic xenoliths taken from Orejana *et al.* (2006). The curve joining small open diamonds represents a simple mixing model illustrating the probable influence of the infiltration of alkaline magmas (metasomatism and alteration) within an isotopically enriched pyroxenitic protolith. The mixing model considers the most radiogenic Gb2 sample as the starting composition $^{87}Sr/^{86}Sr = 0.70917$; $^{143}Nd/^{144}Nd = 0.512087$; Sr 230 ppm; Nd 16 ppm) and the isotopically depleted alkaline host dykes as the main metasomatic agent ($^{87}Sr/^{86}Sr = 0.70350$; $^{143}Nd/^{144}Nd = 0.512637$; Sr 800 ppm; Nd 40 ppm). MORB and OIB fields after Wilson (1989). The model suggests that metasomatism (including alteration) might be caused by the involvement of around 20% of the alkaline component.

diabases as a metasomatic melt, and a Gb2-like composition as the original calc-alkaline pyroxenitic protolith (Fig. 11). The trend described by this model predicts an isotopic modification with a 20% contribution of an alkaline melt component to explain the isotopic composition of the altered ultramafic SCS xenoliths.

Conclusions

The altered ultramafic SCS xenoliths show recrystallization textures, indicating solid-state equilibrium at the lower crustal depths. The host lamprophyric dykes do not show significant hydrothermal alteration. Thus, the secondary phases (chlorite and talc group minerals) present in the ultramafic xenoliths might have formed as a result of selective transformation, mainly of orthopyroxene, as a consequence of volatile exsolution from the host melt. The presence of unaltered clinopyroxene, amphibole and phlogopite phenocrysts in the alkaline dykes suggests that these phases should have been preserved in the xenoliths, if present. The absence of olivine and the predominance of modal clinopyroxene or normative *Hy* and *Di* indicate that these xenoliths were not mantle fragments, but represent cumulate pyroxenites of calc-alkaline affinity.

The presence of Cr–Mg-rich high-*T* hydrous phases (amphibole and phlogopite) indicates significant modal metasomatism at depth. This metasomatic process seems to be heterogeneous, as these xenoliths show three mineral trace element

signatures: type A xenoliths, with LREE-enriched clinopyroxenes with negative HFSE anomalies; type B xenoliths, with clinopyroxenes and amphiboles with high incompatible trace element contents (LILE, HFSE and REE); type C xenoliths, with relatively REE- and HFSE-poor clinopyroxenes and amphiboles. These metasomatic characteristics support crystallization from three different metasomatic agents: carbonated magma, silicate magma and hydrous fluids–melts, respectively, which are derived from the progressive differentiation of a single CO_2–H_2O-rich highly alkaline melt, genetically related to the SCS Permian alkaline lamprophyric magmatism.

The homogeneous Sr–Nd isotopic ratios of the altered xenoliths, together with their sub-alkaline nature, indicate that they formed as pyroxene-rich cumulates, associated with the intrusion of calc-alkaline basic magmas at the base of the crust during an underplating event. The radiogenic Sr composition could be explained by infiltration of an isotopically depleted melt (similar to the depleted SCS alkaline dykes) by an $^{87}Sr/^{86}Sr$-enriched component similar to Gb2 SCS calc-alkaline dykes.

We acknowledge A. F. Larios and J. G. del Tánago for their assistance with the electron microprobe analyses in the CAI of Microscopía Electrónica (UCM); also B. A. Paterson for his collaboration with laser ablation microanalysis at the Department of Earth Sciences of the University of Bristol (UK), and J. M. F. Pérez and J. A. H. Jiménez from the CAI of Geocronología y Geoquímica (UCM) for their help in analysing samples by TIMS. The detailed revision by J. M. Cebriá and G. Ceuleneer greatly increased the quality of the manuscript. We are also indebted to G. Rogers for his revision of the English. This work is included in the objectives of, and supported by, the CGL-2004-02515 project of the Ministerio de Educación y Ciencia of Spain.

References

ALLÈGRE, C. J. & TURCOTTE, D. L. 1987. Implications of a two-component marble-cake mantle. *Nature*, **323**, 123–127.

BEA, F., MONTERO, P. & MOLINA, J. F. 1999. Mafic precursors, peraluminous granitoids, and late lamprophyres in the Avila batholith; a model for the generation of Variscan batholiths in Iberia. *Journal of Geology*, **107**, 399–419.

BEDINI, R. M., BODINIER, J. L., DAUTRIA, J. M. & MORTEN, L. 1997. Evolution of LILE-enriched small melt fractions in the lithospheric mantle: a case study from the East Africa Rift. *Earth and Planetary Science Letters*, **153**, 67–83.

BODINIER, J. L., VASSEUR, G., VERNIÈRES, J., DUPUY, C. & FABRIÉS, J. 1990. Mechanisms of mantle metasomatism: geochemical evidence from the Lherz orogenic peridotite. *Journal of Petrology*, **31**, 597–628.

BRUIJNE, C. H. & ANDRIESSEN, P. A. 2000. Interplay of intraplate tectonics and surface processes in the Sierra de Guadarrama (central Spain) assessed by apatite fission track analyses. *Physics and Chemistry of the Earth*, **25**, 555–563.

CARIGNAN, J., HILD, P., MEVELLE, G., MOREL, J. & YEGHICHEYAN, D. 2001. Routine analyses of trace elements in geological samples using flow injection and low pressure on-line liquid chromatography coupled to ICP-MS; a study of geochemical reference materials BR, DR-N, UB-N, AN-G and GH. *Geostandards Newsletter*, **25**, 187–198.

DALTON, J. A. & WOOD, B. J. 1993. The composition of primary carbonate melts and their evolution through wallrock reaction in the mantle. *Earth and Planetary Science Letters*, **119**, 511–525.

DEER, W. A., HOWIE, R. A. & ZUSSMAN, J. 1976. *Rock-forming Minerals: Volume 3, Sheet Silicates*. Longman, Harlow.

DOWNES, H. 2001. Formation and modification of the shallow sub-continental lithospheric mantle: a review of geochemical evidence from ultramafic xenolith suites and tectonically emplaced ultramafic massifs of western and central Europe. *Journal of Petrology*, **42**, 233–250.

DOWNES, H. & DUPUY, C. 1987. Textural, isotopic and REE variations in spinel peridotite xenoliths, Massif Central, France. *Earth and Planetary Science Letters*, **82**, 121–135.

DOWNES, H., EMBEY-ISZTIN, A. & THIRLWALL, M. F. 1992. Petrology and geochemistry of spinel peridotite xenoiths from the western Pannonian Basin (Hungary): evidence for an association between enrichment and texture in the upper mantle. *Contributions to Mineralogy and Petrology*, **103**, 277–286.

DOWNES, H., SEGHEDI, I., SZAKACS, A. *ET AL.* 1995. Petrology and geochemistry of late Tertiary/Quaternary mafic alkaline magmatism in Romania. *Lithos*, **35**, 65–81.

DOWNES, H., BALAGANSKAYA, E., BEARD, A., LIFEROVICH, R. & DEMAIFFE, D. 2005. Petrogenetic processes in the ultramafic, alkaline and carbonatitic magmatism in the Kola Alkaline Province: A review. *Lithos*, **85**, 48–75.

DUCEA, M. N. & SALEEBY, J. B. 1998. The age and origin of a thick mafic–ultramafic keel from beneath the Sierra Nevada batholith. *Contributions to Mineralogy and Petrology*, **133**, 169–185.

ESCUDER VIRUETE, J., HERNÁIZ, P. P., VALVERDE, P., RODRÍGUEZ, R. & DUNNING, G. 1998. Variscan syncollisional extension in the Iberian Massif: structural, metamorphic and geochronological evidence from the Somosierra sector of the Sierra de Guadarrama (Central Iberian Zone, Spain). *Tectonophysics*, **290**, 87–109.

ESPERANÇA, S. & HOLLOWAY, J. R. 1987. On the origin of some mica-lamprophyres; experimental evidence from mafic minette. *Contributions to Mineralogy and Petrology*, **95**, 207–216.

FÉMÉNIAS, O., COUSSAERT, N., BINGEN, B., WHITEHOUSE, M., MERCIER, J. C. C. & DEMAIFFE, D.

2003. A Permian underplating event in late- to post-orogenic tectonic setting. Evidence from the mafic–ultramafic layered xenoliths from Beaunit (French Massif Central). *Chemical Geology*, **199**, 293–315.

FERNÁNDEZ-SUÁREZ, J., JEFFRIES, T. E., WHITEHOUSE, M. J., ARENAS, R. & VILLASECA, C. 2006. A U-Pb study of zircons from lower crustal xenoliths of the Spanish Central System: a record of Iberian lithospheric evolution from the Neoproterozoic to the Triassic. *Journal of Geology*, **114**, 471–483.

FOLEY, S. F., JACKSON, S. E., FRYER, B. J., GREENOUGH, J. D. & JENNER, G. A. 1996. Trace element partition coefficients for clinopyroxene and phlogopite in an alkaline lamprophyre from Newfoundland by LAM-ICP-MS. *Geochimica et Cosmochimica Acta*, **60**, 629–638.

FREY, F. A. & PRINZ, M. 1978. Ultramafic inclusions from San Carlos, Arizona; petrologic and geochemical data bearing on their petrogenesis. *Earth and Planetary Science Letters*, **38**, 129–176.

GALINDO, C., HUERTAS, M. J. & CASQUET, C. 1994. Cronología Rb–Sr y K–Ar de diques de la Sierra de Guadarrama (Sistema Central Español). *Geogaceta*, **16**, 23–26.

GARRIDO, C. J. & BODINIER, J. L. 1999. Diversity of mafic rocks in the Ronda Peridotite; evidence for pervasive melt–rock reaction during heating subcontinental lithosphere by upwelling asthenosphere. *Journal of Petrology*, **40**, 729–754.

GREEN, D. H. & WALLACE, M. E. 1988. Mantle metasomatism by ephemeral carbonatite melts. *Nature*, **336**, 459–462.

GRÉGOIRE, M., MOINE, B. N., O'REILLY, S. Y., COTTIN, J. Y. & GIRET, A. 2000. Trace element residence and partitioning in mantle xenoliths metasomatized by highly alkaline, silicate- and carbonate-rich melts (Kerguelen Islands, Indian Ocean). *Journal of Petrology*, **41**, 477–509.

GRÉGOIRE, M., BELL, D. R. & LE ROEX, A. P. 2003. Garnet lherzolites from the Kaapvaal craton (South Africa): trace element evidence for a metasomatic history. *Journal of Petrology*, **44**, 629–657.

HART, S. R. & DUNN, T. 1993. Experimental cpx/melt partitioning of 24 trace elements. *Contributions to Mineralogy and Petrology*, **113**, 1–8.

IONOV, D. A. 1998. Trace element composition of mantle-derived carbonates and coexisting phases in peridotite xenoliths from alkali basalts. *Journal of Petrology*, **39**, 1931–1941.

IONOV, D. A. & HOFMANN, A. W. 1995. Nb–Ta-rich mantle amphiboles and micas: implications for subduction-related metasomatic trace element fractionations. *Earth and Planetary Science Letters*, **131**, 341–356.

IONOV, D. A., GRIFFIN, W. L. & O'REILLY, S. Y. 1997. Volatile-bearing minerals and lithophile trace elements in the upper mantle. *Chemical Geology*, **141**, 153–184.

IONOV, D. A., BODINIER, J. L., MUKASA, S. B. & ZANETTI, A. 2002*a*. Mechanisms and sources of mantle metasomatism: major and trace element compositions of peridotite xenoliths from Spitsbergen in the context of numerical modelling. *Journal of Petrology*, **43**, 2219–2259.

IONOV, D. A., MUKASA, S. B. & BODINIER, J. L. 2002*b*. Sr–Nd–Pb isotopic compositions of peridotite xenoliths from Spitsbergen: numerical modelling indicates Sr–Nd decoupling in the mantle by melt percolation metasomatism. *Journal of Petrology*, **43**, 2261–2278.

IRVING, A. J. & FREY, F. A. 1984. Trace element abundances in megacrysts and their host basalts; constraints on partition coefficients and megacryst genesis. *Geochimica et Cosmochimica Acta*, **48**, 1201–1221.

JOHNSON, K. E., DAVIS, A. M. & BRYNDZIA, L. T. 1996. Contrasting styles of hydrous metasomatism in the upper mantle: an ion microprobe investigation. *Geochimica et Cosmochimica Acta*, **60**, 1367–1385.

KEMPTON, P. D. 1987. Mineralogical and geochemical evidence for differing styles of metasomatism in spinel lherzolite xenoliths: enriched mantle source regions of basalts. *In*: MENZIES, M. & HAWKESWORTH, C. J. (eds) *Mantle Metasomatism*. Academic Press, New York, 45–89.

KEMPTON, P. D., HAWKESWORTH, C. J., LÓPEZ-ESCOBAR, L., PEARSON, D. G. & WARE, A. J., 1999. Spinel ± garnet lherzolite xenoliths from Pali Aike, Part 2: trace element and isotopic evidence on the evolution of lithospheric mantle beneath southern Patagonia. *In*: GURNEY, J., GURNEY, J. L., PASCOE, M. D. & RICHARDSON, S. H. (eds.) *The B. J. Dawson Volume, Proceedings of the 7th International Kimberlite Conference*. Red Roof Design, Cape Town, 415–428.

KLEMME, S., VAN DER LAAN, S. R., FOLEY, S. F. & GÜNTHER, D. 1995. Experimentally determined trace and minor element partitioning between clinopyroxene and carbonatite melt under upper mantle conditions. *Earth and Planetary Science Letters*, **133**, 439–448.

LATOURRETTE, T., HERVIG, R. L. & HOLLOWAY, J. R. 1995. Trace element partitioning between amphibole, phlogopite, and basanite melt. *Earth and Planetary Science Letters*, **135**, 13–30.

LITASOV, K. D., FOLEY, S. F. & LITASOV, Y. D. 2000. Magmatic modification and metasomatism of the subcontinental mantle beneath the Vitim volcanic field (East Siberia): evidence from trace element data on pyroxenite and peridotite xenoliths from Miocene picrobasalt. *Lithos*, **54**, 83–114.

MATTIELLI, N., WEIS, D., SCOATES, J. S. *ET AL.* 1999. Evolution of heterogeneous lithospheric mantle in a plume environment beneath the Kerguelen Archipelago. *Journal of Petrology*, **40**, 1721–1744.

MCDONOUGH, W. F. & SUN, S. S. 1995. The composition of the Earth. *Chemical Geology*, **120**, 223–253.

MERCIER, J. C. C. 1980. Single-pyroxene thermobarometry. *Tectonophysics*, **70**, 1–37.

MINARIK, W. G. 1998. Complications to carbonate melt mobility due to the presence of an immiscible silicate melt. *Journal of Petrology*, **39**, 1965–1973.

NAVON, O. & STOLPER, E. 1987. Geochemical consequences of melt percolation; the upper mantle as a chromatographic column. *Journal of Geology*, **95**, 285–307.

NIMIS, P. & ULMER, P. 1998. Clinopyroxene geobarometry of magmatic rocks Part 1: An expanded structural geobarometer for anhydrous and hydrous, basic and ultrabasic systems. *Contributions to Mineralogy and Petrology*, **133**, 122–135.

O'REILLY, S. Y., GRIFFIN, W. L. & RYAN, C. G. 1991. Residence of trace elements in metasomatized spinel lherzolite xenoliths; a proton–microprobe study. *Contributions to Mineralogy and Petrology*, **109**, 98–113.

OREJANA, D., VILLASECA, C. & PATERSON, B. A. 2006. Geochemistry of pyroxenitic and hornblenditic xenoliths in alkaline lamprophyres from the Spanish Central System. *Lithos*, **86**, 167–196.

OTTEN, M. T. 1984. The origin of brown hornblende in the Artfjaellet gabbro and dolerites. *Contributions to Mineralogy and Petrology*, **86**, 189–199.

PAWLEY, A. R. 2003. Chlorite stability in mantle peridotite: the reaction clinochlore + enstatite = forsterite + pyrope + H_2O. *Contributions to Mineralogy and Petrology*, **144**, 449–456.

PAWLEY, A. R. & WOOD, B. J. 1995. The high pressure stability of talc and 10 Å phase: Potential storage sites for H_2O in subduction zones. *American Mineralogist*, **80**, 998–1003.

PERINI, G., CEBRIÁ, J. M., LÓPEZ-RUIZ, J. M. & DOBLAS, M. 2004. Permo-Carboniferous magmatism in the variscan belt of Spain and France: implications on mantle sources. *In*: WILSON, M., NEUMANN, E. R., DAVIES, G. R., TIMMERMAN, M. J., HEEREMANS, M. & LARSEN, B. (eds) *Permo-Carboniferous Magmatism and Rifting in Europe*. Geological Society, London, Special Publications, **223**, 415–438.

REYES, J., VILLASECA, C., BARBERO, L., QUEJIDO, A. J. & SANTOS, J. F. 1997. Descripción de un método de separación de Rb, Sr, Sm y Nd en rocas silicatadas para estudios isotópicos. *In*: *Actas del I Congreso Ibérico de Geoquímica*. CEDEX, Soria, 46–55.

ROCK, N. M. S. 1991. *Lamprophyres*. Blackie, Glasgow.

ROSENBAUM, M. J., WILSON, M. & DOWNES, H. 1997. Enrichment of the Pannonian Carpathian mantle: Pb–Sr–Nd isotope and trace element constraints. *Journal of Geophysical Research*, **102**, 14947–14961.

SCARROW, J., BEA, F., MONTERO, P., MOLINA, J. F. & VAUGHAN, A. P. M. 2006. A precise late Permian $^{40}Ar/^{39}Ar$ age for Central Iberian camptonitic lamprophyres. *Geologica Acta*, **4**, 451–459.

SHAW, C. S. J. 2004. The temporal evolution of three magmatic systems in the West Eifel volcanic field, Germany. *Journal of Volcanology and Geothermal Research*, **131**, 213–240.

SKULSKI, T., MINARIK, W. & WATSON, E. B. 1994. High-pressure experimental trace-element partitioning between clinopyroxene and basaltic melts. *Chemical Geology*, **117**, 127–147.

SUN, S. S. & MCDONOUGH, W. F. 1989. Chemical and isotopic systematics of oceanic basalts; implications for mantle composition and processes. *In*: SAUNDERS, A. D. & NORRY, M. J. (eds) *Magmatism in Ocean Basins*. Geological Society, Special Publications, **42**, 313–345.

VASELLI, O., DOWNES, H., THIRLWALL, M. F. *ET AL.* 1995. Ultramafic xenoliths from Plio-Pleistocene alkali basalts from the Eastern Transylvanian Basin: depleted mantle enriched by vein metasomatism. *Journal of Petrology*, **38**, 23–54.

VERNIÈRES, J., GODARD, M. & BODINIER, J. L. 1997. A plate model for the simulation of trace element fractionation during partial melting and magmas transport in the Earth's upper mantle. *Journal of Geophysical Research*, **102**, 24771–24784.

VILLASECA, C., DOWNES, H., PIN, C. & BARBERO, L. 1999. Nature and composition of the lower continental crust in Central Spain and the granulite-granite linkage: inferences from granulitic xenoliths. *Journal of Petrology*, **40**, 1465–1496.

VILLASECA, C., OREJANA, D., PIN, C., LÓPEZ GARCÍA, J. A. & ANDONAEGUI, P. 2004. Le magmatisme basique hercynien et post-hercynien du Système Central Espagnol: essai de caractèrisation des sources manteliques. *Comptes Rendus de Géosciences*, **336**, 877–888.

WILSHIRE, H. G., 1987. A model of mantle metasomatism. *In*: MORRIS, E. M. & PASTERIS, J. D. (eds) *Mantle Metasomatism and Alkaline Magmatism*. Geological Society of America, special papers, **215**, 47–60.

WILSON, M. 1989. *Igneous Petrogenesis: a Global Tectonic Approach*. Unwin Hyman, Boston, MA.

WITT-EICKSCHEN, G., SECK, H. A., MEZGER, K., EGGINS, S. M. & ALTHERR, R. 2003. Lithospheric mantle evolution beneath the Eifel (Germany): constraints from Sr–Nd–Pb isotopes and trace element abundances in spinel peridotite and pyroxenite xenoliths. *Journal of Petrology*, **44**, 1077–1095.

WOOLLEY, A. R. & KEMPE, D. R. C. 1989. Carbonatites: nomenclature, average chemical compositions, and element distribution. *In*: BELL, K. (ed.) *Carbonatites: Genesis and Evolution*. Unwin Hyman, London, 1–14.

XU, X., O'REILLY, S. Y., GRIFFIN, W. L. & ZHOU, X. 2003. Enrichment of upper mantle peridotite: petrological, trace element and isotopic evidece in xenoliths from SE China. *Chemical Geology*, **198**, 163–188.

XU, Y. G. 2002. Evidence for crustal components in the mantle and constraints on crustal recycling mechanisms: pyroxenite xenoliths from Hannuoba, North China. *Chemical Geology*, **182**, 301–322.

XU, Y. G. & BODINIER, J. L. 2004. Contrasting enrichments in high- and low-temperature mantle xenoliths from Nushan, eastern China: results of a single metasomatic event during lithospheric accretion. *Journal of Petrology*, **45**, 321–341.

YAXLEY, G. M., GREEN, D. H. & KAMENETSKY, V. 1998. Carbonatite metasomatism in the southeastern Australia lithosphere. *Journal of Petrology*, **39**, 1917–1930.

ZANETTI, A., VANNUCCI, R., BOTTAZZI, P., OBERTI, R. & OTTOLINI, L. 1996. Infiltration metasomatism at Lherz as monitored by systematic ion-microprobe investigations close to a hornblendite vein. *Chemical Geology*, **134**, 113–133.

Types of metasomatism in mantle xenoliths enclosed in Neogene–Quaternary alkaline mafic lavas from Catalonia (NE Spain)

G. GALÁN[1], V. OLIVERAS[1] & B. A. PATERSON[2]

[1]*Departament de Geologia, Universitat Autònoma de Barcelona, Edifici C (sur), 08193 Bellaterra-Barcelona, Spain (e-mail: gumer.galan@uab.es)*

[2]*Department of Earth Sciences, University of Bristol, Wills Memorial Building, Bristol BS8 1RJ, UK*

Abstract: Mantle xenoliths in within-plate alkaline mafic lavas from NE Spain are mainly anhydrous spinel lherzolites and harzburgites, grading into each other, and subordinate pyroxenites. Peridotites followed an earlier melt depletion caused by mantle decompression and subsequent metasomatism. Two main types of metasomatism are differentiated affecting mainly the harzburgites: a silicate-melt metasomatism of Fe–Ti type and a carbonatite metasomatism. Both types are recognized in the nearby Pyrenean peridotite massifs, but the presence of hydrous minerals is less frequent in the xenoliths. The two metasomatic styles could have been generated by the intrusion of Cretaceous alkaline magmas, if a chromatographic fractionation–reaction process at decreasing melt mass took place. This would account for the evolution of the original alkaline silicate percolating melt towards a carbonatite-rich melt, allowing the coexistence in both space and time of the two metasomatic styles. Metasomatism in lherzolites could be explained in the same way. The pyroxenite xenoliths are interpreted as cumulates from these alkaline basic magmas that crop out in the area as rare camptonite dykes. Interaction with host lavas is minor and could explain the partial melting, enrichment and disequilibrium observed in a deformed composite xenolith and sporadic veins filled with glass.

Mantle xenoliths from the Tertiary–Quaternary alkaline mafic lavas of the western–central European magmatic province (Wilson & Downes 1991) along with the orogenic ultramafic massifs have served to constrain the evolution of the subcontinental lithospheric mantle (SCLM) in the European plate, as described, for example, by Downes (2001, and references therein), Beccaluva *et al.* (2004) and Féménias *et al.* (2004). These complementary studies indicate that the SCLM was affected by basaltic melt extraction and was locally enriched by metasomatism related to the infiltration of different melts or fluids in a subduction and/or intra-plate context.

The presence of peridotite mantle xenoliths, type I of Frey & Prinz (1978), in Tertiary–Quaternary alkaline mafic lavas from the Catalan volcanic province of NE Spain was first described by Tournon (1968), and they have more recently been the subject of simultaneous studies by Bianchini *et al.* (2007) and by ourselves (Galán 2004; Galán *et al.* 2006; Oliveras & Galán 2006). Here we expand on our preliminary results and are mainly concerned with their petrology, major element geochemistry of both minerals and whole rocks, trace element geochemistry of minerals and, with estimation of their P–T–fO_2 equilibrium conditions. Our aims are: (1) to characterize the different lithologies; (2) to assess the evolution of this part of the SCLM by melt depletion and metasomatic processes; (3) to establish correlations with other European xenoliths and especially with the nearby eastern Pyrenean ultramafic massifs, where melting and particularly metasomatic processes have been well documented by other workers (Bodinier *et al.* 1987*a*, *b*, 1988, 1990, 2004; McPherson *et al.* 1996; Zanetti *et al.* 1996; Woodland *et al.* 1996). According to those researchers, the state of these issues in the eastern Pyrenean examples is as follows: the peridotites are spinel lherzolites and harzburgites that show a continuous variation in their modal compositions. First, they underwent partial melting in the garnet stability field, and were later equilibrated in the spinel lherzolite field. Later, the residues were first invaded by tholeiitic magmas, similar to the Pyrenean Triassic dolerites, and then injected by alkali basalts associated with the Cretaceous alkaline magmatism. The former magmatic event crops out as dry pyroxenite bands and the latter as both amphibole pyroxenite dykes and hornblendite veins. The Cretaceous alkaline injections caused aureoles showing both modal metasomatism in a narrow zone close to the dykes and cryptic metasomatism far from them (Bodinier

From: COLTORTI, M. & GRÉGOIRE, M. (eds) *Metasomatism in Oceanic and Continental Lithospheric Mantle.* Geological Society, London, Special Publications, **293**, 121–153.
DOI: 10.1144/SP293.7 0305-8719/08/$15.00

et al. 1990, 2004). Both types of metasomatism mainly affected the harzburgites. Moreover, trace element concentrations and patterns in all wall rocks, clinopyroxene and amphibole differ away from the dykes; for example, clinopyroxene REE patterns change from convex-upward near the contact, typical of a silicate-melt metasomatism, to extremely fractionated at greater distance, which coupled to depletion of Zr and Ti suggests a carbonatite metasomatism. Woodland *et al.* (1996) supported an earlier carbonatite metasomatism later overprinted locally by the Cretaceous silicate-melt metasomatism. However, Bodinier *et al.* (1990, 2004) favoured the hypothesis that the emplacement of the silicate-melt dykes was linked to chromatographic fractionation–reaction of derivatives, which led to the coexistence, in space and time, of silicate, hydrous and carbonatite metasomatic agents. Nevertheless, the fact that the anhydrous wall-rock harzburgites, away from the contact, show much more Nd-enriched isotopic signature than that deduced from the chromatographic fractionation–reaction model leaves open the likely existence of multi-stage metasomatic events.

Finally, the results of this study will be discussed considering those obtained by Bianchini *et al.* (2007), which provide trace element and Sr–Nd–Hf isotopic compositions for other xenoliths from the same area.

Geological setting

The Catalan within-plate volcanism crops out in three zones (L'Emporda, La Selva, La Garrotxa; Fig. 1), which correspond to Neogene basins and graben structures generated during late Alpine extension, subsequent to the formation of the Pyrenees (Solé Sugrañés *et al.* 1984). The basins are bounded by two main extensional fault systems (NE–SW, NW–SE), which favoured the intrusion of alkaline magmas (Araña *et al.* 1983) and are part of the Tertiary–Quaternary rift system of western and central Europe. Available geochronological data (Donville 1973*a–c*) indicate ages for this volcanism ranging from 10 to 0.11 Ma, with the oldest values being found in lavas from L'Emporda zone and the youngest in lavas from La Garrotxa zone.

Prior to this rifting event, this part of the European lithosphere also shared a common history with others nearby: its structure formed during the Variscan and Alpine orogenies, with rifting episodes between these events: (1) during the Permo-Carboniferous, producing calc-alkaline–transitional and mildly alkaline magmatism (Lago *et al.* 2004; Perini *et al.* 2004); (2) during the Triassic–Jurassic, when continental tholeiites were formed in relation to the early stage of the Atlantic opening (Alibert 1985); (3) during the Cretaceous (85–113 Ma), involving alkaline magmatism (Rossy *et al.* 1992). Neither Alpine magmatism nor that associated with the Triassic–Jurassic extension are documented in the Catalan area, but the Cretaceous alkaline magmatism is shown as scarce lamprophyres (Solé *et al.* 2003). However, these episodes be imprinted on the SCLM underneath.

The lavas are leucite basanites, basanites, alkali basalts and subordinate trachytes (López Ruiz & Rodríguez Badiola 1985), for which Martí *et al.* (1992) suggested heterogeneous mantle sources (lithospheric for the oldest lavas and asthenospheric for the youngest), whereas Cebriá *et al.* (2000) proposed an origin for La Garrotxa mafic lavas by different degrees of partial melting of an enriched, isotopically heterogeneous lithospheric mantle source, as a result of two metasomatic events: a Late Palaeozoic metasomatism causing K enrichment, and a Cretaceous–Palaeogene event associated with the infiltration of asthenospheric melts, before the generation of the Neogene–Quaternary alkaline lavas.

The studied xenoliths were found in alkaline mafic lava flows and pyroclastic deposits from three volcanoes: Sant Dalmai (1 in Fig. 1) in La Selva zone, and Canet d'Adri and La Banya del

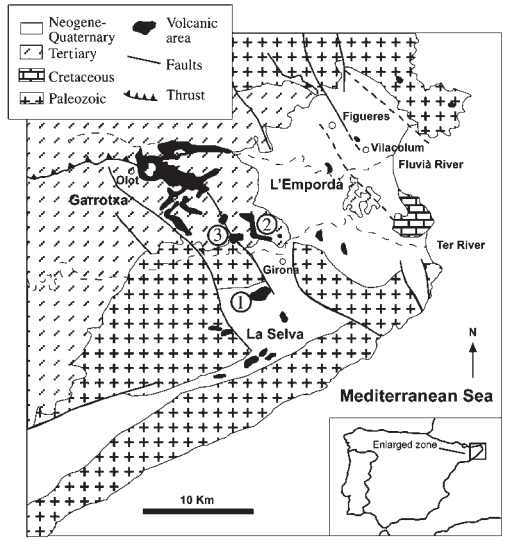

Fig. 1. Simplified geological map of the Catalan volcanism with the location of the three volcanoes where the xenoliths were sampled: 1, St Dalmai; 2, Canet d'Adri; 3, Banya del Boc.

Boc (2 and 3 respectively in Fig. 1) in La Garrotxa zone. The xenoliths are rounded–elongated or angular in shape, and up to 5 cm in size.

Analytical methods

Over 200 xenoliths were collected, of which 60, among the largest, were selected for petrographic study. Those of a sufficient size were point counted to classify them. The cores of 10 xenoliths, among the largest and the least contaminated by their host lavas, were ground using an agate mill for major element analysis and Cr determination by X-ray fluorescence (XRF) using a Siemens SRS-3000 sequential XRF system at SGS Canada Inc. The detection limit for all oxides was 0.01% and the instrument precision on most elements was better than 0.5%. A further 26 representative xenoliths were selected for electron microprobe analysis (EMPA) of the major elements, Ni and Cr of their constituent minerals. Both a Jeol JXA-8600 at the Department of Earth Sciences of the University of Bristol and a Cameca SX50 at the Serveis Científic Tècnics of the Universitat de Barcelona were used for this purpose. Beam current and acceleration voltage were the same in both instruments (15.00 nA and 20.00 kV, respectively) and natural and synthetic standards were used in both cases. Although the counting time and the correction method were different (20–30 s and 16–20 s counting time for peak and background respectively in the Jeol and 10 s for both peak and background in the Cameca instrument; ZAF correction method in the Jeol instrument and PAP in the Cameca), the analytical results are comparable. For glass analyses, the working conditions were different, using 6 nA acceleration voltage and a larger beam spot (5–10 μm) to avoid alkali devolatilization. Both EMPA analysis and mineral mode compositions were used for the estimation by mass balance of major element whole-rock compositions of those xenoliths that were not large enough to be analysed by XRF. Moreover, 14 xenoliths were further selected among those previously analysed by EMPA for measuring mineral trace element contents by laser ablation inductively coupled plasma mass spectrometry (LA-ICP-MS) using a VG Elemental PlasmaQuad 3 + S-Option ICP-MS system equipped with a 266 nm Nd–YAG laser (VG MicroProbe II), at the Department of Earth Sciences of the University of Bristol. The Nd–YAG laser operated at 6 Hz, the beam diameter was *c*. 20 μm and average drill rates were *c*. 2–3 μm s^{-1}. The gas and then an Ar–He mixture transported the ablated material from the sample cell to the plasma torch. All measurements were taken using Thermo Elemental PlasmaLab 'time-resolved analysis' (TRA) data acquisition software, with a total acquisition time of 100 s per analysis, of which 40 s were allowed for background followed by 60 s for laser ablation. Relative element sensitivities were calibrated using NIST 610 glass, and NIST 612 glass was used as a secondary standard. Each analysis was normalized to a major element as internal standard: ^{44}Ca for clinopyroxene and amphibole, ^{29}Si for olivine, orthopyroxene and phlogopite, and ^{49}Ti for spinel. To avoid analytical uncertainties related to variations in the concentration of the internal standards, these element concentrations were measured on the same grains as used for EMPA. Replicate analyses of the NIST 610 and 612 glasses indicate an analytical precision better than 5% for most element concentrations >10 ppm. The data were processed offline with the same PlasmaLab software as used for data collection and various custom-designed Excel spreadsheets. The detection limits are defined as 3.28 SD above the background level, which equates to a 95% confidence level that the measured signal is significantly above background. Detection limits for most elements were <1 ppm, but were (<2 ppm) for Sc and V, and <38 ppm for Co, Ti and Ni. Tables in this paper include, unless otherwise mentioned, major and trace element mineral compositions of the 14 xenoliths selected for LA-ICP-MS analysis. Other mineralogical analytical data can be obtained from the authors upon request.

Petrology

Most of the studied xenoliths are anhydrous spinel lherzolites and harzburgites according to their mineral mode compositions (Fig. 2), although amphibole and phlogopite appear as accessory minerals in sporadic samples (Table 1). Clinopyroxene mode shows a continuous variation from 17 to 6% in the lherzolites and <5% in the harzburgites. Spinel mode also decreases from the lherzolites towards the harzburgites. This continuous variation in the mineral mode compositions has also been documented for the eastern Pyrenean peridotites (Bodinier *et al.* 1988). A few pyroxenites were also found and are considered in this study.

Coarse granular textures (up to 4 mm in diameter) are dominant among all peridotites (Fig. 3a), but there are also porphyroclastic (Fig. 3b) and transitional granular–porphyroclastic forms and, less frequently, mosaic–equigranular (Mercier & Nicolas 1975) or granuloblastic (Harte 1977) textures (Fig. 3c), especially among lherzolites. Coarse granular lherzolites and harzburgites are

Table 1. *Mineral mode compositions of granular peridotite xenoliths and estimated whole-rock compositions*

Rock type:	LHZ	LHZ	LHZ	LHZ	LHZ	LHZ	LHZ	HZ	HZ	HZ	HZ	HZ
Sample:	CA.00.83	BB.12.030*	BB.64.04	BB.16.04	BB.81.04*	SD.98.58	SD.98.2	CA.00.83b	BB.12.041	BB.02.04	BB.74.04	BB.18.29*
(vol%)												
Ol	65.0	52.6	67.7	72.4	72.8	69.2	74.2	79.2	40.5	70.3	71.8	74.4
Cpx	13.0	13.0	9.6	9.0	6.5	7.7	6.1	2.6	1.7	1.3	1.00	0.4
Opx	21.0	31.8	20.6	16.0	18.6	20.3	16.3	18.0	57.5	28.1	26.5	24.7
Spl	1.0	2.6	2.0	2.6	2.1	2.8	3.4	0.2	0.3	0.3	0.7	0.5
Am	–	–	–	–	traces	–	–	–	–	–	–	–
Glass	–	–	–	–	–	–	–	traces	–	–	–	–
Total	100.0	100.0	99.9	100.0	100.0	100.0	100.0	100.0	100.0	100.0	100.0	100.00
Oxides (wt%)												
SiO_2	44.40	45.00	43.99	42.24	42.16	43.45	43.93	43.49	49.22	45.13	44.99	44.68
TiO_2	0.09	0.09	0.08	0.09	0.09	0.13	0.03	0.00	0.02	0.08	0.01	0.00
Al_2O_3	2.55	3.55	2.76	3.10	2.51	3.02	2.52	0.49	1.61	0.89	0.66	0.55
Cr_2O_3	0.45	0.67	0.44	0.44	0.32	0.54	0.58	0.30	0.65	0.43	0.28	0.23
FeO^T	8.16	7.60	8.27	8.84	9.41	8.55	8.71	7.79	6.54	7.92	7.64	6.40
MnO	0.11	0.13	0.14	0.12	0.17	0.14	0.12	0.13	0.13	0.13	0.12	0.12
MgO	41.26	39.76	42.10	43.20	43.85	42.30	42.67	46.95	40.73	44.73	45.70	47.61
CaO	2.81	2.94	2.01	1.79	1.35	1.75	1.39	0.82	1.03	0.65	0.58	0.41
Na_2O	0.18	0.26	0.20	0.17	0.14	0.12	0.04	0.02	0.07	0.03	0.02	0.00
K_2O	0.00	0.00	0.00	0.00	0.00	0.00	0.00	0.00	0.00	0.00	0.00	0.00
TOTAL	100.00	100.00	99.99	99.99	100.00	100.00	100.00	100.00	100.00	99.99	100.00	100.00
Mg-no.	90.0	90.3	90.1	89.7	89.3	89.8	89.7	91.5	91.7	91.0	91.4	93.0
Cr-no.	10.5	11.2	9.7	8.7	7.9	10.6	13.4	29.1	21.3	24.5	22.1	21.9

LHZ, lherzolite; HZ, harzburgite; mineral abbreviations after Kretz (1983).
*Samples also analysed by XRF.

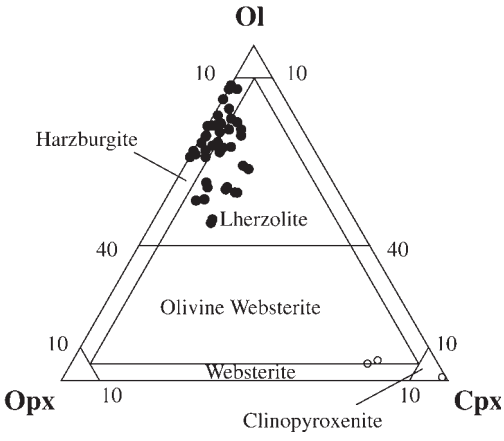

Fig. 2. Classification of the peridotite (●) and the pyroxenite (○) xenoliths based on the mineralogical mode compositions (Le Maitre 2002).

xenomorphic, equigranular or slightly inequigranular rocks, with straight or slightly curved crystal boundaries, and are mostly homogeneous, except for two laminated lherzolites (Harte 1977; BB.81.04, BB154.04), which show milimetre-scale layers in which clinopyroxene and/or spinel increase. Porphyroclastic peridotites show olivine, orthopyroxene (up to 5 mm diameter) and, less frequently, clinopyroxene and spinel porphyroclasts in a finer matrix formed of less deformed neocrystals of the same minerals, which can have grain junctions at 120º (Fig. 3b). One of the most deformed xenoliths is laminated (SD.98.15), with alternating layers enriched in olivine and orthopyroxene (average mineral composition of harzburgite). Both minerals form both porphyroclasts, along with spinel, and neocrystals defining a fluidal finer matrix, with interstitial glass between the neocrystals. Finally, only one lherzolite was found with finer mosaic–equigranular or granuloblastic texture showing crystal boundaries at 120º (Fig. 3c).

Olivine crystals can have very different sizes even in a single non-deformed sample. Rarely, these crystals are tabular and aligned. Both orthopyroxene and clinopyroxene occasionally show mutual lamellae and spinel lamellae in lherzolites. Also, clinopyroxene in lherzolites can have glass inclusions, and may develop spongy rims occasionally (Fig. 3d). Clinopyroxene in harzburgites usually forms smaller crystals than orthopyroxene or olivine. Spinel appears as lamellae, inclusions, isolated interstitial or holly-leaf-shaped crystals (Mercier & Nicolas 1975), and sometimes forms clusters along with olivine and pyroxenes in the lherzolites (Fig. 3e). Occasionally (e.g. in BB.154.04) spinel crystals show corona textures (Fig. 3f) formed of olivine (Fo 90.9 $\pm$ 0.4% (1σ)), clinopyroxene (Wo 44.3 $\pm$ 1.7%; En 50.1 $\pm$ 1.5%; Fs 5.5 $\pm$ 0.3%), plagioclase (An 61.6 $\pm$ 13.3%) (mineral abbreviations after Kretz 1983) and a neospinel that is Cr and Ti enriched (cr-number $= 100 \times Cr/(Cr + Al + Fe^{3+}) = 22.4 \pm 3.5$; mg-number $= 100 \times Mg/(Mg + Fe^{2+}) = 73.4 \pm 0.8$; in cations per formula unit) with respect to the earlier generation. Amphibole forms isolated and disseminated crystals that can include spinel and always show corona textures (Fig. 3g). These corona textures are formed of olivine (Fo 90.5 $\pm$ 0.5%), clinopyroxene (Wo 44.1 $\pm$ 4.6%; En 50.2 $\pm$ 4.7%; Fs 5.6 $\pm$ 0.6%), plagioclase (An 28.9 $\pm$ 3.3%), spinel enriched in Cr, Ti and Fe (cr-number 33.2 $\pm$ 4.6; mg-number 59.3 $\pm$ 5.4) with respect to the spinel in the rock, $\pm$ ilmenite surrounding some of the spinel crystals. Phlogopite appears as relict crystals also with fine reaction corona. Finally, glass is found filling discrete veins along mineral boundaries and cross-cutting them (Fig. 3h).

Pyroxenites are olivine websterites, websterites and clinopyroxenites (Fig. 2), with coarse granular textures. Clinopyroxene is dominant and can contain orthopyroxene lamellae. Olivine may be absent and spinel is rare or absent. Phogopite in tiny isolated crystals was found as an accessory mineral in one sample.

Bulk-rock geochemistry

Bulk-rock analyses of major and minor elements for 10 peridotites are given in Table 2. Three of them were also selected for LA-ICP-MS analysis, whereas the bulk-rock estimates of the other selected xenoliths, which were not large enough to ensure representative sample mass, were based on their modal analyses, previously transformed from volume percent into weight percent using specific gravity of minerals given by Deer *et al.* (1992), and on their mineral chemistry (see Table 1). Comparison of estimates and analytical data for three xenoliths (BB.12.030, BB.81.04 and BB 18.29; Tables 1 and 2) indicates significant differences, especially in sample BB.12.030, showing much higher analysed Al_2O_3 concentration than Al_2O_3 estimated from mode. This is likely to be due to the uncertainty of sampling for both chemistry and mode. Both bulk-rock analyses, when available, and estimates for the other samples are considered in the variation diagrams for basaltic oxides, Cr-number (Cr-number $= 100 \times Cr_2O_3/(Cr_2O_3 + Al_2O_3)$; oxides in moles) and CaO/Al_2O_3 ratio v. Mg-number (Mg-number $= 100 \times MgO/(MgO + FeO^T)$; oxides in moles) (Fig. 4). Mg-number ranges from 89.0 to 92.0, with the lowest values corresponding to lherzolites

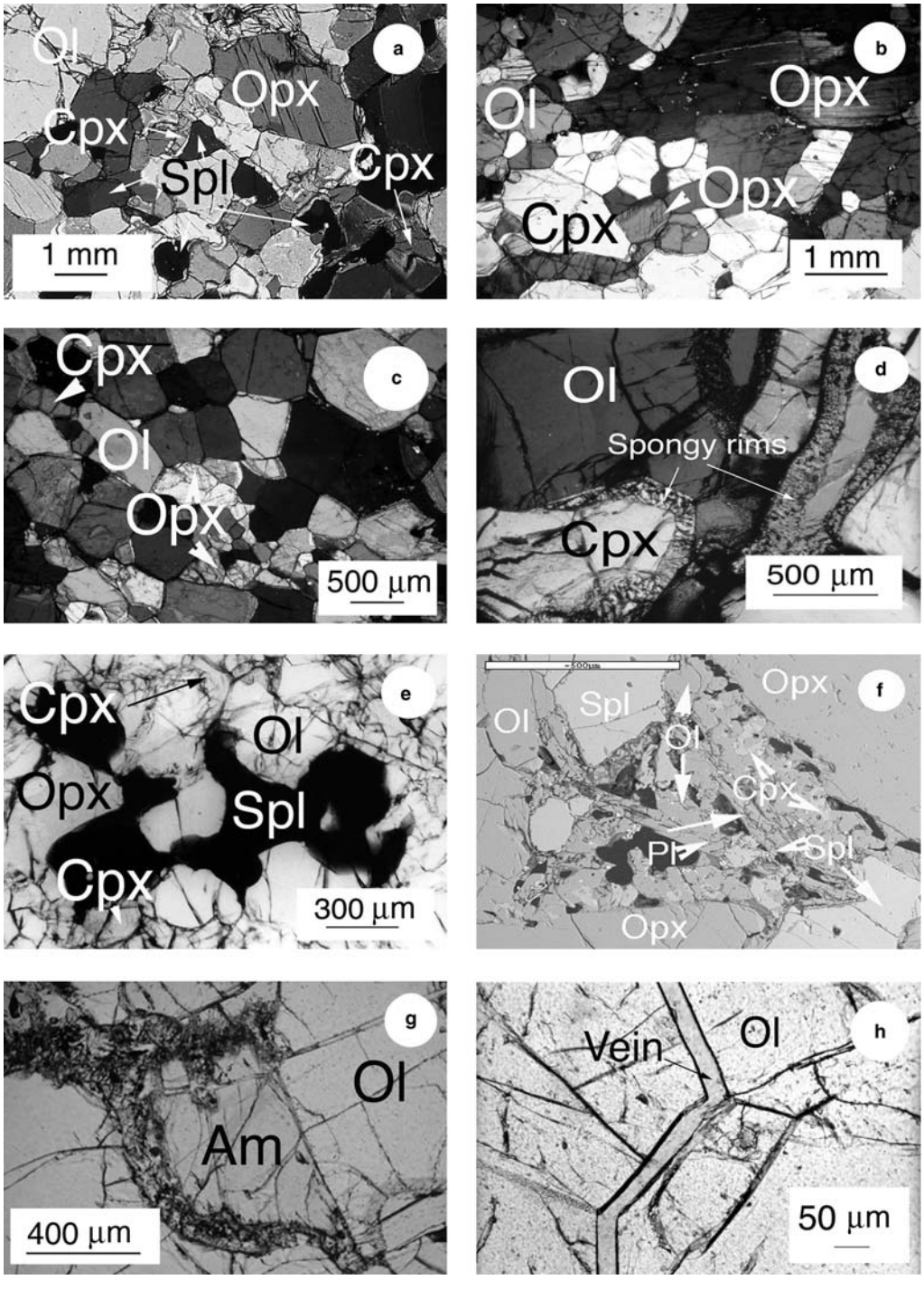

Fig. 3. (**a**) Lherzolite SD.98.2 with granular texture; (**b**) lherzolite BB.45.04 with orthopyroxene porphyroclast at the top right-hand side of the picture, in a finer matrix formed of olivine, orthopyroxene and clinopyroxene, with grain boundaries at 120º; (**c**) mosaic–equigranular or granuloblastic texture in lherzolite BB.26.04; (**d**) spongy rims in clinopyroxene crystals from lherzolite CA.00.83; (**e**) holly-leaf-shaped spinel forming a cluster with orthopyroxene, clinopyroxene and olivine in lherzolite BB.12.030; (**f**) corona texture formed of olivine, clinopyroxene, plagioclase and neospinel around an earlier spinel in lherzolite BB.154.04; (**g**) disseminated amphibole crystal with corona texture in lherzolite BB.81.03; (**h**) glass vein in harzburgite BB.10.799. Mineral abbreviations after Kretz (1983).

Table 2. *Major and minor element compositions of granular peridotite xenoliths*

Rock type:	LHZ	LHZ	LHZ	LHZ	LHZ	HZ	HZ	HZ	HZ	HZ
Sample:	BB.12.030*	BB.139.04	BB.81.04*	BB.179.04	BB.154.04	BB.93.04	BB.96.04	BB.178.04	BB.180.04	BB.18.29*
Oxides (wt%)										
SiO_2	44.60	45.10	43.10	43.70	44.50	44.60	42.40	42.40	43.70	43.50
TiO_2	0.19	0.08	0.03	0.06	0.08	0.10	0.10	0.04	0.04	0.02
Al_2O_3	6.63	2.57	0.71	0.68	1.06	2.63	1.15	0.60	0.94	0.68
Cr_2O_3	0.73	0.42	0.49	0.29	0.51	0.32	0.25	0.41	0.26	0.42
FeO^T	7.83	7.59	7.61	7.68	7.14	7.95	8.33	8.61	7.74	7.39
MnO	0.12	0.12	0.11	0.11	0.11	0.12	0.12	0.13	0.12	0.11
MgO	35.90	41.80	46.80	46.10	45.30	41.30	44.90	47.00	45.60	46.80
CaO	3.34	1.60	0.59	0.39	0.48	1.96	1.95	0.41	0.44	0.25
Na_2O	0.33	0.08	0.08	0.06	0.09	0.12	0.11	0.08	0.07	0.07
K_2O	0.02	bd	0.02	bd	0.03	bd	bd	bd	0.01	bd
Total	100.56	100.20	100.39	99.93	100.09	99.99	100.24	100.64	99.78	100.06
Mg-no.	89.1	90.8	91.6	91.5	91.9	90.2	90.6	90.7	91.3	91.9
Cr-no.	6.9	9.9	31.6	22.2	24.4	7.5	12.7	31.4	15.7	29.3

bd, below detection.
*Samples whose estimated bulk compositions are given in Table 1.

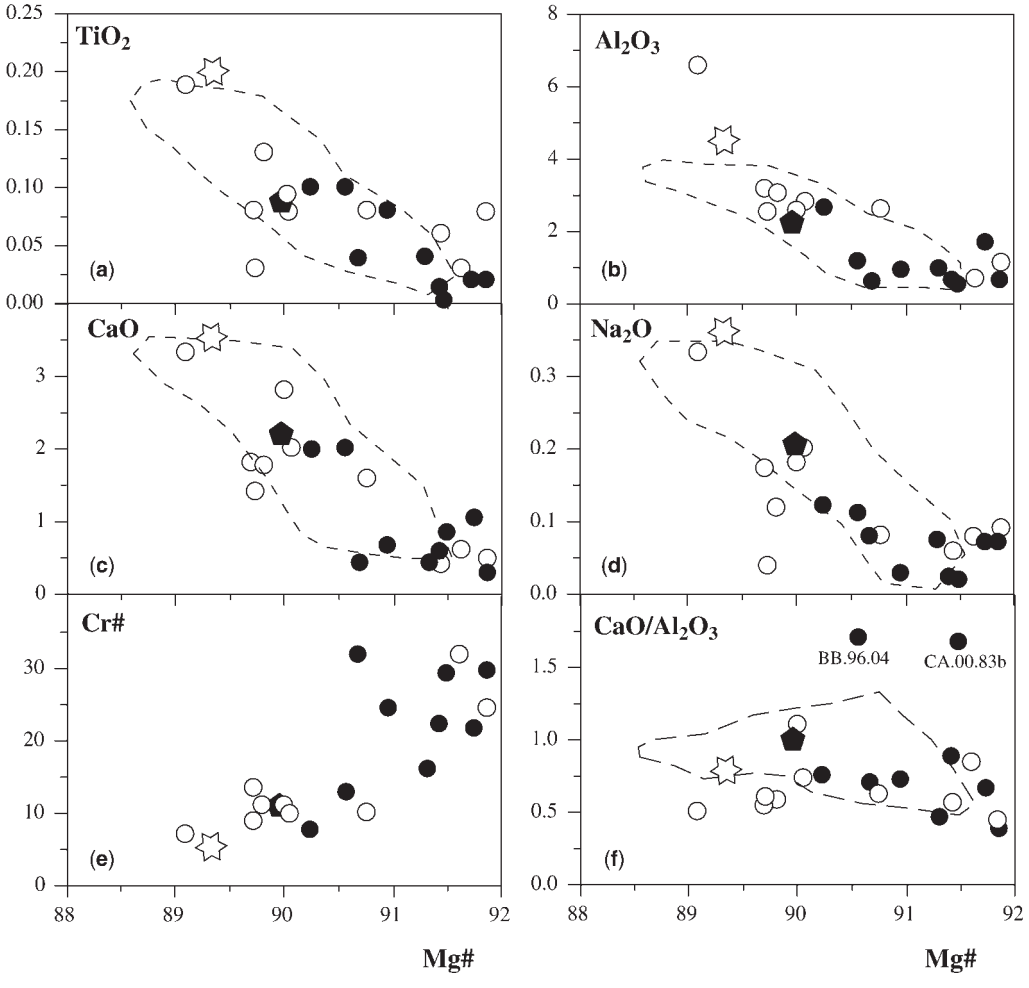

Fig. 4. (**a**–**d**) Major elements (wt %) v. Mg-number; (**e**) Cr-number v. Mg-number; (**f**) CaO/Al_2O_3 v. Mg-number. ○, modal lherzolites; ●, modal harzburgites; ☆, Primitive mantle (McDonough & Sun 1995); ⬟, average subcontinental lithospheric Mantle (McDonough 1990). The dashed line encircles the peridotite compositions of the eastern Pyrenean ultramafic massifs (Bodinier *et al.* 1988).

and the highest to harzburgites, as it is the case for Cr-number (6.9–31.4). It should be observed that lherzolites and harzburgites, as classified by mode, overlap in their geochemical compositions; this is likely to be explained by a lack of representative sample mass. However, it should be observed that trends are consistent, with all basaltic components (TiO_2, Al_2O_3, CaO, Na_2O) decreasing with the degree of melt depletion represented by Mg-number (Fig. 4a–d), whereas Cr-number and Mg-number are positively correlated (Fig. 4e). Also, the CaO/Al_2O_3 ratio stays constant and similar to that of the Primitive Mantle (PM), except for two harzburgites, which show higher values (Fig. 4f). This evolution is similar to that of peridotite xenoliths entrained by mafic lavas of the western–central European province (Zangana *et al.* 1999; Lenoir *et al.* 2000; Beccaluva *et al.* 2004) and of peridotites from the ultramafic massifs of the eastern Pyrenees (Bodinier *et al.* 1988). Finally, except for one sample, the peridotites are more refractory not only than PM (McDonough & Sun 1995), but also than the average SCLM (McDonough 1990).

Major element mineral chemistry

The forsterite content of the peridotite *olivine* (89.0–92.0%) increases from lherzolites to harzburgites and is lower in the pyroxenite olivine (87.7%) (Table 3). Homogeneous compositions characterize each single xenolith and no significant differences between porphyroclast and neocrystal compositions of the porphyroclastic harzburgite SD.98.15 were observed. This sample is also marked by having the lowest forsterite contents despite its refractory modal composition.

Orthopyroxene is aluminian, chromian–aluminian and chromian enstatite (Morimoto 1988), with both mg-number (mg-number = $100 \times Mg/(Mg + Fe^T)$ = (89.7–92.4) and cr-number $100 \times Cr/(Cr + Al)$ = (4.5–19.7) increasing from lherzolites to harzburgites (Table 4). This is also the case for CaO (0.65–1.30%), whereas the opposite is observed for TiO_2 (0.16–0.00%), Al_2O_3 (5.45–2.10%) and Na_2O (0.15–0.03%). Again, the orthopyroxene of the porphyroclastic harzburgite SD.98.15 is an exception, because its compositions are less refractory than those of other harzburgites and more similar to orthopyroxene compositions of lherzolites. Zoning is lacking in isolated crystals, but there are slight increases in both Na_2O and K_2O towards porphyroclast rims and in the orthopyroxene neocrystals of sample SD.98.15. The orthopyroxene of pyroxenites is both aluminian and chromian enstatite, with lower mg-number (87.0–89.5) and similar cr-number (4.5–15.5) compared with peridotite orthopyroxene. It also stands out because of its higher Ti abundances (0.20–0.25%) and variable Al_2O_3 contents (4.73–2.34%) (Table 4).

Clinopyroxene is mostly sodian–chromian–aluminian diopside in lherzolites and chromian–aluminian augite, close to diopside, in most harzburgites (Morimoto 1998), with both mg-number and cr-number increasing towards the sterile rocks (Fig. 5a), as for orthopyroxene. Ca also shows a slight positive correlation with mg-number (Fig. 5b), whereas all Ti, Al^T (Fig. 5c) and Na (Fig. 5d) display a negative correlation, as occurs for clinopyroxene affected by melt depletion (Robinson *et al.* 1998). Greater scatter in both Ca and Na plots indicates that these elements could be also affected by metasomatism. Compositions are homogeneous within a single sample (Table 5), except for the occasional spongy rims in clinopyroxene crystals from lherzolites (Fig. 3d). These rims show depleted compositions of both Al and Na, higher concentrations of Ca, and higher mg-number and cr-number with respect to unaffected zones. Two of these spongy rim compositions are included in Table 5 and in Figure 5. Finally, it should be noted that the Al^{VI}/Al^{IV} ratio shows a rough positive correlation with both Al^T and Na (Fig. 5e and f), suggesting that the jadeite component of clinopyroxene, which is positively associated with pressure, decreases towards the most refractory rocks, as has been observed for the mid-ocean ridge mantle (Seyler & Bonatti 1994). Compositions from core to spongy rims also follow these general trends (Fig. 5). Clinopyroxenes in pyroxenites are either chromian or aluminian augite (Table 5), with variable mg-number (85.3–90.3) and cr-number (5.6–23.8) that both overlap the values for peridotite clinopyroxene, and with higher Al and lower Na than in the latter (Fig. 5).

Spinel compositions are spinel *sensu stricto* in lherzolites and Mg–Al chromite in coarse granular harzburgites, but also spinel *sensu stricto* in the porphyroclastic harzburgite SD.98.15 (Table 6). These compositions are homogeneous within a single sample and in porphyroclasts and neocrystals of sample SD.98.15. The cr-number (cr-number = $100 \times Cr/(Cr + Al + Fe^{3+})$ = 9.4–55.9) and mg-number (mg-number = $100 \times Mg/(Mg + Fe^{2+})$ = 80.8–68.0), both numbers in cations per formula unit, are inversely correlated (Fig. 6).

Amphibole is magnesiohastingsite (Leake 1997), with values for mg-number (86.6) and cr-number (4.15), defined as for pyroxenes, close to those for coexisting clinopyroxene (see Tables 5 and 7) and with 3.20% TiO_2.

Phlogopite in peridotites also has mg-number (88.2) and cr-number (13.5) similar to those of coexisting clinopyroxene (mg-number = 92.4; cr-number = 17.6), but TiO_2 concentration (1.75%) is lower than in amphibole (Table 7), and much lower than in accessory phlogopite of one pyroxenite (10.12%). The latter phlogopite also has slightly lower mg-number (83.9) than that of coexisting olivine (87.7) and pyroxenes (89.4–90.3) (Table 7).

Glass in veins was analysed in three harzburgites (Table 8). The average compositions are intermediate–acid and alkaline, of tephriphonolite, trachyandesite and trachydacite type (Le Maitre 2002), oversaturated and undersaturated. Their total alkali contents (6.5–9.5) are much higher than those of the host mafic lavas and evolved rocks related to them (López Ruiz & Rodríguez Badiola 1985). Finally, both Mg-number (36.1–69.0) and K-number (K-number = $100 \times K_2O/(K_2O + Na_2O)$ = 31.9–46.2; oxides in moles) increase towards the most acid compositions, as has been found in glasses from xenoliths elsewhere (Draper & Green 1997; Coltorti *et al.* 1999).

Trace element mineral chemistry

Olivine mainly concentrates Ni, Co and Mn, and small amounts of Ti and V. It shows homogeneous

Table 3. *Representative major element analyses and formula units of olivine, and average trace element compositions*

Rock type:	Granular lhz													
Sample:	CA.00.83		BB12.030		BB.64.04		BB.16.04		BB.81.04		SD.98.58		SD.98.2	
(wt%)														
SiO_2	40.31		40.21		41.81		40.41		39.51		40.73		41.91	
TiO_2	0.02		0.00		0.01		0.02		0.02		0.05		0.01	
Al_2O_3	0.04		0.01		0.02		0.01		0.02		0.02		0.01	
Cr_2O_3	0.05		0.01		0.04		0.02		0.03		0.01		0.07	
FeO^T	9.62		9.64		9.61		10.13		10.45		9.87		9.62	
MnO	0.10		0.14		0.15		0.14		0.18		0.15		0.12	
MgO	49.26		50.60		50.27		49.39		49.22		48.60		47.93	
NiO	0.38		0.37		0.36		0.39		0.40		0.38		0.36	
CaO	0.13		0.11		0.06		0.06		0.06		0.03		0.00	
Total	99.78		101.10		102.33		100.57		99.89		99.84		100.03	
Cations (O = 4)														
Si	0.991		0.978		1.000		0.987		0.978		1.001		1.023	
Al^{iv}	0.001		0.000		0.000		0.000		0.000		0.000		0.000	
Ti	0.000		0.000		0.000		0.000		0.000		0.001		0.000	
Cr	0.001		0.000		0.000		0.000		0.000		0.000		0.001	
Fe	0.198		0.196		0.190		0.206		0.218		0.203		0.197	
Mn	0.002		0.003		0.003		0.003		0.004		0.003		0.002	
Mg	1.805		1.835		1.793		1.803		1.814		1.781		1.745	
Ni	0.008		0.007		0.007		0.007		0.006		0.008		0.007	
Ca	0.003		0.003		0.000		0.000		0.000		0.001		0.000	
Fo%	90.1		90.3		90.4		89.7		89.3		89.7		89.8	
Trace elements (ppm)	$n = 2$	$\pm 1\sigma$	$n = 4$	$\pm 1\sigma$	$n = 4$	$\pm 1\sigma$	$n = 3$	$\pm 1\sigma$	$n = 4$	$\pm 1\sigma$	$n = 2$	$\pm 1\sigma$	$n = 2$	$\pm 1\sigma$
Ti	19.06	2.2	11.33	1.9	16.73	1.2	19.31	2.4	135.5	169	31.86	5.1	10.89	15
V	4.564	0.2	2.210	0.1	2.684	0.5	3.575	1.2	8.649	7.4	3.192	0.5	4.754	0.0
Mn	1147	24	999.7	17	989.0	4.3	1115	15	877.2	12	na		1310	40
Co	158.9	2.4	140.3	1.4	135.8	0.9	149.7	0.8	117.5	4.3	191.3	4.3	174.1	5.4
Ni	2909	62	2898	27	2746	17	3034	18	2253	84	3518	100	3263	25
Ni/Co	18.31		20.66		20.22		20.27		19.17		18.39		18.74	

Equi, equigranular; lhz, lherzolite; Hz, harzburgite; Px, pyroxenite; p, porphyroclasts; nc, neocrystals; n, number of analyses; na, not analysed; bd, below detection; other abbreviations as in Table 1.

compositions within a single sample (Table 3). Ni and Co values are scattered when plotted against Fo%, but the Ni/Co ratio (18.25–21.50) and Fo% are positively correlated (Fig. 7a). These values are close to the Ni/Co ratio of PM (18.67). It should be noted that the olivine of the porphyroclastic harzburgite (SD.98.15) differs by showing a lower Ni/Co ratio than that of other harzburgites, and that this ratio is lower (13.59) in the olivine of one pyroxenite.

Orthopyroxene has significant concentrations of Ni, Co, Mn, Ti, V and Ga, and lesser amounts of Y and Zr (Table 4). The Ni/Co ratio (11.65–14.50) is lower than in olivine and increases steadily from lherzolites to harzburgites, except for the porphyroclastic harzburgite SD.98.15, the orthopyroxene of which plots closer to that of lherzolites (Fig. 7b). Orthopyroxene from the pyroxenites also has lower Ni/Co ratio (8.85–9.70). All Ti, Ga and Y (Fig. 8a–c) show negative correlation with mg-number for the peridotites, whereas Zr values show scatter when plotted against mg-number, especially for harzburgites (Fig. 8d). However, one coarse granular harzburgite (BB.02.04) is noteworthy for its Ti-enriched orthopyroxene. Also, porphyroclast and neocrystal orthopyroxene compositions of SD.98.15 differ by their higher concentrations of all elements in Figure 8 and by their greater scatter in the plots. Finally, Figure 8 also illustrates that orthopyroxene of pyroxenites differs from the peridotite orthopyroxene trend by showing higher Ti, but lower Y and Zr.

Clinopyroxene concentrates most of the incompatible trace elements, but (1) Rb, Ba, Ta, Pb and Th are often below detection (Table 5); (2) Ti, V, Ga, Nb and Zr are partitioned by spinel and orthopyroxene, as well as by clinopyroxene; (3) Ni and Co are lower than in all olivine, orthopyroxene and spinel (Tables 3–6). Ti is inversely correlated with mg-number (Fig. 9a), reflecting a melt depletion trend among peridotite clinopyroxene. The only exception is the Ti-enriched clinopyroxene of the coarse granular harzburgite BB.02.04. Therefore, Ti is used as a variation index to assess the behaviour of the other trace elements (Fig. 9). Thus, the Ni/Co ratio (14.15–17.47) stays constant

Equi.lhz		Granular Hz					Porphyroclastic Hz		Px	
BB.26.04		CA.00.83b	BB12.041	BB.02.04	BB.74.04	BB18.29	SD.98.15p	SD.98.15nc	BB.83.04	
39.37		40.62	40.54	41.68	41.34	40.61	40.06	40.21	39.56	
0.02		0.00	0.00	0.02	0.01	0.00	0.03	0.04	0.01	
0.02		0.01	0.03	0.02	0.02	0.01	0.00	0.03	0.01	
0.02		0.03	0.03	0.05	0.07	0.04	0.02	0.01	0.04	
10.13		8.51	8.47	8.97	8.61	8.26	10.60	10.09	12.03	
0.13		0.12	0.15	0.13	0.13	0.12	0.16	0.17	0.16	
49.61		51.00	51.19	50.60	51.04	51.70	48.61	48.71	47.80	
0.40		0.39	0.39	0.39	0.44	0.38	0.42	0.36	0.30	
0.04		0.09	0.10	0.10	0.11	0.09	0.10	0.05	0.11	
99.74		100.78	100.90	101.96	101.77	101.23	100.00	99.67	100.02	
0.972		0.985	0.982	1.001	0.993	0.980	0.989	0.992	0.988	
0.000		0.000	0.001	0.000	0.000	0.000	0.000	0.001	0.000	
0.000		0.000	0.000	0.000	0.000	0.000	0.001	0.001	0.000	
0.000		0.001	0.001	0.000	0.000	0.001	0.000	0.000	0.000	
0.210		0.173	0.171	0.179	0.173	0.167	0.219	0.208	0.250	
0.003		0.002	0.003	0.003	0.002	0.002	0.003	0.004	0.003	
1.830		1.844	1.849	1.808	1.827	1.860	1.788	1.792	1.768	
0.007		0.008	0.007	0.007	0.008	0.007	0.008	0.007	0.007	
0.000		0.002	0.003	0.000	0.000	0.002	0.003	0.001	0.000	
89.7		91.4	91.5	91.0	91.4	91.8	89.1	89.5	87.6	
$n=4$	$\pm 1\sigma$	$n=4$	$\pm 1\sigma$ $n=3$	$\pm 1\sigma$		$\pm 1\sigma$ $n=4$	$\pm 1\sigma$	$n=2$	$\pm\sigma$ $n=3$	$\pm 1\sigma$ $n=1$	$n=3$	$\pm 1\sigma$
44.47	21	bd	13.75	6.8	50.85	4.5 4.692	2.4	bd	25.55	3.5 30.5	46.31	10
9.450	52	6.035	1.0 4.720	1.8	7.947	1.1 5.992	0.4	4.281	2.7 2.836	0.9 4.137	4.983	1.2
1069	7.4	na	1122	16	1013	5.0 952.3	8.9	995	5.6 1183	34 1185	1289	11
138.9	3.5	157.3	7.0 157.9	2.9	144.3	3.1 141.8	3.7	155.8	1.6 164.8	3.8 163.4	158	2.2
2685	56	3052	60 3233	60	2836	46 3049	68	3215	5.9 3014	19 2997	2147	25
19.33		19.40	20.47		19.65	21.50		20.64	18.29	18.34	13.59	

for lherzolites and increases slightly towards the most refractory harzburgites (Fig. 9b). All V, Ga, Y, Er and Zr show a rough positive correlation with Ti (Fig. 9c–g), except for Zr of harzburgite BB.18.29 (Fig. 9g). However, a change of slope is observed for both Ga and Y trends, from lherzolites to harzburgites. In contrast, other elements show positive correlation with Ti only for lherzolites and then inverse correlation for harzburgites (e.g. La, Sr, Th) (Fig. 9h–j). Also, one lherzolite (BB.64.04) stands out for its anomalous high concentrations of these three elements and of U (Fig. 9k). Finally, both U and Nb values are scattered (Fig. 9k and l), as is the case for Sc. Thus, Figure 9 illustrates that the behaviour of trace elements consistent with Ti could be due to melt depletion, whereas the scattered values and increased contents of the most incompatible elements, especially in harzburgites, could be due to metasomatism. It should also be noted that one of the spongy rims shows trace element abundances similar to those of the unaffected zone of the clinopyroxene crystal, whereas the other is slightly enriched in Ti, La, Yb, Zr and Nb (Fig. 9). Regarding clinopyroxene in pyroxenites, it is marked (Fig. 9) by lower Ni/Co ratio, and lower V, Y and Yb concentrations than those of peridotites. On the other hand, clinopyroxene rare earth element (REE) and multielement patterns of lherzolites, harzburgites and pyroxenites are variable and differ between these rocks. The ΣREE in clinopyroxene from lherzolites are 2–9 times PM concentration and most REE patterns (Fig. 10a) are either light REE (LREE) depleted or slightly enriched ($(La/Nd)_N = 0.40–1.65$), with heavy REE (HREE) exceeding PM values and non-fractionated ($(Gd/Yb)_N = 0.84–1.31$); a weak positive Eu anomaly is also shown. Furthermore, lherzolite clinopyroxene is also characterized by $(Th/U)_N < 1$ (Fig. 10b), a negative anomaly at Nb, with $(Ti/Nb)_N = 0.77–32.90$, weak negative anomalies at Zr ($(Zr/Sm)_N = 0.16–0.86$) and Ti ($(Ti/Eu)_N = 0.31– 0.57$), and a positive anomaly at Sr, especially in two moderately LREE-enriched lherzolites (SD.98.2 and BB.64.04) ($(La/Nd)_N = 10.83–11.90$) (Fig. 10a). The clinopyroxene-poor lherzolite SD.98.2 also differs in its significant depletion of middle REE (MREE), Hf, Zr and Ti, and its slight HREE fractionation ($(Gd/Yb)_N = 0.61$)). It should be mentioned that no

Table 4. *Representative major element analyses and formula units of orthopyroxene, and average trace element compositions*

Rock type:	Granular lherzolites							Equi. lhz
Sample:	CA.00.83	BB12.030	BB.64.04	BB.16.04	BB.81.04	SD.98.58	SD.98.2	BB.26.04
(wt%)								
SiO_2	53.92	54.82	54.90	55.14	54.86	54.59	58.09	54.23
TiO_2	0.13	0.08	0.13	0.13	0.16	0.16	0.05	0.08
Al_2O_3	5.46	3.83	4.56	4.40	4.70	4.41	2.87	4.02
Cr_2O_3	0.59	0.39	0.38	0.34	0.35	0.37	0.27	0.32
FeO^T	6.20	6.11	6.32	6.56	6.62	6.46	6.32	6.67
MnO	0.15	0.12	0.13	0.16	0.16	0.14	0.10	0.11
MgO	32.17	34.11	32.64	32.61	32.63	32.70	32.73	33.39
NiO	0.12	0.09	0.11	0.11	0.12	0.13	0.12	0.11
CaO	1.18	0.66	0.74	0.67	0.78	0.70	0.49	0.66
Na_2O	0.15	0.11	0.11	0.11	0.11	0.14	0.01	0.06
K_2O	0.00	na	0.01	0.00	0.00	0.01	0.00	0.01
Total	100.09	100.32	100.03	100.23	100.49	99.81	101.05	99.66
Cations (O = 6)								
Si	1.862	1.878	1.896	1.902	1.888	1.889	1.994	1.876
Al^{IV}	0.138	0.122	0.104	0.098	0.112	0.111	0.006	0.124
Al^{VI}	0.084	0.033	0.081	0.081	0.078	0.068	0.110	0.039
Ti	0.003	0.002	0.003	0.003	0.004	0.004	0.001	0.002
Cr	0.016	0.011	0.010	0.009	0.010	0.010	0.007	0.009
Fe^{3+}	0.041	0.082	0.014	0.009	0.023	0.034	0.000	0.077
Fe^{2+}	0.138	0.093	0.169	0.180	0.167	0.153	0.181	0.116
Mn	0.004	0.003	0.004	0.005	0.005	0.004	0.003	0.003
Mg	1.656	1.742	1.680	1.677	1.673	1.686	1.675	1.722
Ni	0.003	0.002	0.003	0.003	0.003	0.004	0.003	0.003
Ca	0.044	0.024	0.027	0.025	0.029	0.026	0.018	0.025
Na	0.010	0.007	0.008	0.007	0.007	0.010	0.001	0.004
K	0.000	0.000	0.000	0.000	0.000	0.001	0.000	0.000
mg-no.	90.2	90.9	90.2	89.9	89.8	90.0	90.2	89.9
cr-no.	6.8	6.4	5.1	4.8	5.0	5.3	5.9	5.2
Wo%	2.3	1.2	1.4	1.3	1.5	1.4	1.0	1.3
En%	88.1	89.7	88.9	88.7	88.4	88.8	89.4	88.8
Fs%	9.5	9.0	9.7	10.0	10.0	9.8	9.7	9.9

Trace elements (ppm)	$n = 2$	$\pm 1\sigma$	$n = 4$	$\pm 1\sigma$	$n = 4$	$\pm 1\sigma$	$n = 4$	$\pm 1\sigma$	$n = 4$	$\pm 1\sigma$	$n = 3$	$\pm 1\sigma$	$n = 2$	$\pm 1\sigma$	$n = 4$	$\pm 1\sigma$
Ti	645.4	53	505.8	21	648.0	21	703.5	27	886	158	770.8	9.0	287.7	4.7	411.8	11
V	104.7	1.1	84.89	4.4	91.43	4.1	90.96	3.2	96.27	5.7	93.82	1.5	103.6	9.8	80.34	2.4
Mn	1055	2.1	1103	48	1041	23	1064	13	1085	8.3	na		1207	73	1084	13
Co	68.55	1.7	63.11	2.9	60.48	1.9	58.76	0.9	61.64	0.8	63.99	2.9	66.74	0.9	58.11	3.5
Ni	853.9	31	771.6	41	749.2	35	714.3	5.4	752.7	12	787.7	28	785.5	39	679.4	14
Ga	5.485	0.0	3.300	0.3	3.657	0.5	3.468	0.3	4.359	0.4	4.311	0.6	3.533	0.1	3.446	0.2
Y	1.407	0.4	0.807	0.1	0.878	0.1	1.107	0.1	1.179	0.2	0.893	0.1	0.794	0.0	1.085	0.2
Zr	1.377	0.0	1.327	0.4	1.473	0.2	1.774	0.2	1.825	0.2	1.611	0.5	0.921	1.3	1.055	0.6
Ni/Co	12.46		12.23		12.39		12.16		12.21		12.31		11.77		11.69	

Abbreviations as in Table 3. Fe^{3+} after Droop (1987).

difference has been observed between the clinopyroxene patterns of the mosaic–equigranular lherzolite BB.26.04 and those of coarse granular lherzolites. Finally, patterns of spongy rims are either slightly LREE enriched or comparable with those of unaffected zones of the clinopyroxene crystal (Fig. 10a and b). The ΣREE in clinopyroxene from harzburgites are higher (2–17 times PM) than in lherzolites, and the patterns (Fig. 10c) are LREE and MREE enriched ($(La/Nd)_N = 1.05–2.24$; $(Sm/Yb)_N$ or $(Sm/Er)_N = 3.43–13.95$) with respect to HREE ($(La/Yb)_N$ or $(La/Er)_N = 2.47–58.47$). The harzburgite clinopyroxene is also characterized by $(Th/U)_N > 1$ in most samples, higher Nb, with $(Ti/Nb)_N = 0.08–2.27$, but always with a negative Nb anomaly, a negative anomaly at Zr ($(Zr/Sm)_N = 0.14–1.28$), except for one sample, and by more significant negative anomaly at Ti ($(Ti/Eu)_N = 0.04–0.43$) than the lherzolite clinopyroxene (Fig. 10d). Again, the Ti-enriched harzburgite BB.02.04 differs from the others by its convex-upward REE pattern, and by less significant negative anomalies at Nb, Zr and Ti (Fig. 10c and d). Convex-upward REE patterns also characterize the clinopyroxene from pyroxenites. This has the lowest ΣREE (1–4 times PM) (Fig. 10e) and also shows weak negative anomalies at Zr ($(Zr/Sm)_N = 0.27–0.34$) and Ti ($(Ti/Eu)_N = 0.43–0.70$), but concentrations of both elements are equal to or exceed those of the PM (Fig. 10f).

Spinel mainly concentrates Ti, V, Co, Ni, Mn and Ga (Table 6). Only the Ni/Co ratio is inversely correlated with *cr*-number (Fig. 11a), whereas Ti, V

Granular Hz										Porphyroclastic Hz				Px	
CA.00.83b		BB12.041		BB.02.04		BB.74.04		BB18.29		SD.98.15p		SD.98.15nc	SD.98.1	SD.83.04	
56.23		56.07		55.83		56.24		56.27		54.63		54.99	55.05	55.34	
0.00		0.04		0.22		0.01		0.00		0.10		0.15	0.25	0.21	
2.07		2.52		2.62		2.31		2.12		4.69		4.63	4.73	2.34	
0.71		0.80		0.77		0.83		0.72		0.36		0.38	0.33	0.66	
5.41		5.33		5.69		5.37		5.16		6.65		6.37	7.92	6.95	
0.14		0.13		0.12		0.12		0.12		0.13		0.12	0.17	0.18	
34.69		34.68		33.40		33.64		35.15		32.37		31.73	29.87	32.96	
0.11		0.09		0.11		0.13		0.10		0.09		0.05	0.08	0.10	
1.05		1.11		1.28		1.28		1.06		0.70		1.44	1.82	1.17	
0.08		0.09		0.07		0.03		0.08		0.09		0.20	0.13	0.01	
na		na		0.00		0.01		na		0.02		0.15	0.00	0.00	
100.48		100.85		100.11		99.97		100.79		99.83		100.26	100.35	100.35	
1.923		1.910		1.929		1.941		1.915		1.895		1.900	1.921	1.921	
0.077		0.090		0.071		0.059		0.085		0.105		0.100	0.079	0.079	
0.007		0.012		0.036		0.035		0.000		0.087		0.089	0.115	0.017	
0.000		0.001		0.006		0.000		0.000		0.003		0.004	0.007	0.005	
0.019		0.021		0.021		0.023		0.019		0.010		0.010	0.009	0.018	
0.056		0.061		0.007		0.003		0.071		0.010		0.013	0.000	0.034	
0.098		0.091		0.157		0.152		0.076		0.183		0.171	0.231	0.168	
0.004		0.004		0.004		0.004		0.004		0.004		0.004	0.005	0.005	
1.769		1.761		1.721		1.731		1.783		1.669		1.635	1.554	1.705	
0.003		0.002		0.003		0.004		0.003		0.003		0.001	0.002	0.003	
0.038		0.040		0.042		0.047		0.039		0.026		0.053	0.068	0.044	
0.005		0.006		0.004		0.004		0.005		0.006		0.013	0.009	0.001	
0.000		0.000		0.000		0.000		0.000		0.001		0.007	0.000	0.000	
92.0		92.1		91.3		91.8		92.4		89.7		89.9	87.1	89.4	
18.6		17.5		16.4		19.7		18.6		4.9		5.2	4.5	15.8	
2.0		2.1		2.2		2.4		2.0		1.4		2.8	3.7	2.3	
90.2		90.2		89.3		89.5		90.6		88.4		87.3	83.9	87.4	
7.9		7.8		8.5		8.0		7.5		10.2		9.8	12.5	10.4	
$n = 4$	$\pm 1\sigma$	$n = 3$	$\pm 1\sigma$	$n = 4$	$\pm 1\sigma$	$n = 4$	$\pm 1\sigma$	$n = 2$	$\pm 1\sigma$	$n = 3$	$\pm 1\sigma$	$n = 1$	$n = 1$	$n = 2$	$\pm 1\sigma$
154.7	12	330.0	6.1	1201.0	11	81.07	4.8	113.6	9.5	803.0	237	925.8	1176	1129	6.4
63.92	3.0	66.66	0.5	123.30	2.4	81.79	5.0	72.63	2.7	96.96	4.0	109.4	112.9	89.02	1.5
na		1034	28	993	13	904.7	13	929.3	5.5	1106	15	1158	1284	1269	21
69.51	2.3	65.16	0.2	59.5	3.5	58.63	0.5	63.28	1.6	70.77	2.5	76.69	83.52	66.29	0.9
842.8	61	852.2	14	761.2	14	850.7	17	848.3	5.9	764.8	67	887.8	807.9	587.3	4.8
2.979	0.8	2.633	0.6	3.155	0.2	1.603	0.1	1.234	0.1	5.820	0.4	4.459	7.803	2.666	0.1
bd		0.402	0.1	0.966	0.2	0.138	0.0	0.296	0.0	1.401	0.3	1.555	1.165	0.699	0.0
1.300	0.4	1.471	0.2	3.437	0.6	0.384	0.1	5.103	0.6	3.611	2.3	4.04	2.347	1.199	0.0
12.13		13.08		12.79		14.51		13.41		10.81		11.58	9.67	8.86	

and Ga remain quasi-constant v. cr-number in most samples (Fig. 11b–d). The exceptions are the porphyroclastic and coarse granular harzburgites (SD.98.15 and BB.02.04, respectively), which also have Ti- and V-enriched spinel. Ga is higher only in the spinel from the porphyroclastic harzburgite, which also shows heterogeneous compositions from crystal core to rim.

Amphibole partitions higher amounts of Ni (D^{Ni}, am/cpx = 2.76), Co (D^{Co}, am/cpx = 2.12), Ga (D^{Ga}, am/cpx = 3.32), Rb, Ba, Nb, Sr, Pb and Ti, lesser amounts of Sc (D^{Sc}, am/cpx = 0.74), and similar amounts of REE, Zr, Th and U than coexisting clinopyroxene (Table 7, Fig. 12a). The Ni/Co ratio is also higher (19.52) than that of the clinopyroxene. Both coexisting minerals are characterized by LREE depletion, except for La, and flat HREE. All these characteristics fit with the compositions of disseminated amphibole either in peridotite massifs or in xenoliths (Vannucci *et al.* 1995) rather than with compositions of vein amphiboles (Ionov *et al.* 1997).

Phlogopite from the clinopyroxenite xenolith (BB.83.04) mainly concentrates large ion lithophile elements (LILE), some high field strength elements (HFSE; Nb, Ta, Ti) and Pb (Table 7), which are much higher than in clinopyroxene, whereas La, Ce, Zr and Hf contents are comparable (Fig. 12b). These compositions, along with the Rb/Sr (0.89) and Zr/Nb (0.53) ratios, are comparable with those of vein biotites (Ionov *et al.* 1997).

Glass in veins from the coarse granular harzburgite CA.00.83b shows high concentrations of all incompatible trace elements, especially of Nb and Ta, but also of Zr and Ti. The first HFSE define a positive anomaly, but there is only a weak negative Ti anomaly (Fig. 12c). The multielement pattern of this glass differs from the patterns of both the host

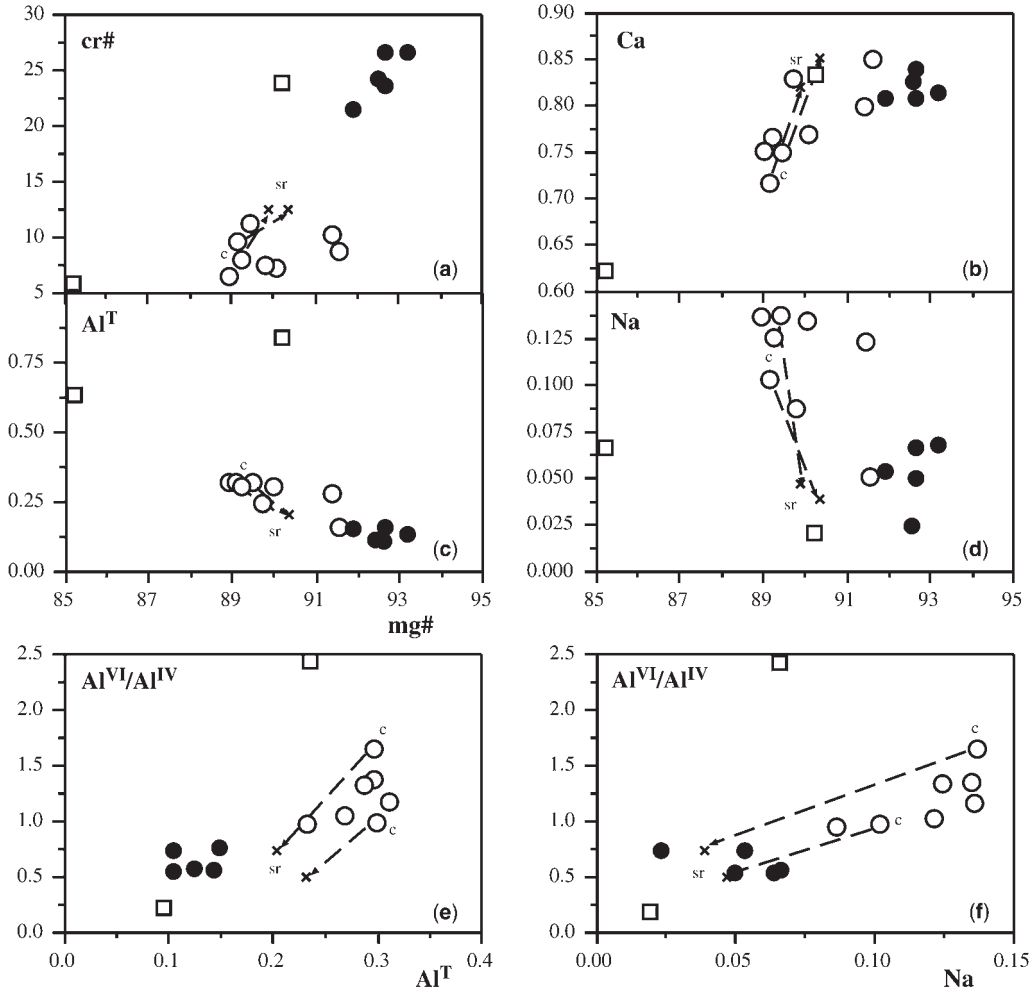

Fig. 5. The mg-number for clinopyroxene v. (**a**) Cr-number, (**b**) Ca, (**c**) Al^T and (**d**) Na; (**e**) Al^{VI}/Al^{IV} v. Al^T; (**f**) Al^{VI}/Al^{IV} v. Na. All elements in cations per formula unit. ○, lherzolite; ×, clinopyroxene spongy rims; ●, harzburgites; □, pyroxenites. The arrows indicate the composition evolution from core (c) to spongy rims (sr).

basaltic lava and the harzburgite clinopyroxene. The latter shows significant negative anomalies for Nb, Ta, Zr and Ti, and Pb is below detection.

P–T–fO_2 equilibrium conditions

Temperatures provided by the orthopyroxene–clinopyroxene thermometer (Brey & Köhler 1990) (TBK90) at 1.5 GPa indicate that lherzolite (1012 ± 71 °C) (±1σ) and harzburgite temperatures (1059 ± 21 °C) overlap significantly, and that pyroxenite temperatures are variable but higher (1064–1257 °C) than those of peridotites. The Ca-in-orthopyroxene thermometer (Brey & Köhler 1990) (TBKCaO90) provides consistent temperatures, within TBK90 ±75 °C, but in this case the values are slightly higher for the coarse granular harzburgites than for the lherzolites (TBKCaO90 for lherzolitesis is 987 ± 62 °C; TBKCaO90 for coarse granular harzburgites is 1087 ± 29 °C; TBKCaO90 for pyroxenites is 1116–1250 °C). TBKCaO90 also gives temperatures for the porphyroclastic harzburgite SD.98.15 that are similar to those of coarse granular peridotite, but in this sample temperature is lower and less uncertain for porphyroclasts (TBKCaO90 is 983 ± 3 °C) than for neoblast compositions (TBKCaO90 is 1105 ± 52 °C).

Pressure estimations have been attempted using the Ca-exchange reaction between olivine and clinopyroxene (Köhler & Brey 1990) (PKB90), considering TBK90 temperatures and Ca contents in olivine measured by EMPA. However, despite using only olivine core compositions, to avoid the effect of secondary fluorescence, the results show high uncertainty for a single sample and scattered values for the whole group of xenoliths. They plot across the spinel lherzolite field and a few samples even cross the boundaries with the garnet lherzolite (O'Neill 1981) and plagioclase lherzolite fields (Gasparik 1987). The PKB90 average for lherzolites is 17.2 ± 10.6 kbar (1σ), with the highest values corresponding to the mosaic–equigranular xenolith BB.26.04 and to the clinopyroxene-poor lherzolite SD.98.2, both being within the garnet lherzolite field, whereas the lowest PKB90 values are close to the plagioclase lherzolite field. The PBK90 average for harzburgites is lower (9.3 ± 7 kbar) and several samples plot within the plagioclase lherzolite field. Finally, the PKB90 value for the pyroxenite BB.83.04, in which olivine and clinopyroxene coexist, is 9.5 ± 1.4 kbar. The large PBK90 range for peridotites suggests that these xenoliths are not in equilibrium for the Ca-exchange reaction between olivine and clinopyroxene. In such a case, only the maximum equilibrium pressures for these peridotites can be known, using the Al–Cr abundance in spinel (Webb & Wood 1986) and P values for the spinel lherzolite–garnet lherzolite boundary of O'Neill (1981): they range from 21.7 ± 0.1 kbar for lherzolites to 32.5 ± 0.1 kbar for harzburgites. The latter values are discarded as too high according to the increasing Cr contents of harzburgite spinel, caused by partial melting.

Finally, estimations of fO_2 are based on the reaction 6fayalite + O_2 = 6ferrosilite + 2magnetite, using the calibration of Wood (1991) (FOW91). Fe^{3+} in spinel studied by EMPA was estimated by charge balance and then corrected following the method of Liermann & Ganguly (2003). The results show that fO_2 values for lherzolites and harzburgites overlap significantly, although average fO_2 for lherzolites is higher (FOW91 $= -0.2 \pm 0.5$) than for harzburgites (FOW91 $= -0.6 \pm 0.5$), where the values are expressed as log units relative to the fayalite–magnetite–quartz buffer (FMQ). This slightly higher fO_2 average for lherzolites could account for the weak positive Eu anomaly of their clinopyroxene REE patterns (Fig. 10a). It should be mentioned that fO_2 for the amphibole-bearing lherzolite BB.81.04 (FOW91 $= 0.1 \pm 0.2$) does not differ from values for the anhydrous lherzolites. Also, no correlation has been observed either between fO_2 and cr-number of spinel or between fO_2 and the $(La/Yb)_N$ or $(La/Er)_N$ value of clinopyroxene, as was observed elsewhere (Wood *et al.* 1990).

Discussion

The xenoliths related to the Neogene–Quaternary within-plate volcanism of NE Spain are mainly formed of anhydrous peridotites, grading from lherzolites to harzburgites. This is in agreement with SCLM compositions documented for the nearby eastern Pyrenean peridotites (Bodinier *et al.* 1988) and for other mantle xenoliths of western–central Europe (Downes 2001, and references therein; Beccaluva *et al.* 2004), and contradicts the existence of a bimodal suite of lherzolites and highly refractory harzburgites, without intermediate compositions, reported recently by Bianchini *et al.* (2007) for the same area. Finally, a few websterite and clinopyroxenite xenoliths are also found.

The pyroxenites

They show characteristics of cumulates from basaltic melts. This is inferred from: (1) lower Fo contents, and lower mg-number and Ni/Co ratio of both olivine and orthopyroxene (Tables 3 and 4, Fig. 7); (2) lower Ni/Co ratio and distinct major and trace element compositions of clinopyroxene (Table 5, Figs 5 and 9) with respect to peridotite clinopyroxene; (3) the convex-upward clinopyroxene REE patterns (Fig. 10e). These patterns are comparable with those of clinopyroxene in both dry pyroxenite bands and amphibole pyroxenite veins in the Pyrenean ultramafic massifs (Bodinier *et al.* 1987*a*, *b*), or with REE patterns of clinopyroxene in veins of composite mantle xenoliths (Witt-Eickschen *et al.* 1993). High Ti and other trace element contents of the accessory phogopite in one of the pyroxenite xenoliths (Table 7) are also in agreement with its origin from veins (Zanetti *et al.* 1996; Ionov *et al.* 1997). Estimates of REE concentrations for the melts in equilibrium with the pyroxenites give patterns (Fig. 13) similar to those of Pyrenean Cretaceous picrites, alkali basalts and teschenites (Rossy *et al.* 1992). D^{REE}, cpx for the estimates were determined after Wood & Blundy (1997), using major element compositions of clinopyroxene and crystallization conditions of 1300 °C and 10 kbar, according to themobarometric data. This Cretaceous alkaline magmatism has been associated with the Fe–Ti metasomatism affecting wall-rock peridotites in the eastern Pyrenean massifs (Bodinier *et al.* 1988, 1990, 2004; McPherson *et al.* 1996; Zanetti *et al.* 1996; Woodland *et al.* 1996), and crops out in the Catalan area as scattered camptonites (Solé *et al.* 2003).

Table 5. *Representative major element compositions and formula units of clinopyroxene, and average trace element compositions*

Rock type:	Granular lhz																			
Sample:	CA.00.83c		CA.00.83sr		BB.12.030		BB.64.04		BB.16.04		BB.81.04		SD.98.58		SD.98.58sr		SD.98.2			
(wt%)																				
SiO_2	50.81		50.42		52.05		51.65		51.72		51.14		51.87		51.47		54.61			
TiO_2	0.41		0.45		0.45		0.51		0.62		0.72		0.75		0.71		0.25			
Al_2O_3	6.99		5.34		6.31		6.72		6.90		7.29		6.92		4.70		3.58			
Cr_2O_3	1.07		1.13		1.02		0.83		0.77		0.74		0.91		0.99		0.50			
FeO^T	3.52		3.36		2.59		3.21		2.91		3.27		3.05		3.07		2.65			
MnO	0.11		0.08		0.10		0.12		0.13		0.10		0.04		0.07		0.08			
MgO	16.28		16.57		15.42		14.94		14.78		14.84		14.55		16.11		16.25			
NiO	0.07		0.07		0.05		0.09		0.04		0.07		0.08		0.02		0.04			
CaO	18.32		20.90		20.75		19.61		19.72		19.29		19.20		21.71		21.91			
Na_2O	1.45		0.66		1.75		1.77		1.92		1.94		1.95		0.55		0.70			
K_2O	0.01		0.01		nd		0.00		0.00		0.00		0.00		0.01		0.01			
Total	99.02		98.99		100.49		99.45		99.51		99.40		99.29		99.41		100.58			
Cations (O = 6)																				
Si	1.847		1.846		1.867		1.875		1.874		1.855		1.886		1.883		1.972			
Al^{IV}	0.153		0.154		0.133		0.125		0.126		0.145		0.114		0.117		0.028			
Al^{VI}	0.147		0.077		0.134		0.163		0.168		0.166		0.183		0.086		0.124			
Ti	0.011		0.012		0.012		0.014		0.017		0.020		0.021		0.020		0.007			
Cr	0.031		0.033		0.029		0.024		0.022		0.021		0.037		0.029		0.014			
Fe^{3+}	0.055		0.067		0.068		0.035		0.037		0.054		0.000		0.003		0.000			
Fe^{2+}	0.052		0.035		0.009		0.062		0.051		0.045		0.093		0.091		0.080			
Mn	0.003		0.002		0.003		0.004		0.004		0.003		0.001		0.002		0.002			
Mg	0.882		0.905		0.824		0.808		0.798		0.802		0.789		0.879		0.875			
Ni	0.002		0.002		0.001		0.003		0.001		0.002		0.002		0.001		0.001			
Ca	0.714		0.820		0.797		0.763		0.766		0.750		0.748		0.851		0.847			
Na	0.102		0.047		0.122		0.125		0.135		0.136		0.137		0.039		0.049			
K	0.001		0.000		0.000		0.000		0.000		0.000		0.000		0.000		0.000			
mg-no.	89.2		89.9		91.5		89.3		90.1		89.0		89.5		90.3		91.6			
cr-no.	9.3		12.5		9.8		7.7		7.0		6.3		11.1		12.5		8.6			
Wo%	41.9		44.9		46.9		45.7		46.4		45.4		45.9		46.7		47.0			
En%	51.8		49.5		48.5		48.4		48.3		48.6		48.4		48.2		48.5			
Fs%	3.4		3.8		4.2		2.3		2.5		3.5		0.1		0.3		0.1			
Trace elements (ppm)	$n = 4$	$\pm 1\sigma$	$n = 1$		$n = 5$	$\pm 1\sigma$	$n = 4$	$\pm 1\sigma$	$n = 6$	$\pm 1\sigma$	$n = 4$	$\pm 1\sigma$	$n = 4$	$\pm 1\sigma$	$n = 2$	$\pm 1\sigma$	$n = 5$	$\pm 1\sigma$		
Sc	50.99	2.7	54.16		70.87	4.1	55.95	0.5	60.84	1.0	51.22	1.3	63.04	2.3	72.50	6.2	76.28	2.3		
Ti	2105	59	2809		2557	74	2657	23	3417	51	3856	80	3990	47	3945	148	1105	104		
V	246.1	1.8	262.6		282.4	6.0	255.5	2.5	285.3	6.9	277.2	5.2	324.1	7.5	327.4	7.9	264.2	6.2		
Mn	804.3	8.1	770.8		665.8	11	669.3	5.9	715.4	31	739.1	5.9	nd		nd		685.8	50		
Co	29.90	2.0	27.9		22.89	1.1	21.78	0.4	23.28	3.0	23.40	0.2	27.71	2.4	27.67	0.6	25.02	2.9		
Ni	425.5	41	394.1		354.3	28	335.7	2.7	371.7	62	351.6	3.6	403.1	30	421.8	47	375.4	48		
Ga	5.285	0.4	4.549		3.778	0.3	4.107	0.1	4.750	0.2	5.155	0.1	6.615	0.4	7.058	0.8	3.195	1.0		
Rb	bd		bd		bd		bd		bd		0.381	0.1	bd		bd		bd			
Sr	38.43	2.8	48.37		77.37	1.7	246.7	2.8	93.61	3.7	119.7	2.4	176.5	3.4	141.8	17	79.38	12		
Y	13.54	0.4	15.66		16.19	0.7	12.66	0.1	16.93	0.8	16.85	0.4	20.55	0.7	17.96	1.3	11.11	0.6		
Zr	13.08	0.4	24.62		31.78	1.5	24.12	0.4	37.97	1.5	32.83	1.0	54.12	0.6	52.44	1.5	1.734	1.0		
Nb	0.389	0.2	0.647		0.172	0.0	0.167	0.0	0.301	0.1	0.064	0.0	1.123	0.2	1.399	0.1	0.788	0.5		
Ba	bd		bd		bd		bd		bd		bd		bd		2.459	1.5	3.648	3.2		
La	0.490	0.1	3.750		0.922	0.1	24.93	0.4	1.751	0.3	4.297	0.3	5.325	0.4	4.952	0.1	4.156	0.1		
Ce	1.810	0.1	12.54		3.868	0.3	17.57	0.6	5.007	0.1	5.963	0.5	10.75	0.4	9.396	0.2	5.038	0.3		
Pr	0.361	0.0	1.806		0.668	0.0	0.863	0.0	0.811	0.1	0.857	0.0	1.425	0.1	1.201	0.1	0.273	0.1		
Nd	2.135	0.2	6.857		4.464	0.2	4.042	0.3	4.794	0.3	5.027	0.3	7.469	0.3	6.870	0.8	0.740	0.2		
Sm	1.045	0.2	1.969		1.529	0.2	1.517	0.2	1.727	0.2	1.931	0.1	2.441	0.3	2.385	0.0	0.420	0.0		
Eu	0.538	0.1	0.965		0.800	0.1	0.669	0.0	0.799	0.1	0.866	0.1	1.140	0.1	0.939	0.1	0.281	0.1		
Gd	1.571	0.1	2.297		2.326	0.7	1.913	0.2	2.288	0.1	2.406	0.2	3.157	0.5	2.859	0.7	1.065	0.2		
Tb	0.379	0.0	0.428		0.441	0.1	0.365	0.0	0.449	0.0	0.502	0.0	0.650	0.1	0.513	0.1	0.248	0.0		
Dy	2.474	0.2	3.606		2.829	0.2	2.172	0.1	3.082	0.3	3.051	0.0	4.234	0.5	3.196	0.7	1.938	0.2		
Ho	0.533	0.0	0.620		0.660	0.1	0.483	0.0	0.656	0.0	0.691	0.0	0.927	0.1	0.736	0.0	0.455	0.1		
Er	1.435	0.2	1.754		1.934	0.2	1.331	0.1	1.770	0.1	1.792	0.1	2.284	0.1	1.997	0.3	1.346	0.2		
Tm	0.231	0.0	0.209		0.260	0.0	0.182	0.0	0.269	0.0	0.267	0.0	0.386	0.0	0.256	0.1	0.173	0.0		
Yb	1.516	0.1	2.089		1.960	0.2	1.180	0.1	1.794	0.1	1.857	0.1	2.646	0.4	1.992	0.3	1.427	0.2		
Lu	0.200	0.1	0.227		0.246	0.0	0.172	0.0	0.245	0.0	0.240	0.0	0.304	0.1	0.266	0.0	0.208	0.0		
Hf	0.449	0.1	0.834		1.026	0.2	0.740	0.0	1.112	0.1	1.099	0.1	1.405	0.1	1.404	0.2	0.267	0.0		
Ta	bd		0.132		bd		bd		bd		bd		bd		bd		bd			
Pb	bd		bd		0.520	0.1	0.673	0.0	bd		bd		bd		0.902	0.2	0.544	0.1		
Th	bd		0.118		bd		2.002	0.0	0.122	0.0	0.389	0.0	0.379	0.1	0.351	0.0	bd			
U	bd		0.057		bd		0.523	0.0	0.068	0.0	0.189	0.0	0.125	0.1	0.188	0.0	0.287	0.0		
Ni/Co	14.23		14.15		15.48		15.41		15.97		15.03		14.55		15.24		15.00			
(La/Yb)N − (La/Er)N	0.22		1.22		0.32		14.38		0.66		1.57		1.37		1.69		1.98			
(La/Nd)N	0.44		1.05		0.40		11.90		0.70		1.65		1.38		1.39		10.83			
(Sm/Yb)N − (Sm/Er)N	0.75		1.02		0.85		1.40		1.05		1.13		1.00		1.30		0.32			
(Gd/Yb)N	0.84		0.89		0.96		1.31		1.03		1.05		0.97		1.16		0.61			
(Th/U)N			0.53				0.98		0.46		0.53		0.78		0.48					
(Ti/Nb)N	2.96		2.37		8.12		8.69		6.20		32.90		1.94		1.54		0.77			
(Ti/Eu)N	0.50		0.37		0.41		0.51		0.55		0.57		0.45		0.54		0.50			
(Zr/Sm)N	0.48		0.48		0.80		0.61		0.85		0.66		0.86		0.85		0.16			
(Zr/Hf)N	0.79		0.80		0.83		0.88		0.92		0.81		1.04		1.01		0.18			
(Nb/Ta)N			0.28																	

c and sr, core and spongy rim compositions, respectively. Other abbreviations as in Table 3.

Equi. lhz		Granular hz										Px			
BB.26.04		CA.00.83b		BB12.041		BB.02.04		BB.74.04		BB.18.29		SD.98.1		BB.83.04	
51.83		53.33		52.89		52.80		53.43		53.40		53.62		52.83	
0.35		0.05		0.12		0.50		0.04		0.03		0.45		0.38	
5.49		2.45		3.40		3.46		2.46		2.88		5.51		2.23	
0.64		1.31		1.54		1.38		1.15		1.55		0.49		1.04	
3.14		2.51		2.49		2.72		2.46		2.33		5.46		3.49	
0.11		0.09		0.07		0.10		0.10		0.08		0.15		0.11	
15.69		17.83		17.74		17.28		18.28		17.95		17.72		18.12	
0.05		0.04		0.04		0.11		0.09		0.06		0.06		0.06	
21.21		21.52		20.90		20.79		21.21		21.01		16.11		21.38	
1.24		0.73		0.93		0.78		0.34		0.94		0.94		0.28	
0.01		nd		nd		0.01		0.01		nd		0.00		0.00	
99.76		99.84		100.12		99.93		99.57		100.22		100.49		99.92	
1.879		1.931		1.906		1.914		1.939		1.921		1.931		1.919	
0.121		0.069		0.094		0.086		0.061		0.079		0.069		0.081	
0.113		0.035		0.050		0.062		0.044		0.043		0.165		0.015	
0.010		0.001		0.003		0.014		0.001		0.001		0.012		0.010	
0.018		0.037		0.044		0.040		0.033		0.044		0.014		0.030	
0.059		0.043		0.059		0.012		0.007		0.056		0.000		0.036	
0.037		0.033		0.016		0.070		0.072		0.014		0.164		0.070	
0.003		0.003		0.002		0.003		0.003		0.002		0.005		0.003	
0.848		0.962		0.953		0.934		0.989		0.963		0.951		0.981	
0.001		0.001		0.001		0.003		0.003		0.002		0.002		0.002	
0.824		0.835		0.807		0.807		0.825		0.810		0.621		0.832	
0.087		0.049		0.065		0.054		0.024		0.066		0.066		0.020	
0.000		0.000		0.000		0.000		0.001		0.000		0.000		0.000	
89.8		92.7		92.7		91.9		92.6		93.2		85.3		90.2	
7.1		26.5		23.4		21.3		23.9		26.5		5.6		23.8	
46.6		44.6		44.0		44.3		43.6		44.0		35.8		43.4	
48.0		51.4		51.9		51.2		52.2		52.2		54.8		51.1	
3.5		2.4		3.3		0.8		0.5		3.2		0.3		2.0	
$n = 2$	$\pm 1\sigma$	$n = 4$	$\pm 1\sigma$	$n = 4$	$\pm 1\sigma$	$n = 4$	$\pm 1\sigma$	$n = 3$	$\pm 1\sigma$	$n = 4$	$\pm 1\sigma$	$n = 4$	$\pm 1\sigma$	$n = 6$	$\pm 1\sigma$
57.03	2.7	62.14	12	55.93	3.0	68.96	1.2	38.49	0.2	65.99	4.9	37.45	3.6	44.32	0.6
1752	85	329.1	10	794.3	58	2622	34	144.4	3.0	268.8	10	2345	277	1956	50
227.9	5.4	179.7	5.9	177.8	8.4	297.5	6.5	137.7	1.8	218.8	12	194.1	11	157.1	4.8
631.1	18	nd		718.7	15	663.8	4.7	613.7	13	674.7	32	1180	71	851.1	48
20.01	0.9	30.23	2.0	27.65	0.3	25.31	0.3	25.90	0.1	27.91	2.1	49.06	3.3	30.33	2.7
314.0	32	454.9	44	436.7	13	390.9	5.6	452.4	6.1	466.6	37	519.6	52	335.0	23
3.560	0.7	2.792	0.5	3.151	0.2	3.529	0.2	1.330	0.3	2.174	0.1	8.189	0.9	2.554	0.2
bd		bd		bd		bd		bd		bd		bd		bd	
25.36	0.3	382.1	43	137.0	14	62.10	0.7	54.76	1.2	184.4	21	56.10	9.4	43.86	0.5
14.70	0.5	2.281	0.1	5.393	0.9	9.012	0.1	0.829	0.1	3.861	0.3	7.164	0.9	4.247	0.1
17.79	0.9	12.23	1.9	18.01	2.4	36.86	0.5	1.789	0.1	71.22	2.7	12.29	2.6	7.954	0.2
<0.150		2.360	0.1	1.088	0.1	0.630	0.1	0.247	0.1	1.303	0.2	<0.150	0.0	<0.150	
3.244	3.7	bd		bd		bd		bd		bd		bd		bd	
0.589	0.1	23.16	1.1	5.391	0.7	2.040	0.1	2.212	0.1	8.706	0.8	1.517	0.4	0.327	0.1
1.212	0.1	53.15	3.7	13.69	2.4	6.055	0.2	4.349	0.1	23.12	3.2	5.904	1.4	1.408	0.1
0.338	0.0	6.021	0.3	1.942	0.3	0.959	0.0	0.630	0.0	3.249	0.2	1.054	0.2	0.343	0.0
2.651	0.3	19.91	1.8	9.949	1.3	5.328	0.2	3.250	0.1	12.53	0.9	6.211	1.3	2.292	0.2
1.561	0.4	3.462	0.3	2.377	0.3	2.243	0.2	0.476	0.1	2.148	0.1	1.741	0.3	0.918	0.2
0.721	0.1	0.971	0.1	0.833	0.2	0.891	0.0	0.164	0.1	0.500	0.1	0.701	0.2	0.356	0.0
1.814	0.2	1.067	0.2	1.773	0.2	2.659	0.1	0.473	0.1	1.205	0.0	1.899	0.3	1.289	0.2
0.334	0.1	0.158	0.0	0.281	0.1	0.422	0.0	0.066	0.0	0.185	0.1	0.291	0.0	0.201	0.0
2.509	0.2	0.789	0.1	1.354	0.3	2.213	0.1	0.225	0.0	0.915	0.2	1.602	0.3	1.075	0.1
0.563	0.0	0.107	0.0	0.242	0.1	0.377	0.0	0.030	0.0	0.152	0.1	0.305	0.1	0.191	0.0
1.384	0.2	0.268	0.1	0.459	0.1	0.799	0.0	0.150	0.0	0.406	0.1	0.673	0.2	0.453	0.1
0.246	0.0	bd		bd		bd		bd		bd		0.099	0.0	0.068	0.0
1.555	0.0	bd		0.453	0.2	0.563	0.0	bd		bd		0.658	0.1	0.404	0.1
0.194	0.1	bd		0.079	0.0	0.061	0.0	bd		0.068	0.0	0.093	0.0	0.054	0.0
0.756	0.1	bd		0.591	0.1	1.607	0.1	bd		1.980	0.2	0.641	0.3	0.314	0.1
bd		0.239	0.0	bd		bd		bd		0.137	0.0	bd		bd	
0.540	0.1	bd		bd		bd		bd		bd		bd		0.228	0.1
bd		1.503	0.2	0.280	0.0	0.146	0.0	bd		1.867	0.3	bd		bd	
0.140	0.0	0.321	0.1	bd		bd		0.081		0.295	0.0	bd		bd	
15.69		15.05		15.79		15.44		17.47		16.72		10.59		11.05	
0.26		58.47		8.09		2.47		10.00		14.49		1.57		0.55	
0.43		2.24		1.05		0.74		1.31		1.34		0.47		0.28	
1.09		13.95		5.70		4.33		3.43		5.71		2.87		2.47	
0.95		3.21		3.17		3.83		2.55		2.39		2.34		2.59	
		1.19								1.62					
		0.08		0.40		2.27		0.32		0.11					
0.31		0.04		0.12		0.38		0.11		0.07		0.43		0.70	
0.44		0.14		0.29		0.64		0.15		1.28		0.27		0.34	
0.63				0.82		0.62				0.97		0.52		0.68	
		0.56								0.54					

Table 6. *Representative major element analyses and formula units of spinel, and average trace element compositions*

Rock type:	Granular lhz					
Sample:	CA.00.83	BB.12.030	BB.64.04	BB.16.04	BB.81.04	SD.98.58
(wt%)						
SiO_2	0.12	0.00	0.06	0.13	0.06	0.10
TiO_2	0.21	0.08	0.15	0.13	0.16	0.18
Al_2O_3	51.91	53.77	54.56	57.77	57.06	53.66
Cr_2O_3	13.72	14.21	11.69	9.63	9.10	12.04
Fe_2O_3	3.77	1.74	3.05	1.89	3.25	3.66
FeO	8.73	9.21	8.83	9.19	8.56	8.93
MnO	0.11	0.10	0.11	0.10	0.10	0.15
MgO	20.52	20.32	20.65	20.96	21.17	20.55
Total	99.08	99.43	99.11	99.80	99.47	98.97
Si	0.025	0.000	0.013	0.027	0.012	0.021
Ti	0.033	0.013	0.024	0.020	0.025	0.028
Al	12.980	13.336	13.504	14.042	13.928	13.317
Cr	2.302	2.364	1.941	1.570	1.490	2.004
Fe^{3+}	0.601	0.276	0.482	0.294	0.507	0.580
Fe^{2+}	1.549	1.620	1.551	1.585	1.483	1.572
Mn	0.019	0.018	0.020	0.017	0.018	0.026
Mg	6.490	6.374	6.466	6.445	6.537	6.452
mg-no.	80.7	79.7	80.7	80.3	81.5	80.4
cr-no.	14.5	14.8	12.2	9.9	9.4	12.6
Trace elements (ppm)	$n = 4$ $\pm 1\sigma$	$n = 2$ $\pm 1\sigma$	$n = 4$ $\pm 1\sigma$	$n = 4$ $\pm 1\sigma$	$n = 6$ $\pm 1\sigma$	$n = 3$ $\pm 1\sigma$
Ti	1052 32	490.7 12	826.0 3.8	752.2 20	997.0 16	2086 174
V	440.7 12	330.3 19	419.9 18	418.1 26	360.5 46	1087 25
Mn	848.0 29	715.7 36	844.0 112	847.5 49	758.1 82	na
Co	221.2 10	232.3 9.7	246.2 12	281.1 20	229.1 29	744.8 49
Ni	2862 119	2497 168	3132 155	3670 302	3072 424	9587 654
Ga	85.81 3	68.84 3.0	72.46 4.4	88.5 5.4	76.73 11	275.6 24
Zr	1.314 0.4	1.16 0.3	bd	bd	bd 0.1	3.281 1.8
Nb	1.164 0.1	1.276 0.1	bd	bd	bd 0.0	2.711 0.2

pc, porphyroclastic core; pr, porphyroclastic rim; other abbreviations as in Table 3. Fe^{3+} estimation is by stoichiometry assuming $\sum$cations = 24.

The compositional heterogeneity of the peridotites is explained by melt depletion and subsequent metasomatisms.

Melt depletion

Melt depletion in peridotites is inferred from: (1) the inverse correlation of all clinopyroxene, orthopyroxene and spinel modes with the olivine mode (Fig. 2, Table 1); (2) the negative correlation of basaltic components with Mg-number and the positive correlation between Cr-number (or cr-number) and Mg-number (or mg-number) in both whole rocks and pyroxenes (Figs 4 and 5), whereas cr-number and mg-number are inversely correlated in spinel (Fig. 6); (3) increasing Fo% in olivine and Ni/Co ratio in olivine and pyroxenes from lherzolites to harzburgites, whereas this ratio decreases in spinel (Figs 7, 9b and 11a); (4) LREE and even MREE depletion in clinopyroxene of most lherzolites (Fig. 10a); (5), decreasing HREE in cpx from lherzolites to harzburgites (Fig. 10a and c). Most co-variation diagrams in this study show no significant gap between the two types of peridotites. Therefore, different melting histories for lherzolites and harzburgites (Bianchini *et al.* 2007) cannot be confirmed.

To approach the degree of melting, trace element concentrations of residual clinopyroxene have been estimated for both batch and fractional melting of a PM source (McDonough & Sun 1995), with a clinopyroxene fraction of 0.20, as given by Norman (1998). Partition coefficients of REE and Y for the clinopyroxene used in this approach were also determined after Wood & Blundy (1997), assuming melting of spinel lherzolites at 1400 °C (Takahashi *et al.* 1993) and 21.0 kbar, which is the maximum estimated pressure for these rocks. These D^{REE}, cpx and D^{Y}, cpx are comparable with those determined experimentally (Hart & Dunn 1993). An Er_N v. Y_N plot (Fig. 14) has been selected to illustrate the degree of depletion, as both elements decrease regularly with Ti (Fig. 9e and f) from lherzolites to harzburgites, except for xenolith BB.02.04, and because heavier REE than Er are not systematically detected

		Granular hz								Porphyroclastic hz	
SD.98.2		CA.00.83b		BB.12.041		BB.02.04		BB18.29		SD.98.15p	SD.98.15nc
0.15		0.00		0.00		0.08		0.00		0.08	0.10
0.17		0.14		0.24		1.00		0.09		0.09	0.13
53.59		21.96		26.39		26.55		23.68		56.28	56.09
13.53		45.71		42.31		39.95		45.64		9.68	9.49
2.49		3.61		2.35		3.61		2.24		3.10	3.85
9.32		12.36		12.13		12.23		11.93		9.71	9.19
0.11		0.21		0.17		0.17		0.20		0.06	0.11
20.24		14.79		15.58		16.16		15.31		20.31	20.71
99.03		98.78		99.15		99.75		99.09		99.31	99.67
0.011		0.000		0.000		0.019		0.000		0.017	0.021
0.010		0.025		0.042		0.179		0.016		0.014	0.020
13.310		6.376		7.464		7.444		6.786		13.853	13.754
2.254		8.904		8.028		7.514		8.773		1.598	1.561
0.394		0.670		0.424		0.647		0.410		0.486	0.603
1.642		2.547		2.433		2.432		2.424		1.696	1.598
0.020		0.044		0.035		0.034		0.041		0.011	0.019
6.360		5.434		5.575		5.731		5.550		6.324	6.424
79.5		68.1		69.6		70.2		69.6		78.9	80.1
14.1		55.8		50.4		48.2		54.9		10.0	9.8
$n = 4$	$\pm 1\sigma$	$n = 3$	$\pm 1\sigma$	$n = 4$	$\pm 1\sigma$	$n = 4$	$\pm 1\sigma$	$n = 2$	$\pm 1\sigma$	n=1 (pc)	$n = 1$(pr)
437.9	114	1092	401	1361	23	5849	64	496.8	4.8	2855	3398
770.5	219	1052	425	725.8	10	1587	40	890.4	5.8	2033	2368
1216	272	na		1226	26	1182	30	1104	9.9	4714	5598
427.4	107	376.5	151	257.9	7.5	246.6	4.1	239.6	5.5	1521	1685
3939	910	1663	731	1561	32	1634	30	1326	45	18430	21050
104.2	30	46.86	25	56.57	2.3	65.72	3.1	31.21	1.0	499.4	612.5
2.173	0.8	4.835	4.7	5.179	0.2	0.964	0.2	4.475	0.2	bd	5.869
1.875	0.7	6.127	3.1	5.478	0.1	0.404	0.1	3.996	0.3	5.621	8.072

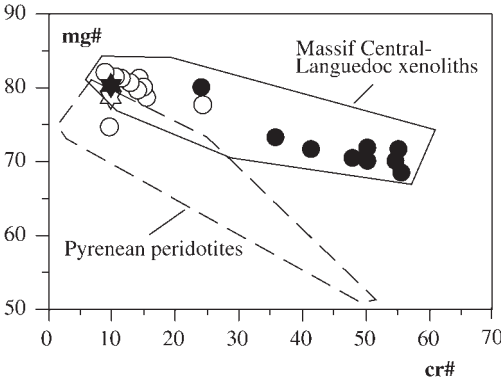

Fig. 6. The mg-number v. cr-number for spinel. ○, lherzolites; ●, harzburgites; ★, porphyroclast; ☆, neocrystal. This figure illustrates that spinel of the studied xenoliths follows the trend defined by spinel in xenoliths from the Massif Central and Languedoc (France), encircled by a continuous line. These are characterized by higher mg-number for similar cr-number with respect to the trend defined by spinel of the Pyrenean peridotites, encircled by a dashed line (Fabriès *et al.* 1987).

in the harzburgite clinopyroxene (Table 5). It is shown that the lherzolite clinopyroxene fits with a low degree of either batch melting (<10%) or fractional melting (<8%), in the spinel lherzolite field. However, the slight HREE fractionation of SD.98.2 clinopyroxene (Fig. 10a) indicates that melting could have started in the garnet lherzolite field. This is consistent with much higher Al^{VI}/Al^{IV} ratio in SD.98.2 clinopyroxene (4.352) with respect to other lherzolite values (1.605–0.961) and, with the PBK90 estimate (23.1 kbar) for sample SD.98.2, which is among the highest pressures for lherzolites. Bianchini *et al.* (2007) came to the same conclusion from the Hf isotopic composition of a clinopyroxene that shows comparable REE and multielement patterns to those of SD.98.2 clinopyroxene. Harzburgite depletion is explained by a higher degree of fractional melting (10–30% in Fig. 14b). Again, no significant gap is observed between the degree of melting in the two types of peridotites. Increasing Er_N by metasomatism is unlikely in harzburgite clinopyroxene, as it displays flat HREE when most HREE are over the detection limit (Fig. 10c). The only exception is

Table 7. *Representative major element analyses and formula units of amphibole and phlogopite, and average trace element compositions*

Rock type:	Granular lhz and hz		Px	
Mineral:	Am*		Phl	
Sample:	BB.81.04		BB.10.799	BB.83.04
(wt%)				
SiO_2	42.12		36.79	37.49
TiO_2	3.18		1.75	10.12
Al_2O_3	14.90		17.19	15.01
Cr_2O_3	0.96		3.93	na
FeO^T	4.67		4.68	5.43
MnO	0.09		0.00	0.04
MgO	16.81		19.70	15.79
NiO	0.14		nd	nd
CaO	10.10		0.12	0.03
Na_2O	4.17		0.04	0.64
K_2O	0.19		10.22	8.90
Total	97.30		94.42	94.42
Cations			*(O = 22)*	
Si	5.959		5.352	5.456
Al^{IV}	2.041		2.648	2.544
Al^{VI}	0.443		0.300	0.031
Ti	0.338		0.191	1.108
Cr	0.107		0.452	
Fe^{3+}	0.550			
Fe^{2+}	0.003		0.569	0.661
Mn	0.011		0.000	0.005
Mg	3.545		4.271	3.424
Ni	0.015			
Ca	1.531		0.019	0.005
Na	1.114		0.011	0.181
K	0.035		1.897	1.652
mg-no.	86.5		88.2	83.8
cr-no.	4.1		13.3	
Trace elements (ppm)	$n = 4$	$\pm 1\sigma$		$n = 5$ $\pm\sigma$
Sc	37.74	0.7		12.98 0.8
Ti	18023	144		56724 2891
V	416.2	4.1		601.2 37
Mn	564.1	5.0		235.9 12
Co	49.66	1.1		72.15 1.7
Ni	969.6	9.7		1292 99
Ga	17.12	1.3		21.32 5.3
Rb	6.877	0.3		43.84 8.1
Sr	421.2	6.5		49.52 44
Y	20.43	0.7		0.185 0.1
Zr	30.00	0.4		16.88 1.5
Nb	2.887	0.2		31.66 2.2
Ba	1820	144		1402 262
La	4.764	0.1		0.408 0.3
Ce	6.700	0.2		1.180 1.4
Pr	1.056	0.1		bd
Nd	5.761	0.6		0.437 0.2
Sm	2.187	0.1		bd
Eu	1.068	0.1		bd
Gd	2.966	0.3		bd
Tb	0.564	0.0		bd
Dy	3.675	0.2		bd
Ho	0.769	0.0		bd

(*Continued*)

Table 7. *Continued*

Rock type:	Granular lhz and hz			Px	
Mineral:	Am*		Phl	Phl	
Sample:	BB.81.04		BB.10.799	BB.83.04	
Er	2.158	0.1		bd	
Tm	0.304	0.0		bd	
Yb	2.001	0.2		bd	
Lu	0.280	0.0		bd	
Hf	0.876	0.0		0.415	0.0
Ta	bd			1.244	0.1
Pb	2.325	0.8		1.626	0.8
Th	0.374	0.0		bd	
U	0.244	0.1		bd	
Ni/Co	19.52				
$(La/Yb)_N - (La/Er)_N$	1.62				
$(La/Nd)_N$	1.60				
$(Sm/Yb)_N - (Sm/Er)_N$	1.19				
$(Gd/Yb)_N$	1.20				
Rb/Sr	0.02			0.89	
Ba/Sr	4.32			28.31	
Zr/Nb	10.4			0.53	
Ti/Zr	601			3361	
Rb/Ba	0.00			0.03	

*Fe^{3+} after Robinson *et al.* (1982).

sample BB.02.04, which differs in showing a clinopyroxene convex-upward REE pattern. It should be noted that these estimates for harzburgites are not as high as those considered by Bianchini *et al.* (2007) (>40%). Therefore, neocrystallization of clinopyroxene in harzburgites by later metasomatism (Bianchini *et al.* 2007) would not be necessary to account for its presence in these refractory rocks.

Melting could occur by mantle decompression, as the Al^{VI}/Al^{IV} ratio in clinopyroxene decreases from lherzolites towards harzburgites (Fig. 5e and f) (Seyler & Bonatti 1994). Unfortunately, the high uncertainty linked to PKB90 results means that we cannot confirm this hypothesis. Moreover, as both Al^{VI}/Al^{IV} ratio and Na also decrease in the refractory compositions of spongy rims, with respect to unaffected zones of clinopyroxene crystals (Figs 3d and 5e, f), decompression, along with probable migration of a low-density fluid during later metasomatism (Carpenter *et al.* 2004), could have triggered local partial melting, at subsolidus temperatures. Thus, LREE and other incompatible trace elements slightly enriched in the spongy rim of sample CA.00.83 (Figs 9 and 10a, b) would be explained by the injection of this later volatile-rich fluid. Any relationship between the development of the clinopyroxene spongy rims and heating by the host lava is discarded, because this texture is not observed at the xenolith borders (Carpenter *et al.* 2004), and because lower orthopyroxene–clinopyroxene temperature was estimated for spongy rims than for clinopyroxene cores (Llovet & Galán 2003). Subsolidus decompression is also supported by the onset of plagioclase in rare corona textures around both spinel and amphibole (Fig. 3f and g).

Types of metasomatism

Evidence of metasomatism exists in both lherzolites and harzburgites, but in the latter it is more significant and widespread. Metasomatism in harzburgites is inferred from: (1) sporadic presence of accessory phlogopite (e.g. BB.17.799, Table 7); (2) slightly higher CaO/Al_2O_3 ratio in two bulk-rock compositions (CA.00.83b and BB.96.04) with respect to the PM (Fig. 4f); (3) Ti increase in orthopyroxene and spinel of two harzburgites (BB.02.04 and SD.98.15) and in the clinopyroxene of one of them (BB.02.04); (4) LREE and other incompatible trace element enrichment (Th, U, Nb, Ta, Sr, Zr, Hf), without increase in Ti (Figs 9 and 10c, d). In lherzolites, metasomatism is reflected by: (1) slight LREE enrichment (BB.81.04 and SD.98.58) and the sporadic presence of accessory amphibole (e.g. in BB.81.04); (2) moderate enrichment and high fractionation of LREE coupled to positive anomaly at Sr in two samples (BB.64.04 and SD.98.2); and (3) development of sporadic spongy rims in clinopyroxene crystals showing refractory

Table 8. *Averages for glass compositions in veins of different granular harzburgite xenoliths*

Sample:	CA.00.83b		BB.10.799		BB.12.48	
(wt%)	$n = 10$	$\pm 1\sigma$	$n = 4$	$\pm 1\sigma$	$n = 7$	$\pm 1\sigma$
SiO_2	59.70	1.2	56.40	1.8	51.25	0.7
TiO_2	2.69	0.1	2.56	0.2	2.45	0.3
Al_2O_3	15.18	0.2	18.51	0.7	18.37	1.4
FeO^T	2.64	0.2	3.16	0.7	7.19	0.7
MnO	0.05	0.0	0.06	0.0	0.16	0.0
MgO	3.29	0.2	2.20	0.0	2.28	0.3
CaO	4.64	1.3	4.95	0.1	6.19	0.8
Na_2O	3.52	0.3	3.18	1.2	5.43	0.4
K_2O	4.58	0.5	3.44	0.6	3.85	0.9
Total	96.28		94.45		97.17	
CIPW norm (wt%)						
Qtz	9.29		10.57		0.00	
Pl	43.48		54.51		38.77	
Or	28.13		21.51		23.40	
Ne	0.00		0.00		12.62	
Di	8.93		0.00		14.10	
Hy	4.87		0.00		0.00	
Ol	0.00		7.57		6.31	
Ilm	5.30		5.15		4.79	
Qtz + Opx	14.16		10.57		0.00	
Ne + Lc	0.00		0.00		12.62	
Mg-no.	68.96		55.40		36.10	
K-no.	46.12		41.58		31.84	
Na_2O/K_2O	0.77		0.92		1.41	
TAS	8.10		6.63		9.28	
$TiO_2 + K_2O$	7.27		6.00		6.30	
$CaO + Na_2O$	8.16		8.13		11.62	
Trace elements (ppm)	$n = 3$	$\pm 1\sigma$				
Sc	19.24	1.5				
Ti	18083	1427				
V	167.3	61				
Co	40.04	13				
Ni	379.9	131				
Ga	88.56	21				
Rb	85.47	23				
Sr	1737	358				
Y	39.06	0.2				
Zr	456.0	105				
Nb	344.2	138				
Ba	707.9	16				
La	138.0	1.4				
Ce	323.3	73				
Pr	26.36	0.8				
Nd	99.55	4.6				
Sm	14.25	1.2				
Eu	4.792	1.0				
Gd	11.84	0.7				
Tb	1.755	0.1				
Dy	8.080	0.9				
Ho	1.532	0.1				
Er	3.955	0.1				
Tm	0.736	0.2				
Yb	3.565	0.3				
Lu	0.491	0.1				
Hf	8.311	1.0				
Ta	8.554	2.6				

(*Continued*)

Table 8. *Continued*

Sample:	CA.00.83b		BB.10.799	BB.12.48
Pb	31.98	4.5		
Th	13.97	1.2		
U	4.410	0.6		
Ni/Co	9.49			
Rb/Ba	0.12			
$(Th/U)_N$	0.81			
$(Nb/Ta)_N$	2.26			
$(La/Yb)_N$	26.3			
$(Gd/Yb)_N$	2.7			
$(Zr/Hf)_N$	1.48			
$(Ti/Nb)_N$	0.03			
$(Ti/Eu)_N$	0.48			
$(Zr/Sm)_N$	1.24			
Ce/Pb	10.1			
Ba/Th	50.7			
Ti/Eu	4100			
U/Nb	0.01			

and LREE-enriched composition (e.g. in CA.00.83) (Fig. 10a and b). Finally, glass filling occasional cross-cutting veins (Fig. 3h) can be found in both lherzolites and harzburgites.

Metasomatism in harzburgites. Two metasomatic styles, mainly cryptic, can be distinguished.

(1) One type is characterized by Ti, Fe, Al, V, Co and Zr enrichment in orthopyroxene, clinopyroxene and spinel (e.g. BB.02.04 and SD.98.15; Figs 8, 9 and 11), along with a convex-upward REE pattern, low $(La/Yb)_N$ and high Ti/Eu ratios in BB.02.04 clinopyroxene (Figs 10c, d and 15). This type of pattern parallels those of pyroxenite xenoliths and dykes (Fig. 10c and e) and could be explained by interaction and diffusional re-equilibration (Bodinier *et al.* 1990) of the harzburgite with an infiltrating alkaline silicate melt, similar to those in equilibrium with the pyroxenites. This metasomatism can be compared with the Fe–Ti metasomatism in wall-rock peridotites, adjacent to Cretaceous amphibole–garnet pyroxenite and hornblendite dykes and veins in the Lherz massif (Bodinier *et al.* 1988, 1990, 2004; McPherson *et al.* 1996; Woodland *et al.* 1996; Zanetti *et al.* 1996). However, the porphyroclastic harzburgite SD.98.15 is a rare xenolith that shows no clinopyroxene and it is also noteworthy for its less refractory compositions and zoning of minerals (Figs 6, 7, 8 and 11). This absence of chemical equilibrium in a small xenolith, together with the existence of melt in its fluidal matrix and the higher temperature provided by the neocrystals, suggests a brief silicate melt metasomatism that

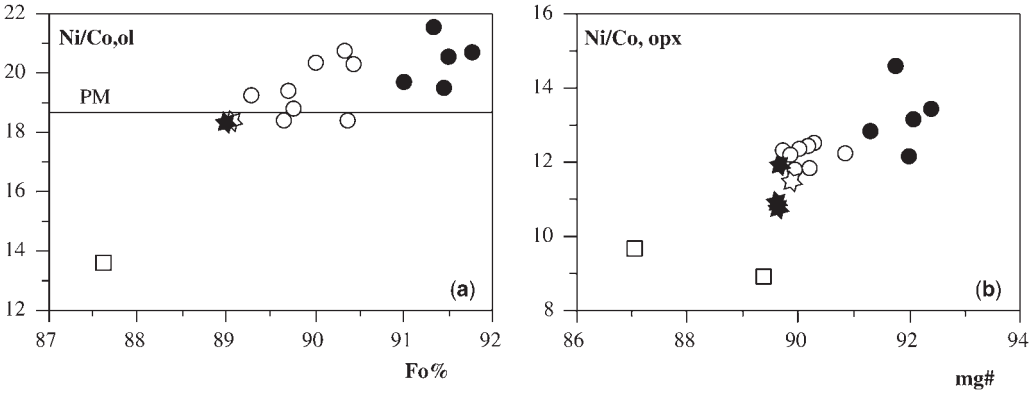

Fig. 7. (**a**) Olivine Ni/Co v. Fo%, both increasing regularly from lherzolites towards harzburgites; (**b**) orthopyroxene Ni/Co v. mg-number, showing similar trend. The Ni/Co value for the Primitive Mantle (McDonough & Sun 1995) is represented in (a). Symbols as in Figs 5 and 6.

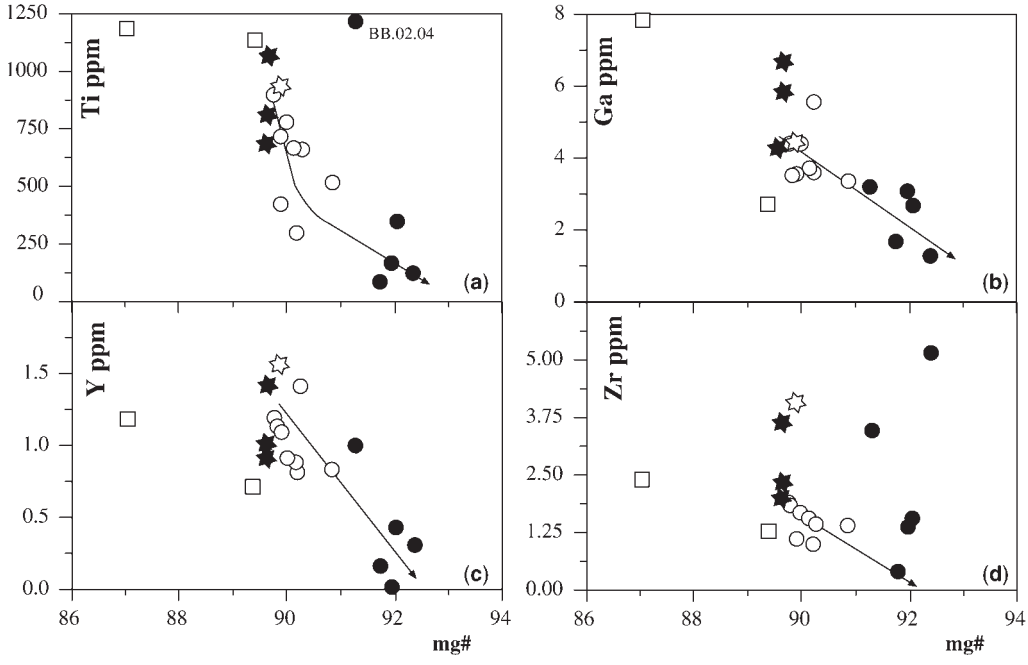

Fig. 8. The mg-number in orthopyroxene v. (**a**) Ti, (**b**) Ca, (**c**) Y and (**d**) Zr. Arrows indicate melt depletion within coarse granular peridotites. Symbols as in Figures 5 and 6.

could be due to heating by the host lava and therefore will not be considered in the following discussion. Highly alkaline melts were also considered by Bianchini *et al.* (2007) as the metasomatizing agent for the granular harzburgites, but of Permo-Triassic age.

(2) The other metasomatic style in harzburgites (BB.18.29, BB.12.04, BB.74.04 and CA.00.83b) is mainly defined by (a) trace element enrichment, except for Ti, in clinopyroxene; (b) higher LREE/HREE ($(La/Yb)_N$ or $(La/Er)_N = 2.47–58.47$) and lower Ti/Eu ratios (Fig. 15); (c) increased Th, U and Nb, but with moderate negative anomalies for Nb and other HFSE (Fig. 10d). These multielement patterns compare better with those of clinopyroxene in xenoliths from the southern domain of the Massif Central, France, than with those with more extreme HFSE negative anomalies in more refractory xenoliths from the northern domain (Downes *et al.* 2003). In addition, they are also comparable with those in distant wall-rock anhydrous harzburgites, injected by a Cretaceous amphibole–garnet pyroxenite dyke and hornblendite veins in the Lherz massif (Pyrenees) (Fig. 10c and d), although the xenolith clinopyroxene is more refractory. This metasomatic style shows characteristics typical of carbonatite metasomatism; also typical are the high $(Zr/Hf)_N$ ratio (4.8) of the clinopyroxene in the most metasomatized harzburgite (CA.00.83b) and the CaO/Al_2O_3 ratio exceeding PM of two harzburgite bulk-rock compositions (Fig. 4f) (Dupuy *et al.* 1992; Ionov *et al.* 1993; Norman 1998; Yaxley *et al.* 1998; Coltorti *et al.* 1999; Blundy & Dalton 2000). However, a similar carbonatite signature has been questioned by other workers (Grégoire *et al.* 2000; Zhang *et al.* 2000; Laurora *et al.* 2001), because it can be also generated by hydrous silicate-melt metasomatism. Furthermore, in the Lherz massif it has been linked to the injection of the alkaline melts in dykes, through melt infiltration in the wall-rock and chromatographic fractionation–reaction at decreasing melt mass, leading to the melt evolution and the formation of carbonate-rich derivatives away from the dyke (Bodinier *et al.* 2004). This model has been also considered for explaining metasomatism in xenoliths (Bedini *et al.* 1997), but in this case it is more difficult to constrain the spatial relationships between the alkaline silicate-melt component and the carbonatite derivatives. For instance, this study cannot provide significant evidence of modal metasomatism causing precipitation of amphibole ($\pm$ clinopyroxene) as a result of percolation–reaction: hydrous minerals are only accessory, and slightly higher CaO/Al_2O_3 ratio than that of PM in some whole rocks could be also due to diffusional

re-equilibration with the infiltrated melt. In addition, the percolation–reaction model in the Lherz massif can account for the LREE enrichment in distal anhydrous wall-rock harzburgites, but not for their low $^{143}Nd/^{144}Nd$ ratios. According to Bodinier *et al.* (2004), the earlier isotopic compositions would remain unaffected, because of the insufficient time elapsed since the dyke injections. $^{143}Nd/^{144}Nd$ and $^{87}Sr/^{86}Sr$ results on harzburgite xenoliths from Catalunya (Bianchini *et al.* 2007) are comparable with those for anhydrous wall-rock harzburgites from Lherz (Bodinier *et al.*

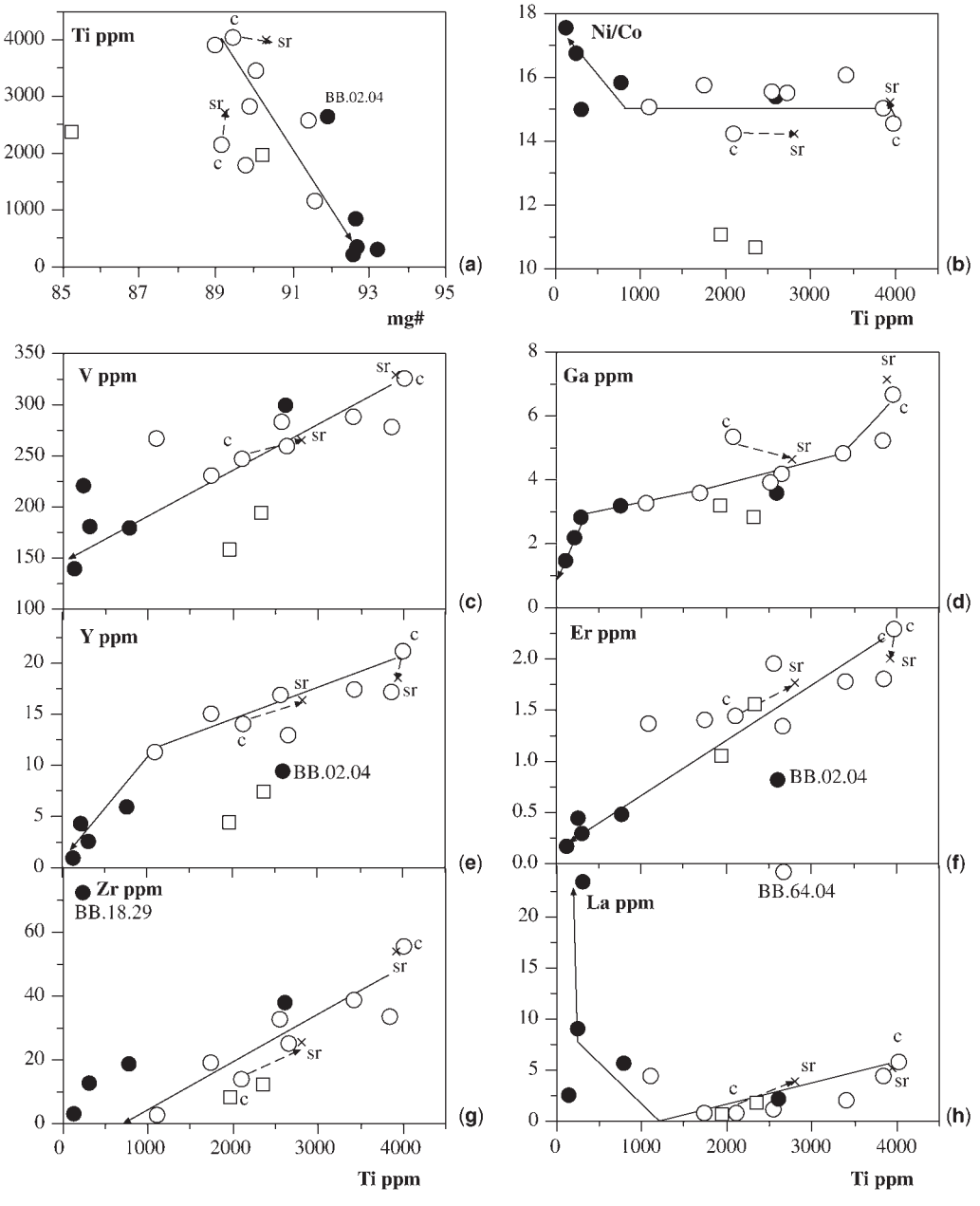

Fig. 9. Variation diagrams for clinopyroxene; (**a**) Ti v. mg-number; (**b–l**) Ni/Co ratio and trace elements v. Ti. Symbols as in previous figures. c and sr, core and spongy rim compositions, respectively.

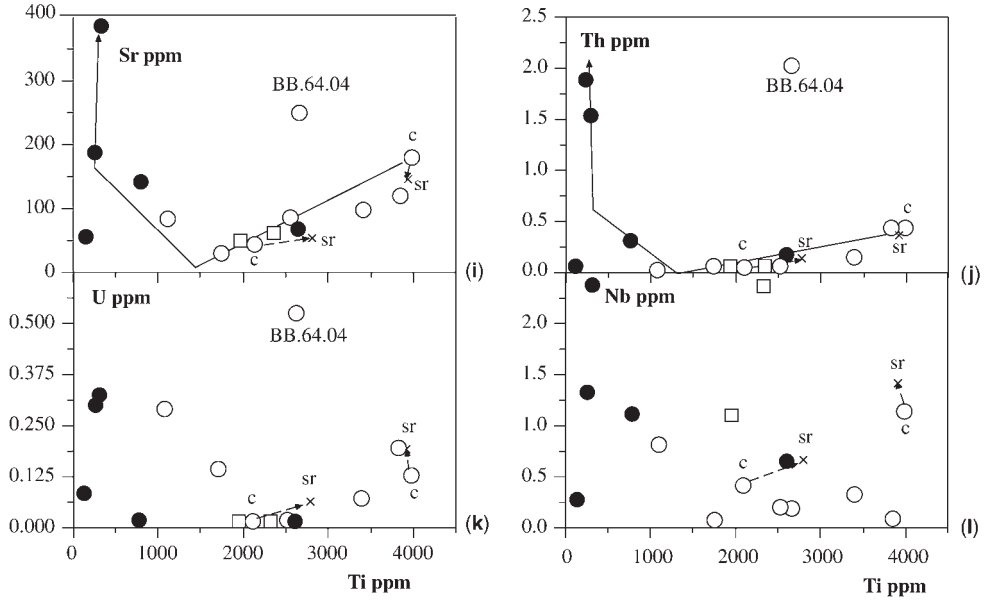

Fig. 9. (*Continued*).

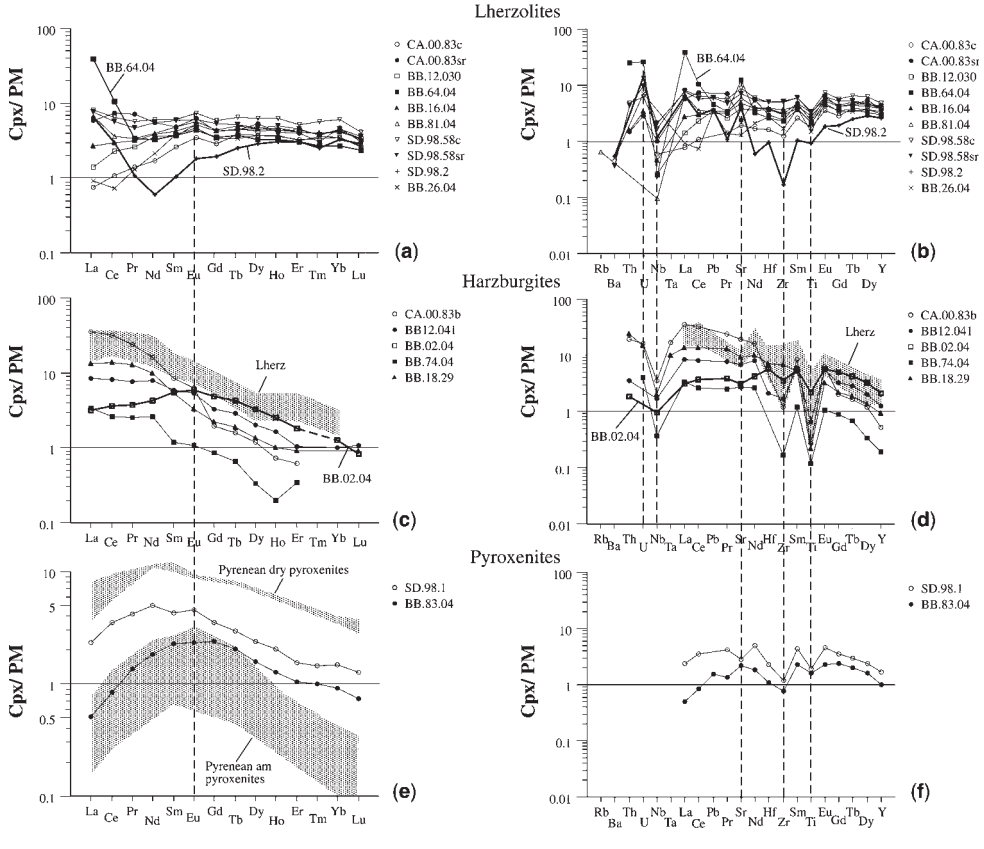

Fig. 10. (**a**–**f**) Clinopyroxene REE and multielement patterns. Clinopyroxene patterns of eastern Pyrenean ultramafic massifs are shown as reference (Bodinier *et al.* 1987*a*, *b*, 2004).

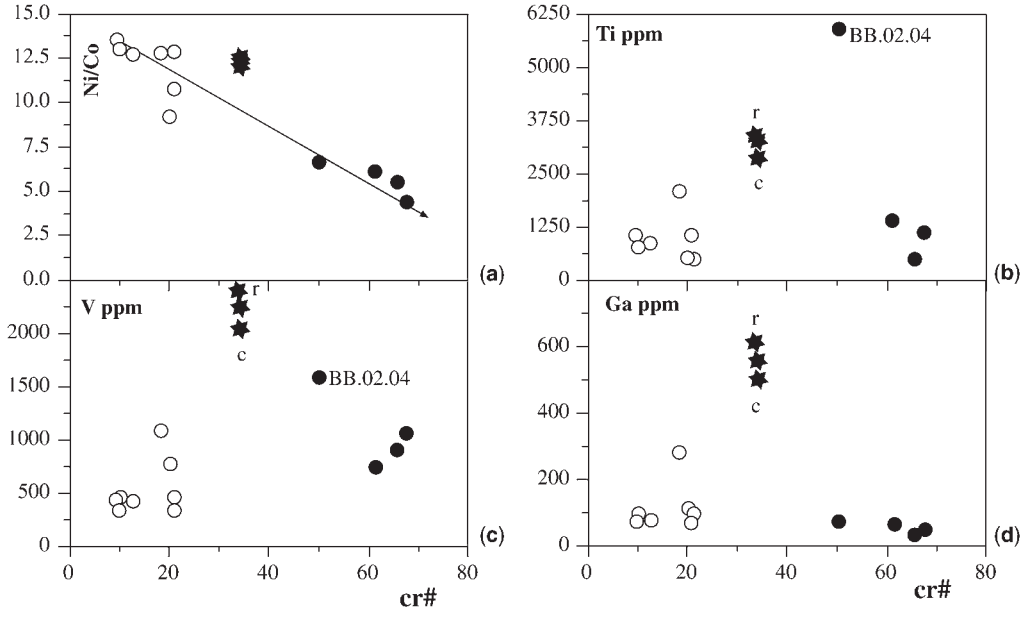

Fig. 11. The cr-number for spinel v. (**a**) Ni/Co ratio, (**b**) Ti, (**c**) V and (**d**) Ga c and r, core and rim compositions, respectively.

2004), but interpretations are controversial. Bianchini *et al.* (2007) considered the isotopic compositions to be related to Permo-Triassic metasomatism, whereas Bodinier *et al.* (2004) favoured their linkage to the much older harzburgite petrogenesis. Finally, McPherson *et al.* (1996) and Woodland *et al.* (1996) suggested an earlier carbonatite metasomatism overprinted by the Cretaceous alkaline–silicate metasomatim in the Lherz massif. Woodland *et al.* also found increasing fO_2 related to the carbonatite metasomatism. However, the results of this study do not provide evidence of fO_2 increase in the carbonatite metasomatized xenoliths, with respect to the Fe–Ti metasomatized sample BB.02.04. Therefore, although multistage metasomatism in harzburgites cannot be completely discarded, the single-stage percolation–reaction model should be favoured for its simplicity.

Metasomatism in lherzolites. The slight evidence of metasomatism in some lherzolites has been related by Bianchini *et al.* (2007) to a subalkaline basic metasomatizing agent, comparable with the Triassic dolerites in the Pyrenees. This would explain the slight LREE enrichment and depleted isotopic compositions of lherzolites. However, those workers did not discard the influence of other alkaline metasomatizing agents, to explain the high LREE fractionation of some clinopyroxene and coexisting amphibole (Bianchini *et al.* 2007, sample Olt8, figs 5 and 6; and our samples BB.64.04 and SD.98.2 in Fig. 10a). Here it is suggested that the Cretaceous alkaline silicate-melt metasomatism could account for all these characteristics, if chromatographic fractionation or reaction took place. In such a case, the lherzolites would be less affected, because they were at greater distance from the dykes. Thus, the amphibole of sample BB.81.04, at equilibrium with coexisting clinopyroxene (Fig. 12a) and depleted of LREE, except for La, would be formed by reaction between a distal lherzolite and a 'residual' late-stage percolating hydrous fluid, depleted of Rb, Th, U, LREE and Zr, because of earlier crystallization of amphibole ± phlogopite (Vannucci *et al.* 1995; Zanetti *et al.* 1996; Ionov *et al.* 1997; Pearson *et al.* 2003; Bodinier *et al.* 2004). This, together with a probably high rock/melt ratio and short time elapsed since the metasomatism, would not affect the primary depleted isotopic composition of lherzolites.

Glass in veins. Glass filling veins has been related to mantle metasomatism as (1) the witness of the infiltrating melt (Edgar *et al.* 1989; Zinngrebe & Foley 1995; Draper & Green 1997); (2) an *in situ* breakdown product of previous metasomatic phases (e.g. amphibole, phlogopite ±

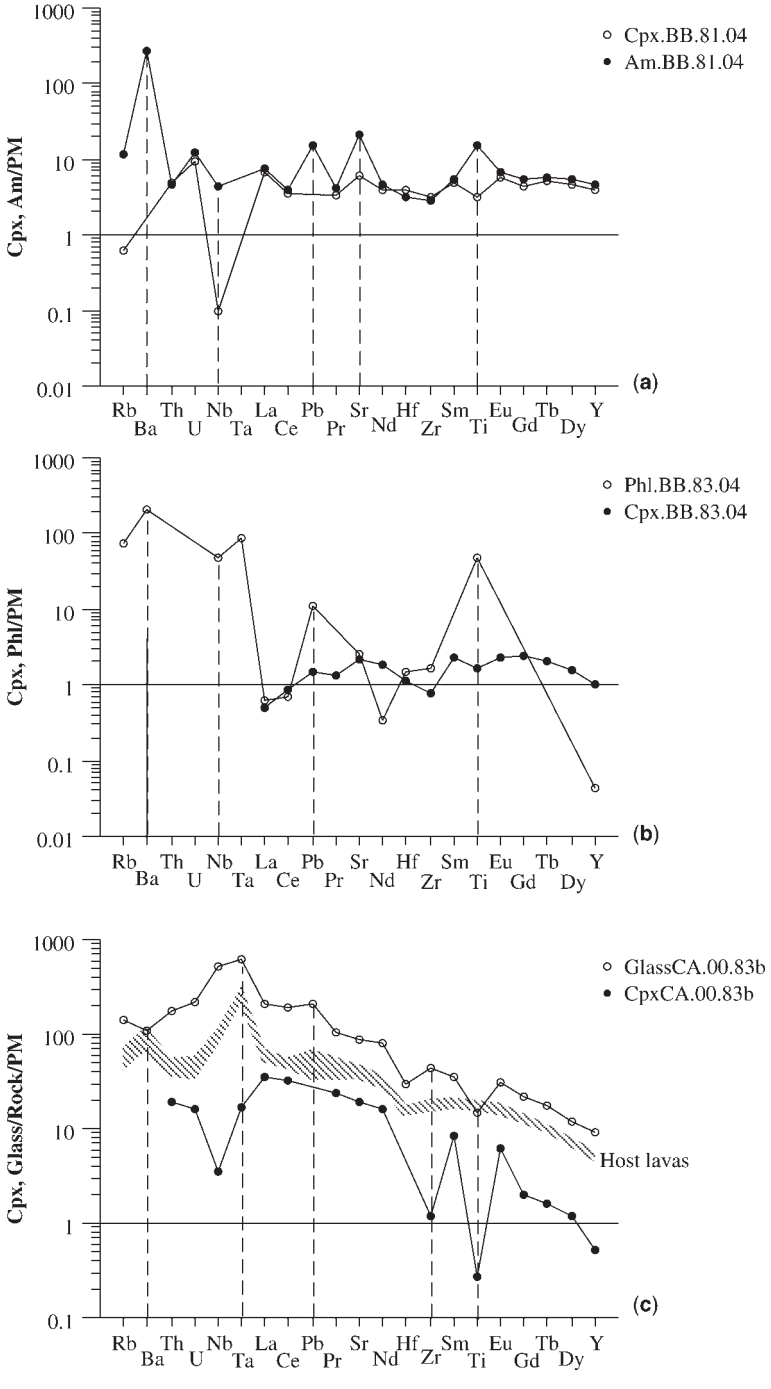

Fig. 12. (**a**) Multielement patterns for coexisting clinopyroxene and amphibole of a coarse granular lherzolite; (**b**) multielement patterns for coexisting clinopyroxene and phlogopite of a pyroxenite; (**c**) multielement patterns for vein glass and clinopyroxene of a coarse granular harzburgite, and for the host lavas (Cebriá *et al.* 2000).

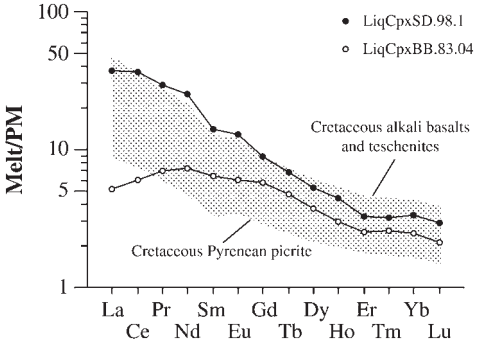

Fig. 13. REE patterns of melts in equilibrium with the pyroxenites, compared with the REE pattern range between the Cretaceous picrite HAB-69 and teschenite BLU-A of Rossy *et al.* (1992) from the Pyrenees. REE partition coefficients for clinopyroxene used in the estimations are La 0.062–0.096, Ce 0.097–0.139, Pr 0.142–0.191, Nd 0.196–0.248, Sm 0.305–0.346, Eu 0.351–0.380, Gd 0.392–0.406, Tb 0.425–0.421, Dy 0.449–0.425, Ho 0.461–0.418, Er 0.462–0.404, Tm 0.456–0.386, Yb 0.445–0.365, Lu 0.431–0.344, for samples SD.98.1 and BB.83.04, respectively.

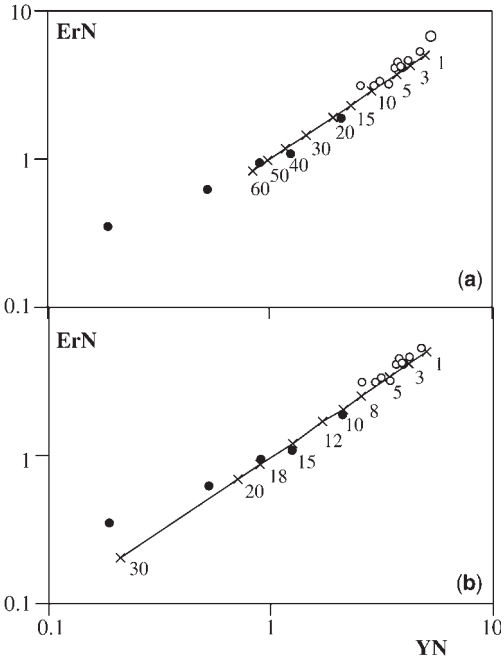

Fig. 14. Er_N v. Y_N of relict clinopyroxene for batch melting (**a**) and fractional melting (**b**). Numbers indicate degree of melting. Other symbols as in Figure 4. D^{Er}, cpx and D^{Y}, cpx used in the modelling were 0.485 and 0.495, respectively.

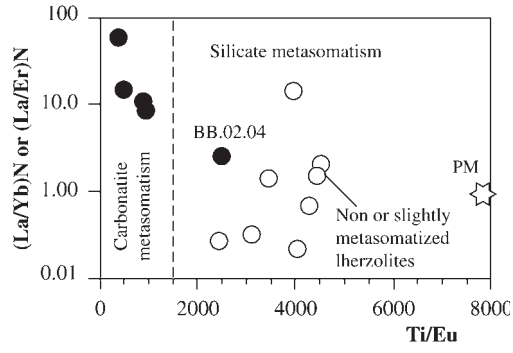

Fig. 15. $(La/Yb)_N$ or $(La/Er)_N$ v. Ti/Eu, with the fields of the carbonatite and silicate metasomatism (Coltorti *et al.* 1999).

clinopyroxene) (Chazot *et al.* 1996; Yaxley *et al.* 1997); or (3) the product reaction of between pristine mantle assemblages and infiltrating metasomatic components (Neumann & Wulff-Pedersen 1997; Coltorti *et al.* 2000). Regarding the shortage of data in this study, the first hypothesis could be excluded, as the glass in harzburgite CA.00.83b, with clinopyroxene showing a carbonatite metasomatic signature, has high enough REE contents to explain the extreme LREE enrichment of the clinopyroxene, but it is very enriched in HFSE to account for the clinopyroxene negative anomalies for these elements (Fig. 12c). On the other hand, an origin as *in situ* breakdown product of earlier amphibole and clinopyroxene could be plausible: its Ce/Pb, Ba/Th, Ti/Eu and U/Nb ratios (Table 8) are intermediate between those of the metasomatized clinopyroxene and amphibole in xenolith BB.81.04 (Yaxley & Kamenetsky 1999). However, this implies that glass post-dates the main metasomatism, although it should be borne in mind that glass does not appear as a breakdown product in amphibole coronae of sample BB.81.04, but plagioclase (Fig. 3g). Finally, regarding the third hypothesis, all Na_2O/K_2O ratio v. normative quartz + orthopyroxene or nepheline + leucite composition, and $TiO_2 + K_2O$ v. $CaO + Na_2O$ composition multielement patterns (Fig. 12c), together with the Rb/Ba (0.12), $(Zr/Sm)_N$ (1.24) and $(Ti/Eu)_N$ (0.48) ratios of glass (Table 8), fit with a reactive Na-alkali silicate melt (Coltorti *et al.* 2000), close to the limit with a carbonatite melt. Therefore, the third hypothesis could also be likely, but the reactive metasomatic melt could be also linked to the host alkaline lava, which would explain the glass preservation (Shaw & Klügel 2002).

Conclusions

The results of this study lead to the following conclusions on the SCLM of NE Spain.

(1) It is mainly formed of anhydrous spinel lherzolites and harzburgites, without any significant gap between them. Minor pyroxenites are also found.

(2) Melt depletion, probably linked to mantle decompression and starting within the garnet lherzolite field, affected the peridotites. Either low degree of batch melting or fractional melting (<10%) could explain the fertility decreases of lherzolites, and up to 30% of fractional melting could account for the most refractory harzburgites.

(3) Subsequent metasomatism affected especially the harzburgites, but also some lherzolites. Only the sporadic presence of amphibole or phlogopite reflects modal metasomatism, whereas the other chemical changes could be related to cryptic metasomatism.

(4) Two main styles of metasomatism can be identified in the harzburgites, one generated by interaction with an alkaline silicate melt and the other by percolation and chromatographic fractionation of a carbonatite melt. However, both metasomatizing agents could be linked, in space and time, by a chromatographic fractionation and reaction process at deacreasing melt mass, leading to the evolution of the initial alkaline melt and to the formation of the carbonate-rich derivatives. Upper Cretaceous alkaline magmas cropping out in the area as lamprophyres are the most likely metasomatizing components.

(5) The slighter evidence of metasomatism observed in lherzolites could be also due to the same metasomatic event, if a chromatographic fractionation or reaction process is assumed.

(6) Only occasional xenoliths showing heterogeneous mineral compositions along with interstitial glass, and the presence of sporadic veins filled with glass could be linked to metasomatism caused by reaction with the host lava.

This study benefited from the support of the European Community Access to Research Infrastructure Action for the Improving of Human Potential Programme, contract HPRI-CT-1999-00008 awarded to B. J. Wood (EU Geochemical Facility, University of Bristol), from a MEC grant (PR2004-0059) to G.G., a DURSI grant to V.O. and from the MCT project BTE2003-08653-C02-01. Comments on an earlier version of this manuscript by M. Grégoire were especially helpful, as were those by J.-M. Dautria and J. C. Garrido.

References

ALIBERT, C. 1985. A Sr–Nd isotope and REE study of late Triassic dolerites from the Pyrenees (France) and the Messejana Dyke (Spain and Portugal). *Earth and Planetary Science Letters*, **73**, 81–90.

ARAÑA, V., APARICIO, A., MARTÍN ESCORZA, C., *ET AL.* 1983. El volcanismo neógeno-cuaternario de Catalunya: caracteres estructurales, petrológicos y geodinámicos. *Acta Geológica Hispánica*, **18**, 1–17.

BECCALUVA, L., BIANCHINI, G., BONADIMAN, C., SIENA, F. & VACCARO, C. 2004. Coexisting anorogenic and subduction-related metasomatism in mantle xenoliths from the Betic Cordillera (southern Spain). *Lithos*, **75**, 67–68.

BEDINI, R. M., BODINIER, J.-L., DAUTRIA, J.-M. & MORTEN, L. 1997. Evolution of LILE-enriched small melt fractions in the lithospheric mantle: a case study from the East African Rift. *Earth and Planetary Science Letters*, **153**, 67–83.

BIANCHINI, G., BECCALUVA, L., BONADIMAN, C., NOWELL, G., PEARSON, G., SIENA, F. & WILSON, M. 2007. Evidence of diverse depletion and metasomatic events in harzburgite–lherzolite mantle xenoliths from the Iberian plate (Olot, NE Spain): Implications for lithosphere accretionary processes. *Lithos*, **94**, 25–45.

BLUNDY, J. & DALTON, J. 2000. Experimental comparison of trace element partitioning between clinopyroxene and melt in carbonate and silicate systems, and implications for mantle metasomatism. *Contributions to Mineralogy and Petrology*, **139**, 356–371.

BODINIER, J.-L., FABRIÈS, J., LORAND, J.-P., DOSTAL, J. & DUPUY, C. 1987*a*. Geochemistry of amphibole pyroxenite veins from the Lherz and Freychinède ultramafic bodies (Ariège, French Pyrenees). *Bulletin de Minéralogie*, **110**, 345–358.

BODINIER, J.-L., GUIRAUD, M., FABRIÈS, J., DOSTAL, J. & DUPUY, C. 1987*b*. Petrogenesis of layered pyroxenites from the Lherz, Freychinède and Prades ultramafic bodies (Ariège, French Pyrenees). *Geochimica et Cosmochimica Acta*, **51**, 279–290.

BODINIER, J.-L., DUPUY, C. & DOSTAL, J. 1988. Geochemistry and petrogenesis of Eastern Pyrenean peridotites. *Geochimica et Cosmochimica Acta*, **52**, 2893–2907.

BODINIER, J.-L., VASSEUER, G., VERNIERES, J., DUPUY, C. & FABRIÈS, J. 1990. Mechanisms of mantle metasomatism: geochemical evidence from the Lherz orogenic peridotite. *Journal of Petrology*, **31**, 597–628.

BODINIER, J.-L., MENZIES, M. A., SHIMIZU, N., FREY, F. A. & MCPHERSON, E. 2004. Silicate, hydrous and carbonate metasomatism at Lherz, France: contemporaneous derivatives of silicate melt–harzburgite reaction. *Journal of Petrology*, **45**, 299–320.

BREY, G. P. & KÖHLER, T. 1990. Geothermobarometry in four-phase lherzolites II. New thermobarometers, and practical assessment of existing thermobarometers. *Journal of Petrology*, **31**, 1353–1378.

CARPENTER, R. L., EDGAR, A. D. & THIBAULT, Y. 2004. Origin of spongy textures in clinopyroxene and spinel from mantle xenoliths, Hessian Depression, Germany. *Mineralogy and Petrology*, **74**, 149–162.

CEBRIÁ, J. M., LÓPEZ-RUIZ, J., DOBLAS, M., OYARZUN, R., HERTOGEN, J. & BENITO, R. 2000. Geochemistry of the Quaternary alkali basalts of Garrotxa (NE Volcanic Province, Spain): a case of double

enrichment of the mantle lithosphere. *Journal of Volcanology and Geothermal Research*, **102**, 217–235.

CHAZOT, G., MENZIES, M. & HARTE, B. 1996. Silicate glasses in spinel lherzolites from Yemen: origin and chemical composition. *Chemical Geology*, **134**, 159–179.

COLTORTI, M., BONADIMAN, C., HINTON, R. W., SIENA, F. & UPTON, B. G. J. 1999. Carbonatite metasomatism of the oceanic upper mantle: evidence from clinopyroxenes and glasses in ultramafic xenoliths of Grande Comore, Indian Ocean. *Journal of Petrology*, **40**, 133–165.

COLTORTI, M., BECCALUVA, L., BONADIMAN, O., SALVINI, L. & SIENA, F. 2000. Glasses in mantle xenoliths as geochemical indicators of metasomatic agents. *Earth and Planetary Science Letters*, **183**, 303–320.

DEER, W. A., HOWIE, R. A. & ZUSSMAN, J. 1992. *An Introduction to The Rock-Forming Minerals*. Pearson Prentice Hall, Harlow.

DONVILLE, B. 1973*a*. Ages potassium–argon des vulcanites du Haut Ampurdan (Nord-Est de l'Espagne). Implications stratigraphiques. *Comptes Rendus de l'Académie des Sciences*, **276**, 2497–2500.

DONVILLE, B. 1973*b*. Ages potassium–argon des vulcanites du Bas Ampurdan. *Comptes Rendus de l'Académie des Sciences*, **276**, 3253–3256.

DONVILLE, B. 1973*c*. Ages potassium–argon des roches volcaniques de la depression de La Selva (NE de l'Espagne). *Comptes Rendus de l'Académie des Sciences*, **277**, 1–4.

DOWNES, H. 2001. Formation and modification of the shallow sub-continental lithospheric mantle: a review of geochemical evidence from ultramafic xenolith suites and tectonically emplaced ultramafic massifs of Western and Central Europe. *Journal of Petrology*, **42**, 233–250.

DOWNES, H., REICHOW, M. K., MASON, P. R. D., BEARD, A. D. & THIRLWALL, M. F. 2003. Mantle domains in the lithosphere beneath the French Massif Central: trace element and isotopic evidence from mantle clinopyroxenes. *Chemical Geology*, **200**, 71–87.

DRAPER, D. S. & GREEN, T. H. 1997. *P–T* phase relations of silicic, alkaline, aluminous mantle-xenolith glasses under anhydrous and C–O–H fluid-saturated conditions. *Journal of Petrology*, **38**, 1187–1224.

DROOP, G. T. R. 1987. A general equation for estimating Fe^{3+} in ferromagnesian silicates and oxides from microprobe analysis, using stoichiometry criteria. *Mineralogical Magazine*, **51**, 431–437.

DUPUY, C., LIOTARD, J. M. & DOSTAL, J. 1992. Zr/Hf fractionation in intraplate basaltic rocks: carbonate metasomatism in the mantle source. *Geochimica et Cosmochimica Acta*, **56**, 2417–2423.

EDGAR, A. D., LLOYD, F. E., FORSYTH, D. M. & BARNETT, R. L. 1989. Origin of glass in upper-mantle xenoliths from the Quaternary volcanics SE of Gees, West Eifel, Germany. *Contributions to Mineralogy and Petrology*, **103**, 277–286.

FABRIÈS, J., FUIGUEROA, O. & LORAND, J. P. 1987. Petrology and thermal history of highly deformed mantle xenoliths from the Montferrier basanites, Languedoc, southern France: a comparison with ultramafic complexes from the north Pyrenean zone. *Journal of Petrology*, **28**, 887–919.

FÉMÉNIAS, O., COUSSAERT, N., BERGER, J., MERCIER, J.-C. C. & DEMAIFFE, D. 2004. Metasomatism and melting history of a Variscan lithospheric mantle domain: evidence from the Puy Beaunit xenoliths (French Massif Central). *Contributions to Mineralogy and Petrology*, **148**, 13–28.

FREY, F. A. & PRINZ, M. 1978. Ultramafic inclusions from San Carlos, Arizona: Petrologic and geochemical data bearing on their petrogenesis. *Earth and Planetary Science Letters*, **38**, 129–176.

GALÁN, G. 2004. Partial melting and metasomatism in the subcontinental lithospheric mantle of NE Spain. *Geochimica et Cosmochimica Acta*, **68**, A723.

GALÁN, G., OLIVERAS, V. & PATERSON, B. 2006. Types of metasomatism in ultramafic xenoliths enclosed in Neogene Quaternary alkaline mafic lavas from Catalonia (NE Spain). *Geophysical Research Abstracts*, **8**, abstract number 05961.

GASPARIK, T. 1987. Orthopyroxene thermobarometry in simple and complex systems. *Contributions to Mineralogy and Petrology*, **96**, 357–370.

GRÉGOIRE, M., MOINE, B. N., O'REILLY, S. Y., COTTIN, J. Y. & GIRET, A. 2000. Trace element residence and partitioning in mantle xenoliths metasomatised by highly alkaline, silicate- and carbonate-rich melts (Kerguelen Islands, Indian Ocean). *Journal of Petrology*, **41**, 477–509.

HART, S. R. & DUNN, T. 1993. Experimental cpx/melt partitioning of 24 trace elements. *Contributions to Mineralogy and Petrology*, **113**, 1–8.

HARTE, B. 1977. Rock nomenclature with particular relation to deformation and recrystallisation textures in olivine-bearing xenoliths. *Journal of Geology*, **85**, 279–288.

IONOV, D. I., DUPUY, C., O'REILLY, S. Y., KOPYLOVA, M. G. & GENSHAFT, Y. S. 1993. Carbonated peridotite xenoliths from Spitsbergen: implications for trace element signature of mantle carbonate metasomatism. *Earth and Planetary Science Letters*, **119**, 283–297.

IONOV, D. A., GRIFFIN, W. L. & O'REILLY, Y. O. 1997. Volatile-bearing minerals and lithophile trace elements in the upper mantle. *Chemical Geology*, **141**, 153–184.

KÖHLER, T. P. & BREY, G. P. 1990. Calcium exchange between olivine and clinopyroxene calibrated as a geothermobarometer for natural peridotites from 2 to 60 kb with applications. *Geochimica et Cosmochimica Acta*, **54**, 2375–2388.

KRETZ, R. 1983. Symbols for rock forming minerals. *American Mineralogist*, **68**, 277–279.

LAGO, M., ARRANZ, E., POCOVÍ, A., GALÉ, C. & GIL-IMAZ, A. 2004. Permian magmatism and basin dynamics in the southern Pyrenees: a record of the transition from late Variscan transtension to early Alpine extension. *In*: WILSON, M., NEUMANN, E.-R., DAVIES, G. R., TIMMERMAN, M. J., HEEREMANS, M. & LARSEN, B. T. (eds) *Permo-Carboniferous Magmatism and Rifting in Europe*. Geological Society, London, Special Publications, **223**, 439–464.

LAURORA, A., MAZZUCHELLI, M., RIVALENTI, G., VANNUCCI, R., ZANETTI, A., BARBIERI, M. A. & GINCOLANI, C. A. 2001. Metasomatism and melting in carbonated peridotite xenoliths from the mantle wedge: the Gobernador Gregores case (southern Patagonia). *Journal of Petrology*, **42**, 69–87.

LEAKE, B. E. 1997. Nomenclature of amphiboles: report of the subcommittee on amphiboles of the International Mineralogical Association, commission on new minerals and mineral names. *Canadian Mineralogist*, **35**, 219–246.

LE MAITRE, R. W. 2002. *Igneous Rocks; A Classification and Glossary of Terms*. Cambridge University Press, Cambridge.

LENOIR, X., GARRIDO, C. J., BODINIER, J. L. & DAUTRIA, J. M. 2000. Contrasting lithospheric mantle domains beneath the Massif Central (France) revealed by geochemistry of peridotite xenoliths. *Earth and Planetary Science Letters*, **181**, 359–375.

LIERMANN, H. P. & GANGULY, J. 2003. Fe^{2+}–Mg fractionation between orthopyroxene and spinel: experimental calibration in the system FeO–MgO–Al_2O_3–Cr_2O_3–SiO_2, and applications. *Contributions to Mineralogy and Petrology*, **145**, 217–227.

LLOVET, X. & GALÁN, G. 2003. Correction of secondary X-ray fluorescence near grain boundaries in electron microprobe analysis: Application to thermobarometry of spinel lherzolites. *American Mineralogist*, **88**, 121–130.

LÓPEZ RUIZ, J. & RODRÍGUEZ BADIOLA, E. 1985. La Región Volcánica Mio-Pleistocena del NE de España. *Estudios Geológicos*, **41**, 105–126.

MARTÍ, J., MITJAVILLA, J., ROCA, E. & APARICIO, A. 1992. Cenozoic magmatism of the Valencia trough (western Mediterranean): relationship between structural evolution and volcanism. *Tectonophysics*, **203**, 145–165.

MCDONOUGH, W. F. 1990. Constraints on the composition of the continental lithospheric mantle. *Earth and Planetary Science Letters*, **101**, 1–18.

MCDONOUGH, W. F. & SUN, S.-S. 1995. The composition of the Earth. *Chemical Geology*, **120**, 223–253.

MCPHERSON, E., THIRLWALL, M. F., PARKINSON, L. J., MENZIES, M. A., BODINIER, J.-L., WOODLAND, A. & BLUSSOD, G. 1996. Geochemistry of metasomatism adjacent to amphibole-bearing veins in the Lherz peridotite massif. *Chemical Geology*, **134**, 135–157.

MERCIER, J. C. C. & NICOLAS, A. 1975. Textures and fabrics of upper mantle peridotites as illustrated by xenoliths from basalts. *Journal of Petrology*, **16**, 454–487.

MORIMOTO, N. 1988. Nomenclature of pyroxenes. *Mineralogy and Petrology*, **39**, 55–76.

NEUMANN, E.-R. & WULFF-PEDERSEN, E. 1997. The origin of highly silicic glass in mantle xenoliths from the Canary Islands. *Journal of Petrology*, **38**, 1513–1539.

NORMAN, M. D. 1998. Melting and metasomatism in the continental lithosphere: laser ablation ICPMS analysis of minerals in spinel lherzolites from eastern Australia. *Contributions to Mineralogy and Petrology*, **130**, 240–255.

OLIVERAS, V. & GALÁN, G. 2006. Petrologia y mineralogia de los xenolitos mantélicos del volcán la Banya del Boc (Girona). *Geogaceta*, **40**, 107–110.

O'NEILL, H. St. C. 1981. The transition between spinel lherzolite and garnet lherzolite, and its use as a geobarometer. *Contributions to Mineralogy and Petrology*, **77**, 185–194.

PEARSON, D. G., CANIL, D. & SHIREY, S. B. 2003. Mantle samples included in volcanic rocks: xenoliths and diamonds. *In*: CARLSON, R. W. (ed.) *Treatise on Geochemistry, Volume 2*. Elsevier, Amsterdan, 171–275.

PERINI, G., CEBRIÁ, J. M., LÓPEZ-RUIZ, J. & DOBLAS, M. 2004. Carboniferous–Permian mafic magmatism in the Variscan belt of Spain and France: implications for mantle sources. *In*: WILSON, M., NEUMANN, E.-R., DAVIES, G. R., TIMMERMAN, M. J., HEEREMAN, M. & LARSEN, B. T. (eds) *Permo-Carboniferous Magmatism and Rifting in Europe.* Geological Society, London, Special Publications, **223**, 415–438.

ROBINSON, P., SPEAR, F. S., SCHUMACHER, J. C., LAIRD, J., CORNELIS, K., EVANS, B. W. & DOULAN, L. 1982. Phase relations of metamorphic amphiboles: Natural occurrence and theory. *In*: VLEBEN, D. R. & RIBBE, P. H. (eds) *Amphiboles: Petrology and Experimental Phase Relations.* Mineralogical Society of America, Reviews in Mineralogy, **9B**, 1–227.

ROBINSON, J. A. C., WOOD, B. J. & BLUNDY, J. D. 1998. The beginning of melting of fertile and depleted peridotite at 1.5 GPa. *Earth and Planetary Science Letters*, **155**, 97–111.

ROSSY, M., AZAMBRE, B. & ALBARÉDE, F. 1992. REE and Sr–Nd isotope geochemistry of the alkaline magmatism from the Cretaceous North Pyrenean Rift Zone (France–Spain). *Chemical Geology*, **97**, 33–46.

SEYLER, M. & BONATTI, E. 1994. Na, Al^4 and Al^6 in clinopyroxenes of continental and suboceanic ridge peridotites: a clue to different melting process in the mantle? *Earth and Planetary Science Letters*, **122**, 281–289.

SHAW, C. S. J. & KLÜGEL, A. 2002. The pressure and temperature conditions and timing of glass formation in mantle-derived xenoliths from Baarley, West Eifel, Germany: the case for amphibole breakdown, lava infiltration and mineral–melt reaction. *Mineralogy and Petrology*, **74**, 163–187.

SOLÉ, J., PI, T. & ENRIQUE, P. 2003. New geochemical data on the Late Cretaceous alkaline magmatism of the northeast Iberian Peninsula. *Cretaceous Research*, **24**, 135–140.

SOLÉ SUGRAÑÉS, L., JULIÁ, R. & ANADÓN, P. 1984. El sistema de fosas neógenas del NE de la Península Ibérica. *In*: LÓPEZ-RUIZ, J. (ed.) *El borde mediterráneo español: evolución del orógeno bético y geodinámica de las depresiones neógenas*. CSIC, Granada, 87–91.

TAKAHASHI, E., SHIMAZAKI, T., TSUZAKI, Y. & YOSHIDA, H. 1993. Melting study of a peridotite KLB-1 to 6.5 GPa, and the origin of basaltic magmas. *Philosophical Transactions of the Royal Society of London, Series A*, **342**, 105–120.

TOURNON, J. 1968. *Le volcanisme de la province de Gérone (Espagne). Études de basaltes quaternaires et de leurs enclaves*. Thèse 3e cycle, Université de Paris.

VANNUCCI, R., PICARDO, G. B., RIVALENTI, G., *ET AL*. 1995. Origin of LREE-depleted amphiboles in the subcontinental mantle. *Geochimica et Cosmochimica Acta*, **59**, 1763–1771.

WEBB, S. A. C. & WOOD, B. J. 1986. Spinel–pyroxene–garnet relationship and their dependence on Cr/Al ratio. *Contributions to Mineralogy and Petrology*, **92**, 471–480.

WILSON, M. & DOWNES, H. 1991. Tertiary–Quaternary extension–related alkaline magmatism in Western and Central Europe. *Journal of Petrology*, **32**, 811–849.

WITT-EICKSCHEN, G., SECK, H. A. & REYS, C. H. 1993. Multiple enrichment processes and their relationships in the subcrustal lithosphere beneath the Eifel (Germany). *Journal of Petrology*, **34**, 1–22.

WOOD, B. J. 1991. Oxygen barometry of spinel peridotites. *In*: LINDSLEY, D. H. (ed.) *Oxide Minerals: Petrologic and Magnetic Significance*. Mineralogical Society of America, Reviews in Mineralogy, **25**, 417–431.

WOOD, B. J. & BLUNDY, J. D. 1997. A predictive model for rare earth elements between clinopyroxene and anhydrous silicate melt. *Contributions to Mineralogy and Petrology*, **129**, 166–181.

WOOD, B. J., TARAS BRYNDZIA, L. & JOHNSON, K. E. 1990. Mantle oxidation state and its relationship to tectonic environment and fluid speciation. *Science*, **248**, 337–345.

WOODLAND, A. B., KORNPROBST, J., MCPHERSON, E., BODINIER, J. L. & MENZIES, M. A. 1996. Metasomatic interactions in the lithospheric mantle: petrologic evidence from the Lherz massif, French Pyrenees. *Chemical Geology*, **134**, 83–112.

YAXLEY, G. M. & KAMENETSKY, V. 1999. *In situ* origin for glass in mantle xenoliths from southeastern Australia: insights from trace element compositions of glasses and metasomatic phases. *Earth and Planetary Science Letters*, **172**, 97–109.

YAXLEY, G. M., KAMENETSKY, V., GREEN, D. H. & FALLOON, T. J. 1997. Glasses in mantle xenoliths from western Victoria, Australia, and their relevance to mantle processes. *Earth and Planetary Science Letters*, **148**, 433–446.

YAXLEY, G. M., GREEN, D. H. & KAMENETSKY, V. 1998. Carbonatite metasomatism in the southeastern Australian lithosphere. *Journal of Petrology*, **39**, 1917–1930.

ZANETTI, A., VANNUCCI, R., BOTTAZZI, P., OBERTI, R. & OTTOLINI, L. 1996. Infiltration metasomatism at Lherz as monitored by systematic ion–microprobe investigations close to a hornblendite vein. *Chemical Geology*, **134**, 113–133.

ZANGANA, N. A., DOWNES, H., THIRLWALL, M. F., MARRINER, G. F. & BEA, F. 1999. Geochemical variation in peridotite xenoliths and their constituent clinopyroxenes from Ray Pic (French Massif Central): implications for the composition of the shallow lithospheric mantle. *Chemical Geology*, **153**, 11–35.

ZHANG, M., SUDDABY, P., O'REILLY, S. Y., NORMAN, M. & QIU, J. 2000. Nature of the lithospheric mantle beneath the eastern part of the Central Asian fold belt: mantle xenolith evidence. *Tectonophysics*, **328**, 131–156.

ZINNGREBE, E. & FOLEY, S. F. 1995. Metasomatism in mantle xenoliths from Gees, West Eifel, Germany: evidence for the genesis of calc-alkaline glasses and metasomatic Ca- enrichment. *Contributions to Mineralogy and Petrology*, **122**, 79–96.

Plume-related stable isotope compositions and fluid–rock interaction processes in the Basal Complex of La Palma, Canary Islands, Spain

A. DEMÉNY[1], R. CASILLAS[2], T. W. VENNEMANN[3], E. HEGNER[4], G. NAGY[1], A. AHIJADO[2], J. DE LA NUEZ[2], P. SIPOS[1], S. PILET[3] & J. MILTON[5]

[1]*Institute for Geochemical Research, Hungarian Academy of Sciences, Budapest, Budaörsi út 45., H-1112, Hungary (e-mail: demeny@geochem.hu)*

[2]*Dpto. de Edafologia y Geologia, Universidad de La Laguna, Avda. Astrofisico Fco. Sánchez, 38206 La Laguna, Tenerife, Spain*

[3]*Institut de Minéralogie et Géochimie, Université de Lausanne, L'Anthropole, CH-1015 Lausanne, Switzerland*

[4]*Institute for Mineralogy, Petrology and Geochemistry, University of München, Theresienstrasse 41/III, D-80333 München, Germany*

[5]*School of Ocean and Earth Science, Southampton Oceanography Centre, European Way, Empress Dock, Southampton SO14 3ZH, UK*

Abstract: Chemical and isotopic compositions of amphiboles, biotites, pyroxenes and feldspars from gabbros and basalts of La Palma, Canary Islands, were studied to determine primary, plume-related compositions and effects of late-stage water–rock interactions. All the studied amphiboles have Sr isotope ratios close to those typical for the mantle, excluding the possibility of significant seawater influence. The pyroxenes and amphiboles also have stable isotope compositions that are typical for mantle-derived phases, whereas biotites and feldspars show signs of interaction with meteoric water. On the basis of the oxygen isotopic compositions, the infiltrating meteoric water derived from precipitation at an approximate elevation of 3500 m above sea level, indicating that La Palma reached this height when the gabbro complexes were formed. The unaltered hydrogen and oxygen isotope compositions of amphiboles show a trend from normal mantle ranges to −90‰ and 5.1‰, respectively; these values are very close to compositions found in other Canary Island complexes by earlier studies, and support the theory that these compositions reflect a plume component originating from depth, rather than local phenomena.

The geochemical characteristics of volcanic rocks from ocean islands are particularly interesting for research on the Earth's mantle as these rocks originate from the deep mantle and hence may provide a unique insight into the evolution of this region. Early studies on ocean island basalts (OIB) observed a slight ^{18}O depletion (Garcia *et al.* 1989; Harmon & Hoefs, 1995) compared with normal upper mantle compositions largely defined by mid-oceanic ridge basalts (MORB) (e.g. Kyser 1986; Mattey *et al.* 1994), although other researchers have argued against any significant primary difference and attributed the decreased ^{18}O content to assimilation of ocean crust that had experienced high-temperature interaction with seawater (Eiler *et al.* 1997; Garcia *et al.* 1998). However, a number of recent studies have supported a primary nature of low ^{18}O content in ocean island (Wiechert *et al.* 1997; Widom & Farquhar 2003; Thirlwall *et al.* 2006) and back-arc complexes (Macpherson *et al.* 2000) and mainly related this feature to recycling of oceanic crust through deep subduction and plume formation. Macpherson *et al.* (2000) suggested an alternative model with low $\delta^{18}O$ values originating from core–mantle interactions. This was later discussed by Thirlwall *et al.* (2006), and they negated ocean crust recycling as an explanation for primary, low $\delta^{18}O$ values in Icelandic rocks. Similar conclusions were supported by radiogenic isotope and trace element data for plume-related magmas indicating a possible component of subducted oceanic crust (e.g. Marcantonio *et al.* 1995; Roy-Barman & Allègre 1995; Widom *et al.* 1999; Sobolev *et al.* 2000).

The basaltic rocks of the submarine series and the first subaerial rocks of Fuerteventura, Canary Islands, contain amphiboles and phlogopites with

From: COLTORTI, M. & GRÉGOIRE, M. (eds) *Metasomatism in Oceanic and Continental Lithospheric Mantle.* Geological Society, London, Special Publications, **293**, 155–175.
DOI: 10.1144/SP293.8 0305-8719/08/$15.00

stable and radiogenic isotope compositions that are interpreted to reflect recycled ocean crust (Demény *et al.* 2004). Shallow-level crustal assimilation as the cause of low $\delta^{18}O$ values can be ruled out as H isotope analyses showed no evidence of a seawater influence (see Demény *et al.* 2004). Instead, the H isotope values are around −95‰, similar to values for other plume-related rocks of the region (Demény *et al.* 2004), and depleted in D relative to typical upper mantle with -70 ± 10‰ (e.g. Boettcher & O'Neil 1980; Kyser & O'Neil 1984; Kyser 1986; Agrinier *et al.* 1993). Demény *et al.* (2004) have raised the possibility that the observed D depletion is characteristic for plume material and may have originated from the deep mantle. H isotope compositions of ocean island basalts are far less frequently studied than O isotope compositions; in view of the sensitivity of the H isotope system to fluid–rock interactions this aspect certainly warrants further research. To examine whether the Fuerteventura volcanic rocks are typical of pristine plume material or simply reflect local alteration, additional plume-related rocks were collected from La Palma, and analysed.

Rocks of the Basal Complex of La Palma were chosen for study, as these rocks represent the initial stage of plume-related magmatic activity, similar to those studied in Fuerteventura. Gabbros of the Basal Complex representing different magmatic stages, as well as basalt-hosted xenoliths and megacrysts, were investigated for their H–O–Sr isotope and trace element compositions.

Geological background

La Palma (Fig. 1) is one of the westernmost and youngest islands of the Canarian Archipelago and it is still in the juvenile stage of development (Carracedo *et al.* 2001). Its geological history started in the Pliocene, when a submarine volcanic edifice was formed. This edifice is composed of pillow lavas, pillow breccias and hyaloclastites, intruded by plugs of gabbros and a dense dyke swarm (Hernández-Pacheco 1971; Hernández-Pacheco & Fernández-Santín 1974; Staudigel 1981; De la Nuez 1984; Staudigel & Schmincke 1984; Staudigel *et al.* 1986; Carracedo *et al.* 2001). The submarine volcanic edifice together with gabbro and dyke intrusions forms the so-called Basal Complex. After a period of uplift, tilting and erosion of the seamount, the subaerial volcanic activity started (Ancochea *et al.* 1994; Guillou *et al.* 1998, 2001; Carracedo et al. 1999*a*,*b*, 2001; Singer *et al.* 2002; Hildenbrand *et al.* 2003). This activity produced the Garafía shield volcano between 1.77 and 1.20 Ma (Ancochea *et al.* 1994; Carracedo *et al.* 2001). The rapid growth and progressive instability of this shield volcano culminated about 1.20 Ma ago in a gravitational landslide of the southern flank of the volcanic edifice, after which a new shield volcano (called Taburiente Volcano) was formed. This younger edifice again was partially destroyed by a new gravitational landslide 560 ka ago. In the interior of the new collapse basin, the Bejenado stratovolcano was formed, and was active until around 400 ka ago (Carracedo *et al.* 2001). During the last stage of volcanism on La Palma a north–south-trending rift was formed (Cumbre Vieja Volcano).

The submarine volcanic edifice of the Basal Complex of La Palma consists of trachytic breccias, overlain by a thick sequence of basaltic pillow lavas, pillow breccias and hyaloclastites. This sequence seems to be NW–SE oriented and dips 50° SW. The age of this unit, determined through the study of Foraminifera found in some hyaloclastites, is Pliocene (3–4 Ma). All these rocks are intruded by various NW–SE-trending gabbros, olivine gabbros, amphibole gabbros and alkali gabbros probably related to the subaerial edifices. The submarine volcanic rocks and gabbros are intruded by a network of basaltic dykes that represents up to 75% of the outcrops. The Basal Complex rocks have also been affected by an intense greenschist-facies hydrothermal metamorphism (Hernández-Pacheco & Fernández-Santín 1974; Staudigel 1981; Staudigel & Schmincke 1984; Schiffman & Staudigel 1994, 1995).

Samples and petrography

The studied samples were collected from several series and rock types. The localities are shown in Figure 1.

(1) Olivine-bearing gabbros (samples LP-02/9, LP-02/18, LP-02/19, LP-04/2, LP-04/4, LP-04/6, LP-04/7, LP-04/9, LP-04/11, LP-04/13 and LP-04/14). The gabbro is composed of idiomorphic, small olivine crystals, interstitial plagioclase, subidiomorphic pink and colourless clinopyroxene, interstitial oxides, kaersutite and biotite as overgrowths on pyroxene (Fig. 2a), and apatite included in kaersutite (Fig. 2b). Metamorphic minerals (related to the hydrothermal greenschist facies) include chlorite, epidote, calcite, albite, actinolite, serpentine and oxides. Sample LP-04/2 contains metamorphic actinolite crystals, which were separated and analysed for H and O isotope compositions. Sample LP-04/6 contains a vein of amphibole-bearing leucogabbro that contains idiomorphic kaersutite, biotite and plagioclase.

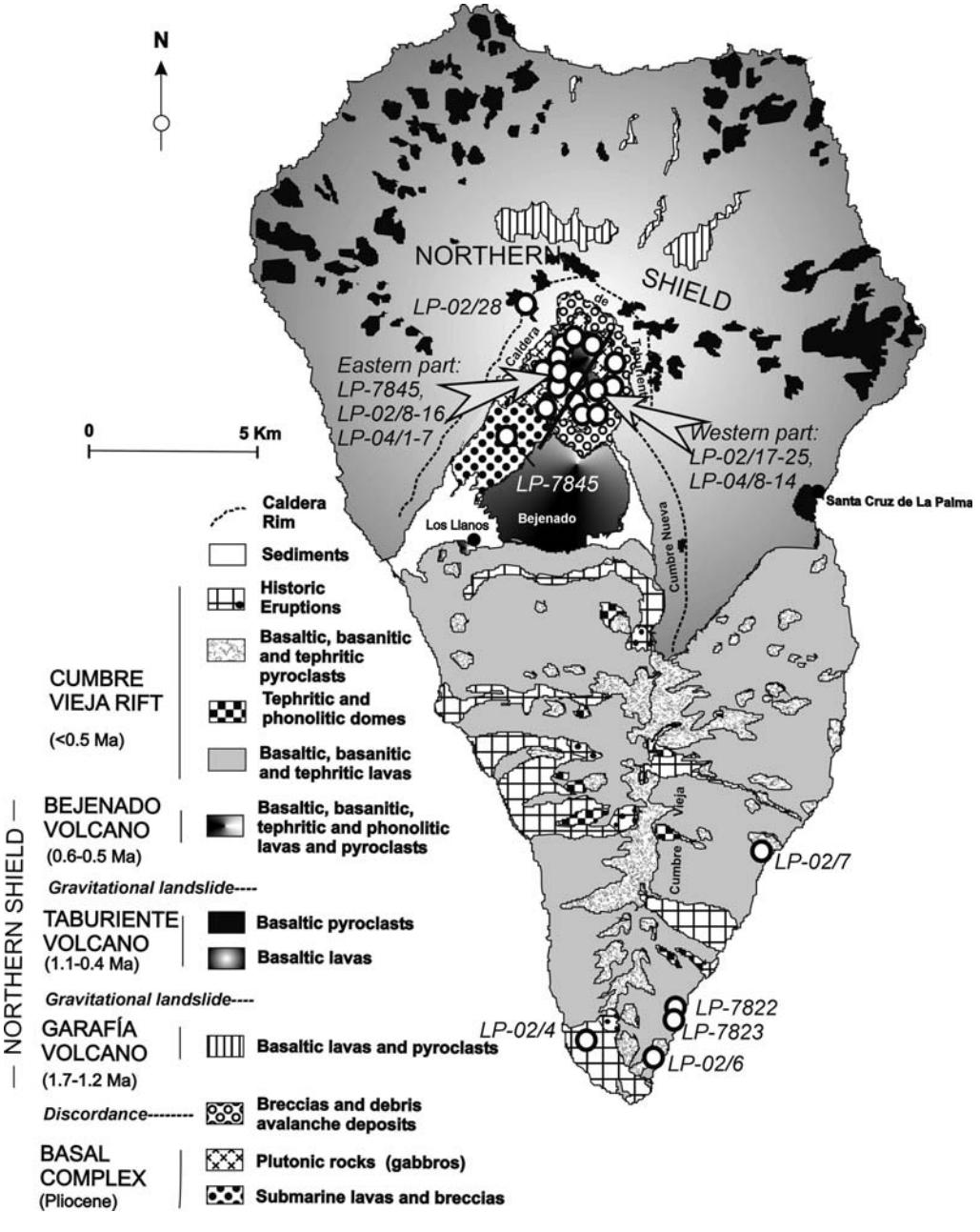

Fig. 1. Geological map of La Palma with sample localities (modified after Carracedo *et al.* 2001). The eastern–western division line in the Basal Complex is artificial and for presentation.

(2) Amphibole-bearing alkaline leucogabbros (samples LP-8359, LP-02/8, LP-02/12, LP-02/17, LP-04/1, LP-04/5, LP-04/10 and LP-04/12). The gabbro is composed of interstitial plagioclase, idiomorphic and prismatic pink clinopyroxene, interstitial oxides, idiomorphic kaersutite (Fig. 2c), idiomorphic biotite (Fig. 2d) and sphene, oxides and apatite as inclusions in kaersutite. Metamorphic minerals (related to the hydrothermal greenschist facies) include chlorite, epidote, calcite, albite, actinolite, serpentine and oxides. Sample LP-04/10 contains a vein of

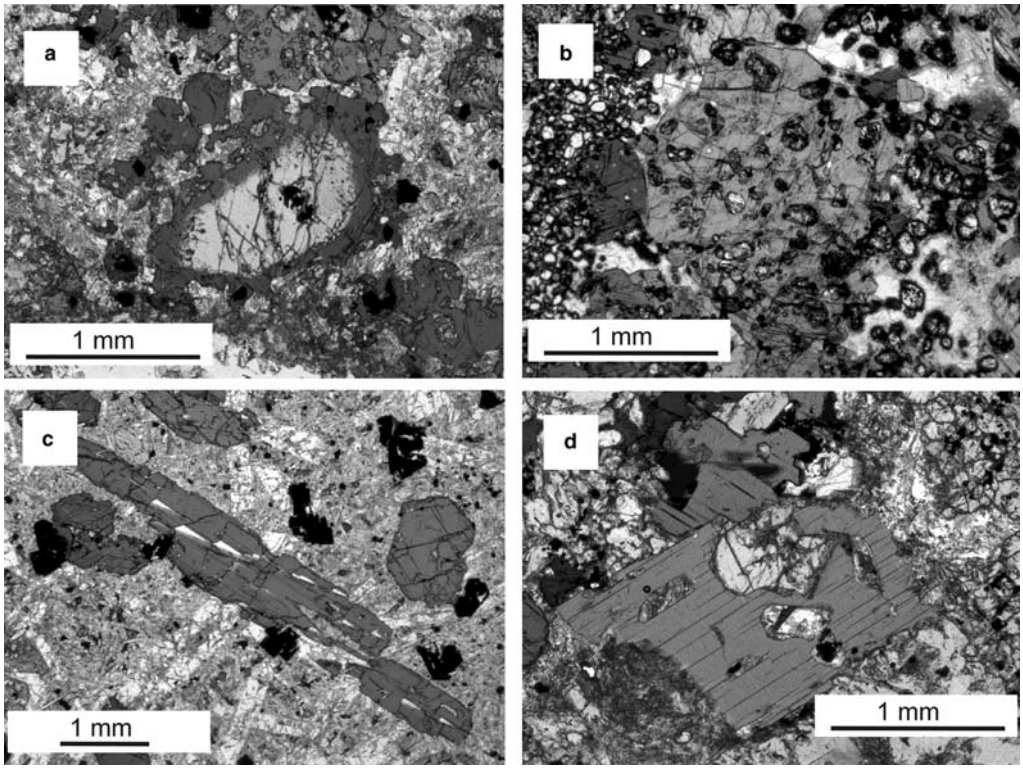

Fig. 2. Optical microscope images of thin sections. Crossed nicols. (**a**). Kaersutite rim around clinopyroxene in olivine-bearing gabbro. Sample LP-04/13. (**b**) Apatite inclusions in kaersutite in olivine-bearing gabbro. Sample LP-02/18. (**c**) Idiomorphic kaersutite crystals in pegmatitic leucogabbro. Sample LP-04/1. (**d**) Biotite in amphibole-bearing leucogabbro. Sample LP-04/10.

amphibole-bearing leucogabbro that contains idiomorphic kaersutite and biotite, and plagioclase.

(3) Amphibole-rich clinopyroxenite (amphibolite; 'a general term, for use in the field, to designate any coarse-grained, holocrystalline igneous rock almost entirely composed of amphibole minerals', *Glossary of Geology*, Bates & Jackson 1983, 1987) (samples LP-02/4, LP-02/7, LP-02/7822 and LP-02/7823) and wehrlite–clinopyroxenite (sample LP-02/6) xenoliths collected from the basaltic rocks of the Cumbre Vieja Ridge and historical eruptions. They contain pink and green clinopyroxene, large kaersutite as overgrowths on pyroxene, and idiomorphic apatite included in pyroxene and oxides. Biotite sometimes occurs as overgrowths on kaersutite. Idiomorphic sphene occurs sporadically.

(4) Amphiboles in basaltic rocks within the Basal Complex and megacrysts in the old submarine pillow-lava basalt in the Basal Complex (sample LP-02/7845). The rock is strongly altered with kaersutite as megacrysts with rounded rims. Minerals related to hydrothermal greenschist-facies metamorphism also occur: calcite, chlorite, epidote, prehnite, pumpellyite and albite.

(5) Xenoliths and xenocrysts in basaltic dykes in the Basal Complex (samples LP-02/16, LP-02/25 and LP-02/28). The xenoliths contain clinopyroxene, kaersutite and oxides (amphibole-bearing clinopyroxenite). The xenocrysts are kaersutites that originated from the disaggregated xenoliths.

Analytical methods

Bulk-rock major element compositions were determined using conventional wet chemistry and gravimetric (SiO_2, loss on ignition (LOI)), atomic absorption spectrometry (AAS; Perkin Elmer AAnalyst/300) and UV-VIS spectrophotometric (UNICAM SP1800-s) analyses. The precision of the analyses is 0.3–1% depending on the element. Bulk-rock trace elements were analysed by X-ray fluorescence (XRF) spectrometry using a Philips 1410 system at the Institute for Geochemical

Research, Hungarian Academy of Sciences. Samples for analysis were milled in an agate mortar to a fine powder (<50 μm). Sample powders of 1.6 g were pressed into pastilles with an additional 0.4 g of boric acid as binder.

The chemical compositions of micas, amphiboles, pyroxenes and olivines were determined with a JEOL JCX-A 733 electron microprobe at the Institute for Geochemical Research, Budapest, using mineral and artificial glass standards. Matrix effects were corrected by the conventional ZAF method.

The H and O isotope compositions were determined at the University of Lausanne, Switzerland. The results are expressed in the δ-notation ($\delta = (R_1/R_2 - 1) \times 1000$, where R_1 and R_2 are the D/H or $^{18}O/^{16}O$ ratios in the sample and the standard, respectively) in permil (‰) relative to V-SMOW. O isotope compositions of silicate minerals were measured using a laser-based method (Rumble & Hoering 1994; Kasemann *et al.* 2001) at the University of Lausanne. The following $\delta^{18}O$ values were obtained for international standards in the course of the study: NBS-28 quartz 9.66 ± 0.05‰ ($n = 10$; theoretical value 9.64‰), NBS-30 biotite 5.12 ± 0.08‰ ($n = 4$; theoretical value 5.1‰), UWG-2 garnet 5.88 ± 0.13‰ ($n = 20$; theoretical value 5.8‰, Valley *et al.* 1995). Based on these data and the reproducibilities of duplicate data, the $\delta^{18}O$ values of samples are exact to within 0.15‰. Water contents and H isotope compositions were determined by TC/EA (high-temperature conversion/elemental analyzer), using a method similar to that described by Sharp *et al.* (2001). The raw data were normalized using NBS-30 biotite and two laboratory standards (Kaol#17 kaolinite and G1 biotite). The H isotope compositions of the laboratory standards obtained in this study reproduced to within ±2‰. The precision of H_2O content measurements performed in parallel is better then 0.1 wt%, on the basis of repeated measurements of NBS-30 and in-house standards.

The Sr isotopic analyses were carried out at the Universität München, Germany. The amphibole separates were cleaned in acetone and ultrapure water using an ultrasonic bath before leaching in 2.5N HCl. Amphibole dissolution and chromatographic procedures followed the methods outlined by Hegner *et al.* (1995). The $^{87}Sr/^{86}Sr$ ratios were measured in a dynamic mass collection mode using a double Faraday cup and are normalized to $^{86}Sr/^{88}Sr = 0.1194$. The NIST 987 Sr-reference material measured during the course of the study yielded $^{87}Sr/^{86}Sr = 0.710220 \pm 10$ (2σ external precision, $n = 22$). The $^{87}Sr/^{86}Sr$ isotopic ratio of the samples of this study are corrected for machine bias and are reported relative to 0.71024 in NIST 987.

Trace element compositions were analysed by laser-ablation (LA)-ICP-MS using a Perkin–Elmer ELAN 6100 DRC type mass spectrometer equipped with a 193 nm excimer laser at the University of Lausanne (for samples from La Palma) and a VG Elemental PQ2+ ICP-MS coupled to a 4D Engineering (Hannover, Germany) excimer laser system at the Southampton Oceanography Centre (for samples from Fuerteventura). The analytical protocol followed the blank–standard–sample–standard pattern. For the purpose of calibration and monitoring instrument performance during the analysis session, polished pieces of the NBS-612 (at the University of Lausanne) and the NIST 610 (at the Southampton Oceanography Centre) standards containing the trace elements of interest were used. After collection, the trace element data were corrected for any instrumental drift, the gas blank was subtracted, and the data were then calibrated against the standards. Ca content determined by electron microprobe analysis was used as internal standards.

Results

Major element compositions of the studied gabbros (Table 1) show a complete transition between plume-related compositions and MORB-related ones (Neumann *et al.* 2000; Fig 3a). Chemical compositions determined by electron microprobe analysis (EMPA) and LA-ICP-MS are listed in Tables 2 and 3, respectively. All the studied amphiboles (except LP-02/19 and LP-04/2) have similar major element compositions (with TiO_2 contents between 5.5 and 7.2 wt%) and plot in the kaersutite–Mg-hastingsite field of the classification diagram of Leake *et al.* (1997), independent of their various host rocks (gabbro, xenocrysts and amphibololite xenoliths in basalts). Samples LP-02/19 and LP-04/2 contain metamorphic actinolite and tremolite, respectively. The Fe^{3+} contents were calculated according to Schumacher (1997; see also Demény *et al.* 2005), the Mg-numbers were calculated for lower and upper Fe^{3+} limits. The Mg-number varies inversely with the TiO_2 and $Na_2O + K_2O$ content. On the basis of Al^{IV} and Ti cation numbers, the amphiboles are similar to the 'primary magmatic amphiboles' crystallized from plume-related magma in the Canary Islands (Fig. 3b). The Al_2O_3 contents of the amphiboles indicate about 0.4–0.7 GPa crystallization pressure (Ernst & Liu 1998), in agreement with the pressures obtained for magma storage within the volcanic edifice of La Palma (Klügel *et al.* 2005; Galipp *et al.* 2006). Trace element compositions show similar spidergram patterns for the studied amphiboles, although some of the elements

Table 1. *Major and trace element contents of gabbros of La Palma (in wt% and ppm, respectively)*

Sample:	8	9	10	11	17	18	19	20A	20B
SiO_2	45.68	44.33	42.34	51.85	44.66	42.08	46.82	40.03	43.76
Al_2O_3	13.28	8.19	11.45	16.73	16.79	8.18	7.91	12.21	18.03
TiO_2	2.61	2.21	3.69	2.30	3.38	3.32	2.64	4.26	2.21
Fe_2O_3	9.69	11.60	14.71	7.39	10.05	13.70	8.70	14.50	7.35
MgO	8.95	16.24	12.32	2.40	5.14	18.18	12.71	6.35	4.64
CaO	13.87	13.51	11.81	4.62	11.67	8.52	17.64	12.51	10.00
K_2O	0.29	0.21	0.45	3.02	1.44	1.62	0.32	2.23	3.14
Na_2O	1.96	0.91	1.70	5.82	2.68	1.51	1.08	4.24	5.81
P_2O_5	0.23	0.18	0.25	0.40	0.25	0.33	0.15	0.50	0.38
LOI	2.34	2.31	0.62	4.14	2.71	1.87	1.28	0.87	2.62
Sum	98.9	99.69	99.34	98.67	98.77	99.31	99.25	97.70	97.94
Sc (0.2)	43	47	38	9	32	31	66	20	16
V (3)	235	181	347	207	300	280	240	374	176
Co (2)	58	56	57	28	36	54	43	59	33
Ni (9)	118	371	214		75	561	165	43	31
Zn (3)	16	43	50	68	50	55	20	60	39
Sr (15)	456	302	452	605	644	97	185	837	1141
Zr (5)	94	83	93	415	148	129	103	229	246

Precisions are shown by numbers in parentheses. All samples belong to the LP-02 sample set.

indicate variations (e.g. U, Th, Nb, Ta, Pb, Sr, Zr, Hf, etc.; see Fig. 4). Most of the pyroxene is diopside. However, samples LP-04/6 and LP-04/10 contain augites. The olivines have forsterite contents from 74 to 81%.

Stable H and O isotope compositions and H_2O contents are listed in Table 4 and shown in Figure 5. The studied amphiboles and biotites collected from the gabbros have rather large δD and $\delta^{18}O$ variations from −110 to −65‰ and from 1.0 to 5.5‰, respectively (Fig. 5b). One of the biotites and a chlorite sample have high H_2O contents (7.28 and 8.58 wt%), suggesting chloritization in the case of the biotite. The other biotite samples all have <3.7 wt% H_2O. The amphiboles have an average H_2O content of 1.2 wt%, although some of the samples yielded lower values. As there is no H_2O wt%–δD correlation (see Fig. 5a), the low water contents could be related to impure separates (considered unlikely, as the samples were carefully hand-picked under binocular microscope) or low water content in the magma and/or the amphibole. The $\delta^{18}O$ and δD values of amphiboles show a slight positive correlation (Fig. 5c), similar to that of phlogopites of early volcanic rocks of Fuerteventura found by Demény *et al.* (2004). The Al_2O_3 content of amphiboles does not correlate with the δD_{amph} values ($R^2 < 0.01$), suggesting that crystallization pressure differences did not cause variations in melt water contents and hence in H

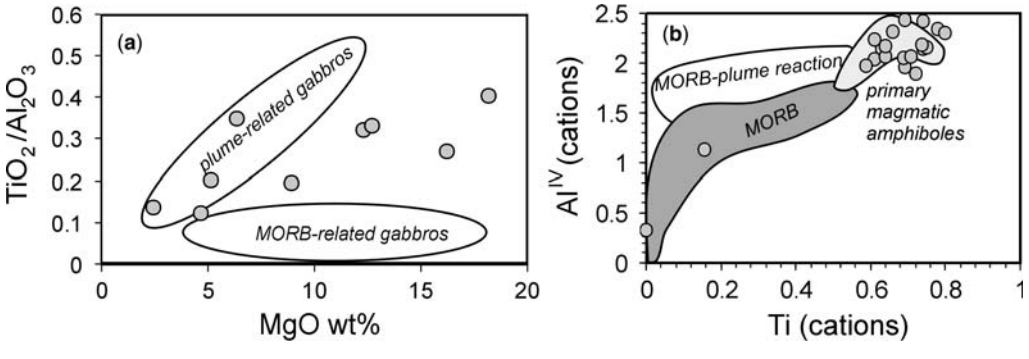

Fig. 3. (**a**) A. TiO_2/Al_2O_3 v. MgO in gabbros of the Basal Complex of La Palma. Fields for plume- and MORB-related gabbros are from Neumann *et al.* (2000). (**b**) Al^{IV} v. Ti for amphiboles hosted by Basal Complex gabbros and amphibololite xenoliths and xenocrysts from basalts of La Palma. Fields for amphiboles of different origins are from Neumann *et al.* (2000). The amphiboles falling into the MORB field are tremolite and actinolite.

Table 2. *Representative chemical compositions (in wt%) of amphiboles, clinopyroxenes and olivines in La Palma determined by electron microprobe analysis*

	Amphiboles							
Sample:	LP-02/4	LP-02/6	LP-02/7	LP-02/8	LP-02/9	LP-02/12	LP-02/17	LP-02/18
SiO_2	36.95	38.91	39.31	40.56	38.21	39.06	40.40	38.52
Al_2O_3	13.93	12.99	12.75	11.30	14.32	12.23	12.04	12.74
TiO_2	6.11	5.57	6.65	5.24	6.78	6.58	6.22	5.46
FeO	11.24	11.27	9.81	12.68	9.66	12.25	11.42	9.65
MgO	12.44	12.18	12.42	12.97	13.88	12.61	12.90	14.22
MnO	0.29	0.21	0.29	0.00	0.11	0.00	0.00	0.09
CaO	11.96	11.97	12.24	11.38	12.22	12.17	11.87	11.96
Na_2O	2.61	2.40	2.75	2.84	2.48	2.43	2.78	2.57
K_2O	1.29	1.37	0.94	0.87	1.06	0.78	0.91	1.59
Total	96.82	96.87	97.16	97.84	98.72	98.09	98.53	96.80
Ion numbers								
Si	5.58	5.85	5.85	6.02	5.58	5.81	5.95	5.76
Al(IV)	2.43	2.15	2.15	1.98	2.42	2.19	2.05	2.24
Al(VI)	0.05	0.15	0.09	0.02	0.04	0.00	0.04	0.00
Ti	0.69	0.63	0.74	0.59	0.74	0.74	0.69	0.61
Fe^{3+}	0.11	0.00	0.00	0.05	0.17	0.02	0.00	0.14
Mg(c)	2.80	2.73	2.76	2.88	3.02	2.80	2.83	3.17
Fe^{2+}(c)	1.31	1.42	1.22	1.53	1.01	1.50	1.41	1.07
Mn(c)	0.04	0.03	0.04	0.00	0.01	0.00	0.00	0.01
Ca	1.93	1.93	1.95	1.82	1.91	1.94	1.87	1.92
Na(b)	0.07	0.07	0.05	0.12	0.09	0.04	0.13	0.09
Na(a)	0.70	0.63	0.75	0.69	0.61	0.66	0.67	0.66
Sample:	LP-02/19	LP-04/1	LP-04/2	LP-04/5	LP-04/6	LP-04/7	LP-04/9	LP-04/10
SiO_2	47.46	40.60	55.78	38.75	40.45	42.00	40.96	39.79
Al_2O_3	7.89	12.07	2.15	13.92	12.72	10.66	11.59	11.70
TiO_2	1.43	5.52		7.12	5.81	6.59	6.23	6.30
FeO	9.82	11.76	2.54	11.05	9.84	10.85	10.01	10.86
MgO	16.26	13.19	23.42	12.56	13.67	13.81	13.60	12.87
MnO	0.00	0.15	0.00	0.19	0.10	0.00	0.15	0.00
CaO	12.37	11.95	12.86	12.26	11.69	11.80	11.17	12.03
Na_2O	2.07	2.89	0.31	2.77	2.92	2.61	2.97	2.76
K_2O		1.04		0.92	1.20	1.26	0.90	0.97
Total	97.29	99.14	97.06	99.54	98.39	99.58	97.57	97.27

(*Continued*)

Table 2. *Continued*

	Amphiboles							
Sample:	LP-02/4	LP-02/6	LP-02/7	LP-02/8	LP-02/9	LP-02/12	LP-02/17	LP-02/18
Ion numbers								
Si	6.87	5.96	7.68	5.66	5.93	6.10	6.04	5.93
Al(IV)	1.13	2.04	0.32	2.34	2.07	1.90	1.96	2.07
Al(VI)	0.21	0.05	0.03	0.06	0.13	0.00	0.05	0.00
Ti	0.16	0.61	0.00	0.78	0.64	0.72	0.69	0.71
Fe^{3+}	0.06	0.00	0.21	0.00	0.00	0.00	0.00	0.01
Mg(c)	3.51	2.89	4.80	2.74	2.99	2.99	2.99	2.86
Fe^{2+}(c)	1.13	1.44	0.08	1.35	1.21	1.32	1.24	1.34
Mn(c)	0.00	0.02	0.00	0.02	0.01	0.00	0.02	0.00
Ca	1.92	1.88	1.87	1.92	1.84	1.84	1.76	1.92
Na(b)	0.00	0.12	0.00	0.08	0.17	0.15	0.24	0.06
Na(a)	0.60	0.70	0.09	0.71	0.66	0.58	0.61	0.74

Sample	LP-04/14	LP-7822	LP-7823	LP-7845	LP-8359
SiO_2	39.81	40.48	39.60	39.46	38.73
Al_2O_3	12.64	12.88	13.24	14.44	13.21
TiO_2	6.76	5.82	5.77	6.13	7.20
FeO	10.09	10.97	10.81	11.99	11.91
MgO	13.47	12.89	13.15	12.82	12.46
MnO	0.12	0.15	0.11	0.15	0.16
CaO	11.94	11.62	11.83	10.77	12.04
Na_2O	2.76	2.89	2.51	2.77	2.60
K_2O	1.04	1.15	1.38	0.66	0.80
Total	98.64	98.85	98.41	99.19	99.11
Ion numbers					
Si	5.84	5.93	5.83	5.68	5.70
Al(IV)	2.16	2.07	2.17	2.32	2.30
Al(VI)	0.02	0.16	0.13	0.13	0.00
Ti	0.75	0.64	0.64	0.66	0.80
Fe^{3+}	0.00	0.00	0.05	0.66	0.00
Mg(c)	2.94	2.81	2.89	2.75	2.73
Fe^{2+}(c)	1.24	1.35	1.28	0.79	1.47
Mn(c)	0.02	0.02	0.01	0.02	0.01
Ca	1.88	1.83	1.87	1.66	1.90
Na(b)	0.12	0.18	0.13	0.34	0.09
Na(a)	0.66	0.65	0.58	0.43	0.65

	Pyroxenes							
Sample:	LP-02/8	LP-02/12	LP-02/17	LP-02/18	LP-02/19	LP-04/2	LP-04/6	
SiO_2	50.19	48.19	50.66	49.62	49.28	49.94	43.41	
Al_2O_3	2.77	4.65	2.72	4.46	3.81	3.58	5.53	
TiO_2	1.24	2.20	1.31	1.94	1.75	1.32	2.11	
FeO	7.24	8.60	7.81	6.29	6.42	5.39	13.04	
MgO	14.81	13.35	13.97	15.03	14.59	15.63	21.53	
CaO	22.70	22.60	22.59	22.40	22.88	22.61	22.07	
Na_2O	0.33	0.54	0.53	0.32	0.35	0.17	0.24	
Total	99.28	100.13	99.59	100.05	99.07	98.63	97.95	
Sample:	LP-04/7	LP-04/9	LP-04/10	LP-04/11	LP-04/13	LP-04/14	LP-8359	
SiO_2	48.86	45.68	45.24	48.57	45.33	47.28	47.77	
Al_2O_3	4.59	5.83	5.55	5.00	7.15	4.87	5.52	
TiO_2	2.45	2.85	2.31	2.79	2.79	2.15	2.64	
FeO	7.19	7.26	10.24	7.15	7.63	6.69	9.25	
MgO	14.02	12.97	20.46	13.40	12.49	13.81	12.10	
CaO	22.49	22.02	22.99	22.88	22.70	22.68	21.65	
Na_2O	0.47	0.36	0.18	0.40	0.37	0.23	0.52	
Total	100.06	96.97	99.22	99.25	98.47	97.70	99.46	
	Olivines							
Sample:	LP-02/18	02/19	LP-04/2	LP-04/6	LP-04/10	LP-04/11	LP-04/13	LP-04/14
SiO_2	39.53	38.17	39.31	37.39	38.78	38.52	38.62	38.44
MgO	42.41	39.39	42.45	37.33	39.58	39.87	39.81	41.39
FeO	18.62	22.41	17.94	23.78	21.71	22.34	20.46	19.99
Total	100.56	99.96	99.69	98.49	100.06	100.72	98.89	99.82

Ion numbers were calculated using the method of Schumacher (1997). The ion numbers shown in this table are based on maximum Fe^{3+}.

Table 3. *Trace element compositions (in ppm) of amphiboles from La Palma (samples 'LP') and Fuerteventura (samples 97/20, 96/54, 97/23, 96/58; see also Demény et al. 2004) determined by LA-ICP-MS*

Sample:	LP-7822	LP-7823	LP-7845	LP-8359	LP-02/4G	LP-02/4F	LP-02/6	LP-02/8	LP-02/9	LP-02/17
Sc				35.6				72.7	52.4	57.5
Rb	2.41	6.84	1.05	4.02	4.16	9.58	7.02	3.02	3.8	3.72
Ba	366	589	179	449	378	621	376	338	517	424
Th	0.12	0.23	0.07	0.14	0.06	1.16	0.2	0.19	0.25	0.17
U	0.11	0.11	0.1	0.04	0.02	0.46	0.15	0.04	0.05	0.03
Ta	1.71	2.39	1.21	4.12	1.22	3.49	1.54	8.19	6.85	5.19
Nb	36.0	46.8	25.9	77.3	26.6	61.0	32.5	160.6	134.2	96.3
La	17.1	21.8	5.8	18.8	11.4	23.4	14.8	33.8	34.6	24.2
Ce	46.5	62.4	22.5	63.0	34.1	62.6	40.5	120.3	110.8	84.0
Pb	0.53	0.50	0.19	1.14	0.29	2.16	0.51	0.38	0.37	0.44
Pr	6.95	9.73	4.27	9.88	5.35	9.16	6.12	19.2	16.1	13.7
Sr	736	1314	640	842	784	1425	801	322	524	645
Nd	35.6	50.6	25.2	49.0	28.0	51.9	32.4	94.3	74.6	68.5
Sm	7.86	12.07	8.14	12.56	6.97	13.40	7.51	24.05	16.73	17.42
Zr	108	152	53	156	78	170	103	294	241	188
Hf	3.57	5.48	2.13	5.35	2.56	6.09	3.34	10.89	7.18	6.25
Eu	2.63	4.05	3.21	4.09	2.24	4.18	2.53	5.37	4.43	5.13
Gd	6.50	10.67	8.06		5.90	11.43	6.27			
Tb	0.94	1.44	1.22	1.52	0.84	1.63	0.86	3.16	2.04	2.09
Dy	4.79	7.47	6.93	8.94	3.71	7.98	4.34	18.74	11.96	12.49
Ho	0.80	1.26	1.21	1.58	0.71	1.41	0.76	3.32	2.08	2.18
Er	1.80	2.87	2.87	3.78	1.50	3.22	1.62	8.18	5.00	5.22
Tm	0.21	0.32	0.35	0.46	0.17	0.37	0.18	1.07	0.68	0.64
Yb	1.31	1.97	2.08	3.06	1.10	2.37	1.12	6.40	4.19	3.98
Lu	0.17	0.24	0.23	0.39	0.14	0.27	0.13	0.80	0.53	0.53

Sample:	LP-02/18	LP-04/1	LP-04/5	LP-04/6	LP-04/9	LP-04/14	97/20	96/54	97/23	96/58
Sc	44.5	67.6	37.4	42.2	54.1	51.8	47.6	47.8	46.9	
Rb	7.14	3.01	4.35	4.62	3.11	4.38	12.67	6.80	11.15	11.68
Ba	137	348	537	657	487	487	366	311	303	264
Th	0.16	0.23	0.11	0.41	0.17	0.20	0.04	0.29	0.03	0.03
U	0.05	0.04	0.02	0.06	0.03	0.05	0.02	0.13	0.04	0.02
Ta	4.05	8.09	3.12	12.31	5.21	4.92	1.52	2.58	1.20	1.04
Nb	64.2	144.5	49.3	239.8	101.3	96.9	21.9	43.8	17.2	14.4
La	14.0	36.1	13.0	54.3	29.5	26.3	10.9	19.3	6.2	6.9
Ce	47.5	128	43.7	161	103	85.8	33.5	52.5	21.3	21.1
Pb	0.38	0.40	0.32	0.66	0.38	0.34	0.30	1.12	0.22	0.28
Pr	7.89	20.1	6.99	22.9	16.5	12.2	5.33	7.22	3.74	3.62
Sr	157	352	1116	464	599	756	696	1077	554	509
Nd	42.9	105.7	37.9	108.2	82.7	56.0	33.3	41.7	23.1	22.0
Sm	10.96	27.57	10.31	24.37	20.45	12.25	8.42	8.95	5.57	5.09
Zr	166	297	120	321	194	182	170	268	110	88
Hf	5.47	11.92	4.28	9.36	6.61	5.44	7.06	8.53	4.60	4.04
Eu	3.11	6.14	3.43	6.89	6.03	3.86	2.45	2.71	1.89	1.71
Gd							6.59	7.19	4.74	4.44
Tb	1.44	3.82	1.31	3.08	2.52	1.39	0.73	0.82	0.58	0.52
Dy	7.96	22.3	7.04	18.12	14.44	7.86	3.86	4.51	3.02	2.83
Ho	1.42	4.00	1.22	3.21	2.48	1.35	0.55	0.67	0.43	0.38
Er	3.64	10.3	2.80	7.84	6.10	3.32	1.23	1.51	0.96	0.83
Tm	0.45	1.26	0.37	1.03	0.72	0.43	0.12	0.18	0.11	0.09
Yb	2.74	7.51	1.76	5.81	4.20	2.57	0.83	1.23	0.59	0.60
Lu	0.36	0.99	0.26	0.78	0.59	0.31	0.09	0.15	0.07	0.06

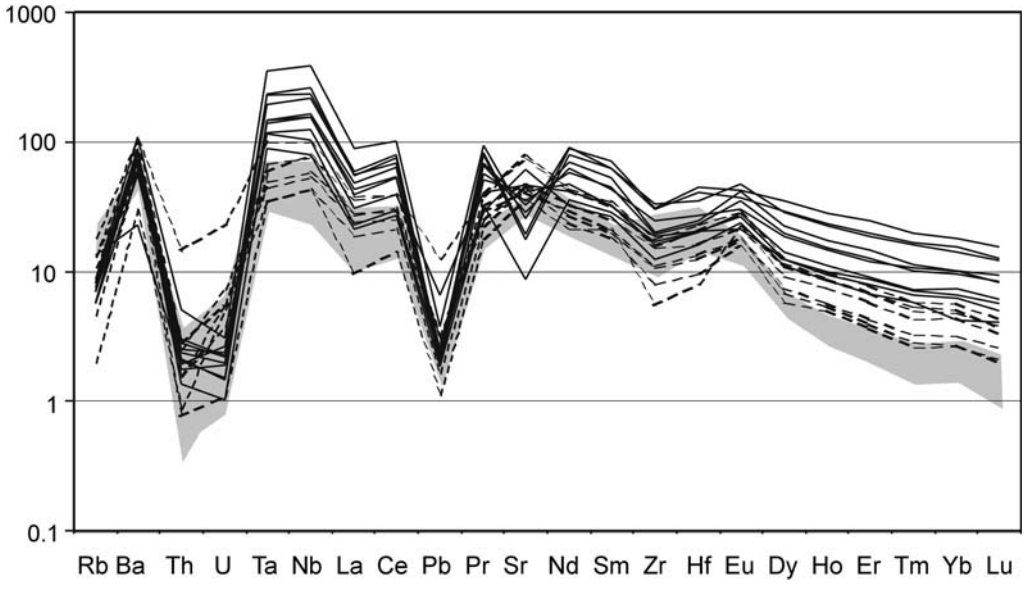

Fig. 4. Trace element contents of amphiboles of La Palma, normalized to primitive mantle (Hofmann 1988). Continuous lines indicate amphiboles from gabbros; dashed lines, amphibololite xenoliths and xenocrysts; the shaded field indicates amphiboles from Fuerteventura.

isotope compositions via fractionation associated with the degassing. Although the Mg-numbers of pyroxenes and olivines are well correlated ($R^2 = 0.98$), the Mg-numbers of amphiboles and pyroxenes have no relationship with the $\delta^{18}O$ values (Fig. 5d), indicating that magma evolution during crystallization did not result in significant O isotope fractionation. The leucogabbro veinlets within mafic gabbros (samples LP-04/6 and LP-04/10) contain augite, but their amphibole has stable isotope compositions identical to those of other amphiboles from the gabbro series. These observations suggest that the changes in H and O isotope compositions are not related to variations in crystallization conditions and rock types.

Sr isotope compositions were also measured on selected samples, and the data are listed in Table 4. Most of the $^{87}Sr/^{86}Sr$ ratios fall into the uncontaminated plume-related range (Hoernle & Tilton 1991), although some samples have lower values.

Discussion

Secondary processes: water–rock interactions and degassing

Before trace element and isotopic compositions are used to interpret primary magmatic processes, it has to be ascertained that the measured compositions truly represent primary magmatic compositions. The very low $\delta^{18}O$ values observed in biotites and chlorites within the gabbros are strong indicators of secondary alteration processes. This is further supported by differences between the oxygen isotope compositions of pyroxene, amphibole and feldspar. Excluding the amphibole separates of samples LP-02/19 (actinolite) and LP-04/2 (tremolite), the gabbro-hosted amphiboles have an average $\delta^{18}O$ value of 5.1‰ ($\pm$0.2‰, $n = 26$), the average $\delta^{18}O$ value for pyroxenes is 5.2 $\pm$ 0.2‰ ($n = 8$), whereas the feldspars, which are most sensitive to alteration, have an average $\delta^{18}O$ value of 4.7 $\pm$ 0.9‰ ($n = 14$) with a large scatter from 3.6 to 6.7‰. The difference in $\delta^{18}O$ between pyroxene and amphibole is in agreement with the theoretical fractionation at 900–1000 °C (Zheng 1993*a*,*b*), although it should be noted that the diopside–hornblende oxygen isotope fractionation is not temperature-sensitive in the range of 700–1000 °C. On the other hand, only two feldspar separates have $\delta^{18}O$ values in high-temperature equilibrium with pyroxene or amphibole compositions (around 6.5‰, using the fractionation equations of Zheng 1993*a*); all the other feldspars have lower $\delta^{18}O$ values. The δD and $\delta^{18}O$ values of amphiboles and biotites plot in two distinct fields within Figure 5b. Although both hinge on values typical for upper mantle derived melts (e.g. Kyser & O'Neil 1984; Kyser 1986; Agrinier *et al.* 1993; Mattey *et al.* 1994; Chazot *et al.* 1997), the

Table 4. *Stable H and O isotope compositions (in ‰ relative to V-SMOW), water contents (in wt%) and Sr isotope ratios of mineral separates from La Palma, Canary Islands*

	H_2O	δD	$\delta^{18}O$	$^{87}Sr/^{86}Sr$		H_2O	δD	$\delta^{18}O$	$^{87}Sr/^{86}Sr$
Amphiboles									
LP-02/4F	1.20	−74	5.2	0.70311	LP-02/28	0.44	−67	5.3	0.70310
LP-02/6a	1.41	−65	5.1		LP-04/2	2.47	−78	3.5	0.70298
LP-02/6b	1.28	−66	5.3		LP-04/5	1.14	−82	5.2	0.70301
LP-02/7	1.17	−83	4.8		LP-04/6	0.82	−87	5.2	0.70304
LP-02/8	1.16	−86	5.1	0.70304	LP-04/7	0.56	−92	5.0	
LP-02/9	1.54	−96	4.7	0.70311	LP-04/9	1.19	−89	4.7	0.70307
LP-02/12	1.17	−99	4.9	0.70309	LP-04/10	0.99	−91	4.9	
LP-02/16	1.21	−75	5.4	0.70307	LP-04/14	0.95	−88	5.1	
LP-02/17	1.20	−93	4.8	0.70311	LP-7822	1.66	−71	5.2	
LP-02/18	1.79	−91	5.0	0.70304	LP-7823	1.34	−77	5.4	0.70309
LP-02/19	0.63	−107	5.1	0.70305	LP-7845	1.38	−100	5.1	0.70295
LP-02/25	1.67	−91	5.3		LP-8359	1.14	−101	5.3	
Biotites									
LP-02/9	3.66	−94	2.9		LP-04/3	7.28	−76	5.2	
LP-02/17	3.38	−87	1.3		LP-04/8	1.79	−89	4.1	
LP-02/18	3.42	−93	1.9		LP-04/9	2.65	−88	3.5	
LP-02/19	2.69	−89	2.7		LP-04/10	2.18	−86	4.5	
LP-04/2	3.57	−76	3.7		LP-04/3(∗)	8.58	−80	1.0	
Pyroxenes					*Feldspars*				
	$\delta^{18}O$		$\delta^{18}O$			$\delta^{18}O$		$\delta^{18}O$	
LP-02/8	5.3	LP-04/12	5.4		LP-02/8	5.1	LP-04/4	3.7	
LP-02/19	4.9	LP-04/13	4.9		LP-02/9	4.1	LP-04/6	6.7	
LP-04/1	5.3	LP-04/14	4.9		LP-02/17	3.6	LP-04/8	6.1	
LP-04/6	5.2				LP-02/19	4.0	LP-04/9	4.4	
LP-04/11	5.4				LP-04/1	5.1	LP-04/10	5.0	
					LP-04/2	5.1	LP-04/11	4.2	
					LP-04/3	4.0	LP-04/14	5.1	

Sample LP-04/3(∗) is a chlorite.

amphiboles have a range of δD values that extends to much lower values, accompanied by a slight decrease of the $\delta^{18}O$ values, whereas the biotite and chlorite have a wide range in $\delta^{18}O$ values as well as δD values, with the former extending to much lower values. This second group for biotites includes only one amphibole with a low $\delta^{18}O$ value. This amphibole (LP-04/2) is a tremolite with elevated water content (see Table 4) and can be attributed to the greenschist-facies hydrothermal metamorphism of the gabbros.

As the rocks were formed as part of an ocean island system, the low $\delta^{18}O$ values may suggest high-temperature interaction with seawater, similar to that observed for ophiolitic rocks (e.g. Muehlenbachs 1986; Alt & Bach 2006; Gao *et al.* 2006). Alternatively, these low values may be attributed to high-temperature interaction with meteoric water, as suggested by Javoy *et al.* (1986) for different rock types from Fuerteventura, La Palma and La Gomera. The isotopic compositions of water in equilibrium with biotite and the chlorite–serpentine separate of sample LP-04/3 can be calculated using the biotite–water and chlorite–water fractionation equations of Wenner & Taylor (1971), Bottinga & Javoy (1973), Suzuoki & Epstein (1976), Cole (1985) and Graham *et al.* (1987). The equilibrium temperatures are not known exactly; however, an unaltered magmatic biotite would typically be in equilibrium with magmatic water at >800 °C, whereas the typical greenschist-facies assemblage would suggest temperatures of 200–400 °C. The $\delta^{18}O$ values of the biotite show a negative relationship with the H_2O content, indicating an alteration effect; thus, the calculations were made assuming a continuous temperature decrease from 800 to 300 °C and an associated change in the $\delta^{18}O$ values from 5.0 to 1.5‰. The water in equilibrium with the chlorite of sample LP-04/3 would represent the infiltrating fluid, and its isotopic compositions were calculated for 200, 300 and 400 °C. The results of the calculations are shown in Figure 6,

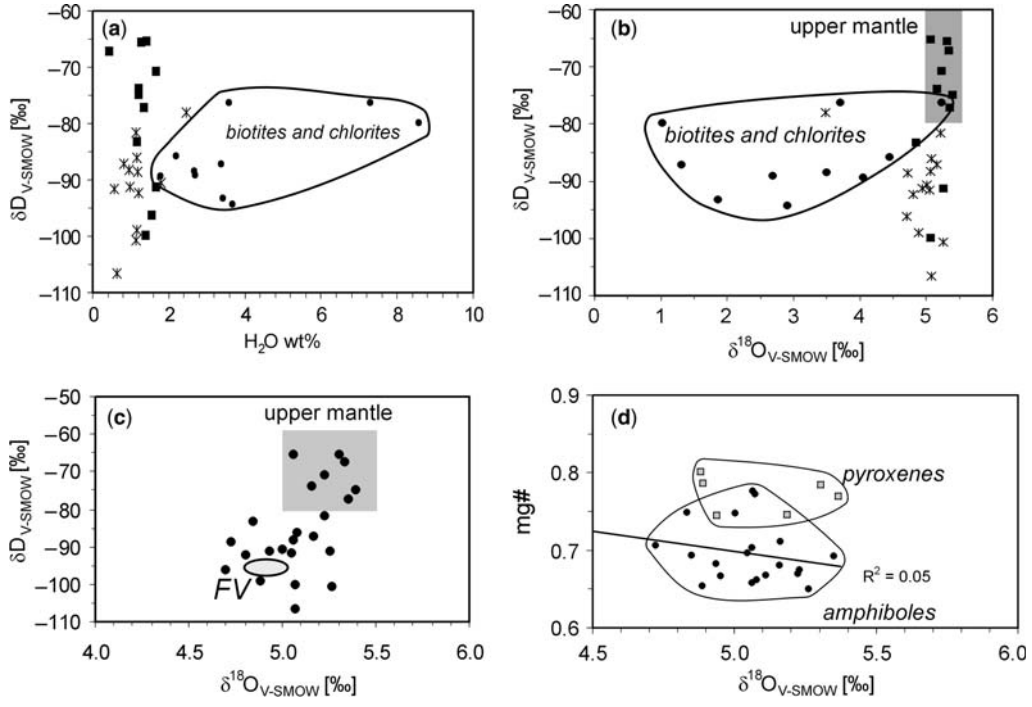

Fig. 5. (**a**, **b**) H_2O contents (in wt%) and H and O isotope compositions (in ‰) of amphiboles, biotites and chlorites in La Palma. ■, amphibololite xenoliths and amphibole xenocrysts; *, amphiboles in gabbros; •, biotites and chlorites in gabbros.(**c**) δD v. $\delta^{18}O$ values in amphiboles. *FV*, primary phlogopite compositions from Fuerteventura (Demény *et al.* 2004). (**d**) Mg-numbers as a function of $\delta^{18}O$ values in amphiboles and pyroxenes. Upper mantle ranges are from Kyser & O'Neil (1984), Kyser (1986), Agrinier *et al.* (1993), Mattey *et al.* (1994) and Chazot *et al.* (1997).

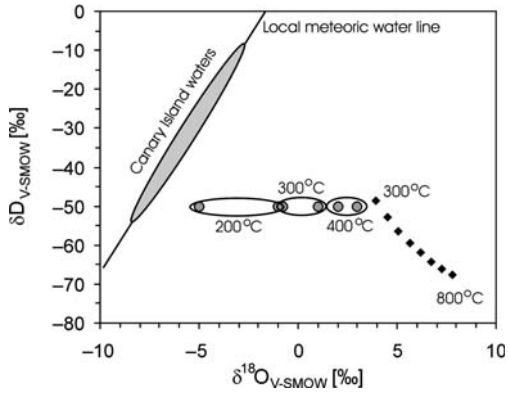

Fig. 6. H and O isotope compositions of waters calculated using the compositions of biotites (◆) and chlorites (grey circles) in gabbros at varying temperatures. The isotopic compositions of Canary Islands meteoric waters are from Gonfiantini *et al.* (1975).

along with the compositions of the Canary Island meteoric waters. The maximum δD value obtained for biotite at 300 °C is very similar to that obtained for chlorite. The distribution of the calculated H and O isotopic compositions of the waters suggests mixing of meteoric and magmatic water, although the direction of the biotite data trend would not exclude seawater infiltration. As whole-rock samples have been noted to have slightly elevated Sr isotope ratios interpreted to be a result of seawater–rock interaction in the gabbros (Hart *et al.* 1999), it may also be expected that secondary amphibole should have higher $^{87}Sr/^{86}Sr$ compared with primary magmatic amphibole, if seawater was indeed important at this stage. However, all of the studied samples, even the actinolite of sample LP-04/2, have Sr isotope compositions typical for normal mantle-derived melts, thus any influence of seawater is not obvious here.

Opposite to the H isotope exchange, where the fluid is usually the dominating phase, the oxygen content of the rock is comparable with that of the fluid phase. The degree of $\delta^{18}O$ change in the fluid and the rock depends on the exchange temperature and the amount of the infiltrating fluid. As

the low-temperature hydrous minerals have clearly been formed in the presence of a secondary fluid, the chlorite compositions may be expected to have equilibrated with the infiltrating fluid, hence providing the best estimate of its composition, too. δD values of chlorites of about −50‰ correspond to δD values of meteoric waters similar to those measured for precipitation at the top of Teide (Tenerife island, elevation 3717 m above sea level (a.s.l.) today (about −50 to −40‰, Gonfiantini *et al.* 1975; Albert-Beltrán *et al.* 1990). This suggests that the elevation of the island may have reached this height, although the present height is 2426 m a.s.l. This estimation is based on the assumption that the altitude effect on H isotope composition of the precipitation was approximately the same during the alteration of the gabbro as it is today. Climate change may affect the isotopic composition of the actual precipitation through variations in the isotopic composition of the source ocean water and temperature. However, given that changes in climate may be expected to be less pronounced for tropical to subtropical ocean islands in terms of changes in the overall H isotope budget of the precipitation (e.g. Darling *et al.* 2003), this estimate is expected to be fairly robust. Based on the reconstruction of the volcanic edifice of La Palma (Carracedo *et al.* 1999*b*), the original height of the Taburiente volcano was at least 3000 m a.s.l., in good agreement with the height inferred above. In a study of the H and O isotope compositions of several Canary Island complexes Javoy *et al.* (1986), also noted similar isotope compositions and inferred a similar height for Fuerteventura. However, their preliminary dataset suggested lower heights for La Palma and La Gomera.

As several of the islands of the Canary archipelago seem to have reached altitudes of about 3000–4000 m during their evolution, this can be perhaps considered to be an upper limit before major collapses of the volcanic edifice. As this statement has important implications for assessment of island evolution and safety, follow-up studies on other islands will be needed to fully explore the significance of isotopic studies in this area.

Next to the rather important change in the ^{18}O contents of biotites with increasing alteration, the amphiboles also show a trend towards D depletion in parallel to a slight ^{18}O depletion (Fig. 5c). Because the change in δD is not associated with a decrease in the H_2O content of the amphiboles, degassing or partial breakdown of amphibole would not provide a plausible explanation (see Demény *et al.* 2006). In contrast, degassing of H_2O from the host magma may explain the decrease in δD values as well as the change in the oxygen isotope composition if the water is degassed at temperatures higher than 500 °C. If such degassing was important, the absence of a relationship between the δD values and the Al_2O_3 contents of the amphiboles ($R^2 < 0.01$) would indicate however, that this is not related to a decrease in crystallization pressure. Further more, the observed shift in $\delta^{18}O$ values may be explained by H_2O degassing from the melt. A basaltic melt can contain *c*. 6 wt% dissolved H_2O (Webster *et al*. 1999), whereas the studied gabbros contain about 0.5–4 wt% H_2O. Using the CO_2–H_2O and basalt–H_2O fractionation relationships of Zheng (1994) and Appora *et al.* (2003), the released H_2O would be enriched in ^{18}O relative to the melt by about 2‰. Degassing of two-thirds of the water content would cause about −0.15‰ shift in the total oxygen content of the melt, assuming that all of the oxygen atoms take part in the exchange process. As already crystallized phases such as pyroxenes may not take part in the exchange between H_2O and the remaining fraction, this estimation is the upper limit of the $\delta^{18}O$ change. Additionally, continuing degassing would result in a stronger change in the amphibole, which is not observed in the present dataset. All these considerations suggest that H_2O degassing is not likely as the major cause of the negative δD and $\delta^{18}O$ shift.

Late-stage alteration in the presence of fluids depleted in D (−70‰ or lower; see above) may also account for the trend in δD values. This would be possible in the presence of the meteoric water such as that which may have caused the alteration of biotite to chlorite. However, as the amphiboles show no textural, chemical or O- and Sr-isotopic signs of late-stage alteration, this possibility is considered to be unlikely for most of the amphiboles.

In summary, although it is clear that the biotite within the rocks analysed has been partially altered to chlorite in the presence of meteoric water, the amphiboles are compatible with having preserved primary magmatic compositions. The variations in primary compositions for the amphiboles may reflect magmatic processes such as magmatic degassing and/or be related to different source components compared with normal mantle-type melts. This possibility will be discussed further below in conjunction with trace element contents and Sr isotope ratios of mineral phases.

Primary compositions

Primary magmatic oxygen isotope compositions are commonly preserved in pyroxene, as these are less sensitive to late-stage diffusive exchange with infiltrating secondary fluids relative to feldspars and micas, for example (Farver 1989). The average $\delta^{18}O$ value (5.2‰) of the pyroxenes is in good agreement with the lowest $\delta^{18}O$ value obtained on clinopyroxenes from Canary Island rocks by Thirlwall *et al.* (1997), and with the pyroxene compositions

reported from Fuerteventura by Demény *et al.* (2004). As discussed above, the amphiboles are in high-temperature equilibrium with the pyroxenes and hence they too would be in equilibrium with typical mantle-derived melts. This would be compatible with their closure temperatures to diffusion (Farver 1989). Oxygen isotope exchange with feldspar at decreasing temperature may also produce a negative $\delta^{18}O$ shift in the amphibole and pyroxene, producing lower than normal mantle $\delta^{18}O$ values. However, the closure temperatures of these minerals should also be taken into account. As Farver (1989) has pointed out, oxygen self-diffusion in hornblende is an order of magnitude faster than in diopside, resulting in closure temperatures around 900–1000 °C in pyroxene and 600–800 °C in amphibole (at 100–1000 °C Ma^{-1} cooling rate and 0.1–1 mm grain size). This means that retrograde oxygen isotope exchange with feldspar would affect the $\delta^{18}O$ values of amphiboles, whereas the pyroxene compositions would remain intact. The *c*. 0.1‰ fractionation between these minerals indicate that no significant retrograde exchange with feldspars occurred. Based on O isotopic fractionations between melt and olivine (*c*. 0.4‰, Eiler *et al.* 2000) and between pyroxene and olivine (0.3–0.4‰, Mattey *et al.* 1994), the basaltic melt compositions should be close to the pyroxene $\delta^{18}O$ values (*c*. 5.2‰). This composition is 0.3–0.5‰ lower than suggested for primary mantle value (5.5–5.7‰, Mattey *et al.* 1994; Eiler 2001).

The observations described above suggest that the trend to slightly lower $\delta^{18}O$ and much lower δD values from typical mantle compositions (Fig. 5c) is not due to late-stage alteration, but rather to magmatic processes. Fractional crystallization can also result in $\delta^{18}O$ variation, but the $\delta^{18}O$ values of amphiboles and pyroxenes show no relationship with their Mg-numbers (Fig. 5d). Demény *et al.* (2004) have observed similar shifts in phlogopites and amphiboles from the submarine and early subaerial volcanic rocks of Fuerteventura. They related the low $\delta^{18}O$ and δD values to a plume component that contained subducted ocean crust material and deep-seated hydrogen. The δD–$\delta^{18}O$ data from La Palma fit the compositions from Fuerteventura, supporting the earlier conclusions. However, the nature of the components or processes that determined the δD–$\delta^{18}O$ distributions in La Palma and Fuerteventura can be further elucidated by trace element and Sr isotope analyses that will be discussed below.

Trace element ratios coupled with radiogenic and stable isotope data can provide essential information on processes such as source heterogeneities, fractional crystallization, partial melting and assimilation. However, the studied rock types hosting the amphiboles have variable mineralogical compositions and crystallization histories, all of which may influence the trace element partitioning and hence trace element content of the amphiboles. The chemical composition of amphibole (Tiepolo *et al.* 2000) and the crystallization conditions (pressure and temperature, Adam & Green 2003) can also affect the amphibole–melt partition coefficient and, thus, the trace element composition of the amphibole. Ce/Pb and Ba/Nb, generally thought to reflect crustal assimilation processes, show a negative correlation ($R^2 = 0.49$), suggesting that assimilation affected the compositions of rocks with the Fuerteventura amphiboles containing the highest amount of a crustal component. However, as trace element content and their ratios in amphiboles can depend on magma evolution and chemistry and crystallization conditions (Adam & Green 2003), these trace element ratio variations should be compared with other variables that are not sensitive to these factors, such as Sr isotope ratio. The Sr isotope ratios are again highest in the Fuerteventura amphiboles, supporting the assumed presence of an assimilated crustal component. This observation raises the question of whether the low $\delta^{18}O$ values found in these amphiboles can also be related to crustal contamination. However, the $\delta^{18}O$ values do not show any correlation with the Sr isotope ratios (Fig. 7a). Instead, the $^{87}Sr/^{86}Sr$ ratios show a relationship with those of Ba/Nb (Fig. 7b). Literature data obtained on amphiboles from other settings (and with variable amounts of a crustal component) have also been plotted in Figure 7b to establish an empirical relationship. There are two main trends that indicate mixing curves determined by different Ba, Nb, and Sr contents in the end-member components. The Canary Islands amphiboles fit the relationship that indicates mixing of uncontaminated mantle material with a component having a high Ba/Nb ratio and no enrichment in Sr, such as observed in the amphiboles from the alkaline basalts and calc-alkaline andesitic rocks of the Carpathian Basin (CB-A and CB-CA, respectively) which record mantle metasomatism by subducted material (see Demény *et al.* 2005). Marks *et al*. (2004) introduced a new variable to detect crustal contamination, the Pb/Pb* value ($Pb/Pb^* = Pb_N/\sqrt{(Ce_N Pr_N)}$) which seems to be independent of mineral–melt partition as pyroxenes and amphiboles fit the same trend in their Pb/Pb*–εNd(T) diagram. The Pb/Pb* and Ba/Nb(N) ratios show a good correlation that trends towards the amphiboles from the Carpathian Basin (Fig. 7c), supporting crustal contamination.

Interestingly, the δD values do display systematic distributions when compared with the Pb/Pb* values (Fig. 7d). The δD–Pb/Pb* plot indicates two trends from a component with low Pb/Pb* ratio (and low Ba/Nb and $^{87}Sr/^{86}Sr$) and a δD value of around −90‰, to higher Pb/Pb* values and (1) higher δD values (up to −67‰, La

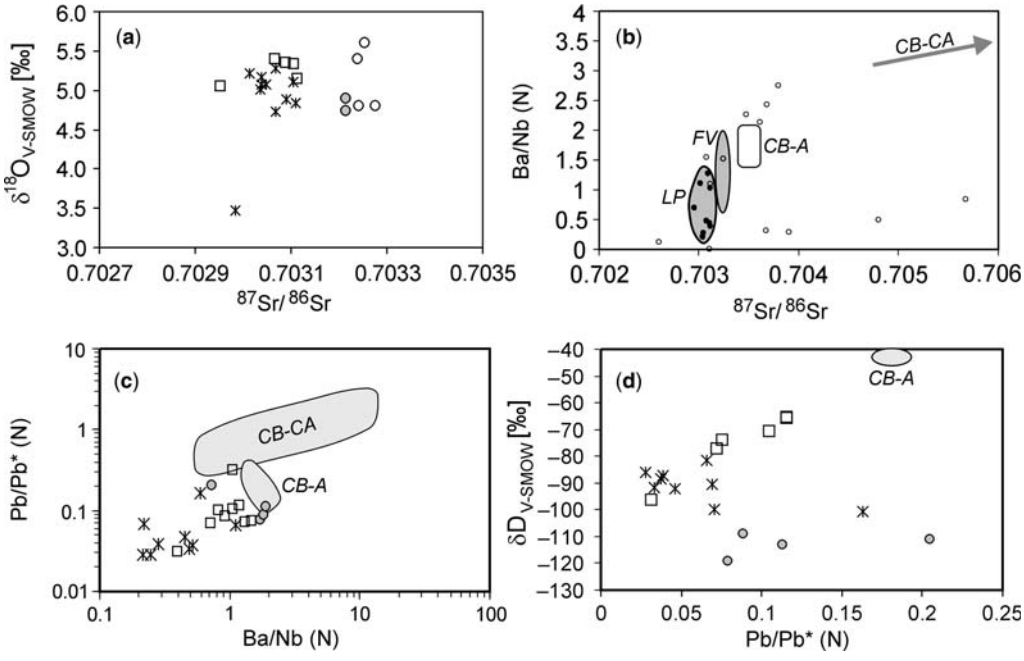

Fig. 7. Co-variations of assimilation-sensitive trace element ratios (Ba/Nb, Pb/Pb*, normalized to primative mantle, Hofmann 1988) and H, O and Sr isotope compositions in amphiboles of La Palma (LP) and Fuerteventura (FV). (**a**, **c**, **d**) □, amphibole xenocrysts and amphibololite xenoliths in basalts of La Palma; *, amphiboles in gabbros of La Palma; grey circles, amphiboles from Fuerteventura; ○, phlogopites from Fuerteventura (Demény *et al.* 2004). (**b**) •, data of the present study; ○, literature data (Downes *et al.* 1995; Zanetti *et al.* 1995; Witt-Eickschen *et al.* 1998; Tribuzio *et al.* 1999, 2000; Powell *et al.* 2004; Demény *et al.* 2005; Orejana *et al.* 2006; A. Demény, unpubl. data). CB-A, alkaline basalts from the Carpathian Basin; CB-CA, Calc-alkaline andesitic rocks from the Caspathian Basin.

Palma, amphibololite xenoliths) and (2) lower δD values (down to −119‰, Fuerteventura amphiboles). The observation that the δD values display co-variations with the Pb/Pb*, Ba/Nb and Sr isotope ratios, whereas the $\delta^{18}O$ values do not, suggests that the crustal component was introduced via a fluid phase, whose infiltration apparently did not affect the oxygen isotope compositions. The gabbros of La Palma belong to the early magmatic activity and may represent the upwelling melt, whereas the amphibololites could have been formed as cumulates in a magma chamber, which makes the contamination more probable. This process may explain the elevated Ba/Nb ratios and δD values in the xenoliths. Demény *et al.* (2004) have observed a difference in δD between phlogopites (δD about −95‰) and amphiboles (δD about −110‰) in Fuerteventura, which they related to early crystallization of phlogopite and later amphibole formation. The present data, however, suggest that the amphiboles were affected by fluid infiltration carrying a crustal component that is reflected by Pb/Pb*, Ba/Nb and $^{87}Sr/^{86}Sr$ increase.

The good agreement between the primary compositions inferred from the amphiboles of the La Palma gabbros ($\delta^{18}O$ about 5.1‰, δD about −90‰) and the phlogopites of the Fuerteventura volcanic rocks ($\delta^{18}O$ about 5.0‰, δD about −96‰) that have close-to-HIMU Sr–Nd–Pb isotope ratios indicates that these compositions are characteristic for the Canary Islands magmas and may represent the pristine plume component, as suggested by Demény *et al.* (2004). The lower than normal mantle $\delta^{18}O$ values can be most probably be explained by subducted ocean crust material, although a deep component originating from the core–mantle boundary could also be possible (Macpherson *et al.* 2000; Thirlwall *et al.* 2006). The crustal contamination model in which the upwelling magmas assimilate ocean crust material that had undergone high-temperature seawater–rock exchange can be excluded on the basis of H and Sr isotope compositions. The origin of the low δD values can also be related to the subduction of ocean crust as the slab undergoes partial devolatilization. Demény *et al.* (2004) have discussed and excluded this possibility. The general plume-related hydrogen isotope composition of about −95‰ in the region around the Canary Islands plume led them to suggest that the hydrogen component is of deep-seated origin. The present dataset further

supports this idea as the primary plume-related composition is similar for the western and eastern Canary Islands and does not vary with time (whereas the age of magmatism for Fuerteventura is about 20 Ma, that for La Palma is about 3 Ma).

Earlier studies have shown lower than normal mantle δD values in plume-related magmas (Deloule *et al.* 1991; Dyar *et al.* 1992; Kyser 1998) that were regarded as a primary feature. Demény *et al.* (2004) raised the possibility that the D depletion may be related to upwelling of material, especially volatile components, from the deep Earth. The enstatite chondrite material that constituted the early Earth and may be preserved in the deep mantle is thought to be highly D depleted (Javoy 1998). Theoretical examinations of hydrogen exchange processes between the deep Earth and the surface have shown that primordial hydrogen can be preserved in the core (Williams & Hemley 2001). As major plumes are rooted at the core–mantle boundary (Hofmann 1997), they may provide pathways for degassing volatiles. Mixing of D-depleted primordial hydrogen with the upper mantle component would produce the observed isotopic compositions.

Conclusions

It has been confirmed that the volcanic rocks of the Canary Islands have oxygen isotopic compositions that are slightly lower than those expected for rocks derived from the upper mantle and that may be attributed to a plume component (see Demény *et al.* 2004). Chemical compositions and stable and radiogenic isotope ratios of rocks from La Palma are similar in this regard to those from Fuerteventura. Amphibole, biotite, pyroxene and feldspar separates from Basal Complex gabbros, as well as amphibole xenocrysts and amphibololite xenoliths in basalts help constrain the petrogenesis of the La Palma rocks. The biotite and feldspar record interaction with meteoric water, whose isotopic composition indicates infiltration from about 3500 m a.s.l. This height has been inferred from stable isotope data for several islands in the archipelago (Javoy *et al.* 1986), thus it has general significance for the assessment of the evolution of the volcanic edifices.

Primary trace element contents and isotopic compositions have been preserved in the amphiboles of La Palma. Variables sensitive to crustal contamination (Ba/Nb and Pb/Pb*) show correlations with Sr isotope ratios, supporting assimilation of a crustal component. The lack of correlation between O and Sr isotope compositions and the relationship between Pb/Pb* ratio and δD values suggest that the crustal component was introduced as part of a fluid phase during metasomatism. The similarities in H and O isotope compositions between the rocks from Fuerteventura and La Palma are compatible with the earlier assumption that these values represent a plume component. Degassing to the same degree in different complexes and rocks producing the same H isotope composition cannot be excluded, but it is regarded as very unlikely. The most plausible explanation for the low $\delta^{18}O$ value is the presence of subducted ocean crust in the plume source, whereas the low δD values could be related to volatiles ascending from depth.

This study was conducted in the framework of Hungarian–Spanish intergovernmental scientific and technological co-operation with support from the Research and Technology Innovation Fund and MEC (E-38/01, E-22/04 and Integrate Action HH2004-0027) and the project CGL 2006-00970/BTE. We also thank the Haciendas de Argual y Tazacorte and the Caldera de Taburiente National Park for their help during the fieldwork. Financial support to A.D. was kindly provided by the Fondation Herbette, allowing for a 3 month stay at the University of Lausanne, where analyses of silicate minerals were conducted. The paper was significantly improved by the detailed reviews by M. Thirlwall and L. Dallai.

References

ADAM, J. & GREEN, T. 2003. The influence of pressure, mineral composition and water on trace element partitioning between clinopyroxene, amphibole and basanitic melts. *European Journal of Mineralogy*, **15**, 831–841.

AGRINIER, P., MÉVEL, C., BOSCH, D. & JAVOY, M. 1993. Metasomatic hydrous fluids in amphibole peridotites from Zabargad Island (Red Sea). *Earth and Planetary Science Letters*, **120**, 187–205.

ALBERT-BELTRÁN, J. F., ARANA, V., DIEZ, J. L. & VALENTIN, A. 1990. Physical–chemical conditions of the Teide volcanic system (Tenerife, Canary Islands). *Journal of Volcanology and Geothermal Research*, **43**, 321–332.

ALT, J. C. & BACH, W. 2006. Oxygen isotope composition of a section of lower oceanic crust, ODP Hole 735B. *Geochemistry, Geophysics, Geosystems*, **7**, article Number Q12008.

ANCOCHEA, E., HERNAN, F., CENDRERO, A., CANTAGREL, J. M., FUSTER, J. M., IBARROLA, E. & COELLO, J. 1994. Constructive and destructive episodes in the building of a young oceanic island, La Palma, Canary Islands, and genesis of the Caldera-de-Taburiente. *Journal of Volcanology and Geothermal Research*, **60**, 243–262.

APPORA, I., EILER, J. M., MATTHEWS, A. & STOLPER, E. M. 2003. Experimental determination of oxygen isotope fractionations between CO_2 vapor and soda–melilite melt. *Geochimica et Cosmochimica Acta*, **67**, 459–471.

BATES, R. L. & JACKSON, J. A. 1987. *Glossary of Geology*. American Geological Institute, Alexandria, Virginia.

BOETTCHER, A. L. & O'NEIL, J. R. 1980. Stable isotope, chemical, and petrographic studies of high-pressure amphiboles and micas: evidence for metasomatism in the mantle source regions of alkali basalts and kimberlites. *American Journal of Science*, **280-A**, 594–621.

BOTTINGA, Y. & JAVOY, M. 1973. Comments on oxygen isotope geothermometry. *Earth and Planetary Science Letters*, **20**, 250–265.

CARRACEDO, J. C., DAY, S. J., GUILLOU, H. & GRAVESTOCK, P. 1999*a*. Later stages of volcanic evolution of La Palma, Canary Islands: Rift evolution, giant landslides and the genesis of the Caldera de Taburiente. *Geological Society of America Bulletin*, **111**, 755–768.

CARRACEDO, J. C., DAY, S. J., GUILLOU, H. & PÉREZ TORRADO, F. J. 1999*b*. Giant Quaternary landslides in the evolution of La Palma and El Hierro, Canary Islands. *Journal of Volcanology and Geothermal Research*, **94**, 169–190.

CARRACEDO, J. C., BADIOLA, E. R., GUILLOU, H., DE LA NUEZ, J. & PÉREZ TORRADO, F. J. 2001. Geology and volcanology of La Palma and El Hierro, Western Canaries. *Estudios Geológicos*, **57**, 175–273.

CHAZOT, G., LOWRY, D., MENZIES, M. & MATTEY, D. 1997. Oxygen isotopic composition of hydrous and anhydrous mantle peridotites. *Geochimica et Cosmochimica Acta*, **61**, 161–169.

COLE, D. R. 1985. A preliminary evaluation of oxygen isotopic exchange between chlorite and water. *Geological Society of America, Abstracts with Programs*, **17**, 550.

DARLING, W. G., BATH, A. H. & TALBOT, J. C. 2003. The O and H stable isotope composition of freshwaters in the British Isles. 2. Surface waters and groundwater. *Hydrology and Earth System Sciences*, **7**, 183–195.

DE LA NUEZ, J. 1984. *El Complejo intrusivo-subvolcánico de La Caldera de Taburiente. La Palma (Canarias)*. Tesis Doctoral, Universidad Complutense de Madrid.

DELOULE, E., ALBARÈDE, F. & SHEPPARD, S. M. F. 1991. Hydrogen isotope heterogeneities in the mantle from ion probe analysis of amphiboles from ultramafic rocks. *Earth and Planetary Science Letters*, **105**, 543–553.

DEMÉNY, A., VENNEMANN, T. W., HEGNER, E. *ET AL*. 2004. H, O, Sr, Nd and Pb isotopic evidence for recycled oceanic crust in the Transitional Volcanic Group of Fuerteventura, Canary Islands, Spain. *Chemical Geology*, **205**, 37–54.

DEMÉNY, A., VENNEMANN, T. W., HOMONNAY, Z., MILTON, A., EMBEY-ISZTIN, A. & NAGY, G. 2005. Origin of amphibole megacrysts in the Plio-Pleistocene basalts of the Carpathian–Pannonian Region. *Geologica Carpathica*, **56**, 179–189.

DEMÉNY, A., VENNEMANN, T. W., HARANGI, SZ., HOMONNAY, Z. & FÓRIZS, I. 2006. H_2O–δD–Fe^{III} relations of dehydrogenation and dehydration processes in magmatic amphiboles. *Rapid Communications in Mass Spectrometry*, **20**, 919–925.

DOWNES, H., SEGHEDI, I., SZAKACS, A. *ET AL*. 1995. Petrology and geochemistry of late Tertiary/Quaternary mafic alkaline volcanism in Romania. *Lithos*, **35**, 65–81.

DYAR, M. D., MCGUIRE, A. V. & MACKWELL, S. J. 1992. Fe^{3+}/H^+ and D/H in kaersutites—misleading indicators of mantle source fugacities. *Geology*, **20**, 565–568.

EILER, J. M. 2001. Oxygen isotope variations of basaltic lavas and upper mantle rocks. *In*: VALLEY, J. W. & COLE, D. R.(eds) *Stable Isotope Geochemistry*. Mineralogical Society of America, Reviews in Mineralogy and Geochemistry, **43**, 319–364.

EILER, J. M., FARLEY, K. A., VALLEY, J. W., HAURI, E., CRAIG, H., HART, S. R. & STOLPER, E. M. 1997. Oxygen isotope variations in ocean island basalt phenocrysts. *Geochimica et Cosmochimica Acta*, **61**, 2281–2293.

EILER, J. M., CRAWFORD, A., ELLIOTT, T., FARLEY, K. A., VALLEY, J. W. & STOLPER, E. M. 2000. Oxygen isotope geochemistry of oceanic-arc lavas. *Journal of Petrology*, **41**, 229–256.

ERNST, W. G. & LIU, J. 1998. Experimental phase-equilibrium study of Al- and Ti-contents of calcic amphibole in MORB—a semiquantitative thermobarometer. *American Mineralogist*, **83**, 952–969.

FARVER, J. R. 1989. Oxygen self-diffusion in diopside with application to cooling rate determination. *Earth and Planetary Science Letters*, **92**, 386–396.

GALIPP, K., KLÜGEL, A. & HANSTEEN, T. H. 2005. Changing depths of magma fractionation and stagnation during the evolution of an oceanic island volcano: La Palma (Canary Islands). *Journal of Volcanology and Geothermal Research*, **155**, 285–306.

GAO, Y., HOEFS, J., PRZYBILLA, R. & SNOW, J. E. 2006. A complete oxygen isotope profile through the lower oceanic crust, ODP Hole 735B. *Chemical Geology*, **233**, 217–234.

GARCIA, M. O., MUENOW, D. W., AGGREY, K. E. & O'NEIL, J. R. 1989. Major element, volatile, and stable isotope geochemistry of Hawaiian submarine tholeiitic glasses. *Journal of Geophysical Research*, **94**, 10525–10538.

GARCIA, M. O., ITO, E., EILER, J. M. & PIETRUSZKA, A. J. 1998. Crustal contamination of Kilauea Volcano magmas revealed by oxygen isotope analyses of glass and olivine from Puu Oo eruption lavas. *Journal of Petrology*, **39**, 803–817.

GONFIANTINI, R., GALLO, G., PAYNE, B. R. & TAYLOR, C. B. 1975. *Environmental isotopes and hydrochemistry in ground water of Gran Canaria. I: Interpretation of environmental isotope and hydrochemical data in ground water hydrogeology*. IAEA, Vienna, 159–170.

GRAHAM, C. M., VIGLINO, J. A. & HARMON, R. S. 1987. Experimental study of hydrogen-isotope exchange between aluminous chlorite and water and of hydrogen diffusion in chlorite. *American Mineralogist*, **72**, 566–579.

GUILLOU, H., CARRACEDO, J. C. & DAY, S. J. 1998. Dating of the Upper Pleistocene–Holocene volcanic activity of La Palma using the unspiked K–Ar technique. *Journal of Volcanology and Geothermal Research*, **86**, 137–149.

GUILLOU, H., CARRACEDO, J. C. & DUNCAN, R. 2001. K–Ar, $^{40}Ar/^{39}Ar$ ages and magnetostratigraphy of Brunhes and Matuyama lava sequences from La

Palma Island. *Journal of Volcanology and Geothermal Research*, **106**, 175–194.

HARMON, R. S. & HOEFS, J. 1995. Oxygen isotope heterogeneity of the mantle deduced from global ^{18}O systematics of basalts from different geotectonic settings. *Contributions to Mineralogy and Petrology*, **120**, 95–114.

HART, S. R., BLUSZTAJN, J., DICK, H. J. B., MEYER, P. S. & MUEHLENBACHS, K. 1999. The fingerprint of seawater circulation in a 500-meter section of ocean crust gabbros. *Geochimica et Cosmochimica Acta*, **63**, 4059–4080.

HEGNER, E., WALTER, H. J. & SATIR, M. 1995. Pb–Sr–Nd isotopic compositions and trace element geochemistry of megacrysts and melilitites from the Tertiary Urach volcanic field: source composition of small volume melts under SW Germany. *Contributions to Mineralogy and Petrology*, **122**, 322–335.

HERNANDEZ-PACHECO, A. 1971. Nota previa sobre el complejo basal de la isla de La Palma (Canarias). *Estudios Geologicos*, **27**, 255–265.

HERNÁNDEZ PACHECO, A. & FERNÁNDEZ SANTÍN, S. 1974. Las formaciones volcánicas submarinas de la Caldera de Taburiente en La Palma (Canarias) y sus transformaciones metasomáticas. *In*: FERRÁN, O. G. (ed.) *Proceedings Symposium on Andean and Antarctic Volcanological Problems*, Santiago, Chile. IAVCEI, 98–111.

HILDENBRAND, A., GILLOT, P. Y., SOLER, V. & LAHITTE, P. 2003. Evidence for a persistent uplifting of La Palma (Canary Islands), inferred from morphological and radiometric data. *Earth and Planetary Science Letters*, **210**, 277–289.

HOERNLE, K. A. & TILTON, G. R. 1991. Sr–Nd–Pb isotope data for Fuerteventura (Canary Islands) basal complex and subaerial volcanics: applications to magma genesis and evolution. *Schweizerische Mineralogische und Petrographische Mitteilungen*, **71**, 3–18.

HOFMANN, A. W. 1988. Chemical differentiation of the Earth: the relationship between mantle, continental crust, and oceanic crust. *Earth and Planetary Science Letters*, **90**, 297–314.

HOFMANN, A. W. 1997. Mantle geochemistry: the message from oceanic volcanism. *Nature*, **385**, 219–229.

JAVOY, M. 1998. The birth of the Earth's atmosphere: the behaviour and fate of its major elements. *Chemical Geology*, **147**, 11–25.

JAVOY, M., STILLMAN, C. J. & PINEAU, F. 1986. Oxygen and hydrogen isotope studies on the basal complexes of the Canary Islands: implications on the conditions of their genesis. *Contributions to Mineralogy and Petrology*, **92**, 225–235.

KASEMANN, S., MEIXNER, A., ROCHOLL, A., VENNEMANN, T., SCHMITT, A. & WIEDENBECK, M. 2001. Boron and oxygen isotope composition of certified reference materials NIST SRM 610/612, and reference materials JB-2G and JR-2G. *Geostandards Newsletter*, **25**, 405–416.

KLÜGEL, A., HANSTEEN, T. H. & GALIPP, K. 2005. Magma storage and underplating beneath Cumbre Vieja volcano, La Palma (Canary Islands). *Earth and Planetary Science Letters*, **236**, 211–226.

KYSER, T. K. 1986. Stable isotope variations in the mantle. *In*: VALLEY, J. W., TAYLOR, H. P., JR & O'NEIL, J. R. (eds) *Stable Isotopes in High Temperature Geological Processes*. Mineralogical Society of America, Reviews in Mineralogy, **16**, 141–164.

KYSER, T. K. 1998. How variable is the hydrogen isotopic composition of the mantle? *Geological Society of America, Abstracts with Programs*, **30**, 271–27.

KYSER, T. K. & O'NEIL, J. R. 1984. Hydrogen isotope systematics of submarine basalts. *Geochimica et Cosmochimica Acta*, **48**, 2123–2133.

LEAKE, B. E., WOOLLEY, A. R., ARPS, C. E. S. *ET AL.* 1997. Nomenclature of amphiboles: Report of the subcommittee on amphiboles of the International Mineralogical Association, commission on new minerals and mineral names. *Canadian Mineralogist*, **35**, 219–246.

MACPHERSON, C. G., HILTON, D. R., MATTEY, D. P. & SINTON, J. M. 2000. Evidence for an ^{18}O-depleted mantle plume from contrasting $^{18}O/^{16}O$ ratios of back-arc lavas from the Manus Basin and Mariana Trough. *Earth and Planetary Science Letters*, **176**, 171–183.

MARCANTONIO, F., ZINDLER, A., ELLIOTT, T. & STAUDIGEL, H. 1995. Os isotope systematics of La Palma, Canary Islands: Evidence for recycled crust in the mantle source of HIMU ocean islands. *Earth and Planetary Science Letters*, **133**, 397–410.

MARKS, M., HALAMA, R., WENZEL, T. & MARKL, G. 2004. Trace element variations in clinopyroxene and amphibole from alkaline to peralkaline syenites and granites: implications for mineral–melt trace-element partitioning. *Chemical Geology*, **211**, 185–215.

MATTEY, D., LOWRY, D. & MACPHERSON, C. 1994. Oxygen isotope composition of mantle peridotite. *Earth and Planetary Science Letters*, **128**, 231–241.

MUEHLENBACHS, K. 1986. Alteration of the oceanic crust and the ^{18}O history of seawater. *In*: VALLEY, J. W., TAYLOR, H. P., JR & O'NEIL, J. R. (eds) *Stable Isotopes in High Temperature Geological Processes*. Mineralogical Society of America, Reviews in Mineralogy, **16**, 425–444.

NEUMANN, E. R., SØRENSEN, V. B., SIMONSEN, S. L. & JOHNSEN, K. 2000. Gabbroic xenoliths from La Palma, Tenerife and Lanzarote, Canary Islands: evidence for reactions between mafic alkaline Canary Islands melts and old oceanic crust. *Journal of Volcanology and Geothermal Research*, **103**, 313–342.

OREJANA, D., VILLASECA, C. & PATERSON, B. A. 2006. Geochemistry of pyroxenitic and hornblenditic xenoliths in alkaline lamprophyres from the Spanish Central System. *Lithos*, **86**, 167–196.

POWELL, W., ZHANG, M., O'REILLY, S. Y. & TIEPOLO, M. 2004. Mantle amphibole trace-element and isotopic signatures trace multiple metasomatic episodes in lithospheric mantle, western Victoria, Australia. *Lithos*, **75**, 141–171.

ROY-BARMAN, M. & ALLÈGRE, C. 1995. $^{187}Os/^{186}Os$ in oceanic island basalts: tracing oceanic crust recycling in the mantle. *Earth and Planetary Science Letters*, **129**, 145–161.

RUMBLE, D. & HOERING, T. C. 1994. Analysis of oxygen and sulfur isotope ratios in oxide and sulfide minerals by spot heating with a carbon dioxide laser in a

fluorine atmosphrere. *Accounts of Chemical Research*, **27**, 237–241.

SCHIFFMAN, P. & STAUDIGEL, H. 1994. Hydrothermal alteration of a seamount complex on La Palma, Canary Islands: Implications for metamorphism in accreted terranes. *Geology*, **22**, 151–154.

SCHIFFMAN, P. & STAUDIGEL, H. 1995. The smectite to chlorite transition in a fossil seamount hydrothermal system: the Basement Complex of La Palma, Canary Islands. *Journal of Metamorphic Geology*, **13**, 487–498.

SCHUMACHER, J. C. 1997. The estimation of ferric iron in electron microprobe analysis of amphiboles: Appendix to the nomenclature of amphiboles. *Canadian Mineralogist*, **35**, 238–246.

SHARP, Z. D., ATUDOREI, V. & DURAKIEWICZ, T. 2001. A rapid method for determination of hydrogen and oxygen isotope ratios from water and hydrous minerals. *Chemical Geology*, **178**, 197–210.

SINGER, B. S., RELLE, M. K., HOFFMAN, K. A., BATTLE, A., LAJ, C., GUILLOU, H. & CARRACEDO, J. C. 2002. Ar/Ar ages from transitionally magnetized lavas on La Palma, Canary Islands, and the geomagnetic instability timescale. *Journal of Geophysical Research—Solid Earth*, **107**, 2307.

SOBOLEV, A. V., HOFMANN, A. W. & NIKOGOSIAN, I. K. 2000. Recycled oceanic crust observed in 'ghost plagioclase' within the source of Mauna Loa lavas. *Nature*, **404**, 986–990.

STAUDIGEL, H. 1981. *Der Basale Complex von La Palma. Submarine vulkanische Processe, Petrologie, Geochemie und sekundare Prozesse im herausgehobenen, submarinen Teil einer ozeanischen Insel und ein Vergleich mit ozeanischer Kruste*. Dissertation Dr Naturw., Ruhr-Universitat Bochum.

STAUDIGEL, H. & SCHMINCKE, H. U. 1984. The Pliocene seamount series of La Palma, Canary Islands. *Journal of Geophysical Research*, **89**, 1195–1215.

STAUDIGEL, H., FERAUD, G. & GIANNERINI, G 1986. The history of intrusive activity on the Island of La Palma (Canary Islands). *Journal of Volcanology and Geothermal Research*, **27**, 299–322.

SUZUOKI, T. & EPSTEIN, S. 1976. Hydrogen isotope fractionation between OH-bearing minerals and water. *Geochimica et Cosmochimica Acta*, **40**, 1229–1240.

THIRLWALL, M. F., JENKINS, C., VROON, P. C. & MATTEY, D. P. 1997. Crustal interaction during construction of ocean islands: Pb–Sr–Nd–O isotope geochemistry of the shield basalts of Gran Canaria. Canary Islands. *Chemical Geology*, **135**, 233–262.

THIRLWALL, M. F., GEE, M. A. M., LOWRY, D., MATTEY, D. P., MURTON, B. J. & TAYLOR, R. N. 2006. Low $\delta^{18}O$ in the Icelandic mantle and its origins: evidence from Reykjanes Ridge and Icelandic lavas. *Geochimica et Cosmochimica Acta*, **70**, 993–1019.

TIEPOLO, M., VANNUCCI, R., OBERTI, R., FOLEY, S., BOTTAZZI, P. & ZANETTI, A. 2000. Nb and Ta incorporation and fractionation in titanian pargasite and kaersutite: crystal-chemical constraints and implications for natural systems. *Earth and Planetary Science Letters*, **176**, 185–201.

TRIBUZIO, R., THIRLWALL, M. F. & MESSIGA, B. 1999. Petrology, mineral and isotope geochemistry of the Sondalo gabbroic complex (Central Alps, Northern Italy): implications for the origin of post-Variscan magmatism. *Contributions to Mineralogy and Petrology*, **136**, 48–62.

TRIBUZIO, R., TIEPOLO, M. & THIRLWALL, M. F. 2000. Origin of titanian pargasite in gabbroic rocks from the Northern Apennine ophiolites (Italy): insights into the late-magmatic evolution of a MOR-type intrusive sequence. *Earth and Planetary Science Letters*, **176**, 281–293.

VALLEY, J. W., KITCHEN, N., KOHN, M. J., NIENDORF, C. R. & SPICUZZA, M. J. 1995. UWG-2, a garnet standard for oxygen isotope ratios: Strategies for high precision and accuracy with laser heating. *Geochimica et Cosmochimica Acta*, **59**, 5523–5531.

WEBSTER, J. D., KINZLER, R. J. & MATHEZ, E. A. 1999. Chloride and water solubility in basalt and andesite melts and implications for magnetic degassing. *Geochimica et Cosmochimica Acta*, **63**, 729–738.

WENNER, D. B. & TAYLOR, H. P., JR 1971. Temperatures of serpentinization of ultramafic rocks based on $^{18}O/^{16}O$ fractionation between coexisting serpentine and magnetite. *Contributions to Mineralogy and Petrology*, **32**, 165–185

WIDOM, E. & FARQUHAR, J. 2003. Oxygen isotope signatures in olivines from São Miguel (Azores) basalts: implications for crustal and mantle processes. *Chemical Geology*, **193**, 237–255.

WIDOM, E., HOERNLE, K. A., SHIREY, S. B. & SCHMINCKE, H. U. 1999. Os isotope systematics in the Canary Islands and Madeira: lithospheric contamination and mantle plume signatures. *Journal of Petrology*, **40**, 279–296.

WIECHERT, U., HOERNLE, K. & GRAHAM, D. 1997. Oxygen isotope evidence for high temperature altered oceanic crust in the Canary Plume. *EOS Transactions, Americal Geophysical Union*, **78**, 825–826.

WILLIAMS, Q. & HEMLEY, R. J. 2001. Hydrogen in deep Earth. *Annual Review of Earth and Planetary Sciences*, **29**, 365–418

WITT-EICKSCHEN, G., KAMINSKY, W., KRAMM, U. & HARTE, B. 1998. The nature of young vein metasomatism in the lithosphere of the West Eifel (Germany): Geochemical and isotopic constraints from composite mantle xenoliths from the Meerfelder Maar. *Journal of Petrology*, **39**, 155–185.

ZANETTI, A., VANNUCCI, R., OBERTI, R. & DOBOSI, G. 1995. Trace-element composition and crystal-chemistry of mantle amphiboles from the Carpatho-Pannonian Region. *Acta Vulcanologica*, **7**, 265–276.

ZHENG, Y.-F. 1993*a*. Calculation of oxygen isotope fractionation between anhydrous silicate minerals. *Geochimica et Cosmochimica Acta*, **57**, 1079–1091.

ZHENG, Y.-F. 1993*b*. Calculation of oxygen isotope fractionation in hydroxyl-bearing silicates. *Earth and Planetary Science Letters*, **120**, 247–263.

ZHENG, Y. F. 1994. Oxygen isotope fractionation in metal monoxides. *Mineralogical Magazine*, **58A**, 1000–1001.

Characterization of the metasomatic agent in mantle xenoliths from Devès, Massif Central (France) using coupled *in situ* trace-element and O, Sr and Nd isotopic compositions

S. TOURON[1,2,3], C. RENAC[2], S. Y. O'REILLY[1], J.-Y. COTTIN[2] & W. L. GRIFFIN[1]

[1]*GEMOC National Key Centre, Department of Earth and Planetary Sciences, Macquarie University, North Ryde, NSW 2109, Australia*

[2]*Département de Géologie–Pétrologie–Géochimie, Laboratoire Transferts Lithosphériques, UMR 6524, Université Jean Monnet, 23 Rue du Docteur Paul Michelon, Saint-Etienne, 42023, France*

[3]*Present address: LRMH—Château de Champs, 29 Rue de Paris, Champs sur Marne, 77420, France (e.mail: stephanie.touron@culture.gouv.fr)*

Abstract: Spinel lherzolites and harzburgites from Mont-Briançon and Marais de Limagne in the Devès volcanic district display coarse-grained to porphyroclastic microstructures and the modal content of volatile-bearing phases increases with the degree of deformation. Clinopyroxene and/or spinel are partly or totally reacted to amphibole. The coupled interpretations of trace-element, rare earth element (REE) and O–Sr–Nd data for clinopyroxene and amphibole indicate that the metasomatized mantle beneath Devès is a mixture of depleted and enriched mantle associated with an alkaline, high field strength element poor, and light rare earth element, U- and Th-rich carbonate-rich silicate fluid–melt metasomatic agent. Oxygen isotope and REE data for clinopyroxene–amphibole pairs indicate a $(La/Yb)_N$ enrichment related to an increasing metasomatic agent/rock ratio.

Because of its physical properties, the subcontinental lithospheric mantle (SCLM) can record large-scale tectonic and metamorphic events, whereas the physical and chemical signatures of these processes tend to be homogenized in the convecting mantle. Investigations of fragments of lithospheric mantle brought to the surface by magmas (mantle xenoliths) provide information beneath each locality about mineralogical and geochemical processes such as melt extraction, interaction with fluids or melts derived from different sources, asthenospheric upwelling, thermal erosion or delamination (O'Reilly *et al.* 2001).

Beneath the French Massif Central, previous geophysical studies have revealed the presence of a deep thermal anomaly (400 km depth) and have distinguished two lithospheric domains separated by the NE–SW 'Sillon Houiller', a major lithospheric structure (Granet *et al.* 1995). Geochemical studies of mantle xenoliths have also shown that this area consists of two geochemically contrasting lithospheric sections on each side of the 45°30′ N parallel (Fig. 1). These southern and northern domains have been interpreted as mantle heterogeneities generated during the Wilson cycle of the Hercynian orogeny (Lenoir *et al.* 2000; Downes *et al.* 2003).

Metasomatic minerals such as amphibole may play an important role in basalt petrogenesis (e.g. Beccaluva *et al.* 1998), and glass may be formed under mantle conditions by its destabilization (Chazot *et al.* 1996; Neumann & Wulff-Pedersen 1997; Neumann *et al.* 2002). Amphibole is usually observed either growing around clinopyroxene and/or spinel (e.g. Francis 1976; Moine *et al.* 2001; Coltorti *et al.* 2007) or in veins (e.g. Francis 1976; O'Reilly *et al.* 1991; Moine *et al.* 2001). Recent studies have also shown that glass can be directly related to amphibole formation (Coltorti *et al.* 2004). Amphibole has been observed in mantle xenoliths from the Massif Central, and previous studies (Boivin 1982; Deloule *et al.* 1991; Lenoir 2000) attributed its origin to an enriched mantle component (Deloule *et al.* 1991), possibly related to the Hercynian subduction in the Massif Central. Nevertheless, the relationships between clinopyroxene and amphibole, their trace-element contents and the isotopic compositions of O, Sr and Nd have not been discussed at the sample scale. This study focuses on mantle xenoliths from Mont-Briançon and Marais de Limagne, two localities in the southern domain (Devès volcanic district, 0.5–3.5 Ma, Maury & Varet 1980). Mont-Briançon is known for the absence of metasomatic parageneses in the peridotite xenoliths (Downes 1987; Lenoir *et al.* 2000), whereas ultramafic xenoliths from Marais de Limagne are

From: COLTORTI, M. & GRÉGOIRE, M. (eds) *Metasomatism in Oceanic and Continental Lithospheric Mantle.* Geological Society, London, Special Publications, **293**, 177–196.
DOI: 10.1144/SP293.9 0305-8719/08/$15.00

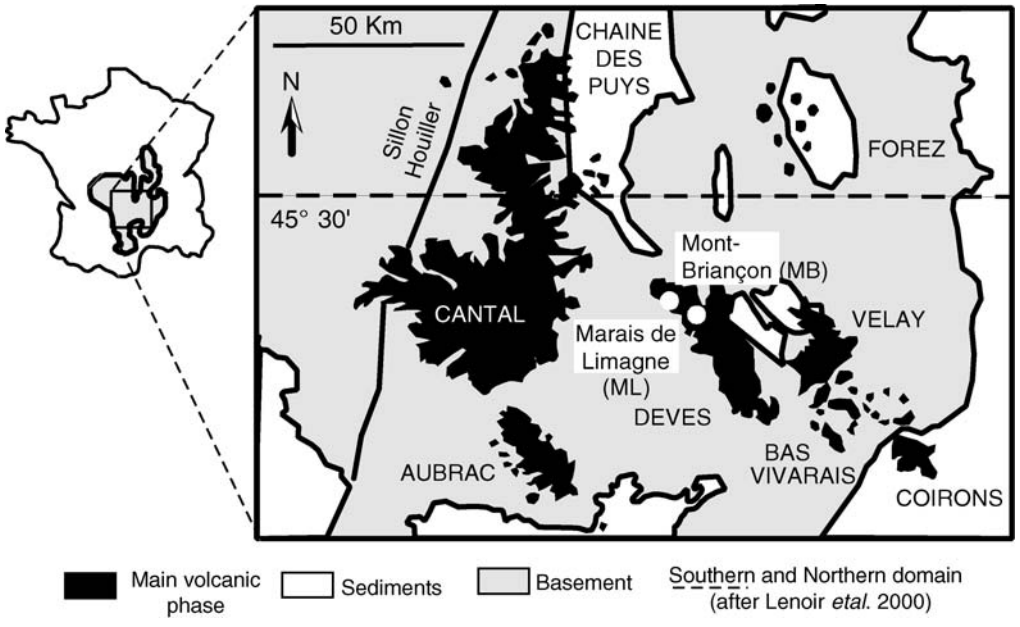

Fig. 1. Simplified map of the Eastern Massif Central showing the boundary (dashed line) between the two contrasting lithospheric domains (after Lenoir *et al.* 2000) and sample localities (MB, Mont-Briançon; ML, Marais de Limagne).

known for their richness in volatile-bearing phases (Jardin 1973; Boivin 1982; Downes 1987; Lenoir *et al.* 2000). Considering sample size and richness in volatile phases (when present) only few samples allowed a full set of geochemical analyses. The textural and paragenetic relationships of primary and metasomatic minerals, their chemical compositions and their O–Sr–Nd isotopic compositions have been used to constrain the geochemical fingerprint of the metasomatic agent and to evaluate the fluid/rock ratio at the sample scale.

Geological setting and sample descriptions

The French Massif Central is one of the most extensive exposures of the Variscan belt within Western Europe (Fig. 1). The Hercynian orogeny was the result of a collision between continental blocks following oceanic closure; uplift continued until Carboniferous time, when the gravitational collapse and peneplanation of the belt began (Le Griel 1988). During the Palaeocene, the Massif Central was uplifted and extended because of the Alpine orogeny (e.g. Michon & Merle 2001). This extension, associated with a mantle upwarping creating an asthenospheric flow, has been interpreted as the result of a hotspot originating either at the upper–lower mantle boundary (Hoernle *et al.* 1995) or *c.* 400 km beneath the Massif Central (Granet *et al.* 1995). This mantle upwelling is present beneath most recent volcanic areas and is responsible for the alkali-basaltic volcanism that occurred from the Eocene until 0.5 Ma ago (Maury & Varet 1980). Numerous mantle-derived xenoliths are found in these lavas. The southern domain of the French Massif Central is characterized by coarse-grained peridotites that are geochemically fertile, whereas protogranular and refractory peridotites are found in the northern area (Lenoir *et al.* 2000; Downes *et al.* 2003).

The two volcanic complexes studied here are located on the basaltic plateau of the Devès volcanic district (0.5–3.5 Ma, Maury & Varet 1980) near the limit between the two contrasting lithospheric domains. In the literature, mantle xenoliths from the strombolian cone of Mont-Briançon (samples MB; Fig. 1) have been described as free of volatile-bearing phases (Downes 1987; Lenoir *et al.* 2000; Touron 2005), whereas peridotite xenoliths from the phreatomagmatic cone at Marais de Limagne (samples ML; Fig. 1) often contain amphibole in various modal contents and rare phlogopite (Downes 1987; Lenoir *et al.* 2000; Touron 2005). Several tens of peridotites were collected in each locality. Peridotites from Mont-Briançon are centimetre- to decimetre-scale and are composed of coarse-grained anhydrous lherzolites as noted by previous studies (Downes 1987; Lenoir *et al.*

2000). Samples from the Marais de Limagne locality are centimetre- to rarely decimetre-sized and comprise a large variety of peridotites (coarse to porphyroclastic microstructures, anhydrous to hydrous lherzolites and harzburgites; Table 1). In this study, the chemical compositions of minerals and their isotopic ratios were obtained on samples characteristic of the main petrographic types and containing primary and metasomatic assemblages.

Analytical methods

Major- and trace-element compositions

Major-element compositions in minerals were determined using a CAMECA Camebax SX50 or a CAMECA SX100 electron microprobe. Silicate phases were analysed with an accelerating voltage of 15 kV and a beam current of 20 nA. Counting time was 10 s on the peak and 5 s for background on both sides of the peak. Lower detection limit were between 0.09 and 0.03 wt%. The mg-number ($= 100Mg/(Fe^{2+} + Mg)$, atoms per formula unit (a.p.f.u.)) of silicates and oxides and the cr-number ($= 100Cr/(Cr + Al)$, a.p.f.u.) of spinel will be used to define the refractory or enriched character of minerals.

Trace elements in clinopyroxenes and amphiboles were analysed with 266 nm and 213 nm lasers connected to an Agilent 7500 Series quadrupole inductively coupled plasma mass spectrometry (ICP-MS) system (frequency 5 Hz, energy 0.5 and 1 mJ; Norman *et al.* 1996). NIST 610 was used as the external standard to calibrate the instrument using values of Norman *et al.* (1996) and Ca contents from electron microprobe as the internal standard. Precision and accuracy on trace elements are documented by repeated analysis of BCR-2G. The oxide production is monitored by measuring $^{248}ThO/^{232}Th$ (Norman *et al.* 1996, 1998). Data were processed on-line using the GLITTER software (Van Achterbergh *et al.* 2001).

Isotopic composition of oxygen

Prior to oxygen extraction, separated olivine and pyroxenes were cleaned in HNO_3 (68%) at 50 °C for 1 h to remove material in dissolution pits and various impurities, then rinsed with MQ H_2O until neutral pH. Optically pure grains were picked for oxygen extraction, which was carried out using BrF_5 in the conventional method (Clayton & Mayeda 1963) for clinopyroxenes and amphiboles, whereas for olivines and orthopyroxenes, O_2 was extracted using a CO_2 laser-heating setup (Sharp 1990). The extraction was performed on one or several grains depending on their weight. O_2 quantities (>25 μmol; e.g. 2–4 mg for laser and 5–8 mg for conventional), yields

Table 1. *Petrographic characteristics of studied samples from Mont-Briançon (MB) and Marais de Limagne (ML) with textural type, microstructure, modal composition and calculated equilibrium temperature (after Brey & Kohler 1990)*

Sample:	MB4	MB32	MB52	ML25	ML40	ML22	ML30
Rock-type:	spinel lherzolite	spinel lherzolite	spinel lherzolite	spinel–amphibole lherzolite	spinel–amphibole lherzolite	spinel–amphibole harzburgite	spinel–amphibole harzburgite
Microstructure:	coarse-grained	coarse-grained	coarse-grained	coarse-equant	porphyroclastic	porphyroclastic	porphyroclastic
Modal contents (%)							
ol	58.5	58.4	67.5	56	52	65	67
opx	23	26.1	19.1	27	27	24	12
cpx	16	12.7	12.2	13	11	4	–
sp	2.5	2.8	1.2	3	1	1	0.1
amp	–	–	–	1	8	7	21
phl	–	–	–	–	1	–	–
Equilibrium temperature (°C)	960	930	950	930	950	920	930

and reproducibility were monitored, with in-house standards and international standards (NBS28; UWG2 and San Carlos olivine provided by J. O'Neil). Uncertainties on the analyses were $\pm 0.3‰$ and $\pm 0.2‰$ for conventional and laser methods, respectively. CO_2 gases were analysed with an ISOPRIME dual-inlet mass spectrometer (Université Jean Monnet). Results were normalized to international standards using the technique described by Coplen (1988).

Sr and Nd extraction and isotopic ratios

Aliquots of inclusion-free pure clinopyroxenes and amphiboles were handpicked using a binocular microscope. The minerals (*c*. 150 mg) were leached in sub-boiling 6 N two-bottle-distilled HCl in pre-cleaned Teflon beakers for 20 min, then rinsed with MQ H_2O until pH neutral. The samples were then re-picked to ensure optical purity. The samples were digested and prepared following conventional procedures (Patchett & Tatsumoto 1980; Blichert-Toft *et al.* 1997; Blichert-Toft 2001). The Sr and Nd solutions were analysed by mass spectrometry using a Nu Plasma multicollector ICP-MS system. The samples were introduced using an MCN-6000 desolvating micro-concentric nebulizer with an uptake of 60 μl min^{-1} and 100 μl min^{-1}, respectively. After each analysis, 2% HNO_3 solution was run for 10–15 minutes as a washout.

The Sr and Nd isotopes and their respective interference-free ^{87}Rb and ^{147}Sm isotope were analysed simultaneously (static-collection mode) in Faraday cups. Interferences of ^{144}Sm on ^{144}Nd were corrected using the recommended ratio $^{144}Sm/^{147}Sm$ of 0.2070. The data were normalized to $^{146}Nd/^{144}Nd = 0.7219$ (Wasserburg *et al.* 1981). Interferences of ^{87}Rb on ^{87}Sr were corrected using the recommended ratio for $^{85}Rb/^{87}Rb$ of 0.38632. The data were normalized to $^{86}Sr/^{88}Sr = 0.1194$. The zero measurement was made by ESA (electrostatic analyser) deflection. External precision of $^{143}Nd/^{144}Nd$ is ± 0.000038 ($n = 12$) for BHVO2 and ± 0.000066 ($n = 13$) for JMC321. External precision of $^{87}Sr/^{86}Sr$ is about ± 0.000032 ($n = 13$) for BHVO2 and 0.000058 for SRM987 (see also http://www.es.mq.edu.au/GEMOC/).

Results

Petrographic observations

The studied lherzolites and harzburgites display a range of microstructure regardless of the rock type (Table 1). All anhydrous lherzolites (MB4, MB32 and MB52) display a coarse-grained microstructure

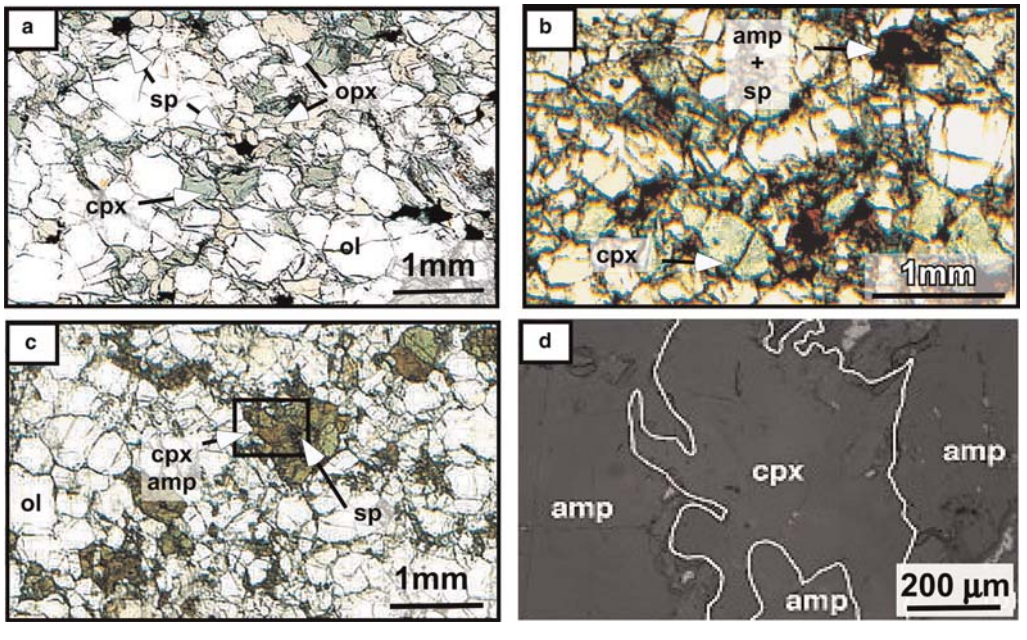

Fig. 2. (**a**) Spinel lherzolite (MB52), (**b**) spinel–amphibole lherzolite (ML40) and (**c**) spinel–amphibole harzburgite (ML30) in transmitted light, and (**d**) spinel–amphibole harzburgite in reflected light (ML30), showing mineral assemblages involving olivine (ol), clinopyroxene (cpx), orthopyroxene (opx), spinel (sp) and amphiboles (amp), such as disseminated amphibole surrounding spinel (b and c) or, as in enlargement of (c), reactive front between clinopyroxene and amphibole (d).

(Fig. 2a). In these xenoliths, olivine (ol), orthopyroxene (opx) and clinopyroxene (cpx) are of similar size (1.5–2 mm), highlighting the primary mineralogical character of these minerals. Spinel (sp) is a minor interstitial phase, usually <1.5 mm across, and does not show any consistent spatial relationship to the other phases. The coarse-grained anhydrous lherzolite MB4 is the sample richest in cpx (16%; Table 1). Amphibole-rich xenoliths are characteristic of the Marais de Limagne locality. Generally, there does not seem to be any consistent relationship between the modal contents of amphibole (amp) and cpx (Touron 2005). Nevertheless, in the few samples presented here, the modal content of amp increases with the degree of deformation (from coarse-grained to porphyroclastic microstructure) and recrystallization, whereas the modal content of cpx decreases. The coarse-equant lherzolite ML25 is amp-poor (1%, Table 1) with millimetre-scale mineral. Spinel is in intergranular positions surrounded by amphibole and is similar in grain size to coexisting ol, opx, cpx and amp. The modal contents of amp in the porphyroclastic lherzolite (ML40) and the two porphyroclastic harzburgites (ML22 and ML30) vary from 5 to 21% (Table 1). In ML22, porphyroclasts of olivine are 3 mm across whereas porphyroclasts of orthopyroxene can be slightly larger (up to 3.5 mm). Granuloblasts are composed of ol, opx, cpx, amp and sp, and range from 0.8 to 1 mm in diameter. Spinel grains define a foliation and amphibole grains can be either disseminated in the granuloblastic matrix or located around spinel (Fig. 2b). In the two amp-rich harzburgites ML22 and ML30, porphyroclasts of ol and opx have grain sizes ranging from 3.5 to 4 mm whereas neoblasts of ol, opx, cpx and amp are 0.2–1 mm in diameter. Spinel is rare, interstitial, and surrounded by amp; its grain size is <0.3 mm in ML22 and <1 mm in ML30. In the amp-rich harzburgite ML30 cpx is relict (Fig. 2c), being corroded and partially or totally replaced to amp (Fig. 2d). Phlogopite (phl) is observed only in lherzolite ML40 (1%; Table 1); it appears to be in textural equilibrium with amp and cpx. In the samples from both localities, no glass has been observed at grain boundaries or near sp, cpx and amp crystals. Nevertheless, it can occur near amphibole in very few samples from Marais de Limagne, probably associated with the destabilization of this mineral and related to possible interaction with host lava (Touron 2005). Therefore, these samples have been discarded from this study.

Major- and trace-element compositions of minerals

None of the minerals studied here show any zoning for major-element compositions. Olivines have mg-number ranging from 0.89 to 0.91, with weak variations of NiO, MnO and CaO contents (Table 2), regardless of the rock types and the modal content of volatile-bearing phases. The opx have mg-number ranging from 0.90 to 0.91 in hydrous harzburgites and homogeneous CaO contents. In contrast to mg-number and CaO, Al_2O_3 contents in opx vary from Al_2O_3-rich in porphyroclasts from the phl–amp-lherzolite to Al_2O_3-poor in amp-rich harzburgite. Spinel has variable Cr_2O_3 contents with cr-number ranging from 0.08 to 0.60. The highest and lowest cr-number values correspond respectively to the amph-rich harzburgite and to an anhydrous lherzolite from Mont-Briançon containing MgO-rich spinel. Cpx is Cr-diopside. Amphibole is pargasitic and hastingsitic or hornblende (ML30) with mg-number varying from 0.89 to 0.91 and from 0.87 to 0.89, respectively. Both cpx and amp are Al_2O_3-rich; the highest Al_2O_3 contents are found in the anhydrous lherzolite from Mont-Briançon (MB4) and the amp-rich harzburgite from Marais de Limagne (ML30). Whereas cpx is MgO- and Cr_2O_3-rich and TiO_2 -poor, coexisting amp is Cr_2O_3- and TiO_2-rich (Table 2). With the exception of the TiO_2 content in cpx, which strongly decreases (form 0.72 to 0.21 wt%) with increasing amp content (from 1 to 8%), no chemical evolution can be observed within cpx from anhydrous to highly hydrous samples. Phl from ML40 is Cr_2O_3 and Al_2O_3-rich with a mg-number of 0.87 (Table 2).

Chondrite (C1) normalized rare earth element (REE) patterns for cpx and amp display wide variations especially in the light REE (LREE from 0.6 to 80 times C1 and from 0.9 to 150 times C1, respectively, Fig. 3a and Table 3). In cpx, the middle REE (MREE) and heavy REE (HREE) are similar within all rock-types, at about 10 times C1. In comparison, the MREE and HREE contents of amp are higher and more than 10 times C1. The highest REE content is observed in amphibole from the most amphibole-rich harzburgite ML30.

LREE depletion is observed in amp and cpx in the anhydrous lherzolites from Mont-Briançon $(La/Yb)_{NC1} = 0.2–0.4$) and in cpx and amp in the amp-poor lherzolite from Marais de Limagne (ML25; $(La/Yb)_{NC1} = 0.1$ for both cpx and amphibole; Fig. 3a and Table 3). These minerals display a similar depletion in most lithophile elements and are characterized by slight negative anomalies in Nb, Ta, Ti and Ba. Moreover, amphibole from the amp-poor lherzolite (ML25, Fig. 3a) displays a positive anomaly in U.

In the amp–phl-bearing lherzolite (ML40), all cpx have similar REE patterns, whereas for amphiboles two types can be observed: those located around spinel display an almost flat REE pattern except for La and Ce, and are notably poorer in LREE than amp disseminated in the matrix

Table 2. *Major-element compositions of minerals expressed as weight percent of oxides, structural formulae, mg-number and cr-number*

Sample:	MB4	MB32	MB52	ML25	ML40	ML40	ML22	ML22	ML30	MB4	MB32	MB52	ML25	ML40	ML40	ML22	ML22	ML30	MB4
Mineral:	Ol	Ol	Ol	Ol	Ol porp.	Ol neob.	Ol porp.	Ol neob.	Ol	Opx	Opx	Opx	Opx	Opx porp.	Opx neob.	Opx porp.	Opx neob.	Opx	Cpx
n:	6	7	7	10	1	4	3	6	7	6	8	7	3	1	1	3	6	4	7
SiO_2	40.69	40.68	40.59	40.67	41.14	40.84	40.83	40.88	40.98	55.43	55.28	55.4	55.32	55.50	55.86	56.44	55.93	57.45	51.57
TiO_2	0.00	0.00	0.00	0.01	0.00	0.00	0.01	0.01	0.02	0.12	0.1	0.08	0.08	0.10	0.07	0.02	0.06	0.02	0.72
Al_2O_3	0.03	0.02	0.02	0.01	0.00	0.01	0.01	0.01	0.01	3.93	3.76	3.66	3.51	4.47	3.62	2.72	3.46	1.65	7.04
Cr_2O_3	0.01	0.02	0.03	0.02	0.00	0.01	0.01	0.02	0.01	0.22	0.31	0.28	0.26	0.31	0.32	0.35	0.39	0.30	0.68
FeO	10.19	9.39	9.73	10.09	10.47	10.52	9.11	9.21	9.98	6.38	6.07	6.15	6.50	6.66	6.93	5.99	6.11	6.26	2.99
MnO	0.13	0.13	0.13	0.16	0.12	0.18	0.15	0.13	0.2	0.13	0.14	0.12	0.15	0.24	0.16	0.15	0.12	0.20	0.08
MgO	48.67	49.28	49.45	48.59	47.93	48.18	49.86	49.87	48.72	32.89	33.41	33.46	33.01	32.64	32.92	34.08	34.00	33.74	14.76
CaO	0.06	0.07	0.05	0.05	0.05	0.04	0.05	0.04	0.04	0.64	0.59	0.63	0.57	0.50	0.66	0.55	0.56	0.59	20.29
Na_2O	0.01	0.01	0.00	0.01	0.01	0.00	0.01	0.01	0.01	0.09	0.09	0.11	0.05	0.07	0.06	0.08	0.07	0.08	1.71
K_2O	0.01	0.01	0.00	0.00	0.00	0.01	0.01	0.01	0.00	0.01	0.01	0.00	0.01	0.00	0.00	0.01	0.01	0.02	0.01
Ni0	0.39	0.39	0.38	0.36	0.44	0.38	0.35	0.36	0.35	0.06	0.11	0.1	0.08	0.02	0.08	0.07	0.11	0.09	0.04
ZnO																			
V_2O_3																			
F																			
Cl	n.d.																		
Total	100.22	100.02	100.41	99.97	100.23	100.26	100.39	100.56	100.37	99.91	99.87	100.02	99.53	100.56	100.77	100.44	100.81	100.45	99.92
Structural formulae																			
Si (IV)	1.00	1.00	0.99	1.00	1.01	1.00	0.99	1.00	1.00	1.92	1.91	1.91	1.92	1.91	1.92	1.92	1.94	1.97	1.87
Al (IV)	0.00	0.00	0.00	0.00	0.00	0.00	0.00	0.00	0.00	0.16	0.15	0.00	0.14	0.18	0.15	0.13	0.11	0.07	0.3
Al (VI)																			
Ti	0.00	0.00	0.00	0.00	0.00	0.00	0.00	0.00	0.00	0.00	0.00	0.15	0.00	0.00	0.00	0.00	0.00	0.00	0.02
Cr	0.00	0.00	0.00	0.00	0.00	0.00	0.00	0.00	0.00	0.01	0.01	0.01	0.01	0.01	0.01	0.01	0.01	0.01	0.02
Fe^{3+}																			
Fe^{2+}	0.21	0.19	0.2	0.21	0.21	0.22	0.19	0.19	0.2	0.18	0.18	0.18	0.19	0.19	0.2	0.17	0.17	0.18	0.09
Mn	0.00	0.00	0.00	0.00	0.00	0.00	0.00	0.00	0.00	0.00	0.00	0.00	0.00	0.01	0.00	0.00	0.00	0.01	0.00
Mg	1.78	1.80	1.80	1.78	1.75	1.76	1.81	1.81	1.78	1.69	1.72	1.72	1.71	1.67	1.69	1.73	1.74	1.73	0.8
Ni	0.01	0.01	0.01	0.01	0.01	0.01	0.01	0.01	0.01	0.00	0.00	0.00	0.00	0.00	0.00	0.00	0.00	0.00	0.00
Ca	0.00	0.00	0.00	0.00	0.00	0.00	0.00	0.00	0.00	0.02	0.02	0.02	0.02	0.02	0.02	0.02	0.02	0.02	0.79
Na	0.00	0.00	0.00	0.00	0.00	0.00	0.00	0.00	0.00	0.01	0.01	0.01	0.00	0.00	0.00	0.00	0.01	0.01	0.12
K	0.00	0.00	0.00	0.00	0.00	0.00	0.00	0.00	0.00	0.00	0.00	0.00	0.00	0.00	0.00	0.00	0.00	0.00	0.00
F																			
Cl																			
OH*																			
Total	3.00	3.00	3.01	3.00	2.99	3.00	3.01	3.00	3.00	4.00	4.01	4.01	4.00	4.00	4.00	4.01	4.00	4.01	
mg-no.	0.89	0.9	0.90	0.90	0.89	0.89	0.91	0.91	0.90	0.90	0.91	0.91	0.90	0.90	0.89	0.91	0.91	0.91	0.90
cr-no.																			

Sample:	MB32	MB52	ML25	ML40	ML22	MB4	MB32	MB52	ML25	ML40	ML22	ML30	ML25	ML40	ML40	ML22	ML30	ML40
Mineral:	Cpx	Cpx	Cpx	Cpx	Cpx	Sp	Sp	Sp	Sp	Sp	Sp	Sp	Amp	Amp dis	Amp sp	Amp	Amp	Phl
n:	7	6	10	4	6	4	7	5	2	3	4	4	2	3	4	10	14	1
SiO2	51.59	51.79	51.44	52.37	53.12	0.06	0.06	0.08	0.07	0.03	0.06	0.05	42.87	43.90	43.62	43.44	45.00	38.97
TiO2	0.56	0.52	0.57	0.36	0.21	0.13	0.1	0.12	0.07	0.05	0.02	0.08	1.58	1.17	0.80	0.73	0.39	1.09
Al2O3	6.55	6.69	6.41	5.51	4.46	58.34	55.57	55.87	57.27	48.16	44.6	19.54	14.78	14.4	14.15	14.3	12.05	17.22
Cr2O3	0.89	0.87	0.62	0.69	0.86	8.06	11.2	11.09	8.86	16.78	22.51	43.65	1.01	0.84	1.15	1.61	2.02	1.10
FeO	2.66	2.73	2.96	3.22	2.73	10.48	10.7	10.98	11.5	14.76	13.11	20.46	4.38	4.71	4.73	4.09	4.50	4.48
MnO	0.07	0.02	0.06	0.08	0.07	0.07	0.08	0.12	0.1	0.14	0.15	0.29	0.02	0.02	0.05	0.05	0.04	0.02
MgO	14.67	14.61	14.68	15.25	15.70	21.88	22.09	21.88	20.78	19.38	19.27	13.86	17.42	17.57	17.43	17.75	17.93	22.3
CaO	20.4	20.6	20.99	21.4	21.33	0.00	0.01	0.01	0.03	0.01	0.01	0.1	11.09	10.98	11.11	10.95	10.50	0.01
Na2O	1.89	1.98	1.56	1.15	1.49	n.d.	n.d.	n.d.	n.d.	n.d.	n.d.	n.d.	3.80	3.49	3.27	3.77	3.58	0.93
K2O	0.00	0.01	0.01	0.01	0.00	n.d.	n.d.	n.d.	n.d.	n.d.	n.d.	n.d.	0.01	0.30	0.76	0.43	0.87	8.61
Ni0	0.03	0.06	0.05	0.03	0.04	0.44	0.35	0.34	0.36	0.34	0.3	0.12	0.11	0.15	0.12	0.07	0.11	0.22
ZnO						0.08	0.08	0.08	0.09	0.15	0.17	0.16						
V2O3						0.08	0.06	0.07	0.08	0.03	0.08	0.1						
F													0.02	0.06	0.03		0.06	0.45
Cl													0.00	0.00	0.06		0.12	0.07
Total	99.33	99.93	99.34	100.14	100.00	99.62	100.3	100.68	99.2	99.83	100.28	98.42	97.08	97.62	97.34	97.19	97.18	95.58
Structural formulae																		
Si (IV)	1.88	1.88	1.80	1.90	1.93	0.00	0.00	0.00	0.00	0.00	0.00	0.00	6.06	6.17	6.18	6.15	6.39	5.45
Al (IV)	0.28	0.29	0.28	0.24	0.19	1.78	1.7	1.71	1.76	1.55	1.44	0.74	1.94	1.83	1.82	1.85	1.61	2.55
Al (VI)													0.53	0.56	0.54	0.53	0.4	0.29
Ti	0.02	0.01	0.02	0.01	0.01	0.00	0.00	0.00	0.00	0.00	0.00	0.00	0.17	0.12	0.09	0.08	0.04	0.11
Cr	0.03	0.02	0.02	0.02	0.02	0.16	0.23	0.23	0.18	0.36	0.49	1.11	0.11	0.09	0.13	0.18	0.23	0.12
Fe^{3+}													0.52	0.55	0.56	0.48	0.53	0.17
Fe^{2+}	0.08	0.08	0.09	0.1	0.08	0.23	0.23	0.24	0.25	0.34	0.3	0.55						0.35
Mn	0.00	0.00	0.00	0.00	0.00	0.00	0.00	0.00	0.00	0.00	0.00	0.01	0.00	0.00	0.01	0.01	0.00	0.01
Mg	0.8	0.79	0.8	0.82	0.85	0.84	0.86	0.84	0.81	0.79	0.79	0.66	3.67	3.68	3.68	3.74	3.79	4.65
Ni	0.00	0.00	0.00	0.00	0.00	0.01	0.01	0.01	0.01	0.01	0.01	0.00	0.01	0.02	0.01	0.01	0.01	0.02
Ca	0.8	0.8	0.82	0.83	0.83	0.00	0.00	0.00	0.00	0.00	0.00	0.00	1.68	1.65	1.69	1.66	1.6	0.00
Na	0.13	0.14	0.11	0.08	0.1	0.00	0.00	0.00	0.00	0.00	0.00	0.00	1.04	0.95	0.9	1.03	0.99	0.25
K	0.00	0.00	0.00	0.00	0.00	0.00	0.00	0.00	0.00	0.00	0.00	0.00	0.00	0.05	0.14	0.08	0.16	1.54
F													0.01	0.03	0.01		0.03	0.20
Cl													0.00	0.00	0.01		0.03	0.02
OH*													1.99	1.97	1.97	2.00	1.94	4.00
Total	4.02	4.02	3.94	4.00	4.01	3.03	3.03	3.03	3.02	3.04	3.03	3.07	17.74	17.69	17.73	17.81	17.75	5.86
mg-no.	0.91	0.91	0.90	0.89	0.91	0.79	0.79	0.78	0.76	0.7	0.72	0.55	0.88	0.87	0.87	0.89	0.88	0.87
cr-no.						0.08	0.12	0.12	0.09	0.19	0.25	0.6						

neob., neoblast, por., porphyroblast, amp dis, amphibole disseminated; amp sp, amphibole associated with spinel; n.d., not determinied; *n*, number of analyses.

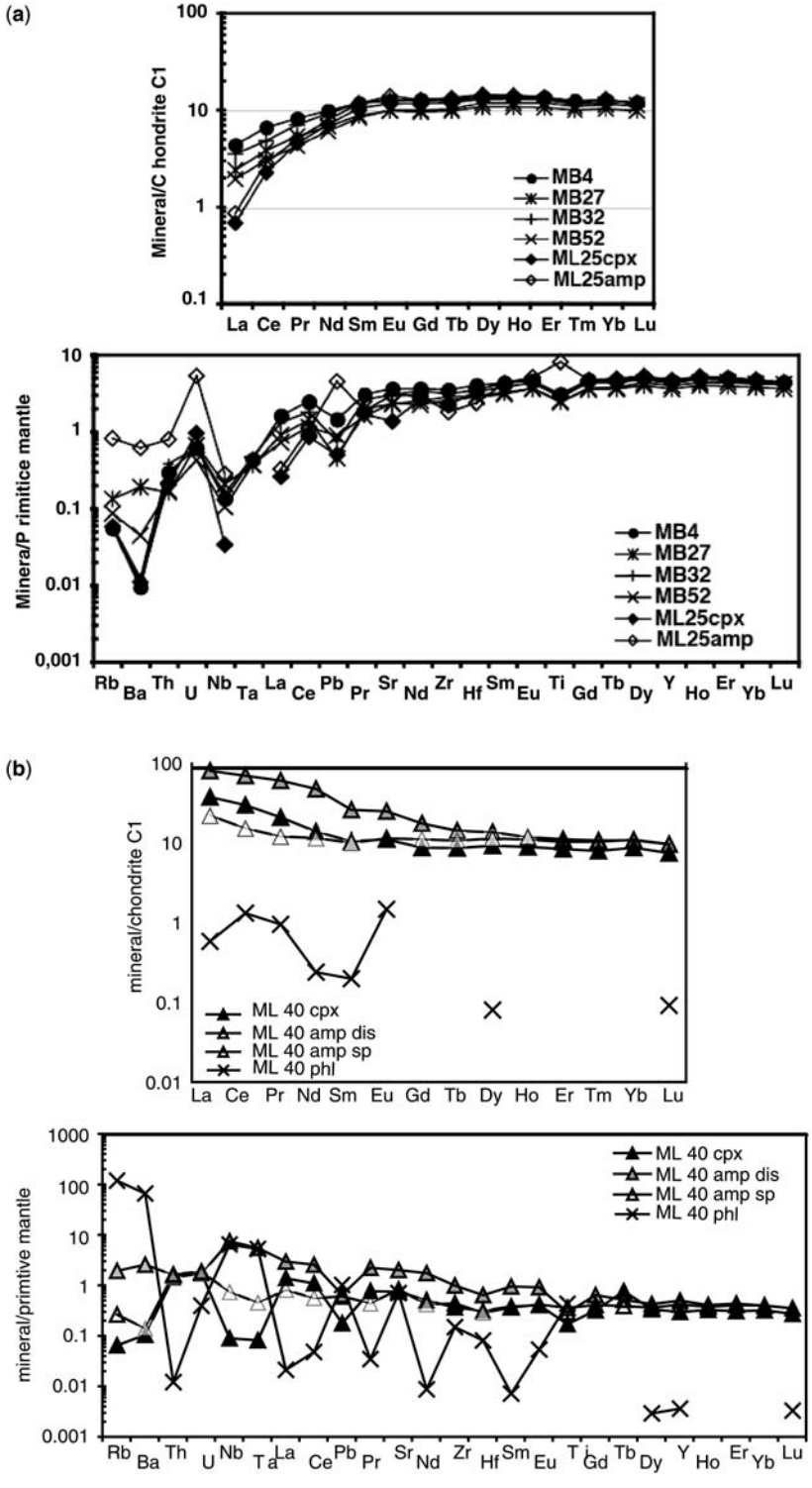

Fig. 3. (*Continued*).

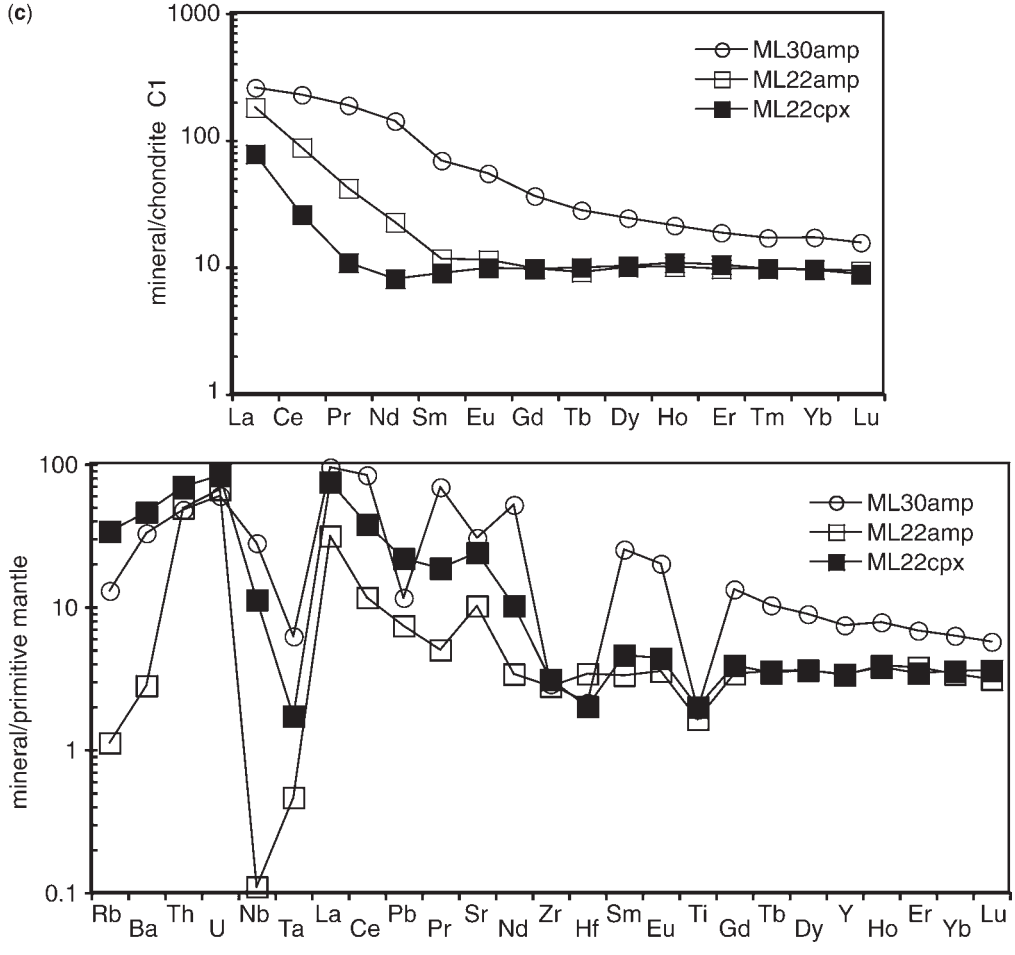

Fig. 3. (*Continued*) Chondrite C1-normalized REE patterns and primitive mantle normalized trace-element patterns (after McDonough & Sun 1995) for cpx, amp and phl of (**a**) anhydrous and hydrous depleted lherzolites (MB4, 27, 32, 52 and ML25), (**b**) two types of amphibole (amp-dis, amphibole disseminated; amp sp, amphibole associated with spinel; see Table 3) in amp-lherzolite ML40, (**c**) hydrous harzburgites (ML22 and 30).

($(La)_{C1} = 20-80$; Fig. 3b and Table 3). The enrichment in Gd and LREE is evident. Primitive mantle-normalized cpx displays strong negative anomalies in Rb, Ba, Nb, Ta and Ti. In contact with spinel, Al_2O_3- and TiO_2-rich amp has a pattern similar to those of coexisting cpx. Disseminated amp is richer in trace elements, although Th, U, Pb, Ti and HREE contents are comparable with those of sp-associated amp and display trace-element patterns similar to those of the coexisting cpx, as observed in other amp-bearing peridotites (Coltorti *et al.* 2004, 2007).

Therefore, amp shows different trace-element signatures related to its petrographic location within the amp–phl bearing lherzolite (ML40). Associated with disseminated amp, phl has a low REE content enriched in Rb, Ba, Nb, Ta, Pb and Sr.

In the amp-bearing harzburgites (ML22; and ML30; Fig. 3c and Table 3), cpx and coexisting amp are enriched in LREE relative to HREE ($(La/Yb)_{NC1} = 3.8-8.2$ for cpx and 2–15.8 for amphiboles). The primitive mantle-normalized diagrams for the most incompatible element-enriched cpx (ML22) show strong negative anomalies in Rb, Ba, Nb, Ta and Ti. Amps in both harzburgites display negative anomalies in Nb, Ta, Zr, Hf and Ti. The strongest enrichment (lithophile elements and REE) or depletion (HFSE) is observed in the most modally metasomatized sample: the amp-rich harzburgite (21% of amphibole for $(La/Yb)_{NPM} = 18$ in ML30).

Table 3. *Average trace-element compositions of cpx, amp and phl expressed in ppm*

Sample:	MB4		MB32		MB52		ML25				ML22				ML40							ML30	
Mineral:	cpx		cpx		cpx		cpx		amp		cpx		amp		cpx		amp dis		amp sp		phl	amp	
n:	9	1SD	9	1SD	7	1SD	7	1SD	6	1SD	7	1SD	13	1SD	3	1SD	3	1SD	3	1SD	1	12	1 SD
Rb	0.04	0.02	–	0.0	0.09	0.05	0.04	0.01	0.51	0.21	0.67	0.58	18.94	1.86	0.4	0.17	11.91	1.85	1.62	1.11	729.55	7.79	1.11
Ba	0.06	0.03	0.12	0.07	0.87	0.54	0.09	0.04	4.2	2.99	18.59	17.18	301.01	26.81	7.08	2.61	173.63	48.19	9.52	0.91	4469.41	216.42	27.72
Th	0.03	0.01	0.03	0.01	0.01	0.01	0.03	0.02	0.07	0.05	3.92	0.42	5.07	0.57	1.15	0.09	1.31	0.07	1.36	0.03	0.01	3.81	0.36
U	0.01	0.01	0.02	0.01	0.01	0.00	0.03	0.02	0.11	0.04	1.35	0.13	1.52	0.16	0.37	0.02	0.35	0.03	0.39	0.01	0.08	1.22	0.09
Nb	0.09	0.02	0.1	0.02	0.07	0.03	0.03	0.02	0.19	0.11	0.07	0.06	4.65	3.37	0.6	0.22	50.27	10.67	4.99	3.2	43.48	18.38	3.62
Ta	0.02	0.01	0.02	0.01	0.01	0.01	–	0.00	–	0.00	0.02	0.01	0.05	0.03	0.03	0.02	2.09	0.88	0.17	0.1	1.99	0.23	0.07
La	1.09	0.03	0.89	0.11	0.49	0.03	0.17	0.01	0.22	0.05	20.3	5.09	43.11	5.41	9.16	0.77	19.64	0.4	5.38	0.77	0.14	61.5	2.26
Ce	4.29	0.17	3.13	0.08	1.98	0.04	1.47	0.07	1.86	0.15	19.46	9.53	53.79	10.69	18.84	1.87	44.16	1.82	9.6	1.7	0.83	140.08	3.31
Pb	0.23	0.06	0.12	0.03	0.14	0.03	0.08	0.01	0.71	0.23	1.11	0.17	3.01	0.28	0.27	0.02	0.94	0.02	0.99	0.03	1.57	1.74	0.78
Pr	0.8	0.05	0.69	0.03	0.42	0.02	0.45	0.02	0.49	0.05	1.27	0.71	3.9	1.00	2.0	0.26	5.79	0.48	1.15	0.11	0.09	17.52	0.51
Sr	76.88	2.51	63.91	1.06	49.16	1.05	28.23	2.73	63.56	4.09	202.33	48.67	448.12	28.75	153.33	16.78	418.52	0.1	167.28	6.69	144.02	610.86	24.47
Nd	4.75	0.16	4.44	0.17	2.93	0.11	3.41	0.22	3.82	0.27	4.25	1.46	10.36	2.73	6.51	0.74	22.39	2.06	5.42	0.35	0.11	64.75	2.12
Zr	38.46	2.08	33.94	1.15	28.26	1.04	24.45	0.77	19.74	1.38	29.27	1.76	27.59	5.1	39.31	3.5	106.74	10.63	47.57	9.18	16.04	30.31	7.23
Hf	1.19	0.09	1.03	0.06	0.84	0.08	0.97	0.07	0.7	0.07	0.96	0.06	0.48	0.11	0.92	0.02	1.87	0.31	0.83	0.13	0.24	0.6	0.07
Sm	1.83	0.14	1.84	0.13	1.3	0.06	1.63	0.07	1.82	0.14	1.35	0.08	1.73	0.27	1.6	0.12	3.96	0.44	1.53	0.06	0.03	10.26	0.48
Eu	0.74	0.04	0.76	0.06	0.59	0.03	0.69	0.05	0.83	0.04	0.55	0.08	0.64	0.06	0.64	0.02	1.45	0.13	0.66	0.04	0.08	3.1	0.14
Ti	3867.4	184.1	3411.1	104.0	3047.5	246.6	3598.5	195.9	10237.9	448.0	1966.9	204.5	2575.0	641.6	23113.8	157.0	3617.2	222.6	4441.8	197.9	5360.5	2311.4	122.7
Gd	2.69	0.12	2.64	0.17	2.09	0.12	2.46	0.16	2.68	0.2	1.85	0.28	1.95	0.23	1.79	0.12	3.59	0.13	2.28	0.08	–	7.24	0.48
Tb	0.48	0.03	0.48	0.03	0.39	0.01	0.45	0.04	0.51	0.01	0.35	0.04	0.33	0.02	0.32	0.01	0.53	0.01	0.4	0.03	–	1.02	0.07
Dy	3.6	0.14	3.35	0.2	3.07	0.16	3.4	0.21	3.74	0.24	2.44	0.33	2.47	0.22	2.33	0.12	3.44	0.37	2.88	0.13	0.02	6.01	0.59
Y	20.5	0.84	19.67	0.63	17.81	0.68	19.49	1.00	21.07	1.13	14.36	1.37	14.43	0.85	13.07	0.72	18.79	0.49	16.05	0.16	0.16	32.0	1.98
Ho	0.78	0.04	0.76	0.02	0.68	0.04	0.76	0.05	0.82	0.06	0.58	0.07	0.55	0.05	0.5	0.01	0.66	0.03	0.62	0.03	–	1.17	0.07
Er	2.28	0.11	2.15	0.11	2.01	0.09	2.19	0.1	2.29	0.27	1.66	0.19	1.56	0.13	1.38	0.11	1.83	0.02	1.69	0.16	–	2.99	0.26
Yb	2.14	0.1	2.01	0.1	1.92	0.08	2.12	0.17	2.21	0.2	1.5	0.2	1.56	0.19	1.45	0.09	1.79	0.09	1.81	0.06	–	2.77	0.26
Lu	0.31	0.03	0.28	0.02	0.29	0.01	0.31	0.02	0.29	0.03	0.21	0.04	0.23	0.02	0.19	0.02	0.24	0.01	0.24	0.0	0.00	0.39	0.03

n, number of point analyses; 1SD one standard deviation on analyses.

Table 4. *$\delta^{18}O$ (‰ V-SMOW), $^{143}Nd/^{144}Nd$ and $^{87}Sr/^{86}Sr \pm 2\sigma$ of minerals from lherzolites and harzburgites*

Sample	Mineral	$\delta^{18}O$	$^{143}Nd/^{144}Nd$	$^{86}Sr/^{87}Sr$
MB4	ol	4.6; 5.5		
	opx	5.8		
	cpx	5.6	0.513195 ± 18	0.702528 ± 10
MB32	ol	5.5; 6		
	opx	5		
	cpx	5.6	0.513076 ± 8	0.703248 ± 8
MB52	ol	5.4; 5.8		
	opx	6.7		
	cpx	5.8	0.513433 ± 18	0.702607 ± 14
ML25	ol	4.9		
	opx	5.6		
	cpx	5.4	0.513282 ± 10	0.703689 ± 12
	amp	5.3		
ML22	ol	4.9; 5.7		
	opx	4.7		
	cpx	6.1	0.513053 ± 10	0.703463 ± 14
	amp	5.8	0.512907 ± 54	0.703394 ± 14
ML40	ol	5.1		
	opx			
	cpx	5.8	0.513051 ± 12	0.703484 ± 14
	amp	5.6	0.512980 ± 12	0.703245 ± 14
ML30	ol	5.4		
	opx	5.1		
	amp	5.9	0.512888 ± 10	0.703372 ± 12

Isotopic composition of oxygen

The $\delta^{18}O$ values obtained for the xenolith minerals ($\delta^{18}O_{ol} = 4.6–6‰$; $\delta^{18}O_{opx} = 4.7–5.8‰$; $\delta^{18}O_{cpx} = 5.4–6.1$; $\delta^{18}O_{amp} = 5.3–5.9‰$ V-SMOW; Table 4) fall within the range of basalt-hosted peridotites worldwide (Boettcher & O'Neil 1980; Ionov *et al.* 1994; Mattey *et al.* 1994; Chazot *et al.* 1997; Fig. 4). $\delta^{18}O$ values for olivine vary within a single sample. These variations are not necessarily related to the number and size of grains analysed, as shown by the coarse-grained anhydrous lherzolites (MB4, MB32 and MB52).

The isotopic composition of oxygen in the different mineral phases are plotted in $\delta^{18}O_{mineral\ A}$ v. $\delta^{18}O_{mineral\ B}$ diagrams (A–B pairs: opx–ol, cpx–ol, amp–ol, amp–cpx), which show equilibrium lines for 900° and 1400 °C (roughly encompassing the spinel-bearing lherzolite field; Fig. 4). Where amphibole is considered, equilibrium is limited to 1100 °C, after Niida & Green (1998) (Chiba *et al.* 1989; Zheng 1992, 1993; Rosenbaum *et al.* 1994).

The mineral pairs (ol–opx and ol–cpx) of the anhydrous lherzolites from Mont-Briançon plot near or away from the two extreme temperature equilibrium lines, indicating an isotopic disequilibrium. Moreover, it has been shown, using a larger set of anhydrous peridotites, that disequilibrium between mineral pairs is common among samples from the Devès volcanic district (Touron 2005).

In the hydrous peridotites, most of the pairs are in equilibrium, except in the porphyroclastic amphibole-rich harzburgite (ML22), where ol–opx and ol–cpx pairs indicate disequilibrium at mantle conditions. Amp–cpx pairs are in equilibrium within mantle conditions regardless of the amp modal content. The minerals from the amp-poor lherzolite (ML25; 1% of amphibole) are isotopically equilibrated whereas mineral pairs from the amp-rich harzburgite (ML22; 7% of amphibole) are not.

Sr and Nd isotopic compositions

$^{87}Sr/^{86}Sr$ isotopic ratios range from 0.702528 to 0.703689 for cpx. However, no such large variation is observed for amp, which is relatively homogeneous: 0.703245–0.703394 (Fig. 5, Table 4). The lowest isotopic ratio was measured in an anhydrous sp-lherzolite from Mont-Briançon (MB4), in agreement with the depleted character already revealed by the major- and trace-element compositions of the pyroxenes. The highest values correspond to cpx in the hydrous xenoliths from Marais de Limagne.

$^{143}Nd/^{144}Nd$ isotopic ratios range from 0.513051 to 0.513433 for cpx; the highest values are observed in cpx from the anhydrous lherzolite MB52, which is the sample most depleted in

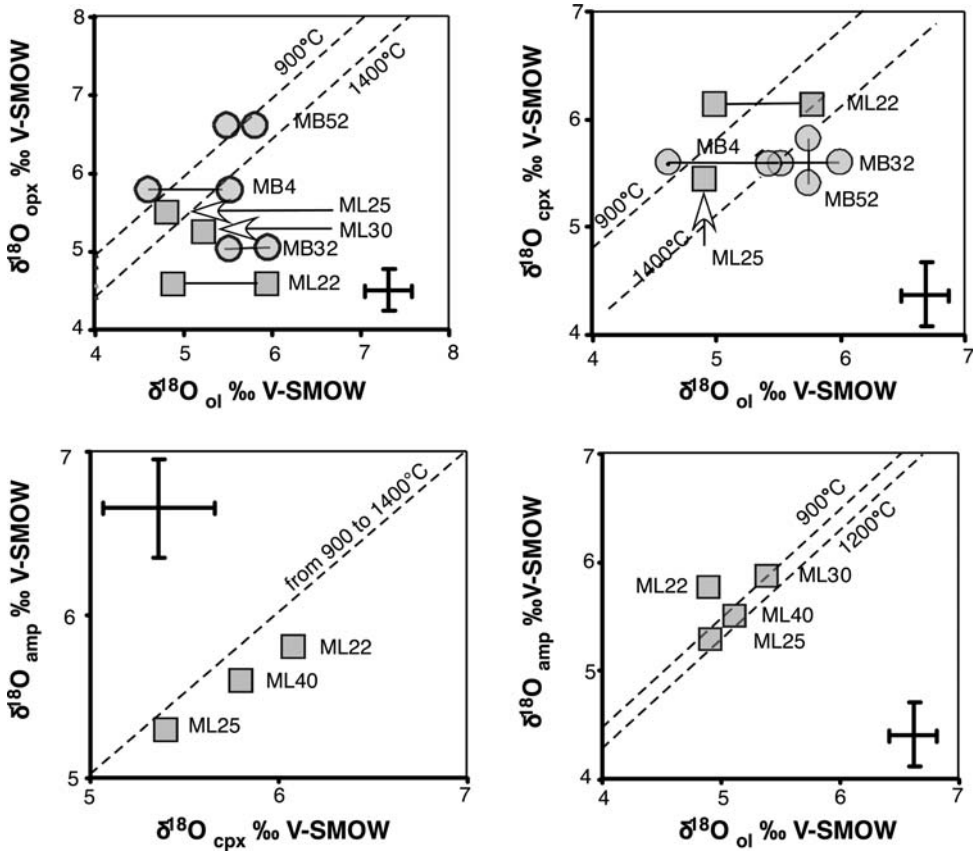

Fig. 4. $\delta^{18}O_{\text{mineral A}}$ v. $\delta^{18}O_{\text{mineral B}}$ (‰ V-SMOW; ol, olivine; opx, orthopyroxenes; cpx, clinopyroxene; amp, amphibole) for mineral separates (shaded circles, ol and pyroxenes from Mont-Briançon (MB); shaded squares, ol, pyroxenes and amp from Marais de Limagne (ML); 2σ error bars are shown.

incompatible elements (Fig. 5, Table 4). In the amp-rich lherzolite and harzburgites, cpx have Nd isotopic ratios lying on the mantle array whereas associated amp has Nd values (0.512888–0.512980) lying below the mantle array. The high $^{143}Nd/^{144}Nd$ ratio of ML25 shows a decoupling between Nd and Sr isotopes, moving away from the mantle array. The $^{87}Sr/^{86}Sr$ and $^{143}Nd/^{144}Nd$ of both cpx and amp, regardless of the modal content of amp, plot within the field of cpx from anhydrous peridotites from the southern domain (Downes *et al.* 2003).

Discussion

Mineralogical and chemical evidence of metasomatic fluids

Mantle rocks studied from Mont-Briançon and Marais de Limagne show evidence of metasomatism revealed by hydrous silicates, without interaction of the host lava (no glass).

All minerals from the different microstructures have homogeneous major oxides, indicating absence of exchange at grain boundaries. This interpretation is supported by the chemical characteristics of cpx (mg-number = 0.89–0.91), which correspond to those predicted for primary peridotitic assemblages (Fabriès *et al.* 1989). The metasomatism involves both secondary re-equilibration of primary cpx and the crystallization of amp and phl as modal phases.

Calculated equilibrium temperatures based on the solubility of Ca in opx (Brey & Kohler 1990) are in agreement with those obtained using the Sachtleben & Seck (1981) thermometer based on Al solubility in opx and coexisting ol and sp (Touron 2005). They range from 920 to 960 °C (Table 1). These temperatures, corresponding to the final recrystallization of the anhydrous silicate phases (ol, opx and sp), are homogeneous

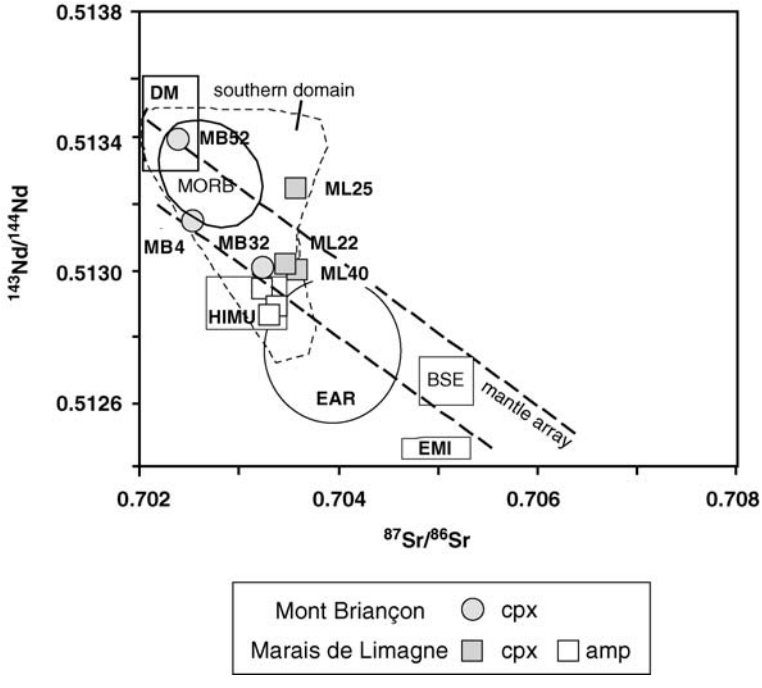

Fig. 5. $^{87}Sr/^{86}Sr$ v. $^{143}Nd/^{144}Nd$ in cpx and amp (field for peridotites from southern Massif Central domains; MORB and EAR after Downes *et al.* (2003) and references therein; main oceanic mantle reservoirs after Zindler & Hart (1986); DM, depleted mantle; BSE, Bulk Silicate Earth; HIMU, High μ; EMI, enriched mantle.

regardless of the amp content and the microstructure. Therefore, all the observed reactions (destabilization and/or re-equilibration of cpx and/or spinel, crystallization of amphibole) are inferred to have occurred under mantle conditions in a limited depth range in the lithosphere. Using the Eastern Australian geotherm (advective and recognized in young intra-plate volcanism, O'Reilly *et al.* 1997) or the geotherm in the Massif Central obtained after geophysical studies (Granet *et al.* 1995, and references therein), these xenoliths should come from *c*. 40 or 50 km, respectively.

The depletion in most lithophile elements, combined with the absence of metasomatic phases in the anhydrous lherzolites from Mont-Briançon, is compatible with a partial melting model (Norman 1998; Fig. 6) requiring less than 2% of melting, consistent with the fertile character of the southern lithospheric domain (Lenoir *et al.* 2000; Downes *et al.* 2003).

In volatile-bearing xenoliths, amp occurs surrounding cpx or sp and/or disseminated in the peridotite. A reaction corresponding to the hydration of cpx has been observed in the most amp-rich harzburgite. Such a reaction is also suggested in other hydrous samples, as the TiO_2 content in cpx decreases with increasing modal content of amp. Moreover, amp generally displays trace-element patterns similar to those of cpx. Variations in LREE enrichment or depletion within cpx and/or amp cannot be explained by primary heterogeneities of host peridotites as a result of large variations in the degree of partial melting (Vannucci *et al.* 1995). Therefore, LREE-depleted amp might result from cpx hydration, a H_2O-rich fluid being a precursor of alkaline melt (Menzies 1983).

Calculated compositions of liquid in equilibrium with cpx and amp were obtained using partioning coefficients (cpx: Hart & Dunn 1993; Blundy *et al.* 1998; amp: Brenan *et al.* 1995; LaTourette *et al.* 1995; Ionov *et al.* 1997; Fig. 7). Most cpx and associated amp appear to have been in equilibrium with liquid of similar compositions. Nevertheless, a hydrous lherzolite (ML40) with two types of amp displays two liquid compositions representing distinct chemical microsystems for amphiboles associated with sp (flat pattern) or with cpx and phl (LREE enrichment). Differences in REE enrichment can be related to chemically different metasomatic agents, indicating a multi-stage metasomatism. Amp associated with sp would correspond to a microsystem formed before the crystallization of disseminated amphibole and

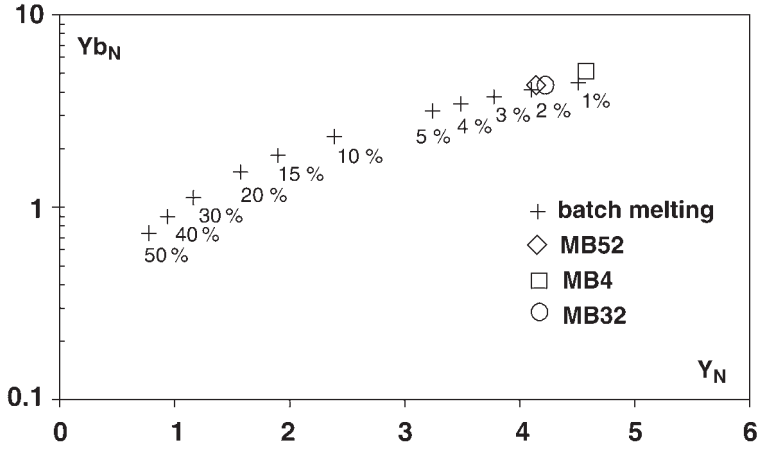

Fig. 6. Modelled degree of melting (after Norman, 1998; normalization values after McDonough & Sun 1995).

preserved from metasomatic infiltration and reaction. This last metasomatic agent is enriched in REE and large ion lithophite element (LILE) and could be derived from a more REE-rich fluid such as an alkaline magma. In other hydrous samples, the modal content of amp increases with REE enrichment and this would suggest an increasing volume of the metasomatic agent.

In conclusion, cpx and/or spinel in samples from Marais de Limagne are partly or totally reacted to amphibole, revealing a progressive transformation that can be described by the infiltration–reaction–crystallization process (Neumann & Wulff-Pedersen 1997). Each end-member of this complex solid–liquid relationship can be dominant in different cases: (1) existence of a potential crystallization substrate (cpx or spinel) for liquidus phase(s) of the melt will favour chemical exchanges between melt and substrate; (2) variation of the volume of percolating agent will favour the infiltration model.

Geochemical signature of the metasomatic agent

Calculated liquids in equilibrium with minerals (Fig. 7) have similar trace-element patterns for coexisting minerals, highlighting once again the chemical equilibrium. From the least modally metasomatized lherzolite (ML25, 1% amp) to the most modally metasomatized harzburgite (ML30, 21% of amp) these liquids become richer in most lithophile elements, and negative anomalies in high field strength elements (HFSE) increase. In ML25, the liquids in equilibrium with cpx and amp have a flat trace-element pattern (about 10 times PM) but display large positive anomalies in U and Th. This liquid is consistent with a sub-alkaline TiO_2-rich fluid or melt (Fabriès *et al.* 1989). The enrichment in lithophile elements is evident in ML30, where negative anomalies in HFSE and high Th and U enrichment suggest a carbonate-rich silicate melt or fluid (e.g. Dautria *et al.* 1992; Ionov *et al.* 1993; Moine 2000; Moine *et al.* 2000).

Origin of the metasomatic agent

The isotopic compositions of Nd and Sr in cpx (Fig. 5) plot in the southern domain (Downes *et al.* 2003) from the depleted mantle (DM) to EAR (European Asthenospheric Reservoir; Granet *et al.* 1995) fields in the mantle array, except those from ML25. However, being poorer in radiogenic Nd, the coexisting amphiboles fall in the HIMU field and very close to the EAR end-member. As the EAR reservoir is regarded as the isotopic fingerprint of the mantle plume beneath the European plate, the melts responsible for the formation of amphibole could result from the mixing between a depleted mantle source (asthenospheric component) and a deeply recycled enriched component (HIMU or EAR). In Figure 8, the cpx and amphiboles plot along a trend from the DM to EMI end-members and define a box) between the depleted and variably enriched mantle. These plots support the mixture of different sources previously proposed for primitive lavas from the Massif Central (Wilson & Downes 1991), but suggest that the HIMU source is not required to explain the Sr–Nd data or the O-isotope data.

Calculated $\delta^{18}O_{fluid}$

Variations in the $\delta^{18}O$ of ol and opx, correlated with the number of fragments analysed, reflect

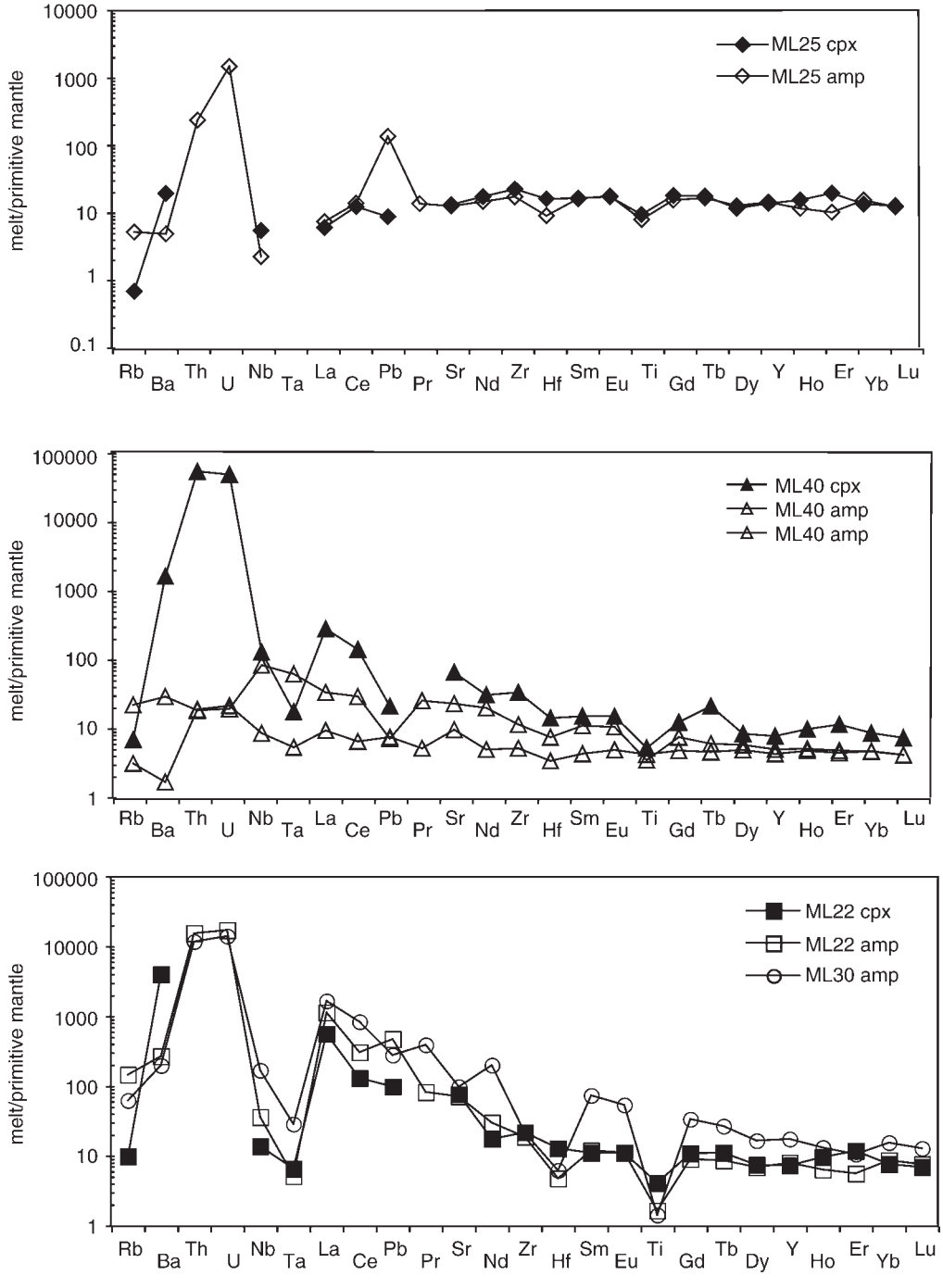

Fig. 7. Primitive mantle normalized calculated liquids in equilibrium with cpx and amp (normalization values from McDonough & Sun 1995) in (**a**) depleted hydrous lherzolite, (**b**) two types of amp-lherzolite and (**c**) hydrous harzburgites.

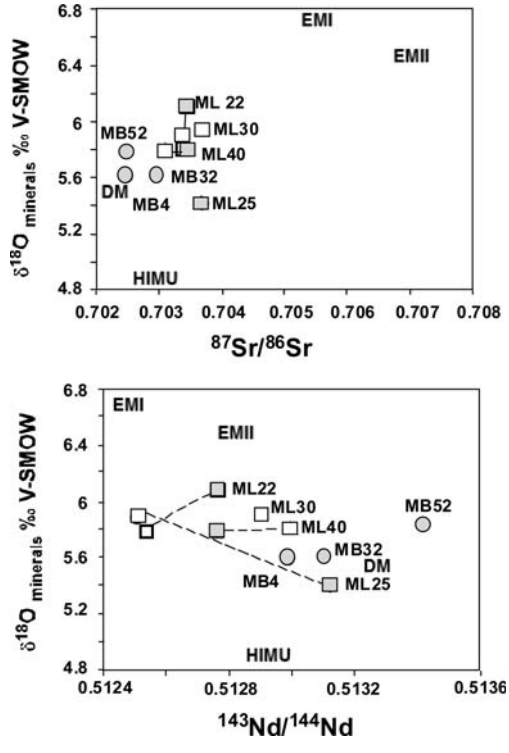

Fig. 8. $\delta^{18}O$ values of amp and cpx v. $^{87}Sr/^{86}Sr$ and $^{143}Nd/^{144}Nd$ (main oceanic mantle reservoirs after Harmon & Hoelfs (1995); DM, depleted mantle; HIMU, High μ; EMI and EMII, enriched mantle. Symbols as in Figure 5.

grain-scale processes such as isotopic zoning induced by different fluids or thermal exchanges. However, as mentioned above, no chemical zoning and no glass have been observed in the xenoliths, excluding late-stage fluid re-equilibration as a cause for these isotopic variations.

$\delta^{18}O_{\text{mineral A}}$ v. $\delta^{18}O_{\text{mineral B}}$ diagrams (Fig. 4) show that ol–opx or ol–cpx pairs from the amp-poor lherzolite are not in equilibrium at mantle conditions (e.g. 900–1400 °C). This isotopic disequilibrium is inconsistent with the petrographic observations. Stable isotope disequilibria have to be related to partial exchange as a result of different rates of oxygen isotope diffusion (Cole & Chakraborty 2001). Diffusion coefficients of oxygen are higher for pyroxenes than for ol and amp (diffusion coefficient: opx > cpx > ol > amp; after Cole & Chakraborty 2001) and/or grain size. Therefore $\delta^{18}O$ values of pyroxenes respond to changes of temperature more rapidly than those for other co-existing minerals.

Accepting the calculated equilibrium temperatures given by the Brey & Köhler (1990) thermometer for each xenolith (which are consistent with the amphibole stability field (Niida & Green 1999) for these spinel-bearing peridotites), liquids in equilibrium with different phases have been calculated using theoretical fractionation factors (Zheng 1992, 1993; Zhao & Zheng 2003; Table 5). Because fractionation factors between all minerals (ol, opx, cpx ad amp) and basalt (as melt) are not available, a $\delta^{18}O_{\text{fluid}}$ ($\delta^{18}O_{Cc}$ (calcite) and $\delta^{18}O_{H_2O}$) has been calculated for each mineral using the oxygen–calcite fractionation factor (Zheng 1993) for an anhydrous melt and mineral–H_2O for amphibole representing a hydrous melt (Table 5). The calculated $\delta^{18}O_{Cc}$ values range from 7.1 to 8.3‰ ($\delta^{18}O_{H_2O}$ values are 8.4 and 9‰) with the exception of the amphibole-poor lherzolite (ML25), which shows larger variations: 6.3–8.3‰. In this amphibole-poor lherzolite, $\delta^{18}O_{Cc}$ values in equilibrium with olivine and opx are respectively 7.5–8.3‰ and 6.3‰, whereas values in equilibrium with cpx and amphibole are respectively 7.9 and 8.2‰. As mentioned above, the apparent lower $\delta^{18}O_{Cc}$ value (opx) can be explained by exchange time and/or grain size effects (the Soret effect, Kyser *et al.* 1998). Such a low $\delta^{18}O_{Cc}$ value could be induced by a thermal anomaly from a mantle upwelling, in agreement with geophysical studies (Granet *et al.* 1995, 2000).

$\delta^{18}O_{Cc}$ values in equilibrium with minerals from the anhydrous lherzolites are similar to those for fluids equilibrated with minerals from hydrous peridotites. This indicates that the melts are homogeneous in $\delta^{18}O$ beneath the northern part of the Devès area. Chazot *et al.* (2003) measured similar $\delta^{18}O_{Cc}$ values in carbonatitic lava from the Velay volcanic district, equilibrated at *c.* 700 °C. Despite the cpx–amp relationship revealed by petrography and trace-element patterns, the calculated $\delta^{18}O_{Cc}$

Table 5. *$\delta^{18}O$ values (‰ V-SMOW) for calculated calcite-rich and H_2O-rich liquids in equilibrium with peridotite minerals at the calculated equilibrium temperature given by the Brey & Köhler (1990) thermometer for each xenolith*

Sample	$\delta^{18}O_{\text{calcite}}$				$\delta^{18}O_{H_2O}$
	ol	opx	cpx	amp	amp
MB4	7.1; 8	7.4	7.3		
MB32	8; 8.5	6.6	7.4		
MB52	7.9; 8.3	8.3	7.5		
ML25	7.4	7.2	7.2	7.7	8.4
ML40	7.5		7.6	8	8.7
ML22	7.5; 8.3	6.3	7.9	8.2	9
ML30	7.9	6.6		8.3	9

values (melts) vary from 7.2 to 8.3‰ V-SMOW. The differences in calculated $\Delta^{18}O_{Cc\ cpx-amp}$ in equilibrium vary from 0.3 to 0.5‰. The decrease of $\Delta^{18}O_{Cc}$ does not vary with the amphibole modal content but seems to be associated with the LREE–enrichment in cpx $(La/Yb)_{NC1} = 0.1–8.5$) and amphibole ($(La/Yb)_{NC1} = 0.1–15.8$).

REE and stable isotope characterization of hydrous metasomatism

The infiltrating fluid or melt responsible for the formation of amphibole and the LREE enrichment in minerals apparently homogenized the $\delta^{18}O$ of the minerals. The metasomatic agent that percolated the Marais de Limagne peridotites could have homogeneous $\delta^{18}O$ and (La/Yb) values. Considering the cpx–amp relationship, proportions of melt have been estimated using the equations for melt/rock ratios (W/R ratio) in an open system from Criss & Taylor (1986) and a temperature of 900 °C (close to calculated equilibrium temperature obtained by geothermometry), to quantify the relative volume of melt and to characterize its initial (La/Yb) ratio. In the calculation, the $\delta^{18}O$ of the initial cpx corresponds to that of the less modally metasomatized peridotite (ML25), and that of the final cpx to the metasomatized peridotite with residual cpx (ML40; the most amp-rich sample ML30, having no cpx); the $\delta^{18}O$ fluid or melt value is the $\delta^{18}O_{Cc}$ in equilibrium with the most LREE-rich amphibole (ML40; $\delta^{18}O_{Cc} = 8‰$). The comparison between the different hydrous samples indicates that W/R increases from 0.25 to 0.47 (Fig. 9). The absolute values of W/R are

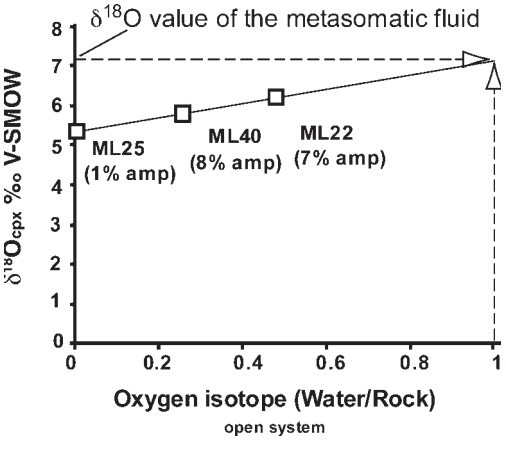

Fig. 9. Calculated W/R ratios at 900 °C v. $\delta^{18}O$ values of cpx (‰ V-SMOW). Dashed line corresponds to W/R = 1 and could represent the $\delta^{18}O$ value of the fluid in equilibrium with cpx.

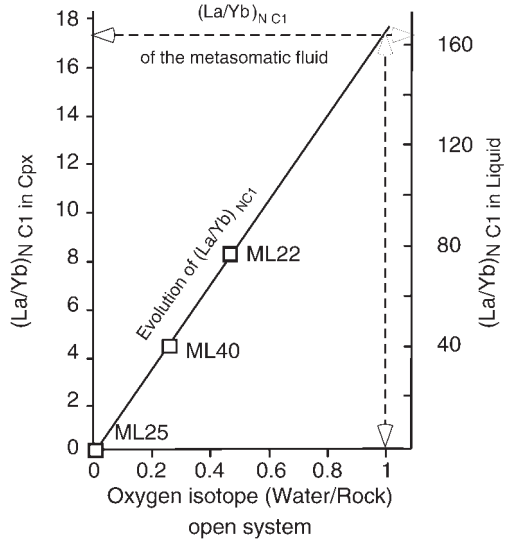

Fig. 10. $(La/Yb)_{NC1}$ of cpx and $(La/Yb)_{NC1}$ of calculated liquids in equilibrium with cpx v. W/R ratios calculated at 900 °C. Dashed line corresponds to evolution of (La/Yb) ratio with increasing W/R ratio.

unrealistic under mantle conditions but the calculation does indicate a relative increase in the proportion of fluid. As mentioned above, $\Delta^{18}O_{Cc\ cpx-amp}$ and W/R ratios are not correlated to the amp content in the peridotites (W/R varies from 0.45 to 0.25 for 7–8% of amp; Fig. 9). This might be related to the fact that the harzburgite has undergone melt extraction before metasomatic re-enrichment. The extrapolation of the W/R ratio up to unity would produce a $\delta^{18}O_{Cpx}$ value of 7‰ in equilibrium with a $\delta^{18}O_{Cc} = 8‰$. This value is slightly lower than those obtained for carbonatites from Velay ($\delta^{18}O = 8.7–24.5‰$; Chazot *et al.* 2003) at 700 °C. Nevertheless, if $\delta^{18}O_{Cc}$ is calculated at this temperature, the results obtained correspond to the lowest values for these carbonatites (Chazot *et al.* 2003).

$(La/Yb)_{NPM}$ ratios of cpx and $(La/Yb)_{NPM}$ ratios of liquids in equilibrium with cpx are plotted v. W/R in Figure 10. For a W/R ratio of unity (chemical equilibrium between percolating fluid and host peridotite), the ratio of the initial percolating melt should be $(La/Yb)_{NPM} = 175$ or $(La/Yb)_{NPM} = 18$ for cpx. This value is comparable with ratios observed in amp-rich harzburgites from Marais de Limagne, similar to ML30 (21% amp and no cpx; Touron 2005).

Conclusions

The lherzolites from Mont-Briançon locality are characterized by the absence of metasomatic

phases, whereas lherzolites and harzburgites from Marais de Limagne show variable modal contents of amphibole (amp) and rare phlogopite (phl).

The anhydrous lherzolites from Mont-Briançon have cpx trace-element patterns compatible with small degrees of partial melting (<5%). Cpx and amp in hydrous peridotites from Marais de Limagne display similar trace-element patterns and the calculated liquids in equilibrium indicate chemical equilibrium between these two phases. The metasomatic agent can be modelled as a subalkaline TiO_2-, Th- and U-rich fluid or melt. Associated with negative anomalies in HFSE, such chemical characteristics are compatible with a carbonate-rich silicate melt or fluid as the metasomatic agent. Nevertheless, this metasomatism did not affect all peridotites equally. Local chemical microsystems were preserved, as indicated by the occurrence of two types of amp within a single lherzolite. This situation suggests a multistage metasomatism.

The isotopic compositions of Sr and Nd of cpx and amp indicate that the metasomatic fluid or melt was derived from a mixing between a depleted MORB mantle (DMM)-type, deeply recycled component and the European Asthenospheric Reservoir (Granet *et al.* 1995). The first set of coupled O, Sr and Nd data on cpx and amphibole allows an improved definition of the isotopic signature of the metasomatized mantle beneath Devès.

The silicate–H_2O–CO_2-rich melt that infiltrated and reacted with the host peridotites has re-equilibrated cpx and amphibole in terms of LREE and O isotopes. Assuming petrographical and geochemical equilibrium, proportions of melt (W/R) have been estimated and have revealed that the volume of melt is not related to the amp content but to the LREE-enrichment, in agreement with the trend of differentiation (from silicate toward silicate–CO_2-rich) of the infiltrating melt.

The authors would like to thank N. Arndt and E. R. Neumann for their constructive reviews. The authors also thank T. Bradley for the polished thick sections, S. Elhlou, C. Lawson and P. Wieland for assistance with the analytical work, and N. Pearson for ever-ready advice, assistance and discussion during the analytical work. This work is part of a 'cotutelle' project between GEMOC, Macquarie University, Sydney and Equipe 'Transferts Lithosphériques', UMR 6524 'Magmas et Volcans', Université Jean Monnet, Saint-Etienne, France. It used instrumentation funded by ARC LIEF and DEST Systemic Infrastructure Grants, Macquarie University and industry. S.T. acknowledges the support of the Région Rhône-Alpes through the program 'EURODOC'. Support for this project was provided by the GEMOC ARC National Key Centre, an ARC Discovery Project grant, a Macquarie University Postgraduate Research Grant (S.T.) and a Macquarie University International Postgraduate Scholarship (S.T.). This is publication number 447 of the GEMOC ARC National Key Centre (www.es.mq.edu.au/GEMOC/).

References

BECCALUVA, L., SIENA, F., COLTORTI, M. *ET AL*. 1998. Nephelinitic to tholeiitic magma generation in a transtensional tectonic setting: an integrated model for the Iblean volcanism, Sicily. *Journal of Petrology*, **39**, 1547–1576.

BLICHERT-TOFT, J. 2001. On the Lu–Hf isotope geochemistry of silicate rocks. *Journal of Geostandards and Geoanalysis*, **25**, 41–56.

BLICHERT-TOFT, J., CHAUVEL, C. & ALBARÈDE, F. 1997. Separation of Hf and Lu for high-precision isotope analysis of rock samples by magnetic sector-multiple collector ICPMS. *Contributions to Mineralogy and Petrology*, **127**, 248–260.

BLUNDY, J. D., ROBINSON, J. A. C. & WOOD, B. J. 1998. Heavy REE are compatible in clinopyroxenes on the spinel lherzolite solidus. *Earth and Planetary Sciences Letters*, **160**, 493–504.

BOETTCHER, A. L. & O'NEIL, J. R. 1980. Stable isotopes, chemical and petrographic studies of high-pressure amphiboles and micas: evidence for metasomatism in the mantle source regions of alkali basalts and kimberlites. *American Journal of Geology*, **280**, 594–621.

BOIVIN, P. A. 1982. *Intéractions entre magmas basaltiques et manteau supérieur: arguments apportés par les enclaves basiques des basaltes alcalins. Exemple du Devès (Massif Central Français) et du volcanisme quaternaire de la région de Carthagène (Espagne)*. Thèse d'Etat Université de Clermont-Ferrand.

BRENAN, J. M., SHAW, H. F., RYERSON, F. J. & PHINNEY, D. L. 1995. Experimental determination of trace-element partitioning between pargasite and a synthetic hydrous andesitic melt. *Earth and Planetary Science Letters*, **135**, 1–11.

BREY, G. P. & KÖHLER, T. 1990. Geothermobarometry in four-phase lherzolites II. New thermobarometers and practical assessment of existing thermobarometers. *Journal of Petrology*, **31**, 1353–1378.

CHAZOT, G., MENZIES, M. A. & HARTE, B. 1996. Silicate glasses in spinel lherzolite from Yemen: origin and chemical compositions. *Chemical Geology*, **134**, 159–179.

CHAZOT, G., LOWRY, D., MENZIES, M. & MATTEY, D. 1997. Oxygen isotopic composition of hydrous and anhydrous mantle peridotites. *Geochimica et Cosmochimica Acta*, **61**, 161–169.

CHAZOT, G., BERTRAND, H., MERGOIL, J. & SHEPPARD, S. M. F. 2003. Mingling of immiscible dolomite carbonatite and trachyte in tuffs from the Massif Central, France. *Journal of Petrology*, **44**, 1917–1936.

CHIBA, H., CHACKO, T., CLAYTON, R. N. & GOLDSMITH, J. R. 1989. Oxygen isotope fractionation involving diopside, magnetite and calcite: application to geothermometry. *Geochimica et Cosmochimica Acta*, **53**, 2985–2995.

CLAYTON, R. N. & MAYEDA, T. K. 1963. The use of bromide pentafluoride in the extraction of oxygen from oxides and silicates for isotopic analysis. *Geochimica et Cosmochimica Acta*, **27**, 43–52.

COLE, D. R. & CHAKRABORTY, S. 2001. Rates and mechanisms of isotopic exchange. *In*: VALLEY, J. W. & COLE, D. R. (eds) *Stable Isotope Geochemistry*. Mineralogical Society of America, Reviews in Mineralogy and Geochemistry, **43**, 83–224.

COLTORTI, M., BECCALUVA, L., BONADIMAN, C., FACCINI, B., NTAFLOS, T. & SIENA, F. 2004. Amphibole genesis via metasomatic reaction with clinopyroxene in mantle xenoliths from Victoria Land, Antarctica. *Lithos*, **2**, 115–139.

COLTORTI, M., BONADIMAN, C., FACCINI, B., NTAFLOS, T. & SIENA, F. 2007. Slab melt and intraplate metasomatism in Kapfenstein mantle xenoliths (Styrian Basin, Austria). *Lithos*, **94**, 66–89.

COPLEN, T. B. 1988. Normalization of oxygen and hydrogen isotope data. *Chemical Geology*, **72**, 293–297.

CRISS, E. E. & TAYLOR, H. P., JR 1986. Meteoritic-hydrothermal systems. *In*: VALLEY, J. W., TAYLOR, H. P., JR & O'NEIL, J. R. (eds) *Stable Isotopes in High Temperature Geological Processes*. Mineralogical Society of America, Reviews in Mineralogy and Geochemistry, **16**, 373–424.

DAUTRIA, J. M., DUPUY, C., TAKHERIST, D. & DOSTAL, J. 1992. Carbonate metasomatism in the lithosphere: peridotitic xenoliths from a melilitic district of the Sahara Basin. *Contributions to Mineralogy and Petrology*, **111**, 37–52.

DELOULE, E., ALBARÈDE, F. & SHEPPARD, S. M. F. 1991. Hydrogen isotope heterogeneities in the mantle from ion probe analyses of amphiboles from ultramafic rocks. *Earth and Planetary Science Letters*, **105**, 543–553.

DOWNES, H. 1987. Relationship between geochemistry and textural type in spinel lherzolites, Massif Central and Languedoc, France. *In*: NIXON, P. H. (eds) *Mantle Xenoliths*. Wiley, Chichester, 125–134.

DOWNES, H., REICHOW, M. K., MASON, P. R., BEARD, A. D. & THIRLWALL, M. F. 2003. Mantle domains in the lithosphere beneath the French Massif Central: trace element and isotopic evidence from mantle clinopyroxenes. *Chemical Geology*, **200**, 71–87.

FABRIÈS, J., BODINIER, J-L., DUPUY, C., LORAND, J.-P. & BENKERROU, C. 1989. Evidence of modal metasomatism in the orogenic spinel lherzolite body from Caussou (Northeastern Pyrenees, France). *Journal of Petrology*, **30**, 199–228.

FRANCIS, D. M. 1976. The origin of amphibole in lherzolite xenoliths from Nunivak Island, Alaska. *Journal of Petrology*, **17**, 357–378.

GRANET, M., WILSON, M. & ACHAUER, U. 1995. Imagine a mantle plume beneath the French Massif Central. *Earth and Planetary Science Letters*, **136**, 281–296.

GRANET, M., JUDENHERC, S. & SOURIAU, A. 2000. Des images du système lithosphere–asthénosphère sous la France et leurs implications géodynamiques: l'apport de la tomographie télésismique et de l'anisotropie sismique. *Bulletin de la Société Géologique de France*, **171**, 149–167.

HARMON, R. S. & HOELFS, J. 1995. Oxygen isotope heterogeneity of the mantle deduced from global ^{18}O systematics of basalts from different geotectonic settings. *Contributions to Mineralogy and Petrology*, **120**, 95–114.

HART, S. R. & DUNN, T. 1993. Experimental cpx/melt partitionning of 24 trace elements. *Contributions to Mineralogy and Petrology*, **113**, 1–8.

HOERNLE, K., ZHANG, Y.-S. & GRAHAM, D. 1995. Seismic and geochemical evidence for large-scale mantle upwelling beneath the eastern Atlantic and western and central Europe. *Nature*, **374**, 34–39.

IONOV, D. A., DUPUY, C., O'REILLY, S. Y., KOPYLOVA, M. G. & GENSHAFT, Y. S. 1993. Carbonated peridotites xenoliths from Spitsbergen: implications for trace element signature of mantle carbonate metasomatism. *Earth and Planetary Science Letters*, **119**, 283–297.

IONOV, D. A., HARMON, R. S., FRANCE-LANORD, C., GREENWOOD, P. B. & ASHCHEPKOV, I. V. 1994. Oxygen isotope composition of garnet and spinel peridotites in continental mantle: Evidence from the Vitim xenolith suite, southern Siberia. *Geochimica et Cosmochimica Acta*, **58**, 1463–1470.

JARDIN, L. 1973. *Les enclaves basiques et ultrabasiques dans les basaltes alcalins de la chaîne du Devès (Haute-Loire, France)*. Thèse de doctorat, Université Claude Bernard, Lyon.

KYSER, T. K., LESHER, C. E. & WALKER, D. 1998. The effects of liquid immiscibility and thermal diffusion on oxygen isotopes in silicate liquids. *Contributions to Mineralogy and Petrology*, **133**, 373–381.

LARDEAUX, J. M., LEDRU, P., DANIEL, I. & DUCHENE, S. 2001. The Variscan French Massif Central—a new addition to the ultra-high metamorphic 'club': exhumation processes and geodynamic consequences. *Tectonophysics*, **332**, 143–167.

LATOURETTE, T., HERVIG, R. L. & HOLLOWAY, J. R. 1995. Trace element partitioning between amphibole, phlogopite and basanite melt. *Earth and Planetary Science Letters*, **135**, 13–30.

LE GRIEL, A. 1988. *L'évolution géomorphologique du Massif Central français*. Essai sur la genèse d'un relief, Université Lyon II.

LENOIR, X. 2000. *Structure et évolution du manteau lithosphérique sous-continental en Europe Occidentale: étude texturale, pétrologique et géochimique des péridotites du Massif de Ronda et du Massif Central*. Thèse de Doctorat, Université Montpellier II.

LENOIR, X., GARRIDO, C. J., BODINIER, J.-L. & DAUTRIA, J.-M. 2000. Contrasting lithospheric mantle domains beneath the Massif Central (France) revealed by geochemistry of peridotite xenoliths. *Earth and Planetary Science Letters*, **181**, 359–375.

MATTEY, D., LOWRY, D. & MACPHERSON, C. 1994. Oxygen isotope composition of mantle peridotites. *Earth and Planetary Science Letters*, **128**, 231–241.

MAURY, R. & VARET, J. 1980. Le volcanisme tertiaire et quaternaire en France. *In*: AUTRAN, A. & DERWURT, D. (eds) *Evolutions géologiques de la France*. Mémoires du BRGM, **107**, 137–159.

MCDONOUGH, W. F. & SUN, S.-s. 1995. The composition of the Earth. *Chemical Geology*, **120**, 223–253.

MENZIES, M. A. 1983. Mantle ultramafic xenoliths in alkaline magmas: evidence for mantle heterogeneity modified by magmatic activity. *In*: HAWKESWORTH, C. J. & NORRY, M. J. (eds) *Continental Basalts and Mantle Xenoliths*. Shiva, Nantwich, 92–110.

MICHON, L. & MERLE, O. 2001. The evolution of the Massif Central rift: spatio-temporal distribution of the volcanism. *Bulletin de la Société géologique de France*, **172**, 69–80.

MOINE, B. N. 2000. *Les enclaves ultramafiques–mafiques riches en volatiles de Kerguelen (TAAF, Océan Indien), transferts de fluides et métasomatism mantellique en contexte intraplaque océanique*. Thèse de Doctorat, Université Jean Monnet, Saint-Etienne.

MOINE, B. N., COTTIN, J. Y., SHEPPARD, S. M. F, GRÉGOIRE, M., O'REILLY, S. Y. & GIRET, A. 2000. Incompatible trace element and isotopic (D/H) characteristics of amphibole- and phlogopite-bearing ultramafic to mafic xenoliths from Kerguelen Islands (TAAF, South Indian Ocean). *European Journal of Mineralogy*, **12**, 761–777.

MOINE, B. N., GRÉGOIRE, M., O'REILLY, S. Y., SHEPPARD, M. F. & COTTIN, J. Y. 2001. High field strength element fractionation in the upper mantle: evidence from amphibole-rich composite mantle xenoliths from Kerguelen Islands (Indian Ocean). *Journal of Petrology*, **42**, 2145–2168.

NEUMANN, E. R. & WULFF-PEDERSEN, E. 1997. The origin of highly silicic glass in mantle xenoliths from the Canary Islands. *Journal of Petrology*, **38**, 1513–1539.

NEUMANN, E. R., WULFF-PEDERSEN, E., PEARSON, N. J. & SPENCER, E. A. 2002. Mantle xenoliths from Tenerife (Canary Islands): Evidence for reactions between mantle peridotites and silicic carbonatite melts inducing Ca metasomatism. *Journal of Petrology*, **43**, 825–857.

NIIDA, K. & GREEN, D. H. 1999. Stability and chemical composition of pargasite amphibole in MORB pyrolite under upper mantle conditions. *Contributions to Mineralogy and Petrology*, **135**, 18–40.

NORMAN, M. D. 1998. Melting and metasomatism in the continental lithosphere: laser ablation ICPMS analysis of minerals in spinel lherzolites from eastern Australia. *Contributions to Mineralogy and Petrology*, **130**, 240–255.

NORMAN, M. D., PEARSON, N. J., SHARMA, A. & GRIFFIN, W. L. 1996. Quantitative analysis of trace elements in geological materials by laser ablation ICPMS: instrumental operating conditions and calibration values of NIST glasses. *Geostandards Newsletter*, **20**, 247–261.

NORMAN, M. D., GRIFFIN, W. L., PEARSON, N. J., GARCIA, M. O. & O'REILLY, S. Y. 1998. Quantitative analysis of trace element abundances in glasses and minerals: a comparison of laser ablation ICPMS, solution ICPMS, proton microprobe, and electron microprobe data. *Journal of Analytical Atomic Spectroscopy*, **13**, 477–482.

O'REILLY, S. Y., GRIFFIN, W. L. & RYAN, C. G. 1991. Residence of trace elements in metasomatized spinel lherzolites xenoliths: a proton-microprobe study. *Contribution to Mineralogy and Petrology*, **109**, 98–113.

O'REILLY, S. Y., GRIFFIN, W. L. & GAUL, O. 1997. Paleogeothermal gradients in Australia: key to 4-D lithosphere mapping. *Journal of Australian Geology and Geophysics*, **17**, 63–72.

O'REILLY, S. Y., GRIFFIN, W. L., POUDJOM-DJOMANI, Y. H. & MORGAN, P. 2001. Are lithospheres forever? Tracking changes in subcontinental lithospheric mantle through time. *GSA Today*, **11**, 4–10.

PATCHETT, P. J. & TATSUMOTO, M. 1980. A routine high-precision method for Lu–Hf isotope geochemistry and cosmochemistry. *Contributions to Mineralogy and Petrology*, **75**, 263–267.

ROSENBAUM, J. M., KYSER, K. T. & WALKER, D. 1994. High temperature oxygen isotope fractionation in the enstatite–olivine–$BaCO_3$ system. *Geochimica et Cosmochimica Acta*, **58**, 2653–2660.

SACHTLEBEN, T. & SECK, H. A. 1981. Chemical control on Al-solubility in orthopyroxene and its implications on pyroxene geothermometry. *Contributions to Mineralogy and Petrology*, **78**, 157–165.

SHARP, Z. D. 1990. A laser-based microanalytical method for the *in situ* determination of oxygen isotope ratios of silicates and oxides. *Geochimica et Cosmochimica Acta*, **54**, 1353–1357.

TOURON, S. 2005. *Empreintes géochimiques du métasomatisme mantellique sous le Massif Central France*. Thèse de doctorat, Université Jean Monnet, Saint-Etienne.

VAN ACHTERBERGH, E., RYAN, C. G., JACKSON, S. & GRIFFIN, W. L. 2001. Data reduction software for LA-ICP-MS. *In*: SYLVESTER, P. (ed.) *Laser-Ablation-ICPMS in the Earth Sciences.* Principles and Applications Short Course Series, Mineralogical Association of Canada, **29**, 239–243.

VANNUCCI, R., PICCARDO, G. B., RIVALENTI, G. *ET AL.* 1995. Origin of LREE-depleted amphiboles in the subcontinental mantle. *Geochimica et Cosmochimica Acta*, **59**, 1763–1771.

WASSERBURG, G. J., JACOBSEN, S. B., DEPAOLO, D. J., MACCULLOCH, M. T. & WHEN, T. 1981. Precise determination of Sm/Nd ratios, Sm and Nd isotopic abundances in standard solutions. *Geochimica et Cosmochimica Acta*, **45**, 2311–2323.

WILSON, M. & DOWNES, H. 1991. Tertiary–Quaternary extension-related alkaline magmatism in Western and Central Europe. *Journal of Petrology*, **32**, 811–849.

ZHAO, Z.-F. & ZHENG, Y. F. 2003. Calculation of oxygen isotopes fractionation in magmatic rocks. *Chemical Geology*, **193**, 59–80.

ZHENG, Y.-F. 1992. Calculation of oxygen isotope fractionation in anhydrous silicate minerals. *Geochimica et Cosmochimica Acta*, **57**, 1079–1091.

ZHENG, Y.-F. 1993. Calculation of oxygen isotope fractionation in hydroxyl-bearing silicates. *Earth and Planetary Science Letters*, **120**, 247–263.

ZINDLER, A. & HART, S. R. 1986. Chemical geodynamics. *Annual Review of Earth and Planetary Sciences*, **14**, 493–571.

Metasomatism of the upper mantle beneath the Hyblean Plateau (Sicily): evidence from pyroxenes and glass in peridotite xenoliths

C. PERINELLI[1], G. T. SAPIENZA[2], P. ARMIENTI[1] & L. MORTEN[2,3]

[1]*Dipartimento di Scienze della Terra, Università di Pisa, via S. Maria 53, 56100 Pisa, Italy (e-mail: cperinelli@dst.unipi.it)*

[2]*Dipartimento di Scienze della Terra e Geologico-Ambientali, Università di Bologna, Piazza Porta San Donato 1, 40126 Bologna, Italy*

[3]*deceased, 18 November 2006*

Abstract: Coarse-grained, protogranular spinel peridotite xenoliths in the Upper Miocene Valle Guffari diatreme display a complex history for the shallow mantle underneath the Hyblean Plateau (SE Sicily). The mineral assemblage and composition (olivine Fo_{89-91}, orthopyroxene En_{88-91}, Cr-diopside $En_{48-49}Fs_{4-6}Wo_{45-48}$, Cr-rich spinel with cr-number = 25–39) record at least one depletion event caused by melt extraction, followed by metasomatic enrichment. One of these samples (HYB40) hosts a fresh glass vein. Rare earth elements (REE) in clinopyroxenes from these peridotites show three patterns: (1) light REE-enriched ($La_n/Yb_n = 7–17$); (2) spoon-shaped ($La_n/Yb_n = 18–20$; $La_n/Sm_n = 21–34$; $Sm_n/Yb_n < 1$); (3) nearly flat ($La_n/Yb_n \sim 3$). Whole-rock and clinopyroxene trace elements indicate that these patterns are associated with more or less complete equilibration with at least two distinct metasomatic melts: an alkaline silicate melt resembling the host basalt and a hawaiitic melt (for peridotite HYB40). *P–T* estimates yield 0.9–1.2 GPa and 870–1050 °C, suggesting that refertilization by metasomatizing melts occurred at the Crust–Mantle boundary or just below. In addition, the *P–T* data coincide with the palaeogeotherm reported by an earlier worker that is consistent with a high geothermal gradient. However, this thermal regime does not fit with the occurrence of an active mantle plume beneath the Hyblean area because of the deduced mantle potential temperatures, which are almost 200°C lower than those typical for a mantle plume. fO_2 calculation gives a redox state above the fayalite–magnetite–quartz buffer FMQ (up to +1.7 Δlog units) related to melt-driven metasomatism.

The ever-growing interest of petrologists in upper mantle xenoliths within volcanic rocks depends on the fact that xenoliths represent small 'fragments' of lithospheric mantle trapped by the ascending magmas. The ascent rate of nodule-bearing alkaline magmas is estimated as a few cm s^{-1} (Spera 1980), hence their geochemical and mineralogical characteristics are considered to remain mostly unmodified. Therefore, geochemical and isotopic investigations on these rocks provide much of our knowledge of petrological features of the upper mantle, and its origin and evolution (e.g. Nixon 1987; Rivalenti *et al.* 1996).

The Hyblean Plateau (southeastern Sicily, Italy) has been affected several magmatic episodes by since at least Triassic times (Cristofolini 1966; Carbone & Lentini 1981; Rocchi *et al.* 1998). Some volcanic events brought to the surface a large number of mantle-derived xenoliths, mainly spinel-facies peridotites and subordinate pyroxenites (Sapienza & Scribano 2000). Garnet-bearing peridotites are absent in the suite. Previous studies of Hyblean peridotites provided petrographic evidence of their depleted character, which has been related to melt extraction (e.g. Sapienza & Scribano 2000). In contrast, studies on whole-rock trace element distribution (e.g. Sapienza & Scribano 2000), Sr–Nd (Tonarini *et al.* 1996) and He isotope systematics (coupled with fluid inclusion study) (Sapienza *et al.* 2005) and *in situ* Re–Os in sulphides (Sapienza *et al.* 2007) indicate that they underwent metasomatic episodes, probably related to the interaction with silicate melt(s). In this study, we present the first data on trace elements of pyroxenes and a glass veinlet from spinel peridotite xenoliths from the Hyblean Plateau, with the aim of deciphering the depletion and enrichment episodes affecting the Hyblean upper mantle. Geochemical data and $P–T–fO_2$ evaluations (in the spinel peridotite stability field) are integrated to document depletion and enrichment events and to characterize the metasomatic agent(s) invading the peridotite matrix. As the Hyblean upper mantle has been considered to be geochemically akin to

From: COLTORTI, M. & GRÉGOIRE, M. (eds) *Metasomatism in Oceanic and Continental Lithospheric Mantle.* Geological Society, London, Special Publications, **293**, 197–221.
DOI: 10.1144/SP293.10 0305-8719/08/$15.00

the northern African upper mantle (Beccaluva *et al.* 2001), a better comprehension of the geochemical processes that have affected this lithosphere portion would add another facet to the petrological and geochemical knowledge of the northern African lithospheric mantle.

Geological setting

The Hyblean Plateau is geographically identified with the southeastern corner of Sicily (southern Italy, central Mediterranean region; Fig. 1), in a complex geodynamic framework dominated by the collision between the European and African plates. It is considered to represent the northern portion of the Pelagian Block, in continuity with the African plate (Burollet *et al.* 1978). However, there is debate regarding the nature of this lithospheric portion, and suggestions have been made regarding its possible oceanic or transitional affinity (Vai 1994; Scribano *et al.* 2006). The Plateau is in contact with the Apennine–Maghrebian Chain through the Gela foredeep in the NW, but the suture is masked by Neogene deposits. The eastern border of the Plateau is sharply joined to the Ionian Basin by the Malta Escarpment.

The plateau is composed of an undeformed *c*. 12 km thick sedimentary sequence consisting of Meso-Cenozoic carbonates and Neogene–Quaternary clastic sequences interrupted by several volcanic layers (Bianchi *et al.* 1987). Although

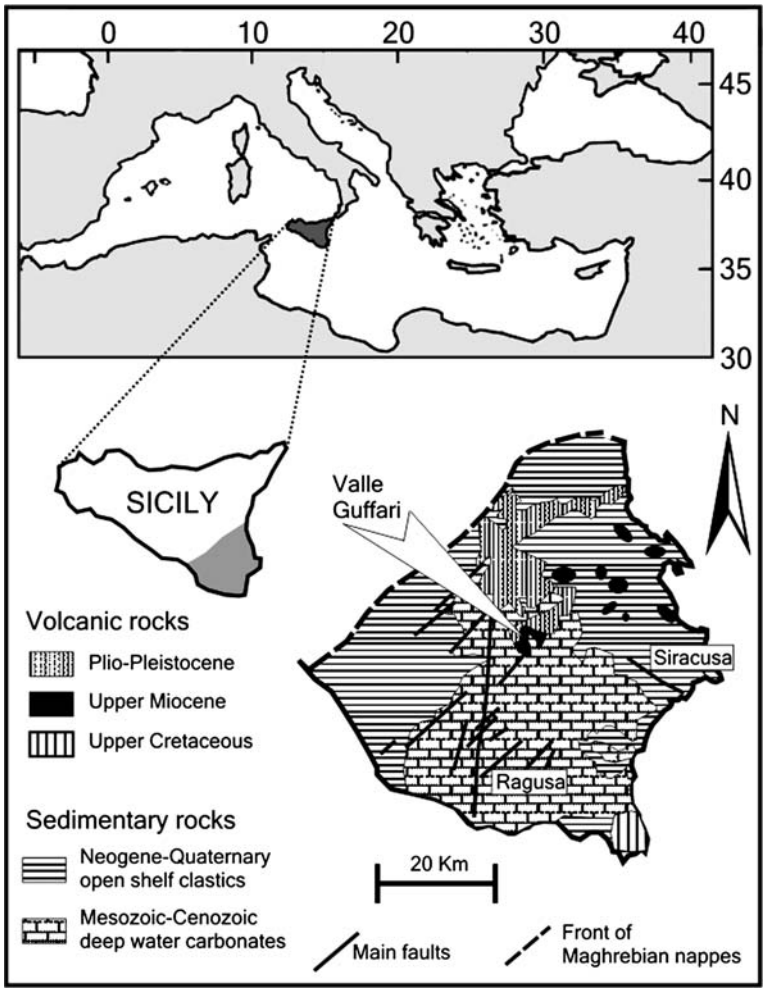

Fig. 1. Geological sketch map of Hyblean Plateau, southeastern Sicily, Italy. The location of Valle Guffari diatreme is reported.

Cristofolini (1966) described Triassic igneous alkali–sodic layers penetrated by commercial drill-holes near Ragusa, the oldest magmatic event recognized in the field consists of Cretaceous alkali basalts, extending over a few square kilometres in the south eastern part of the Plateau (Amore *et al.* 1988). Miocene alkali basaltic lavas and tuff-breccia pipes (the latter described by Carbone & Lentini 1981) crop out in the central–eastern part of the Plateau. These volcanic rocks have an alkaline affinity and range from alkali basalts to basanites and ankaratrites (Bianchini *et al.* 1998). The most recent magmatic episode is represented by Plio-Pleistocene lava flows covering a broad compositional range, from tholeiitic to alkaline (ocean-island basalt (OIB)-like; Beccaluva *et al.* 1998; Trua *et al.* 1998).

Both Quaternary lava flows and Upper Miocene tuff-breccia pipes host a large number of mantle- and crustal-derived xenoliths (Sapienza & Scribano 2000). The Miocene Valle Guffari diatreme (Fig. 1) is the most fruitful for quantity, variety of lithotypes and freshness of samples.

Analytical methods

Whole-rock major element compositions were determined on fused discs by X-ray fluorescence (XRF) (Philips PW 1480), and trace elements were determined for selected samples by inductively coupled plasma-mass spectrometry ICP-MS (Fisons PQ2 Plus®) at Dipartimento di Scienze della Terra, Università di Pisa. Samples were dissolved in screw-top PFA vessels on a hotplate at *c*. 120 °C using on HF–HNO_3 mixture. Analyses were performed by external calibration using basaltic geochemical reference samples as composition- and matrix-matching calibration solutions. The correction procedure includes: (1) blank subtraction; (2) instrumental drift correction using Rh–Re–Bi internal standardization and repeated (every five samples) analysis of a drift monitor; (3) oxide–hydroxide interference correction. Precision, evaluated by replicate dissolutions and analyses of the in-house standard HE-1 (Mt. Etna hawaiite), is generally between 2 and 5% RSD, except for Gd (6%), Tm (7%), Pb and Sc (8%). Detection limits are in the range 0.002–0.02 ng ml^{-1} in the solution (corresponding to 0.002–0.02 ppm for a 1000-fold sample dilution) for all the elements, except for Ba, Pb and Sr (0.1–0.2 ppm).

Major elements of minerals and glass were analysed by CAMECA electron microprobe (CNR–Centro di Studio per gli Equilibri Sperimentali Minerali e Rocce, Dipartimento di Scienze della Terra, Università degli Studi di Roma La Sapienza) operated at 15 kV accelerating voltage and 30 nA beam current. Counting times were 100 s. To reduce alkali loss during glass analysis, we decreased the counting time to 20 s and the beam was defocused to 15 μm. ZAF correction was applied to all data. Synthetic minerals (wollastonite for Si and Ca; rutile for Ti; corundum for Al; olivine for Fe; periclase for Mg; jadeite for Na; orthoclase for K) were used as standards. Metallic standards were used for Cr, Mn and Ni. Analytical precision is 0.5–6% for oxides in the concentration range >50–1.5% wt% and <10% for oxides in the range 0.4–1.5 wt%. Because of the need for accurate evaluation of Ca contents in olivine for equilibrium pressure estimations, the measurement of olivine Ca content was repeated on isolated grains to avoid fluorescence effects from neighbouring pyroxenes: the analytical precision for CaO is <8% and the measured value was lower by about 8–10% than that analysed on thin section.

Trace element concentrations in minerals and glass were determined by laser ablation microprobe–inductively coupled plasma–mass spectrometry (LAM-ICP-MS) at CNR–Istituto di Geoscienze e Georisorse in Pavia (Operating conditions, analytical procedures, accuracy and precision have been described by Bottazzi *et al.* 1994).

Petrography

The petrography of Hyblean peridotite xenoliths was presented in a set of papers (Scribano 1986; Mazzoleni & Scribano 1994; Tonarini *et al.* 1996; Sapienza & Scribano 2000); here we summarize the peridotite features relevant for this study. Eight Hyblean (HYB) spinel peridotites have been selected from the freshest ultramafic xenoliths in the Miocene diatreme pipe of Valle Guffari (Fig. 1). The xenoliths are subrounded and their size ranges from around 5 cm to 9 cm. According to a 1500-point modal estimation these rocks are spinel lherzolites and spinel harzburgites (olivine 59–77 vol%, orthopyroxene 19–30 vol%, clinopyroxene 3–10 vol%, spinel 1–4 vol%). All the minerals of the selected xenoliths are essentially fresh; a low degree of serpentinization occurs only along the cracks within olivine or along grain boundaries.

The most widespread texture is coarse-grained protogranular (Fig. 2a) and only two samples (HYB21 and HYB24) show textures that are intermediate between protogranular and porphyroclastic (Mercier & Nicolas 1975). Coarse (up to 5 mm) kink-banded olivine and smaller orthopyroxene (2–3 mm) grains show curvilinear grain boundaries. Thin exsolution lamellae of clinopyroxene and spinel are often observed in orthopyroxenes

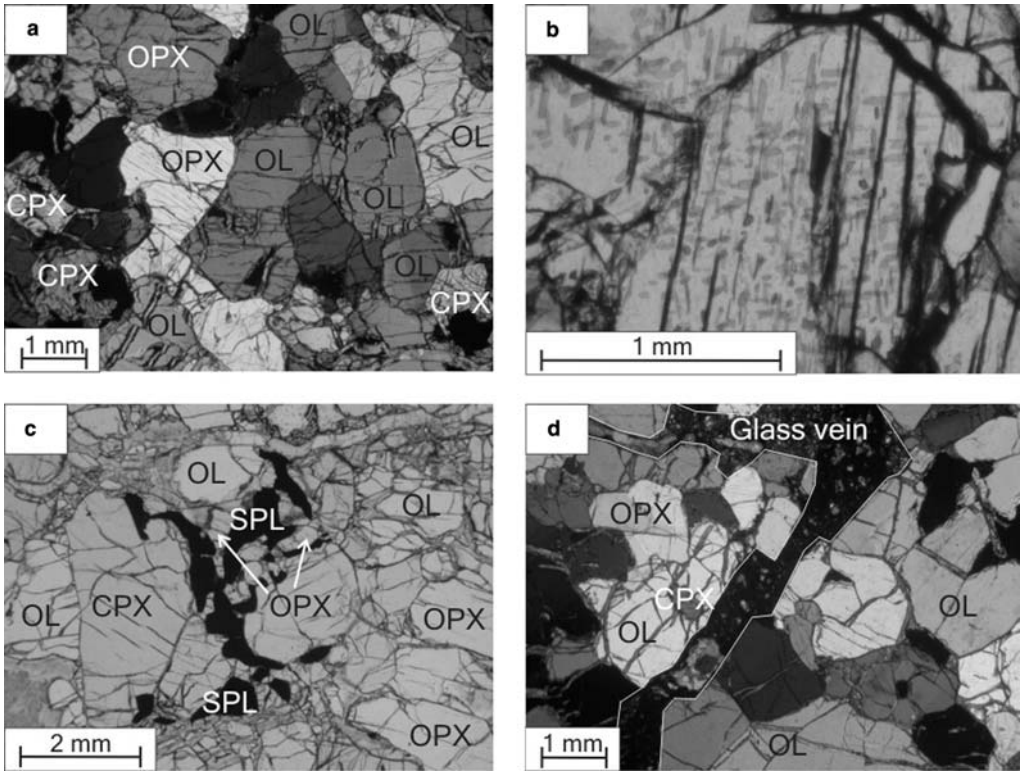

Fig. 2. Photomicrographs in transmitted light: (**a**) coarse-grained protogranular-textured spinel peridotite; (**b**) tiny exsolution lamellae of spinel in clinopyroxene; (**c**) vermicular spinel in contact with orthopyroxene; (**d**) glass vein within sample HYB40. OL, olivine; OPX, orthopyroxene; CPX, clinopyroxene; SPL, spinel.

(Fig. 2b). Clinopyroxene (<2 mm) sometimes displays pyrometamorphic textures (spongy rims) and exsolution of spinel (HYB24 and HYB29). Spinel is usually found as small dispersed grains, but in sample HYB14 it occurs as vermicular inclusions in orthopyroxene (Fig. 2c). Such vermicular spinel may be due to the subsolidus exsolution from a previous Al-rich enstatite (e.g., Morten *et al.* 1989) or the breakdown of earlier garnet. In sample HYB40 a yellowish vein of fresh silicate glass cross-cuts the xenolith (Fig. 2d); the veinlet contains small euhedral olivine (5%) and clinopyroxene (8%) crystals.

Chemical composition

Major elements

Whole rock. Four new bulk-rock analyses of Hyblean peridotites are reported in Table 1. SiO_2 and MgO contents are in the ranges 44.5–45.6 wt% and 39.1–45.3 wt%, respectively. The Mg-number ranges from 89 to 92. CaO (0.8–2.4 wt%) and Al_2O_3 (0.75–1.98 wt%) are negatively correlated with mg-number, and TiO_2 contents are rather scattered. K_2O and Na_2O contents in all samples are very low (<0.06 wt% and <0.11 wt%, respectively). Loss on ignition (LOI) is < 2wt%, testifying to the freshness of the samples.

Olivine. Olivines are homogeneous, with Fo varying from 89 to 91 (Table 2). NiO content ranges from 0.34 to 0.48 wt% and CaO content does not exceed 0.2 wt%. In sample HYB40, the olivines within the glass vein have higher contents of Fo (91–92), NiO (up to 0.51 wt%) and CaO (0.28 wt%) with respect to the olivines of the peridotite matrix (Fo 89, NiO 0.35 wt%, CaO 0.19 wt%).

Orthopyroxene. Orthopyroxenes are enstatites (En_{88-91}) with a narrow (89–92) range of mg-number values ($=100 \times MgO/(MgO + FeO_{tot})$ molar) but relatively large variations in CaO (0.3–1.5 wt%) and Al_2O_3 (2.4–4.9 wt%) abundances. Cr_2O_3 content varies between 0.2 and

Table 1. *Whole-rock major and trace element composition of studied peridotite xenoliths*

	HYB21	HYB29	HYB36	HYB40
wt%				
SiO_2	44.92	44.73	45.59	44.54
TiO_2	0.05	0.06	0.03	0.03
Al_2O_3	1.88	0.96	0.75	1.98
FeO^T	8.58	8.93	7.28	10.24
MnO	0.13	0.14	0.15	0.16
MgO	41.39	41.68	45.28	39.14
CaO	2.23	1.33	0.81	2.39
Na_2O	0.11	0.07	0.09	0.08
K_2O	0.01	0.02	0.06	0.04
P_2O_5	0.06	0.05	0.04	0.01
LOI	1.04	1.80	0.58	2.13
Total	100.4	99.8	100.7	100.7
mg-no.	89.6	89.3	91.7	87.2
ppm				
Sc	14.6	10.2	11.8	16.0
V	68.3	39.1	66.6	32.7
Cr	2076	1844	1856	2563
Co	101	103	102	108
Ni	2081	2092	2029	2244
Rb	0.99	1.03	0.66	0.71
Sr	105	62.3	71.2	88.3
Y	1.12	0.67	1.89	0.85
Zr	2.74	2.46	3.69	3.75
Nb	1.44	0.68	0.44	1.77
Cs	0.02	0.04	0.08	0.05
Ba	1.06	0.50	8.56	32
La	1.78	1.05	0.96	2.34
Ce	2.84	2.43	1.31	4.15
Pr	0.31	0.30	0.17	0.43
Nd	1.19	1.11	0.86	1.55
Sm	0.23	0.21	0.29	0.27
Eu	0.07	0.06	0.10	0.07
Gd	0.21	0.14	0.37	0.20
Tb	0.03	0.02	0.06	0.04
Dy	0.19	0.13	0.37	0.19
Ho	0.04	0.03	0.07	0.03
Er	0.12	0.06	0.18	0.09
Tm	0.02	0.01	0.03	0.01
Yb	0.14	0.07	0.16	0.07
Lu	0.02	0.01	0.02	0.01
Hf	0.06	0.06	0.17	0.07
Ta	0.06	0.04	0.03	0.05
Th	0.21	0.06	0.10	0.08
U	0.05	0.02	0.06	0.06

FeO^T, total Fe; mg-number = molar $(100 \times MgO/(MgO + FeO^T))$.

0.8 wt% (Table 3). These oxides are not correlated with mg-number.

Clinopyroxene. Clinopyroxenes are diopsides ($En_{48-49}Fs_{4-6}Wo_{45-49}$) with typically low TiO_2 contents (often below detection limits). Their mg-number values range from 89 to 92, and are positively correlated with mg-number values of coexisting orthopyroxenes. CaO contents (20.1–24.2 wt%) and mg-number values are positively correlated, whereas Cr_2O_3 (0.3–1.4 wt%), Al_2O_3 (2.4–5.7 wt%) and Na_2O (0.3–1.6 wt%) contents are negatively correlated with mg-number. In sample HYB40 the clinopyroxenes crystallized within the glass vein have a lower mg-number value (90) and higher TiO_2, Al_2O_3 and Cr_2O_3 contents with respect to clinopyroxene from the host peridotite (Table 4).

Spinel. Spinel cr-number (cr = atomic Cr/(Cr + Al) ranges from 0.26 to 0.39. Hence, according to Carswell (1980), these xenoliths may be classified as Cr-spinel peridotites. TiO_2 content in spinels is up to 0.65 wt% (Table 5) and mg-number (=atomic $100 \times Mg/(Mg + Fe^{2+})$) values vary between 0.67 and 0.80 (Table 5 and Fig. 3). Vermicular spinels from symplectitic orthopyroxene–spinel intergrowth in peridotite HYB14 have the highest mg-number and the lowest cr-number values. TiO_2 content in spinels from peridotites HYB23, HYB29 and HYB40 is positively correlated with TiO_2 content in coexisting clinopyroxene (not shown).

Glass vein. The glass vein in sample HYB40 has an alkaline composition (SiO_2 *c.* 50 wt%; $Na_2O + K_2O$ *c.* 6.3 wt%; Table 6) and plots in the field of trachybasalt (specifically hawaiite because $Na_2O - 2 \geq K_2O$) in the total alkalis–silica (TAS) diagram (Fig. 4). Whereas mg-number = 65 and K_2O/Na_2O ratio = 0.33 are consistent with a hawaiitic composition, MgO (<4.5 wt%) and FeO (<5.5 wt%) contents are relatively low and Al_2O_3 (*c.* 20.3 wt%) and TiO_2 (*c.* 3.6 wt%) relatively high.

Trace element composition

Whole rock. New trace-element data are listed in Table 1. The C1-normalized REE pattern and primitive mantle PM-normalized spider diagrams are shown in Figure 5, along with the field for already published peridotite data (Mazzoleni & Scribano 1994; Tonarini *et al.* 1996; Sapienza & Scribano 2000; Sapienza *et al.* 2005). The C1-normalized REE patterns are characterized by light REE (LREE) enrichment relative to heavy REE (HREE) ($La_n/Yb_n = 4–24$; Table 1 and Fig. 5a), whereas the PM-normalized incompatible element profile indicates variable enrichment in large ion lithophile elements (LILE) (e.g. Cs, Sr) and high field strength elements (HFSE) (e.g. Th, U, Nb) (Fig. 5b). Zr/Hf and Nb/Ta ratios range from 22 to 53 and from 13 to 39, respectively. The Zr/Hf ratio in three out of four samples is higher than the PM value (37.1; McDonough & Sun 1995), whereas Zr (2.5–3.8 ppm) and Hf

Table 2. *Major element compositions of selected olivines of spinel peridotites from the Hyblean Plateau, and of olivines within the glass veinlet in peridotite HYB40*

	HYB14				HYB21				HYB23				HYB24			
	rim	rim	core*	rim*	core	rim	core*	rim*	core	rim	core*	core*	core	rim	core*	core*
wt%																
SiO_2	41.73	41.91	41.59	41.28	40.79	40.72	40.98	40.77	40.45	40.73	41.20	40.52	41.39	41.97	41.73	41.25
TiO_2	bd	bd	bd	bd	bd	bd	bd	bd	bd	bd	bd	bd	bd	bd	bd	bd
Al_2O_3	bd	bd	bd	bd	bd	bd	bd	bd	bd	bd	bd	bd	bd	bd	bd	bd
FeO^T	9.05	8.72	8.76	9.12	9.75	9.47	9.25	9.31	9.72	9.34	9.71	9.56	9.19	8.90	9.18	9.06
MnO	bd	0.19	bd	bd	bd	bd	bd	bd	bd	bd	bd	bd	bd	bd	bd	0.15
MgO	49.24	49.16	49.20	48.88	49.41	49.42	49.77	49.86	49.39	48.69	49.24	48.97	49.52	49.50	49.85	48.53
NiO	0.45	bdl.	0.35	0.41	0.43	bdl.	0.41	bd	bd	0.34	0.43	0.41	bd	bd	bd	bd
CaO	0.17	0.20	0.07	0.10	0.12	0.17	0.08	0.10	bd	0.11	0.07	0.08	0.12	0.14	0.08	0.07
Total	100.6	100.2	100.0	99.8	100.5	99.8	100.5	100.0	99.6	99.2	100.6	99.5	100.2	100.5	100.84	99.06
Fo	90.6	90.9	90.9	90.5	90.0	90.3	90.6	90.52	90.1	90.3	90.0	90.1	90.6	90.8	90.6	90.5

	HYB29				HYB34				HYB36				HYB40				
	rim	core	core*	rim*	rim	core	core*	core*	core	core	core*	rim	core	core*	core*	glass	glass
wt%																	
SiO_2	41.30	39.82	40.66	40.45	40.59	40.64	40.50	40.43	40.99	41.19	40.76	40.78	40.96	41.15	40.96	41.33	41.01
TiO_2	bd	bd	bd	bd	bd	bd	bd	bd	bd	bd	bd	bd	bd	bd	bd	bd	bd
Al_2O_3	bd	bd	bd	bd	bd	bd	bd	bd	bd	bd	bd	0.02	bd	bd	bd	bd	bd
FeO^T	8.95	9.52	8.89	8.99	9.60	9.94	9.65	9.74	9.54	8.99	9.07	10.31	10.34	10.34	10.25	9.11	9.09
MnO	bd	bd	bd	bd	bd	bd	bd	bd	0.18	bd	0.17	bd	bd	bd	0.23	bd	bd
MgO	49.46	48.97	49.13	49.31	48.80	48.84	48.76	48.93	49.58	49.23	49.28	48.53	48.71	48.39	48.61	49.70	48.80
NiO	0.34	0.44	0.38	0.41	0.36	0.46	0.39	0.37	0.48	0.47	0.41	0.35	bd	0.42	0.36	0.49	0.51
CaO	0.12	bd	0.08	0.08	0.11	bd	0.06	0.07	bd	bd	0.06	0.19	bd	0.06	0.06	0.25	0.28
Total	100.2	98.8	99.1	99.2	99.5	99.9	99.4	99.5	100.8	99.9	99.8	100.2	100.0	100.4	100.5	100.9	99.7
Fo	90.8	90.2	90.8	90.7	90.1	89.7	90.0	89.9	90.3	90.7	90.6	89.3	89.4	89.3	89.4	90.7	90.5

FeO^T, total Fe; bd, below detection limit; glass, secondary olivine crystallized in glass vein.
*Analysis on single grain.

Table 3. *Major and trace element compositions of selected orthopyroxenes of spinel peridotites from the Hyblean Plateau*

	HYB14			HYB21			HYB23			HYB24		
	core	rim	core	core	rim	core	core	core	core	core	rim	core
wt%												
SiO_2	54.86	54.60	55.15	55.35	55.08	55.69	55.79	55.54	55.51	55.55	55.33	55.23
TiO_2	0.02	bd	bd	0.04	0.04	bd	bd	bd	bd	0.05	0.07	bd
Al_2O_3	4.86	4.58	4.65	4.29	4.17	3.98	3.77	3.47	3.72	4.64	4.41	4.21
FeO^T	5.89	5.97	5.77	5.76	6.00	5.85	5.98	6.20	6.08	5.97	5.78	5.93
MnO	bd	0.14	bd	bd	0.21	bd	bd	bd	bd	bd	bd	0.18
MgO	33.01	33.05	32.79	32.87	32.99	33.57	33.32	33.92	32.97	32.41	33.23	32.84
CaO	1.48	1.32	1.43	1.28	1.30	1.03	1.20	0.79	1.04	1.24	1.25	1.23
Na_2O	bd	bd	bd	0.10	bd	bd	0.18	0.17	0.16	bd	bd	bd
Cr_2O_3	0.80	0.72	0.65	0.75	0.75	0.59	0.45	0.50	0.37	0.72	0.66	0.58
Total	100.9	100.4	100.4	100.4	100.5	100.7	100.7	100.6	99.8	100.6	100.7	100.2
Wo	2.8	2.5	2.8	2.5	2.5	2.0	2.3	1.5	2.0	2.4	2.4	2.4
En	88.3	88.3	88.5	88.8	88.2	89.3	88.8	89.3	88.8	88.4	88.9	88.6
Fs	8.8	9.2	8.7	8.7	9.3	8.7	8.9	9.2	9.2	9.1	8.6	9.0
mg-no.	90.9	90.8	91.0	91.0	90.7	91.1	90.9	90.7	90.6	90.6	91.1	90.8
ppm												
V	100			98	101					102		
Cr	bd			5317	6325					n.a.		
Rb	bd			bd	bd					bd		
Sr	0.57			0.30	0.44					0.97		
Y	0.47			0.63	0.83					0.71		
Zr	0.17			0.36	0.44					1.55		
Nb	0.62			0.32	0.44					0.73		
Cs	bd			bd	bd					bd		
Ba	bd			bd	bd					bd		
La	0.08			0.030	0.054					0.08		
Ce	0.13			0.072	0.10					0.20		
Pr	0.01			0.016	bd					bd		
Nd	bd			0.088	0.10					0.10		
Sm	bd			bd	bd					0.01		
Eu	bd			bd	bd					bd		
Gd	bd			bd	bd					bd		
Tb	bd			bd	bd					bd		
Dy	0.04			bd	bd					0.06		
Ho	0.02			0.019	0.032					0.03		
Er	0.07			0.080	0.095					0.14		
Tm	0.01			bd	bd					0.03		

(*Continued*)

Table 3. *Continued*

	HYB14			HYB21			HYB23			HYB24		
	core	rim	core	core	rim	core	core	core	core	core	rim	core
ppm												
Yb	0.16			0.14	0.22					0.19		
Lu	0.03			0.029	0.037					0.05		
Hf	bd			bd	bd					bd		
Ta	bd			bd	bd					bd		
Pb	bd			bd	bd					bd		
Th	0.02			0.011	0.014					0.007		
U	0.01			0.003	bd					0.009		
	HYB29			HYB34			HYB36			HYB40		
	core	rim	core	core	rim	core	core	rim	core	core	rim	core
wt%												
SiO_2	54.66	55.33	55.29	56.08	55.91	55.87	56.37	56.21	56.15	56.54	56.10	56.42
TiO_2	0.05	0.06	bd	bd	bd	bd	bd	bd		0.14	bd	bd
Al_2O_3	3.70	3.57	3.73	2.43	2.50	2.66	2.67	2.63	2.78	2.57	2.60	2.72
FeO^T	6.46	6.16	6.23	5.95	6.22	5.47	6.05	5.77	5.52	7.14	6.72	6.84
MnO	bd	bd	bd	0.24	bd	0.21	bd	0.17	0.19	0.17	bd	0.00
MgO	32.77	32.95	32.56	34.41	34.62	34.51	34.87	34.83	34.62	33.61	33.73	33.95
CaO	1.35	1.24	1.20	0.53	0.53	0.55	0.31	0.31	0.33	0.34	0.37	0.33
Na_2O	bd	0.12	0.12	bd	bd	0.10	bd	bd		bd	bd	bd
Cr_2O_3	0.73	0.70	0.62	0.43	0.32	0.38	0.39	0.38	0.36	0.23	0.27	0.25
Total	99.7	100.1	99.7	100.1	100.1	99.8	100.7	100.3	99.95	100.7	99.8	100.51
Wo	2.6	2.4	2.3	1.0	1.0	1.0	0.6	0.6	0.6	0.6	0.7	0.6
En	87.7	88.3	88.2	89.9	89.9	90.9	90.6	90.7	91.2	88.6	89.3	89.3
Fs	9.7	9.3	9.5	9.1	9.1	8.1	8.8	8.7	8.2	10.8	10.0	10.1
mg-no.	90.0	90.5	90.3	91.2	90.8	91.8	91.1	91.5	91.8	89.4	89.9	89.8
ppm												
V	92	99								114		
Cr	4673	4941								2428		
Rb	bd	bd								bd		
Sr	1.83	1.79								bd		
Y	0.69	0.72								0.51		
Zr	1.33	1.45								bd		
Nb	0.23	0.25								bd		
Cs	bd	bd								bd		
Ba	bd	bd								bd		
La	0.052	0.083								bd		

Ce	0.26	0.32			bd
Pr	0.035	0.055			bd
Nd		0.21	0.19		bd
Sm	bd	bd			0.10
Eu	bd	0.032			bd
Gd	bd	bd			bd
Tb	bd	0.018			bd
Dy	0.11	0.098			bd
Ho	0.024	0.022			bd
Er	0.070	0.087			0.12
Tm	bd	bd			bd
Yb	bd	0.18			0.14
Lu	bd	0.037			0.04
Hf	bd	bd			0.11
Ta	bd	bd			bd
Pb	bd	bd			bd
Th	0.007	0.008			0.009
U	0.007	0.004			0.004

FeO^T, total Fe; bd, below detection limit; mg-number = molar $(100 \times MgO/(MgO + FeO^T))$.

(0.06–0.17 ppm) contents are always lower than PM (10.5 ppm and 0.28 ppm, respectively; McDonough & Sun 1995). The Nb/Ta ratio and Nb content (0.4–1.8 ppm) are higher than PM values (Nb/Ta = 17.8 and Nb 0.66 ppm; McDonough & Sun 1995) in two out of four samples. Ba is variable, with both positive and negative anomalies ($Ba_N = 0.08–5$). Compatible elements do not show significant variations in abundances in the studied peridotites (Cr 1844–2563 ppm; Ni 2029–2244 ppm; Sc 10–16 ppm; Co 101–108 ppm; V 33–68 ppm). Cr and La are negatively correlated with mg-number.

Orthopyroxene. The REE distribution and contents are similar for all analysed samples (Table 3 and Fig. 6). Their C1-normalized REE patterns are characterized by LREE depletion relative to HREE ($La_N/Yb_N = 0.14–0.34$). In sample HYB14, in spite of the occurrence of vermicular intergrowths with spinel, the absence of a marked HREE enrichment of orthopyroxene suggests that the origin of the intergrowths is not related to the breakdown of an earlier garnet. When normalized to PM values, incompatible trace element patterns of orthopyroxenes display marked positive Nb and Ti anomalies and, in general, negative Sr, La, Ce, Sm and Zr anomalies. Orthopyroxenes from sample HYB40 do not show a positive Nb anomaly and have higher contents of Hf and Ti.

Clinopyroxene. Clinopyroxenes are in general homogeneous; only clinopyroxenes in sample HYB21 show evidences of core–rim zonation (Table 4). C1-normalized REE patterns for clinopyroxenes are characterized by enrichment of LREE with respect to HREE (HREE; $La_N/Yb_N = 2.7–20$; Table 4). In Figure 6, three patterns are recognized: (1) LREE-enriched ($La_n/Yb_n = 7–17$) for samples HYB21, HYB24 and HYB29; (2) spoon-shaped ($La_n/Yb_n = 18–20$; $La_n/Sm_n = 21–34$; $Sm_n/Yb_n < 1$) for sample HYB14; (3) flattened (La_n/Yb_n *c.* 3; Sm_n/Yb_n =2–2.6; La_n/Sm_n *c.* 1.3) for sample HYB40. The REE pattern of clinopyroxene in the HYB40 glass veinlet mimics that of clinopyroxenes in the host peridotite but has a higher ΣREE (Fig. 6). All clinopyroxenes are enriched in U and Th with respect to primitive mantle values and their PM-normalized incompatible trace element patterns show negative Ba, Zr, Hf and Ti anomalies. They lack Sr anomalies, except for rims in HYB21 clinopyroxenes, which display a clear positive Sr anomaly. Rim analysis of HYB21 clinopyroxenes also shows an enrichment of all trace elements with the exception of Nb and Ti, whose values remain similar to those of cores (Table 4). This selective enrichment is probably a result of the different

Table 4. *Major and trace element compositions of selected clinopyroxenes of spinel peridotites from the Hyblean Plateau, and of clinopyroxenes hosted in glass vein from sample HYB40*

	HYB14			HYB21			HYB23			HYB24			HYB29		
	core	rim	core	core	rim	core	core	rim	core	core	rim	core	core	rim	core
wt%															
SiO_2	52.66	52.05	52.98	53.06	52.87	52.67	51.77	52.23	52.25	53.53	53.37	53.24	53.65	53.51	53.51
TiO_2	0.04	0.06	bd	0.09	0.10	bd	0.59	0.57	bd	0.14	0.12		0.16	0.15	bd
Al_2O_3	5.04	4.96	4.67	4.70	4.57	4.75	5.58	5.71	5.56	4.98	5.02	5.08	4.12	4.45	4.45
FeO^T	3.52	3.31	3.19	3.40	3.43	3.19	3.53	3.50	3.27	3.23	3.25	3.38	3.18	3.28	3.28
MnO	bd	bd	bd	bd	bd	bd	bd	bd	bd	bd	bd	bd	bd	bd	bd
MgO	16.08	16.12	16.07	15.99	16.22	16.11	16.01	15.88	15.61	16.16	16.24	15.99	16.33	16.29	16.29
CaO	20.36	20.67	20.89	20.54	20.43	20.42	20.62	20.06	20.03	20.48	20.62	20.77	20.72	20.74	20.74
Na_2O	1.01	0.98	1.05	1.16	1.04	1.09	1.55	1.54	1.34	1.28	1.18	1.23	1.15	1.17	1.17
Cr_2O_3	0.90	1.08	0.76	0.98	0.91	0.98	1.24	1.39	1.04	0.92	0.91	0.90	0.85	1.02	1.02
Total	99.6	99.2	99.6	99.9	99.6	99.2	100.9	100.9	99.1	100.7	100.7	100.6	100.2	100.6	100.5
Wo	44.8	45.2	45.7	45.2	44.7	45.0	45.2	44.7	45.2	45.0	45.1	45.5	45.1	45.1	45.1
En	49.2	49.1	48.9	49.0	49.4	49.5	48.8	49.2	49.0	49.4	49.4	48.7	49.5	49.3	49.3
Fs	6.0	5.7	5.4	5.8	5.9	5.5	6.0	6.1	5.8	5.5	5.5	5.8	5.4	5.6	5.6
mg-no.	89.1	89.7	90.0	89.3	89.4	90.0	89.0	89.0	89.5	89.9	89.9	89.4	90.2	89.9	89.9
ppm															
V	197	194		190	257					224			220	229	
Cr	na	na		na	10600					na			9650	10402	
Sr	92	103		67	406					176			390.7	403	
Y	3.2	3.4		5.0	7.50					6.5			6.9	6.8	
Zr	0.66	0.73		2.58	18.33					13			14.2	14.3	
Nb	bd	3.8		2.57	1.64					6.3			2.44	2.50	
Ba	1.77	1.60		0.69	bd					0.53			0.41	0.50	
La	11.1	11.5		5.9	11.95					14.7			15.8	15.9	
Ce	12.9	12.3		10.1	19.01					26.9			41.5	42.4	
Pr	0.84	0.85		1.09	2.07					2.70			5.1	5.0	
Nd	2.04	1.82		4.1	7.95					9.77			19.6	19.6	
Sm	0.33	0.21		0.76	1.51					1.65			3.24	2.86	
Eu	0.12	0.08		0.25	0.43					0.48			0.82	0.78	
Gd	0.20	0.23		0.89	1.42					1.26			2.34	2.61	
Tb	0.04	0.05		0.15	0.20					0.19			0.29	0.25	
Dy	0.52	0.45		0.86	1.29					1.19			1.72	1.52	
Ho	0.12	0.15		0.20	0.27					0.23			0.27	0.25	
Er	0.38	0.32		0.47	0.81					0.66			0.70	0.69	
Tm	0.07	0.09		0.09	0.11					0.096			0.10	0.10	
Yb	0.38	0.44		0.55	0.72					0.60			0.66	0.76	

Lu	0.05	0.06		0.09	0.08				0.087	0.11	0.09
Hf	0.017	bd		0.06	0.38				0.34	0.44	0.41
Ta	0.11	0.09		0.13	0.43				0.42	0.29	0.27
Pb	bd	bd		bd	0.22				bd	bd	bd
Th	0.81	0.82		0.69	1.37				1.28	0.49	0.49
U	0.20	0.18		0.12	0.36				0.32	0.12	0.10

	HYB34			HYB36			HYB40				
	core	rim	core	core	rim	core	core	rim	core	glass	glass
wt%											
SiO_2	53.50	53.82	53.93	53.05	53.47	53.31	53.30	53.45	53.47	48.00	48.14
TiO_2	bd	bd	bd	0.31	0.27	0.27	0.47	0.51	0.48	2.89	2.15
Al_2O_3	3.44	3.09	3.27	3.06	2.79	3.12	2.45	2.65	2.78	7.64	7.80
FeO^T	3.04	2.84	2.78	2.43	2.52	2.66	2.55	2.51	2.67	3.01	2.86
MnO	bd	bd	bd	bd	bd	bd	bd	bd	bd	bd	bd
MgO	16.99	17.15	17.23	17.03	17.07	17.18	17.04	17.05	17.11	14.65	15.11
CaO	22.02	22.26	21.53	23.93	24.24	23.38	23.58	23.79	23.27	23.34	21.98
Na_2O	1.07	1.13	1.08	0.49	0.48	0.46	0.31	0.29	0.30	0.32	0.42
Cr_2O_3	0.63	0.65	0.55	0.66	0.76	0.57	0.34	0.44	0.35	0.95	1.53
Total	100.7	100.9	100.4	101.0	101.6	101.0	100.0	100.7	100.4	100.8	100.0
Wo	45.8	46.0	45.2	48.3	48.5	47.4	47.8	48.1	47.3	47.8	48.1
En	49.2	49.4	50.3	47.9	47.5	48.4	48.1	48.0	48.4	48.4	47.8
Fs	4.9	4.6	4.6	3.8	3.9	4.2	4.0	4.0	4.2	3.8	4.2
mg-no.	90.9	91.5	91.7	92.5	92.4	92.0	92.3	92.4	92.0	89.7	90.4
ppm											
V							154	181		na	
Cr							na	2820		na	
Sr							44	54		65	
Y							5.6	7.0		12.7	
Zr							13	13		22	
Nb							0.09	0.23		0.57	
Ba							2.54	bd		bd	
La							2.37	2.86		3.6	
Ce							4.0	4.7		6.3	
Pr							0.63	0.74		1.05	
Nd							2.84	4.7		6.8	
Sm							1.15	1.42		2.02	
Eu							0.33	0.49		0.75	
Gd							1.04	1.39		2.64	
Tb							0.17	0.22		0.41	

(*Continued*)

Table 4. *Continued*

	HYB34			HYB36			HYB40			
	core	rim	core	core	rim	core	core	rim	glass	glass
ppm										
Dy							1.06	bd	2.47	
Ho							0.21	0.26	0.47	
Er							0.52	0.80	1.36	
Tm							0.08	bd	bd	
Yb							0.60	0.59	1.29	
Lu							0.07	0.06	0.13	
Hf							0.70	0.79	1.15	
Ta							bd	bd	bd	
Pb							0.84	0.84	0.81	
Th							0.22	0.24	0.26	
U							0.22	0.12	0.12	

FeO^T, total Fe; bd, below detection limit; mg-number = molar ($100 \times MgO/(MgO + FeO^T)$); na, not analysed; glass, secondary clinopyroxene crystallized in glass vein.

diffusive ability of the trace elements into the metasomatic agent (highest for the most incompatible elements such La, Sr; Yu *et al.* 2006). HYB40 clinopyroxenes display a strong negative Nb anomaly and a weak positive Pb anomaly, whereas the negative Zr, Hf and Ti anomalies are very smooth (Fig. 6). With respect to the other samples, HYB40 clinopyroxene also has lower Zr/Hf ratio (17, compared with 32–41 in other samples) and lower Nb content (0.1 ppm, compared with 2.5–6.3 ppm in other samples; Table 4), In this sample, clinopyroxene of the glass vein is richer in incompatible trace elements than the peridotite clinopyroxenes but has very close Zr/Hf (*c*. 19) and Th/U ratios (*c*. 2). In bivariate plots (Fig. 7) Th, U, Sr, Nb and V are positively correlated with La (these are assumed to be the most incompatible elements), whereas Ba, Hf and Zr are negatively correlated. Y and Yb contents do not show any significant correlation with La content.

Glass vein. C1-normalized diagrams show that the glass vein is slightly LREE enriched (La_N/Yb_N *c*. 5; Fig. 8a). PM-normalized incompatible element diagrams are characterized by strong positive Ba, Nb, Pb and Ti anomalies (Fig. 8b). Zr/Hf and Nb/Ta ratios are 27–31 and 13–16 respectively. The glass has major and trace elements composition very different from that of the basaltic host rock (Figs 4 and 8).

P–T conditions and oxygen barometry

P–T–fO_2 estimates of the studied Hyblean peridotites are based on the compositions of mineral phases (Table 7 and Fig. 9). Literature P–T estimates (Nimis 1998; Punturo *et al.* 2000; Sapienza *et al.* 2005) are also reported for comparison. Equilibrium temperatures were calculated using the two-pyroxene geothermometers of Wells (1977) and Brey & Köhler (1990). They yield values in the range 752–1070 °C and 844–1028 °C, respectively. Pressure was estimated using the Köhler & Brey (1990) geobarometer, based on Ca exchange between coexisting olivine and clinopyroxene. It varies in a narrow range, between 0.9 and 1.2 GPa with a maximum error of ± 0.1 GPa, lower than the uncertainty related to geobarometer calibration (± 0.17 GPa; Köhler & Brey 1990). These data agree with the P–T conditions of spinel pyroxenitic xenoliths obtained by Nimis (1998) (Fig. 9a).

The redox state of the xenoliths is reported as Δlog units with respect to the fayalite–magnetite–quartz buffer (FMQ); calculations are based on model of Wood & Virgo (1989), using the temperatures previously calculated. Although the range of estimated pressure is 1.1 ± 0.1 GPa, a uniform equilibration pressure of 1.5 GPa has been used

Table 5. *Representative microprobe analyses of spinels from Hyblean Plateau peridotite xenoliths*

	HYB14	HYB14	HYB21	HYB21	HYB23	HYB23	HYB24	HYB24	HYB24	HYB24	HYB29	HYB29	HYB29	HYB29	HYB34	HYB36	HYB36	HYB40	HYB40
wt%																			
TiO_2	bd	0.41	0.60	0.65	0.64	0.65	bd	bd	bd	0.29	bd	0.35	bd	bd	bd	bd	0.54	0.56
Al_2O_3	44.01	43.97	41.13	40.60	37.41	38.19	41.07	42.67	42.42	36.03	33.96	34.29	36.83	40.23	39.48	41.15	40.96
V_2O_5	bd	bd	bd	0.15	bd	bd	bd	bd	bd	bd	bd	bd	0.17	bd	bd	bd	bd	bd
Cr_2O_3	22.88	22.87	26.28	26.39	28.62	28.23	25.02	23.22	23.71	30.14	31.73	31.65	28.55	24.60	25.89	21.87	20.94
FeO^T	12.59	13.50	13.89	14.56	15.39	15.49	14.71	14.26	14.31	16.26	16.02	16.05	18.79	19.60	18.93	19.34	18.18
MgO	19.53	19.83	18.50	18.42	18.75	18.00	19.28	18.69	18.83	17.72	17.84	17.95	16.30	16.17	16.10	16.88	17.82
MgO	0.38	0.34	bd	bd	bd	bd	bd	bd	bd	bd	bd	bd	bd	bd	bd	bd	bd
Total	99.4	100.9	100.4	100.8	100.8	100.6	100.1	98.8	99.3	100.4	99.6	100.3	100.6	100.6	100.4	99.8	98.5
cr-no.	25.8	25.9	30.0	30.4	33.9	33.1	29.0	26.7	27.3	35.9	38.5	38.2	34.2	29.1	30.5	26.3	25.5
mg-no.	80.1	79.6	76.3	76.0	76.6	73.8	78.9	77.1	77.4	73.9	75.9	75.3	68.7	67.4	67.4	69.4	73.6

FeO^T, total Fe; bd, below detection limit; cr-number = atomic $(100 \times Cr/(Cr + Al))$; mg-number = atomic $(100 \times Mg/(Mg + Fe^{2+}))$.

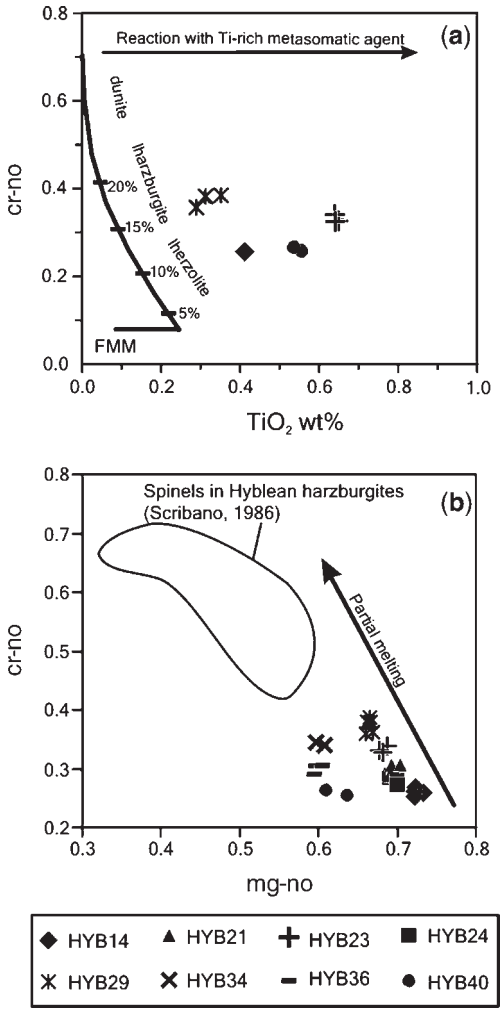

Fig. 3. (**a**) Plot of spinel cr-number v. TiO_2 (wt%). Lines related to partial melting evolution are drawn with marks indicating degree of partial melting. The melt–mantle interaction trend is shown (Pearce *et al.* 2000, and references therein, simplified). FMM, fertile MORB mantle. (**b**) Spinel mg-number v. cr-number. The trend of partial melting (black arrow; drawn by eye) is shown for comparison.

for the fO_2 calculation, to compare our results with the mantle $f\,O_2$ estimated for other parts of Italy (Fig. 9b). Even accounting for an error of ± 1 GPa in the barometric estimates, the relative $f\,O_2$ variation ± 0.3 log units (Canil *et al.* 1990; McCammon & Kopylova 2004). In total, however, all the remaining sources of errors (P, T, X) at most account for $f\,O_2$ variations of ± 0.5 log unit, which is within the oxy-barometer calibration uncertainty (Bryndzia & Wood 1990; Canil *et al.*

Table 6. *Microprobe and LAM-ICP-MS analyses of glass vein*

	HYB40	HYB40	HYB40	HYB40	HYB40	HYB40
wt%						
SiO_2	49.26	49.32	50.35	50.11	49.68	49.73
TiO_2	3.47	3.53	3.56	3.78	3.64	3.56
Al_2O_3	20.09	20.19	20.46	20.47	20.13	20.14
FeO^T	5.16	5.32	5.41	5.57	5.37	5.24
MgO	4.36	4.02	4.39	4.29	4.24	4.38
CaO	9.63	9.50	9.55	9.71	9.62	9.44
Na_2O	4.74	4.99	4.65	4.28	4.90	4.87
K_2O	1.49	1.89	1.52	1.42	1.47	1.50
P_2O_5	0.33	0.33	0.27	0.25	bd	0.29
Total	98.5	99.1	100.2	99.9	99.1	99.2
ppm						
V	405	421				
Cr	30	25				
Rb	11	10				
Sr	554	570				
Y	28.6	30.9				
Zr	80	76				
Nb	26	26				
Cs	0.51	0.48				
Ba	1027	1092				
La	22.5	22.3				
Ce	31.4	29.9				
Pr	4.0	4.0				
Nd	20.6	20.9				
Sm	5.3	5.5				
Eu	1.80	1.94				
Gd	6.2	6.5				
Tb	0.93	bd				
Dy	6.1	6.1				
Ho	1.10	1.10				
Er	3.2	3.2				
Tm	0.43	bd				
Yb	2.76	2.99				
Lu	0.38	0.36				
Hf	2.98	2.50				
Ta	1.91	1.65				
Pb	10.1	10.3				
Th	2.32	2.05				
U	0.96	0.88				

FeO^T, total Fe; bd, below detection limit.

1990). $f\,O_2$ values calculated for our xenoliths range between $+0.2$ and $+1.6$ Δlog units (maximum error ± 0.2 log units) with respect to FMQ (Table 7). Peridotite HYB40 records the most oxidized conditions.

Discussion

Partial melting

According to the literature, the harzburgitic composition, the depletion in basaltic components as Al_2O_3 and Na_2O, and the rather high mg-number values of pyroxenes and Fo content in olivine of the Hyblean peridotites all indicate that these rocks underwent one or more depletion events (Sapienza & Scribano 2000, and references therein).

In this study we observe that although the Zr/Hf ratio (as well as some Nb/Ta values) indicates metasomatic enrichment (Fig. 10b and the next section), whole-rock Zr and Hf (and Nb and Ta in two samples) concentrations are lower than PM values and can be related to partial melting. Similarly, clinopyroxene composition shows Zr (and Hf) contents lower than primitive mantle clinopyroxene trace elements (PMCE: $Zr_{PMCE} = 36.1$ and

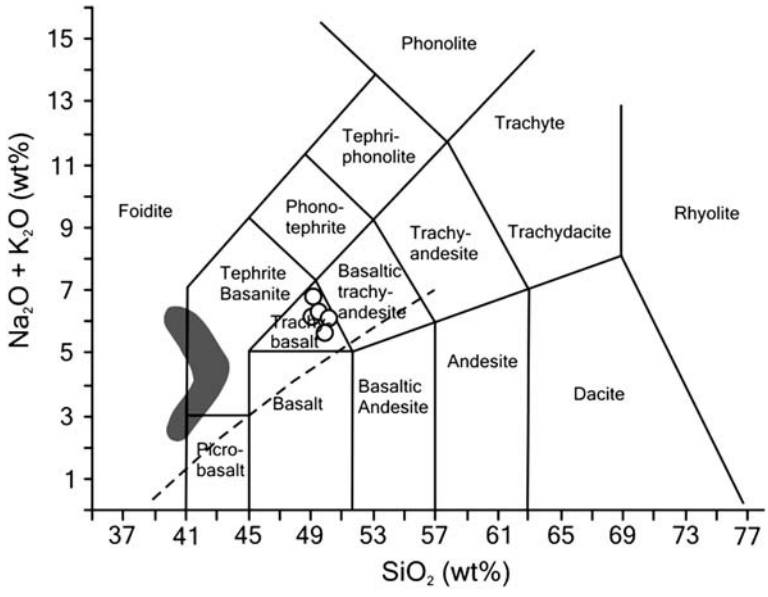

Fig. 4. Total alkalis–silica classification diagram for Hyblean Upper Miocene lavas (shaded field) and glass vein within sample HYB40. The dividing line between alkalic and subalkalic series is after Irvine & Baragar (1971).

$Hf_{PMCE} = 1.34$; calculated by the Hellebrand *et al.* (2002) model, according to Rivalenti *et al.* (1996), whereas Zr/Hf ratios are similar to (or higher than) PMCE, and always above the trend of clinopyroxene evolution for fractional melting reported in Figure 10b. The different affinity of Zr and Hf for clinopyroxene ($^{cpx/melt}D_{Hf} > {}^{cpx/melt}D_{Zr}$; Hart & Dunn 1993) should imply that partial melting lowers the Zr/Hf in the solid residue with respect to the source rock (Weyer *et al.* 2003). Therefore, the observed Zr and Hf trend can be interpreted as the result of an early depletion (which removes mainly Zr but also Hf from clinopyroxenes) followed by a later enrichment that chiefly added Zr.

Our new bulk-rock data fall in the field of the literature Zr and Hf data and their trend is compatible with higher Zr enrichment relative to Hf, after partial melting (Fig. 10b). However, only two samples show Nb and Nb/Ta values comparable with the literature data (Fig. 10a).

The degree of partial melting (F) has been obtained by applying three models.

First, clinopyroxene abundances of HREE were used, on account of their low mobility with respect to LREE during metasomatic events. Following Johnson *et al.* (1990), Norman (1998) and Hellebrand *et al.* (2002), computations are based on the comparison between the REE contents of 'depleted' clinopyroxenes, calculated using a model of fractional melting of a primitive spinel peridotite mantle source, and the REE contents of clinopyroxenes from the studied peridotites (Fig. 11). Modelling is based upon the approach of Hellebrand *et al.* (2002) and provides results in the range $F = 6–13\%$ for the distribution from Dy to Yb.

Second, a narrower range of F is obtained by applying the method proposed by Norman (1998), based on Y and Yb concentration of clinopyroxene; modelling results show that 10–14% of fractional melting can reproduce Y–Yb contents of HYB clinopyroxene.

Third, the equation proposed by Hellebrand *et al.* (2001) was employed. It describes the extent of melting as a function of spinel cr-number; the calculated F range is between 11 and 14%, similar to that obtained by the Norman (1998) model. This suggests that the lowest F estimated by the clinopyroxene HREE model is probably due to the action of metasomatic events that hence slightly modified the HREE abundance of some clinopyroxenes.

In the cr-number v. TiO_2 diagram, the partial melting is characterized by their negative correlation as F increases (Fig. 3a). The spinels, instead, show an increase of TiO_2 at constant cr-number. These enrichments indicate that the 'interacting' end-members are the residual peridotites and a component with higher Ti content and lower mg-number (Fig. 3a). Similarly, the mutual variation of cr-number and mg-number (Fig. 3b) cannot be related only to melt extraction event(s)

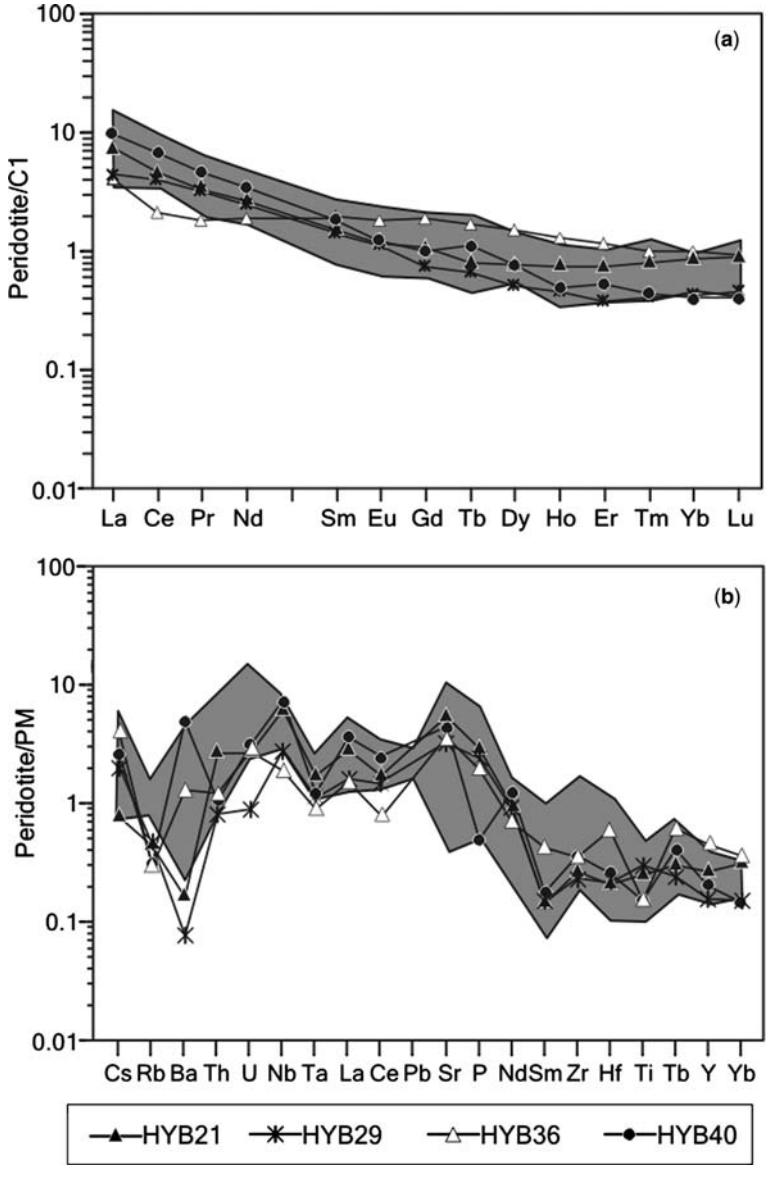

Fig. 5. (**a**) C1-normalized REE pattern and (**b**) PM-normalized multi-element diagram for studied Hyblean peridotite xenoliths. C1- and PM-normalizing values after McDonough & Sun (1995). The shaded field represents literature data (Mazzoleni & Scribano 1994; Tonarini *et al.* 1996; Sapienza & Scribano 2000; Sapienza *et al.* 2005).

(see black arrow in Fig. 3b), as the mg-number for varies for similar cr-number.

Spinel compositions of our Miocene lavas xenoliths are less depleted than those of the harzburgites, found in Quaternary lavas (Scribano 1986; Fig. 3). These data seem to indicate a small-scale spatial heterogeneity rather than to suggest a progressive depletion of the Hyblean upper mantle from the Late Miocene to Quaternary.

Mantle metasomatism

The studied samples do not show modal metasomatism, except for the occurrence of a glass veinlet in peridotite HYB40, which will be discussed in the next section. In contrast, whole-rock and mineral chemistry show evidence of cryptic metasomatism, such as the relations between trace and major elements in bulk-rock chemistry (e.g. negative

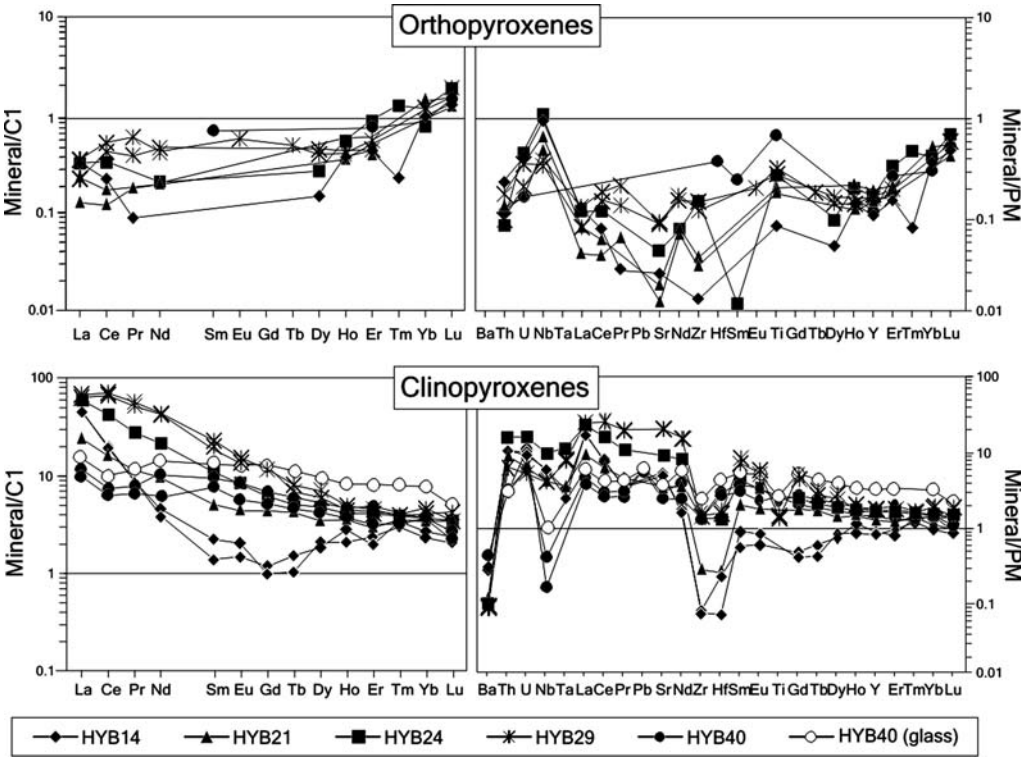

Fig. 6. C1-normalized REE patterns and PM-normalized trace element patterns for pyroxenes of Hyblean spinel peridotites. Clinopyroxene within the HYB40 glass vein is also plotted. C1- and PM-normalizing values from McDonough & Sun (1995).

correlations between mg-number and Cr content and positive correlation between Cr content and Al_2O_3 and Na_2O), the variable trace element enrichments in clinopyroxene, and the irregular Ti and Fe enrichment apparent in Figure 3a and 3b.

Evolution of whole-rock and clinopyroxene Zr/Hf and Nb/Ta ratios can be ascribed to metasomatic processes after an early partial melting event (see the previous section) (Fig. 10), although more data are needed to better define a trend. Both Nb/Ta ratio and Nb content in two out of four Hyblean peridotites are higher than PM values (and also the field of Hyblean peridotites from literature), depicting a trend compatible with their introduction by metasomatic agent(s); a similar process can be invoked for the increase of Zr/Hf ratios (higher than PM). The effect of metasomatism is also confirmed by the composition, of clinopyroxene, the Nb/Ta ratios of which resemble those of the whole rocks (Fig. 10a), and mainly by the positive correlation between Nb and La (see below; Fig. 7).

Given that the Nb and Ta concentrations are controlled by metasomatism, and the low solubility of Nb–Ta in metasomatic fluids (Tatsumi *et al.* 1986), the lack of a negative Nb–Ta anomaly in whole–rock and clinopyroxene spider diagram (Figs 5b and 6) suggests that the metasomatic agent was a melt. The metasomatic event(s) also affected the LREE abundances in clinopyroxenes (Fig. 6); the most pronounced enrichment is experienced by La, thus this element was adopted as an enrichment index. During metasomatism the pair Yb–Y maintains a mutual positive correlation. In contrast both elements are not correlated with La (Fig. 7). This suggests that they did not undergo differential enrichments and were only slightly affected by metasomatism. Metasomatic agents, also control Nb, V, Sr, U and Th contents in clinopyroxene, as shown by the positive correlation with La in the bivariate plots shown in Figure 7.

As clinopyroxene is the main repository for REE and many other trace elements in mantle peridotites (e.g. Eggins *et al.* 1998), we attempt to model the nature of the metasomatic melt by using the clinopyroxene–basaltic melt partition coefficients of Skulski *et al.* (1994).

The differences in composition between our clinopyroxenes document different metasomatizing

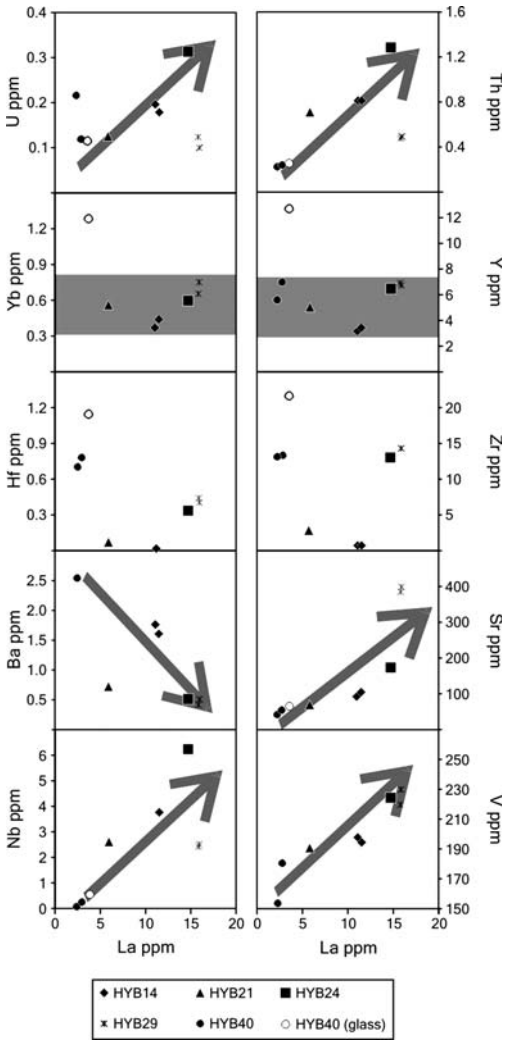

Fig. 7. Covariation diagrams of selected trace elements against La in clinopyroxenes from Hyblean peridotites. Arrows (drawn by eyes) and shaded fields indicate the variation trends of the elements against La.

agents and various extent of metasomatism as a result of various degrees of equilibration with the metasomatic agent. We can assume that the different levels of enrichment in the xenoliths may be due to their distance from the metasomatic source (magma conduit; Xu & Bodinier 2004) and to the progressive equilibrium achieved with it. The spoon-shaped REE patterns in clinopyroxene from peridotites HYB14 and HYB21 probably reflect a situation in which complete equilibration with the metasomatic agent is not reached, hence these compositions were not used for parental melt calculation (Fig. 6).

The modelled melt patterns from HYB24 and HYB29 are parallel to each other and very rich in LREE, up to *c*. 600 times PM (Fig. 12). Liquid from HYB40 clinopyroxenes shows some significant differences, with minor Nb, Sr and LREE contents and lower Zr/Hf ratio (*c*. 16 with respect to 30–35). The theoretical composition of the liquids in equilibrium with peridotite clinopyroxenes can be compared with the compositions of the Hyblean Upper Miocene lavas (Bianchini *et al.* 1998; Rocchi *et al.* 1998; Perinelli 2001; Scribano *et al.* 2006) and the theoretical liquid in equilibrium with clinopyroxene from pyroxenite xenoliths from the same locality (Nimis & Vannucci 1995; Perinelli 2001; Fig. 12). Among the pyroxenites studied by Nimis & Vannucci (1995), we considered only group 1 pyroxenites that still preserve their primary compositions related to the crystallization from an OIB-like melt. Melts deduced from HYB40 clinopyroxenes, particularly that crystallised in the glass vein, resemble the compositions described by Nimis & Vannucci (1995), which therefore could be considered to be responsible for metasomatism in this sample. This suggestion is also confirmed by the glass vein, the composition of which matches that of melts calculated from pyroxenites (Fig. 12). In contrast, host basalt represents a possible metasomatic agent for peridotites HYB24 and HYB29. For these rocks, the LREE enrichment as well as Sr and Zr normalized values of host basalts and theoretical metasomatic agents are comparable. Some differences in Ti content (Fig. 12) could be related to uncertainties in the empirical evaluation of $D^{cpx/liq}$, the dependence of partition coefficients on P–T–X conditions and volatile contents, which makes us consider these calculations as only qualitative. However, the possibility of crystallization of a Ti-rich phase in the metasomatizing melt cannot be ruled out. Nevertheless, the melts considered to have metasomatized HYB24 and HYB40 show some similarities (Zr; MREE, HREE and Y; Fig. 12); HYB24 is possibly enriched only in the most incompatible elements by the host lava in a later phase.

Origin of the glass vein

Several mechanisms have been suggested for glass formation in peridotite xenoliths: (1) *in situ* decompression melting (Chazot *et al.* 1996); (2) host magma infiltration (Garcia & Presti 1987); (3) reaction between percolating melt(s) and host peridotites at mantle depths (Zinngrebe & Foley 1995).

In the Hyblean case, mechanism (1) can be ruled out because of the textural occurrence of the glass vein. To distinguish between options (2) and (3) we compared the geochemical characters of the host basalts and glass vein (Figs 4–8). The

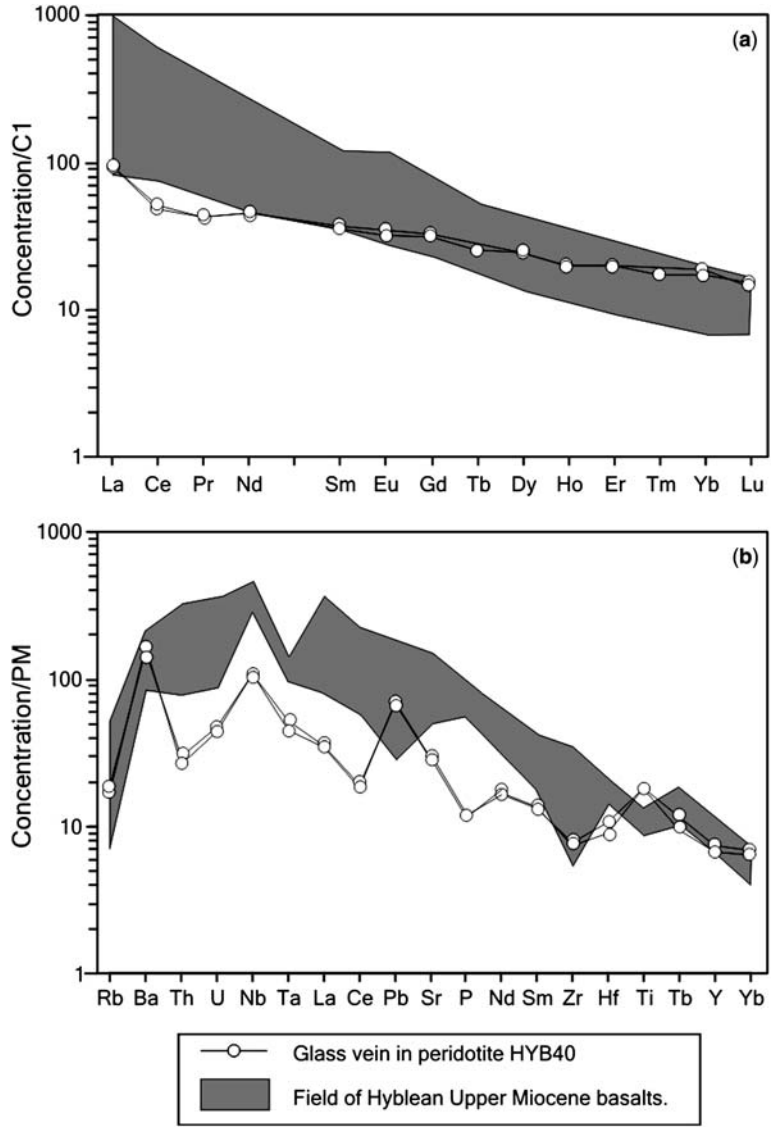

Fig. 8. (**a**) C1-normalized REE patterns and (**b**) PM-normalized trace element patterns for the glass vein of spinel peridotite HYB40. Fields of Upper Miocene lavas are shown for comparison. C1- and PM-normalizing values are from McDonough & Sun (1995).

difference in major-element, REE and trace-element compositions between host basalt (mg-number = 69) and the glass vein is evident: the glass vein is hawaiitic (mg-number = 65) and has higher K_2O/Na_2O ratio (0.33 and 0.19, respectively). Mass-balance calculations based on the glass and phenocryst compositions show that fractionation of a small modal amount of clinopyroxene and olivine cannot explain a derivation from the Upper Miocene magma (Perinelli 2001). Comparison with the Upper Miocene basalts shows that the REE in the glass are less fractionated than those in Upper Miocene lavas, with La_N at the lower limit and Yb_N at the upper limit of the host-rock field (Fig. 8a). Selective trace element relationships expressed by LILE/HFSE (e.g. Ba/Nb_{glass} *c.* 40; $Ba/Nb_{host\text{-}basalt}$ *c.* 11) and LILE/LREE (e.g. Ba/La_{glass} *c.* 47; $Ba/La_{host\text{-}basalt}$ *c.* 7) further stress the lack of parental affinity between the host magma and glass vein. As demonstrated in the previous section, the trace element composition of the glass vein closely resembles that of

Table 7. *Temperature, pressure and oxygen fugacity estimates for peridotites from the Hyblean Plateau*

	T (°C)	P (GPa)	Log $f\,O_2$	Δlog $f\,O_2$ (FMQ)
HYB14	1007 (4)	1.2 (0.02)	−9.06 (0.04)	1.01 (0.04)
HYB21	1053 (8)	1.23 (0.01)	−9.27 (0.18)	0.15 (0.18)
HYB23	1001 (6)	1.13 (0.05)	−9.50 (0.23)	0.65 (0.23)
HYB24	1036 (13)	1.13 (0.05)	−8.59 (0.11)	1.07 (0.11)
HYB29	1034 (11)	1.12 (0.07)	−8.41 (0.07)	1.27 (0.07)
HYB34	957 (9)	0.95 (0.07)	−9.86 (0.1)	0.96 (0.1)
HYB40	873 (10)	0.85 (0.04)	−10.62 (0.03)	1.61 (0.03)

Temperature estimates have been obtained by two-pyroxene geothermometers (Brey & Köhler 1990). Equilibration pressures of peridotites are based on olivine–clinopyroxene Ca exchange reaction (Köhler & Brey 1990). Ca content of olivine was measured on isolated grains. The T and P values for each sample represent the average of three T and P estimates. Standard deviations are given in parentheses. For the $f\,O_2$ calculations a uniform equilibration pressure of 1.5 GPa and the Brey & Köhler (1990) temperature estimations have been used.

melts that generated the pyroxenites. Glass within peridotite HYB40 can therefore be ascribed to the flux of OIB-like liquid in the host peridotite before entrainment into the host lavas. Partial crystallization of the glass indicates that the veining process must have occurred not long before entrainment into the host magma, but leaving enough time for equilibration of clinopyroxenes in the host peridotite with the intruding melt.

P–T–fO₂ conditions

P–T determinations show that the studied rocks equilibrate in the spinel peridotite stability field

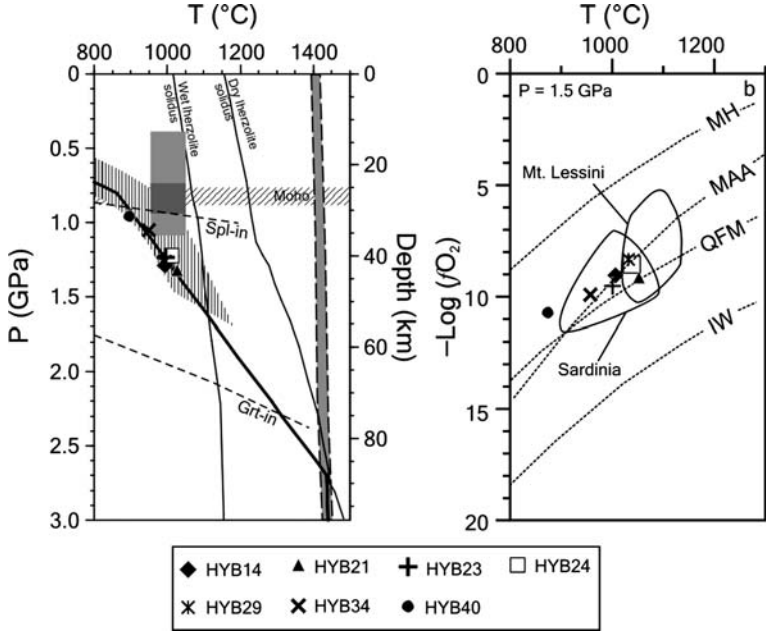

Fig. 9. (**a**) *P–T* estimates for Hyblean peridotite xenoliths. The shaded field includes the range of microthermometric measurements; the dark grey portion indicates the high-frequency interval in which *c*. 60% of measurements fall (Sapienza *et al.* 2005). Vertically hatched field indicates the *P–T* equilibration conditions for Hyblean pyroxenites (Nimis 1998). Peridotite wet ($H_2O < 0.4$ wt%) solidus is after Green *et al.* (1987); peridotite dry solidus is after Takahashi & Kushiro (1983). The shaded field with dashed border indicates the onset of olivine crystallization for alkaline basalts–basanite compositional range. The Moho depth is after Scarascia *et al.* (1994). (**b**) $f\,O_2$–*T* plot for Hyblean peridotites. Curves are: IW, iron–wüstite; FMQ, fayalite–magnetite–quartz; MH, magnetite–hematite; MAA, Mantle Average Array.

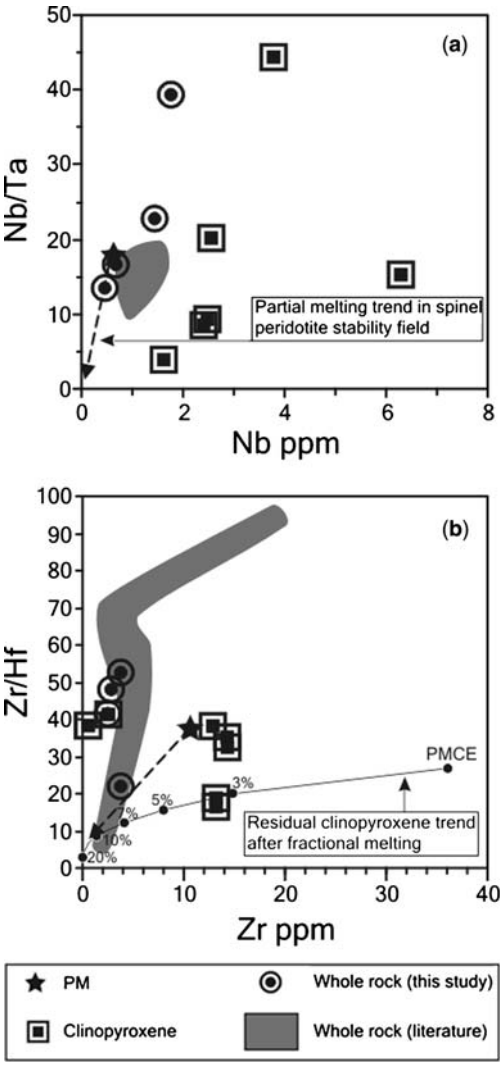

Fig. 10. (**a**) Nb/Ta–Nb and (**b**) Zr/Hf–Zr variation diagrams for whole-rock and clinopyroxenes from Hyblean peridotites. The fractional melting trend of a starting source of primitive spinel peridotite is taken from Weyer *et al.* (2003) and references therein. The trace element composition of clinopyroxene in primitive mantle (PMCE) and the modelled trend for clinopyroxene partial melting residue are estimated using the model of Johnson *et al.* (1990) modified by Hellebrand *et al.* (2002) (black points indicate degree of partial melting). $^{\text{mineral/melt}}D$ are from Ulmer (1989), Hart & Dunn (1993) and Horn *et al.* (1994).

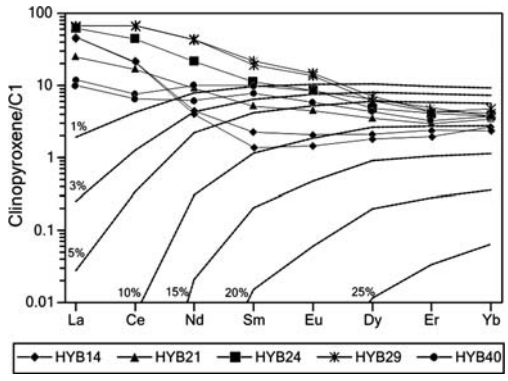

Fig. 11. Comparison between REE patterns of clinopyroxenes from Hyblean peridotites and modelled REE patterns in clinopyroxenes following fractional melting of a spinel peridotite source (Hellebrand *et al.* 2002). Degrees of partial melting are indicated. C1-normalizing values after McDonough & Sun (1995).

(Fig. 9a), and fit the palaeogeotherm calculated by Nimis (1998) for spinel-bearing pyroxenite. Our estimates are also consistent with the entrapment pressures obtained by microthermometric measurements of fluid inclusions hosted in Hyblean peridotites from the same diatreme (Sapienza *et al.* 2005) (0.4–1.1 GPa, at a nominal T of 1000 °C, with a peak between 0.75 and 0.95 GPa; Fig. 9a).

The agreement of different geothermobarometric computations applied to distinct lithotypes (peridotites and pyroxenites) from the same locality corroborates the validity of this palaeogeotherm. Therefore, the metasomatic processes, inferred from fluid inclusions and related to melt–peridotite interaction, took place at, or below, the crust-mantle boundary (up to 1.2 GPa).

The pressure and temperature estimates may be fitted by the equation of heat transport (Philpotts 1990)

$$Tz = Tz_0 + (J_Q^{z0}/k)(z - z_0) - (A_0/2k)(z - z_0)^2$$

that allows us to model a geothermal gradient for Miocene mantle. To match the thermobarometric estimates, the surface heat flux J_Q^{z0} has to be assumed to be 75 mW m^{-2}, close to the range observed in the area (60–70 mW m^{-2}; Arisi Rota & Fichera 1987; Della Vedova *et al.* 1989; Viti *et al.* 1997). Other constants are taken from the standard values reported in the literature: the heat produced in the crust (A_0) is 0.31 μW m^{-3} (Phillpotts 1990) and the thermal conductivity k (W m^{-1} K^{-1}) is assumed to be 2.52 (Philpotts 1990). Whether the high geothermal gradient found may be related to an advective heat-transfer mechanism (Nimis 1998) or to conductive heat transfer from underlying asthenospheric mantle can be decided by looking at the mantle potential temperatures (T_P) of host lavas. For a selection of the less

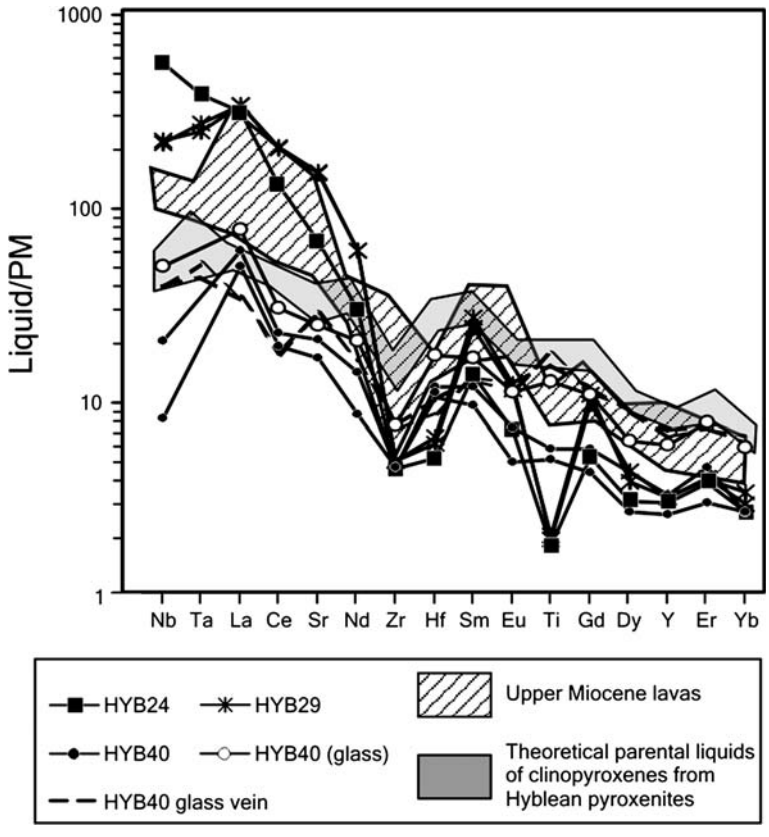

Fig. 12. Trace element compositions of liquids at equilibrium with clinopyroxenes from peridotite xenoliths. Compositions were calculated using the clinopyroxene–liquid partition coefficients of Skulski *et al.* (1994) and Eu after Hart & Dunn (1993). PM-normalizing values after McDonough & Sun (1995). The fields for Upper Miocene lava (Bianchini *et al.* 1998; Rocchi *et al.* 1998; Perinelli 2001; Scribano *et al.* 2006) and parental liquids of clinopyroxenes in pyroxenite xenoliths (Nimis & Vannucci 1995; Perinelli 2001) are shown for comparison (they all are recalculated using clinopyroxene–liquid partition coefficients of Skulski *et al.* (1994) and Eu after Hart & Dunn (1993). The composition of glass in sample HYB40 is also shown.

evolved Miocene lavas (mg-number > 0.6; Rocchi *et al.* 1998) we evaluated the T_P values following the method proposed by Putirka (2005) plotting $X\mathrm{Mg}_{liq}$ against $X\mathrm{Fe}_{liq}$ on the olivine saturation surface (Langmuir & Hanson 1981). As all these lavas lie on an olivine control line at $X\mathrm{Fe}_{liq}$ *c*. 0.07 and the most Fo-rich olivines cluster at a composition of Fo_{90}, the resulting T_P are of about 1430 °C. This value is maintained also by the more recent Plio-Pleistocene lavas and is encountered on the palaeogeotherm at a pressure of about 3.0 GPa, corresponding to the base of the lithosphere where the mantle geothermal gradient becomes adiabatic (Fig. 9a). At this pressure the melting relations are possibly related to the cusp of the dry peridotite solidus at the transition between the spinel and garnet stability fields. The composition of Miocene alkaline lavas also suggests an origin at a depth of about 90 km (Trua 1997; Trua *et al.* 1998). This allows us to reject the hypothesis of Nimis (1998) that an active asscent of mantle (a plume) may be responsible for the values of the thermal gradient. In fact, the thermal gradient and the heat flux of the area have been practically constant in the last 10 Ma, and the mantle potential temperatures are almost 200 °C lower than those of Hawaii and Iceland (Putirka 2005).

The redox state estimated for many Hyblean xenoliths falls within the range for subcontinental lithospheric mantle (FMQ $\pm$ 1; Wood *et al.* 1990). The highest $f\mathrm{O}_2$ values (above FMQ buffer) obtained for the most metasomatized samples (HYB29 = 1.3 Δlog units and HYB40 = 1.6 Δlog units) indicate that the metasomatic agent(s) was slightly more oxidized than the

host mantle. For the other samples, the observed fO_2 variation seems not to be directly related to the metasomatism: the fO_2 for HYB14 (very poorly metasomatized xenolith) is higher (*c.* 1 Δlog units) than fO_2 obtained from the strongly metasomatized HYB24 (0.15 Δlog units). This is in contrast to the common tenet that relates the variations of fO_2 to the action of a metasomatizing agent that leads to a progressive oxidation. Similar behaviour of fO_2 has been observed in peridotite xenoliths of Mt. Lessini and Sardinia (Italy) as well as in other mantle xenoliths from other regions (e.g. Cape Verde Islands; Siena & Coltorti 1993), and has been explained by the 'peculiar effects of fugitive metasomatic agents' that can provide a heterogeneous oxidation of mantle without evident chemical or modal enrichments (Siena & Coltorti 1993, and references therein).

Summary and conclusion

Hyblean peridotites reflect at least a two-stage petrogenetic process. The geochemical characters of spinels and clinopyroxenes indicate a moderate (11–13%) degree of partial melting; Sapienza *et al.* (2006) proposed a minimum Palaeoproterozoic–Archaean age for this event. Depletion was followed by a cryptic metasomatism, which affected the Hyblean lithospheric mantle as shown by whole-rock and clinopyroxene compositions. A minimum Carboniferous age (Tonarini *et al.* 1996) has been proposed for this process. Metasomatism introduced mainly LREE, selective LILE and HFSE into the 'barren' peridotite.

Two distinct metasomatic agents have been recognized.

(1) Siliceous alkaline melt similar to the Upper Miocene host basalt in terms of LREE enrichment, which determined the HFSE enrichment and increased Nb/Ta and Zr/Hf ratios. The more or less complete re-equilibration with this metasomatic agent, calculated from the clinopyroxene compositions, probably depends on the distance between the metasomatic source and the studied clinopyroxenes.

(2) Hawaiitic melt (found in the glass veinlet in sample HYB40), which is not related to the Upper Miocene host basalt. The metasomatizing melts also oxidized the upper mantle, increasing the fO_2 to above FMQ.

Textural and chemical evidence suggests a short interval between the two metasomatic events, which are probably both related to Miocene magmatism.

The peridotites equilibrated in the spinel peridotite stability field. P–T estimates are consistent with the data obtained on pyroxenite xenoliths by Nimis (1998): the thermobarometric data fit a geotherm that has not varied since at least the Late Miocene and that agrees with a mantle potential temperature (1430 °C) of coeval primitive melts at a pressure of 2.7 GPa. This thermal regime does not fit with the occurrence of an active mantle plume beneath the Hyblean area.

The authors are indebted to H. Downes for the constructive comments on an early version of this paper. A. Zanetti is also thanked for assistance during LAM-ICP-MS analysis. M. Benoit and an anonymous reviewer are thanked for constructive comments that improved the paper. This work is part of the PhD thesis of C.P. and is financially supported by the University of Pisa (grants for PhD research). This is the last study in which we could benefit from the fruitful contribution of ideas and enthusiasm of Lauro Morten, to whose memory dedicate this paper.

References

AMORE, C., CARVENI, P., SCRIBANO, V. & STURIALE, C. 1988. Facies ed età del vulcanismo nella fascia sudorientale della Sicilia (Pachino-Capo Passero). *Bollettino della Società Geologica Italiana*, **107**, 481–489.

ARISI ROTA, F. & FICHERA, R. 1987. Magnetic interpretation related to geo-magnetic provinces: the Italian case history. *Tectonophysics*, **138**, 179–196.

BECCALUVA, L., SIENA, F., COLTORTI, M., *ET AL.* 1998. Nephelinitic to tholeiitic magma generation in a transtentional tectonic setting: an integrated model for the Iblean volcanism, Sicily. *Journal of Petrology*, **39**, 1–30.

BECCALUVA, L., BIANCHINI, G., COLTORTI, M., PERKINS, W., SIENA, F., VACCARO, C. & WILSON, M. 2001. Multistage evolution of the European lithospheric mantle: new evidence from Sardinian peridotite xenoliths. *Contributions to Mineralogy and Petrology*, **142**, 284–297.

BIANCHI, F., CARBONE, S., GRASSO, M., *ET AL.* 1987. Sicilia orientale: Profilo geologico Nebrodi-Iblei. *Memorie della Società Geologica Italiana*, **38**, 429–458.

BIANCHINI, G., CLOCCHIATTI, R., COLTORTI, M., JORON, J. L. & VACCARO, C. 1998. Petrogenesis of mafic lavas from the northernmost sector of the Iblean district (Sicily). *European Journal of Mineralogy*, **10**, 301–315.

BOTTAZZI, P., OTTOLINI, L., VANNUCCI, R. & ZANETTI, A. 1994. An accurate procedure for the quantification of Rare Earth Elements in silicates. *In*: BENNINGHOVEN, A. (ed.) *Secondary Ion Mass Spectrometry—SIMS IX*. Wiley, Chichester, 927–930.

BREY, G. P. & KÖHLER, T. P. 1990. Geothermometry in four-phase lherzolites II: new thermobarometers, and practical assessment of of existing thermobarometers. *Journal of Petrology*, **31**, 1353–1378.

BRYNDZIA, L. T. & WOOD, B. J. 1990. Oxygen thermobarometry of abyssal spinel peridotites: The redox

state and C–O–H volatile composition of the Earth's sub-oceanic upper mantle. *American Journal of Science*, **290**, 1093–1116.

BURROLLET, F. P., MUGNIOT, J. M. & SWEENEY, P. 1978. The geology of the Pelagian Block: the margins and basins of southern Tunisia and Tripolitania. *In*: NAIRN, A. E. M., KANES, W. H. & STEHLI, F. G. (ed.) *The Ocean Basins and Margins, Volume. 4b: The Western Mediterranean*. Plenum, New York, 331–359.

CANIL, D., VIRGO, D. & SCARFE, C. M. 1990. Oxidation state of mantle xenoliths from British Columbia, Canada. *Contributions to Mineralogy and Petrology*, **104**, 453–462.

CARBONE, S. & LENTINI, F. 1981. Caratteri deposizionali delle vulcaniti del Miocene superiore negli Iblei (Sicilia sud-orientale). *Geologica Romana*, **20**, 79–101.

CARSWELL, D. A. 1980. Mantle derived lherzolite nodules associated with kimberlites, carbonatite and basalt magmatism: a review. *Lithos*, **13**, 121–138.

CHAZOT, G., MENZIES, M. A. & HARTE, B. 1996. Determination of partition coefficients between apatite, clinopyroxene, amphibole, and melt in natural spinel lherzolites from Yemen: Implications for wet melting of the lithospheric mantle. *Geochimica et Cosmochimica Acta*, **60**, 423–437.

CRISTOFOLINI, R. 1966. Le manifestazioni eruttive basiche del trias superiore nel sottosuolo di Ragusa (Sicilia sud-orientale). *Periodico di Mineralogia*, **35**, 1–28.

DELLA VEDOVA, B., PELLIS, G. & PINNA, E. 1989. Studio geofisico dell'area di transizione tra il Mar Pelagico e la Piana abissale dello Ionio. *In*: Proceedings of VIII GNGTS Meeting, Roma, **1**, 543–558.

EGGINS, S. M., RUDNICK, R. L. & MCDONOUGH, W. F. 1998. The composition of peridotites and their minerals: a laser-ablation ICPMS study. *Earth and Planetary Science Letters*, **154**, 53–71.

GARCIA, M. O. & PRESTI, A. A. 1987. Glass in garnet pyroxenite xenoliths from Kauia island, Hawaii: product of infiltration of host nephelinites. *Geology*, **15**, 904–906.

GREEN, D. H., FALLOON, T. J. & TAYLOR, W. R. 1987. Mantle-derived magmas; roles of variable source peridotite and variable C–H–O fluid compositions. *In*: MYSEN, B. O. (ed.) *Magmatic Processes; Physicochemical Principles; a Volume in Honor of Hatten S. Yoder, Jr.* Geochemical Society Special Publications, **12**, 139–154.

HART, S. R. & DUNN, T. 1993. Experimental cpx/melt partitioning of 24 trace elements. *Contributions to Mineralogy and Petrology*, **113**, 1–8.

HELLEBRAND, E., SNOW, J. E., DICK, H. J. B. & HOFMANN, A. W. 2001. Coupled major and trace elements as indicators of the extent of melting in mid-ocean-ridge peridotites. *Nature*, **410**, 677–681.

HELLEBRAND, E., SNOW, J. E., HOPPE, P. & HOFMANN, A. W. 2002. Garnet-field melting and late-stage refertilization in 'residual' abyssal peridotites from the Central Indian Ridge. *Journal of Petrology*, **43**, 2305–2338.

HORN, I., FOLEY, S. F., JACKSON, S. E. & JENNER, G. A. 1994. Experimentally determined partitioning of high field strength- and selected transition elements between spinel and basaltic melt. *Chemical Geology*, **117**, 193–218.

IRVINE, T. N. & BARAGAR, W. R. A. 1971. A guide to chemical classification of common volcanic rocks. *Canadian Journal of Earth Sciences*, **8**, 523–548.

JOHNSON, K. T. M., DICK, H. J. B. & SHIMIZU, N. 1990. Melting in the oceanic upper mantle: an ion microprobe study of diopside in abyssal peridotites. *Journal of Geophysical Research*, **95**, 2661–2678.

KÖHLER, T. P. & BREY, G. P. 1990. Calcium exchange between olivine and clinopyroxene calibrated as geothermobarometer for natural peridotites from 2 to 60 kb with applications. *Geochimica et Cosmochimica Acta*, **54**, 2375–2388.

LANGMUIR, C. H. & HANSON, G. N. 1981. Calculating melt–mineral equilibria with stoichiometry, mass balance, and single component distribution coefficients. *In*: NAIRN, R. C., NEWTON, A., NAVROTSKY, A. & WOOD, B. J. (eds) *Thermodynamics of Minerals and Melts*. Springer, New York, 247–271.

MAZZOLENI, P. & SCRIBANO, V. 1994. Preliminary geochemical information on selected upper-mantle and lower-crust xenoliths from Hyblean Plateau (South Eastern Sicily). *Mineralogica et Petrographica Acta*, **37**, 295–305.

MCCAMMON, C. & KOPYLOVA, M. G. 2004. A redox profile of the Slave mantle and oxygen fugacity control in the cratonic mantle. *Contributions to Mineralogy and Petrology*, **148**, 55–68.

MCDONOUGH, W. F. & SUN, S. S. 1995. The composition of the Earth. *Chemical Geology*, **120**, 223–253.

MERCIER, J. C. C. & NICOLAS, A. 1975. Textures and fabrics of upper-mantle peridotites as illustrated by xenoliths from basalts. *Journal of Petrology*, **16**, 454–487.

MORTEN, L., TAYLOR, L. A. & DURAZZO, A. 1989. Spinels in harzburgite and lherzolite inclusions from the San Giovanni Ilarione quarry, Lessini Mountains, Veneto Region, Italy. *Mineralogy and Petrology*, **40**, 73–89.

NIMIS, P. 1998. Clinopyroxene geobarometry of pyroxenitic xenoliths from Hyblean Plateau (SE Sicily, Italy). *European Journal of Mineralogy*, **10**, 521–534.

NIMIS, P. & VANNUCCI, R. 1995. An ion microprobe study of clinopyroxenes in websteritic and megacrystic xenoliths from Hyblean Plateau (SE Sicily, Italy): constraints on HFSE/REE/Sr fractionation at mantle depth. *Chemical Geology*, **124**, 185–197.

NIXON, P. H. (ed.) 1987. *Mantle Xenoliths*. Wiley, Chichester.

NORMAN, M. D. 1998. Melting and metasomatism in the continental lithosphere; laser ablation ICPMS analysis of minerals in spinel lherzolites from eastern Australia. *Contributions to Mineralogy and Petrology*, **130**, 240–255.

PEARCE, J. A., BARKER, P. F., EDWARDS, S. J., PARKINSON, I. J. & LEAT, P. T. 2000. Geochemistry and tectonic significance of peridotites from the South Sandwich arc–basin system, South Atlantic. *Contributions to Mineralogy and Petrology*, **139**, 36–53.

PERINELLI, C. 2001. *Modification induced by the metasomatism at high pressure and high temperature in the upper mantle peridotites in active rift, passive margin and intraplate magmatism*. PhD thesis, University of Pisa.

PHILPOTTS, A. R. 1990. *Principles of Igneous and Metamorphic Petrology*. Prentice Hall, Englewood Cliffs, NJ.

PUNTURO, R., KERN, H., SCRIBANO, V. & ATZORI, P. 2000. Petrophysical and petrological characteristics of deep-seated xenoliths from Hyblean Plateau, southeastern Sicily, Italy: suggestions for a lithospheric model. *Mineralogica et Petrographica Acta*, **43**, 1–20.

PUTIRKA, D. K. 2005. Mantle potential temperature at Hawaii, Iceland, and the mid-ocean ridge system, as inferred from olivine phenocrysts: evidence for thermally driven mantle plumes. *Geochemistry, Geophysics, Geosystems*, **6**, doi:10.1029/2005GC.000915.

RIVALENTI, G., VANNUCCI, R., RAMPONE, E., *ET AL*. 1996. Peridotite clinopyroxene chemistry reflects mantle processes rather than continental versus oceanic settings. *Earth and Planetary Science Letters*, **139**, 423–437.

ROCCHI, S., LONGARETTI, G. & SALVADORI, M. 1998. Subsurface Mesozoic and Cenozoic magmatism in south-eastern Sicily: distribution, volume and geochemistry of magmas. *Acta Vulcanologica*, **10**, 395–408.

SAPIENZA, G. & SCRIBANO, V. 2000. Distribution and representative whole-rock chemistry of deep-seated xenoliths from the Iblean Plateau, South-Eastern Sicily, Italy. *Periodico di Mineralogia*, **69**, 185–204.

SAPIENZA, G., HILTON, D. R. & SCRIBANO, V. 2005. Helium isotopes in peridotite mineral phases from Hyblean Plateau xenoliths (south-eastern Sicily, Italy). *Chemical Geology*, **219**, 115–129.

SAPIENZA, G., GRIFFIN, W. L., O'REILLY, S. Y. & MORTEN, L. 2007. Crustal zircons and mantle sulfides: Archean to Triassic events in the lithosphere beneath south-eastern Sicily. *Lithos*, **96**, 503–523.

SCARASCIA, S., LOZEJ, A. & CASSINIS, R. 1994. Crustal structures of the Ligurian, Tyrrhenian and Ionian Sea and adjacent onshore areas interpreted from wide-angle seismic profiles. *Bollettino di Geofisica Teorica ed Applicata*, **36**, 5–19.

SCRIBANO, V. 1986. The harzburgite xenoliths in a Quaternary basanitoid lava near Scordia (Hyblean plateau, Sicily). *Rendiconti della Società Italiana di Mineralogia e Petrologia*, **41**, 245–255.

SCRIBANO, V., SAPIENZA, G., BRAGA, R. & MORTEN, L. 2006. Gabbroic xenoliths in tuff-breccia pipes from the Hyblean Plateau: insights into the nature and composition of the lower crust underneath Southeastern Sicily, Italy. *Mineralogy and Petrology*, **86**, 63–88.

SIENA, F. & COLTORTI, M. 1993. Thermobarometric evolution and metasomatic processes of upper mantle in different tectonic settings: evidence from spinel peridotite xenoliths. *European Journal of Mineralogy*, **5**, 1073–1090.

SKULSKI, T., MINARIK, W. & WATSON, E. B. 1994. High-pressure experimental trace-element partitioning between clinopyroxene and basaltic melts. *Chemical Geology*, **117**, 127–147.

SPERA, F. J. 1980. Aspects of magma transport. *In*: HARGRAVES, R. B. (ed.) *Physics of Magmatic Processes*. Princeton University Press, Princeton, NJ, 265–324.

TAKAHASHI, E. & KUSHIRO, I. 1983. Melting of a dry peridotite at high pressures and basalt magma genesis. *American Mineralogist*, **68**, 859–879.

TATSUMI, Y., HAMILTON, D. L. & NESBITT, R. W. 1986. Chemical characteristics of fluid phase released from a subducted lithosphere and origin of arc magmas: evidence from high-pressure experiments and natural rocks. *Journal of Volcanology and Geothermal Research*, **29**, 293–309.

TONARINI, S., D'ORAZIO, M., ARMIENTI, P., INNOCENTI, F. & SCRIBANO, V. 1996. Geochemical features of Eastern Sicily lithosphere as probed by Hyblean xenoliths and lavas. *European Journal of Mineralogy*, **5**, 1153–1174.

TRUA, T. 1997. *Evoluzione del magmatismo ibleo (Sicilia sud-orientale) dal Cretaceo al Plio-Pleistocene*. PhD thesis, University of Pisa.

TRUA, T., ESPERANCA, S. & MAZZUOLI, R. 1998. The evolution of the lithospheric mantle along the N. African Plate: geochemical and isotopic evidence from the tholeiitic and alkaline volcanic rocks of the Hyblean plateau, Italy. *Contributions to Mineralogy and Petrology*, **131**, 307–322.

ULMER, P. 1989. Partitioning of high field strength elements among olivine, pyroxenes, garnet and calc-alkaline picro-basalt: experimental results and an application. *Annual Report of the Director, Geophysical Laboratory, Carnegie Institution, Washington, DC*, 42–47.

VAI, G. B. 1994. Crustal evolution and basement elements in the Italian area: palaeogeography and characterization. *Bollettino di Geofisica Teorica ed Applicata*, **36**, 411–434.

VITI, M., ALBARELLO, D. & MANTOVANI, E. 1997. Rheological profiles in the Central–Eastern Mediterranean. *Annali di Geofisica*, **40**, 849–864.

WELLS, P. R. A. 1977. Pyroxene thermometry in simple and complex systems. *Contributions to Mineralogy and Petrology*, **62**, 129–139.

WEYER, S., MUNKER, C. & MEZGER, K. 2003. Nb/Ta, Zr/Hf and REE in the depleted mantle: implications for the differentiation history of the crust–mantle system. *Earth and Planetary Science Letters*, **205**, 309–324.

WOOD, B. J. & VIRGO, D. 1989. Upper mantle oxidation state; ferric iron contents of lherzolite spinels by ^{57}Fe Mössbauer spectroscopy and resultant oxygen fugacities. *Geochimica et Cosmochimica Acta*, **53**, 1277–1291.

WOOD, B. J., TARAS BRINDZIA, L. & JOHNSON, K. E. 1990. Mantle oxidation state and its relationship to tectonic environment and fluid speciation. *Science*, **248**, 337–345.

XU, Y. G. & BODINIER, J.-L. 2004. Contrasting enrichments in high- and low-temperature mantle xenoliths from Nushan, Eastern China: results of a single metasomatic event during lithospheric accretion? *Journal of Petrology*, **45**, 321–341.

YU, J.-H., O'REILLY, S. Y., ZHANG, M., GRIFFIN, W. L. & XU, X. 2006. Roles of melting and metasomatism in the formation of lithospheric mantle beneath the Leizhou Peninsula, South China. *Journal of Petrology*, **47**, 355–383.

ZINNGREBE, E. & FOLEY, S. F. 1995. Metasomatism in mantle xenoliths from Gees, West Eifel, Germany: evidence for the genesis of calc-alkaline glasses and metasomatic Ca-enrichment. *Contributions to Mineralogy and Petrology*, **122**, 79–96.

Petrological and geochemical constraints on the composition of the lithospheric mantle beneath the Syrian rift, northern part of the Arabian plate

M. ISMAIL[1], G. DELPECH[2], J.-Y. COTTIN[1], M. GRÉGOIRE[3], B. N. MOINE[1] & A. BILAL[4]

[1]*Département de Géologie–Pétrologie–Géochimie, Université Jean Monnet, UMR-CNRS 6524, 23 rue du Dr P. Michelon, 42023 Saint Etienne Cedex, France*

[2]*UMR-CNRS 8148 IDES, Université Orsay-Paris Sud, 91405 Orsay Cedex, France (e-mail: guillaume.delpech@u-psud.fr)*

[3]*Laboratoire Dynamique Terrestre et Planétaire, UMR-CNRS 5562, Observatoire Midi-Pyrénées, 31400, Toulouse, France*

[4]*Département de Géologie, Université de Damas, BP 9487, Damascus, Syria*

Abstract: A suite of mantle xenoliths from the Neogene–Quaternary volcanic province of Jabel El Arab (Syria) is dominated by spinel ± amphibole harzburgites, with rare lherzolites and wehrlites that were equilibrated at temperatures of 900–1100 °C. The major elements of pristine minerals and trace element compositions of clinopyroxene and amphibole indicate that the lithospheric mantle experienced various degrees of melt extraction (olivine Mg-number = 89.4–91.8, spinel Cr-number = 10.4–46.4), followed by a multistage metasomatic history. The primary clinopyroxene has variable and high Mg-number (89.1–93.6) and highly variable major element concentrations (Al_2O_3 2.7–7.6 wt%, Na_2O 0.5–2.5 wt% and Cr_2O_3 0.4–2.5 wt%). Three groups of harzburgites were identified on the basis of petrographical, mineralogical and geochemical data. Group I harzburgites have compositions indicating a residual origin after polybaric partial melting with $F < 20\%$, which started in the garnet stability field and continued in the spinel stability field. Group II harzburgites are interpreted as a result of a percolation mechanism involving the infiltration of large volumes of undifferentiated basaltic melts through the residual lithosphere. Finally, the mineral major element compositions and the selectively enriched trace element contents of clinopyroxenes in group III harzburgites (high $(La/Sm)_N$ and Th, U, Sr and low high field strength element contents) are attributed to a percolation mechanism involving small volume melt fractions. Such small melt fractions correspond to CO_2-bearing alkaline silicate magmas that have evolved to CO_2-rich melts during repeated percolation-reaction within the Syrian lithospheric mantle. Shortly before eruption, some xenoliths were infiltrated by small silicate melt fractions, which produced discrete reaction zones composed of cpx ± ol ± sp ± glass surrounding reacting primary spinels. The glass in the melt pockets has a trachytic to trachy-andesitic composition and its composition suggests that glass is derived from melting of pre-existing amphibole in the lithospheric mantle, triggered by infiltration of a Na-rich metasomatic agent.

The nature and origin of metasomatic agents in the lithospheric mantle may be difficult to assess because they are often associated with a multistage history and are still widely debated in the literature. Many recent petrological and geochemical studies on mantle metasomatism have focused on the major and trace element compositions of upper mantle xenoliths to decipher the nature of percolating melts or fluids (O'Reilly & Griffin 1988; Hauri *et al.* 1993; Ionov *et al.* 1994; Wulff-Pedersen *et al.* 1996; Coltorti *et al.* 1999; Grégoire *et al.* 2000; Moine *et al.* 2001, 2004; Frezzotti *et al.* 2002; Delpech *et al.* 2004). These studies have described a wide range of melt or fluid compositions as metasomatic media ranging from H_2O-rich to CO_2-rich melts and basaltic to carbonatitic melts occurring in oceanic and continental settings.

Previous studies of mantle xenoliths from the northern part of the Arabian plate beneath the Syrian rift have mostly focused on petrographical descriptions of the xenoliths and their Neogene–Quaternary host basalts, fluid inclusions in peridotites and their P–T equilibrium conditions (Nasir 1994; Laws & Wilson 1997; Medaris & Syada 1998; Nasir & Safarjalani 2000; Bilal & Touret 2001; Al-Mishwat & Nasir 2004; Bilal & Sheleh 2004). The xenolith suite is composed of peridotites (lherzolite, harzburgite, wehrlite) and deep magmatic segregates (pyroxenites, metagabbros). CO_2-bearing fluid inclusions within primary minerals

From: COLTORTI, M. & GRÉGOIRE, M. (eds) *Metasomatism in Oceanic and Continental Lithospheric Mantle.* Geological Society, London, Special Publications, **293**, 223–251.
DOI: 10.1144/SP293.11 0305-8719/08/$15.00

of peridotites indicate $P-T$ conditions corresponding to the spinel lherzolite field (1000 °C, *c*. 1.5 GPa, Bilal & Touret 2001). However, the composition of the Syrian lithospheric mantle is still poorly documented, especially with regard to the relationships between modal compositions, mineral compositions and the physico-chemical conditions.

This paper reports petrographical, mineralogical and geochemical data for a suite of mantle xenoliths from Tel Tannoun, southern Syria. The aim of this study is to assess the type of metasomatism and the nature and origin of melts interacting with the mantle beneath a thinned lithosphere associated with underplating, using detailed petrographical, mineralogical and *in situ* geochemical data.

Geological setting and xenolith occurrence

The Dead Sea fault zone forms the boundary between the African and Arabian plates. Volcanism along the Syrian rift is related to the movement of the Arabian plate towards the Eurasian plate at a velocity of 18 ± 2 mm a^{-1} in a NNW direction (McClusky *et al.* 2000; Fig. 1). The volcanism is divided into two periods: Late Jurassic–early Cretaceous (Cretaceous basalts, Dubertret 1933), and Neogene–Quaternary (Mouty *et al.* 1992; Nasir & Safarjalani 2000). The Neogene–Quaternary alkali basalt volcanism is related to the formation of the Red Sea (24–16 Ma) and Dead Sea rifts (8–0.4 Ma) (Ponikarov 1967; Bohannon *et al.* 1989; Camp & Roobol 1989; Nasir 1994; Baker *et al.* 1997; Chorowicz *et al.* 2005). The Syrian rift thus represents the northern part of the Dead Sea rift, and is the continuation of the Red Sea rift. The Neogene basalts from southern Syria are mostly alkali basalts and basanites (Stein & Katz 1989; Stein & Hofmann 1992; Stein *et al.* 1993; Laws & Wilson 1997). Their chemical composition indicates a typical intraplate setting from the Jurassic to the present (Mouty *et al.* 1992). Some geochemical studies of volcanic rocks from the southern Arabian plate (Yemen, Jordan) have suggested that volcanism originated from the interaction between the Afar mantle plume and the lithosphere (Camp & Roobol 1989; Nasir 1994; Baker *et al.* 1997). More recent geochemical studies of lavas from the northern Arabian plate (Harrat Ash Shaam; Israel, Syria, Jordan) favour instead an origin of the volcanism related asthenospheric upwelling in response to lithospheric extension in this region and do not attribute any role to the Afar mantle plume (Shaw *et al.* 2003; Lustrino & Sharkov 2006; Weinstein *et al.* 2006).

The area of study (Jabel El Arab) represents the northwestern boundary of the Arabian plate (Fig. 1). Most of the Cenozoic volcanic fields of Syria are located along secondary faults in a north–south direction parallel to the Syrian rift. The most widespread occurrence of alkali lavas (Neogene–Quaternary) is concentrated in southern Syria, in a linear zone parallel to the direction of the Syrian rift. The Cenozoic basaltic lavas may be up to 500 m thick and are covered by Tertiary and Quaternary sediments (Nasir & Safarjalani 2000; Al-Mishwat & Nasir 2004). All xenoliths were sampled from the Neogene–Quaternary volcanic field of Jabel El Arab (part of Harrat Ash Shaam),

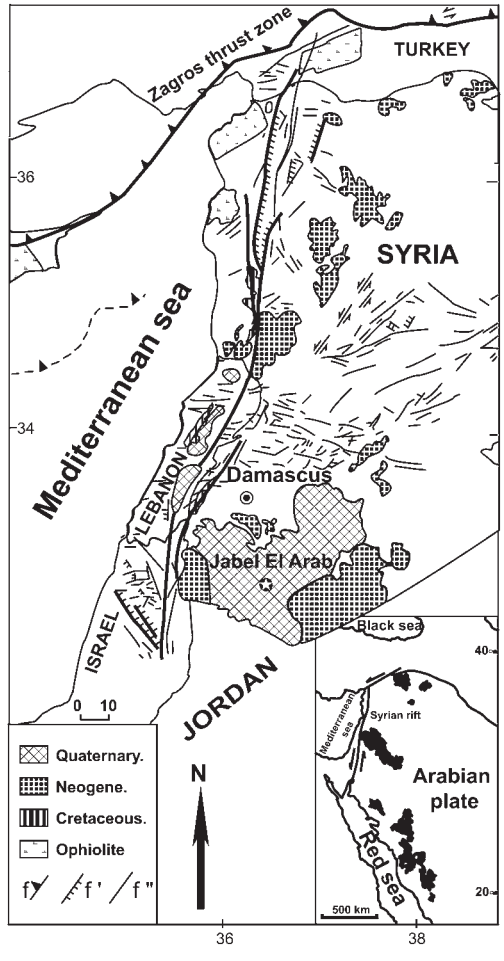

Fig. 1. Geological map of the Syrian rift with the ultrabasic–basic xenolith locality of Tel Tannoun in the Jabel El Arab (star in circle). f, Zagros thrust zone; f′, border faults of the graben in the rift zone; f″, undifferentiated faults.

south of Damascus, near Tel Tannoun (32°57′N, 36°44′E) (Fig. 1). The xenoliths occur in the flanks and craters of Strombolian volcanic cones. Most of the xenoliths are rounded to subrounded, but some have an irregular shape. They range in size from a few centimetres to more than 30 cm. Most are oxidized or display evidence of weathering but the xenoliths selected for this study are fresh or only slightly oxidized. The xenoliths studied can be classified into three groups on the basis of their mineralogical characteristics (Frey & Prinz 1978): spinel lherzolite, spinel ± amphibole harzburgites and spinel wehrlite.

Analytical methods

The modal compositions were determined by point counting (3000 points per thin section). Electron microprobe analyses of minerals were obtained using a CAMECA SX-100 electron microprobe (CNRS-UMR6524, Clermont-Ferrand, France) with a wavelength-dispersive spectrometry (WDS) technique. Operating conditions used a 15 kV accelerating voltage, a 15 nA current for mineral analyses or 8 nA for glass analyses, and a beam diameter of *c*. 2–3 μm. Natural and synthetic minerals were used as standards. Counting times were 10 s on peak and 10 s on background for all elements, and detection limits are typically 0.01–0.04 wt%.

Concentrations of 28 trace elements (rare earth elements (REE), Ba, Rb, Th, U, Nb, Ta, Sr, Zr, Hf, Ti, Y, Cr, Sc, V and Ni) were determined in clinopyroxenes and amphiboles on 120 μm thick polished sections by laser ablation inductively coupled plasma mass spectrometry (LA-ICP-MS) at the Observatoire Midi-Pyrénées (University Toulouse III, France). A CETAC LSX-200 frequency-quadrupled Nd–YAG LA system delivering a wavelength of 266 nm was connected to a Perkin Elmer Elan 6000 ICP-MS instrument (Grégoire *et al.* 2002). A typical analysis consisted of three replicates of 100 readings each, with each replicate representing one sweep of the mass range. The counting time for one sample was typically 160–170 s. The NIST 610 and 612 glass standards were used as external standards. Each analysis was normalized using the Ca wt% values determined by electron microprobe. The ablated material was carried from the laser cell to the ICP-MS system with a mixture of He and Ar. Typical detection limits range from 10 to 20 ppb for REE, Ba, Rb, Th, U, Nb, Ta, Sr, Zr, Hf and Y, and are 100 ppb for V and Sc, and 2 ppm for Ti, Ni and Cr. The typical precision and accuracy for a laser microprobe analysis range from 1 to 10%.

Petrography

The analysed peridotites are spinel harzburgites (13 samples), some of which contain amphibole, one spinel lherzolite, and one spinel wehrlite (Table 1). They contain variable amounts of spinel (0.1–4 vol%) and amphibole (0.1–4.8 vol%). Microstructures vary from coarse-grained, coarse-grained–tabular to rare porphyroclastic, according to the classification of Mercier & Nicolas (1975). Olivine, clinopyroxene and orthopyroxene vary in size from 0.5 to 4 mm, and the pyroxenes show curvilinear grain boundaries. Orthopyroxene is commonly associated with clinopyroxene, and both minerals in some harzburgites display spongy rims. Spinel in the xenoliths is interstitial and has a vermicular shape. It is brown and large (1–3 mm) in some harzburgites (38Th, 43Th and IT13A) and greenish in the lherzolite (51Th) and harzburgite (IT30). Amphibole occurs as grains surrounding the primary spinel or as interstitial crystals in the peridotitic matrix in the harzburgite 33Th (Fig. 2). Harzburgites IT10 and IT49 contain numerous crystals of amphibole that occur around the primary spinel, but in most cases, these amphiboles are not in direct contact with the spinel, as they appear embedded in a matrix of smaller grain size composed of cpx + sp + ol + gl (Fig. 3a; see below). These amphiboles display resorbed grain boundaries that suggest they are not in equilibrium with this fine-grained silicate assemblage. In the porphyroclastic xenolith IT31, most olivine porphyroclasts show undulose extinction and kink-banding and the large orthopyroxene porphyroclasts (≤10 mm in diameter) commonly contain exsolution lamellae of cpx (Fig. 2b). The olivine and orthopyroxene porphyroclasts occur in a matrix of neoblasts of olivine, orthopyroxene and clinopyroxene.

Primary olivine, clinopyroxene and orthopyroxene of the xenolith suite often contain variable amounts of solid and fluid inclusions of CO_2, similar to the inclusions described in the mantle xenoliths from Tel Tannoun (Bilal & Touret 2001).

Nine harzburgites and the wehrlite (30Th, 33Th, 37Th, 52Th, IT1B, IT31, IT10, IT47, IT49 and 23Th) display reaction zones disseminated in the peridotitic matrix (Figs 2d and 3). The reaction zones often occur around primary brown spinel or between primary mineral boundaries. The primary spinel in the reaction zone has spongy rims (Fig. 3c and d). Minerals in reaction zones include subhedral to euhedral clinopyroxene, olivine, small euhedral spinel and glass. Sometimes euhedral small amphiboles occur in some reaction zones but are never associated with the large resorbed amphibole surrounding primary spinels. The small euhedral amphibole may be dispersed

Table 1. *Characteristics of mantle xenoliths from Tel Tannoun*

Sample	Petrographical type	Microstructure	Ol	Opx	Cpx	Sp	Am	Mg-no. (Ol)	Cr-no. (Sp)	*T*(B&K90)	*T*(Wells77)
23Th	Wehrlite	Coarse grained	87.3	0.7	11.2	0.8		90.8 ± 0.1 (4)	45.1 ± 1.1 (2)	922	906
51Th	Lherzolite	Coarse grained–tabular	72.6	14.1	10.1	3.2		89.6 ± 0.1 (5)	10.5 ± 0.1 (3)	1100	1041
30Th	Harzburgite	Coarse grained	82.2	14.5	2.4	0.9		90.7 ± 0.2 (5)	34.8 ± (2)	1016	993
33Th	Harzburgite	Coarse grained	85.4	10.9	2.2	1.1	0.4	91.5 ± 0.1 (5)	45.3 ± 1.1 (2)	952	952
37Th	Harzburgite	Coarse grained–tabular	87.1	10.7	1.5	0.7		90.5 ± 0.3 (5)	23.4 ± (1)	1052	1062
38Th	Harzburgite	Coarse grained–tabular	78.6	13.8	4.8	2.8		91.3 ± 0.1 (2)	36.1 ± 0.2 (2)	924	909
43Th	Harzburgite	Coarse grained	87.9	9.9	1.2	1		91.6 ± 0.1 (6)	35.5 ± 0.2 (2)	937	942
52Th	Harzburgite	Coarse grained–tabular	80	15.5	3.4	1	0.1	90.2 ± 0.1 (2)	76.8 ± (1)	939	916
IT1B	Harzburgite	Coarse grained	79.9	17.7	2.1	0.3		91.0 ± 0.9 (5)		1076	1006
IT10	Harzburgite	Coarse grained	79.4	13.3	1.7	0.8	4.8	90.7 ± 0.6 (4)		952	960
IT13A	Harzburgite	Coarse grained–tabular	71.6	20.2	4.2	4		90.5 ± 0.1 (2)	21.4 ± 0.7 (5)	934	951
IT30	Harzburgite	Coarse grained	84.3	11.5	1.6	2.6		90.5 ± 0.1 (5)	16.2 ± 0.8 (3)	950	931
IT31	Harzburgite	Porphyroclastic	78	13.5	4.6	3.9		90.5 ± 0.1 (4)	20.8 ± 1.5 (3)	925	932
IT47	Harzburgite	Coarse grained–tabular	77.4	18.4	2.4	1.8		90.3 ± 0.1 (5)	16.2 ± 0.1 (3)	1038	1005
IT49	Harzburgite	Coarse grained	76.3	20.2	2.1	0.1	1.3	89.9 ± 0.3 (2)		924	919

The Mg-number of olivine and Cr-number of spinel are average values of a number of analyses indicated in parentheses. *T*(B&K90) and *T*(Wells77) are equilibration temperatures (in °C) calculated from the thermometers of Brey & Köhler (1990*b*) and Wells (1977), respectively.

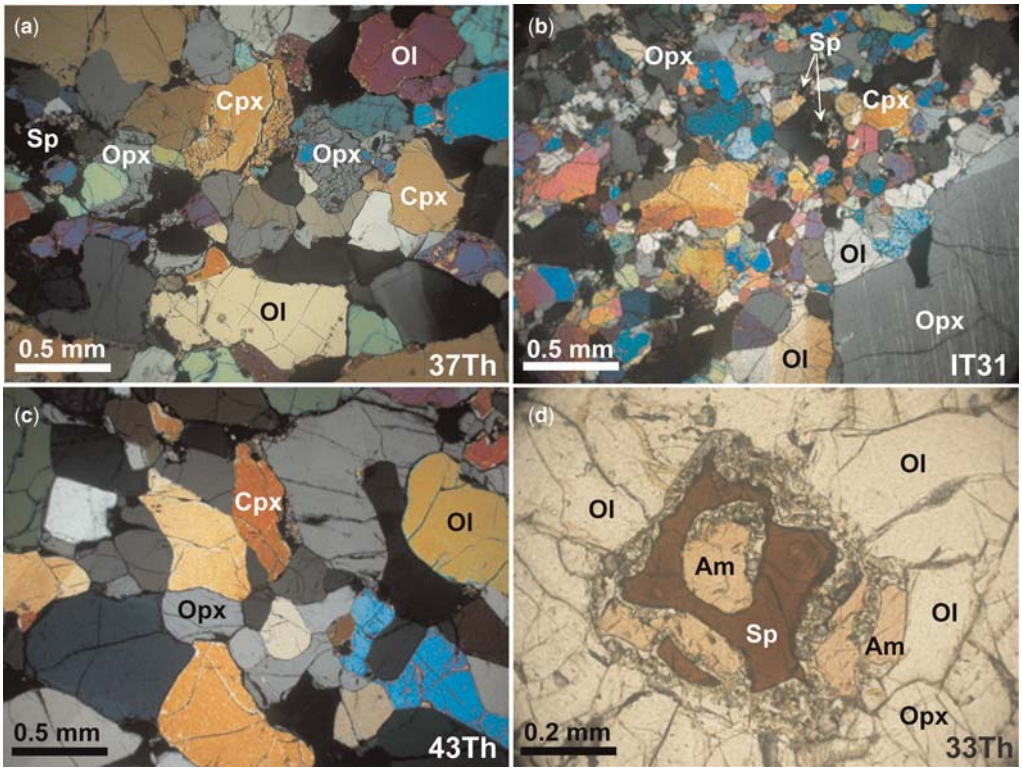

Fig. 2. Photomicrographs of petrographic features of Syrian mantle xenoliths from Tel Tannoun. (**a**) Coarse-grained–tabular microstructure in harzburgite 37Th. (Note the spongy boundaries of orthopyroxene (Opx) and clinopyroxene (Cpx).) (**b**) Porphyroclastic microstructure in harzburgite IT31 with an orthopyroxene porphyroclast containing spinel exsolution lamellae. (**c**) Coarse-grained microstructure in harzburgite 43Th. (**d**) Partly resorbed amphibole around a primary spinel in harzburgite 33Th. The partly resorbed amphibole is embayed in a secondary assemblage composed of euhedral to suheuhedral sp, cpx, olivine and glass.

in the reaction zone but it commonly occurs at the boundary between primary minerals (olivine, orthopyroxene) and the reaction zone and is often associated with small euhedral oxides. Clear glass was observed in the reaction zones of harzburgites and the wehrlite (30Th, 37Th, IT47, IT49 and 23Th). In the wehrlite 23Th, glass also occurs as thin veins along grain boundaries of primary minerals and in many cases these thin veins are connected to adjacent reaction zones. Glass also occurs in the vicinity of the spongy rims of clinopyroxene in harzburgite 30Th and wehrlite 23Th.

Mineral major element compositions (Table 2)

Olivine

Primary olivines in the lherzolite 51Th have homogeneous compositions and the lowest Mg-number (Mg-number $= 100 \times Mg^{2+}/(Mg^{2+} + Fe^{2+})$ in mole fractions $= 89.4–89.7$). Their Mg-number values are slightly more magnesian in the spinel wehrlite (90.1–90.4) but those of the spinel harzburgites are highly variable and the most magnesian, ranging from 90.1 to 91.8. NiO contents in olivines from harzburgites vary from 0.26 to 0.45 wt%, from 0.27 to 0.35 wt% in the lherzolite and from 0.34 to 0.40 wt% in the wehrlite. Concentrations of CaO, Cr_2O_3 and TiO_2 in the primary olivine from the lherzolite and harzburgites are always very low and are <0.2 wt% and <0.1 wt% in the wehrlite. The Al_2O_3 contents of olivines in the lherzolite and harzburgites are always below 0.09 wt%.

The Mg-numbers of secondary ol (Ol II) in reaction zones are higher than those of primary olivines (92.1–93.4). CaO (0.8–0.25 wt%), Cr_2O_3 (0.06–0.64 wt%) and Al_2O_3 (<0.12 wt%) contents of secondary olivines in the wehrlite and harzburgites are higher than those in the primary olivines whereas

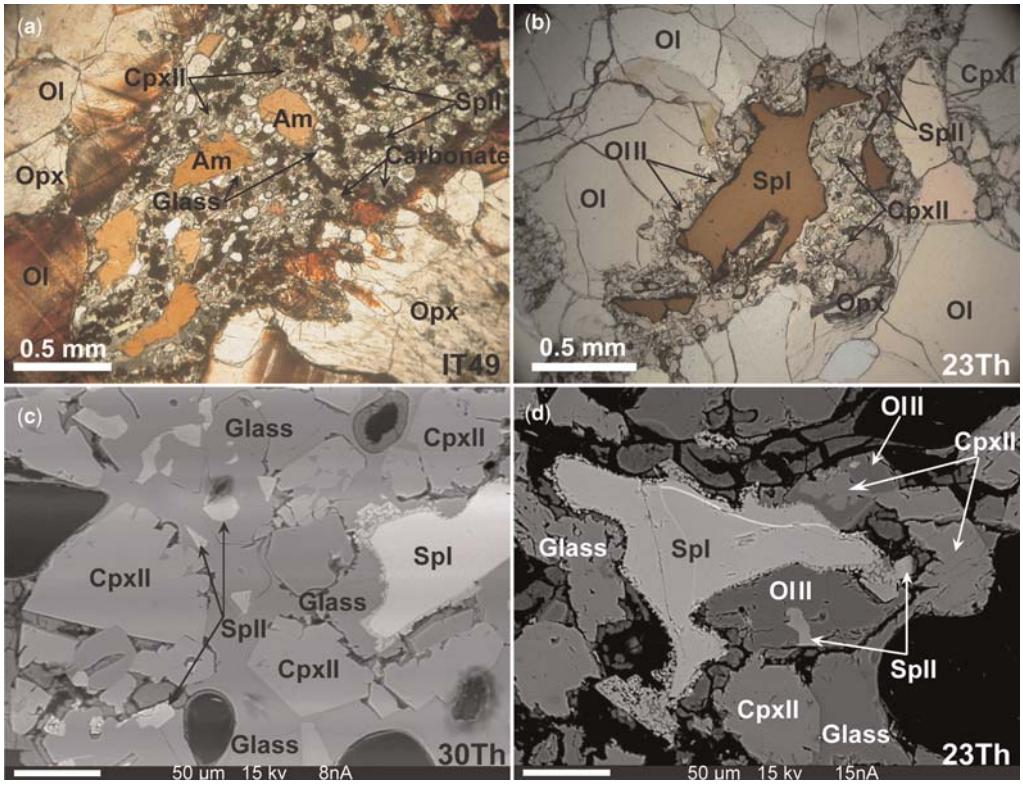

Fig. 3. (**a**, **b**) Photomicrographs of secondary assemblages in reaction zones. (**a**) Reaction zone containing small grains of resorbed amphiboles, secondary spinel (SpII), clinopyroxene (CpxII), glass and carbonate in hydrous harzburgite IT49. (**b**) Reaction zone in anhydrous wehrlite 23Th around primary spinel. (**c, d**) Back-scattered electron images of reaction zones. (c) Secondary euhedral to subeuhedral Sp (SpII) and Cpx (CpxII) embayed in a glass matrix in harzburgite 30Th. (d) Secondary assemblage of OlII, CpxII and SpII in reaction zone embayed in glass around a primary Sp in the wehrlite 23Th.

Table 2. *Representative major element compositions of olivine in Syrian mantle xenoliths*

Sample:	23Th	23Th	51Th	30Th	30Th	33Th	33Th	37Th	37Th	38Th
Assemblage:	I	II	I	I	II	I	II	I	II	I
SiO_2	40.61	40.85	40.19	40.45	41.09	41.42	40.92	40.86	41.35	40.73
TiO_2	0.04	0	0	0.01	0.02	0	0.04	0.03	0.02	0
Al_2O_3	0.01	0	0.02	0.04	0.12	0.01	0.06	0.04	0.06	0.01
Cr_2O_3	0.05	0.12	0	0.06	0.61	0.01	0.50	0.14	0.07	0
FeO^T	9.24	6.22	10.16	9.02	7.51	8.23	6.64	8.45	7.28	8.35
MnO	0.14	0.17	0.16	0.10	0.11	0.14	0.08	0.14	0.14	0.14
MgO	49.10	51.50	48.44	49.57	49.95	49.74	51.02	49.47	50.27	49.68
NiO	0.40	0.36	0.29	0.32	0.32	0.34	0.35	0.29	0.26	0.32
CaO	0.07	0.14	0.07	0.06	0.16	0.07	0.21	0.07	0.14	0.07
Na_2O	0.01	0.04	0.01	0.03	0.02	0	0.03	0.02	0	0
K_2O	0.00	0	0.01	0	0.02	0	0	0.03	0.01	0.01
Total	99.67	99.40	99.36	99.65	99.92	99.96	99.86	99.53	99.60	99.3
mg-no.	90.44	93.63	89.48	90.75	92.21	91.48	93.19	91.26	92.49	91.4

Assemblage I refers to the primary mineralogy and II to the secondary mineralogy. FeO^T determined as total Fe. Mg-number $= 100 \times Mg/(Mg + Fe)$.

the Ol II has similar NiO (0.26–0.43 wt%) and TiO_2 (<0.06 wt%) contents.

Orthopyroxene

The composition of orthopyroxene ranges from $En_{89.1}$ to $En_{91.2}$ in harzburgites, from $En_{88.1}$ to $En_{88.2}$ in the lherzolite and from $En_{89.9}$ to $En_{90.3}$ in the wehrlite. The Mg-number is homogeneous in the lherzolite (89.9–90) and wehrlite (91–91.3) whereas it is variable in the harzburgites (90.6–92.4). The Al_2O_3 contents (0.7–4.9 wt%) are highly variable in the harzburgites but more homogeneous in the lherzolite (5.5 wt%) and wehrlite (2.2–2.7 wt%); the Cr_2O_3 content is in the range of 0.3–0.6 wt% in harzburgites, 0.4–0.5 wt% in the lherzolite and 0.3–0.4 wt% in the wehrlite. Concentrations of Na_2O are relatively high and constant in the lherzolite (0.15 wt%) and in the wehrlite (0.12–0.14 wt%) but more variable in harzburgites (0.03–0.2 wt%).

Clinopyroxene

Primary clinopyroxenes (Cpx I) are Cr-diopsides (En_{48-52} Wo_{43-49} Fs_{3-6}; Fig. 4). Their Mg-number ranges from 89.1 to 89.7 in the lherzolite, from 90.5 to 93.6 in the harzburgites and from 91.7 to 92.7 in the wehrlite. Major element contents of Cpx I in the lherzolite are homogeneous (Fig. 4), whereas Al_2O_3, CaO and Na_2O are highly variable in harzburgites (Al_2O_3 2.71–6.71 wt%; Na_2O 0.53–2.44 wt%). In the wehrlite, Cpx I has relatively homogeneous concentrations with respect to Al_2O_3 and Cr_2O_3, whereas TiO_2, SiO_2 and Na_2O show slight variations, and CaO has more variable contents (19.17–20.88 wt%). Rims of Cpx I in the wehrlite have similar to higher Mg-number, CaO, Al_2O_3, TiO_2 and Cr_2O_3, but lower SiO_2 and Na_2O contents, similar to Cpx II occurring in reaction zones (see below). The primary clinopyroxene compositions show a progressive trend of decreasing Al_2O_3 and increasing CaO with increasing Mg-number from the lherzolite to the harzburgites (Fig. 4), with the wehrlite sample having an intermediate composition.

Subeuhedral to euhedral secondary clinopyroxenes (Cpx II) in the reaction zones are also Cr-diopsides (En_{46-54} Wo_{42-51} Fs_{3-5}) and have highly variable Mg-number, covering the whole range of Cpx I in the harzburgites and the wehrlite (90.4–93.8; Table 4, Fig. 4). Major element concentrations are very variable in Cpx II and the latter are commonly higher in Al_2O_3 (3.71–7.97 wt%), Cr_2O_3 (1.08–4.75 wt%) and TiO_2 (0.6–0.93 wt%) than Cpx I at similar Mg-number. CaO contents in Cpx II are similar to those of Cpx I but their SiO_2 concentrations are commonly lower than those of Cpx I. Finally, the Na_2O contents of Cpx II are less variable than those of Cpx I and do not extend to the high Na_2O contents of some Cpx I.

Spinel

The primary spinel displays large variations in composition ranging from chromite (23Th, 33Th and 52Th) to magnesian and aluminous chromite (30Th, 37Th, 38Th, 43Th, 51Th, IT13A, IT30, IT31 and IT47). The Mg-number and Cr-number ($= 100 \times Cr/(Cr + Al)$ in mole fractions) range from 59.8 to 80.7 and from 10.4 to 46.4, respectively (Table 5, Fig. 5). The spinels in harzburgites

43Th I	52Th I	IT1B I	IT10 I	IT13A1 I	IT30 I	IT31 I	IT31 II	IT47 I	IT49 I
40.93	40.06	40.81	40.95	40.87	40.56	40.69	41.80	40.69	41.451
0	0.01	0.05	0.03	0.01	0.06	0.00	0.00	0.04	0.003
0.01	0.00	0.00	0.02	0.03	0.00	0.02	0.07	0.03	0.026
0	0.04	0.03	0.02	0.05	0.03	0.03	0.03	0.00	0.072
7.98	9.43	8.06	9.21	9.43	9.53	9.18	7.57	9.46	9.503
0.13	0.17	0.15	0.15	0.17	0.10	0.17	0.12	0.20	0.139
50.01	49.11	50.49	49.64	49.75	49.58	49.73	50.26	49.24	48.92
0.3	0.32	0.32	0.31	0.31	0.35	0.37	0.28	0.33	0.294
0.08	0.03	0.09	0.10	0.10	0.04	0.08	0.21	0.13	0.052
0.04	0.02	0.00	0.00	0.01	0.00	0.00	0.02	0.15	0.038
0.01	0.01	0.01	0.00	0.01	0.03	0.02	0.00	0.02	0.031
99.49	99.179	99.992	100.4	100.73	100.28	100.29	100.37	100.3	100.54
91.79	90.28	91.79	90.56	90.38	90.26	90.59	92.21	90.25	90.19

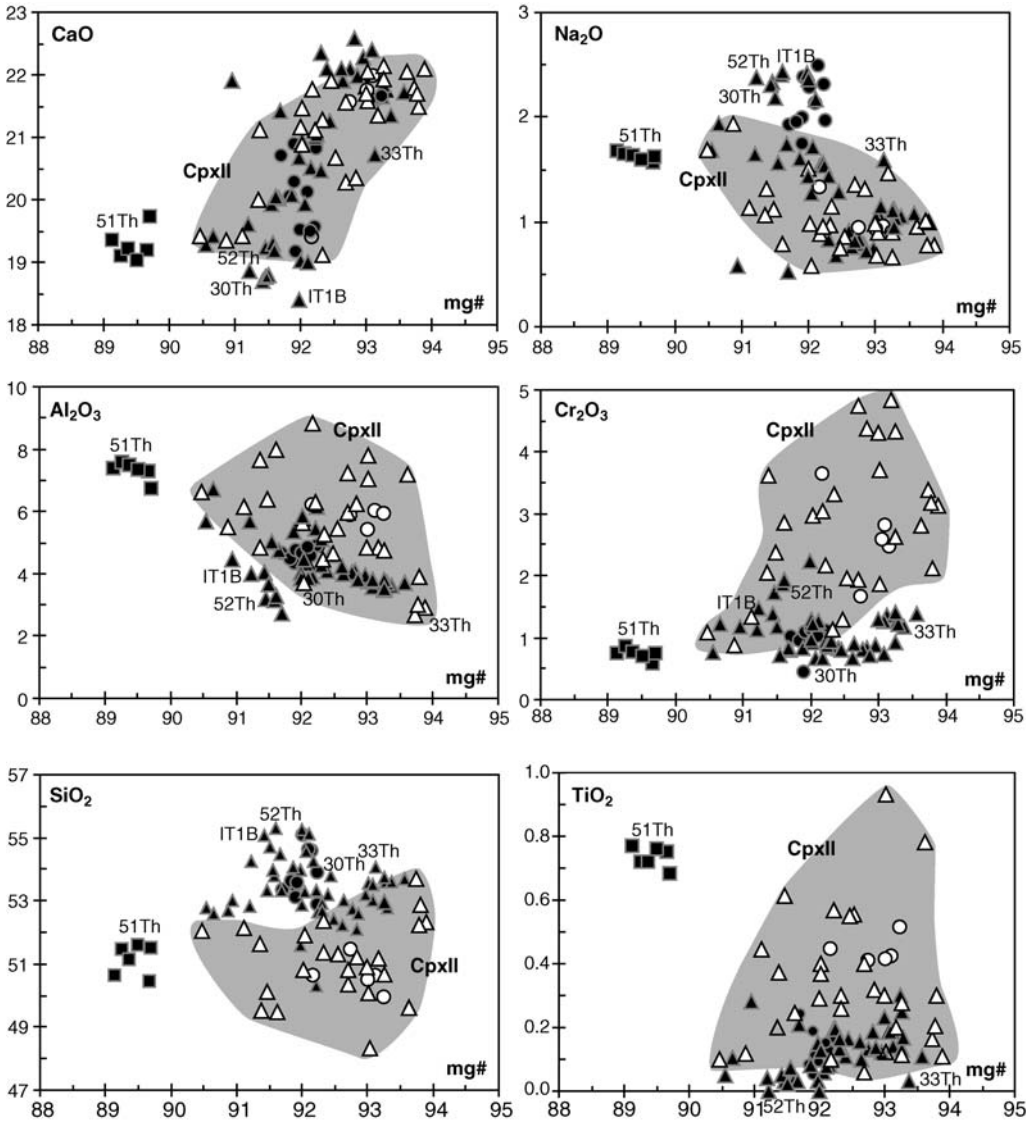

Fig. 4. Major element compositions of primary and secondary clinopyroxenes in mantle xenoliths from Tel Tannoun. ■, primary Cpx in lherzolite; •, primary Cpx in the wehrlite; ▲, primary Cpx in harzburgites; ○, secondary Cpx in the wehrlite; △, secondary Cpx in harzburgites; grey field, secondary clinopyroxenes (Cpx II) from this study.

and wehrlite are more chromiferous than in the lherzolite; the Mg-number v. Cr-number diagram (Fig. 5) shows a linear distribution from low Cr-number–high Mg-number in spinels from the lherzolite to high Cr-number–low Mg-number in spinels from harzburgites and the wehrlite. The TiO_2 content in spinel decreases from the lherzolite (0.23 wt%) to the harzburgites (0.01–0.26 wt%). Secondary spinels in reaction zones commonly have higher Mg-number (72.3–98.6) and Cr-number (22.0–63.6) compared with primary spinel, corresponding to the most chromiferous spinels of the harzburgites and wehrlite. For comparison in Figure 5, the primary and secondary spinels from this xenolith suite extend to much higher Cr-number and lower Mg-number than spinels reported from xenoliths from southern Syria (Table 5; Nasir & Safarjalani 2000). Some harzburgites have primary spinels with Mg-number and Cr-number in spinels that are similar to

xenoliths from the French Massif Central, Hawai or the Kishb Plateau in Saudi Arabia (IT47, IT31, IT30, IT13A, 37Th, Fig. 5). The wehrlite 23Th and some harzburgites (30Th, 33Th, 38Th, 43Th) have primary spinels with higher Cr-number and lower Mg-number; they have similar compositions to spinels reported in xenoliths from Yemen (Chazot *et al.* 1996) or from the French Massif Central (Xu *et al.* 1998).

Amphibole

Amphiboles occurring in three samples are pargasites (33Th) or hornblendes (IT10 and IT49) according to the classification of Leake *et al.* (1997). Their Mg-number ranges from 89.7 to 91.5. The amphiboles are poor in TiO_2 (0.14–0.72 wt%) and rich in Cr_2O_3 (2.50–3.45 wt%) and Na_2O (3.97–4.43 wt%). The amphibole occurring around the spinel (33Th) has higher Ti, Al, Ca and Na contents, and lower Si and K contents than the resorbed amphiboles in reaction zones (IT10 and IT49).

Glass (Table 7)

The major element compositions of glass in reaction zones are highly variable both between and within samples. Overall, they are characterized by relatively high SiO_2 (54.57–62.84 wt%), high Na_2O (4.76–14.85 wt%), high Al_2O_3 (20.59–25.36 wt%) and low TiO_2 (0.05–0.85 wt%) and FeO^T (0.59–3.28 wt%) contents (Fig. 6). The glass compositions vary between sample depending on the occurrence or absence of reacting amphibole in the reaction zones, but also vary within samples without amphibole. In Figure 6, glass compositions in harzburgites where reacting amphibole occurs (IT10, IT49; Fig. 3a) have similar to higher Na_2O (up to 14.85 wt%), higher Al_2O_3, much lower CaO, K_2O and FeO^T and lower TiO_2 than glasses in anhydrous samples. In the anhydrous samples, compositional variations also exist at the scale of a single sample, especially with respect to SiO_2 in harzburgite 37Th and wehrlite 23Th (54.5–60 wt%). On the other hand, glass compositions in anhydrous harzburgite 30Th are more homogeneous in terms of SiO_2 (55.4–56.7 wt%) and have very low TiO_2 contents compared with other anhydrous samples. Glass in the anhydrous wehrlite 23Th has no K_2O, similar to glasses in hydrous harzburgites (Fig. 6). In this sample, glass compositions in reaction zones and in thin veins have similar major element compositions, except that the glasses in the veins have similar to higher SiO_2 contents compared with the most Si-rich glasses in the reaction zones. In the total alkali–silica diagram (Le Bas *et al.* 1986; Fig. 7), the glasses have trachytic to trachy-andesitic compositions, with the exception of the amphibole-bearing harzburgite (IT10), which has a glass with a phonolitic composition, owing to its very high Na_2O and very low K_2O contents. For comparison, the host lavas of the Jabel El Arab xenoliths (this study and Mouty *et al.* 1992) are basalts and basanites (Fig. 7). The host lavas and the glasses in the xenoliths have very different major element compositions. Most glasses have $Na_2O + K_2O > 6$ wt%, and some may contain up to 15.5 wt% in the amphibole-bearing harzburgite IT10, with $Na_2O/K_2O > 1.8$. In terms of their normative composition the glasses are mostly plagioclase (52–92%), orthoclase (0.1–17.1%) and diopside (<10.8%) normative.

Temperature estimates

Temperatures were calculated using the two-pyroxene (Cpx–Opx) thermometers of Wells (1977) and Brey & Köhler (1990*a*), using core major element compositions of minerals only. The temperatures were calculated at an assumed pressure of 1.5 GPa, which corresponds to the average pressure estimated by Bilal & Touret (2001) on the basis of CO_2 fluid inclusions in mantle xenoliths from the same locality. The estimated temperatures for the lherzolite, the wehrlite and the harzburgites are relatively similar and range from 906 °C to 1100 °C.

The temperature estimates in the wehrlite 23Th are the lowest and range from 906 to 922 °C. For the coarse grained–tabular lherzolite 51Th, the temperature estimates are the highest and range from 1041 to 1100 °C. The temperature estimates for the coarse-grained and coarse-grained–tabular harzburgites (909–1076 °C) are higher than those estimated for the porphyroclastic harzburgite (925–932 °C). Nine harzburgites out of 13 have similar equilibration temperatures in the range of 909–960 °C, irrespective of their microstructure and thermometers used. Four harzburgites (IT1B, IT47, 30Th and 37Th) have higher equilibration temperatures (993–1100 °C), with a tendency for temperature estimates using the formulation of Wells (1977) to give lower results. Such deviation to lower estimates of equilibration temperatures using the formulation of Wells (1977) was pointed out by Brey & Köhler (1990*b*) for T >1000 °C in their experiments. A comparison with available equilibration temperatures calculated with the same thermometers for mantle xenoliths from southern Syria (Medaris & Syada 1998; Nasir & Safarjalani 2000) indicates temperatures in the range 990–1150 °C, similar to or slightly higher than the highest temperatures recorded in harzburgites studied here.

Table 3. *Representative major element compositions of orthopyroxene in Syrian mantle Xenoliths*

Sample:	23Th	51Th	30Th	33Th	37Th	37Th	38Th	43Th	52Th
Assemblage:	I	I	I	II	I	II	I	I	I
SiO_2	57.26	53.7	56.29	57.49	55.5	56.09	56.37	56.85	57.97
TiO_2	0.03	0.20	0	0.08	0.06	0.07	0.01	0.10	0.02
Al_2O_3	2.23	5.49	2.75	2.52	3.93	3.76	2.59	2.59	0.71
Cr_2O_3	0.30	0.40	0.30	0.96	0.4	0.38	0.42	0.46	0.40
FeO^T	5.72	6.39	5.75	5.42	5.78	5.97	5.24	5.27	5.70
MnO	0.13	0.12	0.13	0.16	0.16	0.14	0.16	0.1	0.15
MgO	33.72	31.92	33.62	34.18	32.74	33.04	34.20	34.25	34.09
NiO	0.09	0.1	0.09	0.07	0.05	0.05	0.08	0.09	0.08
CaO	0.60	1	0.82	0.72	0.85	0.71	0.62	0.54	0.62
Na_2O	0.14	0.15	0.17	0.09	0.16	0.19	0.06	0.06	0.15
K_2O	0.00	0.03	0.00	0.00	0.03	0	0.00	0.02	0.01
Total	100.22	99.50	99.92	101.68	99.66	100.4	99.75	100.33	99.90
Mg-no.	91.31	89.90	91.24	91.85	91.18	90.77	92.08	92.05	91.43
En	90.26	88.13	89.81	90.60	90.02	89.52	90.99	91.09	90.34
Fs	8.59	9.90	8.63	8.04	8.71	9.11	7.82	7.87	8.47
Wo	1.15	1.97	1.56	1.37	1.27	1.38	1.19	1.04	1.19

Assemblage I refers to the primary mineralogy and II to the secondary mineralogy. FeO^T determined as total Fe. Mg-number $= 100 \times Mg/(Mg + Fe)$.

Trace elements

The REE concentrations of mineral phases (clinopyroxene, amphibole) are given in Table 8 and REE and trace element patterns are presented in Figure 8. Trace element contents of clinopyroxenes correspond to cores of primary clinopyroxenes (Cpx I). No trace element data are available for the harzburgites IT10 and IT49 or for minerals in reaction zones. Primary clinopyroxenes (Cpx I) are more enriched in trace elements than the primitive mantle estimate of McDonough & Sun (1995) by a factor of 2–70 times. Clinopyroxene of the lherzolite 51Th has a nearly flat REE pattern with a slight enrichment in La and Ce compared with primitive mantle values and middle REE (MREE) slightly higher than heavy REE (HREE). It also has lower Ti, Zr, Nb, Sr and Ba contents than other trace elements.

Table 4. *Representative major element compositions of clinopyroxene in Syrian mantle Xenoliths*

Sample:	23Th	23Th	51Th	30Th	30Th	33Th	33Th	37Th	37Th	38Th	43Th	52Th
Assemblage:	I	II	I	I	II	I	II	I	II	I	I	I
SiO_2	53.34	50.63	51.57	48.63	50.35	54.07	48.32	50.30	51.90	53.59	52.97	55.29
TiO_2	0.24	0.45	0.76	0.10	0.06	0.14	0.93	0.57	0.40	0.13	0.25	0.03
Al_2O_3	4.66	6.21	7.31	8.80	7.25	3.63	7.82	6.28	3.71	3.46	3.78	3.27
Cr_2O_3	1.01	3.64	0.68	3.04	1.93	1.36	3.71	2.17	1.23	1.27	1.40	1.94
FeO^T	2.48	2.36	3.26	2.18	2.21	2.15	1.93	2.39	2.63	2.11	2.13	2.56
MnO	0.04	0.12	0.10	0.07	0.01	0.11	0.08	0.03	0.06	0	0.10	0.09
MgO	15.31	15.60	15.52	14.42	15.64	16.36	14.35	15.86	16.86	16.42	16.33	15.70
NiO	0.07	0.04	0.02	0.06	0.04	0.04	0.01	0.03	0.00	0.08	0.03	0.04
CaO	20.69	19.40	19.03	21.77	21.57	20.71	22.04	21.12	21.48	21.82	21.84	19.19
Na_2O	1.92	1.33	1.59	0.89	0.81	1.59	0.90	0.95	0.58	1.12	1.11	2.44
K_2O	0.00	0.02	0.01	0.02	0.02	0	0.00	0.00	0.01	0.02	0.02	0
Total	99.75	99.80	99.85	99.97	99.87	100.16	100.1	99.70	98.85	100.02	99.96	100.55
Mg-no.	91.71	92.17	89.51	92.17	92.70	93.13	93.03	92.22	92.03	93.27	93.26	91.61
En	48.51	50.54	50.03	46.10	48.30	50.41	45.90	48.96	49.95	49.34	49.17	50.76
Fs	4.41	4.30	5.87	3.95	3.83	3.73	3.47	4.16	4.33	3.57	3.57	4.66
Wo	47.10	45.17	44.10	49.99	47.90	45.87	50.66	46.91	45.72	47.11	47.27	44.59

Assemblage I refers to the primary mineralogy and II to the secondary mineralogy. FeO^T determined as total Fe. Mg-number $= 100 \times Mg/(Mg + Fe)$.

IT1B I	IT13A I	IT13A II	IT30 I	IT31 I	IT47 I	IT47 II	IT10 I	IT49 I
57.79	55.87	55.47	55.39	56.57	55.67	55.78	57.16	57.63
0.02	0.00	0.04	0.05	0.03	0.03	0.00	0.00	0.00
1.43	3.16	3.32	3.43	2.92	3.60	4.13	2.18	1.11
0.57	0.39	0.41	0.31	0.39	0.32	0.44	0.52	0.47
5.45	5.88	5.94	6.02	5.85	6.08	5.88	6.14	5.80
0.17	0.18	0.15	0.10	0.11	0.17	0.14	0.15	0.15
34.29	33.96	34.00	33.86	33.70	33.43	33.00	33.60	34.34
0.08	0.07	0.09	0.07	0.09	0.09	0.08	0.07	0.12
0.70	0.67	0.76	0.67	0.60	0.63	1.01	0.79	0.68
0.16	0.03	0.03	0.09	0.05	0.12	0.19	0.20	0.19
0.00	0.00	0.02	0.01	0.02	0.01	0.04	0.00	0.00
100.65	100.21	100.22	100.00	100.32	100.15	100.70	100.80	100.49
91.80	91.16	91.07	90.96	91.12	90.75	90.89	90.69	91.31
90.61	89.98	89.76	89.79	90.07	89.66	89.11	89.32	90.14
8.09	8.73	8.80	8.92	8.78	9.14	8.93	9.17	8.58
1.30	1.29	1.44	1.29	1.15	1.20	1.96	1.51	1.28

The harzburgites have clinopyroxenes with very variable trace element contents and were subdivided into three groups on the basis of the shape of their REE patterns, light REE (LREE)/HREE ratios and major element compositions, as follows.

Group I. Clinopyroxenes are characterized by low abundances of LREE compared with MREE and HREE (IT13A, IT31 and IT47, Fig. 8) and by high Mg-number and Al_2O_3 contents, and low Cr_2O_3 contents (Fig. 4). The harzburgites in which they occur have a coarse-grained or porphyroclastic microstructure. The $(La/Yb)_N$ (where N indicates primitive mantle normalized) ratios are low and range from 0.02 to 0.13. The trace element patterns display a slight enrichment in some of the large ion lithophile elements (LILE; (Th and U) (high for

IT1B I	IT1B II	IT10 II	IT13A1 I	IT30 I	IT31 I	IT31 II	IT47 I	IT47 II	IT49 I	IT49 II
54.26	52.86	51.64	52.09	52.62	53.30	51.32	54.07	52.05	50.67	51.17
0.00	0.30	0.20	0.19	0.20	0.13	0.56	0.08	0.10	0.28	0.20
4.00	3.89	4.82	4.11	6.16	4.45	5.45	5.36	6.61	4.76	4.82
1.47	2.11	2.05	0.83	0.88	0.93	1.96	0.83	1.08	4.32	4.84
2.81	2.04	2.86	2.35	2.32	2.50	2.33	2.55	3.03	1.97	1.98
0.01	0.05	0.05	0.09	0.04	0.04	0.09	0.07	0.08	0.08	0.02
16.21	17.15	16.89	16.86	15.45	16.27	16.21	16.15	16.03	15.20	15.08
0.04	0.01	0.07	0.08	0.02	0.02	0.06	0.05	0.02	0.05	0.05
18.87	21.48	19.99	22.58	21.06	20.96	20.68	20.06	19.43	21.93	21.36
2.38	1.00	1.06	0.79	1.53	1.27	0.86	1.60	1.69	0.90	1.46
0.00	0.00	0.00	0.01	0.00	0.02	0.00	0.04	0.00	0.00	0.01
100.01	100.9	99.61	99.97	100.3	99.88	99.52	100.9	100.1	100.2	101.0
91.23	93.80	91.36	92.83	92.23	92.03	92.54	91.87	90.47	93.26	93.18
51.75	50.84	51.42	49.02	48.46	49.69	50.09	50.47	50.58	47.40	47.81
5.01	3.39	4.89	3.83	4.10	4.31	4.04	4.47	5.36	3.44	3.53
43.27	45.79	43.71	47.19	47.46	46.01	45.88	45.06	44.09	49.17	48.69

Table 5. *Representative major element compositions of spinel in Syrian mantle Xenoliths*

Sample:	23Th	23Th	51Th	30Th	30Th	33Th	33Th	37Th	37Th	38Th	38Th
Assemblage:	II	I	I	I	II	I	II	I	II	I	II
SiO_2	0.01	0.01	0.08	0.06	0.09	0.01	0.04	0.26	0.91	0.03	0.02
TiO_2	0.04	0.06	0.20	0.00	0.04	0.09	0.09	0.26	0.39	0.06	0.06
Al_2O_3	28.73	31.90	56.69	38.81	47.53	32.20	32.74	47.00	33.15	38.39	39.34
Cr_2O_3	42.04	37.34	9.83	30.91	20.01	38.07	36.84	21.39	33.15	31.99	31.29
FeO^T	11.59	12.62	11.02	12.08	9.99	12.52	11.65	10.27	13.59	10.95	9.61
MnO	0.16	0.18	0.06	0.18	0.04	0.16	0.22	0.11	0.17	0.14	0.2
MgO	16.83	16.46	20.67	17.38	19.98	16.86	16.74	19.68	17.02	18.09	18.73
NiO	0.14	0.12	0.32	0.23	0.35	0.16	0.16	0.22	0.15	0.21	0.21
CaO	0.00	0.01	0	0.03	0.16	0.00	0.03	0.06	0.23	0	0.01
Na_2O	0.02	0.02	0	0.00	0.00	0.03	0.01	0.00	0.07	0	0.04
K_2O	0.00	0.00	0.02	0.00	0.02	0.00	0.00	0.00	0.05	0	0
Total	99.55	98.71	98.89	99.67	98.21	100.1	98.51	99.26	98.89	99.86	99.51
Mg-no.	74.19	72.38	80.52	73.56	81.70	73.1	73.39	78.98	72.62	76.06	78.85
Cr-no.	49.54	43.99	10.40	34.84	22.02	44.24	43.04	23.39	40.13	35.86	34.80

Assemblage I refers to the primary mineralogy and II to the secondary mineralogy. FeO^T determined as total Fe. Mg-number $= 100 \times Mg/(Mg + Fe)$. Cr-number $= 100 \times Cr/(Cr + Al)$.

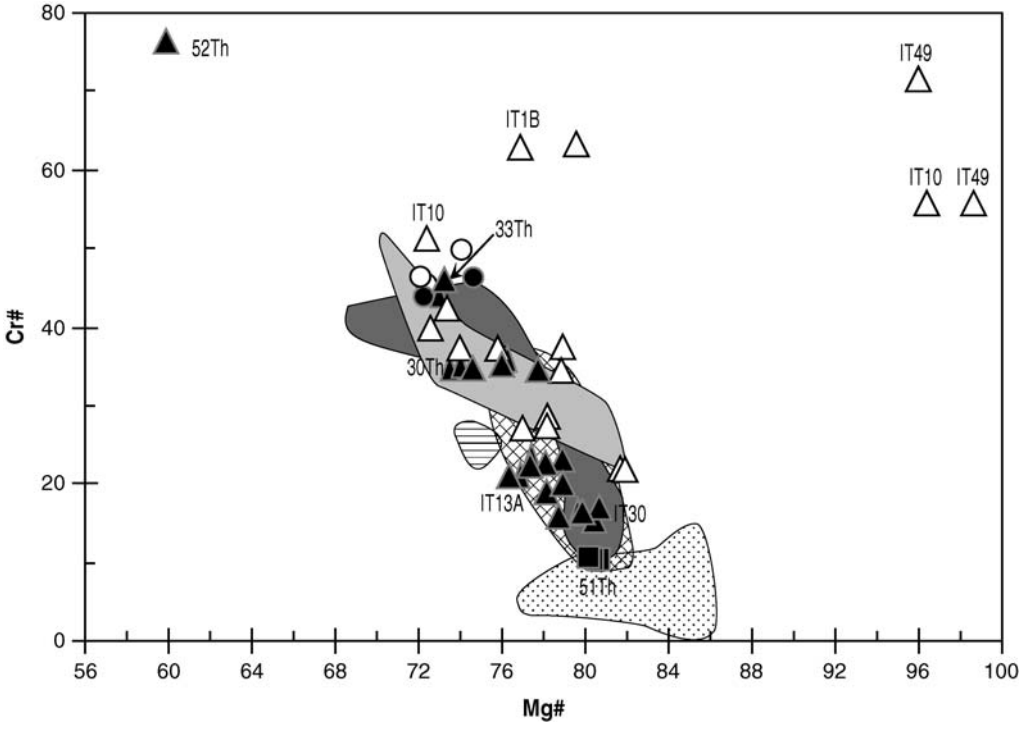

Fig. 5. Cr-number v. Mg-number for spinels in mantle xenoliths from Tel Tannoun. Symbols for rock types as for Figure 4. Fields: strippled, whole xenolith suite of Tel Tannoun (Nasir & Safarjalani 2000); horizontal lines, spinels in harzburgites of Kishb Plateau, Saudi Arabia (Kuo & Essene 1986); light grey, spinels in harzburgites from Yemen (Chazot *et al.* 1996); dark grey, spinel in peridotite xenoliths from Massif Central (Xu *et al.* 1998); crosshatched, spinels in lherzolites from Hawai (Sen 1988).

43Th I	43Th II	52Th I	IT1B II	IT10 II	IT13A I	IT30 I	IT31 I	IT47 I	IT49 II
0.04	0.05	0.02	0.00	0	0.03	0.04	0.00	0.07	0.186
0.24	0.2	0.22	0.03	0.003	0.07	0.01	0.07	0.07	0.264
38.14	36.34	11.85	20.23	25.862	49.56	53.16	49.40	53.31	23.127
30.97	32.93	58.25	52.67	41.555	19.23	14.92	18.70	15.23	44.257
11.84	12.14	16.59	9.09	14.681	10.95	10.34	10.84	10.95	7.959
0.18	0.14	0.25	0.25	0.252	0.09	0.12	0.12	0.10	0.323
17.65	17.42	12.38	17.57	15.936	19.31	20.07	19.52	20.01	22.497
0.18	0.18	0.05	0.12	0.102	0.27	0.30	0.29	0.28	0.207
0	0.02	0.02	0.00	0.116	0.02	0.01	0.02	0.01	0.071
0.04	0	0.00	0.01	0.02	0.00	0.00	0.02	0.00	0.088
0	0	0.01	0.00	0.01	0.00	0.00	0.00	0.01	0.006
99.28	99.42	99.62	99.96	98.537	99.54	98.96	98.98	100.0	98.99
74.75	74.05	59.84	79.62	72.487	100.00	79.74	78.99	78.8	98.58
35.27	37.79	76.75	63.59	51.87	20.64	15.85	20.23	16.08	56.21

IT31) and weak enrichments in Zr, Ba and Ti. Their Sr concentrations are relatively low (12–22 ppm) (Fig. 8).

Group II. Clinopyroxenes from group II are characterized by flat or nearly flat REE patterns (38Th, 43Th and 33Th) and they display the highest Mg-number, and high TiO_2 and Cr_2O_3 contents. They are found in harzburgites with microstructures varying from coarse grained to slightly tabular. These clinopyroxenes have $(La/Yb)_N = 1.4–4.1$, $(La/Sm)_N = 0.7–2.7$ and $(Sm/Yb)_N = 1.6–2$ but weak enrichments in Ba, Nb, Zr and Ti and no enrichment in the most incompatible elements (Rb, Th and U). The clinopyroxene of harzburgite 33Th displays the highest concentrations of Th (3.54 ppm) and U (0.86 ppm). The concentration of Sr in this group ranges from 45 to 104 ppm (Fig. 8).

Group III. Clinopyroxenes from group III are characterized by REE or trace element patterns showing enrichments in the most incompatible trace elements (IT1B, IT30, 23Th, 30Th, 37Th and 52Th), and therefore high $(La/Yb)_N$ ratios ranging from 0.8 to 36. They have the lowest Mg-number and the highest Na_2O values. Their trace element patterns show enrichments in LILE (Th and U) and only weak enrichments in high field strength elements (HFSE; Nb, Ta, Zr and

Table 6. *Representative major element compositions of amphibole in Syrian mantle Xenoliths*

Sample:	33Th	33Th	IT10	IT10	IT10	IT10	IT49	IT49
Assemblage:	II	II	II	II	II	II	II	II
SiO_2	44.22	44.07	45.09	45.85	46.26	45.18	47.39	47.25
TiO_2	0.72	0.72	0.27	0.20	0.14	0.17	0.21	0.22
Al_2O_3	13.28	13.42	12.81	12.54	12.35	12.77	10.16	10.27
Cr_2O_3	2.76	2.63	2.50	2.79	2.71	2.79	3.45	3.29
FeO^T	3.26	3.03	3.63	3.73	3.77	3.77	3.26	3.19
MnO	0.04	0.04	0.09	0.10	0.05	0.07	0.05	0.07
MgO	18.44	18.20	18.10	18.43	18.45	18.44	18.79	18.82
NiO	0.12	0.08	0.08	0.10	0.05	0.10	0.08	0.05
CaO	10.61	10.26	9.62	9.33	9.30	9.39	8.87	8.93
Na_2O	4.05	4.10	3.97	4.24	4.15	4.17	4.43	4.38
K_2O	0.06	0.04	1.05	0.90	0.96	0.96	1.02	0.98
Total	97.55	96.58	97.20	98.21	98.19	97.80	97.72	97.43
Mg-no.	91.062	91.468	89.985	89.905	89.798	89.814	91.21	91.407

Assemblage I refers to the primary mineralogy and II to the secondary mineralogy. FeO^T determined as total Fe. Mg-number $= 100 \times Mg/(Mg + Fe)$.

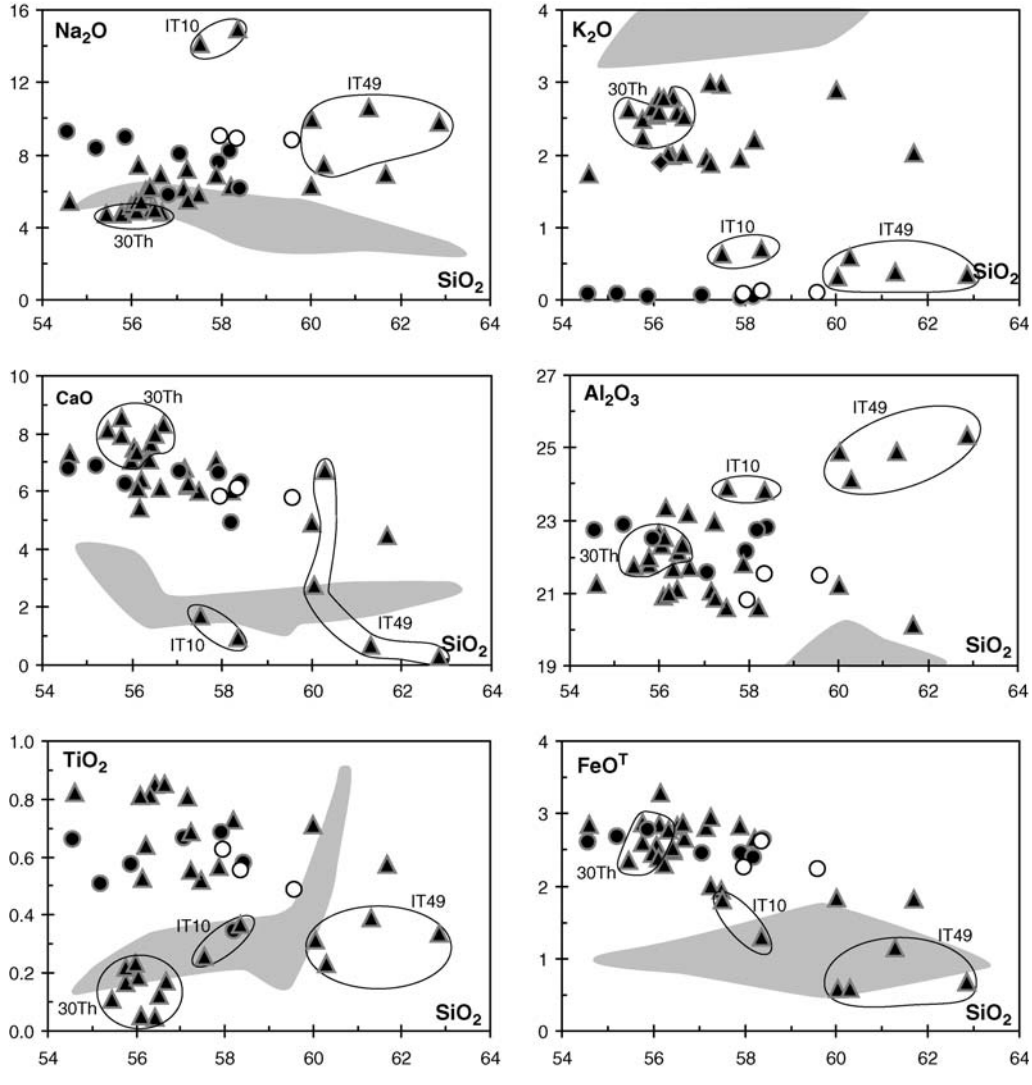

Fig. 6. Major element compositions of glasses in mantle xenoliths from Tel Tannoun. Symbols for rock types as for Figure 4. Grey field is for partial melting experiments of Draper & Green (1997).

Ti), and Rb and Ba compared with their neighbouring elements. The concentration of Sr in group III ranges from 11 to 521 ppm, with most samples containing >104 ppm. Group III clinopyroxenes display various types of REE enrichments. Some of these clinopyroxenes (harzburgites 37Th and IT30, wehrlite 23Th) have a spoon-shaped REE pattern with preferential enrichments in LREE compared with MREE at variable MREE and HREE contents. The MREE–HREE pattern is almost flat and resembles that of group I or group II clinopyroxenes. Some other clinopyroxenes (harzburgites 52Th, 30Th and IT1B) have REE patterns displaying progressive enrichments from HREE to LREE (Fig. 8). The coarse–grained harzburgite IT1B has the highest LREE and MREE contents compared with the other clinopyroxenes. In terms of major elements, two samples with LREE-enriched clinopyroxenes (52Th and IT1B) have significant lower Al_2O_3 and CaO, but higher Na_2O and Cr_2O_3 than LREE–MREE-enriched clinopyroxenes (Fig. 4). Clinopyroxenes from sample 30Th, which has the lowest MREE contents, have major element compositions intermediate between those of other LREE-enriched clinopyroxenes (52Th, IT1B) and LREE–MREE-enriched clinopyroxenes

Table 7. *Representative major element compositions and normative compositions of glass in Syrian mantle Xenoliths*

Sample:	23Th	23Th	23Th	23Th	23Th	23Th	23Th	23Th	23Th	23Th	30Th	30Th	30Th	30Th	30Th	30Th	30Th	30Th	30Th
Assemblage:	II	II	II	II	II	II	II	II (vein)	II (vein)	II (vein)	II	II	II	II	II	II	II	II	II
SiO_2	58.42	57.93	57.08	58.21	55.20	54.57	55.87	58.36	57.97	59.58	55.76	55.44	55.77	56.06	55.98	56.68	56.42	56.12	56.51
TiO_2	0.58	0.68	0.67	0.34	0.51	0.66	0.57	0.56	0.63	0.49	0.17	0.11	0.22	0.19	0.23	0.17	0.05	0.05	0.12
Al_2O_3	22.80	22.15	21.58	22.73	22.88	22.71	22.48	21.54	20.82	21.50	21.78	21.77	21.98	22.32	22.63	21.73	22.14	22.51	22.31
Cr_2O_3	0.06	0.12	0.06	0.00	0.09	0.00	0.07	0.06	0.08	0.04	0.10	0.03	0.00	0.11	0.06	0.10	0.05	0.19	0.07
FeO^T	2.65	2.45	2.45	2.39	2.68	2.61	2.77	2.63	2.25	2.24	2.61	2.36	2.86	2.56	2.45	2.65	2.48	2.85	2.83
MnO	0.06	0.08	0.04	0.05	0.07	0.07	0.04	0.02	0.00	0.02	0.02	0.07	0.04	0.04	0.09	0.00	0.02	0.06	0.05
MgO	3.11	3.07	3.17	2.25	2.66	2.98	3.17	2.62	2.68	2.29	3.11	2.94	2.62	2.84	2.94	3.07	2.66	2.97	2.98
NiO	0.01	0.00	0.00	0.00	0.02	0.00	0.00	0.00	0.00	0.00	0.04	0.03	0.00	0.04	0.00	0.01	0.00	0.02	0.00
CaO	6.29	6.64	6.69	4.90	6.87	6.76	6.25	6.10	5.83	5.78	8.57	8.11	7.93	7.49	7.08	8.34	7.66	7.37	7.97
Na_2O	6.10	7.59	8.07	8.22	8.33	9.25	8.94	8.86	9.07	8.78	4.81	4.77	4.76	5.07	5.17	4.83	4.98	4.92	4.99
K_2O	0.09	0.02	0.05	0.04	0.07	0.07	0.04	0.11	0.07	0.10	2.25	2.62	2.50	2.55	2.64	2.53	2.80	2.58	2.58
Total	100.16	100.73	99.85	99.13	99.38	99.67	100.20	100.86	99.40	100.81	99.20	98.26	98.68	99.26	99.26	100.12	99.25	99.64	100.40
Mg-no.	67.64	69.12	69.69	62.63	63.91	67.05	67.10	63.94	68.00	64.52	68.03	68.92	61.98	66.40	68.14	67.34	65.69	64.96	65.26
Normative compositions																			
Quartz	2.69																		
Plagioclase	82.69	83.75	76.97	88.45	73.66	64.59	70.59	74.99	73.86	80.31	69.63	68.14	71.02	71.18	70.78	69.06	68.73	72.31	69.07
Orthoclase	0.53	0.12	0.3	0.24	0.41	0.41	0.24	0.65	0.41	0.59	13.41	15.78	14.95	15.19	15.72	14.95	16.67	15.31	15.13
Nepheline	0	3.38	7.59	3.44	12.11	18.56	14.1	9.71	10.51	6.62	1.6	1.98	0.77	1.48	2.31	0.97	2.02	0.65	2.03
Corundum	1.25			0.23															
Diopside	0	5.3	8.68	0	7.59	10.83	8.07	9.39	10.60	7.80	9.32	8.03	6.71	4.68	3.27	8.59	6.49	2.93	6.65
Hypersthene																			
Olivine	0	6.16	5.2	7.01	5.26	4.36	5.92	4.22	3.42	3.75	5.72	5.76	6.12	6.8	7.32	5.86	5.87	8.23	6.71
Ilmenite	1.1	1.29	1.27	0.66	0.97	1.25	1.08	1.04	1.20	0.93	0.32	0.21	0.42	0.36	0.46	0.32	0.09	0.09	0.23
Total	100	100	100.01	100.03	100	100	100	100	100	100	100	99.9	99.99	99.69	99.86	99.75	99.87	99.52	99.82

Sample:	37Th	37Th	37Th	37Th	37Th	IT10	IT10	IT47	IT47	IT47	IT47	IT47	IT49	IT49	IT49	IT49
Assemblage:	II	II	II	II	II	II	II	II	II	II	II	II	II	II	II	II
SiO_2	56.43	56.34	57.18	58.23	60.02	58.38	57.54	57.88	57.25	56.15	61.68	56.63	62.84	60.02	60.28	61.30
TiO_2	0.85	0.81	0.80	0.72	0.71	0.36	0.25	0.56	0.68	0.52	0.57	0.85	0.34	0.32	0.24	0.39
Al_2O_3	21.05	21.66	21.03	20.58	21.17	23.80	23.85	21.78	22.92	23.30	20.08	23.14	25.36	24.90	24.13	24.90
Cr_2O_3	0.04	0.07	0.17	0.06	0.04	0.05	0.03	0.43	0.03	0.00	0.00	0.03	0.13	0.37	0.08	0.03
FeO^T	2.51	2.76	2.79	2.63	1.82	1.28	1.80	2.81	2.92	3.28	1.81	2.86	0.68	0.60	0.59	1.16
MnO	0.00	0.07	0.01	0.11	0.07	0.01	0.00	0.02	0.00	0.10	0.09	0.07	0.01	0.00	0.00	0.00
MgO	3.35	3.03	3.08	2.94	2.01	0.42	0.93	2.86	2.11	2.12	1.80	2.38	0.14	2.21	0.57	0.93
NiO	0.00	0.00	0.01	0.01	0.00	0.02	0.01	0.08	0.01	0.03	0.00	0.00	0.02	0.00	0.00	0.00
CaO	7.02	7.03	6.74	5.98	4.85	0.91	1.66	6.98	6.20	5.40	4.42	6.08	0.36	2.78	6.79	0.71
Na_2O	6.16	5.97	6.05	6.21	6.11	14.85	14.05	6.80	7.11	7.36	6.87	6.80	9.90	10.02	7.48	10.68

(*Continued*)

Table 7. *Continued*

Sample:	23Th	23Th	23Th	23Th	23Th	23Th	23Th	23Th	23Th	23Th	30Th	30Th	30Th	30Th	30Th	30Th	30Th	30Th	30Th
Assemblage:	II	II	II	II	II	II	II	II (vein)	II (vein)	II (vein)	II	II	II	II	II	II	II	II	II
K_2O	1.96	1.99	1.94	2.18	2.88	0.69	0.62	1.93	1.86	1.90	2.01	2.00	0.34	0.32	0.59	0.39			
Total	99.37	99.72	99.80	99.64	99.67	100.75	100.74	102.14	101.08	100.16	99.32	100.84	100.12	101.54	100.75	100.50			
Mg-no.	70.36	66.13	66.33	66.57	66.31	36.64	47.94	64.45	56.25	53.56	63.93	59.73	27.20	86.75	63.45	58.72			
Normative compositions																			
Quartz																			
Plagioclase	67.76	70.1	71.42	72	73.8	55.55	52.03	66.79	70.55	69.40	76.70	70.80	85.64	81.88	92.57	82.87			
Orthoclase	11.7	11.76	11.52	12.94	17.08	4.02	3.60	11.23	10.87	11.23	11.94	11.70	2.01	1.83	3.49	2.30			
Nepheline	4.79	3.86	2.46	1.45		33.70	35.88	6.85	7.49	9.58	0.00	6.94	0.00	8.46	0.33	5.74			
Corundum																			
Diopside	8.79	6.84	7.28	6.32	1.8	3.76	6.64	9.16	4.57	1.53	3.20	2.79	0.00	0.00	2.53	0.00			
Hypersthene					4.68						5.52		1.05						
Olivine	5.34	5.9	5.79	5.9	1.3	0.66	1.37	4.91	5.23	7.27	0.00	6.18	0.00	4.28	0.64	2.75			
Ilmenite	1.61	1.54	1.54	1.39	1.35	0.68	0.47	1.04	1.27	0.99	1.08	1.60	0.65	0.59	0.44	0.74			
Total	99.99	100	100.01	100	100.01	98.37	99.99	99.98	99.98	100	98.44	100.01	89.35	97.04	100.00	94.40			

Assemblage I refers to the primary mineralogy and II to the secondary mineralogy. FeO^T determined as total Fe. Mg-number $= 100 \times Mg/(Mg + Fe)$; Cr-number $= 100 \times Cr/(Cr + Al)$.

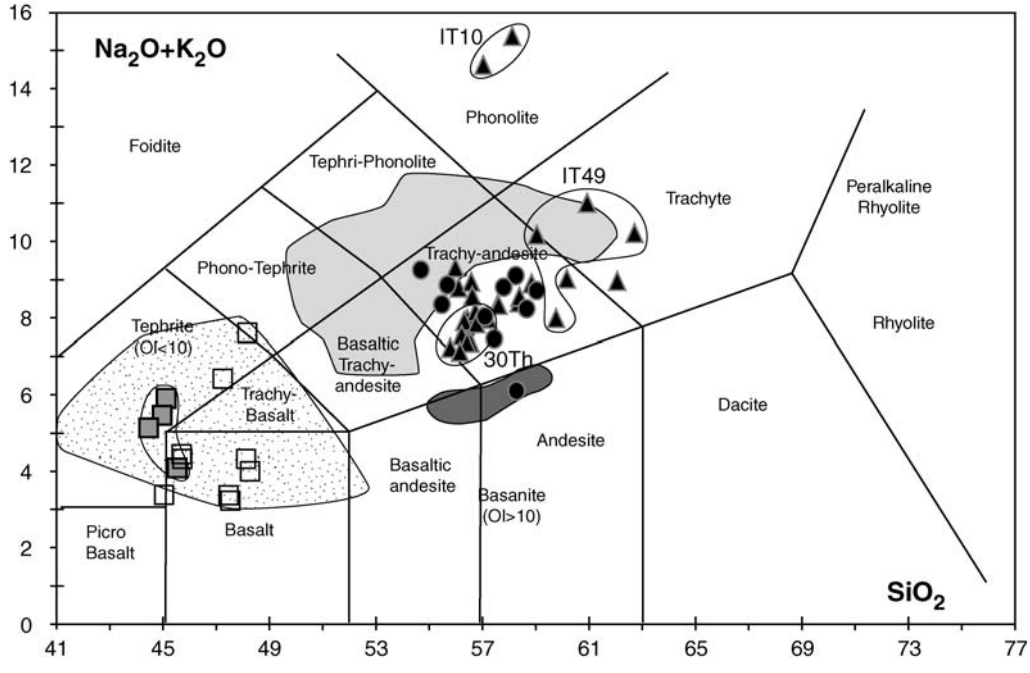

Fig. 7. Total alkalis–Silica diagram of Le Bas *et al.* (1986) for glasses and lavas from Tel Tannoun. Symbols as for Figure 4. Dark grey field is for glasses in reaction zones in anhydrous spinel lherzolites from Yemen (Chazot *et al.* 1996); light grey field is for glasses in reaction zones in hydrous spinel lherzolites from Yemen (Chazot *et al.* 1996); stippled field is for volcanic rocks from southern Syria (Mouty *et al.* 1992); □, basalts from Jabel El Arab (Ismail, unpublished data); grey squares, basalts from Tel Tannoun locality (Ismail, unpubl. data).

(37Th, IT30 and 23Th). Finally, the microstructure in group III harzburgites is similar to that of group II (coarse grained with a tabular tendency).

REE and trace element patterns of the amphibole in harzburgite 33Th (Fig. 8) are similar to those of clinopyroxene in the same rock (group II). However, amphibole in sample 33Th has a higher concentration in trace elements such as U, Th and Sr (U 1.33 ppm, Th 4.85 ppm and Sr 186 ppm) than in the coexisting clinopyroxene (U 0.86 ppm, Th 3.54 ppm and Sr 104 ppm), in agreement with amphibole-bearing xenoliths from Antarctica (Coltorti *et al.* 2004) and Kapfenstein (Coltorti *et al.* 2007).

Discussion

Partial melting history

The studied suite of xenoliths from Syria comprises one lherzolite, one wehrlite and several harzburgites, all of which equilibrated in the spinel stability field (906–1100 °C). Their petrological, mineralogical and geochemical characteristics are comparable with those of type I Cr-diopside mantle peridotites described by Frey & Prinz (1978) and Menzies & Hawkesworth (1987). The major element compositions of the primary mineral phases, particularly the high Mg-number of the primary minerals, low clinopyroxene modal contents, the high Mg-number of olivine and the high Cr-number of spinel (Frey & Prinz 1978; Menzies & Hawkesworth 1987; Boyd 1989; Fabriès *et al.* 1991; Norman 1998), are indicators of partial melting processes in the mantle. In Figure 9, most of the xenoliths from this and other studies (Medaris & Syada 1998; Nasir & Safarjalani 2000) plot off the partial melting trend at low pressure defined by Boyd (1989), indicating that xenoliths rarely preserved their residual partial melting signatures in terms of olivine modal contents and/or Mg-number in olivine (IT13A, group I; 38Th, group II; ± IT1B, group III). Other xenoliths either have olivine contents too high and/or Mg-number too low to be simple melting residues.

The mineralogical and geochemical compositions of minerals in lherzolite 51Th (Figs 4 and 8; Table 2–7) indicate that this sample represents the most fertile rock in the xenolith suite. However, most of the xenolith suite is composed of harzburgites containing minerals with high

Table 8. *Trace element contents (ppm) of clinopyroxenes and amphibole from xenoliths from Tel Tannoun obtained by LA-ICP-MS*

Element	Wehrlite	Lherzolite	Harzburgite											
	23Th	51Th	30Th	33Th-cpx	33Th-Am	37Th	38Th	43Th	52Th	IT1B	IT13A	IT30	IT31	IT47
Sc	90	65	74	111	76	85	93	96	108	133	81	77	86	74
Ti	675	4433	267	727	5476	2140	531	1287	262	270	731	1452	953	646
V	271	274	208	298	431	320	244	223	316	267	224	216	187	213
Cr		4061	4548	9259	16374	6496	7299	6499	8942	7971	5968	6637	5946	5654
Fe		18569	13301	15070	23487	17444	11938	10355	15830	19367	17300	16849	15378	21070
Co											21	19	18	22
Ni	322	300	292	353	969	377	293	244	272	306	302	276	242	317
Ga											1.35	3.29	6.79	3.30
Rb			0.36	0.59	0.67						0.31	0.64		0.00
Sr	33	79	311	104	185	156.5	45	73	146	521	22	11	17	12
Y	8.90	19.33	5.75	8.49	11.42	19.66	5.02	10.78	8.27	9.24	9.09	15.32	11.60	11.05
Zr	14.0	30.9	58.5	23.9	36.6	6.8	25.4	28.1	7.3	8.8	1.9	1.9	14.2	1.4
Nb		0.77	0.80	0.13	6.31	0.23	0.55	0.34			0.15	0.05		0.31
Ba	1.32	0.18	1.80	0.24	36.02	0.65	0.13		0.19	1.03	0.07	0.11		0.10
La	1.07	4.06	12.86	5.18	6.50	23.18	1.45	2.20	14.75	41.98	0.20	2.65	0.04	0.09
Ce	1.31	8.99	19.88	8.43	10.01	29.86	2.51	6.35	29.17	72.24	0.72	4.52	0.54	0.08
Pr	0.18	1.15	1.75	0.94	1.30	2.24	0.43	0.97	2.92	8.21	0.14	0.32	0.16	0.04
Nd	1.23	5.89	5.37	3.97	5.43	6.25	2.68	5.14	10.20	26.92	1.04	1.21	1.21	0.53
Sm	0.54	2.04	0.84	1.19	1.51	1.52	0.94	2.00	2.12	3.37	0.37	0.55	0.81	0.44
Eu	0.24	0.82	0.24	0.47	0.60	0.59	0.31	0.75	0.84	1.11	0.16	0.27	0.42	0.21
Gd	1.01	2.76	0.61	1.55	1.93	2.49	0.96	2.41	1.96	2.22	0.70	1.21	1.41	1.14
Tb	0.20	0.52	0.10	0.27	0.34	0.52	0.15	0.38	0.31	0.30	0.14	0.29	0.32	0.24
Dy	1.48	3.59	0.68	1.64	2.18	3.63	0.99	2.43	1.83	1.63	1.18	2.52	2.21	1.74
Ho	0.34	0.81	0.18	0.32	0.43	0.84	0.21	0.46	0.36	0.32	0.35	0.60	0.44	0.36
Er	0.99	2.13	0.64	0.87	1.24	2.70	0.62	1.27	0.86	0.79	1.08	1.81	1.21	1.20
Yb	0.96	2.10	0.80	0.85	0.97	2.63	0.64	1.07	0.85	0.80	1.04	1.72	1.03	1.36
Lu	0.15	0.33	0.15	0.15	0.14	0.34	0.13	0.19	0.15	0.12	0.15	0.25	0.11	0.18
Hf		1.55	0.56	0.75	1.09	0.60	0.46	0.96	0.49	0.32	0.13	0.25	0.32	0.21
Ta			0.10	0.07	0.19	0.07		0.14						
Pb	0.54									0.35				
Th	2.54	0.17	1.69	3.54	4.85	0.83	0.14	0.17	0.87	0.71	0.05	1.15	0.39	0.10
U	0.74	0.09	0.44	0.86	1.33	0.21			0.24	0.08	0.03	0.26	0.21	0.03
$(La/Sm)_N$	1.24	1.25	9.59	2.73	2.70	9.55	0.97	0.69	4.37	7.81	0.34	3.03	0.03	0.13
$(La/Yb)_N$	0.76	1.32	10.94	4.15	4.56	5.99	1.55	1.40	11.81	35.86	0.13	1.05	0.02	0.05
$(Sm/Yb)_N$	0.61	1.05	1.14	1.52	1.69	0.63	1.60	2.03	2.70	4.59	0.38	0.35	0.86	0.36

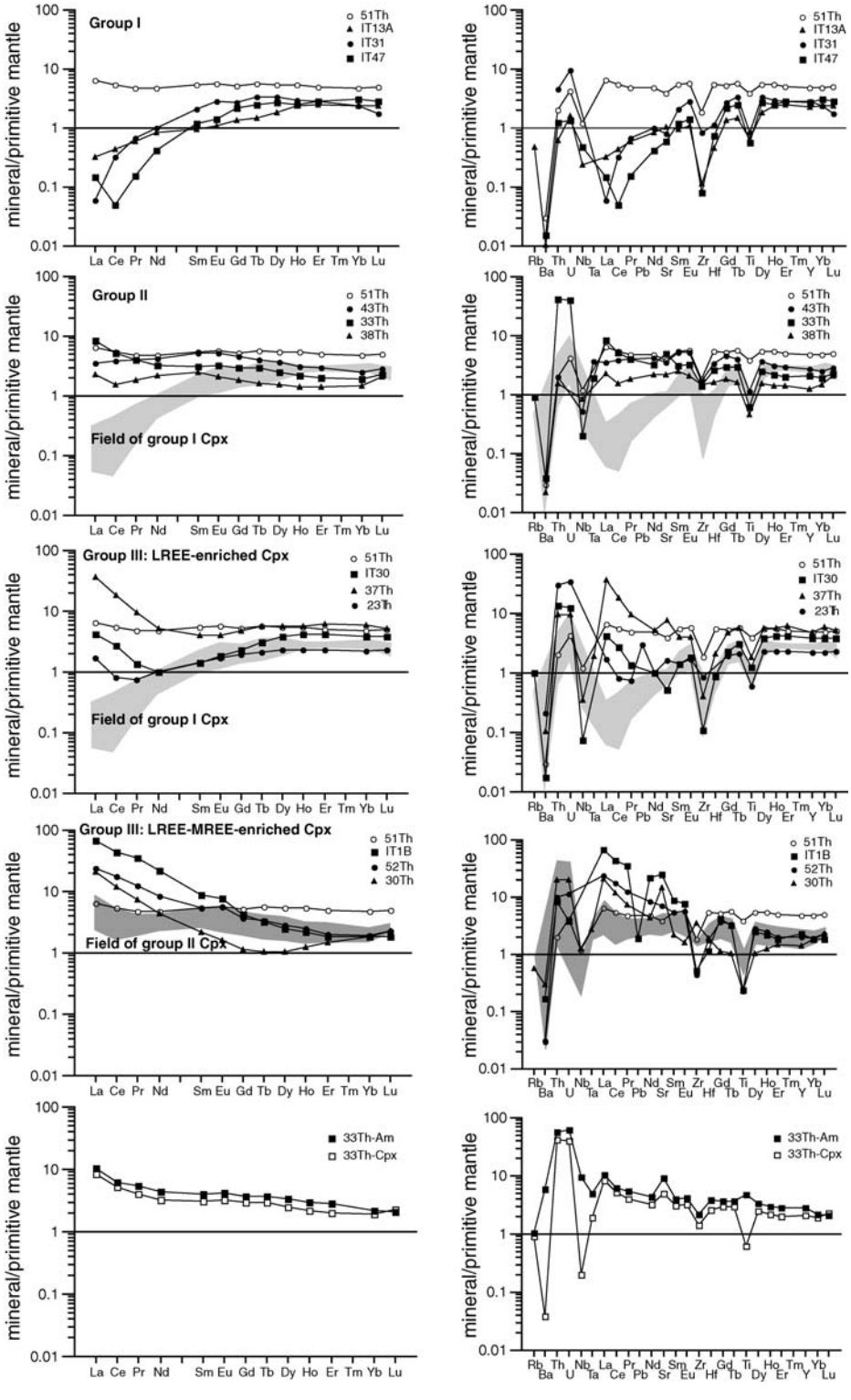

Fig. 8. REE and trace element patterns of primary clinopyroxenes and amphibole from xenoliths from Tel Tannoun. Light grey field is for group I clinopyroxenes; dark grey field is for group II clinopyroxenes. Normalization values are from McDonough & Sun (1995). The lherzolite 51Th is reported for comparison in the three groups.

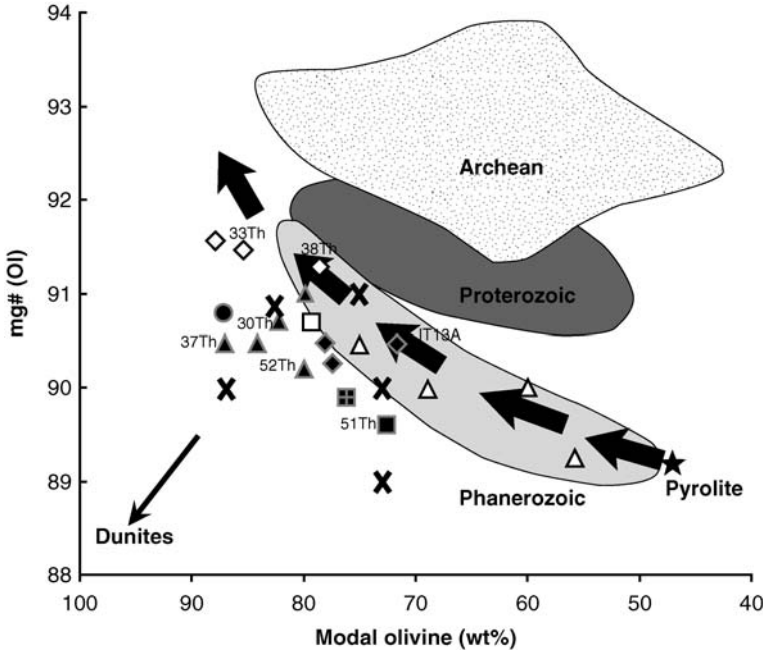

Fig. 9. Olivine modal proportions (vol%) v. olivine Mg-number in xenoliths from Tel Tannoun compared with xenoliths from Archaean, Proterozoic and Phanerozoic terranes (Boyd 1989; Griffin *et al.* 1998). ■, spinel lherzolite; ●, spinel wehrlite; ◆, group I harzburgites; ◇, group II harzburgites; ▲, group III harzburgites; □, harzburgite (IT10); filled square with cross, harzburgite (IT49); △, Syrian lherzolites from Medaris & Syada (1998) and Nasir & Safarjalani (2000); × harzburgites from Medaris & Syada (1998) and Nasir & Safarjalani (2000).

Mg-number (89.2–91.7 for olivine, 90.6–92.4 for orthopyroxene and 90.5–93.6 for clinopyroxene) and high Cr-number in spinels (23.4–46.4). In the clinopyroxene, the Al_2O_3–Mg-number negative correlation between the lherzolite and the harzburgites (Fig. 4) suggests that the major element composition of group I and II clinopyroxenes was mainly controlled by various degrees of partial melting. According to major element variations, the highest Mg-number (90.2–91.8 for olivine, 91.2–92.1 for orthopyroxene and 93.0–93.6 for clinopyoxene) and most refractory compositions in minerals (lowest Al, Ti and Na; Fig. 4) from group II harzburgites imply that they experienced the highest degrees of melting. However, their nearly flat trace element signatures (Fig. 8) and high HREE contents do not resemble those of partial melting residues (Johnson *et al.* 1990) and imply that they were probably re-enriched, even in HREE, during metasomatism (33Th and 43Th). However, the lower HREE contents of harzburgite 38Th (Fig. 8), its modal composition and Mg-number in olivines (Fig. 9) could still be indicative of a high degree of melting.

The group I harzburgites have Mg-number (90.3–90.6 in olivine, 90.3–91.2 in orthopyroxene and 90.5–93 in clinopyroxene and Cr-number in spinel (16.1–23) intermediate between those of minerals from group II and the lherzolite 51Th. Their clinopyroxene REE patterns characterized by depletions in LREE and low (La/Yb) are geochemical fingerprints of residual lithospheric mantle after partial melting (Johnson *et al.* 1990; see modelling below). None the less, some of the most incompatible trace elements are still enriched compared with partial melting residues (Th, U and Nb) and are indicative of later metasomatism by small silicate melt fractions.

The group III harzburgites have minerals characterized by highly variable Mg-number (89.2–91.8 for olivine, 90.8–91.8 for orthopyroxene and 90.5–93.1 for clinopyroxene), and very heterogeneous Cr-number in spinels ranging from 22 to 76.7 (Tables 2–5). The mineral major element variations and clinopyroxene HREE abundances suggest that this group has experienced various degrees of melting. For instance, some LREE–MREE-enriched clinopyroxenes from group III have some of the lowest HREE (IT1B, 30Th and 52Th) and MREE (30Th) abundances, suggesting high degrees of partial melting (Fig. 8). In contrast, the higher abundances of

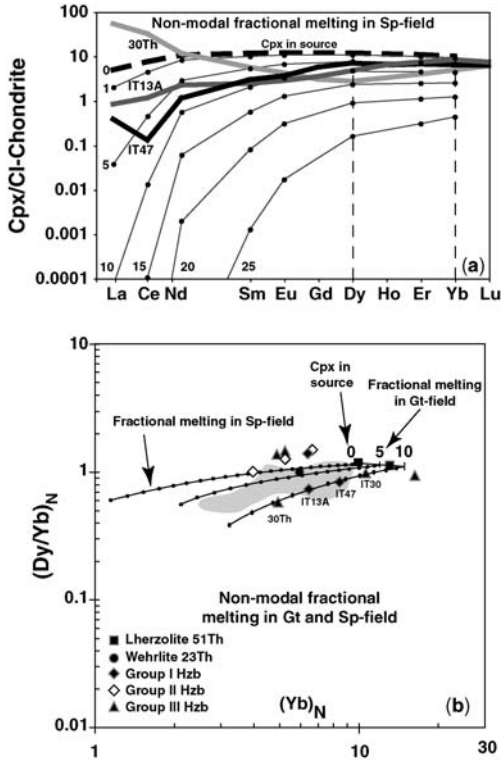

Fig. 10. (**a**) Trace element modelling of residual clinopyroxene in harzburgites 30Th, IT13A and IT47 using the non-modal partial melting equations and parameters of Johnson *et al.* (1990) and CI-chondrite normalization values after McDonough & Sun (1995). Numbers refer to the amount of melting in per cent and the associated residual clinopyroxene composition. (**b**) $(Dy/Yb)_N$ v. Yb_N for clinopyroxenes in xenoliths from this study using the continuous melting model and parameters of Brunelli *et al.* (2006). Symbols as for Figure 9. Light grey field is for clinopyroxenes from the Vema lithospheric section (Brunelli *et al.* 2006). Smallfilled circles on curves are 1% increments of melting.

HREE and flat MREE–HREE patterns for group III (IT30, 23Th and 37Th) clinopyroxenes imply lower degrees of melting, similar to group I harzburgites. The major element variations in some group III clinopyroxenes (IT1B, 52Th and 30Th; high Na and low Al; Fig. 4), coupled with the very high Cr-number in spinel and the enrichments in Th, U, Sr and LREE, highlight instead the effect of metasomatic overprinting as a result of melt–rock reaction.

Trace element abundances can be used to illustrate the extent of the partial melting process. Although the clinopyroxenes from the three groups display variable enrichment in the most incompatible elements (Th, U and LREE), some harzburgites (IT1B, IT13A, IT31, IT47, 30Th, 33Th, 38Th and 52Th) have low Dy, Er, Yb and Lu contents compared with CI-chondrite and primitive mantle estimates (Fig. 8) and may have preserved the trace element signature of partial melting residues. To assess the extent of partial melting, we undertook trace element modelling using the non-modal fractional partial melting equations of Johnson *et al.* (1990) and by assuming that partial melting occurred in the spinel stability field (Fig. 10a). No other REE or REE ratios can satisfactorily be used to assess partial melting conditions, as most LREE/MREE ratios in the clinopyroxenes are greater than unity (e.g. Sm/Yb or Ce/Yb).

The results display some major inconsistencies with a model involving partial melting in the spinel stability field, at least for some harzburgites (Fig 10a). Some clinopyroxenes from group I (IT13A and IT47) and from group III (30Th) have Dy_N values that are too low for their Yb_N values if melting occurred in the spinel stability field, hence they display low $(Dy/Yb)_N$ ratios (IT13A, IT47 and 30Th). Such low $(Dy/Yb)_N$ ratios in clinopyroxenes are a characteristic feature of peridotites that started melting in the garnet stability field and continued to melt in the spinel stability field (Hellebrand *et al.* 2002; Brunelli *et al.* 2006). To account for the low $(Dy/Yb)_N$ ratios (0.56–0.84) at relatively high Yb_N in such clinopyroxenes, 5–10% of melting must have occurred in the garnet stability field, followed by additional melting in the spinel stability field (continuous melting model; see model and parameters of Brunelli *et al.* 2006; Fig. 10b). The total degree of melting for these MREE-depleted samples is $<20\%$ (Fig. 10b). Therefore, the trace element modelling strongly supports a polybaric melting model for some group I and group III harzburgites. However, the occurrence of reaction zones filled with newly formed minerals, the variations in major element compositions and the enrichments in Th, U and LREE in some clinopyroxenes, coupled with the variations in modal composition of the xenolith suite (Figs 4 and 8), preclude a simple partial melting origin. These characteristics would appear to indicate later metasomatic interaction(s) of the residual peridotites with melt(s).

Metasomatic history

Nature of metasomatic agents in the Syrian lithospheric mantle. The microstructural characteristics, and modal and chemical compositions of the primary and secondary assemblages reflect the nature of the metasomatic agent(s) that reacted with the host peridotites. Textural disequilibrium

between distinctive mineral parageneses and the occurrence of minerals in mantle xenoliths such as amphibole, phlogopite or plagioclase, in association with major and trace element enrichments, are indicative of metasomatic processes (O'Reilly & Griffin 1988; Fabriès *et al.* 1989, 1991; Ionov *et al.* 1994; Wulff-Pedersen *et al.* 1996; Coltorti *et al.* 1999; Grégoire *et al.* 2000; Frezzotti *et al.* 2002; Delpech *et al.* 2004; Moine *et al.* 2004).

The petrological, mineralogical and geochemical characteristics of the studied mantle xenoliths indicate that most xenoliths experienced a complex modal and/or cryptic metasomatic history, which modified the major and trace element compositions of the residual lithospheric mantle after various degrees of partial melting. This is indicated by: (1) the occurrence of reaction zones in which secondary minerals are observed; (2) the occurrence of amphibole; (3) the major element variations in primary minerals; (4) the enrichment in strongly incompatible trace elements in clinopyroxenes.

Two major types of metasomatism are inferred to have been responsible for the major and trace element compositions: silicate melt metasomatism involving large melt fractions and silicate melt metasomatism by small melt (volatile-rich) fractions.

Eight harzburgite xenoliths (30Th, 33Th, 37Th, 52Th, IT1B, IT31, IT47 and IT49; Table 1) display evidence of modal metasomatism with the development of reaction zones at the expense of spinel and/or amphibole, as well as spongy rims in the primary clinopyroxene and orthopyroxene (23Th, 30Th, 37Th and 52Th; Fig. 2). These reaction zones occur in the three groups of harzburgites, irrespective of the trace element composition of the primary clinopyroxene. They testify to a late metasomatic event that occurred shortly before entrapment in the host lava. The geochemical evidence for this late metasomatic event will be developed further below.

The primary evidence that suggests metasomatism is the relationship between olivine modal compositions and Mg-number (Fig. 9). From Figure 9, most xenoliths from this suite cannot be simple partial melting residues, including the lherzolite 51Th. The deviation to high olivine modal contents at a given Mg-number and/or to lower Mg-number at a given modal olivine content is a well-known consequence of metasomatism between the residual lithospheric mantle and silicate melts rising to the surface (Kelemen 1990). Such metasomatism may ultimately produce dunites or wehrlites.

The group II harzburgites have the highest olivine modal contents, olivine with the highest Mg-number (91.3–91.8), clinopyroxenes with the highest Mg-number (93–93.6) and relatively low Al, high Ca and low Na contents (Fig. 4). Spinel in this group of harzburgites has variable but high Cr-number and Mg-number (34.8–46.4 and 70.3–77.6, respectively; Fig. 5). These geochemical characteristics indicate that the primary minerals still retain evidence for a high-degree partial melting episode. According to the major element data for olivine, orthopyroxene, clinopyroxene and spinel (Table 2), the group II harzburgites underwent higher degrees of partial melting than the group I harzburgites (see cpx I in Fig. 4 and Sp in Fig. 5). However, the Na contents of group II clinopyroxenes are higher than those in group I clinopyroxenes, contrary to what is expected from partial melting. In addition, the trace element contents of group II clinopyroxenes display relatively flat patterns with very limited trace element fractionation (Fig. 8) and do not resemble the trace element signatures of partial melting residues (Johnson *et al.* 1990; Fig. 10a). This suggests that the Na, Cr and trace element contents of group II clinopyroxenes were further re-enriched during a metasomatic event. This metasomatism also occurred at relatively constant Mg-number (Table 1) or may have even produced slightly more refractory compositions in terms of Mg-number, and at increasing modal olivine contents (Fig. 9; and higher Cpx/Opx ratios) as indicated by experimental work (Kelemen 1990) and natural peridotites (Seyler & Bonatti 1997). The nearly flat trace element patterns in the Syrian xenoliths are similar to those found in clinopyroxenes in metasomatized refractory harzburgites from Ethiopia (Bedini *et al.* 1997).

Such nearly flat trace element patterns of depleted Ethiopian harzburgites and clinopyroxenes are a consequence of an almost complete re-equilibration with a relatively undifferentiated basaltic melt during reactive porous melt flow at high melt/rock ratio and constant bulk Mg/Fe ratio (Bedini *et al.* 1997). Similarly, the mineral chemistry and modal compositions of the group II harzburgites could represent a residual mantle re-equilibrated with basaltic melt during a metasomatic event at high melt/rock ratio. Such a metasomatic event may have taken place during the emplacement of the largest intraplate volcanic field of the Arabian plate (Harrat Ash Shaam) on top of which Quaternary Strombolian cones have formed, which contain the studied xenoliths. Eventually, during metasomatism at decreasing melt/rock ratio, amphibole may have crystallized, such as in harzburgite 33Th. The equilibration temperatures are lower (850–950 °C) than those found by Bedini *et al.* (1997), indicating an origin for the Syrian xenoliths from a relatively shallow upper mantle.

The group III harzburgites are characterized by: (1) intermediate Mg-number values of primary minerals, lower than or equal to those for group I and II; (2) low (samples IT30, 23Th and 37Th) to high

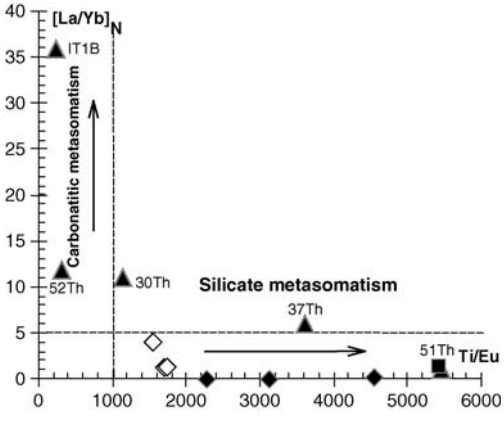

Fig. 11. $(La/Yb)_N$ v. Ti/Eu in clinopyroxenes from Syrian xenoliths (after Coltorti *et al.* 1999). ■, lherzolite (51Th); ◆, group I harzburgites; ◇, group II harzburgites; ▲, group III harzburgites. $(La/Yb)_N$ ratios are normalized to CI-chondrite values from McDonough & Sun (1995).

Cr-number values (samples IT1B, 30Th and 52Th) in spinels; (3) strong enrichment in Th, U, Sr and LREE, associated with depletion in HFSE (except Zr for 30Th) in these clinopyroxenes (Fig. 8). As discussed above, the heterogeneous major elements and HREE contents in group III clinopyroxenes suggest that the metasomatic episode(s) affected harzburgites that had experienced either a low (37Th and IT30) or high degree of melt extraction (IT1B, 30Th and 52Th). The variation of the major element contents in clinopyroxenes and spinels (Figs 4 and 5) and the variation of trace element concentrations or ratios in Cpx I (Figs 8 and 11) suggest that the group III harzburgites were affected by metasomatic media of variable compositions.

If the assumption that some group III harzburgites (IT30, 23Th and 37Th) share some geochemical characteristics with group I melting residues is valid (based on mineral major elements and trace elements in Cpx I), the increase in Al_2O_3 and Na_2O in clinopyroxene at relatively constant Mg-number probably occurred during the metasomatic event that re-enriched the clinopyroxene in the most incompatible trace elements. These clinopyroxenes have high Ti/Eu and moderate $(La/Yb)_N$ (Fig. 11), as well as low $(Nd/Hf)_N$ and $(Gd/Ti)_N$ (not shown); such geochemical indicators suggest that the metasomatic medium in some group III harzburgites (IT30, 23Th and 37Th) was essentially a silicate melt rather than a carbonate-rich melt fraction. These harzburgites contain no volatile-bearing minerals, suggesting that the metasomatic agent was poor in volatile components. The selective enrichments in the most incompatible trace elements and in LREE only indicate that these clinopyroxenes experienced only incipient metasomatism by small silicate melt fractions away from the silicate melt source (Ionov *et al.* 2002).

However, the major element compositions of some other group III clinopyroxenes and spinels (IT1B, 30Th and 52Th) display contrasting geochemical variations. These clinopyroxene compositions extend to lower Al and Ti, but higher Na and Cr contents than other group III clinopyroxenes for a given Mg-number (IT30, 23Th and 37Th; Fig. 4) and their spinels have high Cr-number. In addition, the trace element signatures of these clinopyroxenes (IT1B, 30Th and 52Th) show strong enrichments in Th, U, Sr and LREE (Fig. 8) and are comparatively poor in HFSE. The major and trace element compositions of such clinopyroxenes closely resemble those of clinopyroxenes resulting from carbonatitic metasomatism (Hauri *et al.* 1993; Coltorti *et al.* 1999; Delpech *et al.* 2004; Yaxley *et al.* 1991, 1998). Metasomatism by a carbonatitic melt or fluid should produce extensive reaction zones around the primary orthopyroxene in harzburgites, because orthopyroxene is unstable in the presence of carbonatitic melt at low pressures and will form secondary clinopyroxene, olivine and Cr-rich spinel associated with release of CO_2 (Wyllie & Huang 1976; Yaxley *et al.* 1991, 1998; Dalton & Wood 1993; Coltorti *et al.* 1999; Laurora *et al.* 2001; Dawson 2002). In response to carbonatitic metasomatism, the harzburgitic or lherzolitic lithospheric mantle will ultimately convert to wehrlite. In this context, the wehrlitic samples represent portions of the lithospheric mantle that have reacted the most with the carbonatitic metasomatic agent and therefore should bear indisputable mineralogical and geochemical evidence of such metasomatism. The wehrlite 23Th has Cpx I with relatively high Al_2O_3, CaO and TiO_2 and lower Na_2O compared with Cpx I in the harzburgites showing characteristic features of carbonatitic metasomatism (Fig. 4). Moreover, the trace element compositions of Cpx I in the wehrlite 23Th do not display the strong LREE and Sr enrichments and HFSE depletions often seen in clinopyroxenes metasomatized by carbonatitic melts, but show only a weak enrichment in La and Ce and a strong enrichment in Th and U (Fig. 8). Finally, in the group III harzburgites displaying carbonatitic geochemical fingerprints, as well as in the wehrlite, there is no mineralogical evidence for reaction between a carbonatitic melt and the harzburgitic lithospheric mantle. Therefore, in the Syrian xenoliths, the evidence for metasomatism by a mantle-derived carbonatite is not supported.

Several geochemical studies have pointed out that trace element signatures in clinopyroxenes

similar to those ascribed to carbonatitic metasomatism can be generated by other metasomatic processes such as those resulting from reactive porous melt flow (Bedini *et al.* 1997) or silicate melt metasomatism (Zanetti *et al.* 1999). Some recent studies have also pointed out that silicate- and carbonate-rich melts can be contemporaneous derivatives of a silicate melt (Ionov *et al.* 2002; Bodinier *et al.* 2004; Delpech *et al.* 2004; Moine *et al.* 2004). In the Syrian xenoliths, the 'carbonatitic' geochemical signature of the metasomatic agent in some group III harzburgites (IT1B, 30Th and 52Th) was probably acquired during repeated melt–rock reactions with the heterogeneous wall-rock harzburgites. During this process, the evolution of the geochemical composition of the metasomatic medium can be attributed to crystallization of amphibole, phlogopite or small amounts of Fe–Ti oxides (minerals that would buffer HFSE and/or Rb–Ba and the CO_2/H_2O ratio) during percolation. Amphibole is common in the lithospheric mantle beneath southern Syria (Table 6; Medaris & Syada 1998; Nasir & Safarjalani 2000), and phlogopite has been reported by Medaris & Syada (1998) and Nasir & Safarjalani (2000). The resulting differentiated small melt fraction responsible for metasomatism in some group III harzburgites after percolation away from its source was a CO_2-rich alkali silicate melt that had acquired a 'carbonatitic' trace element signature (Fig. 11). Such metasomatic processes have been described for mantle xenoliths from Kerguelen (Delpech *et al.* 2004; Moine *et al.* 2004), Ethiopia (Bedini *et al.* 1997) and Spitsbergen (Ionov *et al.* 2002) and produced highly fractionated trace element signatures in clinopyroxenes as a result of percolation metasomatism.

Were these metasomatic events in groups II and III related in time and space? In this section, we examine if the different geochemical fingerprints in the group II and III harzburgites could be explained by a single metasomatic event or if we need to invoke a complex multistage metasomatic history. Geochemical studies on peridotites from continental massifs such as Lherz (Fabriès *et al.* 1989, 1991; Bodinier *et al.* 2004) or Ronda (Garrido & Bodinier 1999) have demonstrated that percolation of basaltic melts can affect the mantle rocks on a kilometre scale and that processes involving porous melt flow and chromatographic effects can lead to extreme trace element fractionations in low-temperature, small melt fractions away from the melt source in the upper part of the mantle column. However, in the lower part of the column, close to the melt source, metasomatism by a large volume of silicate melt is likely to result in almost complete re-equilibration of the peridotites with the infiltrating melt. For mantle xenoliths in alkali basalts, we rarely know the spatial relationships between melt source and the metasomatized peridotite so that any direct relationship between trace element fractionation and distance from a melt source is difficult to assess. None the less, Bedini *et al.* (1997), on the basis of relationships between equilibration temperatures, microstructures and geochemical indicators in mantle xenoliths, argued for kilometre-scale percolation in the lithospheric mantle beneath the East African rift.

In the Syrian xenolith suite, there is no relationship between the equilibration temperatures and the microstructures of group I, II and III harzburgites (Table 1), which indicates that all the xenoliths have been sampled from similar depths and that metasomatism affected a heterogeneous residual protolith as shown by the heterogeneous mineral major element compositions and HREE contents in groups II and III. Therefore, it is unlikely that the geochemical fingerprints in this xenolith suite are the result of a kilometre-scale process along a lithospheric mantle column as in Ethiopia. None the less, can group II and III harzburgites result from a single metasomatic event at a shorter distance? Ionov *et al.* (2002) and Bodinier *et al.* (2004) showed that a variety of trace element enrichments can be achieved during a single metasomatic event as a result of chromatographic fractionation during porous melt flow. In this view, harzburgites from group II would be located closer to the melt source (in the vicinity of magma intrusions or magma pathways) as they reacted with larger melt fractions, and harzburgites from group I and III would be situated away from the melt source and affected only by smaller evolved (volatile-rich or not) melt fractions. This would imply that the different types of metasomatism could all be contemporaneous and derivatives of the same original silicate melt source. If such a mechanism is viable, we cannot rule out that group II and III harzburgites have been affected by different metasomatic media at different times. In particular, volcanism in southern Syria (Harrat Ash Shaam) seems to have been continuous since Miocene time, and therefore we cannot discard the possibility of a multistage metasomatic history. To better constrain these hypotheses, a larger set of mantle xenoliths from different locations in northern Syria should be considered in relation to the timing of eruption of the volcanoes in which they are found.

Origin of the reaction zones and glass. The glasses in samples IT10, IT47, IT49 and 23Th (wehrlite), and 30Th and 37Th (harzburgites group IIIA clinopyroxene) have silicic (54.57–62.84 wt%), sodic (4.76–14.85 wt%), calcic (0.4–8.57) and

aluminous (20.59–25.36 wt%) compositions (Figs 6 and 7). The formation of glass in mantle xenoliths has been widely studied (Frey & Green 1974; Francis 1976; Stoch & Seck 1980; Chazot *et al.* 1996; Neumann & Wulff-Pedersen 1997; Yaxley *et al.* 1997; Coltorti *et al.* 1999, 2000) and can be attributed to various processes.

Experimental studies on low-degree melting of peridotite have shown that silicic, aluminous and alkaline melts are in equilibrium with lherzolitic and harzburgitic mineralogy at 1–3 GPa and between 850 and 1350 °C (Draper & Green 1997, 1999). In Figure 6, the glasses have commonly higher Na_2O, CaO, FeO^T and Al_2O_3, much lower K_2O, and somewhat lower SiO_2 than experimental results of Draper & Green (1997, 1999). Therefore, small degrees of partial melting of the lherzolites and harzburgites do not seem to be a realistic mechanism to explain the origin of these glasses.

Can reaction zones originate from infiltration of the host basalt? In Figure 7, the glass compositions encompass the field of trachy-andesites and trachytes but are very different from basalts or basanites from the Tel Tannoun xenolith locality or from Jabel El Arab in terms of SiO_2 and $Na_2O + K_2O$ (Fig. 7). Moreover, petrographic evidence for infiltration of host lava has not been observed in the xenolith suite. Therefore, we discard the possibility that the glasses formed as a result of the host lava infiltration.

The occurrence of amphibole in the reaction zones of harzburgites IT10 and IT49 in disequilibrium with the surrounding silicate matrix (Fig. 3a) can be taken as evidence that part of the glass formed from breakdown of pre-existing amphibole during transport to the surface (Frey & Green 1974; Francis 1976; Stoch & Seck 1980; Chazot *et al.* 1996; Yaxley *et al.* 1997). In this case, glasses would have formed by *in situ* melting of amphibole in a closed system as a result of heating. If so, one would expect the Na_2O/K_2O ratios of the glasses to be similar to that of the residual amphibole in the reaction zone. In Figure 12, glasses in those reaction zones have heterogeneous Na_2O/K_2O ratios varying between 12.6 and 31.6, owing to their heterogeneous and very high Na contents (up to 14.85 wt%), whereas those of residual amphiboles are homogeneous and much lower (4.3–4.4). They also span a large range of FeO^T/MgO ratios, varying from a ratio close to that of the residual amphibole to much higher ratios (0.3–4.8). This evolution is consistent with subsequent fractional crystallization of magnesian olivine and and Mg–Cr-rich spinel from the partial melt (Ol II Mg-number 92.1–93.4, Sp II Mg-number 65.9–91.5; Tables 2 and 5), which will rapidly deplete the melt in MgO. However, the enrichment in Na_2O cannot be realistically explained by

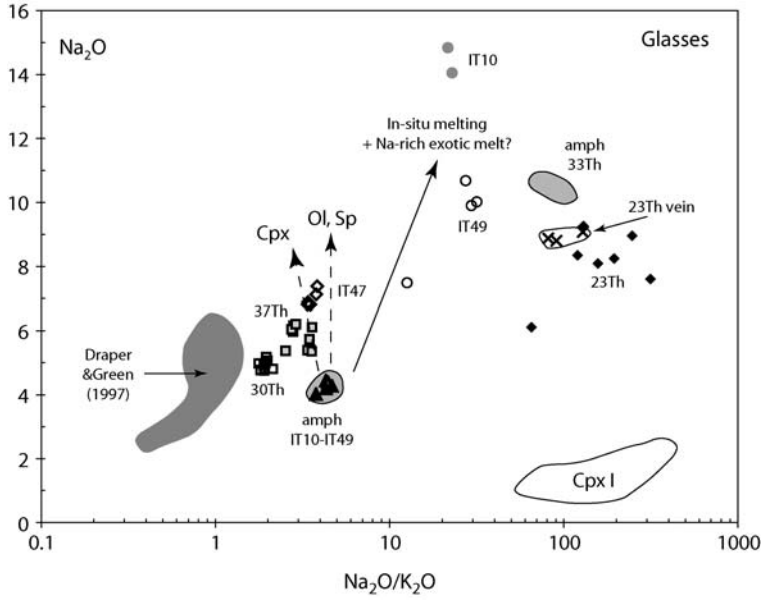

Fig. 12. (Na_2O/K_2O) v. Na_2O for glasses from Syrian xenoliths. Dashed arrows represent the effects on a melt with the composition of residual amphibole of subsequent fractionating olivine, spinel and clinopyroxene. The conticuous-line arrow represents the combined effect of *in situ* melting of amphibole in harzburgites IT10 and IT49 triggered by infiltration of a Na-rich metasomatic agent to produce high Na_2O/K_2O.

subsequent fractional crystallization of secondary clinopyroxenes (Cpx II, Table 4) as it would not increase the Na_2O/K_2O ratio of the melt by a factor of almost 10 (Fig. 12), or possibly after almost complete crystallization of the partial melt in the reaction zone. This is not supported by the petrographic observation and it implies that *in situ* melting of pre-existing amphibole cannot satisfactorily explain the glass compositions in harzburgites IT10 and IT49. Alternatively, these sodic glasses could be explained by addition of an exotic Na-rich (and K- and Ca-poor) melt to these harzburgites, which triggered partial melting of the pre-existing amphiboles. Such Na-rich metasomatic fluid or melt may have originated by melting of amphibole or incongruent melting of clinopyroxene in the nearby lithospheric mantle, but at present we cannot assess its origin.

In anhydrous samples (23Th, 30Th, 37Th and IT47), an origin of the glass in reaction zones by *in situ* melting during decompression of a former hydrous mineral (amphibole or phlogopite) is not supported, as no relics of such minerals have been found. None the less, a metasomatic agent resulting from a small degree of partial melting of pre-existing amphibole may have invaded the xenoliths shortly before eruption, reacted with the primary mineralogy and produced the reaction zones in anhydrous xenoliths. The composition of glasses in reaction zones and veins of the wehrlite supports this idea, as these glasses they display Na_2O/K_2O ratios and TiO_2 contents very similar to those of amphiboles in harzburgite 33Th (Fig. 12, Table 7). Similarly, glass compositions in anhydrous harzburgite IT47 and 37Th have Na_2O/K_2O ratios very similar to those of residual amphiboles in IT10 and IT49 (Table 6 and 7). The decrease in CaO and FeO^T, and increase in Na_2O without clear trends in other major elements in these glasses (Figs 6 and 12) is accounted for by subsequent fractional crystallization of mainly clinopyroxene (Cpx II, Table 4) with only minor olivine (Ol II) and spinel (Sp II) from the metasomatic melt.

Overall, the major element compositions of the glasses in hydrous and anhydrous xenoliths support a major role of melting of pre-existing amphibole in producing small melt fractions now recorded as reaction zones in xenoliths. In hydrous xenoliths, it is clear that *in situ* melting of amphibole has contributed to the glass composition, but melting has certainly been triggered by infiltration of a Na-rich metasomatic agent, which in turn may be derived from earlier melting of pre-existing amphibole or incongruent melting of clinopyroxene in the nearby lithospheric mantle. Support for percolation of these small melt fractions is given by the reaction zones in anhydrous xenoliths, in which the glasses also appear to require a source that contains amphibole. The occurrence of reaction zones in the three groups of harzburgites, irrespective of the clinopyroxene major and trace element compositions, indicates that the infiltration of these small fractions of silicate melt occurred shortly before entrapment in the host lava, and after metasomatism that re-enriched the trace element compositions of clinopyroxenes in group II and III harzburgites. The large difference in composition between Cpx I and Cpx II (Fig. 4) shows that the major and trace element enrichments in Cpx I predate the very late metasomatic event that produced the wehrlitic reaction zones. The last metasomatic event could be the precursor of magmas that entrained the xenoliths and may be related to the youngest Quaternary basanitic volcanic activity. A more detailed study of these reaction zones, including the determination of trace elements in residual amphiboles, glass patches and secondary clinopyroxenes, would help to clarify the origin of the glasses in the Syrian xenoliths.

Conclusions

The conclusions from this study are as follows.

(1) The mineralogical and geochemical data on the Syrian xenolith suite indicate a complex history involving polybaric partial melting at various degrees ($<20\%$) that started in the garnet stability field and continued in the spinel stability field. These xenoliths were further metasomatized by percolating silicate melts.

(2) Some harzburgites (group II) have mineralogical and geochemical compositions indicating a near-re-equilibration with a silicate melt at a relatively high melt/rock ratio, which increased the incompatible trace element abundances while not significantly affecting their major element compositions.

(3) Some harzburgites (group III) have mineralogical and geochemical compositions indicative of metasomatism by small silicate melt fractions, resulting in major element enrichments and selective trace element enrichments in the associated clinopyroxene (high LREE/HREE, but low HFSE). Some of these clinopyroxenes have geochemical fingerprints comparable with metasomatism by carbonate-rich melts.

(4) The occurrence of geochemical fingerprints commonly seen in mantle xenoliths metasomatized by carbonatitic melts can be attributed to progressive reaction and crystallization of an original volatile-bearing silicate melt with the residual peridotites. This led to the generation of CO_2-rich small melt fractions but does not imply metasomatism by a mantle-derived carbonatite.

(5) The occurrence of reaction zones filled with secondary cpx + ol + sp + glass in anhydrous and hydrous xenoliths indicates the percolation of small silicate melt fractions shortly before eruption. The composition of glass supports the idea that these melts originate from partial melting of amphibole in the nearby lithospheric mantle and subsequent fractional crystallization of cpx, ol and sp in reaction zones.

We would like to thank H. Bertrand, F. Sheleh and J. Touret for contributing samples for this study, C. Perrache and C. Laboussière for the polished thin and thick sections, CROUS and Jean Monnet Université-Saint-Etienne (UMR CNRS 6524 'Magmas et Volcans'), Damascus University (F. Sheleh) and Alep (A. Matar) for their assistance during fieldwork. We thank the reviewers H. Downes and B. J. Upton for constructive comments that helped improve the paper, as well as constructive comments from the editor M. Coltorti.

References

AL-MISHWAT, A. T. & NASIR, S. J. 2004. Composition of the lower crust of the Arabian plate: a xenolith perspective. *Lithos*, **72**, 45–48.

BAKER, J. A., MENZIES, M. A., THIRLWALL, M. F. & MCPHERSON, C. G. 1997. Petrogenesis of Quaternary intraplate volcanism, Sana'a, Yemen; implications for plume–lithosphere interaction and polybaric melt hybridization. *Journal of Petrology*, **38**, 1359–1390.

BEDINI, R. M., BODINIER, J. L., DAUTRIA, J. M. & MORTEN, L. 1997. Evolution of LILE-enriched small melt fractions in the lithospheric mantle: a case study from the East African Rift. *Earth and Planetary Science Letters*, **153**, 67–83.

BILAL, A. & SHELEH, F. 2004. Un 'point chaud' sous le système du rift Syrien: données pétrologiques complémentaires sur les enclaves du volcanisme récent. *Comptes Rendus Géoscience*, **366**, 197–204.

BILAL, A. & TOURET, J. L. R. 2001. Les enclaves du volcanisme récent du rift Syrien. *Bulletin de la Société Géologique de France*, **172**, 1–14.

BODINIER, J. L., MENZIES, M. A., SHIMIZU, N., FREY, F. A. & MCPHERSON, E. 2004. Silicate hydrous and carbonate metasomatism at Lherz, France: Contemporaneous derivatives of silicate melt–harzburgite reaction. *Journal of Petrology*, **45**, 299–320.

BOHANNON, R. G., NAESER, C. W., SCHMIDT, D. L. & ZIMMERMANN, R. A. 1989. The timing of uplift, volcanism, and rifting peripheral to the Red Sea; a case for passive rifting? *Journal of Geophysical Research B*, **94**, 1683–1701.

BOYD, F. R. 1989. Compositional distinction between oceanic and cratonic lithosphere. *Earth and Planetary Sciences Letters*, **96**, 15–26.

BREY, G. P. & KÖHLER, T. K. 1990*a*. Geothermobarometry in four-phase lherzolites I. Experimental results from 10 to 60 kb. *Journal of Petrology*, **31**, 1313–1352.

BREY, G. P. & KÖHLER, T. K. 1990*b*. Geothermobarometry in four-phase lherzolites II. New thermobarometers, and practical assessment of existing thermometers. *Journal of Petrology*, **31**, 1353–1378.

BRUNELLI, D., SEYLER, M., CIPRIANI, A., OTTOLINI, L. & BONATTI, E. 2006. Discontinous melt extraction and weak refertilization of mantle peridotites at the Vema lithospheric section (Mid-Atlantic Ridge). *Journal of Petrology*, **47**, 745–771.

CAMP, V. E. & ROOBOL, M. J. 1989. The Arabian continental alkali basalt province: part I. Evolution of Harrat Rahat, Kingdom of Saudi Arabia. *Geological Society of America Bulletin*, **101**, 71–95.

CHAZOT, G., MENZIES, M. & HARTE, B. 1996. Silicate glasses in spinel lherzolite from Yemen: origin and chemical composition. *Chemical Geology*, **134**, 159–179.

CHOROWICZ, J., DHONT, D., AMMAR, O., RUKIEH, M. & BILAL, A. 2005. Tectonics of the Pliocene Homs basalts (Syria) and implications for the Dead Sea Fault Zone activity. *Journal of the Geological Society, London*, **162**, 259–271.

COLTORTI, M., BONADIMAN, C., HINTON, R. W., SIENA, F. & UPTON, B. G. J. 1999. Carbonatite metasomatism of the oceanic upper mantle: evidence from clinopyroxenes and glasses in ultramafic xenoliths of Grande Comore, Indian Ocean. *Journal of Petrology*, **40**, 133–165.

COLTORTI, M., BECCALUVA, L., BONADIMAN, C., SALVINI, L. & SIENA, F. 2000. Glasses in mantle xenoliths as geochemical indicators of metasomatic agents. *Earth and Planetary Science Letters*, **183**, 303–320.

COLTORTI, M., BECCALUVA, L., BONADIMAN, C., FACCINI, B., NTAFLOS, T. & SIENA, F. 2004. Amphibole genesis via metasomatic reaction with clinopyroxene in mantle xenoliths from Victoria Land, Antarctica. *Lithos*, **75**, 115–139.

COLTORTI, M., BONADIMAN, C., FACCINI, B., NTAFLOS, T. & SIENA, F. 2007. Slab melt and intraplate metasomatism in Kapfenstein mantle xenoliths (Styrian Basin, Austria). *Lithos*, **94**, 66–89.

DALTON, J. A. & WOOD, B. J. 1993. The compositions of primary carbonate melts and their evolution through wallrock reaction in the mantle. *Earth and Planetary Science Letters*, **119**, 511–525.

DAWSON, J. B. 2002. Metasomatism and partial melting in upper-mantle peridotite xenoliths from the Lashaine volcano, Northern Tanzania. *Journal of Petrology*, **43**, 1749–1777.

DELPECH, G., GRÉGOIRE, M., O'REILLY, S. Y., COTTIN, J. Y., MOINE, B. N., MICHON, G. & GIRET, A. 2004. Feldspar from carbonate-rich silicate metasomatism in the shallow oceanic mantle under Kerguelen Islands (South Indian Ocean). *Lithos*, **75**, 209–237.

DRAPER, D. S. & GREEN, T. H. 1997. *P–T* phase relations of silicic, alkaline, aluminous mantle-xenolith glasses under anhydrous and C–O–H fluid-saturated conditions. *Journal of Petrology*, **38**, 1187–1224.

DRAPER, D. S. & GREEN, T. H. 1999. *P–T* phase relations of silicic, alkaline, aluminous liquids: new results and applications to mantle melting and metasomatism. *Earth and Planetary Science Letters*, **170**, 255–268.

DUBERTRET, L. 1933. Les grandes nappes basaltiques Syriennes: âge et relations avec la tectonique. *Bulletin de la Société Géologique de France*, **3**, 178–180.

FABRIÈS, J., BODINIER, J. L., DUPUY, C., LORAND, J. P. & BENKERROU, C. 1989. Evidence for modal metasomatism in the orogenic spinel lherzolite body from Caussou (Northeastern Pyrenees, France). *Journal of Petrology*, **30**, 176–199.

FABRIÈS, J., LORAND, J. P., BODINIER, J. L. & DUPUY, C. 1991. Evolution of the upper mantle beneath the Pyrenees: Evidence from orogenic spinel lherzolite massifs. *Journal of Petrology*, Special Issue 'Orogenic Lherzolite and Mantle Processes', 55–76.

FRANCIS, D. M. 1976. Amphibole pyroxenite xenoliths cumulate or replacement phenomena from the upper mantle, Nunivak Island, Alaska. *Contributions to Mineralogy and Petrology*, **58**, 51–61.

FREY, F. A. & GREEN, D. H. 1974. The mineralogy, geochemistry and origin of lherzolite inclusions in Victorian basanites. *Geochimica et Cosmochimica Acta*, **38**, 1023–1059.

FREY, F. A. & PRINZ, M. 1978. Ultramafic inclusions from San Carlos, Arizona. Petrologic and geochemical data bearing on their petrogenesis. *Earth and Planetary Science Letters*, **38**, 1023–1054.

FREZZOTTI, M. L., ANDERSEN, T., NEUMAN, E. R. & SIMONSEN, S. L. 2002. Carbonatite melt CO_2 fluid inclusions in mantle xenoliths from Tenerife, Canary Islands: a story of trapping, immiscibility and fluid–rock interaction in the upper mantle. *Lithos*, **64**, 77–96.

GARRIDO, C. & BODINIER, J. L. 1999. Diversity of mafic rocks in the Ronda peridotite: evidence for pervasive melt–rock reaction during heating of subcontinental lithosphere by upwelling asthenosphere. *Journal of Petrology*, **40**, 729–754.

GRÉGOIRE, M., MOINE, B. N., O'REILLY, S. Y., COTTIN, J. Y. & GIRET, A. 2000. Trace element residence and partitioning in mantle xenoliths metsomatized by alkaline and carbonate-rich melt (Kerguelen Islands, Indian Ocean). *Journal of Petrology*, **41**, 477–509.

GRÉGOIRE, M., BELL, D. R. & LE ROEX, A. P. 2002. Trace element geochemistry of phlogopite-rich mafic mantle xenoliths: their classification and their relationship to phlogopite-bearing peridotite and kimberlites revisited. *Contributions to Mineralogy and Petrology*, **142**, 603–625.

GRIFFIN, W. L., O'REILLY, S. Y., RYAN, C. G., GAUL, O. & IONOV, D. A. 1998. Secular variation in the composition of subcontinental lithospheric mantle. *In*: BRAUN, J., DOOLEY, J. C., GOLEBY, B. R., VAN DER HILST, R. D. & KLOOTWIJK, C. T. (eds) *Structure and Evolution of the Australian Continent*. Geodynamics series, American Geophysical Union, Washington, **26**, 1–26.

HAURI, E. H., SHIMIZU, N., DIEU, J. J. & HART, S. R. 1993. Evidence for hotspot-related carbonatite metasomatism in the oceanic upper mantle. *Nature*, **365**, 221–227.

HELLEBRAND, E., SNOW, J. E., HOPPE, P. & HOFMANN, A. W. 2002. Garnet-field melting and late-stage refertilization in 'residual' abyssal peridotites from the Central Indian Ridge. *Journal of Petrology*, **43**, 2305–2338.

IONOV, D. A., HOFMANN, A. W. & SHIMIZU, N. 1994. Metasomatism induced melting in mantle xenoliths from Mongolia. *Journal of Petrology*, **35**, 753–785.

IONOV, D. A., BODINIER, J. L., MUKASA, S. B. & ZANETTI, A. 2002. Mechanisms and sources of mantle metasomatism: major and trace element compositions of peridotite xenoliths from Spitsbergen in the context of numerical modelling. *Journal of Petrology*, **43**, 2219–2259.

JOHNSON, K. T. M., DICK, H. J. B. & SHIMIZU, N. 1990. Melting in the oceanic upper mantle: an ion microprobe study of diopside in abyssal peridotites. *Journal of Geophysical Research*, **95**, 2661–2678.

KELEMEN, P. B. 1990. Reaction between ultramafic rock and fractionating basaltic magma I. Phase relations, the origin of calc-alkaline magma series, and the formation of discordant dunite. *Journal of Petrology*, **31**, 51–98.

KUO, L.-C. & ESSENE, E. J. 1986. Petrology of spinel harzburgite xenoliths from the Kishb Plateau, Saudi Arabia. *Contributions to Mineralogy and Petrology*, **93**, 335–346.

LAURORA, A., MAZZUCCHELLI, M., RIVALENTI, G., VANNUCCI, R., ZANETTI, A., BARBIERI, M. A. & CINGOLANI, C. A. 2001. Metasomatism and melting in carbonated peridotite xenoliths from the mantle wedge: The Gobernador Gregores case (Southern Patagonia). *Journal of Petrology*, **42**, 69–87.

LAWS, E. & WILSON, M. 1997. Tectonics and magmatism association with Mesozoic passive continental margin development in the Middle East. *Journal of the Geological Society, London*, **154**, 459–464.

LEAKE, B. E., WOOLLEY, A. R., ARPS, C. E. S. *ET AL.* 1997. Nomenclature of amphiboles, report of the Subcommittee on Amphiboles of the International Mineralogical Association Commission on new minerals and mineral names. *Mineralogical Magazine*, **61**, 295–321.

LE BAS, M. J., LE MAITRE, R. W., STRECKEISEN, A. & ZANETTIN, B. A. 1986. Chemical classification of volcanic rocks based on the total alkali–silica diagram. *Journal of Petrology*, **27**, 745–750.

LUSTRINO, M. & SHARKOV, E. 2006. Neogene volcanic activity of western Syria and its relationship with Arabian plate kinematics. *Journal of Geodynamics*, **42**, 115–139.

MCCLUSKY, S., BALASSANIAN, S., BARKA, A. *ET AL.* 2000. Global positioning system constraints on plate kinematics and dynamics in the eastern Mediterranean and Caucasus. *Journal of Geophysical Research*, **105**, 5695–5719.

MCDONOUGH, W. F. & SUN, S.-S. 1995. The composition of the Earth. *Chemical Geology*, **120**, 223–253.

MEDARIS, L. G. & SYADA, G. 1998. Spinel peridotite xenoliths from the Al Ashaer volcano, Syria: A contribution to the elemental composition and thermal state of subcontinental Arabian lithosphere. *International Geology Review*, **40**, 305–324.

MENZIES, M. A. & HAWKESWORTH, C. J. 1987. Upper mantle processes and composition. *In*: NIXON, P. H. (eds) *Mantle Xenoliths*. Wiley, Chichester, 725–738.

MERCIER, J. C. C. & NICOLAS, A. 1975. Textures and fabrics of upper-mantle peridotites as illustrated by

xenoliths from basalts. *Journal of Petrology*, **16**, 454–487.

MOINE, B. N., GRÉGOIRE, M., O'REILLY, S. Y., SHEPPARD, S. M. F. & COTTIN, J. Y. 2001. High field strength element (HFSE) fractionation in the upper mantle: evidence from amphibole-rich composite mantle xenoliths from the Kerguelen Islands (Indian Ocean). *Journal of Petrology*, **42**, 2145–2167.

MOINE, B. N., GRÉGOIRE, M., O'REILLY, S. Y. *ET AL.* 2004. Carbonatite melt in oceanic upper mantle beneath the Kerguelen Archipelago. *Lithos*, **75**, 239–252.

MOUTY, M., DELALOYE, M., FONTIGNIE, D., PISKIN, O. & WAGNER, J. 1992. The volcanic activity in Syria and Lebanon between Jurassic and Actual. *Schweizerische Mineralogische und Petrographische Mitteilungen*, **72**, 91–105.

NASIR, S. 1994. Geochemistry and petrogenesis of Cenozoic volcanic rocks from northwestern part of the Arabian continental alkali basalt province. *Journal of African Geoscience Reviews*, **1**, 455–467.

NASIR, S. & SAFARJALANI, A. 2000. Lithospheric petrology beneath the northern part of the Arabian plate in Syria: evidence from xenoliths in alkali basalts. *Journal of African Earth Science*, **30**, 149–168.

NEUMANN, E. R. & WULFF-PEDERSEN, E. 1997. The origin of highly silicic glass in mantle xenoliths from the Canary Islands. *Journal of Petrology*, **38**, 1513–1539.

NORMAN, M. D. 1998. Melting and metasomatism in the continental lithosphere: laser ablation ICPMS analysis of minerals in spinel lherzolites. *Contributions to Mineralogy and Petrology*, **130**, 240–255.

O'REILLY, S. Y. & GRIFFIN, W. L. 1988. Mantle metasomatism beneath western Victoria, Australia, I: Metasomatic processes in Cr-diopside lherzolites. *Geochimica et Cosmochimica Acta*, **52**, 433–447.

PONIKAROV, V. P. 1967. *The Geology of Syria, explanatory notes on the geologic map of Syria, scale 1:500 000: part I. Stratigraphy, igneous rocks and tectonics*. Ministry of Industry, Damascus.

SEN, G. 1988. Petrogenesis of spinel lherzolites and pyroxenites suite xenoliths from the Koolau shield, Oahu, Hawaii: implications for petrology of the post-eruptive lithosphere beneath Oahu. *Contributions to Mineralogy and Petrology*, **10**, 61–91.

SEYLER, M. & BONATTI, E. 1997. Regional-scale melt–rock interaction in lherzolitic mantle in the Romanche Fracture Zone (Atlantic Ocean). *Earth and Planetary Science Letters*, **146**, 273–287.

SHAW, J. E., BAKER, J. A., MENZIES, M. A., THIRLWALL, M. F. & IBRAHIM, K. M. 2003. Petrogenesis of the largest intraplate volcanic field on the Arabian plate (Jordan): a mixed lithosphere–asthenosphere source activated by lithospheric extension. *Journal of Petrology*, **44**, 1657–1679.

STEIN, M. & HOFMANN, A. W. 1992. Fossil plume head beneath the Arabian lithosphere? *Earth and Planetary Science Letters*, **114**, 193–209.

STEIN, M. & KATZ, A. 1989. The composition of the subcontinental lithosphere beneath the Israel; inferences from peridotitic xenoliths. *Israel Journal of Earth Sciences*, **38**, 75–87.

STEIN, M., GARFUNKEL, Z. & JAGOUTZ, E. 1993. Chronothermometry of peridotitic and pyroxenitic xenoliths: Implications for the thermal evolution of the Arabian lithosphere. *Geochimica et Cosmochimica Acta*, **57**, 1325–1337.

STOCH, H. G. & SECK, H. A. 1980. Geochemistry and mineralogy of two spinel peridotite suites from Dreiser Weiher, W. Germany. *Geochimica et Cosmochimica Acta*, **44**, 457–470.

WEINSTEIN, Y., NAVON, O., ALTHERR, R. & STEIN, M. 2006. The role of lithospheric mantle heterogeneity in the generation of Plio-Pleistocene alkali basaltic suites from NW Harrat Ahaam (Israel). *Journal of Petrology*, **47**, 1017–1050.

WELLS, P. R. A. 1977. Pyroxene thermometry in simple and complex system. *Contributions to Mineralogy and Petrology*, **62**, 129–139.

WULFF-PEDERSEN, E., NEUMANN, E. R. & JENSEN, B. B. 1996. The upper mantle under La Palma, Canary Islands: formation of Si–K–Na-rich melt and its importance as a metasomatic agent. *Contributions to Mineralogy and Petrology*, **125**, 113–139.

WYLLIE, P. J. & HUANG, W. L. 1976. Carbonatite and melting reaction in the system $CaO–MgO–SiO_2$ at mantle pressures with geophysical and petrological applications. *Contributions to Mineralogy and Petrology*, **54**, 79–107.

XU, Y. G., MENZIES, M. A., BODINIER, J. L., BEDINI, R. M., VROON, P. & MERCIER, J.-C. C. 1998. Melt percolation and reaction atop a plume: evidence from the poikiloblastic peridotite xenoliths from Borée (Massif Central, France). *Contributions to Mineralogy and Petrology*, **132**, 65–84.

YAXLEY, G. M., CRAWFORD, A. J. & GREEN, D. H. 1991. Evidence for carbonatite metasomatism in spinel peridotite xenoliths from western Victoria, Australia. *Earth and Planetary Science Letters*, **107**, 305–317.

YAXLEY, G. M., KAMENETSKY, V., GREEN, D. H. & FALLOON, T. J. 1997. Glass in mantle xenoliths from western Victoria, Australia, and their relevance to mantle processes. *Earth and Planetary Science Letters*, **148**, 433–446.

YAXLEY, G. M., GREEN, D. H. & KAMENETSKY, V. 1998. Carbonatite metasomatism in Southern Australian lithosphere. *Journal of Petrology*, **39**, 1917–1930.

ZANETTI, A., MAZZUCCHELLI, M., RIVALENTI, G. & VANNUCCI, R. 1999. The Finero phlogopite peridotite massif: an example of subduction-related metasomatism. *Contributions to Mineralogy and Petrology*, **134**, 107–122.

The role of HIMU metasomatic components in the North African lithospheric mantle: petrological evidence from the Gharyan lherzolite xenoliths, NW Libya

L. BECCALUVA[1], G. BIANCHINI[1], R. M. ELLAM[2], M. MARZOLA[1], K. M. OUN[3], F. SIENA[1] & F. M. STUART[2]

[1]*Dipartimento di Scienze della Terra, Università di Ferrara, 44100 Ferrara, Italy (e-mail: bcc@unife.it)*

[2]*Isotope Geoscience Unit, Scottish Universities Environmental Research Centre, East Kilbride G75 0QF, UK*

[3]*Geology Department, Al-Fateh University, Tripoli, Libya*

Abstract: The Neogene–Quaternary alkali-basalt–hawaiite lavas of the Gharyan volcanic field (NW Libya) contain mantle xenoliths. These mostly consist of protogranular spinel lherzolites with superimposed metasomatic textures represented by reaction patches where primary orthopyroxene (opx), clinopyroxene (cpx) and spinel (sp) are the main reacting phases. The secondary parageneses include clinopyroxene (cpx2), olivine (ol2) and feldspar (feld) as reaction rims around opx, spongy-textured clinopyroxene with recrystallized portions (cpx2 $\pm$ feldspar), and brown spinel destabilized in a higher Cr/(Cr + Al) black vermicular aggregate (sp2) generally associated with feldspar microlites. Cpx2 are typically depleted in Na_2O and Al_2O_3 relative to cpx; feldspar includes both alkali-feldspar (Or 17–51) and plagioclase (An 23–64). Bulk rocks have flat heavy rare earth element (HREE) patterns (1.2–2.3 times chondrite) and are variably enriched in light REE (LREE; La_N/Yb_N up to 6.6). The constituent clinopyroxenes are characterized by flat HREE distributions (8–14.5 times chondrite) and variable LREE enrichment with La_N/Yb_N up to seven, which generally conform to the bulk-rock chemistry. Samples relatively unaffected by metasomatism have clinopyroxene Sr–Nd isotopic composition ($^{87}Sr/^{86}Sr$ down to 0.7023, $^{143}Nd/^{144}Nd$ up to 0.5139) that approaches the depleted mantle (DM), suggesting that the lithospheric mantle beneath the area underwent a long-term depletion probably by pre-Palaeozoic extraction of basic melts. The remaining samples approach $^{87}Sr/^{86}Sr$ *c.* 0.7030, $^{143}Nd/^{144}Nd$ *c.* 0.5130, with $^{206}Pb/^{204}Pb$ up to 19.66. These data imply that the causative agents of metasomatism were Na-alkali silicate melts with a clear HIMU affinity, in accordance with the isotopic signature of the host lavas ($^{87}Sr/^{86}Sr = 0.7032$, $^{143}Nd/^{144}Nd = 0.5130$, $^{206}Pb/^{204}Pb = 19.60$). This prevalent HIMU geochemical signature is comparable with that recorded in Cenozoic alkaline basic lavas and associated mantle xenoliths from other occurrences of the northern–central African lithosphere, suggesting a common regional sub-lithospheric component. The relatively low $^3He/^4He$ of the Gharyan xenoliths (5.3–6.5 R_a) indicates that this component originates within the upper mantle and is unrelated to the deep-seated mantle plume source of the Ethiopian–Yemen plateau basalts. Therefore, the Cenozoic volcanic districts of the Saharan belt could be related to smaller-scale shallow mantle upwellings (also referred to as 'hot fingers') triggered by intraplate reactivation of regional tectonic lineaments within the Pan-African cratonic basement, as a foreland reaction of the African–Europe collisional system.

In the Saharan belt of North Africa, south of the Maghrebian orogenic system, Cenozoic intraplate volcanism occurs in Morocco (Atlas), Algeria (Hoggar), in several volcanic fields in Libya and Chad (e.g. Gharyan, Jebel Haruj, Tibesti), as well as in Sudan (Jebel Marra). The distribution of this within-plate anorogenic volcanism in the north African plate is related to extensional tectonics and may be considered the surface expression of a variety of processes involving interactions between the lithosphere and the convecting mantle below. Such volcanism is associated either with localized domal basement uplifts or with the development of rift systems. It is still unclear if magma sources are homogeneous, or if each province is a distinct entity in terms of mantle geochemical components. Furthermore, it has yet to be established whether mantle plumes have any role in the production of this magmatism, and the role of pre-existing lithospheric architecture (and its far-field stress regime) in controlling the location of the major

From: COLTORTI, M. & GRÉGOIRE, M. (eds) *Metasomatism in Oceanic and Continental Lithospheric Mantle.* Geological Society, London, Special Publications, **293**, 253–277.
DOI: 10.1144/SP292.12 0305-8719/08/$15.00

volcanic districts, and their geochemical characteristics, remains unclear.

Mantle xenoliths often exhumed in alkaline volcanic rocks in these areas can provide important constraints on the composition and mineralogy of the mantle lithosphere and its role as a magma source component. Unfortunately, detailed investigations are still scarce, and in particular there are very few isotope data in the literature (Dautria *et al.* 1987, 1992; Raffone *et al.* 2001, 2004; Beccaluva *et al.* 2006*a*, *b*).

The aim of this paper is to investigate mantle xenoliths from the Gharyan district, the northernmost volcanic field of Libya (Fig. 1). Gharyan consists of a large (3000 km^2 and a few tens of metres thick) basaltic plateau of Early Eocene age characterized by magmas that are transitional in composition between tholeiitic and alkaline. Additionally, Late Eocene phonolite domes and younger (12–1 Ma) volcanic centres erupted alkaline basic melts (Liégeois *et al.* 2005, and references therein). The latter contain the peridotite xenoliths that are the subject of this paper. These mantle xenoliths display widespread pyrometamorphic textures (Siena *et al.* 1991, and references therein) and therefore may represent a convenient case study to investigate the development of metasomatic reactions and the nature of their agent of metasomatism (Coltorti *et al.* 2000).

We present new major and trace element analyses carried out both on whole rocks (X-ray fluorescence (XRF); inductively coupled plasma mass spectrometry (ICP-MS)) and minerals (*in situ* analyses by electron microprobe analysis (EMPA) and laser ablation microprobe (LAM)-ICP-MS) as well as Sr–Nd–Pb–He isotope analyses of hand-picked mineral separates. The goal is to reconstruct the compositional evolution of the lithospheric mantle beneath the area, and to interpret the observed metasomatic components in terms of geochemical fluxes between different reservoirs (e.g. lithospheric v. sub-lithospheric mantle components) on a regional scale.

Petrography, mineral and bulk-rock composition

The mantle xenoliths from Gharyan (up to 5–6 cm in size) are dominantly lherzolites that typically show protogranular textures characterized by a four-phase mineral assemblage. 'Primary' olivine, orthopyroxene, clinopyroxene and spinel are widely overprinted in pyrometamorphic domains (Fig. 2) containing spongy (sieve-textured) clinopyroxene and reaction patches with 'secondary' microcrysts of olivine, clinopyroxene, spinel and feldspar.

Primary olivine (ol) consists of large kink-banded crystals (up to 1 mm) with Fo ranging between 89.0 and 89.7. Lower Fo content (down to Fo 85.5) is recorded by olivine microcrysts

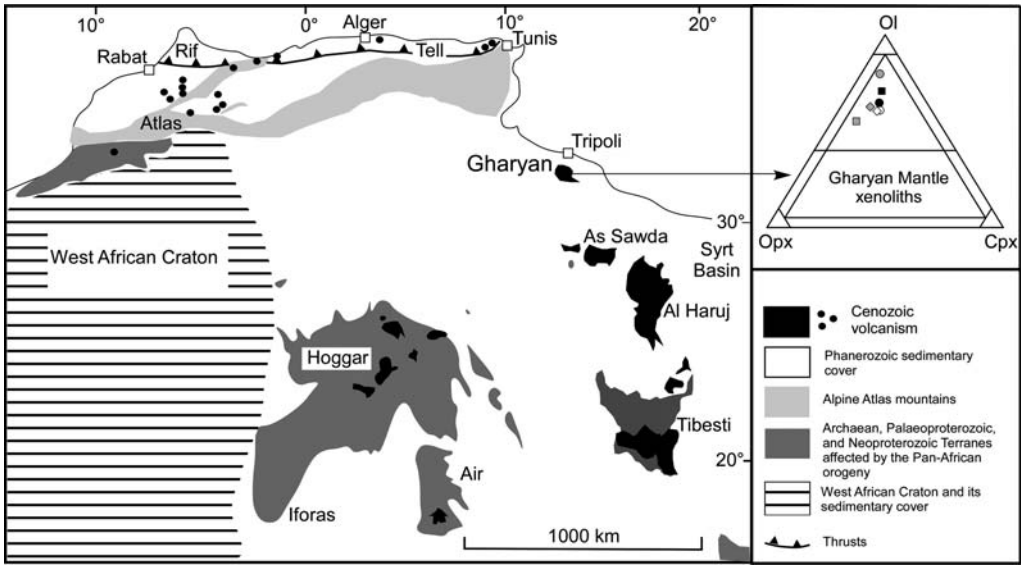

Fig. 1. Simplified geological map of North Africa indicating the locations of the main Cenozoic volcanic fields (after Liégeois *et al.* 2005, modified). Also shown is the modal composition of the Gharyan mantle xenoliths in terms of olivine (ol), orthopyroxene (opx) and clinopyroxene (cpx).

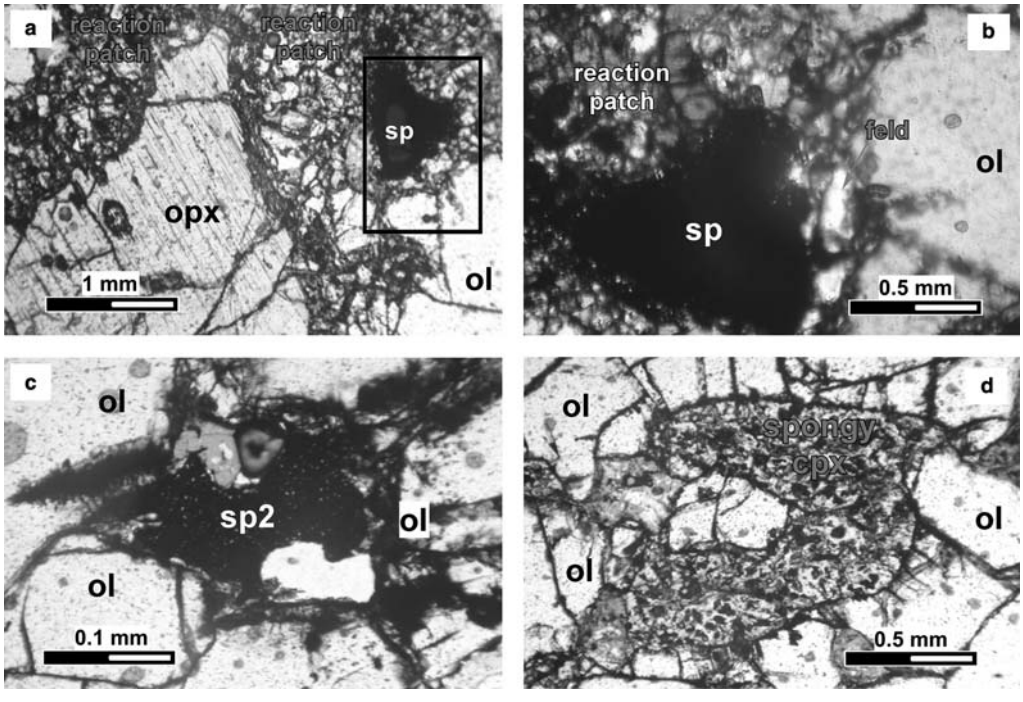

Fig. 2. Photomicrographs of Gharyan mantle xenoliths illustrating petrographic evidence of metasomatic reactions. (**a**) Destabilized orthopyroxene surrounded by a reaction aggregate of secondary olivine, clinopyroxene and feldspar, and spinel crystal with brown Al_2O_3-rich core and black high Cr-number rim; (**b**) magnification of the spinel reaction rim showing the presence of secondary feldspar; (**c**) vermicular aggregate of secondary black spinel intergrowth with feldspar; (**d**) destabilized spongy clinopyroxene surrounded by olivine crystals.

(ol2) in reaction patches. The evidence of strain and deformation in these olivine crystals, together with the absence of cumulate textures, rules out a cumulate origin of these xenoliths.

Orthopyroxene (opx) is rarely intact, usually showing 'corroded' crystal rims with reaction coronas (Fig. 2) containing complex fine-grained aggregates of secondary olivine, clinopyroxene and feldspar. 'Core' opx composition varies in the following ranges: Wo 1.0–1.7, En 87.7–89.4, Fs 9.1–10.6, with Mg-number $(Mg/(Mg + Fe))$ 0.89–0.91 and Cr-number $(Cr/(Cr + Al))$ 0.03–0.06. Enrichment in CaO (Wo up to 4.2; En down to 85.9) characterizes opx crystal rims at the interface with clinopyroxene, as recorded in sample E27A.

Clinopyroxene (cpx) shows a compositional variation in relation to its textural position. Large equilibrated diopsidic crystals are characterized by the following compositions: Wo 45.1–48.5, En 47.0–49.4, Fs 4.0–6.6, with Mg-number 0.88–0.93, Cr-number 0.04–0.09, Na_2O wt% 0.94–1.76 and TiO_2 wt% 0.3–0.6 (Fig. 3a); endiopside secondary clinopyroxene (cpx2) consists of spongy destabilized crystals (Fig. 2) and secondary microcrysts in reaction patches, typically characterized by a lower Na_2O content (down to 0.3%) sometimes associated with TiO_2 enrichment with respect to the primary compositions (Fig. 3a and b).

Spinel (sp) is typically holly-leaf or lobate in shape, and generally characterized by brown cores with Mg-number 0.78–0.82 and Cr-number 0.09–0.11, and black rims (sp2) with lower Mg-number (down to 0.44) and higher Cr-number (up to 0.73), resulting in a fine aggregate of vermicular Cr–Fe–Ti-rich spinel intergrowth with feldspar microliths (Figs 2 and 3c). Similar textures in which primary spinel crystals are progressively destabilized toward the rims have been described in other mantle xenolith suites and related to metasomatic reactions (Siena *et al.* 1991; Beccaluva *et al.* 2001*a*).

Feldspar (feld) occurs only in the reaction fine-grained patches and is not texturally equilibrated with the primary phases of the peridotite mineral assemblage. An extremely wide compositional range can be observed (even within a single sample), varying between andesine–labradorite plagioclase (An 23–64) to variously potassic alkaline feldspar (Or 17–51), and conforming with the

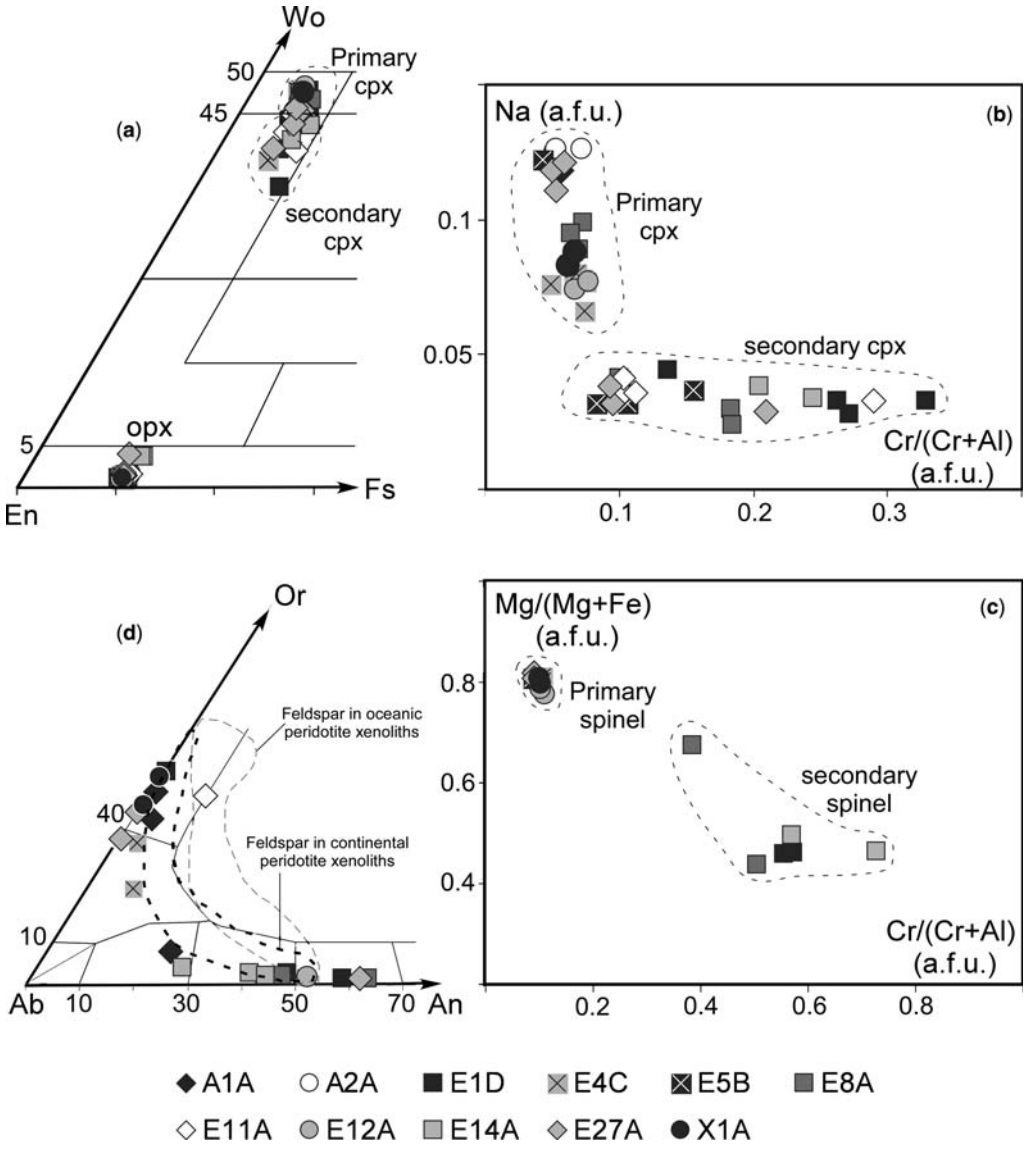

Fig. 3. Mineral compositions of Gharyan mantle xenoliths. (**a**) Wollastonite (Wo)–enstatite (En)– ferrosilite (Fs) classification diagram for pyroxenes. (**b**) Na v. Cr/(Cr + Al) for clinopyroxene and (**c**) Mg/(Mg + Fe) v. Cr/(Cr + Al) for spinel in atoms per formula units (a.f.u.). (**d**) Albite (Ab)–anorthite (An)–orthoclase (Or) classification diagram for feldspars, showing compositional fields for metasomatic feldspars in oceanic and continental peridotite xenoliths (after Bonadiman *et al*. 2005).

overall feldspar field from continental peridotite xenoliths (Fig. 3d). As recently observed in several xenolith populations (Ionov *et al.* 1999; Grégoire *et al.* 2000; Beccaluva *et al.* 2001*a*; Delpech *et al.* 2004; Bonadiman *et al.* 2005), the presence of alkali feldspar can be considered an important marker of metasomatic processes, thus precluding the interpretation of this phase as crystallized from infiltrated host-lava.

Application of the two-pyroxene geothermometer of Brey & Köhler (1990) using the composition of large equilibrated crystals from the samples least affected by secondary textures gives nominal equilibration temperatures in the range of

890–1060 °C, with the lowermost values in sample X1A and the highest in sample E5B.

Major element mass-balance calculations between the mineral phases and whole-rock composition (Tables 1 and 2; Fig. 1) indicate that all the samples are lherzolites, with the following modal abundance: ol 59–77%, opx 12–34%, cpx 8–17%, sp 1–3%.

In the Al_2O_3 v. MgO diagram of Figure 4a the Gharyan peridotites are compared with primitive mantle (PM) composition, abyssal peridotites and other xenolith suites from Cenozoic volcanic occurrences in the African plate (Hoggar; Iblean district, Sicily), and its northern Adriatic promontory represented by the Veneto Volcanic Province

Table 1. *Major (wt%) and trace element (ppm) whole-rock analyses of representative mantle xenoliths from Gharyan and their host lavas*

Type:	Lh	Lh	Lh	Lh	Lh	Lh	Lh	Host lavas		
Sample:	A2A	E1D	E11A	E12A	E14A	E27A	X1A	A2	E1	E22
SiO_2	44.80	43.33	45.27	42.88	45.55	45.19	44.94	48.04	49.83	49.73
TiO_2	0.15	0.12	0.13	0.06	0.13	0.12	0.10	2.27	1.95	1.95
Al_2O_3	3.41	2.89	3.54	2.37	3.45	3.32	3.02	14.27	15.06	14.99
FeO_{TOT}	9.29	9.23	7.19	9.29	7.64	7.36	8.01	9.91	10.41	10.51
MnO	0.15	0.16	0.13	0.14	0.14	0.13	0.14	0.16	0.16	0.16
MgO	38.33	40.55	39.68	43.14	39.81	40.65	40.27	7.93	7.95	8.05
CaO	3.54	2.98	3.57	1.95	2.79	2.81	3.29	9.69	9.65	9.62
Na_2O	0.28	0.49	0.39	0.14	0.39	0.33	0.20	5.17	3.87	3.88
K_2O	0.03	0.18	0.03	0.01	0.08	0.06	0.00	1.05	1.12	1.11
LOI								1.52		
Ni	1765	1797	1713	1974	1654	1846	1942	249	262	259
Co	111	113	110	113	105	112	115	48	49	48
Cr	2203	1707	1882	1634	1951	1939	2120	255	305	309
V	71	50	73	50	73	74	73	191	188	182
Rb	1	n.d.	n.d.	n.d.	n.d.	n.d.	n.d.	9	17	17
Ba	nd	18	14	8	7	n.d.	5	559	384	376
Sr	51	59	77	39	73	31	16	774	522	524
Sc	19.2	n.d.	19.1	13.5	18.6	18.2	21.8	18.3		23.3
Y	3.78	2.59	3.70	1.36	2.82	2.60	2.33	24.7		21.0
Zr	9.88	16.4	12.6	3.33	7.20	4.93	2.89	232		139
Hf	0.21	0.23	0.28	0.09	0.23	0.16	0.12	4.79		3.60
Nb	1.30	1.00	1.96	0.83	1.30	1.06	1.06	71.0		40.9
Ta	0.29	0.20	0.21	0.21	0.20	0.17	0.58	4.23		2.42
La	0.58	2.04	3.56	1.23	2.25	1.63	0.45	45.8		36.6
Ce	1.37	4.90	6.89	1.63	4.60	2.74	0.55	90.1		63.7
Pr	0.19	0.52	0.92	0.16	0.64	0.33	0.06	9.80		7.92
Nd	1.04	2.63	3.85	0.52	2.61	1.36	0.37	41.7		30.8
Sm	0.27	0.49	0.77	0.13	0.59	0.35	0.19	7.11		6.56
Eu	0.11	0.14	0.24	0.06	0.20	0.12	0.08	2.08		2.08
Gd	0.38	0.48	0.79	0.22	0.63	0.48	0.24	6.82		6.71
Tb	0.07	0.08	0.12	0.04	0.11	0.09	0.05	0.84		0.91
Dy	0.51	0.48	0.75	0.26	0.65	0.64	0.40	4.49		5.05
Ho	0.11	0.09	0.14	0.06	0.14	0.13	0.09	0.66		0.79
Er	0.34	0.27	0.41	0.19	0.42	0.39	0.29	1.91		2.24
Tm	0.05	0.03	0.06	0.04	0.07	0.06	0.05	0.20		0.26
Yb	0.36	0.26	0.39	0.19	0.39	0.38	0.30	1.44		1.68
Lu	0.04	0.03	0.04	0.03	0.05	0.04	0.05	0.16		0.20
Th	0.08	n.d.	0.40	0.23	0.19	0.20	0.18	6.07		4.04
U	0.06	n.d.	0.11	0.13	0.08	0.04	0.09	1.56		1.09
ol	59	69	59	77	53	61	63			
opx	22	17	23	12	34	25	20			
cpx	17	13	16	8	10	12	15			
sp	2	1	2	3	3	2	2			
feld	–	trace	trace	trace	trace	trace	trace			

Mineral modal proportions (%) of xenoliths were obtained by mass-balance calculation of bulk-rock and mineral analyses. Lh, lherzolite; ol, olivine; opx, orthopyroxene; cpx, clinopyroxene; sp, spinel; feld, feldspar; n.d., not detected; LOI, loss on ignition.

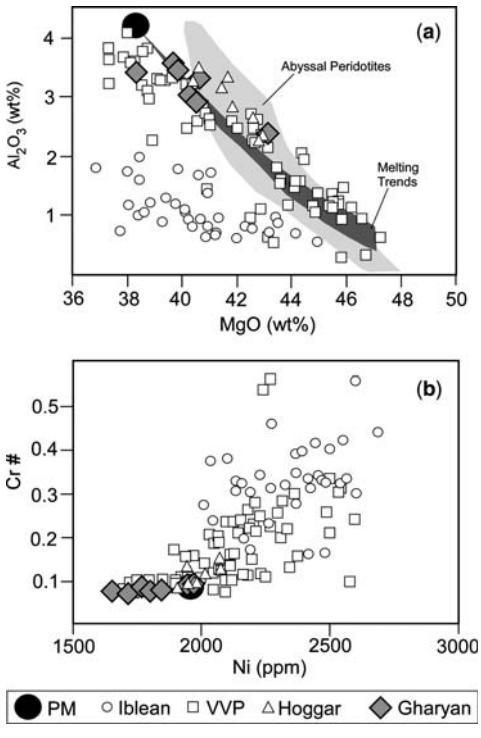

Fig. 4. Variations of Al_2O_3 v. MgO (**a**) and Cr-number ($Cr_2O_3/(Cr_2O_3 + Al_2O_3)$) v. Ni (**b**) for the Gharyan mantle xenoliths. Literature data for other mantle xenoliths from the African plate (Hoggar; Iblean district, SE Sicily) and its northern Adriatic promontory (Veneto Volcanic Province, VVP) are reported for comparison (Beccaluva *et al*. 2001*a*, 2005, 2006*a*, *b*). Also shown in (**a**) are the field for abyssal peridotites and the partial melting trends from a fertile mantle composition (PM) after Niu (1997).

(VVP; Beccaluva *et al.* 2005, references therein, and authors' unpublished data). Depletion trends by partial melting of a fertile mantle source have also been reported by Niu (1997). It should be noted that the Gharyan lherzolites are comparable with those from Hoggar, overlapping the least depleted portion of the mantle melting trend. Notably, the Gharyan mantle appears to be rather fertile, as is also supported by its relatively low Cr-number ($Cr_2O_3/(Cr_2O_3 + Al_2O_3)$) ratio as well as nickel content (Fig. 4b).

Chondrite (Ch)-normalized rare earth element (REE) patterns of Gharyan lherzolites are reported in Figure 5. It is noteworthy that nearly flat heavy rare earth element (HREE) patterns range between 1.2 and 2.3 times chondrite, with the highest and lowest content corresponding to cpx-rich (16–17%) and cpx-poor (8%) samples, respectively. This confirms that HREE are mainly concentrated

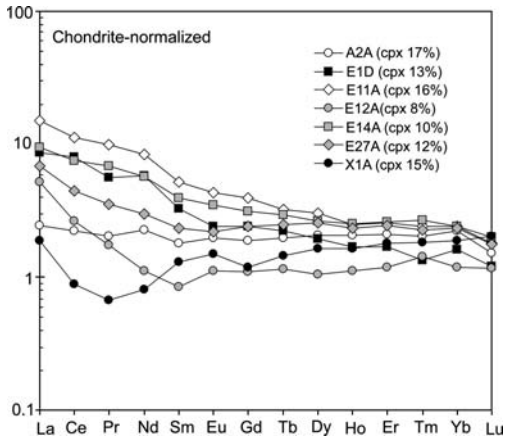

Fig. 5. Chondrite-normalized REE patterns for bulk-rock peridotite xenoliths from Gharyan. Normalizing factors after McDonough & Sun (1995).

in clinopyroxene (Bedini & Bodinier 1999; Coltorti *et al.* 1999; Beccaluva *et al.* 2001*b*), and therefore represent an indication of the depletion degree of mantle material. On the other hand, most samples show light REE (LREE) enrichments to a variable extent and shape ($La_N/Yb_N = 3–6.6$ times), which are commonly ascribed to metasomatic processes.

Pyroxene trace element composition

In situ trace element analyses represent the more reliable data to define the diverse contributions of depletion and enrichment processes as well as to recognize the possible contamination of mantle material by the host lava, which are otherwise difficult to unravel solely by whole-rock analyses.

The REE patterns of constituent clinopyroxenes are characterized by flat HREE patterns (8–14.5 times Ch) and variable LREE enrichment with La_N/Yb_N up to seven (Fig. 6; Table 3). Sample A2A has relatively flat patterns with a slight depletion in LREE (La, Ce, Pr), suggesting a comparable slight depletion of the pristine mantle domain unaffected by metasomatic enrichments. Other samples such as E4C and X1A show spoon-shaped REE patterns with HREE around nine and 11 times Ch, respectively, a significant depletion in Nd, Pr (Pr_N/Yb_N down to 0.1) and an increase in the lightest REE, particularly evident for La (La_N/Yb_N up to 1.7). These patterns can be interpreted as the result of melting episodes (and extraction of basic melts) followed by slight cryptic metasomatic processes that reintroduced the most incompatible (more mobile) elements. The remaining samples are characterized by variably enriched LREE (La_N/Yb_N up to seven)

Table 2. *Representative electron microprobe analyses of mineral phases from the Gharyan mantle xenoliths*

	A1A Lh									A2A Lh								
Mineral:	ol	ol	opx	opx	cpx	cpx	feld	feld	feld	ol	ol	opx	opx	cpx	cpx	cpx	sp	sp
Label:	1C	2H	2A	2B	1D	2I	2E	2F	2L	3A	3C	3B	3D	2A	2B	2C	1A	1B
SiO_2	40.94	41.17	55.61	55.75	52.23	52.19	61.19	65.28	66.67	41.13	41.24	55.67	55.25	52.32	52.28	52.55	0.04	0.08
TiO_2	0.02	0.02	0.10	0.12	0.47	0.55	0.26	0.25	0.25	0.03	0.00	0.16	0.12	0.53	0.63	0.60	0.17	0.19
Al_2O_3	0.04	0.02	4.43	4.27	6.37	6.62	23.13	19.19	19.34	0.01	0.07	4.63	4.64	6.81	6.58	6.72	57.03	57.40
FeO_{TOT}	10.19	10.56	6.79	6.45	3.17	3.25	0.34	0.47	0.36	10.08	10.38	7.00	6.72	3.07	3.03	3.24	12.61	11.52
MnO	0.16	0.13	0.18	0.23	0.14	0.05	0.04	0.02	0.03	0.09	0.23	0.20	0.07	0.01	0.08	0.01	0.02	0.14
MgO	48.58	48.62	32.78	32.56	15.33	15.01	0.04	0.08	0.04	48.76	49.13	32.41	32.41	15.20	15.10	15.09	20.68	20.45
CaO	0.05	0.08	0.78	0.74	19.93	20.07	4.89	0.67	0.19	0.05	0.07	0.80	0.74	19.41	19.27	19.43	0.02	0.00
Na_2O	0.00	0.00	0.13	0.16	1.72	1.69	8.08	6.11	6.01	0.05	0.03	0.05	0.14	1.78	1.79	1.80	0.00	0.01
K_2O	0.00	0.00	0.00	0.00	0.01	0.00	1.35	6.50	7.99	0.00	0.01	0.00	0.01	0.00	0.01	0.00	0.00	0.00
Cr_2O_3	0.01	0.00	0.27	0.33	0.53	0.61	–	–	–	0.03	0.01	0.23	0.28	0.57	0.77	0.56	9.15	9.43
NiO	0.01	0.01	–	–	–	–	–	–	–	0.44	0.38	–	–	–	–	–	0.43	0.34
Total	99.99	100.61	101.06	100.62	99.91	100.05	99.31	98.56	100.87	100.67	101.53	101.15	100.38	99.70	99.54	100.00	100.15	99.56

	E1D Lh													
Mineral:	ol	ol	opx	opx	cpx2	cpx2	cpx2	cpx2	cpx2	sp2	sp2	feld	feld	feld
Label:	2E	2 N	2A	2B	2C	2M	3D	5A	5C	1A	1D	1E	2L	5D
SiO_2	40.80	41.02	55.58	55.56	54.73	55.22	52.22	53.70	53.41	0.07	0.14	53.94	66.99	56.43
TiO_2	0.02	0.00	0.14	0.11	0.42	0.25	0.71	0.47	0.36	3.92	3.73	0.14	0.26	0.14
Al_2O_3	0.00	0.01	4.19	4.25	1.20	1.02	4.11	2.12	3.43	15.90	17.04	28.68	17.82	26.75
FeO_{TOT}	11.78	11.35	6.75	6.69	3.89	5.30	3.40	3.27	3.38	31.39	31.50	0.85	1.02	0.52
MnO	0.31	0.18	0.15	0.17	0.14	0.18	0.13	0.15	0.07	0.38	0.36	0.00	0.02	0.00
MgO	47.71	47.95	32.93	32.29	19.16	19.86	16.02	17.68	17.21	9.86	9.92	0.05	0.12	0.07
CaO	0.18	0.06	0.61	0.67	20.42	18.03	22.81	21.46	21.07	0.16	0.18	12.35	0.11	9.70
Na_2O	0.00	0.00	0.11	0.13	0.47	0.40	0.57	0.47	0.63	0.00	0.04	4.77	5.32	5.71
K_2O	0.00	0.00	0.00	0.02	0.02	0.01	0.03	0.00	0.00	0.00	0.00	0.21	8.48	0.44
Cr_2O_3	0.08	0.00	0.31	0.32	0.90	0.56	0.71	1.11	0.79	31.66	31.59	–	–	–
NiO	0.01	0.01	–	–	–	–	–	–	–	0.14	0.21	–	–	–
Total	100.88	100.58	100.76	100.22	101.37	100.82	100.71	100.44	100.34	93.47	94.71	101.00	100.15	99.77

(*Continued*)

Table 2. *Continued*

E4C Lh																	
Mineral:	ol	ol	opx	opx	opx	opx	opx	cpx	cpx	cpx	cpx	cpx	sp	sp	feld	feld	feld
Label:	1A	1B	1F	2B	2C	3D	6B	1G	1H	3B	4A	4B	1I	4F	6D	6E	6I
SiO_2	40.81	40.75	55.40	55.69	55.38	55.56	55.26	52.57	52.49	52.39	52.63	52.76	0.07	0.09	66.12	65.79	54.97
TiO_2	0.02	0.00	0.12	0.06	0.08	0.12	0.08	0.39	0.35	0.34	0.27	0.29	0.16	0.09	0.32	0.38	0.12
Al_2O_3	0.00	0.00	3.25	3.53	3.57	3.75	3.72	4.62	4.54	5.01	4.95	4.80	54.76	55.49	19.73	20.83	27.45
FeO_{TOT}	10.33	10.44	6.65	6.66	6.84	6.41	6.69	2.83	2.90	2.70	2.72	2.82	11.59	11.01	0.36	0.31	0.40
MnO	0.14	0.20	0.17	0.11	0.08	0.18	0.20	0.06	0.05	0.19	0.01	0.09	0.16	0.11	0.00	0.03	0.00
MgO	48.59	48.88	33.55	33.20	33.04	33.02	33.18	15.87	15.91	15.88	15.73	15.70	20.27	20.16	0.03	0.00	0.00
CaO	0.02	0.05	0.54	0.50	0.57	0.77	0.52	22.27	22.21	22.06	21.91	21.92	0.03	0.05	0.78	1.73	10.43
Na_2O	0.00	0.02	0.02	0.04	0.00	0.05	0.00	1.09	1.11	1.08	1.08	1.14	0.01	0.00	7.06	7.70	5.35
K_2O	0.00	0.00	0.00	0.00	0.03	0.01	0.00	0.00	0.00	0.04	0.00	0.01	0.00	0.01	5.86	3.93	0.28
Cr_2O_3	0.00	0.02	0.29	0.21	0.23	0.33	0.22	0.55	0.53	0.54	0.40	0.52	9.70	9.81	–	–	–
NiO	0.31	0.34	–	–	–	–	–	–	–	–	–	–	0.25	0.21	–	–	–
Total	100.20	100.70	100.01	99.99	99.84	100.20	99.89	100.30	100.19	100.24	99.71	100.05	97.01	97.02	100.24	100.70	99.01

E5B Lh														
Mineral:	ol	ol	ol2	opx	opx	opx	cpx	cpx2	cpx2	cpx2	sp	sp	feld	feld
Label:	2H	2I	3E	2E	2F	3A	3L	3G	3I	3M	2A	3B	3C	3D
SiO_2	40.63	41.05	41.08	54.86	55.09	54.53	51.91	52.27	51.62	52.96	0.07	0.10	58.24	66.69
TiO_2	0.00	0.00	0.00	0.15	0.19	0.10	0.52	0.58	0.52	0.57	0.20	0.32	0.13	0.25
Al_2O_3	0.00	0.02	0.00	4.98	4.86	4.85	7.24	3.73	4.91	2.68	55.99	57.00	26.54	18.79
FeO_{TOT}	10.06	10.27	10.20	6.64	6.69	6.46	3.57	3.62	3.25	3.27	11.83	11.57	0.46	0.71
MnO	0.08	0.25	0.22	0.06	0.14	0.22	0.08	0.10	0.13	0.10	0.09	0.16	0.00	0.03
MgO	48.61	48.74	48.23	32.77	32.32	32.84	14.62	16.91	16.57	16.92	20.48	20.77	0.11	0.70
CaO	0.06	0.03	0.29	0.81	0.74	0.78	19.34	22.00	21.88	22.86	0.00	0.03	8.88	1.36
Na_2O	0.00	0.00	0.02	0.10	0.17	0.12	1.73	0.46	0.46	0.53	0.00	0.02	6.28	6.36
K_2O	0.00	0.01	0.02	0.02	0.02	0.00	0.00	0.03	0.00	0.01	0.04	0.05	0.37	4.50
Cr_2O_3	0.00	0.00	0.12	0.27	0.21	0.30	0.48	0.65	0.67	0.73	8.35	8.15	–	–
NiO	0.01	0.01	0.01	–	–	–	–	–	–	–	0.33	0.36	–	–
Total	99.46	100.37	100.19	100.66	100.43	100.21	99.50	100.35	100.02	100.64	97.37	98.52	101.01	99.38

E8A Lh

Mineral:	ol	ol	opx	opx	cpx	cpx	cpx	cpx2	cpx2	cpx2	sp2	sp2	feld	feld	feld
Label:	3A	3B	1A	1B	2E	4A	4C	2F	4B	4D	2A	3C	2B	2D	3D
SiO_2	40.54	40.59	55.56	55.55	52.27	52.62	52.83	51.57	51.26	52.08	0.08	0.04	51.09	55.14	56.25
TiO_2	0.00	0.00	0.13	0.08	0.36	0.40	0.39	0.77	0.59	0.45	0.99	6.81	0.06	0.17	0.19
Al_2O_3	0.00	0.00	3.95	3.76	5.67	5.49	5.65	3.72	4.83	2.99	30.96	20.60	29.40	26.26	26.80
FeO_{TOT}	12.57	11.01	6.24	6.41	2.87	2.98	3.10	3.95	3.37	3.63	20.00	26.68	0.59	0.56	0.61
MnO	0.17	0.14	0.13	0.11	0.04	0.15	0.14	0.11	0.09	0.14	0.22	0.33	0.02	0.00	0.00
MgO	46.75	48.42	33.37	33.16	15.39	15.47	15.61	16.13	16.67	17.29	15.22	10.42	0.07	0.16	0.08
CaO	0.09	0.05	0.63	0.62	21.27	21.29	21.51	22.26	21.65	21.95	0.19	0.57	13.29	9.62	9.67
Na_2O	0.01	0.00	0.05	0.05	1.41	1.36	1.28	0.42	0.59	0.34	0.01	0.03	4.20	5.98	5.94
K_2O	0.01	0.00	0.01	0.00	0.00	0.00	0.02	0.00	0.00	0.00	0.00	0.01	0.21	0.35	0.33
Cr_2O_3	0.06	0.04	–	–	0.65	0.56	0.63	1.26	0.79	1.00	28.96	31.18	–	–	–
NiO	0.29	0.27	–	–	–	–	–	–	–	–	0.28	0.21	–	–	–
Total	100.49	100.51	100.19	99.78	99.93	100.31	101.17	100.19	99.84	99.87	96.92	96.88	99.12	98.83	100.21

E11A Lh

Mineral:	ol	ol	opx	opx	cpx2	cpx2	cpx2	cpx2	feld
Label:	1D	2A	1A	2D	2B	2C	2E	1G	1F
SiO_2	41.08	41.43	55.25	55.76	52.44	52.48	53.08	52.57	64.70
TiO_2	0.00	0.01	0.02	0.06	0.25	0.24	0.20	0.72	0.69
Al_2O_3	0.03	0.01	4.62	4.52	4.50	5.06	4.27	2.62	17.26
FeO_{TOT}	10.34	10.51	6.81	6.65	3.65	3.22	3.42	4.72	1.03
MnO	0.16	0.14	0.12	0.09	0.09	0.10	0.17	0.12	0.01
MgO	48.43	48.88	32.05	32.47	17.20	16.67	17.64	17.57	1.64
CaO	0.13	0.10	0.84	0.72	21.03	20.86	20.34	19.14	2.20
Na_2O	0.01	0.02	0.11	0.17	0.51	0.58	0.51	0.47	5.01
K_2O	0.00	0.00	0.01	0.01	0.01	0.00	0.00	0.00	7.80
Cr_2O_3	0.01	0.03	0.32	0.31	0.76	0.88	0.82	1.58	–
NiO	0.01	0.01	–	–	–	–	–	–	–
Total	100.20	101.15	100.14	100.76	100.45	100.08	100.43	99.51	100.35

E12A Cpx-poor Lh

Mineral:	ol	opx	opx	cpx	cpx	sp	sp	feld
Label:	1I	1B	1M	1G	1H	1C	1D	1L
SiO_2	41.36	55.85	55.89	52.61	53.40	0.04	0.04	55.08
TiO_2	0.04	0.08	0.09	0.33	0.37	0.07	0.12	0.13
Al_2O_3	0.00	3.45	3.54	4.60	4.51	55.01	54.96	27.11
FeO_{TOT}	10.48	6.82	6.55	2.91	2.96	12.69	12.50	0.62
MnO	0.14	0.19	0.12	0.12	0.13	0.05	0.12	0.00
MgO	49.14	33.13	33.29	15.67	15.75	19.35	19.63	0.12
CaO	0.05	0.53	0.54	22.53	22.01	0.03	0.02	10.82
Na_2O	0.01	0.03	0.06	1.05	1.10	0.00	0.02	5.47
K_2O	0.02	0.00	0.00	0.00	0.00	0.02	0.02	0.27
Cr_2O_3	0.02	0.28	0.22	0.49	0.57	10.07	9.38	–
NiO	0.01	–	–	–	–	0.36	0.34	–
Total	101.27	100.36	100.30	100.31	100.81	97.70	97.14	99.61

(*Continued*)

Table 2. *Continued*

	E14A Lh										
Mineral:	ol	ol2	opx	opx	cpx2	cpx2	sp2	sp2	feld	feld	feld
Label:	1A	1F	1L	1M	1E	1P	1G	1H	1C	1D	1I
SiO_2	39.79	39.93	55.15	54.29	51.76	52.76	0.14	0.20	55.65	54.70	59.79
TiO_2	0.02	0.05	0.14	0.19	0.90	0.48	3.64	4.65	0.10	0.15	0.16
Al_2O_3	0.03	0.01	2.99	2.89	2.35	2.62	19.26	10.98	26.48	26.77	24.17
FeO_{TOT}	13.66	10.46	7.25	7.03	4.80	4.21	24.81	26.37	0.53	0.84	0.40
MnO	0.23	0.10	0.14	0.19	0.13	0.07	0.21	0.31	0.00	0.01	0.00
MgO	45.36	48.33	32.15	32.09	16.77	17.83	11.12	10.03	0.04	0.31	0.00
CaO	0.10	0.06	1.93	1.95	20.87	20.11	0.16	0.57	8.34	8.94	5.70
Na_2O	0.01	0.00	0.07	0.07	0.48	0.54	0.00	0.02	6.52	6.18	7.94
K_2O	0.00	0.00	0.00	0.00	0.00	0.02	0.02	0.09	0.43	0.32	0.67
Cr_2O_3	0.00	0.02	0.39	0.34	1.14	1.00	38.27	43.57	–	–	–
NiO	0.01	0.01	–	–	–	–	0.26	0.16	–	–	–
Total	99.20	98.98	100.22	99.05	99.20	99.64	97.90	96.95	98.08	98.23	98.82

	E27A Lh															
Mineral:	ol	ol	opx	opx core	opx rim	cpx	cpx	cpx core	cpx rim	cpx2	cpx2	sp	sp	feld	feld	feld
Label:	1M	2H	1A	2A	2C	1Q	1R	2G	2E	1B	1D	1G	1H	1C	1F	2D
SiO_2	40.88	40.78	55.44	55.35	56.76	52.11	52.30	52.35	54.16	52.13	52.42	0.09	0.06	52.05	67.03	67.37
TiO_2	0.00	0.01	0.10	0.15	0.12	0.49	0.44	0.43	0.14	0.52	0.47	0.16	0.17	0.07	0.23	0.23
Al_2O_3	0.04	0.00	4.82	4.57	2.08	6.67	6.71	6.74	2.32	3.33	4.12	56.15	56.27	29.55	18.79	17.92
FeO_{TOT}	10.21	10.18	6.31	6.55	6.23	3.22	3.47	3.37	3.39	3.64	3.32	11.17	11.15	0.33	0.29	0.49
MnO	0.12	0.22	0.21	0.17	0.10	0.12	0.07	0.05	0.16	0.17	0.07	0.03	0.15	0.00	0.00	0.01
MgO	49.13	48.80	32.35	32.72	32.79	15.31	15.36	15.55	19.03	17.65	17.05	20.60	20.41	0.13	0.04	0.21
CaO	0.09	0.06	0.88	0.70	2.12	20.00	19.95	19.84	20.13	21.34	22.04	0.00	0.00	13.02	0.03	0.00
Na_2O	0.00	0.00	0.12	0.09	0.07	1.59	1.69	1.75	0.41	0.45	0.54	0.00	0.00	4.39	7.39	6.38
K_2O	0.01	0.02	0.00	0.00	0.00	0.00	0.01	0.00	0.00	0.02	0.02	0.00	0.00	0.21	6.06	6.84

Cr_2O_3	0.00	0.00	0.34	0.31	0.57	0.57	0.54	0.62	0.90	0.51	0.63	8.30	8.34	–	–	–
NiO	0.01	0.01	–	–	–	–	–	–	–	–	–	0.40	0.43	–	–	–
Total	100.50	100.08	100.58	100.60	100.83	100.08	100.54	100.71	100.64	99.77	100.69	96.90	96.99	99.76	99.86	99.45

X1A Lh

Mineral:	ol	ol	opx	opx	cpx	cpx	sp	sp	feld	feld
Label:	1A	2I	1E	2A	1B	1D	1C	2G	2D	2F
SiO_2	41.19	39.39	55.65	56.24	52.55	52.70	0.03	0.06	67.40	68.21
TiO_2	0.00	0.02	0.10	0.11	0.43	0.31	0.10	0.09	0.39	0.14
Al_2O_3	0.01	0.03	3.58	3.66	5.22	5.26	56.04	56.93	18.94	18.79
FeO_{TOT}	10.29	10.07	6.65	6.71	3.06	2.99	12.14	11.64	0.67	0.55
MnO	0.13	0.11	0.13	0.15	0.06	0.05	0.11	0.13	0.05	0.05
MgO	48.60	48.86	32.90	33.49	15.34	15.24	20.13	20.80	0.09	0.04
CaO	0.04	0.06	0.56	0.60	21.56	21.29	0.00	0.01	0.08	0.02
Na_2O	0.03	0.01	0.06	0.06	1.26	1.17	0.01	0.00	6.04	5.48
K_2O	0.00	0.00	0.00	0.00	0.00	0.00	0.00	0.00	6.92	8.22
Cr_2O_3	0.01	0.04	0.23	0.28	0.57	0.52	9.54	9.56	–	–
NiO	0.01	0.01	–	–	–	–	0.39	0.41	–	–
Total	100.31	98.60	99.86	101.29	100.05	99.54	98.50	99.63	100.58	101.50

Mineral abbreviations as in Table 1; suffix '2' refers to secondary compositions.

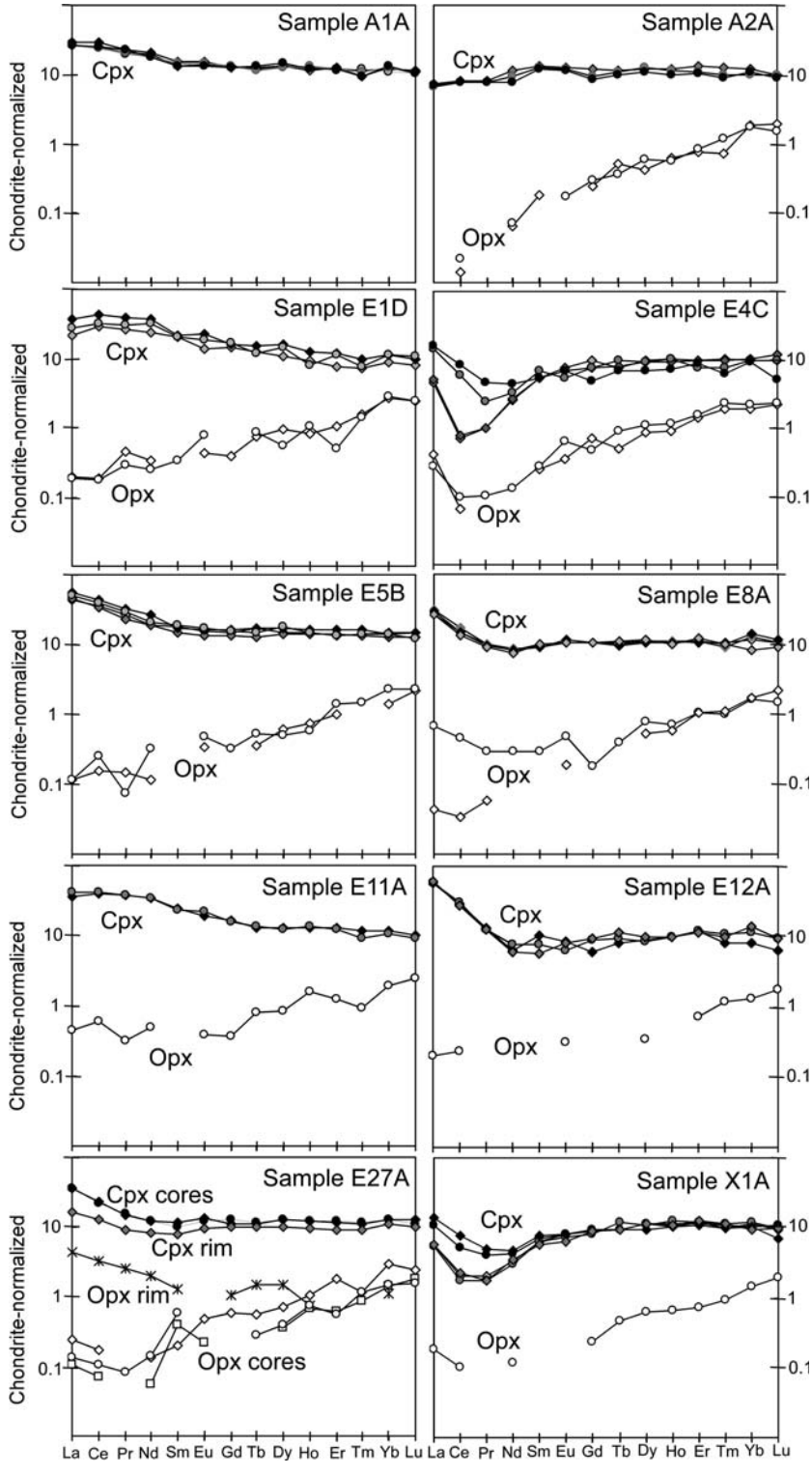

Fig. 6. Chondrite-normalized REE patterns of clinopyroxenes and orthopyroxenes from Gharyan peridotite xenoliths. Normalizing factors after McDonough & Sun (1995).

Table 3. *Representative in situ trace element analyses by LAM-ICP-MS of pyroxenes*

	A1A Lh					A2A Lh				
Mineral:	cpx	cpx	cpx	cpx	cpx	cpx	cpx	cpx	opx	opx
Label:	1A	2B	3A	3B	3C	1A	1D	1E	3B	3D
Rb	0.03	<0.01	<0.01	<0.03	<0.02	0.07	<0.02	0.03	<0.02	<0.02
Ba	0.11	0.15	0.17	<0.10	0.86	0.18	0.17	<0.04	<0.02	0.03
Sr	118	138	118	117	115	80.3	78.07	78.08	0.22	0.27
Y	18.3	18.4	17.8	17.1	16.7	18.5	15.18	14.97	0.99	1.03
Zr	32.6	31.1	31.8	31.8	30.8	29.7	26.44	27.14	1.51	1.65
Hf	1.03	1.02	0.90	0.85	0.98	0.84	0.73	0.91	0.04	0.08
Nb	1.43	1.34	1.35	1.18	1.32	0.59	0.49	0.56	0.02	0.02
Ta	0.14	0.08	0.06	0.05	0.07	0.03	0.02	0.01	<0.01	<0.01
La	6.38	6.92	6.55	6.42	6.21	1.74	1.62	1.64	<0.01	<0.01
Ce	15.3	18.2	15.0	14.9	15.8	4.97	4.81	4.84	0.01	0.01
Pr	1.95	2.15	1.83	1.89	2.08	0.76	0.73	0.70	<0.01	<0.01
Nd	8.83	9.31	8.30	8.17	8.09	5.27	4.29	3.54	0.03	0.03
Sm	1.96	2.28	2.15	2.22	1.97	2.01	1.84	1.75	0.03	<0.03
Eu	0.77	0.88	0.75	0.84	0.76	0.69	0.68	0.65	<0.01	0.01
Gd	2.61	2.54	2.58	2.62	2.54	2.38	1.85	1.68	0.05	0.06
Tb	0.44	0.46	0.43	0.42	0.47	0.40	0.40	0.36	0.02	0.01
Dy	3.31	3.28	3.22	3.14	3.60	3.02	3.05	2.71	0.11	0.15
Ho	0.65	0.69	0.71	0.74	0.66	0.66	0.64	0.55	0.03	0.03
Er	1.98	1.96	1.82	1.93	1.92	2.15	1.75	1.69	0.12	0.13
Tm	0.24	0.29	0.29	0.28	0.24	0.32	0.25	0.22	0.02	0.03
Yb	2.00	1.95	1.72	2.05	2.19	1.89	1.61	1.79	0.30	0.28
Lu	0.27	0.28	0.26	0.27	0.25	0.25	0.24	0.22	0.05	0.04
Pb	0.36	0.35	0.28	0.38	0.30	0.26	0.26	0.15	<0.02	<0.02
Th	0.76	0.82	0.69	0.73	0.80	0.15	0.12	0.15	<0.01	<0.01
U	0.19	0.27	0.13	0.19	0.14	0.04	0.06	<0.06	0.01	<0.01

(*Continued*)

Table 3. *Continued*

	E1D Lh					E4C Lh					
Mineral:	cpx	cpx	cpx	opx	opx	cpx	cpx	cpx	cpx	opx	opx
Label:	3A	5A	5B	2A	2I	3B	3C	1C	4D	5A	5B
Rb	0.19	0.52	0.32	<0.01	<0.01	0.08	<0.02	0.08	0.02	0.02	0.01
Ba	2.79	7.27	3.15	<0.06	0.53	<0.07	0.12	0.59	0.08	0.15	0.11
Sr	94.9	125	97.1	0.71	0.78	4.67	4.56	18.7	20.3	0.28	0.29
Y	13.0	18.2	16.0	1.22	1.26	13.6	13.7	14.1	10.5	1.56	1.66
Zr	24.2	35.8	27.8	2.33	2.56	4.31	3.97	4.71	7.62	0.50	0.45
Hf	0.94	1.17	1.00	0.04	0.05	0.42	0.26	0.32	0.26	0.03	<0.04
Nb	0.81	0.80	0.24	<0.06	0.02	0.01	<0.01	0.02	0.09	<0.07	<0.01
Ta	0.02	0.06	0.08	<0.01	0.01	<0.01	<0.01	<0.01	0.02	<0.01	<0.01
La	5.01	8.78	6.61	0.05	0.04	1.10	1.19	3.52	3.85	0.10	0.07
Ce	18.1	26.5	20.0	0.11	0.11	0.44	0.48	3.57	5.25	0.04	0.06
Pr	2.47	3.59	2.86	0.04	0.03	0.10	0.09	0.23	0.42	<0.01	0.01
Nd	11.1	17.3	14.9	0.15	0.12	1.15	1.21	1.51	2.04	<0.04	0.06
Sm	3.03	3.23	3.08	<0.03	0.05	0.78	0.78	1.04	0.78	0.04	0.04
Eu	0.79	1.27	1.04	0.02	0.04	0.44	0.38	0.30	0.38	0.02	0.04
Gd	2.92	3.24	3.36	0.08	<0.03	1.90	1.54	1.55	0.97	0.14	0.09
Tb	0.46	0.56	0.43	0.03	0.03	0.28	0.28	0.35	0.25	0.02	0.03
Dy	2.61	3.92	3.61	0.24	0.13	2.35	2.31	2.34	1.66	0.21	0.27
Ho	0.52	0.67	0.44	0.05	0.06	0.55	0.52	0.57	0.40	0.05	0.06
Er	1.19	1.88	1.79	0.17	0.08	1.56	1.54	1.20	1.41	0.22	0.25
Tm	0.19	0.24	0.19	0.04	0.04	0.26	0.24	0.19	0.16	0.05	0.06
Yb	1.41	1.80	1.81	0.43	0.46	1.59	1.62	1.60	1.53	0.31	0.36
Lu	0.20	0.25	0.27	0.06	0.06	0.25	0.30	0.24	0.13	0.06	0.06
Pb	0.23	0.36	0.31	0.02	0.06	0.70	0.54	0.79	0.69	0.06	0.05
Th	0.27	0.34	0.12	0.01	0.02	0.94	1.09	1.02	1.22	0.26	0.16
U	0.09	0.06	0.09	0.01	0.01	0.42	0.47	0.39	0.38	0.05	0.07

	E5B Lh						E12A Cpx-poor Lh			
Mineral:	cpx	cpx	cpx	cpx	opx	opx	cpx	cpx	cpx	opx
Label:	3H	4A	3F	4D	3A	3B	1F	1G	1H	1B
Rb	0.15	<0.05	0.16	0.17	<0.02	<0.02	0.10	0.01	0.04	<0.02
Ba	4.99	0.16	6.53	2.45	0.19	0.21	1.01	0.18	2.79	0.25
Sr	146	199	146	185	0.38	0.38	119	123	113	0.69
Y	20.1	22.6	21.1	20.9	1.34	1.26	13.7	13.1	12.3	0.63

Zr	33.3	39.6	34.9	36.5	1.82	1.97	4.53	3.97	3.34	0.28
Hf	1.11	1.28	1.13	1.42	0.05	0.06	0.37	0.44	0.31	<0.03
Nb	1.21	1.38	0.56	1.38	<0.02	0.02	0.03	0.04	0.04	0.05
Ta	0.02	0.05	0.01	0.05	0.01	<0.01	<0.01	<0.01	0.02	<0.01
La	10.9	13.0	10.5	11.7	0.03	0.03	13.61	14.1	13.6	0.05
Ce	21.0	26.8	22.0	24.1	0.09	0.15	17.79	19.0	15.7	0.14
Pr	2.16	2.95	2.48	2.70	0.01	0.01	1.26	1.18	1.01	<0.01
Nd	8.84	12.0	8.79	9.63	0.05	0.15	2.88	3.51	2.55	<0.01
Sm	2.23	2.57	2.64	2.75	<0.06	<0.03	1.51	1.14	1.04	<0.01
Eu	0.74	0.93	0.88	0.94	0.02	0.03	0.48	0.36	0.39	0.02
Gd	2.69	3.21	2.96	3.09	<0.06	0.07	1.23	1.80	1.59	<0.01
Tb	0.45	0.63	0.62	0.53	0.01	0.02	0.29	0.33	0.37	<0.01
Dy	3.52	4.15	3.67	4.44	0.15	0.12	2.17	2.09	2.39	0.09
Ho	0.76	0.92	0.82	0.82	0.04	0.03	0.53	0.54	0.57	0.64
Er	2.22	2.62	2.10	2.14	0.16	0.23	1.90	1.90	1.72	<0.01
Tm	0.34	0.41	0.35	0.35	<0.02	0.04	0.21	0.27	0.25	0.12
Yb	2.05	2.24	2.34	2.23	0.23	0.37	1.33	1.82	1.92	0.03
Lu	0.32	0.37	0.36	0.31	0.06	0.06	0.16	0.24	0.22	0.21
Pb	0.27	0.66	0.30	0.52	0.04	0.05	1.16	0.84	0.83	<0.00
Th	1.24	1.40	0.57	1.04	<0.01	0.01	2.00	2.06	2.34	0.03
U	0.33	0.29	0.14	0.27	0.01	<0.01	0.27	0.75	0.77	0.02

	E8A Lh						E11A Lh		
Mineral:	cpx	cpx	cpx	cpx	opx	opx	cpx	cpx	opx
Label:	2H	5A	5B	2E	1A	4A	2B	2C	2D
Rb	0.07	<0.04	<0.03	0.04	0.24	<0.01	0.77	0.92	0.10
Ba	0.95	0.09	0.68	0.28	2.88	0.53	37.0	22.9	0.66
Sr	50.6	46.4	40.7	41.5	3.05	0.07	166	122	2.38
Y	16.1	15.8	15.8	15.5	1.15	0.83	17.4	17.6	1.40
Zr	17.8	17.4	17.1	18.4	1.13	0.76	45.9	47.9	3.12
Hf	0.79	0.82	0.63	0.70	0.07	<0.03	1.55	1.60	0.02
Nb	0.03	0.01	0.14	0.07	0.09	<0.01	1.55	2.17	0.07
Ta	<0.01	<0.01	0.06	<0.01	<0.01	<0.01	0.11	0.08	0.02
La	7.36	6.80	6.25	6.46	0.16	0.01	9.83	8.68	0.11
Ce	10.3	9.29	8.40	9.12	0.28	0.02	25.1	24.3	0.37
Pr	0.92	0.87	0.82	0.92	0.03	0.01	3.53	3.46	0.03
Nd	3.90	3.69	3.49	3.78	0.13	<0.03	15.6	15.4	0.23
Sm	1.35	1.36	1.50	1.50	0.04	<0.03	3.39	3.54	<0.04
Eu	0.59	0.65	0.60	0.60	0.03	0.01	1.24	1.09	0.02
Gd	2.14	2.13	2.05	2.10	0.04	<0.03	3.06	3.32	0.07

(*Continued*)

Table 3. *Continued*

	E8A Lh						E11A Lh		
Mineral:	cpx	cpx	cpx	cpx	opx	opx	cpx	cpx	opx
Label:	2H	5A	5B	2E	1A	4A	2B	2C	2D
Tb	0.38	0.34	0.40	0.37	0.01	<0.01	0.49	0.46	0.03
Dy	2.68	2.57	2.87	2.74	0.19	0.13	3.10	3.19	0.21
Ho	0.62	0.57	0.55	0.60	0.04	0.03	0.75	0.70	0.09
Er	1.73	1.77	1.91	1.71	0.16	0.17	1.93	2.07	0.20
Tm	0.23	0.25	0.25	0.27	0.02	0.03	0.23	0.29	0.02
Yb	2.06	2.32	1.35	1.90	0.26	0.27	1.72	1.86	0.30
Lu	0.26	0.28	0.23	0.27	0.04	0.05	0.23	0.25	0.06
Pb	1.07	1.16	1.47	1.04	0.06	0.06	0.29	0.60	0.08
Th	1.48	1.39	1.18	1.30	0.05	<0.01	0.77	0.81	0.03
U	0.43	0.38	0.41	0.42	0.01	<0.01	0.17	0.15	<0.01

	E27A Lh						
Mineral:	cpx core	cpx core	cpx rim	opx rim	opx core	opx	opx
Label:	2F	2G	2E	2D	2A	1A1 N	1B1
Rb	0.06	<0.01	2.71	0.54	0.05	<0.02	<0.02
Ba	0.30	0.14	2.91	4.15	0.37	0.05	1.06
Sr	101	98.8	54.9	16.1	1.00	0.26	0.26
Y	16.4	16.8	13.6	1.40	1.21	0.98	0.98
Zr	12.7	13.1	6.34	1.20	0.82	0.84	0.72
Hf	0.81	0.69	0.32	0.14	0.06	0.04	<0.03
Nb	2.05	2.09	0.40	0.35	0.09	0.03	0.10
Ta	0.07	0.10	0.04	0.08	<0.01	<0.01	<0.01
La	8.34	8.68	3.91	1.05	0.06	0.02	0.03
Ce	13.5	13.8	7.66	2.03	0.10	0.04	0.06
Pr	1.43	1.37	0.84	0.24	<0.01	<0.01	0.01
Nd	5.64	5.50	3.77	0.91	0.06	0.03	0.07
Sm	1.50	1.73	1.16	0.19	0.03	0.06	0.09
Eu	0.68	0.77	0.53	<0.03	0.03	0.01	<0.01
Gd	2.53	2.16	2.03	0.21	0.12	<0.03	<0.02
Tb	0.41	0.40	0.36	0.05	0.02	<0.01	0.01
Dy	3.10	3.15	2.44	0.37	0.17	0.09	0.10
Ho	0.67	0.66	0.52	0.04	0.06	0.04	0.04
Er	1.90	1.89	1.42	<0.01	0.28	0.10	0.09
Tm	0.29	0.28	0.23	<0.01	0.03	0.02	0.03

Yb	2.01	2.01	1.74	0.18	0.47	0.23	0.24
Lu	0.28	0.32	0.26		0.06	0.04	0.04
Pb	0.63	0.52	0.75	4.61	0.12	0.15	<0.01
Th	1.47	1.34	0.47	0.48	<0.01	0.02	0.01
U	0.41	0.42	0.09	0.11	0.01	0.01	0.01

X1A Lh

Mineral:	cpx	cpx	cpx	cpx	cpx	opx
Label:	1B	1D	1Z	3B	4A	4C
Rb	<0.01	<0.02	<0.02	0.07	<0.05	<0.02
Ba	0.05	<0.04	0.13	0.14	0.27	0.14
Sr	45.7	18.5	16.7	45.2	20.4	0.70
Y	15.4	15.0	15.3	15.1	15.3	1.00
Zr	6.11	5.08	5.40	11.3	5.00	1.33
Hf	0.43	0.47	0.56	0.55	0.28	0.03
Nb	0.07	0.04	0.04	0.20	0.08	0.01
Ta	0.01	<0.01	0.01	<0.01	<0.01	0.01
La	2.64	1.34	1.29	3.31	1.39	0.04
Ce	3.17	1.26	1.08	4.82	1.38	0.06
Pr	0.38	0.19	0.17	0.47	0.16	<0.01
Nd	1.94	1.56	1.41	2.16	1.63	0.05
Sm	1.02	0.95	0.95	1.16	0.85	<0.03
Eu	0.46	0.45	0.42	0.45	0.35	<0.01
Gd	1.88	1.79	1.63	1.77	1.80	0.05
Tb	0.33	0.34	0.43	0.34	0.34	0.02
Dy	2.82	2.83	2.70	2.29	2.86	0.15
Ho	0.64	0.58	0.69	0.58	0.60	0.04
Er	1.84	1.94	1.97	1.76	2.04	0.11
Tm	0.27	0.25	0.29	0.24	0.29	0.02
Yb	1.64	1.87	1.92	1.70	1.50	0.23
Lu	0.27	0.24	0.25	0.18	0.25	0.05
Pb	0.69	0.50	0.43	0.52	0.53	0.15
Th	1.65	1.46	1.43	1.84	1.29	0.12
U	0.46	0.48	0.48	0.47	0.44	0.03

Abbreviations as in Table 1.

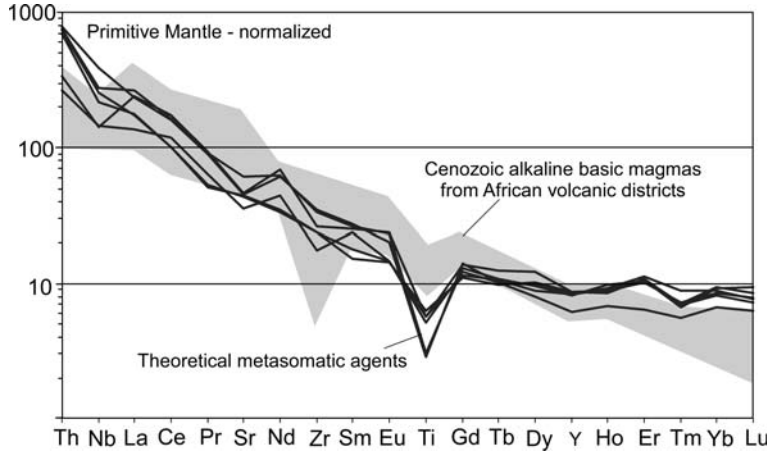

Fig. 7. Primitive mantle (PM)-normalized trace element patterns of the computed metasomatic agents that affected the Gharyan lithospheric mantle. Calculations were performed on the basis of composition of the most metasomatized clinopyroxenes, using distribution coefficients from the GERM web site (http://www.earthref.org/GERM/). Normalizing factors after Sun & McDonough (1989). Also shown for comparison is the compositional field of Cenozoic alkaline lavas (alkali-basalts, basanites and melilitites) from volcanic districts of the African plate (Beccaluva *et al*. 1998; Janney *et al*. 2002; Azzouni-Sekkal *et al*. 2007).

related to marked enrichment effects that totally mask the pre-metasomatic history. Among these, samples E1D and E11A have humped LREE patterns with Ce_N/Yb_N slightly higher than La_N/Yb_N, as is often observed for magmatic clinopyroxenes (Jeffries *et al.* 1995; Foley *et al.* 1996; Dobosi & Jenner 1999). They could be interpreted as the result of more effective metasomatic processes with modal growth of clinopyroxene under conditions of higher fluid/matrix ratio.

Trace element modelling has been carried out based on the composition of these clinopyroxenes and experimental partition coefficients have been determined for clinopyroxene–basic melts (GERM dataset: http://earthref.org/GERM) to identify the nature of the metasomatizing agent (Fig. 7). Most incompatible elements of the calculated metasomatic agents fit fairly well with the composition of Na alkaline basic lavas (alkali-basalts, basanites and melilitites) from Cenozoic volcanic districts of the African plate.

Orthopyroxene shows very low REE composition, and when plotted in chondrite-normalized diagrams generally displays LREE-depleted patterns. In samples E1D and E5B, where clinopyroxene (of probable neo-formation) records clear metasomatic effects, orthopyroxene does not show any evidence of LREE enrichment. This suggests that, in this case, orthopyroxene is a reacting phase that is effectively consumed during the reaction with the metasomatizing agent. In other samples (E4C, E8A and E27A), the REE patterns of the orthopyroxenes mimic at sub-chondritic level the spoon-shaped patterns of the coexisting clinopyroxene. This effect is probably related to metasomatic processes occurring with a low fluid/matrix ratio that did not trigger clinopyroxene growth and orthopyroxene consumption.

Diffusive processes between metasomatized clinopyroxene and coexisting orthopyroxene seem to be represented in sample E27A, where clinopyroxene or orthopyroxene cores and their interface rims have been analysed. It can be observed that the LREE content of the opx gradually increases from the core (La_N *c*. 0.1–0.3) toward the interface with the clinopyroxene (La_N *c*. 4), and that the LREE conent of the cpx gradually decreases from the core (La_N *c*. 36) toward the rim (La_N *c*. 16).

Sr–Nd–Pb isotope variations

To overcome any ambiguous interpretation of the geochemical components of the pristine mantle and the subsequent metasomatic enrichments, isotopic analyses have been carried out on carefully separated (and chemically leached) clinopyroxenes. Sr–Nd–Pb isotope compositions of the cpx separates (Table 4 and Fig. 8) show the following compositional ranges: $^{87}Sr/^{86}Sr = 0.70227–0.70304$, $^{143}Nd/^{144}Nd = 0.51296–0.51387$, $^{206}Pb/^{204}Pb = 18.76–19.66$, $^{207}Pb/^{204}Pb = 15.6–15.75$, $^{208}Pb/^{204}Pb = 38.46–39.47$. Nd_N/Yb_N of both whole rock and clinopyroxene are inversely

Table 4. *Sr–Nd–Pb isotope compositions of clinopyroxene separates (cpx) from the Gharyan mantle xenoliths and their host lavas (w.r.)*

Rock type	Sample	Analysed fraction	$^{87}Sr/^{86}Sr$	$^{143}Nd/^{144}Nd$	$^{206}Pb/^{204}Pb$	$^{207}Pb/^{204}Pb$	$^{208}Pb/^{204}Pb$	Sm/Nd age CHUR (Ga)	Sm/Nd age DM (Ga)
Anhydrous peridotite xenoliths									
Lh	A2A	cpx	0.70227	0.51330	18.76	15.60	38.46		
Lh	E1D	cpx	0.70304	0.51296	19.48	15.70	39.29		
Lh	E11A	cpx	0.70297	0.51298	19.66	15.75	39.47		
Lh (cpx poor)	E12A	cpx	0.70304	0.51341	–	–	–		
Lh	E14A	cpx	0.70284	0.51303	19.65	15.69	39.35		
Lh	E27A	cpx	0.70295	0.51319	19.61	15.68	39.32		
Lh	X1A	cpx	0.70290	0.51387	–	–	–	1.17	0.85
Host lavas									
Alkaline basalt	A2	w.r.	0.70319	0.51299	19.60	15.71	39.40		
Hawaiite	E1	w.r.	0.70320	0.51295	19.40	15.69	39.23		

Abbreviations as in Table 1. Sm–Nd model ages (Ga) referred to chondrite uniform reservoir (CHUR) and depleted mantle (DM) are calculated for the relatively unmetasomatized sample X1A using averaged Nd and Sm contents of clinopyroxene (Table 3) and the model parameters by Faure (1986).

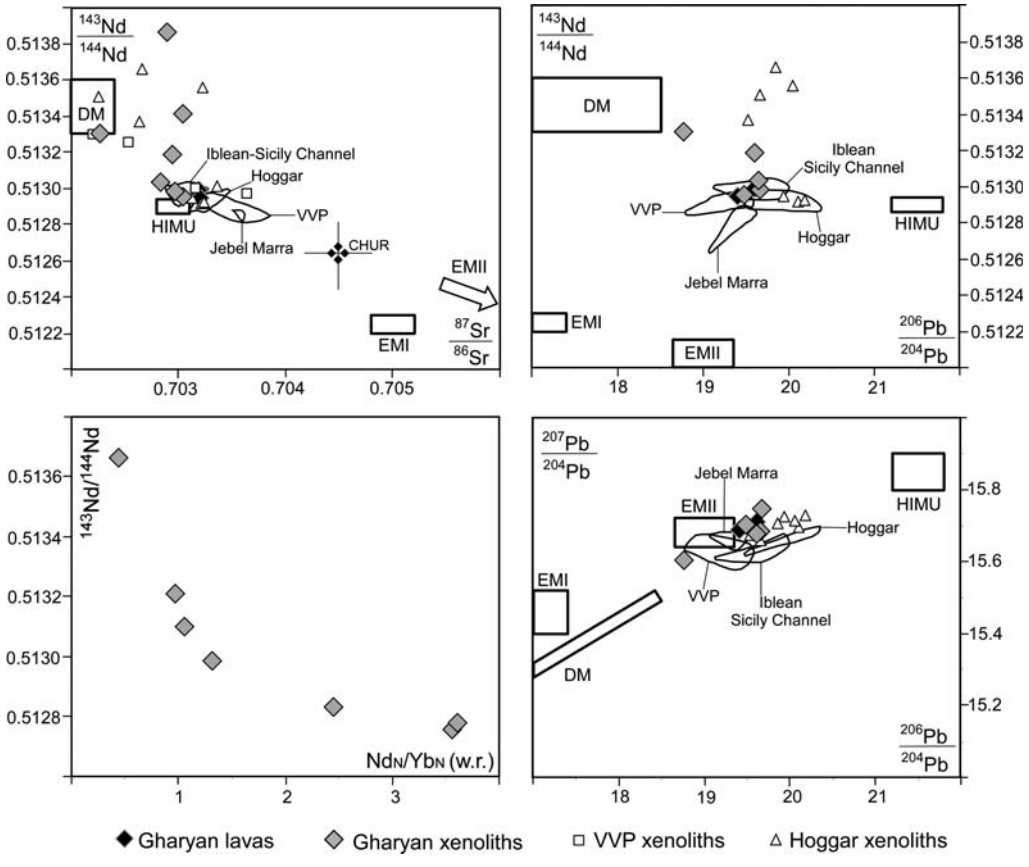

Fig. 8. Sr–Nd–Pb isotopic variations for clinopyroxene separates from the Gharyan mantle xenoliths, compared with those from Hoggar (Beccaluva *et al*. 2006*a*, *b*) and the Veneto Volcanic Province (VVP, Beccaluva *et al*. 2007). Also shown are compositions of Gharyan host lavas and other alkaline basic lavas from Hoggar (Allègre *et al*. 1981), Jebel Marra (Davidson & Wilson 1989; Franz *et al*. 1999), and the Iblean–Sicily Channel districts (Beccaluva *et al*. 1998; Civetta *et al*. 1998; Bianchini *et al*. 1999). Isotopic mantle end-members (DM, HIMU, EMI and EMII) are after Zindler & Hart (1986).

correlated with $^{143}Nd/^{144}Nd$, with the higher $^{143}Nd/^{144}Nd$ being recorded in samples less affected (or totally unaffected) by metasomatism. Sm–Nd model age calculations of the less metasomatized sample X1A give ages of 0.85 and 1.17 Ga relative to depleted mantle (DM) and chondrite uniform reservoir (CHUR), respectively. These data, although limited, seem to confine the main depletion melting events to pre-Palaeozoic times.

The extremely high $^{143}Nd/^{144}Nd$ of sample X1A (approaching 0.5139) is coupled with a higher Sm_N/Nd_N (1.6–2 in cpx, and 1.6 in the whole rock). This may suggest that sample X1A was affected by partial melting in the presence of residual garnet (leaving high Sm/Nd in the system), and subsequently re-equilibrated in the spinel peridotite facies, ultimately leading to the observed very radiogenic $^{143}Nd/^{144}Nd$ composition (Downes *et al.* 2003; Bianchini *et al.* 2007).

In the Sr v. Nd isotopic diagram (Fig. 8) the least metasomatized samples plot in the upper-left part of the diagram close to the DM end-member. In contrast, the most metasomatized xenoliths ($^{87}Sr/^{86}Sr$ *c*. 0.7030, $^{143}Nd/^{144}Nd$ *c*. 0.5130) cluster around the high μ (HIMU) mantle end-member. This latter is also the dominant component of all the Cenozoic alkaline lavas from North African districts (Hoggar, Allègre *et al.* 1981; Jebel Marra, Davidson & Wilson 1989; Franz *et al.* 1999; Iblean and Sicily Channel districts, Beccaluva *et al.* 1998; Civetta *et al.* 1998; Bianchini *et al.* 1999), including those from Gharyan.

Pb isotopic data confirm that the Gharyan mantle xenoliths can be interpreted as the result of mixing

between DM and HIMU components. However, it has to be noted that the enrichment in ^{206}Pb and ^{208}Pb is significant also in samples that have previously been considered to be relatively unaffected by metasomatism on the basis of REE and Nd isotopes. For example, E27A is characterized by $^{206}Pb/^{204}Pb = 19.61$, $^{208}Pb/^{204}Pb = 39.32$, Nd_N/Yb_N *c*. 1, $^{143}Nd/^{144}Nd = 0.5132$, and $^{87}Sr/^{86}Sr = 0.70295$. This apparent incongruence between the Sm–Nd and the U–Pb systems may be attributed to different elemental behaviour during metasomatism, with Pb being much more mobile than Nd (and Sr) and hence a more sensitive indicator of incipient metasomatic events.

He isotopes

Helium isotope determinations have been made on gases trapped in olivine and pyroxene from several xenoliths. They show a narrow $^{3}He/^{4}He$ range (5.3–6.5 R_a; Table 5) that is similar to ratios measured in peridotite xenoliths and lavas from Hoggar (Pik *et al.* 2006; Beccaluva & Stuart, unpubl. data), the Cameroon line (e.g. Barfod *et al.* 1999), and the Etna–Iblean plateau and Sicily Channel (Marty *et al.* 1994; Martelli *et al.* 2004; Sapienza *et al.* 2005; Stuart, unpubl. data). The measured $^{3}He/^{4}He$ values are lower than the DM sampled by mid-ocean ridge basalts (8 ± 1 R_a) and show no sign of the deep mantle signature such as that of the Ethiopia–Afar plume (Pik *et al.* 2006). Similar $^{3}He/^{4}He$ values are recorded by Cenozoic intraplate volcanism throughout Europe (Buikin *et al.* 2005), Africa (Pik *et al.* 2006) and the eastern–central Atlantic Ocean (Hilton *et al*. 2000), which are typical of basalts with strong HIMU-like Pb isotope and trace element ratios (e.g. Barfod *et al.* 1999; Hilton *et al.* 2000). Therefore He isotopes are consistent with the Sr–Nd–Pb isotope data and provide further evidence for a rather uniform HIMU sublithospheric component beneath the North Africa lithosphere.

Conclusions

Mantle xenoliths from the Gharyan volcanic field represent a lithospheric mantle that equilibrated in the spinel lherzolite facies (8–17% of cpx) at temperatures between 890 and 1060 °C. They represent slightly to moderately depleted mantle material likely to have resulted from extraction of basic melts that occurred during pre-Palaeozoic times.

Subsequent metasomatic effects are indicated by the widespread pyrometamorphic textures represented by reaction patches with secondary mineral parageneses that include cpx2, ol2 and feldspar as reaction rims around opx, spongy textured clinopyroxene with recrystallized portions (cpx2 + feldspar), and brown spinel destabilized in a black vermicular aggregate (sp2) generally associated with feldspar microlites.

Trace element analyses of both bulk-rocks and constituent pyroxenes show variable enrichments in incompatible element (LREE, Th, U, etc.) possibly caused by interaction with Na-alkali silicate basic melts similar to those from North African volcanic districts.

Porous flow appears to be the general mechanism of metasomatism, although with variable effects (enrichments) depending on the fluid/matrix ratio, fluid mobility and reaction kinetics, which cause different equilibrium attainment reflected in variable trace element patterns. Some of these effects could be theoretically accommodated by chromatographic fractionation as proposed for mantle reactive porous flow models by Bodinier *et al.* (2004, and references therein).

Most cpx separates from the Gharyan xenoliths show Sr–Nd–Pb isotope compositions ($^{87}Sr/^{86}Sr$ *c*. 0.7030, $^{143}Nd/^{144}Nd$ *c*. 0.5130, $^{206}Pb/^{204}Pb$ up to 19.66) that indicate a prevalent HIMU metasomatic signature. Significantly, an analogous imprint also characterizes the host lavas ($^{87}Sr/^{86}Sr$ 0.7032, $^{143}Nd/^{144}Nd$ 0.5130, $^{206}Pb/^{204}Pb$ 19.60).

A coherent Sr–Nd–Pb signature approaching DM is recorded by a single sample ($^{87}Sr/^{86}Sr$

Table 5. *Helium isotope composition of olivine and orthopyroxene separates from the Ghayan anhydrous peridotite xenoliths*

Rock type	Sample	Analysed fraction	$^{4}He(CM^3$ STP $g^{-1})$	Error	$^{3}He/^{4}He$ (R/R_a)	Error
Lh	A2A	opx	7.6E − 09	3.8E − 10	5.29	0.48
Lh	E11A	ol	1.9E − 08	8.3E − 10	6.50	0.48
Lh	E11A	opx	8.6E − 08	3.4E − 09	6.13	0.21
Lh	E12A	opx	6.8E − 09	3.4E − 10	5.75	0.64
Lh	E27A	ol	1.5E − 08	7.4E − 10	6.44	0.36
Lh	X1A	opx	1.1E − 07	4.2E − 09	6.08	0.13

R_a is the atmospheric $^{3}He/^{4}He$ ratio.

0.70227, $^{143}Nd/^{144}Nd$ 0.51330, $^{206}Pb/^{204}Pb$ 18.76) relatively unaffected by metasomatic reactions, whereas some other samples characterized by Sr–Nd ratios ($^{87}Sr/^{86}Sr$ *c*. 0.70295, $^{143}Nd/^{144}Nd$ *c*. 0.51319) approaching DM, but a HIMU affinity for Pb isotopes ($^{206}Pb/^{204}Pb$ *c*. 19.61), may be attributable to the higher mobility of Pb relative to Sr and Nd during metasomatism. Our results allow us to conclude that the Na-alkali silicate agent(s), characterized by a clear HIMU signature, affected to a variable extent a depleted lithospheric mantle section (DM) under the investigated area. This prevalent HIMU fingerprint compares favourably with the geochemical features of alkaline basic lavas and associated mantle xenoliths from other volcanic districts of North Africa, suggesting a common sub-lithospheric metasomatic agent across the area.

One possibility is that the sub-lithospheric component is associated with a large-scale mantle plume extending from the eastern Atlantic to the circum-Mediterranean and Central Europe since the late Cretaceous (Cebriá & Wilson 1995; Hoernle *et al.* 1995; Wilson & Bianchini 1999; Wilson & Patterson 2001). However, the available data indicate that such a sub-lithospheric mantle component also extends southward to central Africa (Pik *et al.* 2006). Moreover, the relatively low $^{3}He/^{4}He$ isotopic ratios confirmed by the analyses on the Gharyan xenoliths (5.3–6.5 R_a) suggest that this sub-lithospheric component originates within the upper mantle, in contrast to the high ratios recorded in the Ethiopian–Yemen plateau basalts (up to 20 R_a), which are attributed to deep-seated mantle plume(s) possibly rising from the core–mantle boundary (Pik *et al.* 2006). This is in accordance either with remarkable degassing of shallow mantle domains or with the addition of recycled components to the upper mantle (Moreira & Kurz 2001).

Therefore, the volcanic districts of the Saharan belt could have been related to small, second-order, 'hot fingers' triggered by intraplate rifting related to tectonic reactivation of the Pan-African cratonic basement (Azzouni-Sekkal *et al.* 2007). This, in turn, may be considered a far-field foreland reaction to the Africa–Europe collisional system (Liégeois *et al.* 2005).

Appendix: analytical methods

Rock samples were selected from the freshest chips and powdered in an agate mill. For determination of major and trace elements (Ni, Co, Cr, V and Sr), samples were analysed as powder pellets by XRF, using a wavelength-dispersive automated Philips PW 1400 spectrometer at the Department of Earth Sciences, Ferrara University. Accuracy and precision for major elements are estimated as better than 3% for Si, Ti, Fe, Ca and K, and 7% for Mg, Al, Mn and Na; for trace elements (above 10 ppm) they are better than 10%. REE, Sc, Y, Zr, Hf, Nb, Th and U were analysed by ICP-MS at the Department of Earth Sciences, Ferrara University, using a VG Plasma Quad2 plus system. Accuracy and precision, based on the replicated analyses of samples and standards, are estimated as better than 10% for all elements well above the detection limit.

Mineral compositions were obtained at the CNR-IGG Institute of Padova with a Cameca-Camebax electron microprobe (fitted with three wavelength-dispersive spectrometers) at an accelerating voltage of 15 kV and specimen current of 15 nA, using natural silicates and oxides as standards. Trace element analyses on pyroxenes were carried out at the CNR-IGG of Pavia by LAM-ICP-MS, using an Elan DRC-e mass spectrometer coupled with a Q-switched Nd–YAG laser source (Quantel Brilliant). The CaO content was used as internal standard. Precision and accuracy, better than 10% for concentrations at ppm level, were assessed by repeated analyses of NIST SRM 612 and BCR-2 standards.

Sr–Nd–Pb isotopic analyses on separated (by hand-picking) clinopyroxene (*c*. 100–200 mg) and whole rocks were carried out at SUERC. Samples were initially leached with 2.5M HCl and then digested with a mixture of HF–HNO_3–HCl. Sample preparation followed methods similar to those described by Hardarson *et al.* (1997). Sr samples were analysed using a VG Sector 54-30 mass spectrometer in multidynamic mode using an exponential correction for mass fractionation and $^{86}Sr/^{88}Sr = 0.1194$. Nd and Pb isotopes were analysed using a Micromass IsoProbe MC-ICP-MS system Pb was measured using the method similar to that described by Ellam (2006). NIST SRM981 gave $^{206}Pb/^{204}Pb = 16.940 \pm 7$, 15.496 ± 6, 36.708 ± 15 (2 SD, $n = 22$). Nd was measured in multidynamic mode. Isotope ratios were collected as six blocks of 20 dynamic (three mass) cycles with an on-peak zero measurement for each block determined in a blank solution of the 5% (v/v) nitric acid used to make up the sample solutions. Mass bias was corrected using $^{144}Nd/^{146}Nd = 0.7219$ and an exponential law. The internal laboratory Nd 'standard' (JM) gave $^{143}Nd/^{144}Nd = 0.511481 \pm 15$ ($n = 10$), which is within error of the long-term thermal ionization mass spectrometry (TIMS) mean of 0.511499 ± 10 (all errors 2 SD). Two determinations on the BCR-1 geostandard gave $^{143}Nd/^{144}Nd = 0.512615 \pm 14$ (2 SE) and 0.512629 ± 14 (2 SE). Each $^{143}Nd/^{144}Nd$ measurement consumed *c*. 150 ng of Nd. Mineral separates for helium isotope analysis were picked under a binocular microscope and washed ultrasonically in HNO_3 then water, prior to a final treatment with Analar acetone. Helium was extracted from all minerals by *in vacuo* crushing and analysed at SUERC using procedures modified only slightly from those of Stuart *et al.* (2000).

The authors gratefully acknowledge J. P. Liégeois and J. Y. Cottin for their perceptive and constructive criticism, which greatly improved the manuscript. Further thanks go to R. Tassinari for XRF and ICP-MS whole-rock analyses, and to R. Carampin and A. Zanetti for their assistance during the EPMA and LA-ICP-MS analyses.

References

ALLÈGRE, C. J., DUPRÉ, B., LAMBERT, B. & RICHARD, P. 1981. The subcontinental versus suboceanic debate. Lead–neodymium–strontium isotopes in a primary basalt in a shield area: the Ahaggar volcanic suite. *Earth and Planetary Science Letters*, **52**, 85–92.

AZZOUNI-SEKKAL, A., BONIN, B., BENHALLOU, A., YAHIAOUI, R. & LIÉGEOIS, J. P, 2007. Tertiary alkaline volcanism of the Atakor Massif (Hoggar, Algeria). *In*: BECCALUVA, L., BIANCHINI, G. & WILSON, M. (eds) *Cenozoic Volcanism in the Mediterranean Area*. Geological Society of America, Special Papers, **418**, 321–340.

BARFOD, D., BALLENTINE, C. J., HALLIDAY, A. N. & FITTON, J. G, 1999. Noble gases in the Cameroon line and the He, Ne and Ar isotopic compositions of high μ (HIMU) mantle. *Journal of Geophysical Research*, **104**, 29509–29527.

BECCALUVA, L., SIENA, F., COLTORTI, M., *ET AL*. 1998. Nephelinitic to tholeiitic magma generation in a transtensional tectonic setting: an integrated model for the Iblean volcanism, Sicily. *Journal of Petrology*, **39**, 1547–1576.

BECCALUVA, L., BONADIMAN, C., COLTORTI, M., SALVINI, L. & SIENA, F. 2001*a*. Depletion events, nature of metasomatizing agent and timing of enrichment processes in lithospheric mantle xenoliths from Veneto Volcanic Province. *Journal of Petrology*, **42**, 173–187.

BECCALUVA, L., BIANCHINI, G., COLTORTI, M., PERKINS, W. T., SIENA, F., VACCARO, C. & WILSON, M. 2001*b*. Multistage evolution of the European lithospheric mantle: new evidence from Sardinian peridotite xenoliths. *Contributions to Mineralogy and Petrology*, **142**, 284–297.

BECCALUVA, L., BIANCHINI, G., BONADIMAN, C., COLTORTI, M., MACCIOTTA, G., SIENA, F. & VACCARO, C. 2005. Within-plate Cenozoic volcanism and lithospheric mantle evolution in the western–central Mediterranean area. *In*: FINETTI, I. (ed.) *Crop Project—Deep Seismic Exploration of the central Mediterranean Italy*. Elsevier, Amsterdam, 641–664.

BECCALUVA, L., AZZOUNI-SEKKAL, A., BENHALLOU, A., BIANCHINI, G., ELLAM, R., MARZOLA, M. & SIENA, F. 2006*a*. Geochemical evidence of strongly alkaline-carbonated HIMU metasomatism in mantle xenoliths from the Manzaz–Atakor District (Hoggar, Algeria). *Geophysical Research Abstracts*, **8**, abstract 01304.

BECCALUVA, L., AZZOUNI-SEKKAL, A., BENHALLOU, A., BIANCHINI, G., ELLAM, R., MARZOLA, M. & SIENA, F. 2006*b*. Evidence of strongly alkaline-carbonated HIMU metasomatism in mantle xenoliths from the Manzaz–Atakor District (Hoggar, Algeria). *In*: *Abstracts volume of the 4th International Geological Correlation Program IGCP-485, Algiers, December 2006*, 15.

BECCALUVA, L., BIANCHINI, G., BONADIMAN, C., *ET AL*. 2007. Intraplate lithospheric and sublithospheric components in the Adriatic domain: nephelinite to tholeiite magma generation in the Paleogene Veneto Volcanic Province, Southern Alps. *In*: BECCALUVA, L., BIANCHINI, G. & WILSON, M. (eds) *Cenozoic Volcanism in the Mediterranean Area*. Geological Society of America, Special Papers, **418**, 131–152.

BEDINI, R. M. & BODINIER, J.-L. 1999. Distribution of incompatible trace elements between the constituents of spinel peridotite xenoliths: ICP-MS data from the East African Rift. *Geochimica et Cosmochimica Acta*, **63**, 3883–3900.

BIANCHINI, G., BELL, K. & VACCARO, C. 1999. Mantle sources of the Cenozoic Iblean volcanism (SE Sicily, Italy): Sr–Nd–Pb isotopic constraints. *Mineralogy and Petrology*, **67**, 213–221.

BIANCHINI, G., BECCALUVA, L., BONADIMAN, C., NOWELL, G., PEARSON, G., SIENA, F. & WILSON, M. 2007. Evidence of diverse depletion and metasomatic events in harzburgite–lherzolite mantle xenoliths from the Iberian plate (Olot, NE Spain): implications for lithosphere accretionary processes. *Lithos*, **94**, 25–45.

BODINIER, J.-L., MENZIES, M. A., SHIMIZU, N., FREY, F. A. & MCPHERSON, E. 2004. Silicate, hydrous and carbonate metasomatism at Lherz, France: contemporaneous derivatives of silicate melt–harzburgite reaction. *Journal of Petrology*, **45**, 299–320.

BONADIMAN, C., BECCALUVA, L., COLTORTI, M. & SIENA, F. 2005. Kimberlite-like metasomatism and 'garnet signature' in spinel-peridotite xenoliths from Sal, Cape Verde archipelago: relics of a subcontinental mantle domain within the Atlantic Oceanic lithosphere? *Journal of Petrology*, **46**, 2465–2493.

BREY, G. P. & KÖHLER, T. P. 1990. Geothermobarometry in four-phase lherzolites II. New thermobarometers and practical assessment of existing thermobarometers. *Journal of Petrology*, **31**, 1353–1378.

BUIKIN, A., TRIELOFF, M., HOPP, J., ALTHAUS, T. & KOROCHANTSEVA, E. 2005. Noble gas isotopes suggest deep mantle plume source of late Cenozoic mafic alkaline volcanism in Europe. *Earth and Planetary Science Letters*, **230**, 143–162.

CEBRIÁ, J. M. & WILSON, M. 1995. Cenozoic mafic magmatism in Western/Central Europe: a common European Asthenospheric Reservoir? *Terra Nova Abstracts, Supplement*, **7**, 162.

CIVETTA, L., D'ANTONIO, M., ORSI, G. & TILTON, G. R, 1998. The geochemistry of volcanic rocks from Pantelleria island, Sicily Channel: petrogenesis and characteristics of the mantle source region. *Journal of Petrology*, **39**, 1453–1492.

COLTORTI, M., BONADIMAN, C., HINTON, R. W., SIENA, F. & UPTON, B. G. J. 1999. Carbonatite metasomatism of the oceanic upper mantle: evidence from clinopyroxenes and glasses in ultramafic xenoliths of Grande Comore, Indian Ocean. *Journal of Petrology*, **40**, 133–165.

COLTORTI, M., BECCALUVA, L., BONADIMAN, C., SALVINI, L. & SIENA, F. 2000. Glasses in mantle xenoliths as geochemical indicators of metasomatic agents. *Earth and Planetary Science Letters*, **183**, 303–320.

DAUTRIA, J. M., LIOTARD, J. M., CABANES, N., GIROD, M. & BRIQUEU, L. 1987. Amphibole-rich xenoliths and host alkali basalts: petrogenetic constraints and implications on the recent evolution of the upper mantle beneath Ahaggar (Central Sahara, Southern Algeria). *Contributions to Mineralogy and Petrology*, **95**, 133–144.

DAUTRIA, J. M., DUPUY, C., TAKHERIST, D. & DOSTAL, J. 1992. Carbonate metasomatism in the lithospheric mantle: peridotitic xenoliths from a melilititic district of the Sahara basin. *Contributions to Mineralogy and Petrology*, **111**, 37–52.

DAVIDSON, J. P. & WILSON, I. R. 1989. Evolution of an alkali basalt–trachyte suite from Jebel Marra volcano, Sudan, through assimilation and fractional crystallization. *Earth and Planetary Science Letters*, **95**, 141–160.

DELPECH, G., GRÉGOIRE, M., O'REILLY, S. Y., COTTIN, J. Y., MOINE, B., MICHON, G. & GIRET, A. 2004. Feldspar from carbonate-rich silicate metasomatism in the shallow oceanic mantle under Kerguelen Islands (South Indian Ocean). *Lithos*, **75**, 209–237.

DOBOSI, G. & JENNER, G. A. 1999. Petrologic implications of trace element variation in clinopyroxene megacrysts from the Nógrád volcanic province, North Hungary: a study by laser ablation microprobe-inductively coupled plasma-mass spectrometry. *Lithos*, **46**, 731–749.

DOWNES, H., REICHOW, M. K., MASON, P. R. D., BEARD, A. D. & THIRLWALL, M. F. 2003. Mantle domains in the lithosphere beneath the French Massif Central: trace element and isotopic evidence from mantle clinopyroxenes. *Chemical Geology*, **200**, 71–87.

ELLAM, R. M. 2006. New constraints on the petrogenesis of the Nuanetsi picrite basalts from Pb and Hf isotope data. *Earth and Planetary Science Letters*, **245**, 153–161.

FAURE, G. 1986. *Principles of Isotope Geology*, 2nd edn. Wiley, Chichester.

FOLEY, S. F., JACKSON, S. E., FRYER, B. J., GREENOUGH, J. D. & JENNER, G. A. 1996. Trace element partition coefficients for clinopyroxene and phlogopite in an alkaline lamprophyre from Newfoundland by LAM-ICP-MS. *Geochimica et Cosmochimica Acta*, **60**, 629–638.

FRANZ, G., STEINER, G., VOLKER, F., PUDLO, D. & HAMMERSCHMIDT, K. 1999. Plume related alkaline magmatism in central Africa—the Meidob Hills (W Sudan). *Chemical Geology*, **157**, 27–47.

GRÉGOIRE, M., LORAND, J. P., O'REILLY, S. Y. & COTTIN, J. Y. 2000. Armalcolite-bearing, Ti-rich metasomatic assemblages in harzburgitic xenoliths from the Kerguelen Islands: implications for the oceanic mantle budget of high-field strength elements. *Geochimica et Cosmochimica Acta*, **64**, 673–694.

HARDARSON, B. S., FITTON, J. G., ELLAM, R. M. & PRINGLE, M. S. 1997. Rift relocation—a geochemical and geochronological investigation of a palaeo-rift in northwest Iceland. *Earth and Planetary Science Letters*, **153**, 181–196.

HILTON, D. R., MCPHERSON, C. G. & ELLIOT, T. R. 2000. Helium isotope ratios in mafic phenocryst and geothermal fluids from La Palma, the Canary Islands (Spain): implications for HIMU mantle source. *Geochimica et Cosmochimica Acta*, **64**, 2119–2132.

HOERNLE, K., ZHANG, Y. S. & GRAHAM, D. 1995. Seismic and geochemical evidence for large-scale mantle upwelling beneath the Eastern Atlantic and Western and Central Europe. *Nature*, **374**, 34–39.

IONOV, D. A., GRÉGOIRE, M. & PRIKHOD'KO, V. S. 1999. Feldspar–Ti-oxide metasomatism in off-cratonic continental and oceanic upper mantle. *Earth and Planetary Science Letters*, **165**, 37–44.

JANNEY, P. E, LE ROEX, A. P., CARLSON, R. W. & VILJOEN, K. S. 2002. A chemical and multi-isotope study of the Western Cape olivine melilitite province, South Africa: implications for the sources of kimberlites and the origin of the HIMU signature in africa. *Journal of Petrology*, **43**, 2339–2370.

JEFFRIES, T. E., PERKINS, W. T. & PEARCE, N. J. G. 1995. Measurement of trace element in basalts and their phenocrysts by laser probe microanalysis inductively coupled plasma mass spectrometry (LPMA-ICP-MS). *Chemical Geology*, **121**, 131–144.

LIÉGEOIS, J. P., BENHALLOU, A., AZZOUNI-SEKKAL, A., YAHIAOUI, R. & BONIN, B. 2005. The Hoggar swell and volcanism: reactivation of the Precambrian Tuareg shield during Alpine convergence and West African Cenozoic volcanism. *In*: FOULGER, G. R., NATLAND, J. H., PRESNALL, D. C. & ANDERSON, D. L. (eds) *Plates, Plumes and Paradigms*. Geological Society of America, Special Papers, **388**, 379–400.

MARTELLI, M., NUCCIO, P. M., STUART, F. M., BURGESS, R., ELLAM, R. M. & ITALIANO, F. 2004. Helium–strontium isotope constraints on mantle evolution beneath the Roman Comagmatic Province, Italy. *Earth and Planetary Science Letters*, **224**, 295–308.

MARTY, B., TRULL, T., LUSSIEZ, P., BASILE, I. & TANGUY, J.-C. 1994. He, Ar, O, Sr and Nd isotope constraints on the origin and evolution of Mount Etna magmatism. *Earth and Planetary Science Letters*, **126**, 23–39.

MCDONOUGH, W. F. & SUN, S. S. 1995. The composition of the earth. *Chemical Geology,* **120**, 223–253.

MOREIRA, M. & KURZ, M. D. 2001. Subducted oceanic lithosphere and the origin of the 'high μ' basalt helium isotopic signature. *Earth and Planetary Science Letters*, **189**, 49–57.

NIU, Y. 1997. Mantle melting and melt extraction processes beneath ocean ridges: evidence from abyssal peridotites. *Journal of Petrology*, **38**, 1047–1074.

PIK, R., MARTY, B. & HILTON, D. R. 2006. How many plumes in Africa? The geochemical point of view. *Chemical Geology*, **226**, 100–114.

RAFFONE, N., ZANETTI, A., CHAZOT, G., DENIEL, C. & VANNUCCI, R. 2001. Geochemistry of mantle xenoliths from Ibalrhatene (Mid Atlas, Morocco): insights into the lithospheric mantle evolution during continental rifting. *In*: *Abstracts volume of the Eleventh*

Annual Goldschmidt Conference, May 2001, Hot Springs, USA, Abs. no. 3323.

RAFFONE, N., ZANETTI, A. M., CHAZOT, G., PIN, C. & VANNUCCI, R. 2004. Multiple steps of melt percolation through lithospheric mantle recorded by REE and HFSE zoning in cpx and amph of wehrlites from Azrou (mid Atlas, Morocco). *In*: *Abstracts volume of the 32nd IGC, Florence, August 2004*, Abs. no. 255-8.

SAPIENZA, G., HILTON, D. R. & SCRIBANO, V. 2005. Helium isotopes in peridotite mineral phases from Hyblean Plateau xenoliths (south-eastern Sicily, Italy). *Chemical Geology*, **219**, 115–129.

SIENA, F., BECCALUVA, L., COLTORTI, M., MARCHESI, M. & MORRA, V. 1991. Ridge to hot-spot evolution of the Atlantic lithospheric mantle: evidence from Lanzarote peridotite xenoliths (Canary Islands). *Journal of Petrology, Special Issue 'Orogenic Lherzolites and Mantle Processes'*, 271–290.

STUART, F. M., ELLAM, R. M., HARROP, P. J., FITTON, J. G. & BELL, B. R. 2000. Constraints on mantle plumes from the helium isotopic composition of basalts from the British Tertiary Igneous Province. *Earth and Planetary Science Letters*, **177**, 273–285.

SUN, S.-S. & MCDONOUGH, W. F. 1989. Chemical and isotopic systematics of oceanic basalts: implications for mantle composition and process. *In*: SAUNDERS, A. D. & NORRY, M. J. (eds) *Magmatism in the Oceanic Basins*. Geological Society, London, Special Publications, **42**, 313–346.

WILSON, M. & BIANCHINI, G. 1999. Tertiary–Quaternary magmatism within the Mediterranean and surrounding regions. *In*: DURAND, B., JOLIVET, L., HORVÁTH, F. & SÉRAME, M. (eds), *The Mediterranean Basins: Tertiary Extension within the Alpine Orogen*. Geological Society, London, Special Publications, **156**, 141–168.

WILSON, M. & PATTERSON, R. 2001. Intraplate magmatism related to short-wavelength convective instabilities in the upper mantle: evidence from the Tertiary–Quaternary volcanic province of Western and Central Europe. *In*: ERNST, R. E. & BUCHAN, K. L. (eds) *Mantle Plumes: their Identification through Time*. Geological Society of America, Special Papers, **352**, 37–58.

ZINDLER, A. & HART, S. R. 1986. Chemical geodynamics. *Annual Review of Earth and Planetary Sciences*, **14**, 493–571.

Metasomatism induced by alkaline magma in the upper mantle of northern Victoria Land (Antarctica): an experimental approach

C. PERINELLI[1], A. ORLANDO[2], A. M. CONTE[3], P. ARMIENTI[1], D. BORRINI[4], B. FACCINI[5] & V. MISITI[6]

[1]*Dipartimento di Scienze della Terra, Università di Pisa, via S. Maria 53, 56100 Pisa, Italy (e-mail: cperinelli@dst.unipi.it)*

[2]*CNR–IGG, UO di Firenze, via G. La Pira, 4, 50121 Firenze, Italy*

[3]*CNR–IGG, UO di Roma, p.le Aldo Moro 5, 00185 Roma, Italy*

[4]*Dipartimento di Scienze della Terra, Università di Firenze, via G. La Pira, 4, 50121 Firenze, Italy*

[5]*Dipartimento di Scienze della Terra, Università di Ferrara, via Saragat 1, 44100 Ferrara, Italy*

[6]*INGV Sezione di Sismologia e Tettonofisica, via di Vigna Murata 605, 00143 Roma, Italy*

Abstract: Magma generation in the Ross Sea system is related to partial melting of strongly metasomatized mantle sources where amphibole most probably plays a crucial role. In this context, metasomatism induced by a mela-nephelinite melt in lithospheric mantle of the Mt. Melbourne Volcanic Province (northern Victoria Land (NVL), Antarctica) was investigated experimentally studying the effects of melt interaction with lherzolite at 1.5–2.0 GPa and $T = 975–1300\ ^{\circ}C$, and wehrlite at 1.0 GPa and $T = 1050–1250\ ^{\circ}C$. The experiments were designed to induce melt infiltration into the ultramafic rocks. The observed modifications in minerals are compared with those found in mantle xenoliths from NVL. The effects of metasomatic modifications are evaluated on the basis of run temperature, distance from the infiltrating melt and the diffusion rates of chemical components. Both in lherzolite and wehrlite, clinopyroxene exhibits large compositional variations ranging from primary diopside to high-Mg–Cr–(Na) augitic and omphacitic clinopyroxenes in lherzolite, and to low-Mg and high-Ti–Al–Fe–Na augites in wehrlite. Olivine (in wehrlite) and spinel (in lherzolite) are also compositionally modified: the former shows enrichment in Fe and the latter displays a higher Cr/(Cr + Al) ratio. The systematic variations in mineral compositions imply modifications of the chemistry of the infiltrating melt as recorded by the glass veinlets and patches observed in some charges. In experiments involving wehrlite paragenesis, the glass composition approaches that of melt patches associated with both amphibole-free and amphibole-bearing natural samples, and is related to olivine + clinopyroxene crystallization coupled with primary clinopyroxene dissolution at the contact between the metasomatizing melt and the solid matrix. Even if amphibole crystallization was not attained in the experiments, we were able to explain the occurrence of amphibole in the natural system considering that in this case a hot metasomatizing melt infiltrates a cooler matrix.

The Ross rift system and accompanying Cenozoic volcanism of the Mt. Melbourne Volcanic Province (northern Victoria Land (NVL), Antarctica) has been related either to the occurrence of a long-lasting mantle plume or to the top-down control of the tensile state of the lithosphere (Rocholl *et al.* 1995; Rocchi *et al.* 2006). Alkali-basaltic eruptions brought to the surface abundant mantle xenoliths, mainly represented by both amphibole-free and amphibole-bearing spinel peridotites and cumulitic pyroxenites–wehrlites, which can provide information on the thermal state and the chemical and mineralogical composition of lithospheric mantle.

Previous studies have revealed a significant mineralogical and compositional heterogeneity of NVL upper mantle, as a result of the combined effects of partial melting and both modal and cryptic metasomatic processes (Coltorti *et al.* 2004, 2006; Perinelli *et al.* 2006). Modal metasomatism of NVL mantle xenoliths is recognizable by the occurrence of pargasitic to kaersutitic amphibole, usually associated with glass. Amphibole may form veins or grow as disseminated grains around clinopyroxene and/or spinel. Disseminated and vein amphiboles have similar major and trace element composition and their genesis

From: COLTORTI, M. & GRÉGOIRE, M. (eds) *Metasomatism in Oceanic and Continental Lithospheric Mantle.* Geological Society, London, Special Publications, **293**, 279–302.
DOI: 10.1144/SP293.13 0305-8719/08/$15.00

is attributed to the reaction of lherzolitic rocks with an infiltrating magma, possibly an undersaturated, TiO_2-rich Na alkaline silicate melt (Coltorti *et al.* 2004). According to Coltorti *et al.* the reaction that generates amphibole first produces progressive modifications on primary mantle paragenesis forming secondary olivine (ol2-nat), clinopyroxene (cpx-A) and spinel (sp2-nat), and consuming orthopyroxene. These neoformed phases represent 'precursors' of amphibole as well as being associated with it. Coltorti *et al.* (2004) inferred that the possible metasomatic agent was similar to the most undersaturated rock found in the province, a nephelinite cropping out at Greene Point (sample SAX20, Orlando *et al.* 1997; Perinelli *et al.* 2006). An analogous nephelinitic melt has been considered by Perinelli & Armienti (2005) to be responsible for the metasomatic events recognized in wehrlites and pyroxenites cropping out in the same area.

The concurrent presence of amphibole-free and amphibole-bearing spinel peridotites and pyroxenites has been documented in several areas worldwide (Xu & Bodinier 2004, and references therein). They may result from the same metasomatic event (Xu & Bodinier 2004) but are related to two different mechanisms: (1) 'wall-rock' metasomatism, caused by the transport of melt in fractures (veins and dykes); (2) 'diffuse' metasomatism related to percolation of small melt fractions along grain boundaries in a solid matrix. The differences in metasomatic assemblage and mineral compositions (major and trace elements) in the xenoliths can be explained by the P–T control on amphibole stability and the progressive chemical variation of infiltrating melts (Xu & Bodinier 2004).

Despite the interest in completely highlighting how 'diffuse' and/or 'wall-rock' metasomatism acts, few experimental studies on interaction of alkaline melts with mantle rocks have been undertaken (e.g. Sen & Dunn 1994; Shaw *et al.* 1998; Rapp *et al.* 1999; Shaw 1999). Therefore, to better understand the processes involved in the metasomatism in NVL mantle, a series of high-pressure–high-temperature experiments were performed to simulate *in situ* the effect of different extents of metasomatism. In particular, the aim of the experiments was to investigate the reactions affecting lherzolite or wehrlite phases during interaction with alkaline melts, and to test the possibility that ensuing reactions generate amphibole.

The experiments were performed at pressure conditions of 1.5–2.0 GPa for lherzolite and 1.0 GPa for wehrlite in a P–T range close to the conditions of metasomatism that may have occurred in nature, according to Perinelli *et al.* (2006).

Starting materials

Nephelinite–lherzolite runs at high T ($>1100\ ^\circ$C)

In these runs we used fine-grained ($<100\ \mu$m) nephelinite SAX20 (sampled at Greene Point) containing olivine phenocrysts (Fo_{71-78}) (Table 1) in a groundmass of diopsidic clinopyroxene, feldspar ($Ab_{49}Or_{47}An_4$), nepheline ($Ne_{66-70}Ks_{3-6}Qtz_{23-30}$) and spinel (magnetite$_6$–ulvöspinel$_{94}$ series).

Anhydrous lherzolite ($<50\ \mu$m) from a xenolith (sample 154L, provided by M. Coltorti) was chosen as representative of unmetasomatized mantle. Mineral compositions are given in Table 1.

Nephelinite–lherzolite runs at low T ($<1100\ ^\circ$C)

In these runs we used the 154 L lherzolite and a SAX20 glass_5bru glass obtained melting in air SAX20 powder at 1400 °C (quenched after 2 min) in a Deltech DT-31VT-OS2 vertical quench furnace and remelting the resulting glass at the same temperaure, after grinding. Natural brucite ($Mg(OH)_2$) powder (5 wt%, 99.9% pure) was added to the (anhydrous) glass, as its decomposition at run conditions (Irving *et al.* 1977) supplies water to the system (Table 1). Moreover, another glass (SAX20-2.5TiO_2glass_5bru) was prepared by adding 2.5 wt% TiO_2 to SAX20 prior to the two melting cycles at 1400 °C; as in the preparation of the previous starting material, 5 wt% of 99.9% pure brucite was added to the mixture before loading the capsule.

MgO and TiO_2 additions allow the bulk composition of the glass to approach that of metasomatic melts inferred by Coltorti *et al.* (2004) (Table 1) and water released by brucite enhances reaction rates and counterbalances the water loss during glass synthesis.

Nephelinite–wehrlite runs

Nephelinite SAX20 was used with a fresh wehrlite (BRP19), free of any metasomatic feature, sampled at Browning Pass, on the coast of Ross Sea, NVL. This rock consists of *c.* 50% olivine (Fo_{81}), *c.* 50% diopsidic clinopyroxene and a trace of Cr-spinel (Table 1).

Experimental and analytical procedures

Nephelinite–lherzolite runs

At $T > 1100\ ^\circ$C nephelinite powder was placed at the bottom of a graphite capsule, to avoid Fe loss,

Table 1. *Representative composition of minerals in lherzolite and in wehrlite together with whole-rock composition of nephelinite SAX20 and other synthetic starting materials used in the runs. Metasomatizing melts inferred by Coltorti et al. (2004) are also reported for comparison*

	Lherzolite 154L				Wehrlite BRP19			SAX20*	SAX20glass_5bru nominal	SAX20-2.5TiO_2glass_5bru nominal	melt1†	melt2†
	ol1	opx1	cpx1	sp1	ol1	cpx1	sp1					
SiO_2	40.73	55.93	52.81	bdl	40.55	51.18	0.05	40.78	39.19	38.23	39.68	47.74
TiO_2	bdl	bdl	0.07	0.01	bdl	0.67	2.18	3.62	3.48	5.74	7.48	5.66
Al_2O_3	bdl	3.25	3.19	48.04	bdl	4.16	26.84	11.81	11.35	11.07	12.13	10.49
FeO^T	8.79	5.59	1.93	11.32	17.57	6.01	28.53	14.50	13.93	13.59	3.74	5.66
MnO	0.09	0.18	0.14	0.02	0.19	0.10	0.10	0.28	0.27	0.26		
MgO	50.20	34.17	16.99	18.49	41.53	16.43	11.42	9.33	12.26	12.04	17.91	13.32
CaO	0.02	0.55	23.56	bdl	0.18	19.75	bdl	9.23	8.87	8.65	14.96	9.9
Na_2O	n.d.	0.04	0.39	n.d.	n.d.	0.64	n.d.	5.31	5.10	4.98	4.04	4.01
K_2O	bdl	bdl	bdl	bdl	bdl	bdl	bdl	1.54	1.48	1.44		2.83
Cr_2O_3	bdl	0.66	0.79	20.76	bdl	0.92	29.99	0.08	0.08	0.08		
NiO	0.40	n.d.	n.d.	n.d.	bdl	bdl	bdl	0.03	0.03	0.03		
P_2O_5	n.d.	n.d.	n.d.	n.d.	n.d.	n.d.	n.d.	1.60	1.54	1.50		
H_2O	n.d.	n.d.	n.d.	n.d.	n.d.	n.d.	n.d.	0.90	1.47	1.47		
Total	100.23	100.37	99.87	98.64	100.02	99.86	99.11	99.01	99.05	99.08	99.94	99.61
Fo	91.05				80.81							
En		90.38	48.44			48.26						
Fs		8.57	3.31			10.07						
Mg-no.				0.75			0.50					
Cr-no.				0.22			0.43					

ol1, olivine; opx1, orthopyroxene; cpx1, clinopyroxene; sp1, spinel; H_2O value refers to LOI. bdl, below detection limit; n.d., not determined; Fo, En, Fs, forsteritic, enstatitic, ferrosilitic components, respectively; Mg-number = $Mg/(Mg + Fe^{2+})$; Cr-number = $Cr/(Cr + Al)$.

*From Orlando *et al*. (1997).

†Metasomatizing melts from Coltorti *et al*. (2004).

and in close contact with lherzolite powder; the nephelinite/lherzolite ratio was *c.*1 in all runs. The graphite capsule (4 mm long) was then inserted into an outer Pt capsule (o.d. 3.0 mm, i.d. 2.8 mm, length *c.* 7–8 mm), which was welded shut. Experiments were performed at 1.5 and 2.0 GPa, at temperatures in the range 1150–1300 °C; runs lasted up to 95 h. No H_2O was added to the charges.

$Ag_{50}Pd_{50}$ capsules were used in runs at $T < 1100$ °C. The melt–peridotite couples were assembled as sandwiches of lherzolite between either SAX20glass_5bru or SAX20-2.5TiO_2-glass_5bru powders, again with a melt/lherzolite ratio of *c.* 1. Because of the lower temperatures of these experiments, longer durations (190–212 h) were used.

All of these experiments (Table 2) were carried out in a $\frac{1}{2}$ inch piston-cylinder apparatus (at CNR–IGG HP–HT Laboratory, Florence) using a salt–Pyrex–crushable alumina assembly and the 'hot piston-out' technique. Pressure was calibrated using the reaction ferrosilite = fayalite + quartz at 1000 °C (Bohlen *et al.* 1980). Further experimental details have been given by Orlando & Borrini (2001). Temperature was measured by a Pt_{100}–$Pt_{90}Rh_{10}$ thermocouple and no correction for the effect of pressure was applied to the thermocouple e.m.f. The pressure was considered accurate to ±0.05 GPa and temperature to ±5 °C of stated values.

Oxygen fugacity during the experiments at $T > 1100$ °C was estimated according to the calculated Fe^{3+} in spinel coexisting with olivine and orthopyroxene (Ballhaus *et al.* 1990) and the C–COH buffer (Ulmer & Luth 1991). The two independent estimates are consistent, and give values of $\Delta FMQ < -1.2$ (where FMQ is the fayalite –magnetite–quartz buffer).

Run products were analysed on a JEOL JXA-8600 electron microprobe operated at 15 kV accelerating voltage and 10 nA beam current. Count times ranged from 10 to 40 s (same times for backgrounds) and alkali loss was minimized by defocusing the electron beam to 15 μm. Data were corrected for the matrix effect using the Bence & Albee (1968) method and errors were estimated according to Vaggelli *et al.* (1999).

Nephelinite–wehrlite runs

These samples were prepared by packing a layer of wehrlite powder over a layer of nephelinite powder in a graphite capsule, to obtain a wehrlite/nephelinite ratio of *c.* 1 in all charges. The graphite capsule was put into a Pt capsule, stored in an oven at 110 °C overnight to remove humidity, and then welded shut. The final length of capsules was 8–9 mm.

All nephelinite–wehrlite experiments were run in a 3/4 inch piston-cylinder apparatus, at the HP–HT Laboratory of Experimental Volcanology and Geophysics of Istituto Nazionale di Geofisica e Vulcanologia (INGV), Rome.

Experiments were performed at 1.0 GPa at 1250–1050 °C; run times were in the range 5–48 h (Table 2). Experiments performed at 1150 °C and 1050 °C were repeated with *c.* 3%water in the capsules. Below we identify as 'hydrous' the experiments with H_2O added in the charge and 'anhydrous' the runs without H_2O addition, although in the latter experiments water is present because of its occurrence in nephelinite (Table 1).

The pressure cell consists of an assembly of NaCl–Pyrex, with a graphite heater and magnesia inner sleeves. The dimensions of this assembly allowed volatile-free and volatile-added charges to be run at the same time. Al_2O_3 (anhydrous runs) or pyrophyllite (water-bearing runs) powder was packed around the capsules (Freda *et al.* 2001). The temperature was controlled by a $W_{95}Re_5$–$W_{74}Re_{26}$ (type C) thermocouple. The thermocouple tip was placed in the middle of *c.* 10 mm long hotspot between the two capsules (for further details see Misiti *et al.* 2006). The thermocouple was encapsulated in an Al_2O_3 sleeve. The temperature was considered accurate to ±3 °C of stated values.

Pressure was calibrated against the NaCl melting point (Bohlen *et al.* 1980) at 1004 °C at 1.0 GPa and 1090 °C at 1.5 GPa. Pressure correction was +250 bar.

Experiments were first pressurized to the target pressure and then heated at a rate of 200 °C min^{-1} to 20 °C below the target temperature. A slower rate of 40 °C min^{-1} was applied within the last 20 °C of heating to avoid overshooting. The experiment was ended by switching off the heating power while maintaining pressure constant. The initial quench rate was about 2000 °C min^{-1}. The pressure is considered accurate to ±0.05 GPa and possible pressure effects on the e.m.f. of the thermocouple were ignored.

Oxygen fugacity estimated according to Ulmer & Luth (1991) is for all experiments $\Delta FMQ < -1.3$. Experimental conditions and results are summarized in Table 2.

Back-scattered electron (BSE) images of nephelinite–wehrlite runs were collected at the Dipartimento di Scienze della Terra of Pisa University, using a Philips XL30 SEM.

Microanalyses of phase composition were performed on polished carbon-coated mounts by a four-spectrometer Cameca SX50-52 electron microprobe using a 15 keV accelerating voltage, a 15 nA beam current (at CNR–IGAG, Rome).

Table 2. *Experimental assemblage, run conditions and results*

Run	Starting material	Capsule	P (GPa)	T (°C)	Duration (h)	Detected phases
169	154L SAX20	C–Pt	1.5	1150	3	*lh*: ol1, opx1, cpx1, sp1, cpx2, sp2 *nf*: glass, cpx, ol, sp, ne
167	154L SAX20	C–Pt	1.5	1200	4	*lh*: ol1, opx1, cpx1, sp1, cpx2, sp2 *nf*: glass, cpx, ol, sp
170	154L SAX20	C–Pt	1.5	1250	49	*lh*: ol1, opx1, cpx1, sp1, cpx2, sp2, $<<$glass *nf*: glass, cpx, ol
166	154L SAX20	C–Pt	1.5	1300	75	*lh*: ol1, opx1, cpx1, sp1, cpx2, sp2, $<<$glass *nf*: glass
173	154L SAX20	C–Pt	2.0	1300	95	*lh*: ol1, opx1, cpx1, sp1, cpx2, sp2 *nf*: glass, cpx, ol, rhönite, sp
178	*154L* *SAX20-2.5TiO$_2$glass_5bru*	$Ag_{50}Pd_{50}$	2.0	975	212	*lh*: ol1, opx1, cpx1, sp1, cpx2, sp2 *nf*: glass, ol, cpx, sp
177	*154L* *SAX20-2.5TiO$_2$glass_5bru*	$Ag_{50}Pd_{50}$	2.0	1025	190	*lh*: ol1, opx1, cpx1, sp1, (ol2), (opx2), cpx2, sp2, $<$glass2 *nf*: glass, oxides, cpx, ap
176	*154L* *SAX20glass_5bru*	$Ag_{50}Pd_{50}$	2.0	1025	190	*lh*: ol1, opx1, cpx1, sp1, (ol2), (opx2), cpx2, sp2, $<$glass2 *nf*: glass, ol, cpx, rhönite, ap
141	BRP19 SAX20	C–Pt	1.0	1250	5	*py*: ol1, cpx1, ol2, cpx2, glass *nf*: glass
140	BRP19 SAX20	C–Pt	1.0	1200	8	*py*: ol1, cpx1, ol2, cpx2, $<$glass *nf*: glass, ol
144	BRP19 SAX20	C–Pt	1.0	1175	8	*py*: ol1, cpx1, ol2, cpx2, $<$glass *nf*: glass, ol
150	BRP19 SAX20	C–Pt	1.0	1150	8	*py*: ol1, cpx1, ol2, cpx2, $<$glass *nf*: glass, ol, cpx, oxides
153	BRP19 SAX20	C–Pt	1.0	1150	24	*py*: ol1, cpx1, ol2, cpx2, glass *nf*: glass, ol, cpx, oxides
154	BRP19 SAX20	C–Pt	1.0	1050	48	*py*: ol1, cpx1, ol2, cpx2, glass *nf*: glass, ol, cpx, oxides, ne
153*	BRP19 SAX20	C–Pt	1.0	1150	24	*py*: ol1, cpx1, ol2, cpx2, glass *nf*: glass, ol, cpx, oxides
154*	BRP19 SAX20	C–Pt	1.0	1050	48	*py*: ol1, cpx1, ol2, cpx2, glass, $<$ sp2 *nf*: glass, ol, cpx, oxides, rhönite, ap

C–Pt, double capsules with graphite inside Pt; *lh*, *nf*, *py* in the *Detected phases* column refer to phases found in lherzolitic, nephelinitic and pyroxenitic portions of the capsule, respectively; ol, olivine; opx, orthopyroxene; cpx, clinopyroxene; sp, spinel; ap, apatite; ne, nepheline; suffixes *1* and *2* refer to original and neo-formed phases, respectively; $<$, scarce; $\ll$, rare.
*Experiments with *c*. 3 wt% H_2O added in the charge.

Matrix effect corrections (ZAF) were performed using the algorithm of Philibert (1963) and Duncumb & Reed (1968). A focused beam was used for minerals, whereas glasses were analysed with a 10 μm diameter beam to minimize volatilization of sodium; a 5 μm diameter beam was used for small volumes of glass in the lowest-temperature experiments.

Results

Nephelinite–lherzolite runs

Phases detected in experimental products are reported in Table 2 and chemical analyses of lherzolite are shown in Tables 3–5. In experimental runs glass is seldom found in lherzolite and is not related to the distance from the lherzolite–nephelinite interface or to the occurrence and the composition of neoformed phases (see below).

Runs at high T (>1100 °C). Nephelinite was completely molten at 1.5 GPa and 1300 °C. At lower temperatures it was partially molten and clinopyroxene + olivine, spinel and nepheline progressively saturated the liquid at decreasing temperature. In the run at 2.0 GPa glass coexisted with clinopyroxene, olivine, spinel and rhönite (Table 2).

The lherzolite area of the charges contains small, rare glass pockets (mostly not analysable by electron microprobe) with the exception of the run performed at the lowest temperature (Fig. 1a).

In the lherzolitic portion of the capsules at 1250 °C, some glass analyses attain a SiO_2-rich latitic composition; the original phases, olivine (ol1), clinopyroxene (cpx1), orthopyroxene (opx1) and spinel (sp1) are accompanied by scattered neoformed subhedral clinopyroxene (cpx2, Fig. 1a) and spinel (sp2). Analyses of neoformed phases in the lherzolitic portion of the charges are reported in Tables 3–5.

At 1.5 GPa, cpx2 is augite in all the runs. With respect to the original phases, there are increases in MgO (from 16.5–17.4 to 26 wt%), Na_2O (from 0.4–0.8 to 2.2 wt%) and Cr_2O_3 (from 0.4–0.9 to 2.7 wt%), whereas CaO decreases (from 22.6–23.8 to 7.6 wt%). In particular, in the run carried out at 1150 °C neoformed clinopyroxene is mainly found around orthopyroxene crystals together with glass that is not analysable (Fig. 1b).

At 2.0 GPa cpx2 has a higher Na_2O content (2.3–4.1 wt%) than cpx2 synthesized at 1.5 GPa; the CaO content is generally low (9.7–14.2 wt%) and Cr_2O_3 and MgO content are in the range of 1.2–1.8 and 17.4–18.4 wt%, respectively. According to the Morimoto (1989) classification, most of the analysed crystals are omphacite. Neoformed spinel (sp2) occurs as subhedral crystals or coronas around original crystals in all the runs, as shown in Figure 1c. Sp2 crystals generally show higher Cr-number ($Cr/(Cr + Al)$; up to 0.85) and lower Mg-number ($Mg/(Mg + Fe^{2+})$; down to 0.63) with respect to sp1 crystals. The highest Cr_2O_3 content (67.2 wt%) was found in experiments at 1150 °C.

Runs at low T (<1100 °C). BSE images reveal that some olivine crystals close to the lower interface sank into the nephelinitic portion and reacted from Fo_{90} to Fo_{85}. In these runs interaction occurred despite the low temperature, probably because of the reactivity of glass as starting material and the long durations utilized (190–212 h).

In the run with SAX20glass_5bru, in the nephelinitic portions of the capsule, glass is dominant and olivine (Fo_{78}), augitic clinopyroxene, rhönite and apatite crystals are commonly found. In the lherzolite, neoformed phases join the original ones: olivine crystals equilibrated to Fo_{86} close to the lower interface (ol2) and small (<20 μm) enstatitic orthopyroxene crystals (opx2) enriched in Na_2O (0.5–1.4 wt%) and CaO (1.1–1.6 wt%) relative to opx1 are sometimes found scattered in sporadic glass patches along the capsule walls. Glass analyses show very low totals (<70 wt%), probably because of the combined effect of water content and poorly polished surfaces of micro-vesicular or friable glass (e.g. see Peterson & Newton 1990). Neoformed augite and omphacite, enriched in Na_2O (up to 3.3 wt%) and Cr_2O_3 (up to 2.5 wt%) and depleted in CaO (16.2–19.8 wt%) with respect to cpx1, are found throughout the lherzolitic portion together with high Cr-number (0.39–0.54)–low Mg-number (0.59–0.60) neoformed spinel.

In runs with SAX20-2.5TiO_2glass_5bru (Ti-doped), at 1025 °C, glass is the dominant phase in the nephelinitic portions of the charge; however, small (<10 μm) ilmenite–hematite crystals are scattered in the glass together with scarce clinopyroxene and apatite. As in the undoped run, we detected in the peridotite high-Na_2O and -CaO orthopyroxene (opx2) in (nephelinitic) glass pockets and high-Na_2O, -Cr_2O_3 and low-CaO neoformed augitic and omphacitic clinopyroxene. High Cr-number (0.64–0.65) spinels (sp2) are commonly present throughout the lherzolitic portion; their TiO_2 contents (1.2–1.8 wt%) are greater than in sp1 and in sp2 of the undoped run. Furthermore, the Mg-number (0.48–0.50) is the lowest among the analysed spinels in all experiments.

At 975 °C some clinopyroxene, olivine and spinel crystals are scattered in the glass in the nephelinitic portions of the capsule. Some olivine (Fo_{90}) crystals, probably from the lherzolitic portion, are present in the lower nephelinitic

Table 3. *Representative electron microprobe analyses of cpx2 in lherzolite*

Run	169	169	169	167	167	167	167	167	170	170	166	
P (GPa)/T (°C)	1.5/1150	1.5/1150	1.5/1150	1.5/1200	1.5/1200	1.5/1200	1.5/1200	1.5/1200	1.5/1250	1.5/1250	1.5/1300	
SiO_2	54.59	54.29	53.51	47.67	53.39	53.97	54.10	54.19	54.31	54.34	53.27	
TiO_2	bdl	bdl	0.11	2.35	0.17	0.18	0.41	0.03	0.18	0.20	0.09	
Al_2O_3	0.71	0.70	1.94	8.82	3.98	4.06	4.49	2.96	3.24	4.92	3.23	
Cr_2O_3	1.91	1.47	0.83	0.81	1.93	1.82	0.86	1.85	1.20	2.71	1.77	
FeO^T	2.44	2.58	3.18	7.39	5.59	5.54	6.21	5.73	4.28	3.24	3.57	
MnO	0.32	0.14	bdl	0.22	0.08	0.17	0.28	0.30	0.28	0.23	0.11	
MgO	19.42	19.19	19.29	14.02	22.63	21.96	22.00	25.96	20.42	17.00	20.11	
CaO	19.91	20.79	20.13	15.96	10.51	11.17	10.71	7.62	14.77	15.37	16.95	
Na_2O	0.70	0.83	0.59	2.31	1.17	1.23	1.47	0.83	1.04	2.24	0.93	
K_2O	0.04	bdl	0.04	0.14	bdl	bdl	0.09	bdl	bdl	bdl	bdl	
Total	100.04	99.99	99.62	99.69	99.45	100.10	100.62	99.47	99.72	100.25	100.03	
mg-no.	93.39	92.96	91.50	77.10	87.78	87.55	86.27	88.94	89.43	90.30	90.90	
SiO_2/Al_2O_3	76.89	77.56	27.58	5.40	13.41	13.29	12.05	18.31	16.76	11.04	16.49	
Run:	178	178	176	176	176	177	177	173	173	173	173	173
P (GPa)/T (°C)	2/975	2/975	2/1025	2/1025	2/1025	2/1025	2/1025	2/1300	2/1300	2/1300	2/1300	2/1300
SiO_2	54.06	54.49	54.95	54.95	53.40	54.83	53.53	51.66	53.18	53.65	53.77	53.43
TiO_2	0.05	0.08	0.09	0.11	0.17	0.29	0.87	1.38	0.37	0.57	0.66	0.10
Al_2O_3	3.28	2.91	1.65	1.60	4.20	3.85	6.18	7.88	7.13	7.30	8.39	6.44
Cr_2O_3	0.75	1.05	2.52	2.31	0.64	0.97	2.08	1.09	1.66	1.29	1.29	1.83
FeO^T	1.86	1.94	2.20	2.24	3.70	3.79	5.75	8.84	4.20	4.25	4.13	3.78
MnO	0.05	0.06	0.09	0.21	0.26	0.14	0.17	0.29	0.17	0.21	0.15	0.06
MgO	17.41	16.93	18.25	18.83	16.55	16.46	14.08	14.72	18.36	17.55	17.37	18.05
CaO	20.72	21.46	19.43	18.96	18.60	18.13	14.02	11.12	11.97	10.93	9.72	14.18
Na_2O	1.53	1.34	1.25	1.27	1.89	2.45	3.90	3.41	2.75	3.63	4.14	2.27
K_2O	0.19	0.27	bdl	bdl	0.04	bdl	bdl	0.07	bdl	bdl	bdl	0.04
Total	99.90	100.53	100.43	100.48	99.45	100.91	100.58	100.46	99.79	99.38	99.62	100.18
mg-no.	94.32	93.93	93.64	93.72	88.81	88.51	81.29	74.71	88.58	87.99	88.18	89.44
SiO_2/Al_2O_3	16.48	18.73	33.30	34.34	12.71	14.24	8.66	6.56	7.46	7.35	6.41	8.30

mg-number $= Mg \times 100/(Mg + Fe^T)$; bdl, below detection limit.

Table 4. *Representative electron microprobe analyses of sp1 and sp2 in lherzolite*

Run	169	169	167	170	173	176	176	176	177	177	178
	sp1	sp2	sp2	sp1	sp1	sp1	sp2	sp2	sp2	sp2	sp1
P (GPa)/*T* (°C)	1.5/1150	1.5/1150	1.5/1200	1.5/1250	2/1300	2/1025	2/1025	2/1025	2/1025	2/1025	2/975
TiO_2	0.07	0.11	0.11	0.59	0.32	0.10	0.15	0.07	1.81	1.21	bdl
Al_2O_3	46.42	35.42	22.56	44.05	42.63	46.83	33.68	24.29	14.68	15.89	49.45
Cr_2O_3	22.89	36.15	47.64	22.40	27.73	22.84	32.62	42.74	41.53	41.40	21.67
FeO^T	12.43	12.77	11.79	17.25	11.54	12.06	20.49	18.60	31.57	31.04	10.78
MnO	0.11	0.15	0.16	0.14	0.08	0.13	0.42	0.32	0.47	0.51	0.13
MgO	18.68	17.30	16.67	15.18	18.49	18.93	13.72	13.14	10.49	10.84	19.81
CaO	0.02	0.06	0.14	0.15	0.02	0.07	0.14	0.05	0.12	0.08	0.00
Total	100.62	101.96	99.07	99.76	100.79	100.96	101.22	99.21	100.67	100.97	101.84
Cr-no.	0.25	0.41	0.59	0.25	0.30	0.25	0.39	0.54	0.65	0.64	0.23
Mg-no.	0.75	0.72	0.75	0.63	0.75	0.76	0.59	0.60	0.48	0.50	0.78

Mg-number $=Mg/(Mg + Fe^{2+})$ where Fe^{2+} was calculated on the basis of stoichiometry and charge balance; Cr-number $= Cr/(Cr + Al)$; bdl, below detection limit.

Table 5. *Representative electron microprobe analyses of glasses in lherzolite*

Run	170	170	170
P (GPa)/T (°C)	1.5/1250	1.5/1250	1.5/1250
SiO_2	54.64	56.96	58.27
TiO_2	1.37	0.55	0.44
Al_2O_3	21.55	21.47	22.26
Cr_2O_3	bdl	0.08	0.13
FeO^T	3.61	2.90	2.58
MnO	0.11	bdl	0.03
MgO	3.58	3.10	3.49
CaO	2.72	2.04	2.05
Na_2O	4.38	4.99	5.31
K_2O	3.68	3.91	4.29
Total	95.64	96.00	98.85

bdl, below detection limit.

section. Neoformed clinopyroxene and spinel crystals are found in the (central) lherzolitic portion of the charge. In particular, cpx2 shows slight Na_2O enrichment (up to 1.53 wt%) and CaO depletion (down to 20.7 wt%) with respect to cpx1.

Nephelinite–wehrlite runs

At 1.0 GPa the nephelinite layer of anhydrous experiments is completely molten at 1250 °C; at 1200 °C olivine crystallizes, joined by clinopyroxene at 1150 °C, and by spinel and nepheline at 1050 °C. In the hydrous experiments performed at 1150 °C and 1050 °C, crystal assemblages in nephelinite are the same as the anhydrous experiments but lack nepheline; rhönite and apatite occur at lower temperature. It is evident that at different temperatures different melt composition start to interact with the wehrlitic layer and their composition are reported in Table 8 and shown in the total alkalis–silica (TAS) diagram (large symbols in Fig. 3a).

Melts are in contact with the wehrlite through a reaction area whose extent depends on experimental temperature and run duration. The influence of the experimental time is shown by the replicated anhydrous experiment at 1150 °C: in the shorter run (8 h) the reactions are limited to a *c.* 250 μm wide area whereas in the longer runs (24 h) the reaction affects all the wehrlite layer.

Run at T = *1250 °C.* The wehrlite layer is strongly infiltrated and three sub-layers can be recognized (Fig. 2): in the boundary layer (layer I), 300 μm wide closest to nephelinite melt, clinopyroxene (cpx1) dissolved completely, resulting in a mush of olivine + melt (Fig. 2a). The melt composition in this region is controlled by the contribution of cpx1 dissolution in the nephelinite; the resulting

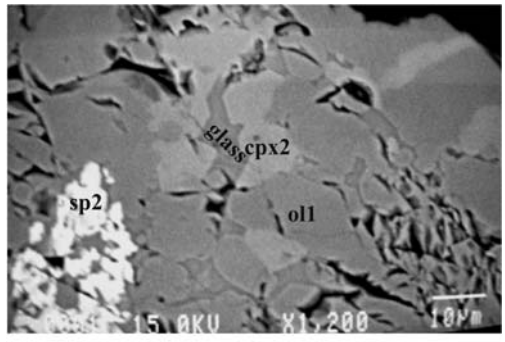

(a)

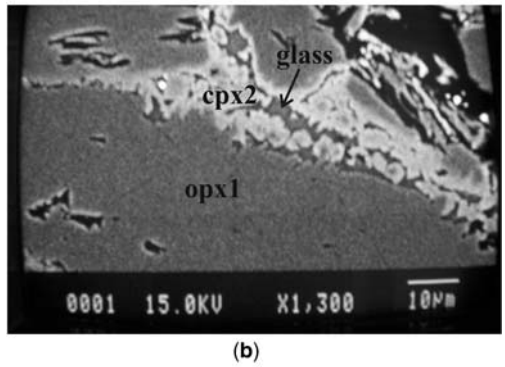

(b)

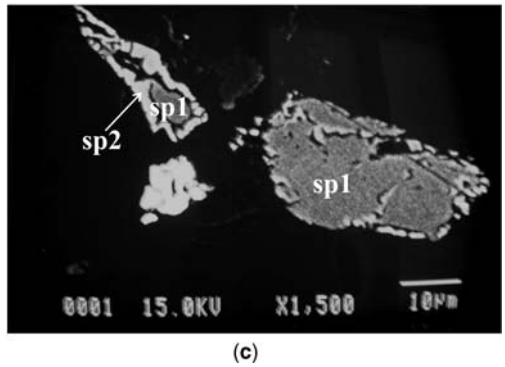

(c)

Fig. 1. Backscattered electron images of representative run products in lherzolite. (**a**) Run 170 (1250 °C and 1.5 GPa); (**b**, **c**) run 169 (1150 °C and 1.5 GPa).

melt is enriched in SiO_2 and CaO, and depleted in alkalis (mainly Na_2O), TiO_2 and P_2O_5 (Tables 6–8; Fig. 3a–d). The mg-number is close to that of nephelinite.

The olivine grains become more rounded or show embayed rims; the composition is depleted in iron (Fo 82.6) relative to primary olivine (Fo 80.8; ol1). Calculated partition coefficients ($K_{D\ Mg/Fe}$) for Mg and Fe (all Fe as FeO) between

Table 6. *Representative electron microprobe analyses of ol2 in wehrlite*

Run	141 ol1*	141 ol2†	141 ol2	141 ol1‡	140 ol2§	140 ol2	140 ol2§	153 ol2§	153 ol2¶	153 ol2§	153‖ ol2§	153‖ ol2
T (°C)	1250	1250	1250	1250	1200	1200	1200	1150	1150	1150	1150	1150
SiO_2	39.06	39.57	40.19	40.02	38.77	38.56	38.69	37.99	38.53	39.21	38.19	38.88
TiO_2	bdl	bdl	bdl	bdl	0.02	0.14	0.03	bdl	bdl	bdl	bdl	bdl
Al_2O_3	0.12	bdl	bdl	bdl	0.09	0.32	0.03	0.04	0.03	0.03	0.24	0.05
FeO	16.00	14.58	15.43	14.33	23.16	23.95	21.36	22.91	21.18	19.85	21.21	24.00
MnO	0.39	0.21	0.30	0.10	0.42	0.40	0.49	0.36	0.37	0.34	0.48	0.44
MgO	42.75	44.10	44.09	44.77	36.43	35.83	38.86	37.07	39.57	39.81	38.32	36.91
CaO	0.42	0.39	0.58	0.35	0.44	0.50	0.32	0.62	0.56	0.47	0.54	0.50
NiO	0.24	0.18	0.12	0.18	0.27	0.19	0.19	0.10	0.15	0.23	bdl	0.11
Cr_2O_3	0.17	bdl	0.20	0.12	0.04	0.02	bdl	0.09	0.14	0.02	0.12	0.07
Total	99.15	99.03	100.91	99.87	99.64	99.91	99.97	99.18	100.54	99.96	99.10	100.94
Fo	82.65	84.36	83.59	84.78	73.71	72.73	76.43	74.26	76.91	78.14	76.31	73.28

Run	154 ol2	154 ol2¶	154 ol2¶	154‖ ol2	154‖ ol2	154‖ ol2¶	154‖ ol2¶
T (°C)	1050	1050	1050	1050	1050	1050	1050
SiO_2	37.25	37.57	39.81	37.69	38.16	39.83	39.63
TiO_2	bdl	bdl	bdl	bdl	bdl	bdl	bdl
Al_2O_3	0.03	0.22	0.02	0.02	0.19	bdl	0.25
FeO	32.52	28.82	20.16	30.69	27.68	19.30	17.84
MnO	0.73	0.59	0.35	0.56	0.43	0.34	0.21
MgO	28.99	32.31	39.35	30.59	33.46	40.10	41.18
CaO	0.53	0.43	0.23	0.50	0.41	0.35	0.07
NiO	0.02	0.09	0.17	0.09	0.10	0.19	0.17
Cr_2O_3	0.10	bdl	0.20	bdl	0.08	bdl	0.22
Total	100.18	100.03	100.29	100.14	100.51	100.10	99.57
Fo	61.38	66.64	77.67	63.99	68.31	78.81	76.43

*Restitic olivine in layer.
†Restitic olivine in layer II.
‡Restitic olivine in layer III.
§Analysis at the rim of ol1 at nephelinite–wehrlite boundary layer.
¶Away from nephelinite–wehrlite boundary layer.
‖Wet experiments.
Fo, forsterite; bdl, below detection limit.

olivine and the associated melt range from 0.23 to 0.26. The highest $K_{D\ Mg/Fe}$ values approach the equilibrium values of 0.3 ± 0.03 for mafic melts (Roeder & Emslie 1970).

Layer II, about 600 μm wide, is composed of olivine, clinopyroxene and interstitial melt that may contain neocrysts of olivine and clinopyroxene (Fig. 2a and b). The melt fraction of this layer is very low relative to layer I and the glass occurs in interstitial patches rarely connected to olivine + melt layer by very thin veins. Neoformed olivines crystallized in the largest glass blebs are subequant and up to 25 μm in size whereas neoformed clinopyroxenes are anhedral and similar in size to the neoformed olivines. The primary crystals generally preserve their original shape, showing slightly rounded rims when they occur close to the small glass blebs; sometimes original olivines close to the large blebs show an overgrowth of neoformed olivine (Fig. 2b).

The compositional variation observed in the primary phases consists in the enrichment of forsterite component in olivine (from Fo *c.* 80 in ol1 to an average of Fo 84.3 in ol2) and depletion in TiO_2, Al_2O_3, FeO and Na_2O, as well as an increase in mg-number, in clinopyroxenes (Table 7). These compositional changes indicate a restitic character for these crystals (Hirose & Kawamoto 1995; Shaw *et al.* 2006).

Compositions of the interstitial glass pools, reported in Table 8, differ significantly from those of glasses at the nephelinite–wehrlite interface ('boundary layer'). Moving towards layer III, as melt pools decrease in size, the compositions change, displaying an increase in SiO_2, Al_2O_3, FeO and alkalis (Na_2O to a minor extent), and a decrease of TiO_2, CaO, P_2O_5 and mg-number (Table 8 and Fig. 3).

The secondary olivine (ol2) grown in the largest melt pools has similar composition to restitic olivine (an average of Fo 83.5) whereas secondary clinopyroxene (cpx2) is enriched in TiO_2 (1.1–2.7 wt%), Al_2O_3 (4.2–7.2 wt%), FeO (6.2–10.4 wt%) and Na_2O (1.0–1.6 wt%) (Fig. 4a–c) with respect to cpx1 (Tables 6 and 7). The mg-number of cpx2 ranges from 66 and 74 (Table 7).

Restitic olivine has $K_{D\ Mg/Fe}^{ol/liquid}$ between 0.03 and 0.19, whereas $K_{D\ Mg/Fe}^{ol/liquid}$ between ol2 and the associated melt ranges from 0.14 to 0.17, all consistently lower than equilibrium values. The lowest $K_{D\ Mg/Fe}^{ol/liquid}$ values are related to glass with the highest SiO_2 content. $K_{D\ Mg/Fe}^{cpx/liquid}$ (all Fe as FeO) of restitic clinopyroxene falls outside the equilibrium range of 0.25–0.32 (Nielsen & Drake 1979; Shaw *et al.* 1998), and varies between 0.08 and 0.12. Conversely, the $K_{D\ Mg/Fe}$ values for cpx2 and melt pairs are close to equilibrium values, ranging from 0.26 to 0.38.

In layer III, the most distal from the nephelinite–wehrlite interface (Fig. 2a), olivine and clinopyroxene have compositions similar to those of 'restitic' crystals in layer II but fractions of secondary melt are very low and are not large enough to be analysed.

Runs at $T < 1250\ ^{\circ}C$. As in the 1250 °C run, the wehrlite layer shows various degree of interaction with infiltrated melts. In all experiments the boundary layers (on average 250 μm wide) are characterized by the highest melt fraction; the reaction between liquid and wehrlite results in a decrease in clinopyroxene abundance and growth of neoformed olivine, which occurs either as discrete grains or rims on the original crystals. In the remaining wehrlite, the infiltrating melt forms small patches or a network of thin veins and interstitial glass pools spreading across the entire wehrlite layer. In the short duration (8 h) experiment at 1150 °C the melt–rock interaction area is restricted to a narrow area (about 100 μm in diameter).

Minerals

The neoformed olivine crystallized at the boundary layer is depleted in the Fo component with respect to ol1, approaching the composition of olivine crystallizing in the nephelinite area (from Fo76 for ol2 at 1200 °C to Fo61 for ol2 at 1050 °C; Table 6). Dissolution of initial clinopyroxene in this region strongly decreases from the run at 1200 °C to that at 1050 °C.

In the wehrlite, primary olivine and clinopyroxene do not show significant textural variations and olivine neocrysts may grow in the largest melt pools. The olivine neocrysts progressively approach the composition of ol1 (Table 6). Original clinopyroxene (cpx1) develops narrow (up to 50 μm) and irregular reaction rims (cpx2; Fig. 2c) enriched in TiO_2 (up to 1.25 wt% at 1200 °C; up to 5.55 wt% at 1050 °C), Al_2O_3 (up to 5.4 wt% at 1200 °C; up to 8.9 wt% at 1050 °C), FeO (up to 6.5 wt% at 1200 °C; up to 9.2 wt% at 1050 °C) and Na_2O (0.8 wt% at 1200 °C; up to 1.4 wt% at 1050 °C). These enrichments are coupled with decreasing mg-number values (Table 7 and Fig. 3a–d) (see also Shaw *et al.* 2006, and references therein). It is noteworthy that the cpx2 compositions of each experimental run are related to the composition of the reacting melt, which in turn depends on the experimental temperature (Fig. 3e). Some of the scatter observed in each compositional trend is due to the irregular extent of the melt–rock reactions (Fig. 2c).

In the hydrous experiments at 1150 °C and 1050 °C, cpx1 dissolution at the interface with the

Table 7. *Representative electron microprobe analyses of cpx2 in wehrlite*

Run	141 cpx restitic	141 cpx2*	141 cpx2*	140 cpx2†	140 cpx2‡	153 cpx2‡	153 cpx2*	153§ cpx2†	153§ cpx2†	154 cpx2‡	154 cpx2‡	154 cpx2*
T (°C)	1250	1250	1250	1200	1200	1150	1150	1150	1150	1050	1050	1050
SiO_2	54.11	47.89	50.09	50.54	49.63	46.73	50.88	48.57	51.56	45.29	47.76	50.63
TiO_2	0.28	2.71	1.45	1.25	1.08	2.84	1.55	2.47	1.24	3.92	2.30	1.12
Al_2O_3	1.46	6.17	4.79	5.44	4.91	7.72	5.03	5.54	3.38	7.90	6.61	4.87
Cr_2O_3	1.39	0.31	0.23	0.88	0.88	0.57	0.73	0.28	0.75	0.07	0.15	0.65
FeO^T	4.17	10.24	8.75	6.55	6.24	6.13	4.93	7.79	5.73	9.13	8.24	6.42
MnO	0.10	0.36	0.23	0.16	0.11	bdl	0.07	0.11	0.05	0.26	0.33	bdl
MgO	16.35	11.24	13.52	14.44	15.84	12.80	14.51	12.75	15.19	10.31	12.73	15.22
CaO	21.05	20.14	19.51	19.93	20.44	21.71	21.37	20.83	21.81	22.41	20.46	19.71
Na_2O	0.55	1.40	1.54	0.74	0.81	1.19	1.11	1.18	0.64	1.00	1.15	0.83
Total	99.46	100.46	100.11	99.93	99.95	99.69	100.18	99.53	100.36	100.29	99.73	99.45
mg-no.	87.49	66.18	73.37	79.72	81.90	78.83	83.99	74.48	82.54	66.81	73.36	80.87
SiO_2/Al_2O_3	37.06	7.76	10.46	9.29	10.11	6.05	10.12	8.77	15.25	5.73	7.23	10.40

Run	154§ cpx2‡	154§ cpx2c‡ (rim)	154§ cpx2‡	154§ cpx2‡
T (°C)	1050	1050	1050	1050
SiO_2	46.94	45.83	44.53	46.91
TiO_2	2.70	2.49	5.33	2.94
Al_2O_3	7.54	8.95	10.64	7.80
Cr_2O_3	bdl	bdl	0.42	0.08
FeO^T	9.65	8.78	7.70	9.30
MnO	0.19	0.13	0.16	0.25
MgO	10.30	10.61	9.60	10.30
CaO	21.52	21.43	20.99	20.79
Na_2O	1.04	1.11	1.29	1.32
Total	99.88	99.33	100.66	99.67
mg-no.	87.49	66.18	73.37	79.72
SiO_2/Al_2O_3	37.06	7.76	10.46	9.29

*cpx2 neocrysts in glass blebs far from SAX20–wehrlite boundary layer.
†Clinopyroxene reacted rim analysed far from SAX20–wehrlite boundary layer.
‡cpx2 at boundary layer.
§Wet experiments.
mg-number= $Mg \times 100/(Mg + Fe^T)$; bdl, below detection limit.

Table 8. *Representative electron microprobe analysis of glasses in wehrlite*

Run	141 glass*	141 glass*	141 glass*	141 glass†	141 glass†	141 glass†	141 glass†	140 nephelinite derived melt	140 glass*	140 glass†	153 nephelinite derived melt	153 glass*	153 glass†
T (°C)	1250	1250	1250	1250	1250	1250	1250	1200	1200	1200	1150	1150	1150
SiO_2	45.86	46.28	48.26	47.34	49.23	50.63	51.69	42.24	45.12	46.28	42.4	42.56	44.52
TiO_2	2.66	2.47	2.05	2.72	2.15	1.95	2.13	3.48	4.09	3.91	4.23	4.25	4.36
Al_2O_3	9.74	9.34	8.29	9.84	9.12	13.13	13.34	13.21	13.88	14.16	14.07	13.94	14.67
Cr_2O_3	0.22	0.76	0.28	0.26	0.35	0.52	0.06	0.06	0.10	bdl	bdl	0.05	bdl
FeO^T	13.64	13.47	13.14	12.37	12.13	17.28	13.38	14.35	11.84	11.84	13.85	12.74	11.41
MnO	0.23	0.29	0.26	0.23	0.31	0.35	0.25	0.34	0.31	0.25	0.25	0.28	0.37
MgO	9.11	9.42	8.13	6.00	5.10	2.01	1.20	6.58	4.82	3.15	4.56	3.63	1.74
CaO	12.24	12.45	13.64	14.52	14.49	7.61	9.47	10.22	12.82	12.81	11.73	12.66	11.45
Na_2O	4.10	4.17	4.37	4.78	5.56	4.62	5.34	5.90	5.19	5.60	5.69	5.94	7.32
K_2O	1.17	1.16	1.06	1.12	1.25	1.84	2.37	1.96	1.84	1.99	1.95	2.35	2.48
P_2O^5	1.03	0.19	0.50	0.83	0.30	0.06	0.78	1.64	na	na	1.28	1.61	1.68
mg-no.	54.35	55.49	52.45	46.37	42.83	17.16	13.79	44.98	42.06	32.17	36.99	33.69	21.38
SiO_2/Al_2O_3	4.71	4.96	5.82	4.81	5.40	3.86	3.87	3.20	3.25	3.27	3.01	3.05	3.03

Run	153‡ nephelinite derived melt	153‡ glass*	153‡ glass†	154 nephelinite derived melt	154 glass*	154 glass*	154 glass†	154 glass§	154‡ nephelinite derived melt	154‡ glass*	154‡ glass*	154‡ glass*	154‡ glass†
T (°C)	1150	1150	1150	1050	1050	1050	1050	1050	1050	1050	1050	1050	1050
SiO_2	42.60	43.93	45.76	47.85	49.76	49.4	55.03	50.2	46.74	47.59	48.26	49.9	51.25
TiO_2	3.85	3.94	3.31	2.40	1.88	2.45	1.46	1.69	2.56	2.46	2.20	2.11	1.73
Al_2O_3	13.14	15.28	16.69	19.40	21.01	20.15	22.31	21.75	19.43	19.76	19.98	21.51	23.13
Cr_2O_3	0.14	0.01	bdl	0.03	bdl	0.16	0.04	bdl	bdl	0.08	bdl	0.11	0.07
FeO^T	13.97	10.92	9.49	11.20	6.67	9.33	3.40	5.76	10.26	9.57	9.04	6.76	4.44
MnO	0.30	0.17	0.25	0.18	0.06	0.20	0.01	0.03	0.23	0.26	0.23	0.21	0.09
MgO	5.85	3.26	1.77	2.20	1.96	1.86	1.66	1.95	2.22	2.23	2.30	2.02	1.70
CaO	11.49	11.79	9.62	6.07	4.53	5.36	2.79	3.68	6.58	5.89	5.75	4.93	3.58
Na_2O	5.43	6.61	8.81	6.47	9.62	6.97	7.92	10.51	8.45	8.54	8.37	8.79	10.31
K_2O	2.00	2.04	2.05	3.10	3.67	3.44	4.45	3.82	2.94	3.07	3.12	3.66	3.70
P_2O^5	1.24	2.06	2.26	1.11	0.84	0.68	0.92	0.60	0.60	0.54	0.76	0.45	0.37
mg-no.	42.75	34.74	24.95	25.97	34.36	26.22	46.54	37.64	27.84	29.35	31.22	34.76	40.57
SiO_2/Al_2O_3	3.24	2.88	2.74	2.47	2.37	2.45	2.47	2.31	2.41	2.41	2.42	2.32	2.22

*Glass blebs at SAX20–wehrlite boundary layer.
†Glass blebs in the wehrlite layer.
‡Wet experiments.
§Glass analysed along the capsule wall.
mg-number $= Mg \times 100/(Mg + Fe^T)$; bdl, below detection limit; na, not analysed.

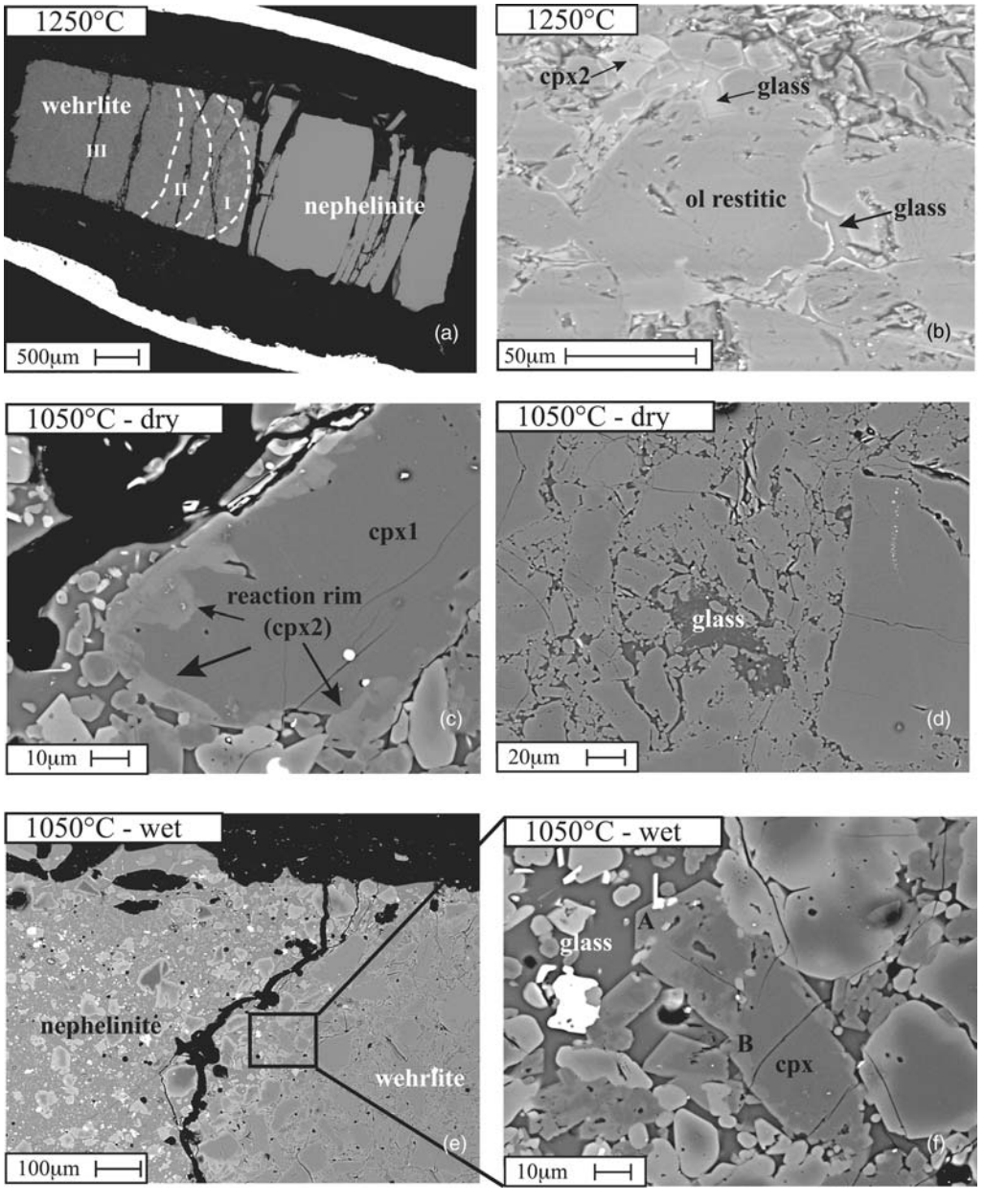

Fig. 2. Backscattered electron images of representative run products in wehrlite. (**a**, **b**) Run 141 (1250 °C), (**c**, **d**) run 154 (1050 °C); (**e**, **f**) run 154* (1050 °C, wet run). I, II and III refer to different reaction areas observed in 1250 °C run. cpx2, clinopyroxenes produced by melt–rock reaction; ol restitic, olivine that underwent partial melting (1250 °C). In (f) A refers to the growth rim on primary clinopyroxene; B refers to the reaction rim of the same crystal.

melt is reduced with respect to the anhydrous counterparts. A small amount of cpx1 dissolved completely (at 1150 °C) or partially (at 1050 °C) in an area about 200 μm wide (Fig. 2e and f). The neoformed phases found both at the interface and inside the wehrlite layer show the same kind of compositional modifications and textural features as recognized in the anhydrous experiments (Fig. 4a–c). In the 1050 °C run a Ti-rich spinel also crystallizes at the boundary layer (Fig. 2f).

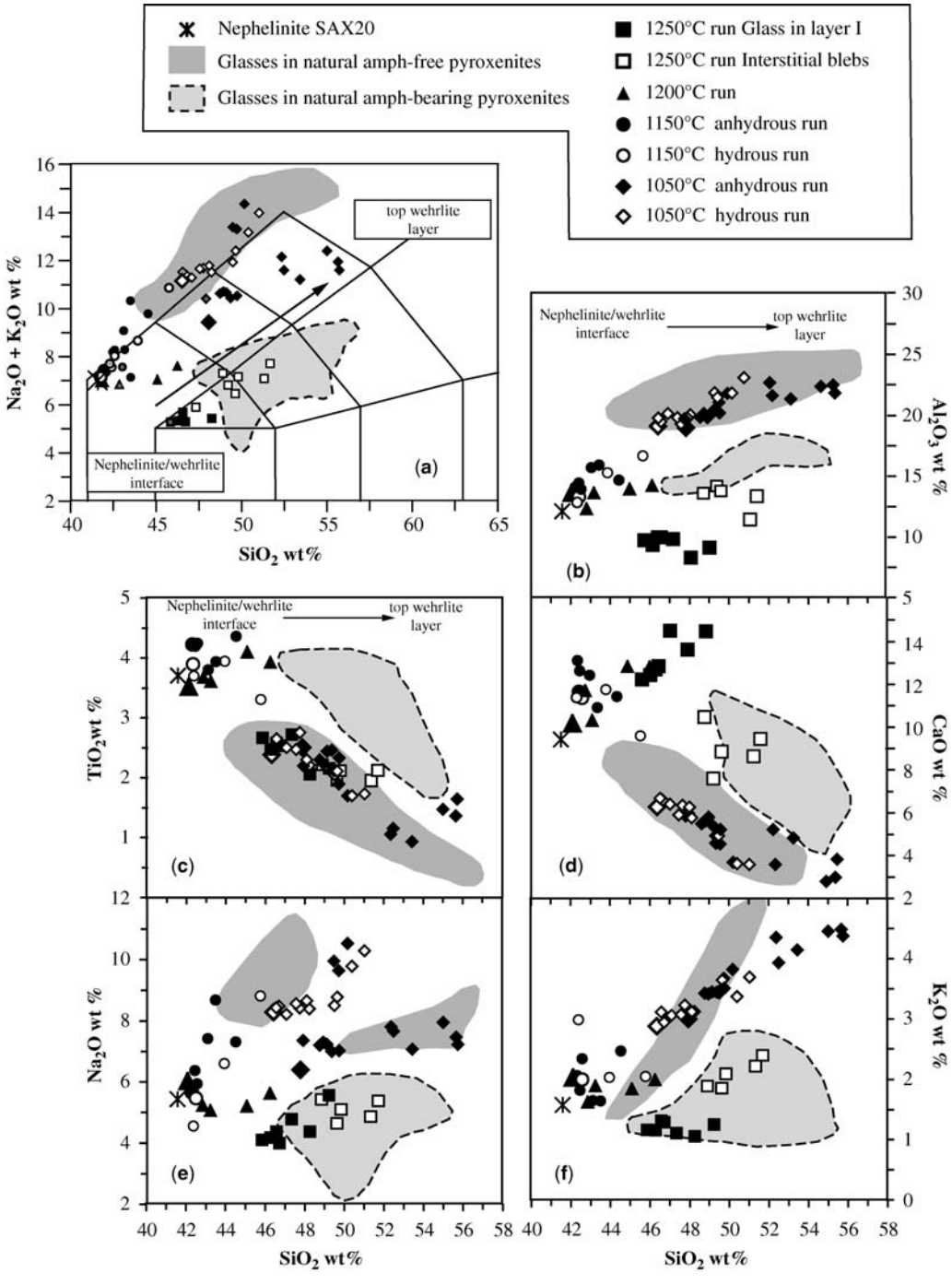

Fig. 3. (**a**) Experimental glasses from nephelinite–wehrlite runs plotted in the TAS classification diagram (Le Bas *et al.* 1986); (**b**–**f**) compositional variation diagrams for experimental glasses. The arrows indicate compositional variations resulting from the continuous interaction of infiltrating melts with the wehrlite. The large symbols represent the nephelinite-derived melts; asterisk indicates the melt composition at the boundary layer that starts infiltration. Also shown are fields for interstitial glasses occurring in natural wehrlites (Perinelli & Armienti unpublished).

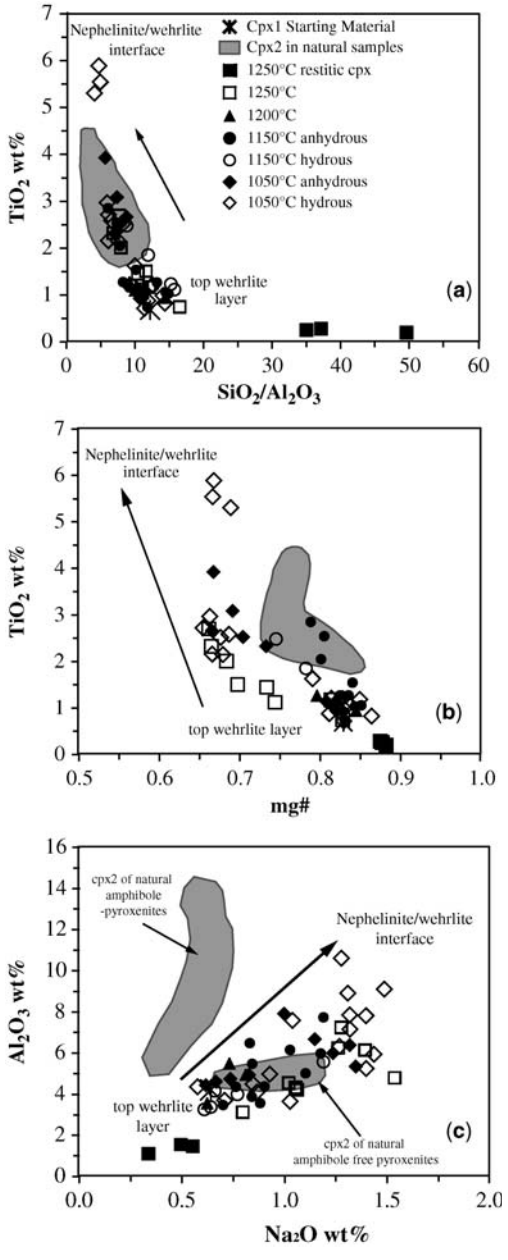

Fig. 4. (**a**) TiO_2 v. SiO_2/Al_2O_3, (**b**) TiO_2 v. mg-number, and (**c**) Al_2O_3 v. Na_2O, for synthesizing clinopyroxenes in nephelinite–wehrlite experiments. Also shown is secondary clinopyroxene related to metasomatism of natural wehrlites (grey area; Perinelli & Armienti 2005). The long arrows indicate compositional variations induced by metasomatism on original clinopyroxene as a function of distance from the nephelinite–wehrlite boundary layer.

Glasses

A network of melt veins and/or interstitial glass pools is observed in all the experiments. This is connected to the nephelinite. Melt compositions of the analysable glass are reported in Table 8.

In the 1200 °C and 1150 °C experiments, including the longest duration run at 1150 °C, most of the interstitial pools were too small to be analysed. Glasses analysed at the boundary layer show weak chemical modifications with respect to nephelinite, except for alkalis (mainly Na_2O), which were enriched in the experiments at 1150 °C. The same enrichment was not observed in glasses from the 1200 °C run, the chemistry of which records instead the higher contribution of clinopyroxene dissolution (Table 8; Fig. 3a–f).

In the hydrous and anhydrous experimental runs performed at 1050 °C, the melts occurring at the boundary layer and invading wehrlite have the most differentiated compositions (Fig. 3a), being derived by high degrees of nephelinite crystallization at this temperature; further inside the rock, these melts show an increase in SiO_2 (to 55%) and K_2O (to 4.5%) and a depletion in CaO, P_2O_5 (not shown) and TiO_2 (although these last two elements show an increase at the top of wehrlite; Fig. 3c). In these runs, Na_2O content in the melt patches is influenced by the presence of water, which prevented the nepheline crystallization in the hydrous nephelinite-derived melt; as a consequence, Na_2O concentrations in wet experiments are higher than in anhydrous ones, reaching 10 wt% in the distal interstitial patches. Similar Na content is attained in the water-free runs only in the melt portions that occur along the wall of the graphite capsule (Fig. 3e).

It is noteworthy that the mg-number values shown a good covariance with SiO_2 (not shown).

In terms of mineral–melt Mg and Fe exchange equilibrium we found that olivine $K_D^{ol/liquid}{}_{Mg/Fe}$ (0.27–0.33) and clinopyroxene $K_D^{cpx/liquid}{}_{Mg/Fe}$ (0.2–0.28) in the boundary layer approach equilibrium values for the highest temperature experiment (1200 °C) or the longest duration runs (1050 °C, 48 h). In the wehrlite layer the $K_D^{ol/liquid}{}_{Mg/Fe}$ values are generally lower (0.15–0.18) than those calculated for the boundary layer, although $K_D^{cpx/liquid}{}_{Mg/Fe}$ shows a very wide range (0.12–0.35), with most values falling in the range 0.24–0.30, indicating equilibrium between most of the clinopyroxenes and associated melts. The low K_D values for olivine may be due to the high SiO_2 content of the glass occurring in this area (Draper & Green 1997; Shaw *et al.* 1999).

$K_D^{phases/liquid}{}_{Mg/Fe}$ values computed for 1150 °C experiments are constantly low (<0.19 and <0.18

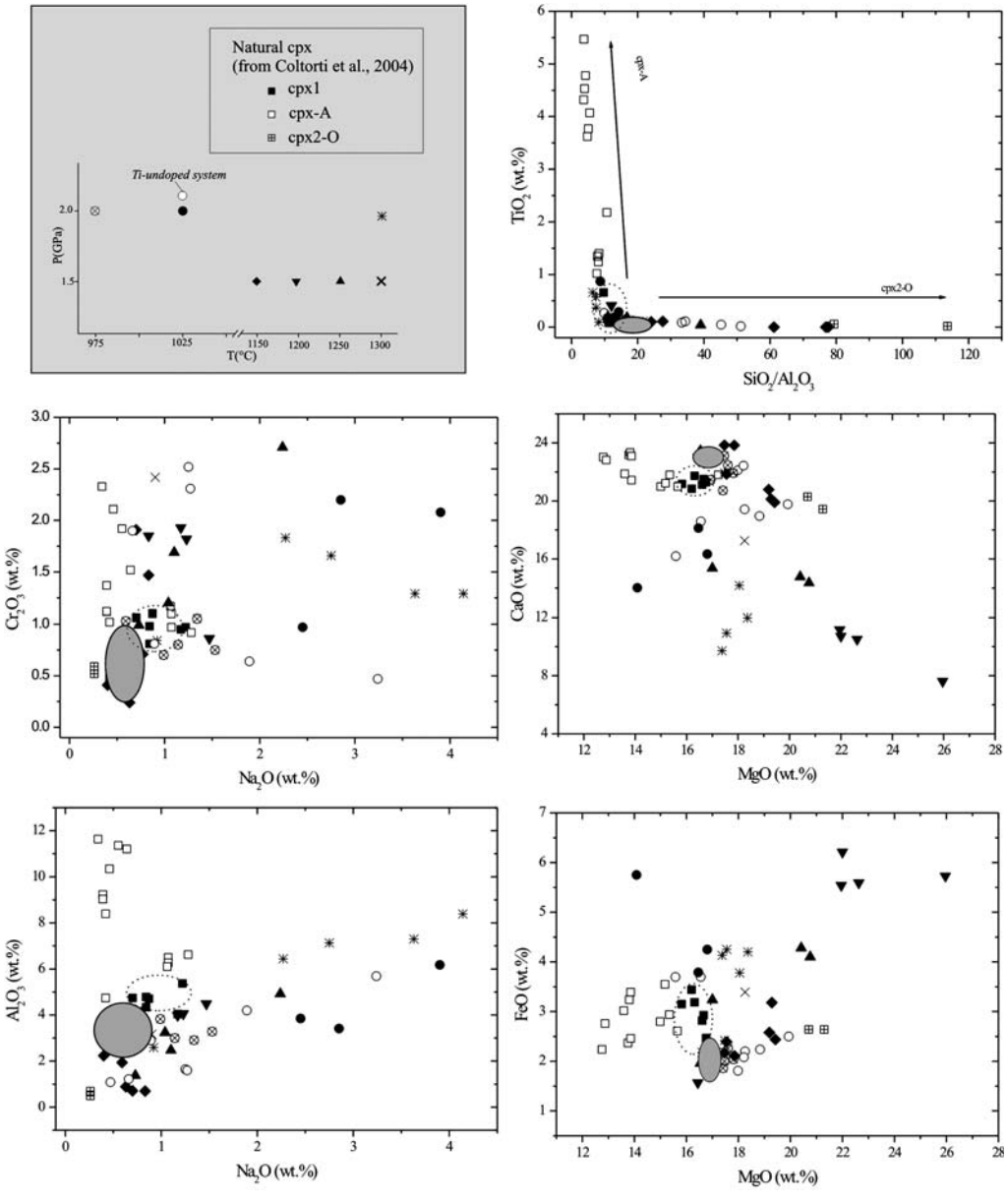

Fig. 5. Composition of experimental (this paper) and natural clinopyroxenes (from Coltorti *et al.* 2004). The shaded area and dotted line indicate the compositional field of cpx1 of lherzolite 154L (this paper) and cpx1 from Coltorti *et al.* (2004), respectively. The arrows in the upper right diagram indicate out compositional variations induced by metasomatism on cpx1, as reported by Coltorti *et al.* (2004).

for olivine and clinopyroxene, respectively). These low K_D values are not linked to the occurrence of high SiO_2 melts and may be related to the run duration being too short to attain equilibrium.

Discussion

The ubiquitous occurrence of neoformed clinopyroxene and spinel in the lherzolite and clinopyroxene and olivine in the wehrlite indicates that both

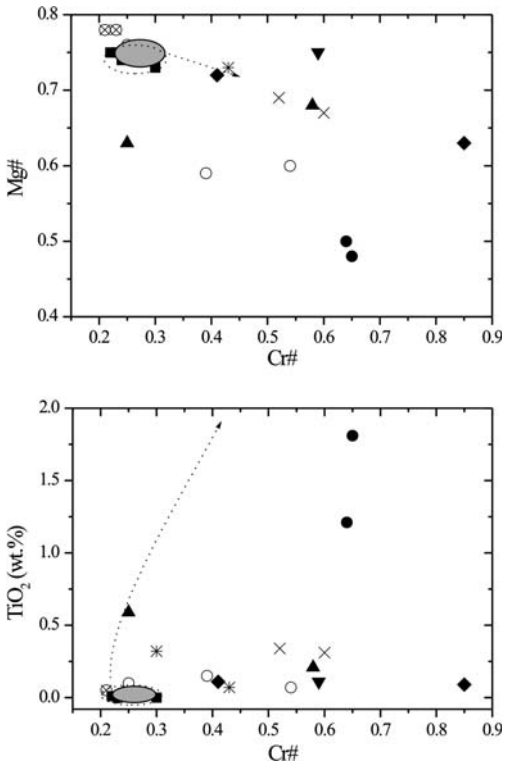

Fig. 6. (**a**) Cr-number v. Mg-number and (**b**) Cr-number v. TiO_2, in experimental spinel. Legend as in Figure 5. The dotted arrows indicate compositional variations induced by metasomatism on original spinels from mantle xenoliths (Coltorti *et al.* 2004).

underwent a chemical modification at the experimental conditions. The modifications observed in lherzolite and wehrlite will be discussed below.

Nephelinite–lherzolite reaction

The distribution and the paucity of the glass do not allow a reaction front to be clearly identified in the lherzolitic portion of the charges. This can be ascribed to fast kinetics of the melt infiltration process, which reaches an early completion even in the shortest run, as a consequence of the low viscosity of nephelinite-derived melts. This affects the spatial distribution and chemical composition of the neoformed phases, which do not show regular compositional variations from the lherzolite–nephelinite interface to the internal parts of the peridotite.

Neoformed minerals (cpx2, sp2) could form either by a partial melting process of lherzolite or by metasomatic reactions. However, the chemical variations recorded in cpx2 are not compatible with partial melting (e.g. their Na_2O and Al_2O_3 contents) and, although the Cr-number increase from sp1 to sp2 could be due also to partial melting (e.g. Matsukage & Kubo 2003), the fact that Cr-number variations are unrelated to temperature of the experiments rules out this hypothesis. Moreover, an increase of Cr-number in spinels is reported to occur as a result of metasomatic reactions in lherzolite (e.g. Francis 1976; Neal 1988; Sen & Dunn 1994). In addition, the fact that TiO_2 content in sp2 increases if a Ti-doped nephelinite is used clearly indicates that neoformed phases result from interaction with the alkaline melt. Textures observed in lherzolite for neoformed phases point to rock–melt interaction. In particular, the occurrence of cpx2 together with glass in association with orthopyroxene (and olivine) is reported to be a consequence of orthopyroxene interaction with silica-undersaturated melts (Shaw *et al.* 1998; Shaw 1999). Moreover, sp2 coronas observed around original spinel crystals closely resemble those reported by Shaw *et al.* (2006) in mantle peridotite xenoliths that underwent interaction with silica-undersaturated melts.

The main compositional features of cpx2 and sp2 can be compared with those of natural phases thought to be a consequence of reaction with metasomatizing melts. In Figures 5 and 6 the compositions of neoformed clinopyroxene and spinel in the lherzolitic portion of the capsule are given, together with that of original phases in lherzolite 154L. Furthermore, clinopyroxenes from unmetasomatized xenoliths and clinopyroxene associated with amphibole (cpx-A) and secondary clinopyroxenes (i.e. in the reaction rim of orthopyroxene, cpx2-O) studied by Coltorti *et al.* (2004) are also reported for comparison.

The higher Na_2O contents and the concomitant increase in Al_2O_3 and Cr_2O_3 (Fig. 5) of cpx2 synthesized at 2 GPa is a result of the entrance of trivalent cations (Al, Cr, Fe) at the M1 site as a result of the decrease in cell volume at increasing pressure. Such a high Na_2O increase is not observed in crystals formed at 1.5 GPa or in natural lherzolitic samples in which cpx-A coexists with pargasitic amphibole (containing *c.* 3 wt% Na_2O).

The Cr_2O_3 contents in cpx2 are comparable with those of cpx-A, whereas cpx2-O shows contents similar to some cpx2 formed at 1150 °C. MgO enrichment (Fig. 5) associated with CaO depletion occurs in the experimentally produced clinopyroxenes but not in cpx-A.

The SiO_2/Al_2O_3 v. TiO_2 diagram has been used by Coltorti *et al.* (2004) to show the chemical variations of both cpx-A and cpx2-O. In particular, according to those workers, TiO_2 in cpx-A approaches 6 wt% (Fig. 5) Some cpx2 crystals (formed at 2 GPa) show TiO_2 enrichments to

1 wt%, whereas SiO_2/Al_2O_3 ratios of cpx2 formed at low temperature (especially at 1150 °C) approach those of cpx2-O.

In summary, cpx2 chemistry does not match that of natural samples, although SiO_2/Al_2O_3 ratios detected in cpx2-O (from natural metasomatized lherzolites) is approached by some cpx2 synthesized at low temperature.

For spinel, Cr-number and Mg-number appear to be inversely correlated and TiO_2 content approaches 2.0 wt% in runs performed using the Ti-doped starting material (Fig. 6). No worthwhile comparison can be drawn between these findings and the data reported by Coltorti *et al.* (2004) because of the paucity of the analytical data for spinels reported by those workers. However, it can be noted that a general Cr-number and TiO_2 increase and a slight Mg-number decrease were also observed in natural sp2 (Fig. 6).

Finally, analyses of glass obtained at 1250 °C approach the composition of some Si-rich glasses found in xenoliths where interaction involving orthopyroxene occurs (Shaw *et al.* 1998; Shaw 1999). In the discrimination diagram $CaO + Na_2O$ v. $TiO_2 + K_2O$ proposed by Coltorti *et al.* (2000) to identify the nature of the metasomatic agents, these glasses plot in the field pertaining to metasomatism caused by Na-alkaline silicate melt.

Nephelinite–wehrlite reaction

The effects of metasomatic reactions recognized in the wehrlite–nephelinite experimental runs were compared with those observed in metasomatized wehrlites and pyroxenites from Browning Pass, Baker Rocks and Mt. Overlord (NVL), Antarctica. These metasomatized rocks, both amphibole-free and amphibole-bearing, are interpreted to be the result of successive infiltration of rising alkaline melt(s) into pyroxenite bodies formed by a fractionation process at different conditions of pressure and temperature (Perinelli & Armienti 2005).

The compositional features recorded by clinopyroxene in our experiments reveal the most representative effects of the reactions with the infiltrating melt. The differences between original and secondary clinopyroxenes, and the comparison of the latter with the cpx2 in natural samples, are evaluated on the basis of their TiO_2, Na_2O, SiO_2 and Al_2O_3 contents and mg-number, which are the most distinguishable chemical parameters. Experimental neoformed clinopyroxenes define a trend of decreasing SiO_2/Al_2O_3 with increasing TiO_2, from the less to the more reacted crystals (Fig. 4a); these last overlap the trend defined by neoclinopyroxenes in natural metasomatized pyroxenites (Fig. 4a). The enrichment of TiO_2 in experimental cpx2 is also associated to the increase of FeO content, which, in terms of mg-number, shows a trend similar to that of natural cpx2 although the latter displays a more limited mg-number variation (Fig. 4b). It is noteworthy that in the area of the experimental boundary layer, the distribution of TiO_2 and FeO enrichments along the reaction rims surrounding primary clinopyroxenes may be not correlated. For instance, the clinopyroxene shown in Figure 2f has similar mg-number (point A mg-number = 68.9 and point B mg-number = 68.3) along the entire reaction rim, and this results in equilibrium with the adjacent melt in term of $K_D^{cpx/liquid}{}_{Mg/Fe}$ (0.24 and 0.25, respectively), but the TiO_2 content is very different (point A TiO_2 5.33 wt% and point B TiO_2 2.49 wt%). This may be due to the different diffusive rates of these elements and to the amount of glass adjoining the crystal: the higher diffusive velocity of Fe (and Mg) with respect to Ti allows crystal–liquid equilibrium to be reached also when the amount of adjacent glass is low; when the clinopyroxene borders large melt pools and the crystal can grow, the new composition approaches that of clinopyroxenes crystallized in the nephelinite area that show very high TiO_2 content (up to 6 wt%).

The mutual variation of Na_2O and Al_2O_3 of experimental cpx2 follows a smooth positive trend that includes also some natural secondary clinopyroxenes found in the metasomatized amphibole-free pyroxenites. Most of the natural cpx2, instead, defines a steeper trend with a slight (or no) Na_2O increase (Fig. 4c). These natural cpx2 grains almost all occur in amphibole-bearing samples, suggesting that the crystallization of amphibole may affect the Na_2O behaviour in clinopyroxene. Sen & Dunn (1994) in their experimental work on melt–lherzolite interaction observed a similar relationship between amphibole crystallization and Na_2O content of associated clinopyroxene.

In this framework, the compositional modifications recorded by clinopyroxene in our reaction experiment on wehrlite are like those observed in both experimental and natural mantle rock–melt systems where the reactions involves high melt/rock volume ratio (e.g. Sen & Dunn 1994; Shaw *et al.* 1998, 2006; Shaw 1999; Coltorti *et al.* 2004; Perinelli *et al.* 2006; see the section 'Nephelinite–lherzolite reaction' of the present paper). The occurrence of amphibole, therefore, seems to be the sole parameter affecting the compositions of secondary pyroxenes in the variously metasomatized mantle rocks.

Glasses

All the glasses represent melts generated from the nephelinite. The temperature-dependent path of

nephelinite-derived melts is illustrated in the basalt tetrahedron CaTs–Di–Ol–Q pertaining to the CMAS system (Fig. 7). Nephelinite-derived compositions lie on an olivine control line down to 1150 °C; at lower temperatures clinopyroxene crystallization drives the metasomatizing melts towards a phono-tephritic composition. At the various temperatures, these are the melts that are provided to the boundary layer and start infiltration (Fig. 7).

The processes that affect the nephelinite-derived melts at the boundary layer are themselves evident in the pseudo-ternary projection from the quartz (Q) component of the basalt tetrahedron CaTs–Di–Ol–Q of Figure 7. Boundary-layer melts from

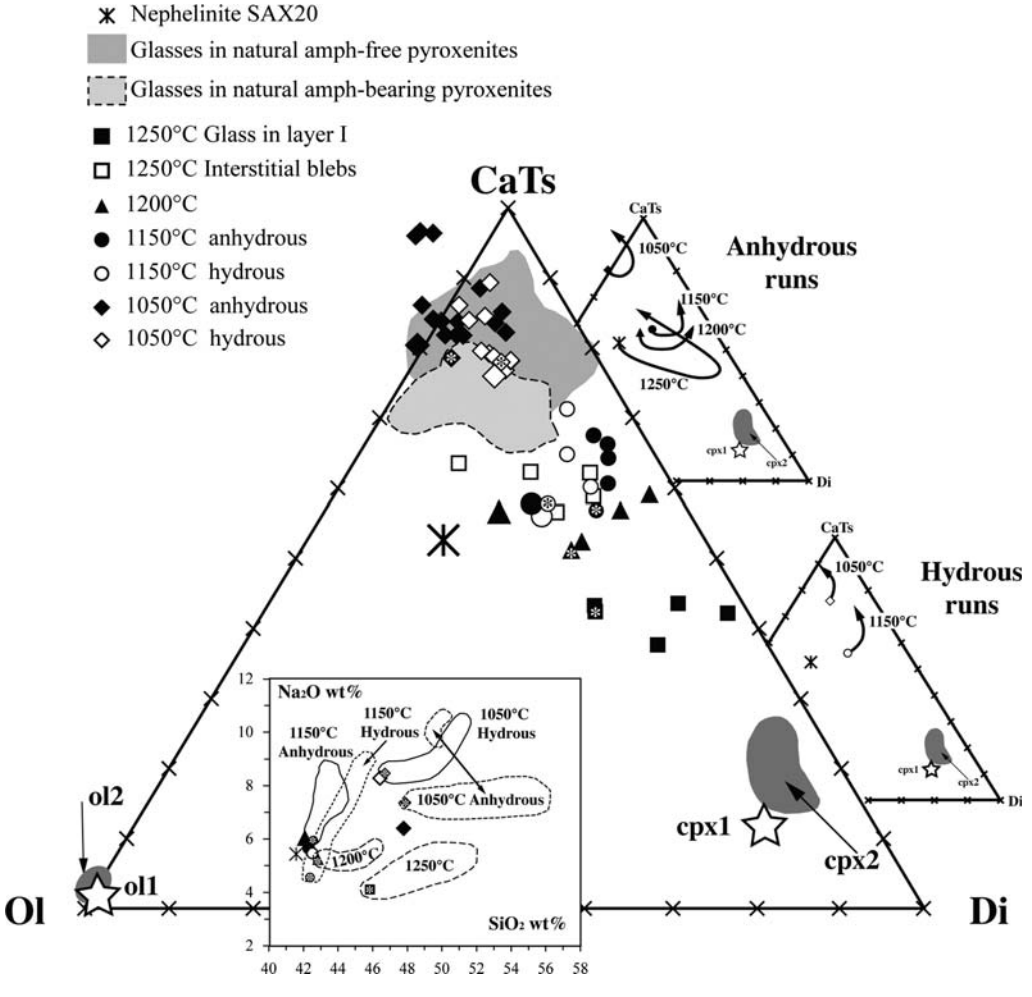

Fig. 7. Synthetic glasses plotted on the pseudo-ternary projection from quartz (Q) in the basalt tetrahedron CaTs–Di–Ol–Q pertaining to the CMAS system (O'Hara 1968), where $C = (CaO - 3.33P_2O_5 + 2Na_2O + 2K_2O) \times 56.08$, $M = (FeO + MnO + NiO + MgO - TiO_2) \times 40.31$, $A = Al_2O_3 + Cr_2O_3 + Fe_2O_3 + Na_2O + K_2O + TiO_2) \times 101.96$ and $S = (SiO_2 - 2Na_2O - 2K_2O) \times 60.09$ (all oxides in molar proportion). Symbols as in Figure 3; ol1, cpx1 and cpx2 refer to primary olivine, primary clinopyroxene and secondary clinopyroxene, respectively. In the two smaller pseudo-ternary projections the trends of liquid evolution from the nephelinite-derived melts to interstitial melts are shown for both anhydrous and hydrous experiments at the various temperatures used. The effect of alkali diffusion on the liquid compositions is shown in the inset SiO_2 v. Na_2O diagram. From this diagram it is evident that the glasses at the boundary layer of anhydrous experiments are affected by clinopyroxene dissolution mainly in the runs at the highest temperature. In the hydrous runs the clinopyroxene dissolution had negligible effect. In all experiments, the composition of melts formed in wehrlite is controlled by crystallization of new olivines and clinopyroxenes as well as by the alkali diffusion process.

higher-temperature anhydrous experiments (1250 °C–1150 °C) are influenced to a different extent by the effect of the preferential dissolution of primary clinopyroxene, which implies an increase in the abundance of cpx-derived oxides, SiO_2 and CaO (see Fig. 3). Melts from the 1150 °C hydrous run reveal, with respect to its anhydrous analogue, a negligible contribution of cpx1 dissolution and a significant crystallization of both secondary olivine and clinopyroxene. Similarly, boundary layer melts of lower-temperature runs (1050 °C), when anhydrous, show a very low assimilation of primary clinopyroxene; when hydrous, they show essentially the crystallization of neoformed olivine + clinopyroxene. These 1050 °C glasses, both hydrous and anhydrous, display a rise in alkalis and a decrease in calcium contents (Fig. 3).

The control of assimilation–crystallization processes on the composition of boundary layer melts in both hydrous and anhydrous runs is shown in more detail in the small projections of Figure 7. They show that cpx1 dissolution has a significant role in anhydrous experiments, whereas in hydrous runs, the compositional effect on the glasses of cpx1 assimilation may be hidden by the contemporaneous crystallization of neo-crystals of the same phase. Moreover, all boundary layer melts are affected by olivine crystallization. A cursory inventory of olivine and clinopyroxene amounts involved in the formation of boundary layer melts may be performed using Figure 7 and applying the lever rule. For anhydrous melts, at 1250 °C, up to 15% of olivine crystallization is necessary together with consistent (up to 40%) clinopyroxene assimilation. At lower temperatures, much lower amounts of olivine crystallization (0–5%) and clinopyroxene assimilation (10%) are required. For hydrous melts olivine and clinopyroxene crystallization always occur. It should be noted that the amount of glass is very low, and the above percentages do not imply a large amount of melting of the original paragenesis. Boundary layer melts thus appear to be controlled by clinopyroxene dissolution and/or crystallization in a way that can be recognized as a reaction front (Lundstrom 2003; Morgan & Liang 2003).

When boundary layer melts migrate through the wehrlite, they change in composition as a result of both the nucleation of new phases and reaction with pre-existing clinopyroxene and olivine. As a consequence, they progressively become enriched in SiO_2, Al_2O_3 and alkalis and depleted in TiO_2 and P_2O_5 (Fig. 3). However, the observed trends in Harker diagrams (Fig. 3 and inset in Fig. 7) seem to indicate that a diffusive flux of Na_2O and K_2O also occurrs from the nephelinite–wehrlite boundary layer into wehrlite; the interstitial pools are thus enriched in the faster diffusing elements (Na_2O and K_2O) compared with the slower diffusing TiO_2 and P_2O_5, according to a process well documented in other experimental studies ('uphill diffusion' of Shaw *et al.* 1998; see also Lundstrom 2003; Morgan & Liang 2003, and references therein). The competing behaviour between the differently diffusing TiO_2 and Na_2O is evident if we consider that the continuing clinopyroxene–melt interaction in wehrlite should reduce sodium and titanium content in the melt as a result of their absorption by clinopyroxene; instead, TiO_2 displays the expected trend whereas Na_2O increases (Fig. 3).

The continuing clinopyroxene–melt interaction in fact should change both Na_2O and TiO_2 in the same way and the decoupling of these two elements shown in Figure 3 could be explained by their different diffusivity. Moreover, the differences in the Na_2O–SiO_2 enrichment trends, shown by wet and dry experiments at 1050 °C, underline the strong effect of water on the alkali diffusivity (Freda & Scarlato 2001, and references therein).

Finally, the highest Na content attained in the water-free runs found in the melt portions along the wall of the graphite capsule may be explained by a melt advection process (Lundstrom 2003).

Although chemical transport by diffusion may have some effect on glass compositions, the different behaviour of the elements in experimental melts mainly depends on the melt/rock ratio (Navon & Stolper 1987; Bodinier *et al.* 1990; Bedini *et al.* 1997; Vernières *et al.* 1997; Ionov *et al.* 2002). For high melt/rock ratios, the compositional modification of the reactant liquid is prevented or limited to a thin layer at the melt–rock boundary (nephelinite–wehrlite interface). Low melt/rock ratios cause progressive compositional changes of percolating melt as a result of its continuous interaction with the rock assemblage. Therefore, the compositional variations of infiltrating melts and reacted phases are a function of the distance from the melt source (i.e. from the nephelinite layer) and depend on the rate of melt infiltration in addition to the reaction processes.

The compositions of experimental glasses when compared with those of natural samples reveal some significant similarities: in particular, the alkali-rich melt compositions from hydrous and anhydrous runs at 1050 °C mimic the alkali-rich glasses found in natural metasomatized amphibole-free pyroxenites (Fig. 3b–e). This suggests that in evolved T–X systems such as those experimentally reproduced at the lowest temperature, the compositions of melts probably were not suitable to form amphibole. Moreover, water content could have hindered amphibole nucleation; in fact, despite water addition in the 1050 °C run, the metasomatized assemblage contains only some spinel, a

phase that precedes amphibole nucleation in systems with low water activity (King *et al.* 2000).

Melts from runs at 1200 °C and interstitial melts at 1250 °C approach natural low-alkali melt compositions (Fig. 3a) associated with amphibole-bearing pyroxenites, although amphibole is absent in these experiments.

Lack of amphibole among experimental products

Amphibole is a phase that directly reveals metasomatism of mantle rocks and occurs in many mantle xenoliths from NVL. In our experiments, amphibole was not detected, in lherzolite or wehrlite. This was expected in high-T experiments ($T > 1100$ °C); in lower-T runs amphibole formation could have been hampered by some parameters controlling its P–T stability field in mantle rocks, such as bulk-rock composition, particularly alkali and Ti contents in lherzolite, and water content (e.g. Wallace & Green 1991; Niida & Green 1999). However, considering for comparison the Sen & Dunn (1994) reaction experiments, it can be observed that, although they used an amphibolite-derived melt as metasomatizing agent, amphibole nucleated as small (1–10 μm) grains, only at 975 °C (and not at 1025 °C) at the same pressure as our experiments (2.0 GPa).

A further parameter that may have hindered the amphibole crystallization is the melt/rock ratios in the experimental charges, which, as pointed out by Rapp *et al.* (1999), can affect the nature of chemical reactions and thus the mineralogy of the resulting assemblages.

Finally, although amphibole is outside its stability field at $T > 1100$ °C, we noted that in the wehrlite–nephelinite system the composition of melts from high-temperature runs approaches natural melt compositions associated with amphibole-bearing pyroxenites. This leads us to consider that the lack of amphibole in the runs might be due to the experimental configuration; this imposes a constant temperature on the system, a condition that does not reproduce exactly the condition of the natural environment, where a hot metasomatizing melt infiltrates a colder matrix. Therefore, high-T experimental melts could represent suitable precursors of melts able to form amphibole, but to crystallize this phase it should infiltrate a matrix at lower temperature, which is excluded by the configuration of the experiments.

Relying upon this evidence, it is possible to consider that in the mantle, where a nephelinitic magma such as SAX20 at 1200 °C passes through a relatively cool wehrlite (850-1050 °C; Perinelli & Armienti 2005; Perinelli *et al.* 2006), at the magma–wall-rock contact, the wehrlite undergoes a transient heating that induces clinopyroxene dissolution. The resultant melts, enriched in clinopyroxene components, may percolate into cooler wall rock while reacting with the wehrlitic mineral assemblage. Moreover, during their migration, melts crystallize secondary clinopyroxene and they progressively become enriched in water to achieve amphibole saturation. Similar processes, which can be accounted for in terms of 'wall-rock' metasomatism and 'diffuse' metasomatism (Xu & Bodinier 2004, and references therein), probably lead to the amphibole crystallization also in lherzolitic rocks, although our experiments with lherzolite paragenesis did not provide any indication of these processes.

Our experiments, however, do not rule out the possibility that natural glasses associated with amphibole may originate by interaction with a metasomatic agent different from SAX20 nephelinite (i.e. a low-alkali and high-TiO_2 hydrous liquid).

Concluding remarks

Although our experiments on nephelinite–lherzolite–wehrlite assemblages did not produce amphibole, considerable chemical modifications are observed in both lherzolitic and wehrlitic wehrlite assemblages portions of the charges. Moreover, the runs on nephelinite wehrlite assemblages show that compositional variations and their extent depend on melt/rock ratio and are a function of the distance from the melt source (i.e. from the nephelinite layer).

Clinopyroxene shows compositional variations in both lithotypes: it changes from diopside to high-Mg–Cr–(Na) augites and omphacites in lherzolite and to low-Mg and high-Ti–Al–Fe–Na augites in the wehrlite. Its chemical variations partially fit the modifications of clinopyroxenes found in xenoliths and thought to be a result of reactions between a metasomatizing melt such as SAX20 and a lherzolite (wehrlite). In particular, we were able to reproduce experimentally at low temperatures, the high SiO_2/Al_2O_3 ratios of secondary clinopyroxenes found as reaction rims of orthopyroxenes in lherzolite, whereas even the use of Ti-doped nephelinite did not cause the Ti increase observed in clinopyroxene of natural lherzolite. On the other hand, the Ti, Al and Na increase in natural clinopyroxenes of amphibole-free pyroxenites is fairly well matched by crystals formed in wehrlite.

Furthermore, spinel (in lherzolite) and olivine (in wehrlite) were compositionally modified by metasomatic melts: Cr-number increases and Mg-number decreases in spinel, and forsterite decreases in olivine.

Nephelinite–lherzolite experiments produced scarce interstitial glass; the only analysable patches, from the 1.5 GPa-1250 °C experiment,

have compositions that approach some melts related to orthopyroxene–melt reaction found in natural xenoliths. In contrast, experiments on the nephelinite–wehrlite system provided a variety of melts that fit to some extent the natural glasses. In particular, the runs at $T < 1150\ ^{\circ}C$ produced melts that mimic the trends shown by high-alkali and low-TiO_2 glasses found in the amphibole-free natural pyroxenites. Boundary layer glasses of high-temperature ($T > 1150\ ^{\circ}C$) runs could be the precursor of glasses associated with amphibole-bearing pyroxenites. They are significantly affected by primary clinopyroxene dissolution and simultaneous crystallization of the neoformed phases. The lack of amphibole nucleation in the experiments was probably due to the fact that the fixed temperature imposed by the experimental setting does not allow achievement of a stability field for amphibole, which can form in nature in an evolving T–X regime where a hot metasomatizing melt infiltrates a colder matrix.

This mechanism can be identified with a moving reaction front that, although implying a relatively low amount of melt, may induce widespread metasomatic effects in a wide mantle region. The variable metasomatic style recognized in NVL can be accounted for in terms of a process like this, where the infiltration of rising basaltic melts, which are also responsible for the formation of pyroxenitic lenses and dykes of variable thickness, modifies the chemical and mineralogical mantle composition, as well as its thermal regime (Armienti & Perinelli, unpublished). Such or variably metasomatized mantle source is probably responsible for the Cenozoic magmatism, although the role played by amphibole (and clinopyroxene) in the magma generation is still a matter of considerable debate.

We are grateful to C. Shaw and M. Toplis for their very constructive reviews. The authors thank M. Coltorti for helpful discussions and encouragement, F. Olmi, C. Petrone (CNR-IGG) and M. Serracino (CNR-IGAG) for help during EPM analyses, and F. Colarieti and M. Tamponi for the assistance in SEM analysis.

References

BALLHAUS, C. G., BERRY, R. F. & GREEN, D. H. 1990. Oxygen fugacity controls in the Earth's upper mantle. *Nature*, **348**, 437–440.

BEDINI, R. M., BODINIER, J.-L., DAUTRIA, J.-M. & MORTEN, L. 1997. Evolution of LILE-enriched small melt fractions in the lithospheric mantle: a case study from the East African Rift. *Earth and Planetary Science Letters*, **153**, 67–83.

BENCE, A. E. & ALBEE, A. L. 1968. Empirical correction factors for the electron microanalysis of silicates and oxides. *Journal of Geology*, **76**, 382–402.

BODINIER, J.-L., VASSEUR, G., VERNIÈRES, J., DUPUY, C. & FABRIÈS, J. 1990. Mechanisms of mantle metasomatism: geochemical evidence from the Lhèrz orogenic peridotite. *Journal of Petrology*, **31**, 597–628.

BOHLEN, S. R. B., ESSENE, E. J. & BOETTCHER, A. L. 1980. Reinvestigation and application of olivine–quartz–orthopyroxene barometry. *Earth and Planetary Science Letters*, **47**, 1–10.

COLTORTI, M., BECCALUVA, L., BONADIMAN, C., SALVINI, L. & SIENA, F. 2000. Glasses in mantle xenoliths as geochemical indicators of metasomatic agents. *Earth and Planetary Science Letters*, **183**, 303–320.

COLTORTI, M., BECCALUVA, L., BONADIMAN, C., FACCINI, B., NTAFLOS, T. & SIENA, F. 2004. Amphibole genesis via metasomatic reaction with clinopyroxene in mantle xenoliths from Victoria Land, Antarctica. *Lithos*, **75**, 115–139.

COLTORTI, M., BONADIMAN, C., FACCINI, B., MELCHIORRE, M., NTAFLOS, T & SIENA, F. 2006. Mantle xenoliths from Northern Land, Antarctica: evidence for heterogeneous lithospheric mantle. *In*: *16th Goldschmidt Conference, 27 August–1 September 2006, Melbourne, Australia, Abstracts*, A108.

DRAPER, D. S. & GREEN, T. H. 1997. P–T phase relation of silicic, alkaline, aluminous mantle-xenolith glasses under anhydrous and C–O–H fluid- saturated conditions. *Journal of Petrology*, **38**, 1187–1224.

DUNCUMB, P. & REED, S. J. B. 1968. The calculation of stopping power and backscatter effects in electron probe microanalysis. *In*: HEINRICH, K. F. J. (ed.) *Quantitative Electron Probe Microanalysis*. NBS Special Publications, **298**, 133–154.

FRANCIS, D. M. 1976. The origin of amphibole in lherzolite xenoliths from Nunivak Island, Alaska. *Journal of Petrology*, **17**, 357–378.

FREDA, C. & SCARLATO, P. 2001. La diffusione nei fusi silicatici. *Quaderni di Geofisica, Istituto Nazionale di Geofisica e Vulcanologia*, **14**, 1–23.

FREDA, C., BAKER, D. R. & OTTOLINI, L. 2001. Reduction of water loss from gold–palladium capsules during piston-cylinder experiments by use of pyrophyllite powder. *American Mineralogist*, **86**, 234–237.

HIROSE, K. & KAWAMOTO, T. 1995. Hydrous partial melting of lherzolite at 1 GPa: the effect of H_2O on the genesis of basaltic magmas. *Earth and Planetary Science Letters*, **133**, 463–473.

IONOV, D. A., BODINIER, J.-L., MUKASA, S. B. & ZANETTI, A. 2002. Mechanisms and sources of mantle metasomatism: major and trace element composition of peridotite xenoliths from Spitsbergen in the context of numerical modelling. *Journal of Petrology*, **43**, 2219–2259.

IRVING, A. J., HUANG, W. L. & WYLLIE, P. J. 1977. Phase relations of portlandite, calcium hydroxide and brucite, magnesium hydroxide to 33 kilobars. *American Journal of Science*, **277**, 313–321.

KING, P. L., HERVIG, R. L., HOLLOWAY, J. R., DELANEY, J. S. & DYAR, M. D. 2000. Partitioning of Fe^{3+}/Fe_{total} between amphibole and basanitic melt as a function of oxygen fugacity. *Earth and Planetary Science Letters*, **178**, 97–112.

LE BAS, M. J., LE MAITRE, R. W., STRECKEISEN, A. & ZANETTIN, R. 1986. A chemical classification of volcanic rocks based on the total alkali–silica diagram. *Journal of Petrology*, **27**, 745–750.

LUNDSTROM, C. C. 2003. An experimental investigation of diffusive infiltration of alkalis into partially molten peridotite: implications for mantle melting processes. *Geochemistry, Geophysics, Geosystems*, **4**, 1–25.

MATSUKAGE, K. & KUBO, K. 2003. Chromian spinel during melting experiments of dry peridotite (KLB-1) at 1.0–2.5 GPa. *American Mineralogist*, **88**, 1271–1278.

MISITI, V., FREDA, C., TADDEUCCI, J., ROMANO, C., SCARLATO, P., LONGO, A., PAPALE, P. & POE, B. T. 2006. The effect of H_2O on the viscosity of K-trachytic melts at magmatic temperatures. *Chemical Geology*, **235**, 124–137.

MORGAN, Z. & LIANG, Y. 2003. An experimental and numerical study of kinetics of harzburgite reactive dissolution with applications to dunite dike formation. *Earth and Planetary Science Letters*, **214**, 59–74.

MORIMOTO, N. 1989. Nomenclature of pyroxenes. *Canadian Mineralogist*, **27**, 143–156.

NAVON, O. & STOLPER, E. 1987. Geochemical consequence of melt percolation: the upper mantle as chromatographic column. *Journal of Geology*, **95,** 285–307.

NEAL, C. R. 1988. The origin and composition of metasomatic fluids and amphiboles beneath Malaita, Solomon Islands. *Journal of Petrology*, **29**, 149–179.

NIELSEN, R. L. & DRAKE, M. J. 1979. Pyroxene-melt equilibria. *Geochimica et Cosmochimica Acta*, **43**, 1259–1272.

NIIDA, K. & GREEN, D. H. 1999. Stability and chemical composition of pargasitic amphibole in MORB pyrolite under upper mantle conditions. *Contributions to Mineralogy and Petrology*, **135**, 18–40.

O'HARA, M. J. 1968. The bearing of phase equilibria studies in synthetic and natural systems on the origin and evolution of basic and ultrabasic rocks. *Earth-Science Reviews*, **4**, 69–133.

ORLANDO, A. & BORRINI, D. 2001. Solubility of Ti in andradite under upper mantle conditions: preliminary results. *Periodico di Mineralogia*, **70**, 99–110.

ORLANDO, A., ARMIENTI, P., CONTICELLI, S., VAGGELLI, G. & MANETTI, P. 1997. Petrological investigations on the primitive Cainozoic lavas of Northern Victoria Land, Antarctica. *In*: RICCI, C. A. (ed.) *The Antarctic Region: Geological Evolution and Processes*. Terra Antartica Publications, Siena, 523–529.

PERINELLI, C. & ARMIENTI, P. 2005. Pyroxenites and megacrysts in alkaline basaltic magmas from northern Victoria Land (Antarctica): constraint on the thermal evolution of sub-continental lithosphere. *Ofioliti*, **30**, 231.

PERINELLI, C., ARMIENTI, P. & DALLAI, L. 2006. Geochemical and O-isotope constraints on the evolution of lithospheric mantle in the Ross Sea rift area (Antarctica). *Contributions to Mineralogy and Petrology*, **151**, 245–266.

PETERSON, J. W. & NEWTON, R. C. 1990. Experimental biotite-quartz melting in the KMASH-CO_2 system and the role of CO_2 in the petrogenesis of granites and related rocks. *American Mineralogist*, **75**, 1029–1042.

PHILIBERT, J. 1963. A method for calculating the absorption correction in electron probe microanalysis. *In*: PATTEE, H. H., COSSLETT, V. E. & ENGSTRÖM, A. (eds) *X-ray Optics and X-ray Microanalysis*. Academic Press, New York, 379–392.

RAPP, R. P., SHIMIZU, N., BORMAN, M. D. & APPLEGATE, G. S. 1999. Reaction between slab-derived melts and peridotite in the mantle wedge: experimental constraints at 3.8 GPa. *Chemical Geology*, **160**, 335–356.

ROCCHI, S., ARMIENTI, P., DI VINCENZO, G., CARDINI, I., ROSSETTI, F. & STORTI, F. 2006. Tight link between Cenozoic magmatism and local-regional fault activity in the West Antarctic Rift. *Terra Antartica Reports*, **12**, 73–80.

ROCHOLL, A., STEIN, M., MOLZAHN, M., HART, S.R. & WÖRNER, G. 1995. Geochemical evolution of rift magmas by progressive tapping of a stratified mantle source beneath the Ross Rift, Antarctica. *Earth and Planetary Science Letters*, **131**, 207–224.

ROEDER, P. L. & EMSLIE, R. F. 1970. Olivine-liquid equilibrium. *Contribution to Mineralogy and Petrology*, **29**, 275–289.

SEN, C. & DUNN, T. 1994. Experimental modal metasomatism of a spinel lherzolite and the production of amphibole-bearing peridotite. *Contributions to Mineralogy and Petrology*, **119**, 422–432.

SHAW, C. S. J. 1999. Dissolution of orthopyroxene in basanitic magma between 0.4 and 2 GPa: further implications for the origin of Si-rich alkaline glass inclusions in mantle xenoliths. *Contributions to Mineralogy and Petrology*, **135**, 114–132.

SHAW, C. S. J., THIBAULT, Y., EDGAR, A. D. & LLOYD, F. E. 1998. Mechanisms of orthopyroxene dissolution in silica-undersaturated melts at 1 atmosphere and implications for the origin of silica-rich glass in mantle xenoliths. *Contributions to Mineralogy and Petrology*, **132**, 354–370.

SHAW, C. S. J., HEIDELBACH, F. & DINGWELL, D. B. 2006. The origin of reaction textures in mantle peridotite xenoliths from Sal Island, Cape Verde: the case for 'metasomatism' by the host lava. *Contributions to Mineralogy and Petrology*, **151**, 681–697.

ULMER, P. & LUTH, R. W. 1991. The graphite–COH fluid equilibrium in P, T, fO_2 space; an experimental determination to 30 kbar and 1600 °C. *Contributions to Mineralogy and Petrology*, **106**, 265–272.

VAGGELLI, G., OLMI, F. & CONTICELLI, S. 1999. Quantitative electron microprobe analysis of reference silicate mineral and glass samples. *Acta Vulcanologica*, **11**, 297–303.

VERNIÈRES, J., GODARD, M. & BODINIER, J.-L. 1997. A plate model for the simulation of trace element fractionation during partial melting and magma transport in the Earth's upper mantle. *Journal of Geophysical Research*, **102**, 24771–24784.

WALLACE, M. E. & GREEN, D. H. 1991. The efffect of bulk rock composition on the stability of amphibole in the upper mantle: implications for solidus positions and mantle metasomatism. *Mineralogy and Petrology*, **44**, 1–19.

XU, Y. G. & BODINIER, J.-L. 2004. Contrasting enrichments in high- and low-temperature mantle xenoliths from Nushan, Eastern China: results of a single metasomatic event during lithospheric accretion? *Journal of Petrology*, **45**, 321–341.

Palaeozoic subduction-related and kimberlite or carbonatite metasomatism in the Scottish lithospheric mantle

C. BONADIMAN[1], M. COLTORTI[1], S. DUGGEN[2,3,4], L. PALUDETTI[1], F. SIENA[1], M. F. THIRLWALL[2] & B. G. J. UPTON[5]

[1]*Department of Earth Sciences, University of Ferrara, via Saragat 1, 44100 Ferrara, Italy (e-mail: constanza.bonadiman@unife.it)*

[2]*Department of Geology, Royal Holloway University of London, Egham, TW20 0EX, UK*

[3]*Geological Institute, University of Copenhagen, Øster Voldgade 10, 1350 Copenhagen K, Denmark*

[4]*Present address: Leibniz Institute of Marine Sciences, IFM-GEOMAR, Division Dynamics of the Ocean Floor, Wischhofstrasse 1–3, 24148 Kiel, Germany*

[5]*School of GeoSciences, The University of Edinburgh, Grant Institute, The King's Buildings, West Mains Road, Edinburgh EH9 3JW, UK*

Abstract: Mantle xenoliths entrained in late Carboniferous to mid-Permian silica-poor basic magmas from northern Scotland were investigated using major and trace element compositions of minerals and isotopic compositions of whole-rocks and clinopyroxenes. The aim of the study was to gain more precise information on the nature of the lithospheric mantle beneath this terrane, including evidence for its metasomatic modification and evolution. This study concerns peridotites from two localities in the ENE and WSW of the Scottish Northern Highlands Terrane: Rinibar (South Ronaldsay, Orkney) and Streap Com'laidh (near Glenfinnan). Two groups of clinopyroxenes can be distinguished both at Streap Com'laidh (Type-S1 and Type-S2) and Rinibar (Type-R1 and Type-R2) based on different trace element contents and isotopic ratios. Type-S1 is characterized by an almost flat profile from middle rare earth elements (MREE) to heavy REE (HREE) accompanied by an overall light REE (LREE) enrichment. It shows the highest Th and U, coupled with low Sr, Zr and TiO_2 contents. Type-S2 exhibits humped LREE-enriched patterns and a steep decrease from Nd to Yb. It has the lowest Th and U, coupled with the highest Sr, TiO_2 and Zr contents. Both groups of clinopyroxenes present analogous isotopic features. They have measured $^{87}Sr/^{86}Sr$ values from 0.70652 to 0.70826, $^{144}Nd/^{143}Nd$ from 0.512093 to 0.512687 and $^{176}Hf/^{177}Hf$ from 0.282727 to 0.283088. These isotopic features could be explained by the addition in the mantle wedge of a slab component, made up of altered oceanic crust plus a moderate quantity of subducted sediments. The most recent subduction event in the geological history of Scotland is at about 400 Ma. It may have been during this convergent stage that the metasomatism affecting the sub-Streap lithospheric mantle occurred. Type-R1 is characterized by the lowest concentrations of Ba, Rb, Sr, LREE and U–Th, associated with remarkably high levels of Ti and Zr. These clinopyroxenes have measured $^{87}Sr/^{86}Sr$ ranging from 0.70330 to 0.70383, $^{144}Nd/^{143}Nd$ from 0.512643 to 0.512761 and $^{176}Hf/^{177}Hf$ from 0.282705 to 0.282899. In contrast, Type-R2 shows the highest concentrations of Ba, Rb, Sr, LREE and U–Th, and pronounced Ti and Zr negative anomalies. They have measured $^{87}Sr/^{86}Sr$ isotopic ratios similar to Type-R1, but lower $^{144}Nd/^{143}Nd$ (0.512431–0.512524) and higher $^{176}Hf/^{177}Hf$ (0.282921–0.283014). Calculated melt in equilibrium with Type-R1 is very similar to inferred primary kimberlitic magmas and the clinopyroxene trace element profiles may have resulted from an efficient chemical exchange between a percolating melt and the peridotite host rock. On the other hand the calculated Type-R2 melt overlaps the field of Proterozoic carbonatites. Significantly, at the age of 550 ($\pm$50) Ma, the two groups have almost identical Sr–Nd compositions, similar to average depleted mid-ocean ridge basalt mantle (DMM) at 550 Ma. This strongly suggests contemporaneous overprinting of DMM by kimberlitic and carbonatitic metasomatic agents at *c*. 550 Ma, which may be related to the opening of the Iapetus Ocean following the break-up of the Rodinia supercontinent. These data indicate a complex metasomatic history of the Scottish lithospheric mantle, which relate different geological events, most probably prior to the juxtaposition of the various tectonic blocks that nowadays constitute the Northern Highland Terranes.

From: COLTORTI, M. & GRÉGOIRE, M. (eds) *Metasomatism in Oceanic and Continental Lithospheric Mantle.* Geological Society, London, Special Publications, **293**, 303–333.
DOI: 10.1144/SP293.14 0305-8719/08/$15.00

The petrological characteristics of the Scottish lithosphere as it was in late Palaeozoic time have been investigated through a study of spinel peridotite xenoliths in late Carboniferous–early Permian alkali basaltic dykes from two localities in the Scottish Northern Highland Terrane; that is, the tectonic unit bounded by the Great Glen Fault to the south and east and the Moine Thrust to the west and north (Fig. 1). The localities are Rinibar (Orkney Islands) and Streap Com'laidh (Inverness-shire). The Streap Com'laidh xenolithic dyke was first described by Walker & Ross (1954) followed by a more detailed description by Praegel (1981). The Rinibar occurrence has not previously been reported.

Intraplate magmatism was widespread in Britain and Ireland in the Carboniferous to the early Permian. A review of this activity in Scotland has been given by Upton *et al.* (2004). A wide assortment of mantle and lower crustal xenoliths, together with high-pressure phenocrysts and megacrysts, was entrained by some of the silica-poor mafic magmas (basanite to mela-nephelinite compositions). The Carboniferous–Permian volcanic province in the British Isles provides a rare (possibly unique?) opportunity to sample pre-Mesozoic mantle xenoliths that were entrained by basaltic magmatism as opposed to kimberlitic, lamproitic or lamprophyric magmatism. The majority of the occurrences are in Scotland (Upton *et al.* 1983; Watson 1985; Hunter & Upton 1987; Menzies & Halliday 1988; Downes *et al.* 2001). Studies of deep crustal and upper mantle xenoliths within the Northern Highland Terrane include those from Tingwall (Orkney), Duncansby Head (NE Scottish mainland; Upton *et al.* 2001) and Gribun (Isle of Mull; Upton *et al.* 1998). Further data on lower crustal xenoliths from the terrane have been provided by Halliday *et al.* (1993).

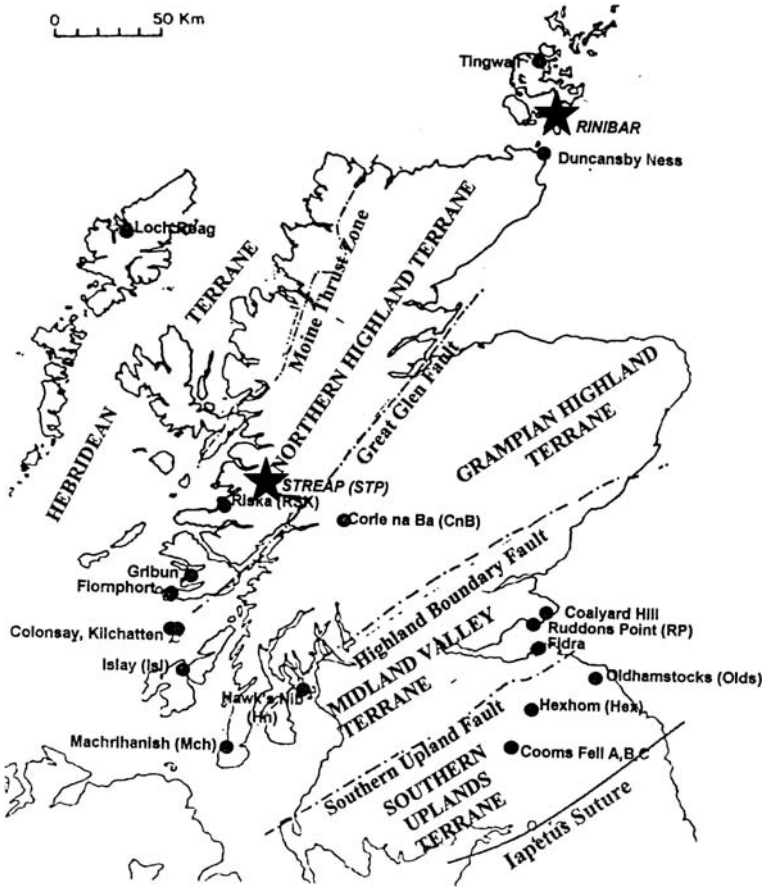

Fig. 1. Simplified map of Scotland terranes showing the boundaries of the main tectonic units and the location of the main pre-Mesozoic mantle xenolith occurrences (after Upton 2004). Stars indicate the Rinibar and Streap Com'laidh xenolith location.

Mineralogical and geochemical studies of mantle xenoliths in the province are few, as the majority have been extensively hydrated or carbonated, rendering them unsuitable for detailed analysis. However, the advent of analytical techniques such as *in situ* laser-ablation inductively coupled plasma-mass spectrometry (LA-ICP-MS) and high-precision radiogenic isotope analysis of mineral separates by thermal ionization mass spectrometry (TIMS) and multi-collector (MC)-ICP-MS has permitted acquisition of critical new data. In this study we present data for representative xenoliths from Rinibar and Streap Com'laidh (henceforth abbreviated to Streap), including *in situ* major and trace element mineral analyses acquired through electron microprobe analysis (EMPA) and LA-ICP-MS, and high-precision Sr–Nd–Hf isotopic data obtained by TIMS and MC-ICP-MS on whole rock and separated clinopyroxenes. The petrological and geochemical characteristics of the xenoliths throw light on the nature of the fluids and melts that were responsible for the metasomatism of the pre-Mesozoic lithospheric mantle beneath northern Scotland. They point to the operation of two distinct metasomatic styles, one intraplate and the other subduction-related, both very different from the xenoliths' host lavas. Streap xenolith-bearing dykes show the typical characteristics of an ocean island basalt (OIB)-like mantle source (Upton *et al.* 2004; Kirstein *et al.* 2006).

Geological setting

Xenoliths occur abundantly in a mafic dyke *c*. 1 m wide, cutting Devonian sandstones, SE of Rinibar on the western coast of the South Ronaldsay, Orkney (UK Grid reference [412 929]). The xenoliths appear to be wholly composed of spinel-bearing lherzolites and pyroxenite megacrysts. On Orkney, and in the far NE of the Scottish mainland, a group of volcanic necks and vents, associated with hundreds of small mafic, NE–SW-trending dykes, also cut Devonian sandstones. Whole-rock K/Ar dating on some of these dykes indicated an age of 252 $\pm$ 10 Ma (Baxter & Mitchell 1984).

Another Permian NE–SW dyke swarm, dating from *c*. 290 Ma, occurs further south in the Northern Highland Terrane (extending from Glenfinnan to Cluanie Lodge) (Walker & Ross 1954; Upton 2004). The Streap dyke, at [945 844], is part of this swarm and cuts Proterozoic (Moine) metasedimentary rocks. The dyke is *c*. 70 cm wide and contains a wide variety of xenoliths (spinel lherzolites, websterites, granulite-facies metagabbros and quartzo-feldspathic gneisses together with a megacryst suite (Walker & Ross 1954; Praegel 1981; Upton *et al.* 1983). Spinel lherzolite xenoliths dominate the suite, constituting *c*. 90% of the total and measuring up to 15 cm across. Praegel (1981) presented seven whole-rock analyses of the lherzolites together with mineral data for the four principal components.

Both occurrences are located within the Northern Highland Terrane, which is one of the five main terranes that constitute Scotland. From south to north, these terranes are the Southern Uplands, Midland Valley, Grampian Highland, Northern Highland and, to the NW of the Moine Thrust Zone, the Hebridean Terrane (Fig. 1). The terranes are believed to have been amalgamated into their present relationships by 400 Ma at the latest. Uncertainty exists as to where the Northern Highland Terrane lay in earlier times, but magnetic studies suggest that by around 1.2 Ga, it was an integral part of a supercontinent located in the southern hemisphere. The break-up of Rodinia led, at *c*. 600 Ma, to the opening of the Iapetus Ocean. This subsequently underwent complex closure throughout the Ordovician and Silurian, resulting in the Caledonian Orogeny. The final 'docking' of the Northern Highland Terrane with respect to its neighbouring Grampian and Hebridean Terranes appears to have been effected during the (Silurian) Scandian phase of the orogeny.

Prior to Caledonian deformation the North Highlands Terrane is inferred to have been a relatively stable continental region affected by extensional tectonics between *c*. 1000 and 600 Ma. Extension gave rise to shallow marine faulted basins within which sediments accumulated and were subsequently metamorphosed to form the Moine Supergroup. The terrane was subjected to an extensional phase at *c*. 870 Ma when tholeiitic basalt magmas formed a major dyke swarm, later to be amphibolitized and deformed in the Caledonian Orogeny. After this, the terrane remained little affected by magmatism until intrusion of late Caledonian (mainly salic) plutons at 430–410 Ma, related to WNW-directed subduction (Thirlwall 1988). By latest Carboniferous times the terrane had been incorporated within the supercontinent of Pangaea. Stresses within this led to fracturing, small-fraction mantle melting and consequent intrusion of alkaline mafic dykes. Some of these dykes contain the xenoliths that form the subject of this paper.

Petrography

Streap is among the very few British and Irish localities where fresh peridotite xenoliths can be found containing primary olivines and orthopyroxenes. Those from Rinibar show greater weathering and the ferromagnesian silicates show secondary hydration, commonly concentrated along fractures

in pyroxenes and olivine, as well as the development of calcite veins accompanied by tiny crystals of magnetite and clay minerals. Primitive mantle textures, however, are still preserved in the great majority of the samples. The spinel-bearing ultramafic xenoliths occur abundantly, mainly as rounded or, more rarely, angular nodules between 10 and 20 cm in diameter. The Rinibar and Streap xenoliths are typically fine-grained ($\leq$0.5 mm for all minerals), with protogranular to porphyroclastic textures (Mercier & Nicolas 1985). Those from Streap have the finest grain size, with all minerals varying between 200 and 400 μm diameter.

Mineral modes for samples with loss on ignition (LOI) $<$ 6 wt% were calculated from whole-rock and mineral data using mass-balance calculations. For the more weathered samples, modes were calculated using the procedure proposed by Niu (1997) for altered peridotites. In both cases results were cross-checked with petrographic observations. Short descriptions and modes of all the studied samples are given in Table 1.

At both localities the peridotites are predominantly lherzolites (following the Streckeisen (1976) classification), although samples ST1 and ST4 from Streap are not readily classifiable. Although both are formally lherzolites, ST1 has 7% of modal opx and is therefore considered a wehrlite, whereas ST4, with 30% of modal cpx, is a cpx-rich lherzolite. Sample EN5 from Rinibar, with 33% modal olivine, is classified as olivine websterite.

Table 1. *Mineral mode relative percentages of Streap and Rinibar xenoliths*

Sample	Rock type	LOI	ol	opx	cpx	sp	phl
Streap							
ST1	Wehrlite	2.38	47	7	43	2	0.9
ST3*	Lherzolite		60	27	12	1	
ST4	Cpx rich-lherzolite	1.49	49	20	30	1	
ST5	Lherzolite	0.57	62	25	12	1	
ST7*	Lherzolite		60	30	9	1	
ST13	Lherzolite	2.27	65	16	18	0.3	
Rinibar							
AN1	Lherzolite	6.87	78	11	10	1	0.4
CN2	Lherzolite	9.79	55	30	14	1	
CN4	Lherzolite	6.51	81	7	9	1	1.8
EN4	Lherzolite	9.95	63	25	9	3	
EN5	Ol-websterite	5.25	33	10	56	1	
EN7	Lherzolite	13.1	72	13	11	3	1.8
EN8	Lherzolite	8.92	65	24	10	1	
FN3	Lherzolite	5.08	69	9	20	2	
FN4	Lherzolite	3.14	64	21	15	0.6	
GN5	Lherzolite	10.3	62	17	20	2	
HN11	Lherzolite	11.2	72	14	12	2	

LOI, loss on ignition (wt%); ol, olivine; opx, orthopyroxenes; cpx, clinopyroxenes; sp, spinels; phl, phlogopites.
*Because of the very small size of the xenolith whole-rock analyses were not carried out, thus mineral modes were estimated on the basis of petrographic observations.

The olivines have sizes $<$0.5 mm and show the characteristic rounded grain boundaries of protogranular peridotites. The Rinibar olivines are often fractured and severely weathered, whereas the Streap olivines are very fresh and show no deformation apart from occasional undulose extinction. Orthopyroxenes, occasionally kink-banded, exhibit subrounded habits with grain size varying from 0.2 to 0.5 mm. These sizes are generally less than those typical for minerals in peridotite xenoliths (2–10 mm) (Pearson *et al.* 2003, and reference therein). Emerald green clinopyroxenes in the Streap peridotites are very fresh, primitive grains with crystal sizes comparable with those of the orthopyroxenes. In contrast, the primary Rinibar clinopyroxenes commonly exhibit a spongy texture with secondary clinopyroxenes, olivines and spinels.

Small amounts of phlogopite are present in samples AN1, CN4, EN7, GN5, HN2 (Rinibar) and ST1 (Streap), and sample FN3 (Rinibar) also has very small amphibole crystals in the spongy rim of the primary clinopyroxenes. The phlogopites occur as brown, reddish brown to yellow tabular crystals, disseminated in the peridotite matrix, or concentrated in veinlets. In Rinibar samples AN1 and GN5 the phlogopites occur in polycrystalline aggregates in association with clinopyroxenes and dark spinels as lamellar intergrowths.

Analytical methods

Major element compositions of minerals were determined by EMPA, using a Cameca CAMEBAX instrument, at the Istituto di Geoscienze e Georisorse, CNR, Padua (Italy). An acceleration voltage of 15 keV and sample currents of 20 μA with 100 s counting time were used. Oxides and natural and synthetic minerals were used as standards. Matrix corrections were performed using the the PAP procedure in the CAMECA software. Analytical precision (2σ) is better than $\pm$2% for elements in the range 10–20 wt% oxide, better than 5% for elements in the range 2–10 wt% oxide, and better than 10% for elements in the range 0.5–2 wt% oxide. The concentrations of trace elements in clinopyroxenes and orthopyroxenes were obtained by LA-ICP-MS at the Istituto di Geoscienze e Georisorse, CNR, Pavia (Italy). Precision and accuracy (both better than 10% for concentrations at ppm level) were assessed by repeated measurements of SNR NIST 612 and BCR-2 standards. The data obtained have been processed with the GLITTER software package (Van Achterberg *et al.* 2001). Calcium was used as an internal standard for quantifying

clinopyroxenes, and magnesium for orthopyroxenes. The calibration protocol involves standardization at the beginning, middle and end of each analytical run to correct for within-run instrumental drift. During each run BCR-2 was analysed as an unknown sample. Full details of the analytical parameters and quantification procedures have been given by Tiepolo *et al.* (2003).

High-precision Sr–Nd–Hf-isotope analysis by TIMS and MC-ICP-MS was conducted to gain evidence concerning the nature of the metasomatic agents that affected the Streap and Rinibar peridotites. The Sr, Nd and Hf isotope composition of the Rinibar xenoliths was obtained on acid-washed clinopyroxene separates to avoid possible cryptic alteration. However, the radiogenic isotope analyses for the Streap xenoliths were obtained on whole-rock dissolutions; separation of clinopyroxenes from the Streap samples was impossible because of their anomalously fine-grained nature.

Sr–Nd–Hf isotope analyses were performed on 100–125 mg fresh clinopyroxene separates and whole-rock powders at the Department of Geology, Royal Holloway University of London, using a multi-collector VG354 mass spectrometer (Sr and Nd) and an IsoProbe MC-ICP-MS system for Hf. The chemical procedures were performed in clean laboratories and all acids were purified by sub-boiling distillation and were blank-tested for Sr. As the blank-test for Sr gave very low values, it is valid to assume that the Nd and Hf blanks would also be very low. The whole-rock powders and clinopyroxene samples were acid washed with 6N HCl in poly-tetrafluorethylene (PTFE) Savillex beakers on a hot plate and rinsed with 18.2 MΩ water to minimize the effects of alteration. Dissolution was achieved with 6M HCl to which was added a few drops of concentrated HF (a mixture that effectively breaks down clinopyroxene), evaporation and subsequent addition of a concentrated HNO_3–HF mixture, which left only a few tiny grains of unsoluble spinel in some of the clinopyroxene separate samples. Following evaporation the residue was converted to nitrate and dissolved in 10% HNO_3 and passed through *c*. 50 mg of TRU-Spec resin loaded on pipette-tip columns to separate the light rare earth elements (LREE); Nd was separated from the remaining LREE by two passes on anion resin exchange columns. The first eluent containing the matrix elements, and Sr and Hf, that was collected from the TruSpec columns was evaporated, dissolved with 8 N HNO_3 and passed through SrSpec resin loaded in pipette-tip columns to separate Sr from the matrix and Hf. Sr was further purified with a second pass on the SrSpec resin. Hf was then separated from the heavy REE (HREE) and high field strength elements (HFSE) and purified with a two-step column chemistry using cation resin followed by Ln resin (Anczkiewicz *et al.* 2004).

Sr was run multi-dynamically on single Re filaments using a TaF_5 sandwich-loading technique. Nd was loaded on single Re filaments with dilute H_3PO_4 and silica gel and run multi-dynamically as NdO^+. Further details of the analytical procedures have been reported in the literature (Thirlwall 1991*a*, *b*). The external reproducibility (2σ) of this method is currently ± 0.000014 for $^{87}Sr/^{86}Sr$ and ± 0.000006 for $^{143}Nd/^{144}Nd$. Hf was analysed using a static procedure on the IsoProbe (Thirlwall & Anczkiewicz 2004). Over the 3 days of analysis the JMC475 standard yielded $^{176}Hf/^{177}Hf = 0.282191 \pm 10$ (2σ, $n = 11$), and the measured data have been corrected to JMC475 $^{176}Hf/^{177}Hf = 0.282165$.

Major element, trace element and isotopic data

The degree of weathering in the Rinibar xenoliths is too high to permit whole-rock major and trace element modelling. Consequently, for quantitative assessment, particularly relating to the geochemical nature of the Palaeozoic lithospheric mantle, our detailed major and trace element analytical work was restricted to the minerals (Tables 2–7).

The mg-number of the Streap olivines ranges between 87.4 and 91.3, except for the wehrlite ST1, which has olivines with mg-number 83.1. The Ni contents vary between 1230 and 2670 ppm (Table 2, Fig. 2). The mg-number for the Rinibar olivines (87.3–92.2) are comparable, but they are generally richer in Ni (1720–3620 ppm). Olivine from lherzolite AN1 has anomalously low mg-number (85.4–85.7). The more iron-rich olivines do not represent secondary recrystallized crystals but are primary grains. The predicted total variation of olivine mg-numbers in the upper mantle secular evolution is in the range of 86.3 (the lowest value as Bulk Silicate Earth (BSE) primordial olivine) to 92.5 (the most restitic mantle peridotites) (O'Neill & Palme 1998). AN1 olivines lie at the lowest limit, indicating a composition more fertile than BSE primordial olivine. This, however, does not agree with its modal contents (cpx *c*. 9 vol%). This olivine-rich and cpx-poor lherzolite with low mg-number in olivines has probably undergone processes that modified its original modal and geochemical composition (e.g. metasomatism at high melt/rock ratio). Compared with olivines from Archaean cratons and off-craton Phanerozoic settings, the Streap olivines fall in the Phanerozic field, whereas some of the Rinibar samples fall into the field for selected cratonic areas (Kelemen *et al.* 1998).

Table 2. *Representative major element analyses of olivines from Streap and Rinibar xenoliths*

	Streap									Rinibar			
	lh						cpx-rich lh	wh		lh			
	ST3	ST3	ST5	ST5	ST13	ST13	ST4	ST1	ST1	AN1	AN1	CN2	CN2
wt%													
SiO_2	40.77	40.77	41.25	41.02	40.97	40.71	40.23	38.73	38.88	39.25	39.46	40.97	40.92
FeO	9.90	10.13	8.50	8.39	10.14	10.05	11.81	15.06	15.93	13.97	13.58	9.73	9.79
MnO	0.15	0.04	0.15	0.13	0.18	0.24	0.15	0.24	0.31	0.19	0.33	0.14	0.17
MgO	49.39	49.68	49.52	49.48	48.59	48.91	46.05	43.29	44.15	45.80	45.64	49.58	49.28
CaO	0.06	0.05	0.06	0.04	0.03	0.00	0.11	0.05	0.01	0.05	0.11	0.04	0.04
Cr_2O_3	0.02	0.04	0.00	0.00	0.01	0.00	0.02	0.00	0.04	0.00	0.08	0.00	0.00
NiO	0.30	0.21	0.30	0.29	0.29	0.16	0.32	0.11	0.16	0.25	0.26	0.45	0.37
Si	0.995	0.992	1.006	1.005	1.004	0.998	1.008	1.000	0.988	0.988	0.992	0.996	0.998
Fe	0.202	0.206	0.173	0.172	0.208	0.206	0.247	0.325	0.339	0.294	0.285	0.198	0.200
Mn	0.003	0.001	0.003	0.003	0.004	0.005	0.003	0.005	0.007	0.004	0.007	0.003	0.004
Mg	1.795	1.802	1.800	1.806	1.774	1.788	1.720	1.666	1.672	1.719	1.710	1.796	1.791
Ca	0.002	0.001	0.001	0.001	0.001	0.000	0.003	0.001	0.000	0.001	0.003	0.001	0.001
Cr	0.000	0.001	0.000	0.000	0.000	0.000	0.000	0.000	0.001	0.000	0.002	0.000	0.000
Ni	0.006	0.004	0.006	0.006	0.006	0.003	0.006	0.002	0.003	0.005	0.005	0.009	0.007
Mg-no.	89.9	89.7	91.2	91.3	89.5	89.7	87.4	83.7	83.2	85.4	85.7	90.1	90.0

mg-number = 100 × Mg/(Mg + Fe) (atomic formula units).

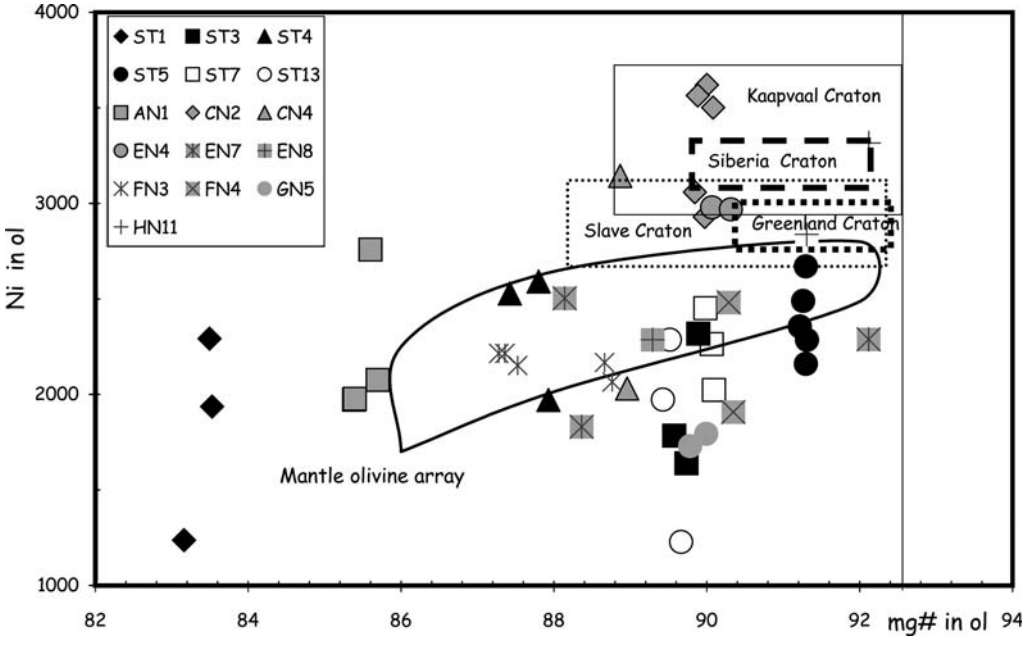

Fig. 2. Ni (ppm) v. mg-number in Rinibar (grey symbols) and Streap (filled and open symbols) olivines. The vertical line indicate the predicted upper limit for mg-number (92.5) of olivine from the most restitic mantle peridotites (O'Neill & Palme 1998). Fields of olivines from Archaean craton peridotites, both garnet and spinel facies, are from Kelemen *et al.* (1998); Phanerozoic mantle olivine array is from Takahashi (1987).

Rinibar											
lh											
CN4	CN4	EN4	EN4	EN7	EN8	FN3	FN3	FN4	GN5	GN5	HN11
40.87	40.65	41.16	40.68	40.71	40.89	40.23	40.33	40.84	40.72	39.97	40.93
10.73	10.75	9.82	9.47	11.31	10.38	11.76	12.01	9.30	9.99	9.82	8.58
0.19	0.16	0.20	0.14	0.32	0.14	0.25	0.27	0.14	0.16	0.17	0.09
48.05	48.59	50.01	49.58	48.19	48.57	46.32	46.22	48.84	49.27	49.54	50.59
0.10	0.10	0.04	0.07	0.08	0.06	0.08	0.09	0.07	0.03	0.03	0.05
0.01	0.06	0.00	0.08	0.05	0.01	0.04	0.02	0.02	0.00	0.03	0.02
0.40	0.26	0.38	0.38	0.23	0.29	0.27	0.28	0.24	0.22	0.23	0.36
1.003	0.995	0.994	0.993	0.997	1.002	1.006	1.007	1.004	0.996	0.984	0.992
0.220	0.220	0.198	0.193	0.232	0.213	0.246	0.251	0.191	0.204	0.202	0.174
0.004	0.003	0.004	0.003	0.007	0.003	0.005	0.006	0.003	0.003	0.003	0.002
1.757	1.773	1.800	1.804	1.759	1.773	1.726	1.720	1.789	1.796	1.818	1.828
0.003	0.003	0.001	0.002	0.002	0.002	0.002	0.002	0.002	0.001	0.001	0.001
0.000	0.001	0.000	0.001	0.001	0.000	0.001	0.000	0.000	0.000	0.001	0.000
0.008	0.005	0.007	0.007	0.005	0.006	0.006	0.006	0.005	0.004	0.005	0.007
88.9	89.0	90.1	90.3	88.4	89.3	87.5	87.3	90.3	89.8	90.0	91.3

As for the olivines, mg-number values for the orthopyroxenes from both localities range from 89.7 to 91.8. The orthopyroxenes from samples ST1 and ST4 also have the lowest mg-number, clustering around 85 and 88, respectively (Table 3). Within a single sample, the mg-number values of the orthopyroxenes are similar to, or slightly greater than, those of the olivines, as the Fe–Mg partition coefficient (K_d) between olivine and orthopyroxene is *c*. 1 (Brey & Köhler 1990). CaO contents vary between 0.37 and 1.05 wt%, with no distinction between the two suites (Table 3). However, the Streap orthopyroxenes have, on average, higher Al_2O_3 (2.3–5.5 wt%) and lower Cr_2O_3 (0.19–0.38 wt%) than those from Rinibar (Al_2O_3 1.7–4.1 wt%; Cr_2O_3 0.23–0.53 wt%). The LREE in the Streap orthopyroxenes are lower, by a factor of 10, than those of Rinibar, whereas the middle REE (MREE) and HREE are more uniform, with chondrite-normalized patterns showing a decrease from HREE to MREE ($(Sm/Yb)_N$, 0.08–0.15). The LREE enrichment in the Rinibar orthopyroxenes is accompanied by high Sr, U and Th, but not by Ti and Zr, suggesting the possibility that they have interacted with a melt rich in highly incompatible elements (Table 7).

In the Streap clinopyroxenes mg-number is limited to 91–93, except for samples ST1 and ST4, which, analogously to orthopyroxenes and olivines, show the lowest values (86–88.5). In contrast, the Rinibar clinopyroxenes exhibit a continuous spectrum of mg-number from 89 to 93, with sample AN1 showing the lowest values (Table 4). For all samples, the mg-number of the clinopyroxenes is greater than that of the coexisting olivines (and orthopyroxenes). This is consistent with the Fe–Mg K_d for olivine–clinopyroxene, determined experimentally at $T = 1000\,^{\circ}C$ and $P = 1.5$ GPa ($^{ol-cpx}K_d = 1.16$; Brey & Köhler 1990). Fe–Mg distribution coefficients for the Streap clinopyroxenes and olivines range between 1.15–1.17 (i.e. close to the values indicated by Brey & Köhler (1990)), suggesting that the silicates in the peridotites were in equilibrium. On the other hand, the Fe–Mg distribution coefficient for the Rinibar clinopyroxene–olivine pairs vary from 1.01 to 1.2, indicating disequilibrium between the two phases.

In the Streap peridotites, the Al_2O_3 and TiO_2 contents vary from 3.8 to 7.3 wt% and 0.57 to 1.05 wt%, respectively, whereas the primary clinopyroxenes from Rinibar show somewhat lower Al_2O_3 (1.7–6.7 wt%) and TiO_2 (<0.5 wt%) contents (Table 4). When compared with primary clinopyroxenes, the few grains of secondary clinopyroxenes from Rinibar, which are always related to spongy pyroxene grains, are richer in CaO and, to a lesser extent, TiO_2, with highly variable Na_2O. However, in view of their scarcity and extremely small size, which prevents detailed analytical study, they are not considered any further here and are not reported in Table 4.

On the basis of their REE and incompatible trace element distribution, two types of clinopyroxenes can be distinguished among the Streap xenoliths (Table 7; Fig. 3a and b). The first (Type-S1) is characterized by an almost flat profile from MREE to HREE ($(Sm/Yb)_N$ 0.91–1.66)

Table 3. *Representative major element analyses of orthopyroxenes from Streap and Rinibar xenoliths*

	Streap								
	lh							cpx-rich lh	wh
	ST3	ST3	ST5	ST7	ST7	ST13	ST13	ST4	ST1
wt%									
SiO_2	55.44	55.27	55.23	55.33	54.83	55.05	55.46	53.81	54.07
TiO_2	0.11	0.15	0.14	0.16	0.17	0.12	0.13	0.29	0.16
Al_2O_3	4.09	4.53	4.41	4.16	3.99	4.13	3.48	5.40	2.94
Fe_2O_3	0.22	0.42	0.00	0.19	0.53	0.29	0.44	0.05	0.40
FeO	5.87	6.00	5.35	6.05	5.43	6.52	6.35	7.32	9.54
MnO	0.14	0.03	0.15	0.11	0.17	0.22	0.25	0.12	0.25
MgO	33.33	33.62	33.09	33.25	33.72	33.20	33.88	31.03	30.92
CaO	0.73	0.71	0.79	0.67	0.65	0.46	0.37	1.02	0.47
Na_2O	0.13	0.11	0.13	0.11	0.13	0.05	0.03	0.15	0.07
K_2O	0.00	0.00	0.00	0.00	0.00	0.00	0.00	0.00	0.02
Cr_2O_3	0.26	0.31	0.35	0.26	0.21	0.30	0.19	0.34	0.28
Si	1.904	1.883	1.908	1.902	1.888	1.896	1.902	1.879	1.912
Ti	0.003	0.004	0.004	0.004	0.005	0.003	0.003	0.007	0.004
Al	0.165	0.182	0.180	0.168	0.162	0.168	0.141	0.222	0.123
Fe III	0.006	0.011	0.000	0.005	0.014	0.007	0.011	0.001	0.011
Fe II	0.169	0.171	0.154	0.174	0.156	0.188	0.182	0.214	0.282
Mn	0.004	0.001	0.004	0.003	0.005	0.006	0.007	0.003	0.007
Mg	1.706	1.707	1.704	1.703	1.731	1.703	1.732	1.615	1.630
Ca	0.027	0.026	0.029	0.025	0.024	0.017	0.014	0.038	0.018
Na	0.009	0.007	0.009	0.008	0.009	0.003	0.002	0.010	0.005
K	0.000	0.000	0.000	0.000	0.000	0.000	0.000	0.000	0.001
Cr	0.007	0.008	0.009	0.007	0.006	0.008	0.005	0.009	0.008
Mg no.	91.0	90.9	91.7	90.7	91.7	90.1	90.5	88.3	85.3

mg-number $= 100 \times Mg/(Mg + Fe)$ (atomic formula units).

accompanied by an overall LREE enrichment ($(La/Yb)_N$ 0.61–4.54). It shows the highest Th and U contents (up to 4.7 ppm and up to 1.3 ppm, respectively), coupled with low Sr (78–208 ppm), Zr (27–36 ppm) and TiO_2 (0.47–0.72 wt%) contents (Table 7). Cpx in ST3, on the whole, presents a type-S1 profile, but with a spoon-shaped LREE distribution, with a minimum at Pr (Fig. 3a and b). The second type (Type-S2) exhibits humped LREE-enriched patterns ($(La/Yb)_N$ 4.53–12.0), with maxima at Pr (Nd) and a steep decrease from Nd to Yb ($(Sm/Yb)_N$ 4.63–7.03). Compared with Type-S1, these clinopyroxenes have the lowest Th (0.06–0.59 ppm) and U (0.03–0.17 ppm), coupled with the highest Sr (183–241 ppm), TiO_2 (0.57–1.05 wt%) and Zr (21–73 ppm) (Fig. 3c and d). The patterns of both types show positive Eu anomalies ($(Eu_N/((Sm + Gd)_N/2) = Eu^*$, 1.1–1.36).

The Rinibar clinopyroxenes are LREE-rich with humped, strongly positive, fractionated patterns. $(La/Yb)_N$ ranges from 6.86 to 32.2 with a maximum at Ce. On the basis of their incompatible trace element distributions, they are divisible into two groups. Type-R1 is characterized by the lowest concentrations of Ba (and Rb), Sr, LREE and U–Th, associated with remarkably large Ti and Zr (and Hf) anomalies varying from moderately negative to slightly positive (Fig. 4a and b). Type-R2 shows the highest concentrations of Ba (and Rb), Sr, LREE, U and Th, somewhat lower Nb (and Ta) concentrations, and pronounced Ti and Zr (Hf) negative anomalies. Sample CN2 has the highest overall REE concentrations; it also has the highest Th and U (Th 7.04 ppm; U 1.84 ppm) and it is the only sample of Rinibar having cpx with $La_N > Ce_N$ (Fig. 4c and d).

On the basis of their textures, all spinels in the Streap lherzolites can be classified as 'primary' spinel and are compositionally rather homogeneous (Table 5). They are extremely fertile in terms of aluminium contents (cr-number $= (Cr/(Cr + Al) \times 100)$, 8.40–18.8) and show mg-number (80–84) and TiO_2 contents (0.05–0.18 wt%) compatible with mantle conditions (Barnes & Roeder 2001). Spinels from ST1 and ST4 are relatively rich in TiO_2 (0.40–0.60 wt%) and have cr-number values of 9.86–18.8 associated with low mg-number (61–78). In contrast, the Rinibar spinels are strongly zoned with cr-number ranging from 8.26 to 71.8 and,

Rinibar								
lh								
CN2	CN2	EN4	EN4	EN8	EN8	FN4	GN5	GN5
55.77	56.19	55.96	56.15	55.70	55.61	54.71	56.51	55.88
0.04	0.02	0.02	0.00	0.06	0.07	0.10	0.00	0.04
4.12	3.06	2.24	2.23	3.88	4.22	4.54	1.76	2.26
0.20	0.33	0.16	0.40	0.25	0.53	0.14	0.10	0.58
6.63	6.18	5.84	5.83	6.83	6.13	5.89	6.14	5.61
0.14	0.15	0.06	0.15	0.16	0.18	0.16	0.16	0.24
33.10	33.94	33.66	34.24	33.16	33.84	32.63	33.65	34.20
0.87	0.84	0.64	0.73	0.72	0.79	0.90	0.79	0.82
0.08	0.05	0.10	0.04	0.06	0.08	0.11	0.12	0.11
0.01	0.00	0.06	0.03	0.02	0.00	0.00	0.01	0.02
0.53	0.29	0.37	0.44	0.34	0.35	0.45	0.23	0.34
1.901	1.919	1.945	1.930	1.905	1.885	1.895	1.960	1.923
0.001	0.001	0.001	0.000	0.002	0.002	0.003	0.000	0.001
0.166	0.123	0.092	0.090	0.157	0.168	0.185	0.072	0.092
0.005	0.008	0.004	0.010	0.006	0.014	0.004	0.003	0.015
0.189	0.176	0.170	0.168	0.195	0.174	0.171	0.178	0.162
0.004	0.004	0.002	0.004	0.004	0.005	0.005	0.005	0.007
1.682	1.727	1.743	1.754	1.690	1.709	1.685	1.739	1.754
0.032	0.031	0.024	0.027	0.026	0.029	0.034	0.029	0.030
0.005	0.003	0.007	0.003	0.004	0.005	0.008	0.008	0.007
0.001	0.000	0.003	0.001	0.001	0.000	0.000	0.001	0.001
0.014	0.008	0.010	0.012	0.009	0.009	0.012	0.006	0.009
89.9	90.8	91.1	91.3	89.7	90.8	90.8	90.7	91.5

on the whole, they show higher cr-number and TiO_2 contents (up to 2.04 wt%) than those from Streap.

Phlogopites are present in a few samples from both xenolith groups, and in these the mg-number values mimic those of the coexisting pyroxenes (Table 6). However, whereas the disseminated phlogopites in the Streap xenoliths have low Ba, Zr (and Hf) and extremely low Nb (5–6 ppm) contents, those in the Rinibar samples are enriched in both LILE (Ba up to 39 000 ppm) and HFSE (Nb, 130–150 ppm) (Table 7).

Sr, Nd and Hf isotopic data for the xenoliths are reported in Table 8, along with the internal error (2σ). The Type-R1 clinopyroxenes have measured $^{87}Sr/^{86}Sr$ values ranging from 0.70330 to 0.70383, $^{143}Nd/^{144}Nd$ from 0.512643 to 0. 512761 and $^{176}Hf/^{177}Hf$ from 0.282705 to 0.282899. Although the Type-R2 clinopyroxenes have similar measured $^{87}Sr/^{86}Sr$ isotopic ratios, they have lower $^{143}Nd/^{144}Nd$ (0.512431–0.512524) and higher $^{176}Hf/^{177}Hf$ (0.282921–0.283014) than the Type-R1 clinopyroxenes. The two groups of Streap xenoliths, separated on the basis of their trace element contents, are none the less isotopically indistinguishable in terms of Nd–Hf systematics. In turn, the Type-S1 xenolith group shows a slight tendency towards more radiogenic Sr. However, when compared with data from mineral separates and whole rocks of nine peridotite xenoliths from Streap (Menzies & Halliday 1988), which have trace element distribution closely comparable with our data for both Type-S1 and Type-S2 xenoliths, no difference has been observed. Typically, they have measured $^{87}Sr/^{86}Sr$ values from 0.70652 to 0.70826, $^{143}Nd/^{144}Nd$ from 0.512093 to 0.512687 and $^{176}Hf/^{177}Hf$ from 0.282727 to 0.283088. Only the ST1 samples record very low Nd and Hf isotope ratios (measured $^{143}Nd/^{144}Nd$ 0.512093 and $^{176}Hf/^{177}Hf$ 0.282562) with marginally higher radiogenic Sr. Compared with both Rinibar types of clinopyroxenes, Streap whole-rock xenoliths have more radiogenic Sr, whereas the Nd and Hf isotope ratios are clearly distinct only for two samples (Table 8).

Physico-chemical constraints on the nature and evolution of the Scottish lithosphere

Thermal and rheological contraints

Fine-grained protogranular textures have been observed in peridotite xenoliths from various

Table 4. *Representative major element analyses of clinopyroxenes from Streap and Rinibar xenoliths*

	Streap												Rinibar						
	lh							cpx-rich lh			wh		lh						
	ST3	ST5	ST5	ST7	ST7	ST13	ST13	ST4	ST4	ST4	ST1	ST1	AN1	AN1	CN2	CN2	CN2	CN4	CN4
wt%																			
SiO_2	52.30	52.22	52.49	51.60	51.84	52.11	52.04	50.67	50.84	51.08	49.90	50.89	52.89	53.22	53.51	53.12	53.27	52.01	51.37
TiO_2	0.55	0.61	0.55	0.61	0.72	0.67	0.75	1.04	1.03	0.89	0.73	0.69	0.53	0.46	0.10	0.13	0.10	0.35	0.42
Al_2O_3	6.36	6.67	6.75	6.54	6.67	3.77	6.91	7.31	7.30	6.93	5.04	3.82	2.15	3.26	3.50	4.16	3.97	4.34	3.46
Fe_2O_3	0.35	0.20	0.24	0.42	0.28	0.37	0.40	0.19	0.23	0.22	0.67	0.70	0.32	0.71	0.55	0.53	0.57	0.44	0.26
FeO	2.84	2.31	2.50	2.44	2.49	2.07	2.16	3.94	3.76	3.68	3.81	3.63	2.90	3.44	2.59	2.69	2.58	3.04	2.70
MnO	0.20	0.08	0.10	0.07	0.10	0.02	0.15	0.10	0.12	0.11	0.11	0.16	0.14	0.09	0.08	0.09	0.14	0.15	0.11
MgO	15.36	15.52	15.35	15.24	15.24	16.59	14.26	15.06	15.01	15.33	14.33	15.36	16.52	15.43	17.61	16.81	17.04	15.89	15.76
CaO	20.19	19.62	19.68	19.78	19.87	23.38	20.41	18.72	18.84	18.92	22.02	22.44	22.27	20.40	21.64	21.42	21.48	19.80	22.59
Na_2O	1.64	1.80	1.88	1.81	1.75	0.49	2.18	1.54	1.63	1.54	0.94	0.74	0.77	1.90	0.80	1.04	1.00	1.47	0.54
K_2O	0.03	0.00	0.01	0.00	0.02	0.00	0.01	0.01	0.01	0.00	0.03	0.00	0.00	0.00	0.02	0.02	0.03	0.00	0.05
Cr_2O_3	0.81	0.70	0.72	0.54	0.62	0.96	0.69	0.59	0.62	0.63	0.70	0.41	1.43	1.53	0.62	0.51	0.45	1.15	1.60
Si	1.878	1.884	1.885	1.876	1.876	1.885	1.877	1.850	1.851	1.860	1.856	1.880	1.929	1.924	1.914	1.909	1.912	1.908	1.896
Ti	0.015	0.017	0.015	0.017	0.020	0.018	0.020	0.029	0.028	0.024	0.020	0.019	0.015	0.012	0.003	0.004	0.003	0.010	0.012
Al	0.269	0.284	0.286	0.280	0.285	0.161	0.294	0.315	0.314	0.297	0.221	0.166	0.092	0.139	0.148	0.176	0.168	0.188	0.151
Fe III	0.009	0.005	0.007	0.012	0.008	0.010	0.011	0.005	0.006	0.006	0.019	0.019	0.009	0.019	0.015	0.014	0.015	0.012	0.007
Fe II	0.085	0.070	0.075	0.074	0.075	0.063	0.065	0.120	0.115	0.112	0.119	0.112	0.088	0.104	0.077	0.081	0.077	0.093	0.083
Mn	0.006	0.002	0.003	0.002	0.003	0.001	0.004	0.003	0.004	0.003	0.003	0.005	0.004	0.003	0.002	0.003	0.004	0.005	0.003
Mg	0.822	0.834	0.822	0.826	0.822	0.895	0.767	0.819	0.814	0.832	0.794	0.845	0.898	0.831	0.939	0.900	0.911	0.869	0.867
Ca	0.777	0.758	0.757	0.771	0.771	0.906	0.789	0.732	0.735	0.738	0.878	0.888	0.870	0.790	0.829	0.825	0.826	0.778	0.893
Na	0.114	0.126	0.131	0.127	0.123	0.034	0.152	0.109	0.115	0.109	0.068	0.053	0.054	0.133	0.055	0.072	0.070	0.105	0.039
K	0.001	0.000	0.001	0.000	0.001	0.000	0.000	0.001	0.000	0.000	0.001	0.000	0.000	0.000	0.001	0.001	0.001	0.000	0.002
Cr	0.023	0.020	0.020	0.016	0.018	0.027	0.020	0.017	0.018	0.018	0.021	0.012	0.041	0.044	0.018	0.014	0.013	0.033	0.047
mg-no.	90.6	92.3	91.6	91.8	91.6	93.4	92.2	87.2	87.6	88.1	87.0	88.3	91.1	88.9	92.4	91.7	92.2	90.3	91.3

	Rinibar																	
	lh																	
	CN4	EN4	EN5	EN5	EN7	EN7	EN8	FN3	FN3	FN4	FN4	FN4	GN5	GN5	GN5	HN11	HN11	HN11
wt%																		
SiO_2	52.27	52.85	51.11	51.99	54.77	54.15	52.50	53.63	53.45	52.06	52.07	51.10	53.95	53.74	49.62	53.94	54.65	51.83
TiO_2	0.49	0.60	0.38	0.34	0.23	0.21	0.18	0.05	0.18	0.21	0.35	0.48	0.07	0.10	0.42	0.25	0.18	0.86
Al_2O_3	2.85	3.00	4.58	4.11	1.90	2.15	4.84	2.81	3.75	6.20	6.10	6.75	3.81	1.96	6.00	2.56	2.96	3.29
Fe_2O_3	0.23	0.45	0.81	0.66	0.51	0.53	0.34	0.48	0.34	0.24	0.26	0.42	0.52	0.22	0.58	0.39	0.15	0.30
FeO	2.79	2.70	2.60	2.73	3.09	2.75	2.88	3.04	3.49	2.87	2.80	2.64	2.66	2.88	2.16	2.44	2.30	2.03
MnO	0.07	0.17	0.14	0.07	0.17	0.06	0.12	0.12	0.13	0.09	0.10	0.11	0.16	0.15	0.01	0.03	0.10	0.05
MgO	16.23	17.02	16.33	16.75	16.79	16.10	16.20	16.40	15.77	15.96	15.92	15.32	16.27	17.61	15.87	16.42	15.85	15.98
CaO	22.40	22.79	22.12	22.16	21.18	21.48	21.64	20.30	19.96	19.60	19.89	19.99	19.67	22.02	21.32	20.14	19.59	22.32
Na_2O	0.65	0.55	0.74	0.68	1.45	1.57	0.92	1.53	1.66	1.41	1.41	1.51	1.93	0.50	0.75	1.75	2.15	0.95
K_2O	0.02	0.00	0.01	0.02	0.01	0.02	0.00	0.00	0.00	0.01	0.00	0.01	0.00	0.00	0.02	0.04	0.07	0.00
Cr_2O_3	1.49	1.10	0.33	0.34	1.05	1.22	0.40	0.84	0.85	0.86	0.83	0.95	0.84	0.67	2.41	2.19	2.31	2.50
Si	1.914	1.899	1.868	1.886	1.962	1.958	1.900	1.954	1.942	1.886	1.884	1.859	1.945	1.951	1.819	1.949	1.968	1.887
Ti	0.013	0.016	0.010	0.009	0.006	0.006	0.005	0.001	0.005	0.006	0.009	0.013	0.002	0.003	0.012	0.007	0.005	0.024
Al	0.123	0.127	0.197	0.176	0.080	0.092	0.206	0.120	0.161	0.265	0.260	0.289	0.162	0.084	0.259	0.109	0.126	0.141
Fe III	0.006	0.012	0.022	0.018	0.014	0.014	0.009	0.013	0.009	0.006	0.007	0.012	0.014	0.006	0.016	0.011	0.004	0.008
Fe II	0.085	0.081	0.079	0.083	0.093	0.083	0.087	0.093	0.106	0.087	0.085	0.080	0.080	0.087	0.066	0.074	0.069	0.062
Mn	0.002	0.005	0.004	0.002	0.005	0.002	0.004	0.004	0.004	0.003	0.003	0.003	0.005	0.004	0.000	0.001	0.003	0.002
Mg	0.886	0.912	0.889	0.906	0.896	0.868	0.874	0.891	0.854	0.862	0.858	0.831	0.874	0.953	0.867	0.884	0.850	0.867
Ca	0.879	0.878	0.866	0.861	0.813	0.832	0.839	0.792	0.777	0.761	0.771	0.779	0.760	0.857	0.837	0.780	0.756	0.871
Na	0.046	0.038	0.053	0.048	0.101	0.110	0.065	0.108	0.117	0.099	0.099	0.106	0.135	0.036	0.053	0.123	0.150	0.067
K	0.001	0.000	0.000	0.001	0.001	0.001	0.000	0.000	0.000	0.000	0.000	0.000	0.000	0.000	0.001	0.002	0.003	0.000
Cr	0.043	0.031	0.009	0.010	0.030	0.035	0.011	0.024	0.025	0.025	0.024	0.027	0.024	0.019	0.070	0.063	0.066	0.072
mg-no.	91.2	91.8	91.8	91.6	90.6	91.3	90.9	90.5	89.0	90.8	91.0	91.2	91.6	91.6	92.9	92.3	92.5	93.3

mg-number = 100 × Mg/(Mg + Fe) (atomic formula units).

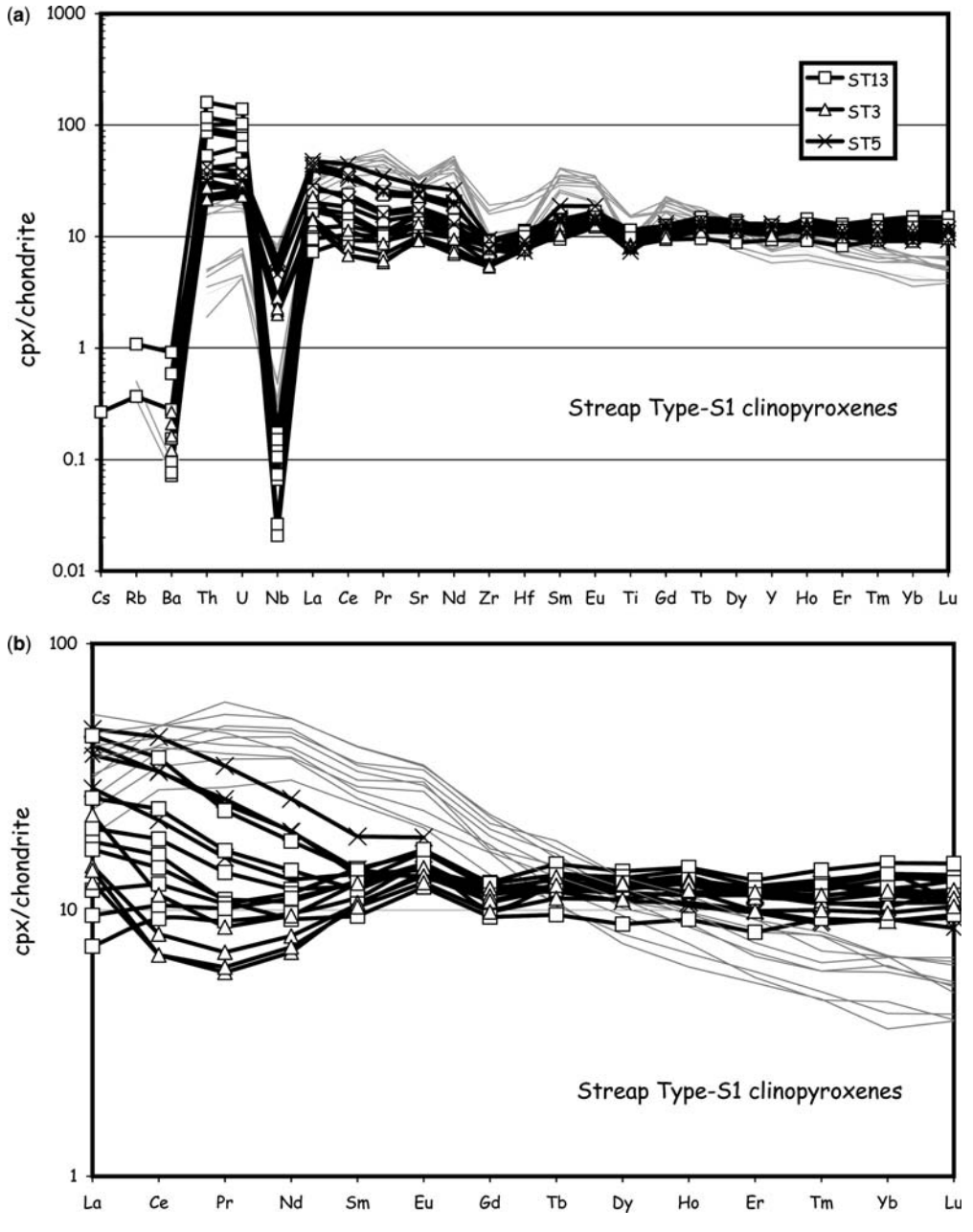

Fig. 3. Chondrite-normalized REE (**a**) and incompatible trace element (**b**) plots of Streap Type-S1 clinopyroxenes; Type-S2 (thin grey profiles) are reported for comparison. Chondrite-normalized REE (**c**) and incompatible trace element (**d**) plots of Streap Type-S2 clinopyroxenes; Type-S1 (thin grey profiles) are reported for comparison. Normalizing factors from McDonough & Sun (1995).

Scottish localities (Hunter & Upton 1987; Menzies *et al.* 1987; Downes *et al.* 2001). However, such textures are globally rare in spinel peridotite xenoliths of intraplate Cenozoic (Phanerozoic?) magmas (Pearson *et al.* 2003, and reference therein). Fine-grained protogranular textures are also very scarce in mantle xenoliths in pre-Mesozoic kimberlites and lamproites (Dawson 1980; Pearson

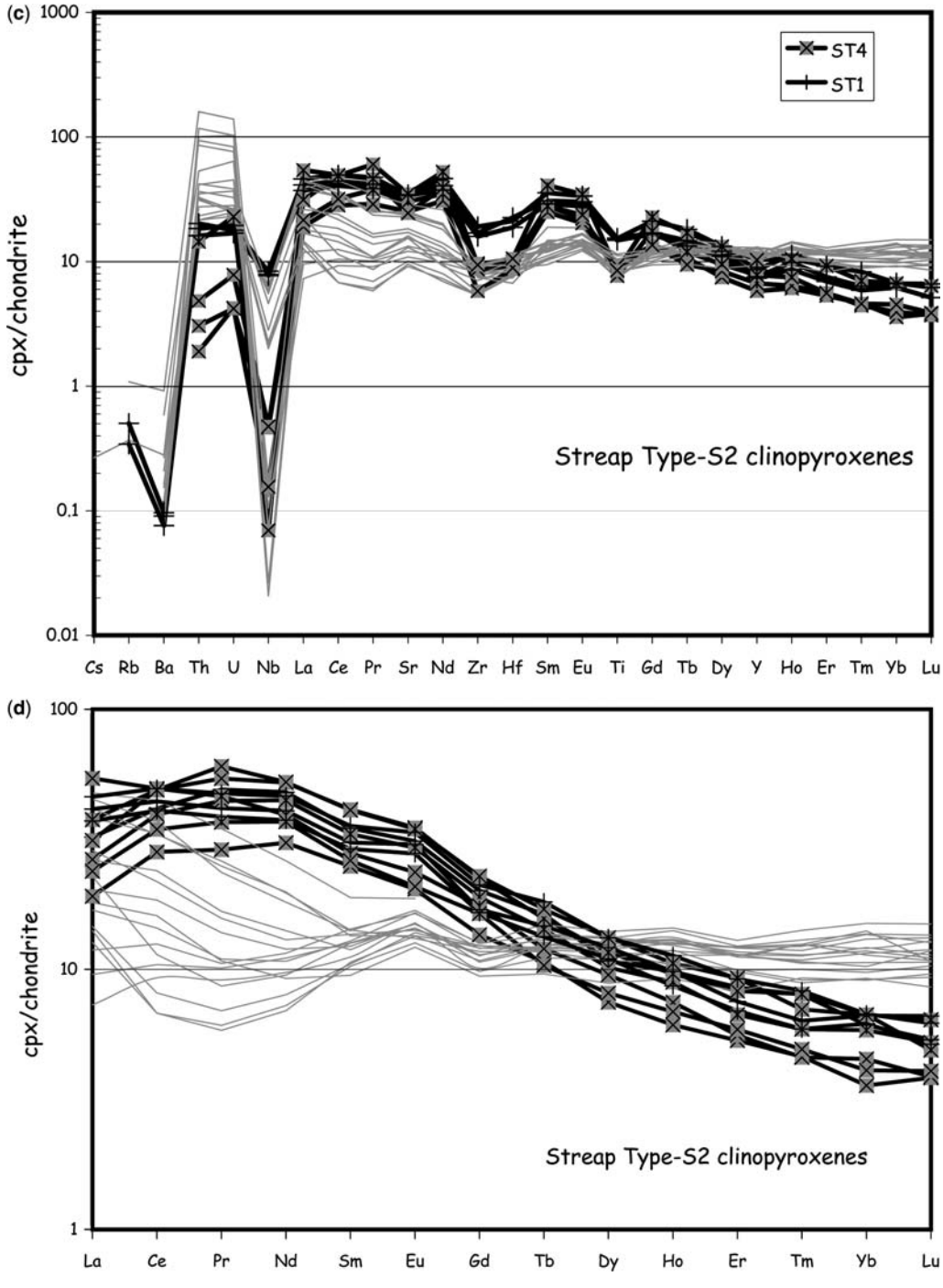

Fig. 3. (*Continued*).

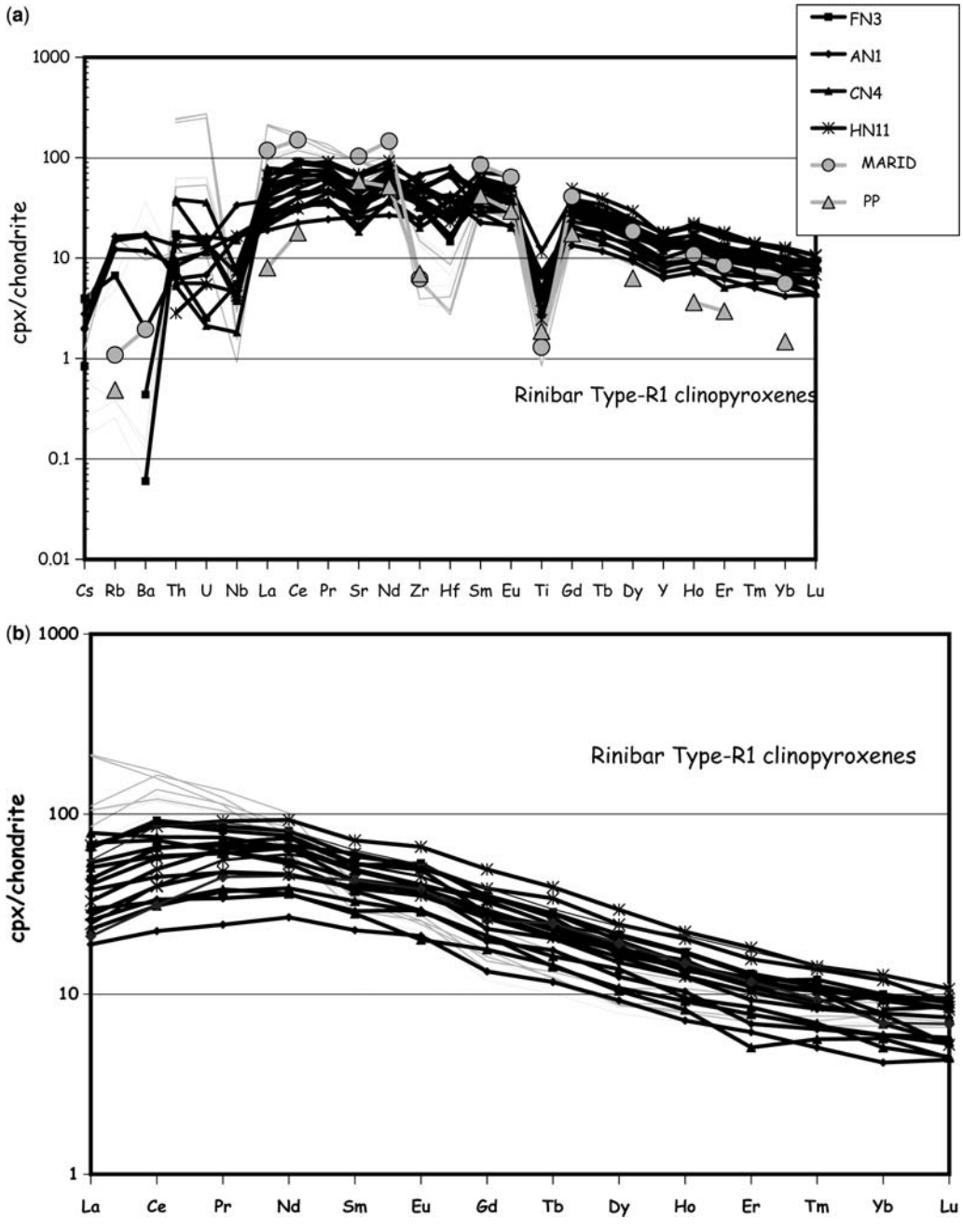

Fig. 4. Chondrite-normalized REE (**a**) and incompatible trace element (**b**) plots of Rinibar Type-R1 clinopyroxenes; Type-R2 (thin grey profiles) and clinopyroxenes from MARID peridotites and garnet–phlogopite peridotites (PP) from the Kimberley pipes (South Africa) (Grègoire *et al.* 2002) are also reported for comparison. Chondrite-normalized REE (**c**) and incompatible trace element (**d**) plots of Rinibar Type-R2 clinopyroxenes; Type-R1 (thin grey profiles) and carbonatite-metasomatized Cr-diopsides from spinel peridotite xenoliths from Kutch (Western India, Karmalkar & Rege 2002), southern Patagonia (Gorring & Kay 2000) and Comores (Coltorti *et al.* 1999) are also reported for comparison. Normalizing factors from McDonough & Sun (1995).

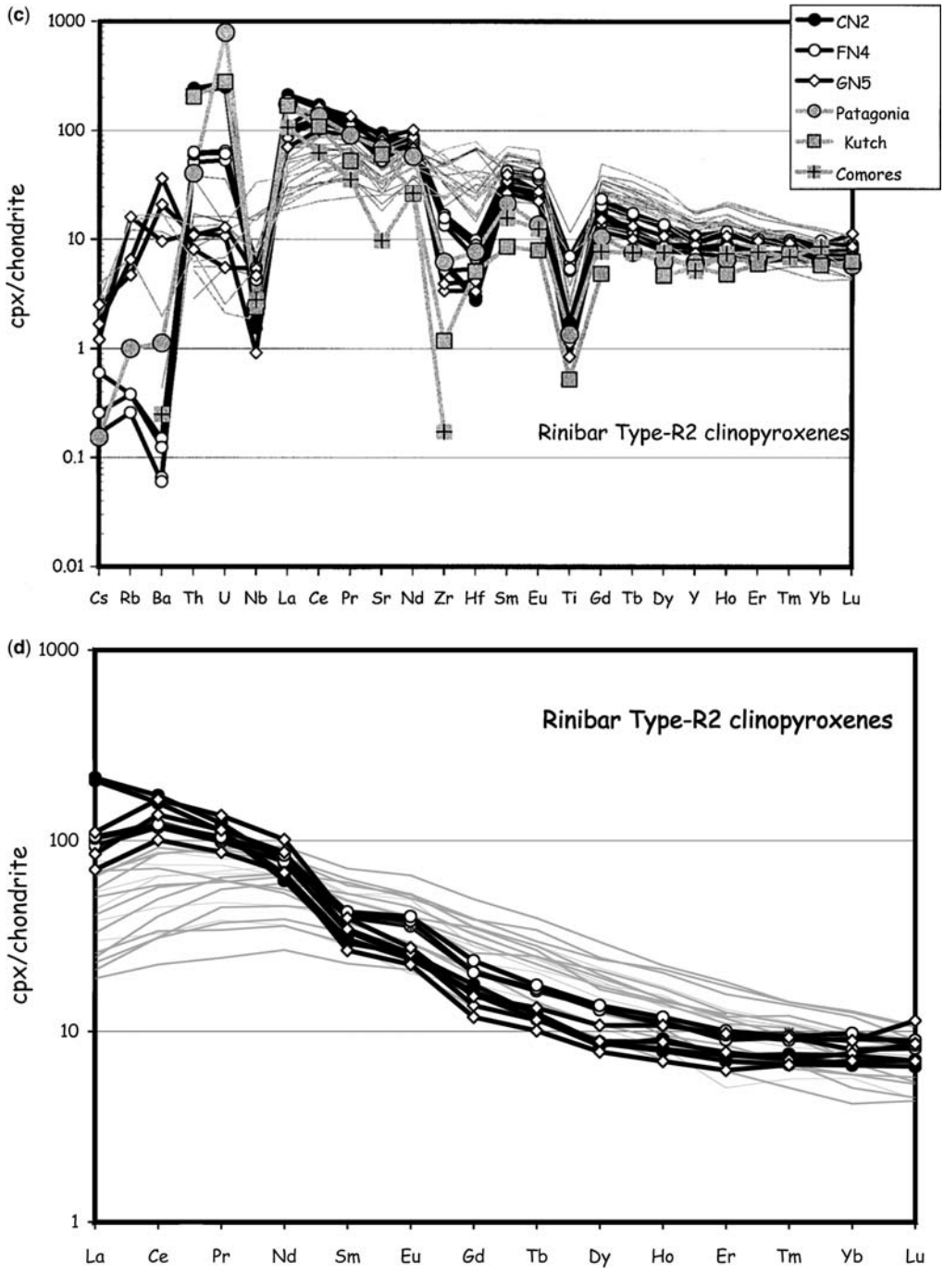

Fig. 4. (*Continued*).

Table 5. *Representative major element analyses of spinels from Streap and Rinibar xenoliths*

	Streap										Rinibar				
	lh						cpx-rich lh		wh		lh				
	ST3	ST3	ST5	ST5	ST7	ST13	ST4	ST4	ST1	ST1	AN1	AN1	CN2	CN2	CN4
wt%															
SiO_2	0.06	0.05	0.08	0.08	0.07	0.06	0.09	0.09	0.02	0.04	0.09	0.09	0.11	0.04	0.09
TiO_2	0.15	0.18	0.13	0.13	0.12	0.05	0.56	0.56	0.39	0.60	1.60	2.04	0.08	0.06	0.46
Al_2O_3	56.32	56.28	54.90	55.08	58.19	57.30	52.91	52.48	42.83	38.41	13.06	22.01	44.74	44.04	37.68
Fe_2O_3	3.65	2.97	2.57	2.30	2.08	1.58	4.49	4.67	10.29	13.14	11.34	8.87	5.40	5.77	5.22
FeO	7.82	8.31	7.02	7.07	8.22	8.84	10.21	9.71	16.00	16.88	19.00	16.62	10.35	9.81	11.70
MnO	0.12	0.12	0.07	0.05	0.11	0.05	0.11	0.09	0.21	0.16	0.48	0.35	0.11	0.23	0.15
MgO	21.11	20.85	21.06	21.12	20.99	20.33	18.92	19.13	14.18	12.77	10.04	12.83	18.65	18.61	16.58
Cr_2O_3	9.00	9.53	9.97	10.24	7.94	8.67	8.47	8.33	12.72	13.24	42.63	35.67	20.27	20.47	25.10
NiO	0.33	0.33	0.31	0.28	0.32	0.28	0.36	0.35	0.07	0.24	0.19	0.25	0.25	0.26	0.21
Si	0.002	0.001	0.002	0.002	0.002	0.002	0.002	0.002	0.001	0.001	0.003	0.003	0.003	0.001	0.003
Ti	0.003	0.003	0.003	0.003	0.002	0.001	0.011	0.012	0.009	0.014	0.040	0.048	0.002	0.001	0.010
Al	1.734	1.735	1.729	1.729	1.788	1.783	1.699	1.695	1.465	1.361	0.511	0.811	1.442	1.430	1.288
Fe	0.070	0.060	0.050	0.050	0.040	0.030	0.090	0.100	0.220	0.300	0.280	0.210	0.110	0.120	0.110
Fe II	0.170	0.180	0.160	0.160	0.180	0.200	0.230	0.220	0.390	0.420	0.530	0.430	0.240	0.230	0.280
Mn	0.003	0.003	0.002	0.001	0.002	0.001	0.002	0.002	0.005	0.004	0.014	0.009	0.003	0.005	0.004
Mg	0.822	0.813	0.838	0.838	0.815	0.800	0.768	0.781	0.613	0.572	0.497	0.597	0.760	0.764	0.716
Cr	0.186	0.197	0.211	0.216	0.164	0.181	0.182	0.181	0.292	0.315	1.119	0.881	0.438	0.446	0.575
Ni	0.007	0.007	0.007	0.006	0.007	0.006	0.008	0.008	0.002	0.006	0.005	0.006	0.005	0.006	0.005
cr-no.	9.7	10.2	10.9	11.1	8.4	9.2	9.7	9.6	16.6	18.8	68.7	52.1	23.3	23.8	30.9
mg-no.	82.9	81.9	84.0	84.0	81.9	80.0	77.0	78.0	61.1	57.7	48.4	58.1	76.0	76.9	71.9

cr-number = 100 × Cr/(Cr + Al) (atomic formula units).
mg-number = 100 × Mg/(Mg + Fe) (atomic formula units).

et al. 2003). Among the very few examples that we know of are those from the Palaeozoic (590–470 Ma) kimberlites of eastern Finland (Kukkonen & Peltonen 1999; Kukkonen *et al.* 2003), which have peridotite textures comparable with those from Rinibar. The subcontinental mantle that they represent is interpreted to have stabilized in the late Archaean (3.5–2.7 Ga). Fine-grained protogranular textures are also reported for a group of pyroxenites (orthopyroxenites and mica clinopyroxenites) in the Mesozoic Weltevreden and Mzongwana kimberlites in South Africa (Doyle *et al.* 2004), which have been interpreted as reaction products between 'megacryst magma' and mantle peridotite. Very fine-grained peridotite textures (with olivines 60–70 μm in diameter) are also known from xenoliths from a mantle wedge above a subduction zone, attributed to the strong shearing that characterizes such environments (Arai *et al.* 2004). Coarse textures (i.e. grain size >5 mm), are considered to be characteristic of the subcratonic lithospheric mantle (Silver *et al.* 1999; Pearson *et al.* 2003). The grain growth occurs when there is a local destabilization of the grain structure induced by a thermal injection accompanied by a long-term residence in a high-temperature–low-stress regime (Silver *et al.* 1999). This is believed to be characteristic of the Archaean subcratonic mantle, where abnormally large crystals occur (e.g. olivines up to 30 mm; Pearson *et al.* 2003). These probably grew in higher geothermal regimes than those of Phanerozoic subcontinental mantle (Francis 2003). Under a dynamic recrystallization regime, stress dominates over the temperature effect, leading to smaller grains at higher stress (Karato *et al.* 1980; de Bresser *et al.* 1998, 2001). The very fine grain size of the Scottish xenoliths may reflect efficient dynamic recrystallization. This matches neither cratonic mantle roots nor the Phanerozoic mantle.

Equilibrium temperature estimates for the Streap and Rinibar xenoliths were calculated using the opx–cpx Fe–Mg exchange thermometer (Brey & Köhler 1990). Both populations record very similar range of temperatures (Streap 840–1000 °C; Rinibar 870–1000 °C), with only sample ST4 showing higher temperatures (1180–1200 °C). It is noteworthy that these are only slightly higher than equibration temperatures (820–800 °C) estimated for the ultramafic cumulate suites that are inferred to overlie the lithospheric lherzolites in the Northern Highland Terrane

Rinibar															
lh															
CN4	EN4	EN4	EN5	EN5	EN7	EN7	EN8	EN8	FN3	FN3	FN4	FN4	GN5	HN11	HN11
wt%															
0.19	0.07	0.09	0.05	0.06	0.05	0.20	0.15	0.09	0.12	0.20	0.06	0.06	0.06	0.05	0.06
1.42	0.13	0.14	0.14	0.17	1.01	1.82	0.03	0.04	0.73	0.76	0.18	0.22	0.16	0.51	0.54
21.90	30.39	30.59	55.95	56.45	14.13	15.14	52.73	51.85	25.18	27.03	48.49	49.60	25.79	13.23	14.84
6.47	6.58	6.40	3.86	4.52	10.88	10.16	4.49	4.03	9.41	7.96	3.92	3.42	5.67	5.02	5.67
15.65	11.54	12.22	9.45	9.37	13.75	21.03	9.49	8.88	14.42	14.92	8.50	9.00	12.27	13.16	12.63
0.33	0.27	0.33	0.11	0.08	0.29	0.55	0.12	0.07	0.27	0.25	0.09	0.11	0.23	0.28	0.29
12.47	15.98	15.82	19.91	20.31	13.33	8.70	19.77	19.58	12.88	12.66	19.54	19.47	15.21	12.71	13.38
36.59	33.43	34.52	8.32	7.58	45.02	39.98	11.96	12.09	30.32	29.08	15.32	15.06	39.63	50.17	48.74
0.22	0.25	0.23	0.31	0.16	0.13	0.12	0.30	0.40	0.18	0.21	0.24	0.28	0.09	0.03	0.09
0.006	0.002	0.003	0.001	0.002	0.002	0.007	0.004	0.002	0.004	0.007	0.002	0.002	0.002	0.002	0.002
0.034	0.003	0.003	0.003	0.003	0.024	0.046	0.001	0.001	0.018	0.018	0.004	0.004	0.004	0.013	0.013
0.832	1.061	1.053	1.742	1.744	0.537	0.595	1.651	1.654	0.957	1.022	1.574	1.594	0.917	0.521	0.572
0.160	0.150	0.140	0.080	0.090	0.260	0.250	0.090	0.080	0.230	0.190	0.080	0.070	0.130	0.130	0.140
0.420	0.290	0.300	0.210	0.210	0.370	0.590	0.210	0.200	0.390	0.400	0.200	0.210	0.310	0.370	0.350
0.009	0.007	0.008	0.002	0.002	0.008	0.016	0.003	0.002	0.007	0.007	0.002	0.002	0.006	0.008	0.008
0.599	0.705	0.689	0.784	0.793	0.641	0.432	0.783	0.790	0.619	0.605	0.802	0.791	0.684	0.633	0.652
0.932	0.783	0.797	0.174	0.157	1.148	1.053	0.251	0.259	0.773	0.737	0.334	0.325	0.945	1.326	1.260
0.006	0.006	0.005	0.007	0.003	0.003	0.003	0.006	0.009	0.005	0.005	0.005	0.006	0.002	0.001	0.002
52.8	42.5	43.1	9.1	8.3	68.1	63.9	13.2	13.5	44.7	41.9	17.5	16.9	50.8	71.8	68.8
58.8	70.9	69.7	78.9	79.1	63.4	42.3	78.9	79.8	61.3	60.2	80.0	79.0	68.8	63.1	65.1

(Upton *et al.* 1998, 2001). These temperatures are, on average, lower than those recorded by mantle xenoliths (1000–1100 °C) in Phanerozoic alkali basalts from around the world (Downes *et al.* 2001; Pearson *et al.* 2003) but match the temperatures reported for the shallowest cratonic mantle and off-cratonic mantle roots (Francis 2003; Griffin *et al.* 2003; King 2005).

No reliable pressure values were obtained using the ol–cpx Ca exchange barometer of Köhler & Brey (1990), because of the disequilibrium of calcium between the two phases, but as spinel is

Table 6. *Representative major element analyses of phlogopites from Streap and Rinibar xenoliths*

	Streap			Rinibar								
	wh			lh								
	ST1	ST1	ST1	AN1	AN1	AN1	CN4	CN4	CN4	GN5	EN7	EN7	EN7
wt%													
SiO_2	36.95	36.46	36.39	34.69	38.16	37.72	37.81	37.08	37.73	31.31	35.80	34.60	35.22
TiO_2	4.64	4.90	4.27	7.23	5.75	6.25	3.35	3.38	3.52	6.21	5.05	6.58	6.74
Al_2O_3	14.85	14.82	15.18	15.15	15.21	12.27	16.10	16.24	16.05	16.62	15.26	15.18	15.73
FeO	6.53	6.69	6.40	7.60	7.25	8.27	4.68	4.65	4.70	9.47	8.37	9.74	6.88
MnO	0.04	0.00	0.02	0.06	0.12	0.09	0.00	0.02	0.08	0.02	0.09	0.13	0.02
MgO	19.78	19.25	19.80	17.53	19.89	19.04	20.98	20.95	20.86	15.90	17.53	17.48	18.43
Na2O	0.61	0.62	0.64	0.49	0.72	0.58	0.77	0.78	0.76	1.15	0.88	0.80	0.83
K2O	9.08	8.57	8.68	7.61	8.82	7.56	8.34	8.21	8.23	6.19	7.94	7.14	8.24
Cr_2O_3	0.56	0.62	0.73	0.05	0.04	0.00	1.49	1.34	1.96	0.11	0.00	0.00	0.12
NiO	0.09	0.06	0.04	0.11	0.09	0.11	0.18	0.28	0.16	0.00	0.13	0.08	0.06
mg-no.	84.4	83.7	84.6	80.4	83.0	80.4	88.9	88.9	88.8	75.0	78.9	76.2	82.7

mg-number = 100 × Mg/(Mg + Fe) (atomic formula units).

Table 7. *Trace element compositions (ppm) of clinopyroxenes (cpx), orthopyroxenes (opx) and phlogopites (phl) of Streap and Rinibar xenoliths*

	Streap									
	Type-S1									
	ST3				ST5					
ppm	cpx	cpx	cpx	cpx	cpx	cpx	cpx	cpx	opx	opx
Cs	<0.04	<0.04	<0.04	<0.04						
Rb	<0.09	<0.09	<0.09	<0.08						
Ba	0.39	0.50	0.65	0.29						0.01
Th	0.68	0.80	0.63	0.62	0.95	0.90	1.06	1.22		0.001
U	0.20	0.21	0.18	0.17	0.19	0.18	0.24	0.28	0.05	0.05
Nb	0.53	0.69	0.49	0.56	1.47	1.36	1.13	1.55		
La	3.47	5.40	3.01	3.34	9.06	10.5	6.80	11.3	0.03	
Ce	4.97	6.98	4.15	4.15	20.3	21.6	13.3	27.3	0.08	0.08
Pr	0.66	0.82	0.55	0.58	2.37	2.40	1.49	3.30		0.01
Sr	73.1	94.6	69.5	66.5	183	177	124	208	0.4	0.37
Nd	3.73	4.44	3.24	3.39	9.27	9.43	6.07	12.2		0.09
Zr	20.7	22.0	20.7	20.9	28.8	29.4	29.6	36.6	1.94	1.22
Hf	0.87	0.84	0.88	0.82	0.72	0.79	0.96	0.98	0.05	0.04
Sm	1.60	1.93	1.63	1.57	2.06	2.27	2.09	2.89		0.03
Eu	0.80	0.84	0.78	0.73	0.78	0.86	0.82	1.09		
Gd	2.48	2.32	2.22	2.02	2.53	2.70	2.54			
Tb	0.45	0.50	0.46	0.41	0.45	0.47	0.44	0.51	0.02	
Dy	3.15	3.22	3.19	2.78	2.99	3.11	2.95	3.33	0.15	0.12
Y	17.0	17.6	16.4	16.1	19.8	19.0	20.6	20.4	1.37	1.01
Ho	0.67	0.73	0.72	0.67	0.59	0.61	0.64	0.70	0.04	0.03
Er	1.89	1.85	1.93	1.64	1.62	1.72	1.88	1.87	0.18	0.16
Tm	0.27	0.28	0.29	0.26	0.23	0.26	0.27	0.32	0.03	0.02
Yb	1.81	1.96	2.00	1.66	1.57	1.70	1.74	1.93	0.24	0.26
Lu	0.27	0.30	0.28	0.26	0.22	0.24	0.30	0.27	0.05	0.04
$(La/Yb)_N$	1.38	1.98	1.08	1.45	4.13	4.42	2.79	4.21		
$(Sm/Yb)_N$	0.99	1.09	0.91	1.05	1.46	1.48	1.33	1.66		

the only aluminous phase, it is reasonable to consider the range of 1.2–1.8 GPa as the barometric conditions at the time of the xenolith entrainment.

In summary, the thermal and rheological data indicate that the lithospheric mantle beneath the SW and the NE parts of the Northern Highlands Terrane, as sampled by the dykes at Rinibar and Streap, differs from the simple 'pure' Archaean to Phanerozoic cratonic and Phanerozoic off-cratonic environments. We might infer that these xenoliths represent portions of both cratonic and off-cratonic Proterozoic mantle.

Pre-Palaeozoic Rinibar and Streap mantle composition

The concentrations of major and trace elements in the minerals from most of the Rinibar and Streap xenoliths vary with mg-number. However, there is no clear depletion trend that can be attributed to melt extraction. For the Rinibar samples, it is difficult to constrain the melting conditions prior to metasomatism, as the abundances of even those elements least likely to have been influenced by metasomatism (i.e. HREE, Zr and Y) vary widely and do not relate to the major refractory indicators. Moreover, it is highly probable that the clinopyroxenes are 'originally' secondary in nature, as suggested by many workers for the origin of the clinopyroxenes and garnets in the Archaean subcontinental lithospheric mantle (e.g. Stachel *et al.* 1998; Griffin *et al.* 1999; Bonadiman *et al.* 2004; Spengler *et al.* 2006). Some indications, however, of the Pre-Palaeozoic nature of the Scottish lithosphere can be deduced from a few key major and trace elements in the minerals. For example, the Al_2O_3 and Cr_2O_3 contents of the pyroxenes of the two suites are strikingly different, with the Rinibar orthopyroxenes and clinopyroxenes (at comparable mg-number), having lower Al_2O_3 and higher Cr_2O_3 than those from Streap (Fig. 5). In

						Type-S2									
ST13						ST1									
cpx	cpx	cpx	cpx	cpx	cpx	cpx	cpx	cpx	cpx	cpx	cpx	cpx	opx	phl	
0.05	<0.04	<0.04	<0.04	<0.04	<0.04									1.59	
0.13	<0.10	<0.10	<0.09	0.38	<0.08										
0.67	<0.04	0.37	0.23	2.21	0.18								0.004	13493	
2.72	2.49	1.02	3.40	4.64	1.20	0.06	0.15	0.13	0.45	0.53	0.42	0.10			
0.62	0.57	0.27	0.76	1.03	0.33	0.03	0.05	0.05	0.16	0.19	0.17	0.03		0.01	
0.01	0.03	0.03	0.02	0.04	0.04	0.04	0.12	0.09	0.07	0.06	0.02	0.07		5.27	
4.28	4.00	1.73	6.24	10.69	2.26	4.53	7.00	6.27	7.64	8.92	12.9	5.65	0.01		
9.85	8.82	5.68	14.66	22.81	6.38	17.3	27.5	24.1	25.4	30.0	30.3	21.2	0.02		
1.02	1.04	0.87	1.59	2.24	0.96	2.74	4.94	4.22	4.67	5.15	4.40	3.50	0.01		
112	117	79	133	165	88.1	183	242	199	206	234	178	196	0.20	212	
4.31	5.01	4.54	6.58	8.46	5.16	14.3	23.0	20.9	22.4	24.4	18.3	17.3	0.04		
27.3	36.0	31.6	36.0	35.0	30.2	22.5	41.0	35.8	35.4	40.8	33.5	31.0	1.25	3.68	
0.94	1.12	0.94	1.19	1.18	1.07	0.93	1.29	1.33	1.13	1.25	0.95	1.05	0.01	0.08	
1.45	1.97	1.71	1.82	2.15	1.93	3.81	6.19	5.07	5.34	6.30	4.28	4.01	0.01		
0.71	0.96	0.82	0.88	0.98	0.87	1.18	1.77	1.70	1.81	2.03	1.37	1.21			
1.94	2.47	2.08	2.19	2.58	2.34	2.79	4.24	3.89	4.13	4.59	3.61	3.37			
0.36	0.49	0.46	0.45	0.51	0.46	0.40	0.57	0.53	0.61	0.59	0.45	0.39	0.01		
2.25	3.04	3.19	3.26	3.39	3.21	1.90	3.00	2.58	2.74	2.95	2.42	2.06	0.04		
14.7	19.9	17.1	16.9	17.3	16.7	9.12	15.5	12.2	14.5	16.9	12.3	10.5	0.63	0.94	
0.52	0.71	0.75	0.74	0.71	0.74	0.35	0.58	0.51	0.56	0.54	0.42	0.39	0.02		
1.37	2.02	1.88	2.00	2.01	1.89	0.88	1.40	1.11	1.41	1.37	0.92	0.97	0.10		
0.24	0.32	0.32	0.30	0.31	0.29	0.12	0.17	0.15	0.20	0.20	0.12	0.13	0.01		
1.54	2.39	2.05	2.22	2.32	2.06	0.61	1.00	0.99	1.04	1.14	0.77	0.70	0.12		
0.24	0.27	0.33	0.34	0.32	0.29	0.10	0.13	0.13	0.14	0.12	0.10	0.10	0.02		
1.99	1.20	0.61	2.01	3.31	0.79	5.34	5.04	4.53	5.28	5.62	12.00	5.83		4.14	
1.05	0.91	0.93	0.91	1.03	1.04	6.96	6.90	5.67	5.72	6.15	6.18	6.41			

other words, the latter have 'more fertile compositions' than the Rinibar pyroxenes.

In the discrimination diagram of Ramsay & Tompkins (1994) (Fig. 5), it can be seen that the Streap clinopyroxenes have the chromium and aluminium contents expected for diopsides in off-craton environments (both spinel and garnet stability fields) whereas most of the Rinibar clinopyroxenes plot in the field for cratonic garnet lherzolites.

The high Al_2O_3 contents and flat chondrite-normalized MREE–HREE profiles of the Type-S1 clinopyroxenes suggest that they originally formed, and experienced long-term equilibration, in the spinel stability field (Beccaluva *et al.* 2001; Neumann *et al.* 2004; Bonadiman *et al.* 2005; Hellebrand *et al.* 2005). The high normalized HREE values (Yb_N, 9–15 × chondrite) of these pyroxenes also reflect the fertile character of the pre-metasomatic peridotite. Because the HREE contents correlate with the cr-number of the coexisting spinel, we can employ the modelling technique proposed for abyssal peridotites by Hellebrand *et al.* (2001). An estimate of the degree of partial melting can be obtained using the simple equation for a near-fractional melting model based on cr-number of spinel ($F(\%) = 10.3\ln(\text{Cr-number}_{sp}) + 25.0$; Hellebrand *et al.* 2005). This indicates a range between 1 and 6% for the Streap population. Similar estimates (*c.* 4%) were also obtained using the $(Sm/Yb)_N$ v. Yb_N grid (Hellebrand *et al.* 2001, 2005) in which we replace the starting point ('DMM cpx in spinel facies') with the $Cpx_{PM\text{-}sp}$ (primitive mantle clinopyroxene composition in the spinel stability field, as defined by Bonadiman *et al.* (2005)).

As reported above, the mg-number values of clinopyroxenes in both suites are comparable, but the Streap clinopyroxenes consistently have higher Al_2O_3 and TiO_2 contents (Table 2). Clinopyroxene MREE–HREE chondrite-normalized profiles are also distinct between Rinibar and Type-S1 of Streap. From these simple considerations, it appears that the Rinibar and Streap samples, prior

Table 7. *(Continued)*

	Rinibar															
	Type-R1															
	ST4			CN4						HN11						
ppm	cpx	cpx	cpx	cpx	cpx	cpx	cpx	phl	phl	cpx	cpx	cpx	cpx	cpx	cpx
Cs	<0.04	<0.04	<0.04					7.61	3.88						
Rb	0.18	<0.09	0.12					305	364						
Ba	0.23	0.22	0.18					36672	38766						
Th	0.47	0.59	0.54	0.28	0.15	1.04	0.16			0.38	0.08				
U	0.13	0.13	0.14	0.08	0.02	0.10	0.04			0.10	0.04				
Nb	1.90	2.06	1.94		0.45			134	149	1.72	1.12	1.04	1.84	2.06	4.08
La	8.82	10.93	9.80	12.7	12.0	18.7	5.45			15.9	7.79	9.66	5.79	13.1	4.97
Ce	25.0	30.3	27.1	40.0	35.8	45.7	18.9			52.3	30.3	34.9	24.5	52.5	19.0
Pr	3.67	4.51	3.96	6.36	5.75	7.06	3.53			8.69	6.09	5.86	5.28	8.53	4.26
Sr	248	247	250	210	190	314	133	381	532	496	326	413	272	470	234
Nd	17.5	21.7	19.0	31.3	30.4	30.5	18.1			43.4	31.4	25.9	28.0	38.0	21.2
Zr	61.6	74.0	65.7	182	189	191	90.9	44.8	31.2	204	153	149	132	229	182
Hf	2.01	2.25	2.40	7.18	7.46	7.28	4.05	0.77	0.40	4.07	2.81	2.43	2.44	2.95	3.87
Sm	4.44	5.45	4.70	7.55	7.40	6.43	5.02			10.9	9.25	6.62	8.07	9.65	6.58
Eu	1.62	1.95	1.75	2.35	2.30	2.12	1.66			3.82	2.90	2.25	2.62	3.04	2.22
Gd	3.40	4.34	3.49	6.80	7.18	5.74	4.34			10.1	7.93	6.04	6.63	7.99	5.29
Tb	0.50	0.68	0.55	0.91	1.00	0.79	0.61			1.47	1.27	0.84	0.92	1.11	0.93
Dy	2.79	3.36	3.08	4.66	4.22	4.43	3.50			7.48	6.19	4.37	5.29	6.05	4.87
Y	11.6	13.5	11.9	22.2	20.6	19.6	14.1	0.22		26.3	27.5	20.7	24.1	28.5	20.7
Ho	0.49	0.64	0.56	0.76	0.79	0.77	0.54			1.26	1.15	0.81	0.95	1.20	0.84
Er	1.15	1.52	1.25	1.98	1.82	1.92	1.40			3.00	2.59	2.04	2.08	2.87	1.93
Tm	0.15	0.21	0.16	0.27	0.27	0.27	0.18			0.36	0.35		0.28	0.36	0.24
Yb	1.05	1.15	1.13	1.33	1.16	1.58	0.86			2.17	2.03	1.40	1.55	2.13	1.18
Lu	0.13	0.16	0.17	0.19	0.14	0.21	0.11			0.27	0.23	0.22	0.21	0.27	0.17
$(La/Yb)_N$	6.02	6.85	6.23	6.86	7.39	8.49	4.55			5.27	2.75	4.96	2.68	4.42	3.02
$(Sm/Yb)_N$	4.69	5.29	4.63	6.30	7.08	4.53	6.49			5.60	5.05	5.26	5.79	5.03	6.19

to metasomatism, represented distinct mantle domains. The Streap Type-S1 peridotites could represent typical sp-facies, off-craton, lithospheric mantle, whereas we suggest that the Rinibar samples were evolved from a garnet-bearing source in a cratonic environment. Alternatively, as will be discussed below, the HREE profiles of the Rinibar samples could indicate equilibrium with melt generated in the garnet stability field.

Metasomatic style of Rinibar

The Rinibar clinopyroxenes are characterized by humped REE patterns with a maximum at Pr (Nd) and $(Sm/Yb)_N$ varying between 5.0 and 6.2, accompanied by the moderately to strong Ti (Zr and Hf) negative anomalies (Fig. 4a–d). The degree of MREE–HREE positive fractionation depends on the presence of garnet in the peridotite source, which preferentially takes up the HREE; for example $(Sm/Yb)_N$ values in the Slave and Kaapvaal cratons are typically >15 (i.e. Griffin *et al.* 1999; Grégoire *et al.* 2003; Kopylova & Caro 2004). Less steep MREE–HREE clinopyroxene profiles (i.e. $5 < (Sm/Yb)_N < 15$) are a function of the appearance of spinel and the relative destabilization of garnet, as shown by a minority of mantle xenoliths brought to the surface in kimberlites (e.g. Griffin *et al.* 2003; Stachel *et al.* 1998). Peridotite clinopyroxenes that have been always in equilibrium with spinel have almost flat to negatively fractionated HREE profiles ($(Sm/Yb)_N$ ratios varying from *c.* 1 to <1; Hellebrand *et al.* 2005). In some cases, the persistence of positively fractionated MREE–HREE profiles for clinopyroxenes in the spinel stability field is considered to indicate former residence in garnet-bearing mantle (see Bonadiman *et al.* 2005). The pronounced convexities of the LREE profiles are consistent with lower $^{cpx/liq}K_d$ of La with respect to Ce, which can be obtained only if the clinopyroxene crystallized from a primitive basic melt (Suhr *et al.* 1998; Asimow *et al.* 2001). These clinopyroxene profiles, especially those of Type-R1, are similar to those from MARID peridotites and

Type-R1					Type-R2							
FN3			AN1		CN2			FN4			GN5	
cpx	cpx	cpx	cpx	cpx	cpx	cpx	opx	cpx	cpx	cpx	cpx	cpx
0.74	<0.03	0.16	0.38	0.52				<0.03	0.11	0.05	0.32	0.23
2.35	<0.07	<0.09	5.75	5.20				<0.09	0.13	0.13	2.28	5.61
4.75	0.14	1.05	41.3	40.2			0.07	0.16	0.36	0.30	87.4	23.0
0.22	0.50	0.50	0.18	0.39	7.08	6.49	0.06	1.48	1.75	1.81	0.23	0.33
0.02	0.11	0.10	0.05	0.10	2.02	1.84	0.04	0.39	0.47	0.48	0.04	0.08
1.35	1.07	0.91	4.05	8.27	0.71	0.38		1.04	1.31	1.31	1.32	0.22
10.34	15.75	15.40	4.49	8.96	49.1	50.7	0.10	22.3	24.9	24.4	20.2	26.2
39.5	53.7	56.3	13.7	27.4	96.9	106	0.37	72.1	78.0	72.9	83.8	101
6.58	7.68	8.11	2.31	4.50	10.7	11.7	0.05	9.40	9.82	9.72	10.8	12.9
246	331	465	186	235	691	675	1.05	406	387	381	553	625
34.5	35.4	37.7	12.5	21.3	31.3	35.7	0.18	36.3	40.5	39.2	40.7	47.4
124	125	122	96.2	260	24.0	21.6	2.3	57.1	64.9	52.2	13.0	15.2
2.60	1.55	1.71	4.05	8.45	0.31	0.32	0.05	0.92	1.05	0.71	0.36	0.44
7.96	8.12	8.92	3.47	6.04	4.66	5.12	0.05	6.09	6.45	6.29	5.26	6.02
3.09	2.85	3.02	1.22	2.22	1.39	1.42	0.03	2.07	2.07	2.21	1.49	1.59
7.05	5.74	7.25	2.75	4.74	3.22	3.32	0.09	4.19	4.38	4.18	2.81	3.13
1.05	0.89	1.05	0.44	0.76	0.43	0.46	0.01	0.61	0.61	0.63	0.43	0.50
5.45	4.51	5.04	2.35	3.81	2.14	2.20	0.17	3.39	3.26	3.30	2.25	2.73
21.9	18.4	22.3	10.0	15.5	13.7	13.5	1.23	14.4	15.5	15.4	14.0	17.2
0.97	0.88	0.83	0.40	0.71	0.52	0.45	0.05	0.64	0.66	0.62	0.50	0.61
2.16	1.80	1.98	1.02	1.54	1.25	1.16	0.20	1.49	1.62	1.59	1.29	1.61
0.29	0.23	0.31	0.13	0.21	0.18	0.17	0.04	0.24	0.25	0.23	0.18	0.24
1.63	1.65	1.70	0.71	1.33	1.16	1.13	0.36	1.36	1.59	1.55	1.30	1.52
0.24	0.21	0.23	0.11	0.19	0.18	0.17	0.07	0.21	0.22	0.23	0.22	0.29
4.54	6.84	6.51	4.54	4.84	30.26	32.15		11.73	11.27	11.33	11.12	12.41
5.42	5.46	5.84	5.43	5.06	4.45	5.03		4.96	4.52	4.52	4.48	4.41

Table 8. *Measured Sr–Nd–Hf isotopic values of bulk rocks and clinopyroxenes of Streap and Rinibar xenoliths, respectively*

Sample	Rock type		$(^{87}Sr/^{86}Sr)_m$	2σ	Rb	Sr	$(^{143}Nd/^{144}Nd)_m$	2σ	Sm	Nd	$(^{176}Hf/^{177}Hf)_m$	2σ	Lu	Hf
Streap														
Type-S1														
ST5	lh	whole rock	0.70710	11	1	39	0.512687	17	0.41	1.67	0.283088	60	0.05	0.13
ST13	lh	whole rock	0.70652	10	10	190	0.512550	5	1.45	4.31	0.282735	12	0.32	1.11
Type-S2														
ST1	wh	whole rock	0.70826	12	7	199	0.512093	5	2.96	11.7	0.282537	8	0.08	0.68
ST4	cpx-rich lh	whole rock	0.70797	9	7	229	0.512615	5	2.04	8.30	0.282727	17	0.07	1.10
Rinibar														
Type-R1														
AN1	lh	cpx	0.70347	12	5.07	205	0.512761	4	4.65	18.8	0.282799	12	0.14	6.51
CN4	lh	cpx	0.70383	12	2.10	212	0.512643	6	6.07	25.3	0.282706	7	0.15	5.66
FN3	lh	cpx	0.70331	11	2.35	348	0.512757	4	8.34	35.9	0.282848	8	0.23	1.95
HN11	lh	cpx	0.70330	12	2.00	352	0.512743	16	8.14	29.9	0.282705	27	0.21	2.90
Type-R2														
CN2	lh	cpx	0.70377	11	0.50	682	0.512431	4	4.74	32.0	0.283014	28	0.17	0.31
FN4	lh	cpx	0.70381	9	0.12	390	0.512480	5	6.33	38.9	0.282921	10	0.22	0.91
GN5	lh	cpx	0.70345	12	3.15	586	0.512524	5	5.12	40.0			0.23	0.46

Trace element analyses are in ppm. Rb and Sr analyses of Streap were carried out by XRF, whereas Sm, Nd, Lu and Hf were Determined ICP-MS. Trace element analyses of Rinibar clinopyroxene separates were carried out by LAM-ICP-MS.

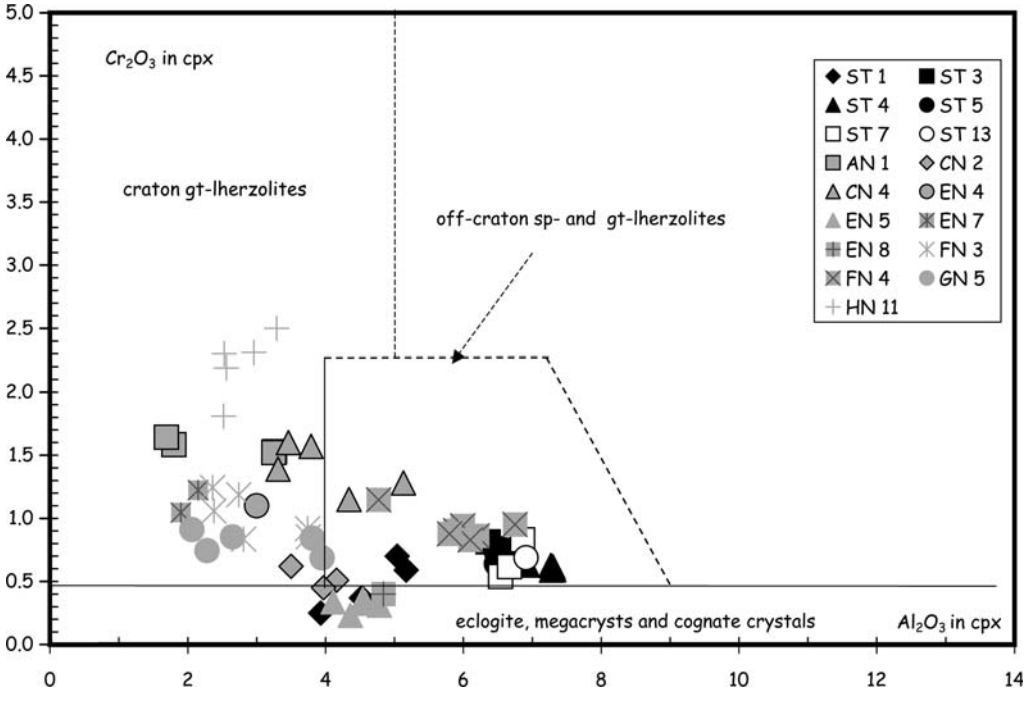

Fig. 5. Cr_2O_3 v. Al_2O_3 discriminating plot for craton and off-craton Cr-diopsides in both spinel and garnet stability field (Ramsay & Tompkins 1994).

garnet–phlogopite peridotites from the Kimberley pipes (South Africa, Grégoire *et al.* 2003) (Fig. 4b). On the other hand, the Type-R2 trace element profiles mimic those of peridotites interacted with carbonatite melts (Fig. 4d).

In terms of major element contents, the Type-R1 clinopyroxenes appear approximately equilibrated with orthopyroxene (and olivine), suggesting that their crystallization resulted from an equilibrium between a hypothetical melt and the original peridotite matrix. To put further constraints on the origin of the clinopyroxenes, we calculated the hypothetical melts in equilibrium with clinopyroxene, using the $^{cpx/melt}K_d$ of Green *et al.* (2000) and Keshav *et al.* (2005) (Fig. 6a). The calculated melt type is very similar (except for HREE) to the 'inferred primary kimberlitic magmas' for two of the Kimberley pipes (Le Roex *et al.* 2003). Trace element profiles are, however, better accounted for by considering the MARID liquid proposed by Grégoire *et al.* (2002). The MARID paragenesis was interpreted by those workers as having resulted from an efficient chemical exchange between a percolating melt of kimberlitic composition and its peridotite host rock. Such an exchange could have occurred via an extensive reaction between highly depleted mantle peridotite and percolating melt, either by continuous melt feeding a mantle column (Vernières *et al.* 1997; Ionov *et al.* 2002) or through impregnation by an interconnected melt network (e.g. Moine *et al.* 2001; Speigelman & Kelemen 2002; Piccardo *et al.* 2007).

Major element contents of the Type-R2 Rinibar clinopyroxenes also imply the same on-craton imprinting, but their trace element budget differs in showing strong Sr, U, Th and LREE enrichment accompanied by remarkable Zr (and Hf) negative anomalies. These features have been documented in Cr-diopsides from spinel peridotite xenoliths that reflect strong carbonatitic metasomatism of continental (e.g. Kutch, Karmalkar & Rege 2002; southern Patagonia, Gorring & Kay 2000) as well as oceanic lithosphere (Coltorti *et al.* 1999).

The hypothetical Type-R2 melts, calculated on the basis of the $^{cpx/carb}K_d$ of Klemme *et al.* (1995), overlap the field of Proterozoic carbonatite melts from the Canadian, North Atlantic, Kaapvaal and Baltic Cratons (Ionov & Harmer 2002; Downes *et al.* 2005; Tappe *et al.* 2006; Fig. 6b). The Type-R2 melts are also similar to those calculated in equilibrium with type-R1 pyroxenes, except for the more accentuated Zr (and Hf) negative anomalies. The slighter fractionated MREE–HREE patterns of the calculated carbonatitic melts with respect to the Proterozoic carbonatic melts could indicate that the final residence of

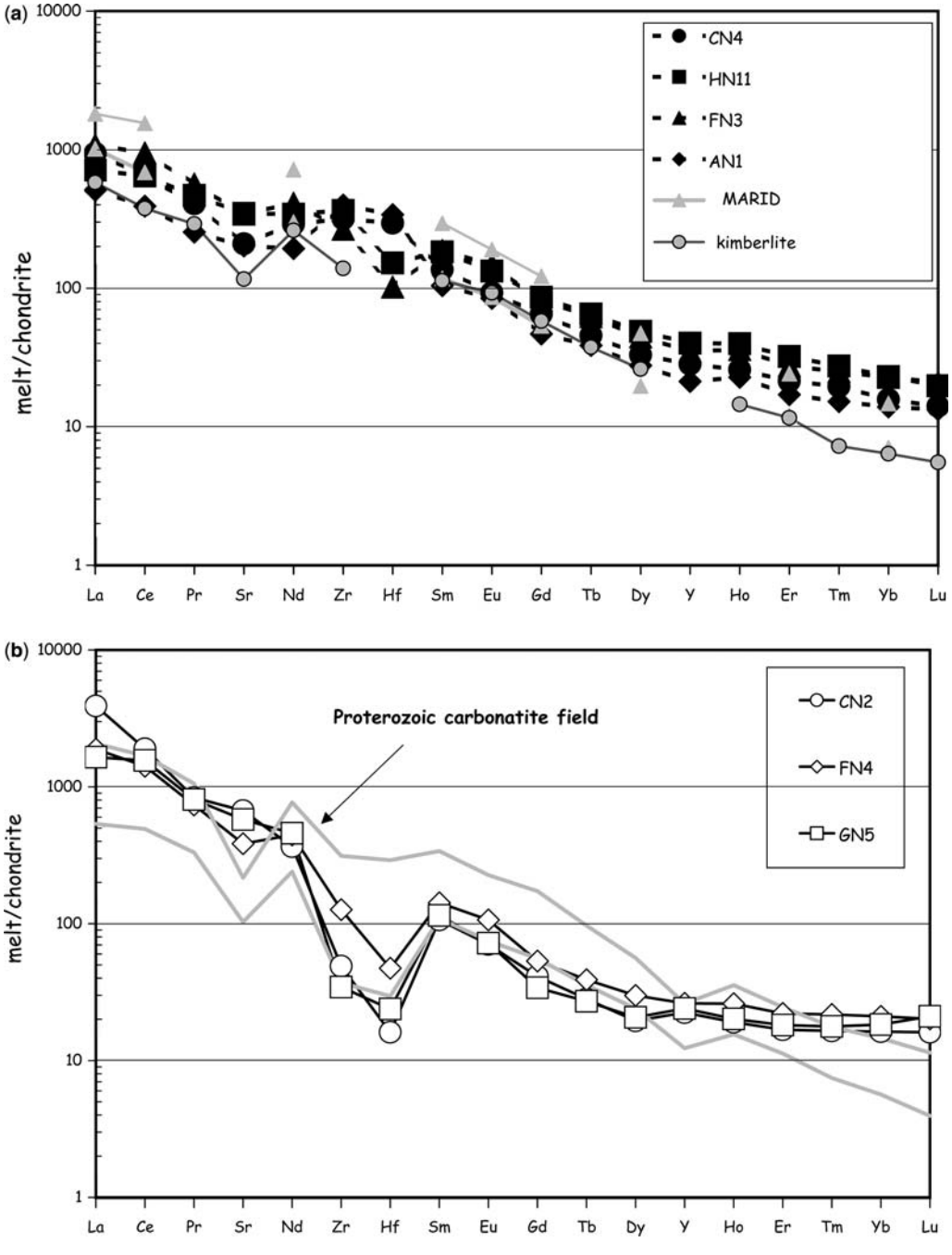

Fig. 6. (**a**) Chondrite-normalized incompatible trace element diagram of calculated melts in equilibrium with Rinibar Type-R1 clinopyroxenes. Inferred primary kimberlite of Kimberley pipes from Le Roex *et al.* (2003) and MARID liquid proposed by Grégoire *et al.* (2002) are reported for comparison. (**b**) Chondrite-normalized incompatible trace elements diagram of calculated melts in equilibrium with Rinibar Type-R2 clinopyroxenes. Proterozoic carbonatite field (outlined by grey lines) from Ionov & Harmer (2002), Downes *et al.* (2005) and Tappe *et al.* (2006). Normalizing factors are from McDonough & Sun (1995).

clinopyroxenes in equilibrium with these melts must have been the spinel-bearing peridotite field. In summary, the trace elements of the clinopyroxenes suggest that both silicate (kimberlitic) and carbonatitic magmas affected this part of the Northern Highland Terrane lithosphere, interacting with the (probably depleted) subcratonic mantle. The relatively high, but still fractionated, HREE profiles of the clinopyroxenes suggest the evolution from garnet to spinel stability field of the peridotite source, or a prolonged interaction with a carbonatic or kimberlitic melt that originated in the garnet stability field and afterwards moved towards a spinel peridotite environment. This scenario constrains the barometric conditions at the time of the melt–lithosphere interaction to lower than 2.1 GPa (Gasparik 2003).

Sr, Nd and Hf isotopic data for the Type-R1 (kimberlite-type) and Type-R2 (carbonatite-type) clinopyroxene groups are closely similar, with perfect overlapping of the Sr isotopic data. The principal difference is for the Nd-isotopic compositions, which depict two distinct fields in the Nd v. Sr isotope co-variation diagram at 252 Ma, the age of the xenolith-bearing dyke (Fig. 7a). Significantly, at the age of 550 ($\pm$50) Ma, the two groups

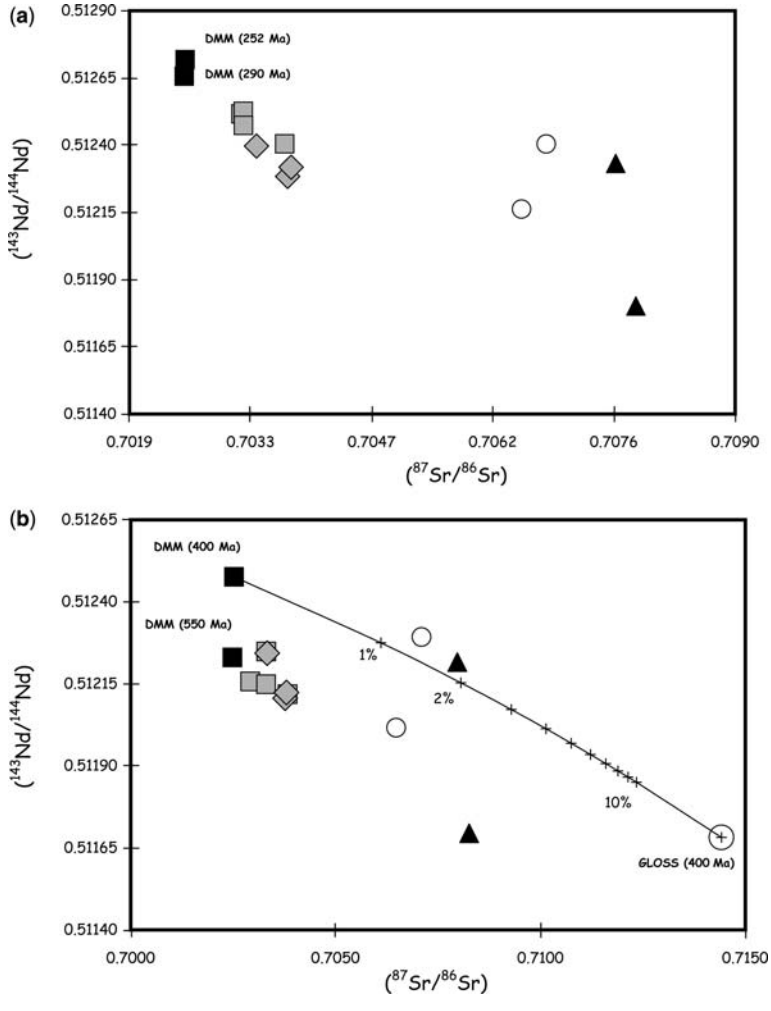

Fig. 7. ^{143}Nd/^{144}Nd v. ^{87}Sr/^{86}Sr co-variation diagrams for Scottish samples corrected for the ages of (**a**) the Rinibar (252 Ma) and Streap (290 Ma) xenolith-bearing dykes and for (**b**) 550 Ma (Rinibar) and 400 Ma (Streap). LA-ICP-MS data of the clinopyroxenes used for the age corrections, as reported in Table 8. Grey squares, Rinibar Type-R1 clinopyroxenes; grey diamonds, Type-R2 clinopyroxenes; open circles, Streap Type-S1 whole-rock; black triangles, StreapType-S2 whole-rock. GLOSS, Global Subducted Sediments (Plank & Langmuir 1998) corrected at 400 Ma. Average DMM from Workman & Hart (2005).

have almost identical Sr–Nd compositions (Fig. 7b), similar to average DMM at 550 Ma (Workman & Hart 2005). This strongly suggests contemporaneous overprinting of DMM by kimberlitic and carbonatitic metasomatic agents at *c*. 550 Ma and not at *c*. 250 Ma, when the xenoliths were emplaced at crustal levels by alkaline magmas. This is supported by the systematics in the Nd–Hf-isotope diagram, in which the kimberlitic-type Rinibar samples fall into the DMM (550 Ma) field and the carbonatitic-type Rinibar samples form a vertical array from this field. The downward vertical array in the Nd–Hf-isotope diagram points to a metasomatic agent with relatively low $^{176}Hf/^{177}Hf$ (Fig. 8), suggesting that the metasomatic agent must have had a low Lu/Hf ratio for a long time.

Contemporaneous kimberlite and carbonatite magmatism is not unusual, as indicated by the majority of the pre-Mesozic lithospheric carbonatites, which are spatially and temporally related to kimberlites and which have Sr and Nd isotopic ratios similar to those of the Type-R1 and Type-R2 clinopyroxenes from Rinibar (e.g. in the Canadian, Finnish, Kola and Kaapvaal Cratons; Agashev *et al.* 2001; Kukkonen *et al.* 2003; Le Roex *et al.* 2003; Eglington & Amstrong 2004; Downes *et al.* 2005; Tappe *et al.* 2006) (Fig. 9). Accordingly, a common origin for both carbonatitic and silicate magmatism has been invoked. The two magma types were generated in the same mantle region by similar melting processes. This also accords with experimental results on the melting of a carbonated mantle at 6 GPa, which show that kimberlites and carbonatites can be formed from the same source by variable degree of partial melting (Dalton & Presnall 1998). Analogously, kimberlite and carbonatite metasomatism that affected the Rinibar lithospheric mantle at 550 $\pm$ 50 Ma may be considered as derived from variable degrees of partial melting of a similar source.

Metasomatic style in the Streap xenoliths

The Streap clinopyroxenes show geochemical features completely different from those of Rinibar clinopyroxenes. The enrichments in Sr, U, Th and LREE contents can be explained by interaction of originally different lithospheric mantle with metasomatic melts. The U/Th ratio closely reflects the chondritic ratio (U/Th 0.23–0.26, Table 8; PM 0.25, McDonough & Sun 1995), and indicates that the hypothetical melt interacting with the lherzolites had the $^{cpx/melt}U/Th$ partition coefficients of *c*. 1 predicted ($^{cpx/melt}U/Th$, 0.98–1.19; Wood *et al.* 1999; Lundstrom *et al.* 2000, and references therein) for clinopyroxenes on the mantle solidus in equilibrium with basaltic melts at 1.0–1.5 GPa. Among the wide assortment of mantle, crustal xenoliths and megacrysts (Upton *et al.* 1999, 2001, 2003) representing the complexity of the juxtaposed Scottish tectonic blocks, Sr–Nd isotopic signatures comparable with those of Streap have been observed, so far, only for the Loch Roag (Hebridean Terrane) mantle xenoliths and a few Fidra (Southern Uplands Terrane) metagabbroic granulites (Fig. 9) (Menzies *et al.* 1987; Downes *et al.* 2001). The Streap mantle xenoliths show the highest radiogenic Sr yet recorded from any of the

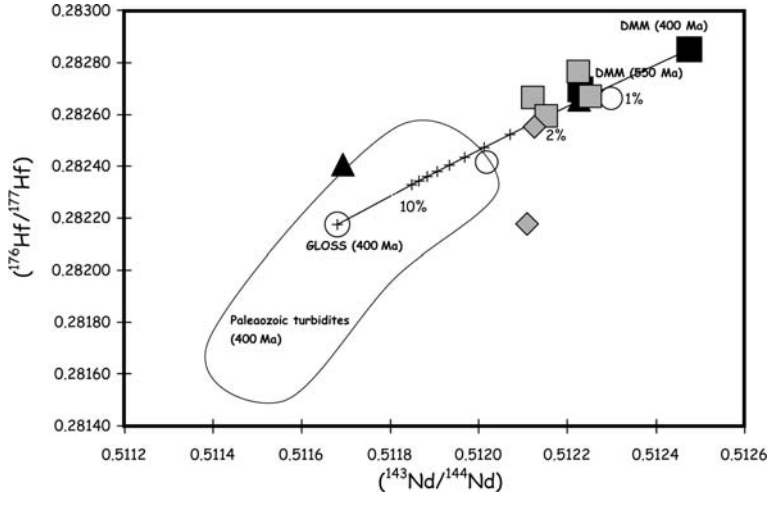

Fig. 8. $^{176}Hf/^{177}Hf$ v. $^{143}Nd/^{144}Nd$ co-variation diagram of Rinibar and Streap samples corrected for the age of 550 Ma and 400 Ma, respectively. Field of Palaeozoic turbidites from Vervoort *et al.* (1999). LA-ICP-MS data of the clinopyroxenes used for the age corrections, as reported in Table 8. Symbols as in Figure 7.

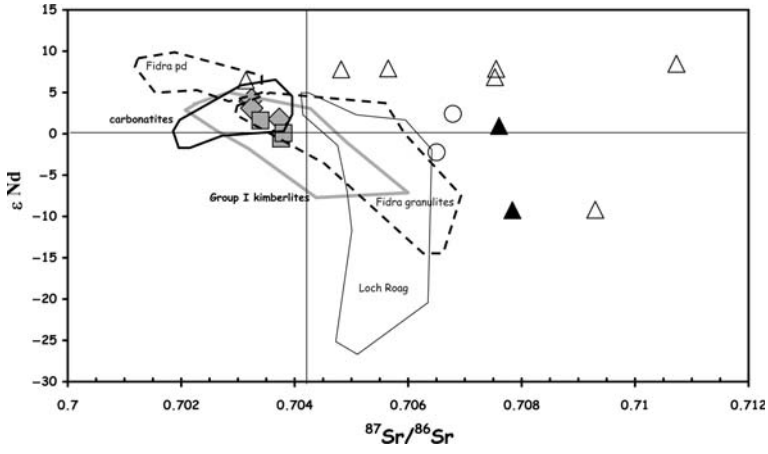

Fig. 9. εNd v. $^{87}Sr/^{86}Sr$ for Rinibar and Streap samples corrected for the ages of the xenolith-bearing dykes. εNd values were calculated using $^{143}Nd/^{144}Nd$ and $^{147}Sm/^{144}Nd$ ratios for a chondritic uniform reservoir $(CHUR)_0$ of 0.512638 and 0.1967, respectively (Blichert-Toft & Albarède 1997). LA-ICP-MS data of the clinopyroxenes used for the age corrections, as reported in Table 8. Streap separate clinopyroxenes (open triangles) are also reported for comparison (Menzies & Halliday 1988). Fields of Fidra peridotite and granulite xenoliths are from Downes *et al.* (2001); Loch Roag xenoliths from Menzies *et al.* (1987) and Menzies & Halliday (1988); Proterozoic carbonatites from Agashev *et al.* (2001), Eglington & Amstrong (2004) and Downes *et al.* (2005). Group I kimberlite field from Le Roex *et al.* (2003), Davies *et al.* (2006) and Tappe *et al.* (2006). Symbols as in Figure 7.

Scottish terranes. A subduction event has been already invoked by Menzies & Halliday (1988) to account for these anomalous isotopic features. Additionally, Thirlwall (1982) argued for a NW-dipping subduction zone on the basis of the northwesterly increase of Sr, Ba, K, P and REE in the Siluro-Devonian volcanic rocks. In this context, Streap could represent shallow, less contaminated, sub-arc lithospheric mantle. However, extreme lateral heterogeneity of the Scottish lithospheric mantle has been already noted, and the data should be handled with caution (e.g. Menzies & Halliday 1988; Upton *et al.* 1999; Downes *et al.* 2001).

A very dilute hydrous fluid as metasomatic agent must be discounted because of the high U–Th contents coupled with their unfractionated ratios and elevated Th/Nd in some of the Streap samples (Wood *et al.* 1999; Foley *et al.* 2001). Uranium is enriched by the action of H_2O-rich fluids, derived from the dehydration of minerals in the subducted slab at high water/rock ratios (Bailey & Ragnarsdottir 1994) but, on the basis of dehydration and melting experiments with marine sediments, Th is mobilized by melts rather than fluids (Johnson & Plank 1999). Conversely, positive Eu anomalies, with respect to Sm and Gd, have been recorded in deep-sea hydrothermal fluids as a result of exchange mechanisms between fluids and plagioclase during prolonged rock–fluid interaction (Douville *et al.* 1999). It therefore appears that dehydration or melting of variable portions of altered oceanic crust could be involved in the subduction process. Menzies & Halliday (1988) reported analyses of separated clinopyroxenes from Streap with very high $^{87}Sr/^{86}Sr$ (0.70755–0.71073), at almost constant $^{143}Nd/^{144}Nd$ (0.512712–0.512680). This too could reflect involvement of dehydration or melting of altered oceanic crust. It is, however, highly unlikely that altered oceanic crust alone could account for these high radiogenic Sr values, and sediment subduction has also to be considered. The most recent subduction event that occurred in the geological history of Scotland is reported at about 400 Ma, thus we correct the Streap Sr–Nd isotopic data for this age. In Figure 7b Streap samples fall between the average DMM (400 Ma) (Workman & Hart 2005) and subducted sediments (400 Ma), and, notably, they overlap with the field of Palaeozoic turbidites (Global Subducted Sediments, Plank & Langmuir 1998; Palaeozoic turbidites, Vervoort *et al.* 1999; Fig. 8). Simple bulk mixing between average DMM and average subducted sediments suggests up to 10% of the Sr and Nd coming from subducted sediments (Fig. 7b). This is consistent with some Streap cpx having elevated Th/LREE. It was recently argued that subduction-zone lavas and hence the slab components (=metasomatic agents) in the melting region of the mantle wedge inherit elevated Th/LREE from subducted sediments (Plank 2005). The high aluminium, together with the positive Eu

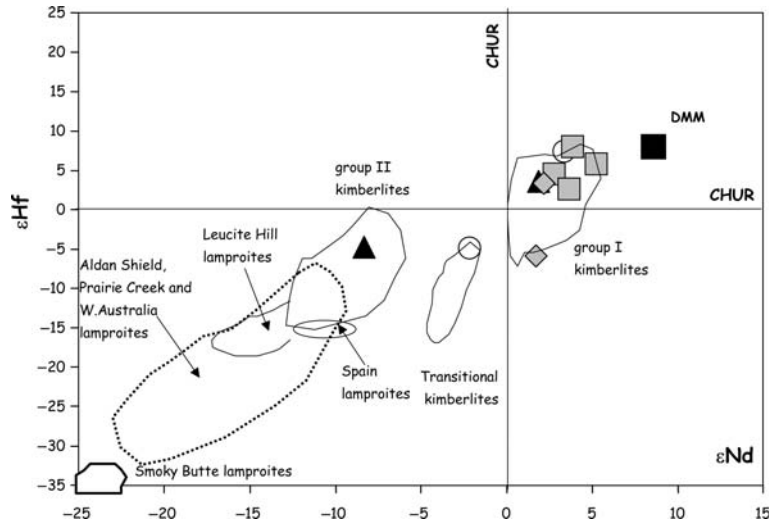

Fig. 10. εHf v. εNd at the time of Rinibar and Streap xenolith emplacements. εNd values were calculated using $^{143}Nd/^{144}Nd$ and $^{147}Sm/^{144}Nd$ ratios for a chondritic uniform reservoir $(CHUR)_0$ of 0.512638 and 0.1967, respectively (Blichert-Toft & Albarède 1997). εHf were calculated using $^{176}Hf/^{177}Hf$ and $^{176}Lu/^{177}Hf$ ratios for a chondritic uniform reservoir $(CHUR)_0$ of 0.282772 and 0.032, respectively (Blichert-Toft & Albarède 1997). LA-ICP-MS data of the clinopyroxenes used for the age corrections, as reported in Table 8. Also shown for comparison are the fields of Group I, II, Transitional kimberlites and lamproites from Davies *et al.* (2006). Symbols in Figure 7.

anomaly, of these clinopyroxenes also suggests that plagioclase played a significant role in the genesis of the metasomatic melts. Considering that the clinopyroxene does not preferentially retain Eu with respect to Gd and Sm, the positive Eu anomalies should be a signature of the metasomatic melt; consequently, plagioclase (as the phase that preferentially accommodates Eu with respect to neighbouring REE), should be present in the source of such melt, and should be completely exhausted during partial melting. As the barometric evaluation for Streap (and Rinibar) xenoliths conflicts with the presence of plagioclase in the peridotite source, the Eu positive anomaly of the metasomatic agent could have been produced by partial melting of oceanic crust and subducted sediments. Further evidence for the involvement of sediment in the geochemistry of the Streap samples can be deduced from the Nd–Hf isotopic systematics (Figs 8 and 10). The majority of the Scottish xenoliths lie between CHUR and the DM field but two Streap samples plot in the fourth quadrant of this diagram. Significantly, these two samples plot in the field of Palaeozoic turbidites, indicating that up to 10% of sediments may have been involved in the subduction process (Fig. 8). Negative to extremely negative εHf, accompanying by similarly negative εNd, is also a characteristic signature of the majority of the lamproites worldwide (Davis *et al.* 2006 and references therein), indicating that these magmas were derived from mantle sources affected by a long-term LREE enrichment and low Lu/Hf ratio. Accordingly, Davies *et al.* (2006) demonstrated that lamproite sources contain a significant subduction-related component (oceanic crust plus sediments) that was stored for a long time (>1 Ga) in the subcontinental lithospheric mantle (Fig. 10).

The extreme elemental and isotopic variability of the Streap clinopyroxenes is explicable in terms of a hydrous melt derived from altered oceanic crust plus an important contribution from sediments that interacted with a heterogeneous mantle column. In this model, several factors may be responsible for mobilizing elements and forming fluid or melts, including (1) variation in the proportion of melt and fluid produced from the slab (oceanic crust ± sediments) fluxing the mantle wedge and controlling U–Th variability, Zr, Hf and Eu enrichments; (2) the proportion of spinel and garnet in the mantle wedge (yielding different HREE profiles and variable Zr and Hf enrichments); (3) the degree of melt–peridotite interaction.

Conclusion

Geochemical and isotopic features of clinopyroxenes from two localities in Northern Scotland highlight several chemically heterogeneous mantle

domains. Clinopyroxenes from Rinibar identified two metasomatic styles, one carbonatitic and one silicate (kimberlite-like). Based on the similarity of trace element patterns of the calculated metasomatic melts it is proposed that they derived from the same source with variable degrees of partial melting. This is also supported by the similarity of Sr and Nd isotopic ratios at 550 $\pm$ 50 Ma. This age is crucial for Scotland and for global tectonics. It corresponds to the opening of the Iapetus Ocean following the break-up of the Rodinia supercontinent. At about the same time (550 Ma) the Canadian and Finnish Shields were also affected by kimberlitic and carbonatitic magmatism. Late Proterozoic–Early Phanerozoic carbonatite magmatism is also recognized within Scotland (Loch Borralan, Northern Highland Terrane; Young *et al.* 1994). Moreover, the megacrysts in the Carbo-Permian basanites and melanephelinites appear to represent a coherent suite across Scotland from the Hebridean Terrane (Loch Roag) to the Southern Uplands (Burn-Between-the-Laws). Their genesis, involving high LREE and Nb, arguably involved carbonatitic melt fractions (Long *et al.* 1994; Upton *et al.* 1999). The emplacement of very small fraction partial melts (and related metasomatism) in relation to the rifting and drifting of the Iapetus Ocean could be compared with the opening of the Atlantic Ocean, where Early to Late Cretaceous kimberlite and alkaline–carbonatite complexes are found on both side of the ocean in Brazil and Angola.

At 500 Ma the tectonic regime changed from divergent to convergent as Iapetus began to close and Baltica started to approach Laurentia. It may have been during this convergent stage (*c*. 400 Ma) that the metasomatism affecting the sub-Streap lithospheric mantle occurred. Clinopyroxenes from this locality show trace element and isotopic features that can be explained by metasomatic fluids from a subducted slab. A substantial amount of sediments (*c*. 10%) is also necessary to explain the isotopic features of these samples. The various terranes that now constitute Scotland came into conjunction at the end of the Caledonian Orogeny, and were certainly contiguous by 416 Ma. The Rinibar clinopyroxenes record no subduction-related imprinting. This could imply that either the north easternmost portion of the Highland Terrane lithospheric mantle was unaffected by the subduction or, alternatively, the subduction-related metasomatism recorded in the Streap mantle may be older, and occurred when the two lithospheric blocks were far apart.

We thank H. Downes for stimulating discussion regarding the Scottish mantle xenoliths. Interesting comments in the reviews of M. Menzies and G. Delpech helped to improve the manuscript. A UK Royal Society–Leverhulme Trust Senior Research Fellowship to M.F.T allowed S.D. to spend more than a year at RHUL. S. D's work at the University of Copenhagen was funded by the German Research Foundation, DFG (DU 426/1-1,2) and further supported by the Danmarks Grundforskningsfond.

References

AGASHEV, A. M., POKHILENKO, N. P., MCDONALD, J. A., TAKAZAWA, E., VAVILOV, M. A., SOBOLOEV, N. V. & VATANABE, T. 2001. A unique kimberlite–carbonatite primary association on the Snap Lake dyke system, Slave craton: evidence from geochemical and isotopic studies. *Abstracts Volume 'The Slave–Kaapvaal Workshop, Merreckville'*.

ANCZKIEWICZ, R., PLATT, J. P., THIRLWALL, M. F. & WAKABAYASHI, J. 2004. Franciscan subduction off to a slow start: Evidence from high precision Lu–Hf garnet ages on high grade blocks. *Earth and Planetary Science Letters*, **225**, 147–161.

ARAI, S., TAKADA, S., MICHIBAYASHI, K. & KIDA, M. 2004. Petrology of peridotite xenoliths from Iraya volcano, Philippines, and its implication for dynamic mantle-wedge processes. *Journal of Petrology*, **45**, 369–389.

ASIMOW, P. D., HIRSCHMANN, M. M. & STOLPER, E. M. 2001. Calculation of peridotite partial melting from thermodynamic models of minerals and melts, IV. Adiabatic decompression and the composition and mean properties of mid-ocean ridge basalts. *Journal of Petrology*, **42**, 963–998.

BAILEY, E. H. & RAGNARSDOTTIR, K. V. 1994. Uranium and thorium solubilities in subduction zone fluids. *Earth and Planetary Science Letters*, **124**, 119–129.

BARNES, S. J. & ROEDER, P. L. 2001. The range of spinel compositions in terrestrial mafic and ultramafic rocks. *Journal of Petrology*, **42**, 2279–2302.

BAXTER, A. N. & MITCHELL, J. G. 1984. Camptonite–monchiquite dyke swarms of northern Scotland; age relationships and their implications. *Scottish Journal of Geology*, **20**, 297–308.

BECCALUVA, L., BONADIMAN, C., COLTORTI, M., SALVINI, L. & SIENA, F. 2001. Depletion events, nature of metasomatizing agent and timing of enrichment processes in lithospheric mantle xenoliths from the Veneto Volcanic Province. *Journal of Petrology*, **42**, 173–188.

BLICHERT-TOFT, J. & ALBARÈDE, F. 1997. The Lu–Hf isotope geochemistry of chondrites and evolution of the mantle–crust system. *Earth and Planetary Science Letters*, **148**, 243–258.

BONADIMAN, C., COLTORTI, M., GRIFFIN, W. L. & O'REILLY, S. Y. 2004. Composition of clinopyroxenes from mantle xenoliths as indicators of lithospheric evolution. *In*: *Abstracts, 32nd International Geological Congress, August 2004, Florence, Italy.*

BONADIMAN, C., BECCALUVA, L., COLTORTI, M. & SIENA, F. 2005. Kimberlite-like metasomatism and 'garnet signature' in spinel-peridotite xenoliths from Sal, Cape Verde Archipelago: relics of a subcontinental mantle domain within the Atlantic oceanic lithosphere? *Journal of Petrology*, **46**, 2465–2493.

BREY, G. P. & KÖHLER, T. 1990. Geothermobarometry in four-phase lherzolites II. New thermobarometers, and practical assessment of existing thermobarometers. *Journal of Petrology*, **31**, 1353–1378

COLTORTI, M., BONADIMAN, C., HINTON, R. W., SIENA, F. & UPTON, B. G. J. 1999. Carbonatite metasomatsim of the oceanic upper mantle: evidence from clinopyroxenes and glasses in ultramafic xenoliths of Grande Comore, Indian Ocean. *Journal of Petrology*, **40**, 133–165.

DALTON, J. A. & PRESNALL, D. C. 1998. The continuum of primary carbonatitic–kimberlitic melt compositions in equilibrium with lherzolite: data from the system $CaO–MgO–Al_2O_3–SiO_2–CO_2$ at 6 GPa. *Journal of Petrology*, **39**, 1953–1964.

DAVIES, G. R., STOLZ, A. J., MAHOTKIN, I. L., NOWELL, G. M. & PEARSON, D. G. 2006. Trace element and Sr–Pb–Nd–Hf isotope evidence for ancient, fluid-dominated enrichment of the source of Aldan Shield lamproites. *Journal of Petrology*, **47**, 1119–1146.

DAWSON, J. B. 1980. *Kimberlites and their Xenoliths*. Springer, Berlin.

DE BRESSER, J. H. P., PEACH, C. J., REIJS, J. P. J. & SPIERS, C. J. 1998. On dynamic recrystallization during solid-state flow: effects of stress and temperature. *Geophysical Research Letters*, **25**, 3457–3460.

DE BRESSER, J. H. P., TER HEEGE, J. & SPIERS, C. J. 2001. Grain size reduction by dynamic recrystallization: can it result in major rheological weakening? *International Journal of Earth Sciences*, **90**, 28–45.

DOUVILLE, E., BIENVENU, P., CHARLOU, J. L., DONVAL, J. P., FOUQUET, Y., APPRIOU, P. & GAMO, T. 1999. Yttrium and rare earth elements in fluids from various deep-sea hydrothermal systems. *Geochimica et Cosmochimica Acta*, **63**, 627–643.

DOWNES, H., UPTON, B. G. J., HANDRYDE, E. A. J. W. & THIRLWALL, M. F. 2001. Geochemistry of mafic and ultramafic xenoliths from Fidra (Southern Uplands, Scotland): implications for lithospheric processes in Permo-Carboniferous times. *Lithos*, **58**, 105–124.

DOWNES, H., BALAGANSKAYA, E., BEARD, A., LIFEROVICH, R. & DEMAIFFE, D. 2005. Petrogenetic processes in the ultramafic, alkaline and carbonatitic magmatism in the Kola Alkaline Province: A review. *Lithos*, **85**, 48–75.

DOYLE, P. M., BELL, D. R. & LE ROEX, A. P. 2004. Fine-grained pyroxenites from the Gansfontein kimberlite, South Africa: Evidence for megacryst magma–mantle interaction. *South African Journal of Geology*, **107**, 285–300.

EGLINGTON, B. M. & AMSTRONG, R. A. 2004. The Kaapvaal Craton and adjacent orogens, southern Africa: a geochronological database and overview of the geological development of the craton. *South African Journal of Geology*, **107**, 13–32.

FOLEY, S. F., PETIBON, C. M., JENNER, G. A & KJARSGAARD, B. A. 2001. High U/Th partitioning by clinopyroxene from alkali silicate and carbonatite metasomatism: an origin for Th/U disequilibrium in mantle melts? *Terra Nova*, **13**, 104–109.

FRANCIS, D. 2003. Cratonic mantle roots, remnants of a more chondritic Archean mantle? *Lithos*, **71**, 135–152.

GASPARIK, T. 2003. *Phase Diagrams for Geoscientists: An Atlas of the Earth's Interior*. Springer, Berlin.

GORRING, M. T. & KAY, S. M. 2000. Carbonatite metasomatized peridotite xenoliths from southern Patagonia: implications for lithospheric processes and Neogene plateau magmatism. *Contributions to Mineralogy and Petrology*, **140**, 55–72.

GREEN, T. H., BLUNDY, J. D., ADAM, J. & YAXLEY, G. M. 2000. SIMS determination of trace element partition coefficients between garnet, clinopyroxene and hydrous basaltic liquids at 2–7.5 GPa and 1080–1200 °C. *Lithos*, **53**, 165–187.

GRÉGOIRE, M., BELL, D. R. & LE ROEX, A. P. 2002. Trace element geochemistry of glimmerite and MARID mantle xenoliths: their relationship to kimberlite and to phlogopite-bearing peridotite revisited. *Contributions to Mineralogy and Petrology* **142**, 603–625.

GRÉGOIRE, M., BELL, D. R. & LE ROEX, A. P. 2003. Garnet lherzolites from the Kaapvaal Craton (South Africa): trace element evidence for a metasomatic history. *Journal of Petrology*, **43**, 629–657.

GRIFFIN, W. L., DOYLE, B. J., RYAN, C. G. *ET AL*. 1999. Layered mantle lithosphere in the Lac de Gras area, Slave Craton: composition, structure and origin. *Journal of Petrology*, **40**, 705–727.

GRIFFIN, W. L., O'REILLY, S. Y., ABE, N. *ET AL*. 2003. The origin and evolution of Archean lithospheric mantle. *Precambrian Research*, **127**, 19–41.

HALLIDAY, A. N., DICKIN, A. P., HUNTER, R. N., DAVIES, G. R., DEMPSTER, T. J., HAMILTON, P. J. & UPTON, B. G. J. 1993. Formation and composition of the lower continental crust: evidence from Scottish xenolith suites. *Journal of Geophysical Research*, **98**, 581–607.

HELLEBRAND, E., SNOW, J. E. & HOFMANN, A. W. 2001. Coupled major and trace elements as indicators of the extent of melting in mid-ocean-ridge peridotites. *Nature*, **410**, 677–681.

HELLEBRAND, E., SNOW, J. E., MOSTEFAOUI, S. & HOPPE, P. 2005. Trace element distribution between orthopyroxene and clinopyroxene in peridotites from the Gakkel Ridge: a SIMS and NanoSIMS study. *Contributions to Mineralogy and Petrology*, **150**, 486–504.

HUNTER, R. H. & UPTON, B. G. J. 1987. The British Isles — a Palaeozoic mantle sample. *In*: NIXON, P. H. (ed.) *Mantle Xenoliths.* John Wiley, Chichester, 107–118.

IONOV, D. A. & HARMER, R. E. 2002. Trace element distribution in calcite–dolomite carbonatites from Spitskop: inferences for differentiation of carbonatite magmas and the origin of carbonates in mantle xenoliths. *Earth and Planetary Science Letters*, **198**, 495–510.

IONOV, D. A., BODINIER, J.-L., MUKASA, S. B. & ZANETTI, A. 2002. Mechanisms and sources of mantle metasomatism: major and trace element Compositions of peridotite xenoliths from Spitsbergen in the context of numerical modelling. *Journal of Petrology*, **43**, 2219–2259.

JOHNSON, M. C. & PLANK, T. 1999. Dehydration and melting experiments constrain the fate of subducted sediments. *Geochemistry, Geophysics, Geosystems*, **1** Paper Number 1999GC000014.

KARATO, S., TORIUMI, M. & FUJII, T. 1980. Dynamic recrystallization of olivine single crystals during high-temperature creep. *Geophysical Research Letters*, **7**, 649–652.

KARMALKAR, N. R. & REGE, S. 2002. Cryptic metasomatism in the upper mantle beneath Kutch: Evidence from spinel lherzolite xenoliths. *Current Sciences*, **82**, 1157–1165.

KELEMEN, P. B., HART, S. R. & BERNSTEIN, S. 1998. Silica enrichment in the continental upper mantle via melt/rock reaction. *Earth and Planetary Science Letters*, **164**, 387–406.

KESHAV, S., CORGNE, A., GUDFINNSSON, G. H., BIZIMIS, M., MCDONOUGH, W. F. & FEI, Y. 2005. Kimberlite petrogenesis: Insights from clinopyroxene–melt partitioning experiments at 6 GPa in the $CaO–MgO–Al_2O_3–SiO_2–CO_2$ system. *Geochimica et Cosmochimica Acta*, **69**. 2829–2845.

KING, S. D. 2005. Archean cratons and mantle dynamics. *Earth and Planetary Science Letters*, **234**, 1–14.

KIRSTEIN, L. A., DAVIS, G. R. & HEEREMANS, M. 2006. The petrogenesis of Carboniferous–Permian dyke and sill intrusions across northern Europe. *Contributions to Mineralogy and Petrology*, **152**, 721–742.

KLEMME, S., LAAN, S., FOLEY, S. F. & GUNTHER, D. 1995. Experimentally determined trace and minor element partitioning between clinopyroxene and carbonatite melt under upper mantle conditions. *Earth and Planetary Science Letters*, **133**, 439–448.

KÖHLER, T. & BREY, G. P. 1990. Calcium exchange between olivine and clinopyroxene calibrated as geothermobarometer for natural peridotites from 2 to 60 kb with applications. *Geochimica et Cosmochimica Acta*, **54**. 2375–2388.

KOPYLOVA, M. G. & CARO, G. 2004. Mantle xenoliths from the Southeastern Slave Craton: evidence for chemical zonation in a thick, cold lithosphere. *Journal of Petrology*, **45**, 1045–1067.

KUKKONEN, I. T. & PELTONEN, P. 1999. Xenolith-controlled geotherm for the central Fennoscandian Shield: implications for lithosphere–asthenosphere relations. *Tectonophysics*, **304**, 301–315.

KUKKONEN, I. T., KINNUNEN, K. A. & PELTONEN, P. 2003. Mantle xenoliths and thick lithosphere in the Fennoscandian Shield. *Physics and Chemistry of the Earth*, **28**, 349–360.

LE ROEX, A. P, BELL, D. R. & DAVIS, P. 2003. Petrogenesis of Group I kimberlites from Kimberley, South Africa: evidence from bulk-rock geochemistry. *Journal of Petrology*, **44**, 2261–2286.

LONG, A. M., MENZIES, M. A., THIRLWALL, M. F., UPTON, B. G. J. & ASPEN, P. 1994. Carbonatite mantle interaction: a possible origin for megacryst/xenolith suites in Scotland. *In*: MEYER, H. O. A. & LEONARDOS, O. H. (eds) *Proceedings of the Fifth International Kimberlite Conference 2*. Companhia de Pesquisa de Recursos Minerais, Special Publications, 467–477.

LUNDSTROM, C. C., GILL, J. & WILLIAMS, Q. 2000. A geochemically consistent hypothesis for MORB generation. *Chemical Geology*, **162**, 105–126.

MCDONOUGH, W. F. & SUN, S. S. 1995. The composition of the Earth. *Chemical Geology*, **120**, 223–253.

MENZIES, M. & HALLIDAY, A. N. 1988. Lithospheric mantle domains beneath the Archean and Proterozoic crust of Scotland. *Journal of Petrology, Special Issue*, 275–302.

MENZIES, M. A., ROGERS, N., TINDLE, A. & HAWKESWORTH, C. J. 1987. Metasomatic and enrichment processes in lithospheric peridotites, an effect of astenosphere–lithosphere interaction. *In*: MENZIES, M. A. & HAWKESWORTH, C. J. (eds) *Mantle Metasomatism.* Academic Press, London, 313–364.

MERCIER, J.-C. C. & NICOLAS, A. 1975. Textures and fabrics of upper-mantle peridotites as illustrated by xenoliths from basalts. *Journal of Petrology*, **16**, 454–487.

MOINE, B. N., GRÉGOIRE, M., O'REILLY, S. Y., SHEPPARD, S. M. F. & COTTIN, J. Y. 2001. High field strength element fractionation in the upper mantle: evidence from amphibole-rich composite mantle xenoliths from the Kerguelen Islands (Indian Ocean). *Journal of Petrology*, **42**, 2145–2167.

NEUMANN, E. R., GRIFFIN, W. L., PEARSON, N. J. & O'REILLY, S. Y. 2004 The evolution of the upper mantle beneath the Canary Islands: information from trace elements and Sr isotope ratios in minerals in mantle xenoliths. *Journal of Petrology*, **45**, 2573–2612.

NIU, Y. 1997. Mantle melting and melt extraction processes beneath ocean ridges: evidence from the abyssal peridotites. *Journal of Petrology*, **38**, 1047–1074.

O'NEILL, H. S. T. & PALME, H. 1998. Composition of the silicate Earth: implications for accretion and core formation. *In*: JACKSON, I. (eds) *The Earth's Mantle*. Cambridge University Press, Cambridge, 3–126.

PEARSON, D. G., CANIL, D. & SHIREY, S. B. 2003. Mantle samples included in volcanic rocks: xenoliths and diamonds. *In*: CARLSON, R. W., HOLLAND, H. D. & TUREKIAN, K. K. (eds) *Treatise on Geochemistry* 2. Elsevier, Amsterdam, 171–275.

PICCARDO, G. B., ZANETTI, A. & MUNTENER, O. 2007. Melt/peridotite interaction in the Lanzo south peridotite: field, textural and geochemical evidence. *Lithos*, **94**, 191–209.

PLANK, T. 2005. Constraints from thorium/lanthanum on sediment recycling at subduction zones and the evolution of the continents. *Journal of Petrology*, **46**, 921–944.

PLANK, T. & LANGMUIR, C. H. 1998. The chemical composition of subducting sediment and its consequences for the crust and mantle. *Chemical Geology*, **145**, 325–394.

PRAEGEL, N.-O. 1981 Origin of ultramafic inclusions and megacrysts in a monchiquite dyke at Streap, Inverness-shire, Scotland. *Lithos*, **14**, 305–322.

RAMSAY, R. R. & TOMPKINS, L. A. 1994. The geology, heavy mineral concentrate mineralogy, and diamond prospectivity of the Boa Esperança and Cana Verde pipes, Corrego D'anta, Minas Gerais, Brazil. *In*: MEYER, H. O. A. & LEONARDOS, O. H. (eds) *Proceedings of the Fifth International Kimberlite Conference 2*. Companhia de Pesquisa de Recursos Minerais, Special Publications, 329–345.

SILVER, P. G., MAINPRICE, D., BEN ISMAIL, W., TOMMASI, A. & BARRUOL, G. 1999. Mantle structural geology from seismic anisotropy. *In*: FEI, Y., BERTKA, C. & MYSEN, B. O. (eds) *Mantle Petrology: Field Observations and High Pressure Experimentation. A Tribute to Francis R. (Joe) Boyd.* Geochemical Society, Special Publications, **6**, 79–103.

SPENGLER, D., VAN ROERMUND, H. L. M., DRURY, M. R., OTTOLINI, L., MASON, P. R. D. & DAVIES, G. R. 2006. Deep origin and hot melting of an Archaean orogenic peridotite massif in Norway. *Nature*, **440**, 913–917.

SPIEGELMAN, M. & KELEMEN, P. B. 2002. Extreme chemical variability as a consequence of channelized melt transport. *Geochemistry, Geophysics, Geosystems*, **4**, 1–18.

STACHEL, T., VILJOEN, K. S., BREY, G. & HARRIS, J. W. 1998. Metasomatic processes in lherzolitic and harzburgitic domains of diamondiferous lithospheric mantle: REE in garnets from xenoliths and inclusions in diamonds. *Earth and Planetary Science Letters*, **159**, 1–12.

STRECKEISEN, A. L 1976. To each plutonic rock its proper name. Earth-Science Reviews, **12**, 1–33.

SUHR, G., SECK, H. A., SHIMIZU, N., GUNTHER, D. & JENNER, G. 1998. Circulation of refractory melts in the lowermost oceanic crust: evidence from a trace element study of dunite-hosted clinopyroxenes in the Bay of Islands Ophiolite. *Contributions to Mineralogy and Petrology*, **131**, 136–154.

TAKAHASHI, E. 1987. Origin of basaltic magmas—implications from peridotite melting experiments and an olivine fractionation model. *Bulletin of the Volcanological Society of Japan*, **30**, 17–40.

TAPPE, S., FOLEY, S. F., JENNER, G. A. *ET AL.* 2006. Genesis of ultramafic lamprophyres and carbonatites at Aillik Bay, Labrador: a consequence of incipient lithospheric thinning beneath the North Atlantic craton. *Journal of Petrology*, **47,** 1261–1315.

THIRLWALL, M. F. 1982. A triple-filament method for rapid and precise analysis of rare-earth elements by isotope dilution. *Chemical Geology*, **35**, 155–166.

THIRLWALL, M. F. 1988. Geochronology of Late Caledonian magmatism in northern Britain. *Journal of the Geological Society, London*, **145**, 951–957.

THIRLWALL, M. F. 1991*a*. High-precision multicollector isotopic analysis of low levels of Nd as oxide. *Chemical Geology (Isotope Geo-sciences Section)*, **94**, 13–22.

THIRLWALL, M. F. 1991*b*. Long-term reproducibility of multicollector Sr and Nd isotope ratio analysis. *Chemical Geology (Isotope Geo-sciences Section)*, **94**, 85–104.

THIRLWALL, M. F. & ANCZKIEWICZ, R. 2004. Multidynamic isotope ratio analysis using MC-ICP-MS and the causes of secular drift in Hf, Nd and Pb isotope ratios. *International Journal of Mass Spectrometry*, **235**, 59–81.

TIEPOLO, M., BOTTAZZI, P., PALENZONA, M. & VANNUCCI, R. 2003. A laser probe coupled with ICP-double-focusing sector-field mass spectrometer for *in situ* analysis of geological samples and U–PB dating of zircon. *Canadian Mineralogist*, **41**, 259–272.

UPTON, B. G. J. 2004. *Volcanoes and the Making of Scotland*. Dunedin Academic Press, Edinburgh.

UPTON, B. G. J., ASPEN, P. & CHAPMAN, N. A. 1983. The upper mantle and deep crust beneath the British Isles: evidence from inclusion suites in volcanic rocks. *Journal of the Geological Society, London*, **140**, 105–122.

UPTON, B. G. J., ASPEN, P., REX, D. C., MELCHER, F. & KINNY, P. 1998. Lower crustal and possible shallow mantle samples from beneath the Hebrides: evidence from a xenolithic dyke at Gribun, western Mull. *Journal of the Geological Society, London*, **155**, 813–828.

UPTON, B. G. J., HINTON, R. W., ASPEN, P., FINCH, A. & VALLEY, J. W. 1999. Megacrysts and associated xenoliths: evidence for migration of geochemically enriched melts in the upper mantle beneath Scotland. *Journal of Petrology*, **40**, 935–956.

UPTON, B. G. J., ASPEN, P. & HINTON, R. W. 2001. Pyroxenite and granulite xenoliths from beneath the Scottish Northern Highlands Terrane: evidence for lower-crust/upper-mantle relationships. *Contributions to Mineralogy and Petrology*, **142**, 178–197.

UPTON, B. G. J., ASPEN, P. & HINTON, R. W. 2003. Garnet pyroxenite xenoliths and pyropic megacrysts in Scottish alkali basalts. *Scottish Journal of Geology*, **39**, 169–184.

UPTON, B. G. J., STEPHENSON, D., SMEDLEY, P. M., WALLIS, S. M. & FITTON, J. G. 2004. Carboniferous and Permian magmatism in Scotland. *In*: NEUMANN, E.-R., DAVIES, G. R., TIMMERMAN, M. J., HEEREMANS, M & LARSEN, B. T. (eds) *Permo-Magmatism and Rifting in Europe*. Geological Society, London, Special Publications, **223**, 195–218.

VAN ACHTERBERG, E., RYAN, C. G., JACKSON, S. E. & GRIFFIN, W. L. 2001. Data reduction software for LA-ICPMS. *In*: SYLVESTER, P. (ed.) *Laser Ablation ICPMS in the Earth Sciences.* Mineralogical Association of Canada, **29,** 239–243.

VERNIÈRES, J., GODARD, M. & BODINIER, J. L. 1997. A plate model for the simulation of trace element fractionation during partial melting and magma transport in the Earth's upper mantle. *Journal of Geophysical Research, B, Solid Earth and Planets*, **102**, 24771–24784.

VERVOORT, J. D., PATCHETT, P. J., BLICHERT-TOFT, J. & ALBARÈDE, F. 1999. Relationships between Lu–Hf and Sm–Nd isotopic systems in the global sedimentary system. *Earth and Planetary Science Letters*, **168**, 79–99.

WALKER, G. P. L. & ROSS, J. V. 1954. A xenolithic monchiquite dyke near Glenfinnan, Inverness-shire. *Geological Magazine*, **91**, 463–472.

WATSON, J. 1985. Northern Scotland as an Atlantic–North Sea divide. *Journal of the Geological Society, London*, **142**, 221–243.

WOOD, B. J., BLUNDY, J. D. & ROBINSON, J. A. C. 1999. The role of clinopyroxene in generating U-series disequilibrium during mantle melting—implications for uranium series disequilibria in basalts. *Geochimica et Cosmochimica Acta*, **63**, 1613–1620.

WORKMAN, R. K. & HART, S. R. 2005. Major and trace element composition of the depleted MORB mantle (DMM). *Earth and Planetary Science Letters*, **231**, 53–72.

YOUNG, B. N., PARSONS, I. & THREADGOULD, R. 1994. Carbonatite near the Loach Borralan intrusion, Assynt. *Journal of the Geological Society, London*, **151**, 945–954.

Reconstruction of mantle sections beneath Yakutian kimberlite pipes using monomineral thermobarometry

I. V. ASHCHEPKOV[1], N. P. POKHILENKO[1], N. V. VLADYKIN[2], A. Y. ROTMAN[3], V. P. AFANASIEV[1], A. M. LOGVINOVA[1], S. I. KOSTROVITSKY[2], L. N. POKHILENKO[1], M. A. KARPENKO[4], S. S. KULIGIN[1], E. V. MALYGINA[1], Y. B. STEGNITSKY[3], N. A. ALYMOVA[2] & O. S. KHMELNIKOVA[1]

[1]*Institute of Geology and Mineralogy SD RAS, Koptyug ave 3, Novosibirsk, Russia (e-mail: Igor.Ashchepkov@uiggm.nsc.ru)*

[2]*Institute of Geochemistry SD RAS, Favorsky Str. 1a, Irkutsk, 664033, Russia*

[3]*Central Science and Research Geology and Prospecting Institute of the Stock Company 'ALROSA', Chernyshevsky Str, 7, Mirny, 678170 Russia*

[4]*Aykhal Mining Enterprise of Stock Company 'ALROSA', Almazny Str., 3-26, Aykhal, 678170 Russia*

Abstract: Four original monomineral methods for mantle peridotite associations are used to reconstruct $P-T$ conditions beneath the kimberlite pipes of Yakutia. The clinopyroxene Jd–Di method gives the closest coincidence with Opx barometry in accord with all physico-chemical boundaries. Garnet thermometers calibrated using Opx, Gar–Cpx and Ni-garnet thermometers and two variants of barometers were developed separately for pyroxenites and peridotites. A Cr–Sp thermobarometer uses the monomineralic version of the Ol–Sp thermometer and a newly calibrated Cr–Sp barometer. A picroilmenite method uses the Ol–Sp thermometer and a pressure-calibration of the geikielite component. Each mantle column is divided into two (upper and lower) sections by a pyroxenite layer located near 40 kbar. Below the pyroxenite layer, the lower section comprises 3–4 lithologically distinct horizons, with a thermally perturbed layer at the base. Above the pyroxenite layer are 3–5 lithologically distinct horizons, which are more fertile than the lower sections. Splitting of the geotherms characterizes most $P-T$ diagrams and is ascribed to multistage melt percolation processes typical for the mantle beneath kimberlite pipes. The largest pipes are diamond-bearing and have a highly depleted peridotite lens above the asthenospheric layer.

Monomineral thermobarometry (McGregor 1974; Finnerty & Boyd 1987; Ryan *et al.* 1996; Nimis & Taylor 2000; Ashchepkov 2002, 2003, 2006*a*, *b*; Ashchepkov *et al.* 2005*a*, *b*; Ashchepkov & Vishnyakova 2006) of kimberlite megacrysts and xenocrysts permits the reconstruction of mantle lithological and chemical structure and thermal state. $P-T$ diagrams and lithological columns may be produced (Griffin *et al.* 1999*a*, *b*; Ashchepkov *et al.* 2003*a*) for pipes where polymineral mantle xenoliths are not well preserved. Even heavy-mineral concentrate from diamond and other placers containing only garnets, ilmenites and chromites now yields geotherm positions (Ashchepkov *et al.* 2005*b*, *c*) and the detailed structure and rock sequences in the lithospheric mantle. The new version of garnet thermobarometry (Ashchepkov 2006) correlates well with traditional methods of $P-T$ estimations, based on polymineral associations (e.g. Nickel & Green 1985; Krogh 1988; Brey & Kohler 1990). They reproduce closely the pressures obtained with Al–Opx (McGregor 1974) and Gar–Opx barometers (Nickel & Green 1985; Brey & Kohler 1990).

In developing new methods our goal was to construct a series of self-consistent methods. For this purpose we used a database containing electron microprobe analysis (EPMA) results from more than 2300 associations of polymineralic xenoliths from the published literature and more than 16 000 original analyses of xenocrysts and xenolith minerals from Siberian kimberlites.

The reconstruction of the structure of the lithospheric mantle permits us to decipher the processes of continental lithosphere genesis and the influence of subduction and plumes on the lower horizons of the lithosphere (Sobolev 1977; Dobretsov & Kirdyashkin 1994; Griffin *et al.* 1999*a*, *b*). The majority of diamond was captured by kimberlites from the lower part of the lithospheric mantle (Kharkiv *et al.* 1968;

From: COLTORTI, M. & GRÉGOIRE, M. (eds) *Metasomatism in Oceanic and Continental Lithospheric Mantle.* Geological Society, London, Special Publications, **293**, 335–352.
DOI: 10.1144/SP293.15 0305-8719/08/$15.00

Sobolev 1977; Boyd & Finnerty 1980; Dawson 1980; Sobolev *et al.* 1984, 1997; Pokhilenko *et al.* 1991; Jacob *et al.* 1994; Logvinova *et al.* 2001).

Study of the mantle xenoliths and xenocrysts allows the determination of mantle structure (Nixon & Boyd 1973; Sobolev 1977) and the mapping of mantle lithosphere (Griffin *et al.* 1999*a*, *b*). Because of the high degree of xenolith alteration in many pipes, the determination of mantle structure by this method has been restricted to Udachnaya (Boyd *et al.* 1997), Obnazhennaya (Taylor *et al.* 2003) and Mir (Beard *et al.* 1996; Snyder *et al.* 1997; Roden *et al.* 1999). Thermobarometric estimates using garnet (Ryan *et al.* 1996; Griffin *et al.* 1999*a*, *b*) permit the construction of a lithological profile of the lithospheric mantle and have been used also to determine the evolution of the mantle in the northern part of the Siberian Platform (Pokhilenko *et al.* 1999). This variant of garnet thermobarometry gives pressure estimates that sometimes are very different from those determined with the polymineralic methods. The use of garnets alone does not permit complete imaging of mantle sequences.

New methods

The new methods we used are calibrated or compared with the baseline provided by the orthopyroxene method, which includes the Opx thermometer of Brey & Köhler (1990) combined with Al–Opx barometer of McGregor (1974). The new methods compare favourably with the results from other published xenolith thermobarometers (e.g. Bertrand & Mercier 1985; Nickel & Green 1985; Brey & Köhler 1990).

Clinopyroxene

The methods described in the previous papers (Ashchepkov 2002, 2003) use the correlation of the Jd content in clinopyroxene with the pressure estimated with the Al–Opx barometer (McGregor 1974)

$$P_0 = 0.19 \times Kd^{3/4} \times T\,(^\circ\mathrm{C})/(1 + \mathrm{Fe}) - 35\ln(1273/T\,(^\circ\mathrm{C})) \times (\mathrm{Al} + \mathrm{Ti} + 2.5\mathrm{Na} + 1.5\mathrm{Fe}^{3+})$$

where $Kd = (\mathrm{Na/Ca}) \times [\mathrm{Mg}/(\mathrm{Al}^{\mathrm{VI}} + \mathrm{Cr} + \mathrm{Ti} - \mathrm{Fe}^{3+})]$ (formula units) and a second approximation

$$P = 0.00006P_0^3 - 0.0156P_0^2 + 1.6757P_0 \ (R^2 = 0.8245).$$

The temperatures are calculated using the monomineralic clinopyroxene thermometer (Nimis & Taylor 2000) with an additional correction

$$T = -0.000001T_{\mathrm{NT2000}}^2 + 0.9575T_{\mathrm{NT2000}} + 107.01 + 33.85(\mathrm{Cr_2O_3} + \mathrm{TiO_2}) - 137.5 - 25.8(\mathrm{FeO} - 4.2) - 11.2\mathrm{Na_2O} + \mathrm{TiO_2}.$$

Garnet

We use separate schemes for common peridotites and for pyroxenite and peridotites impregnated by melts from the garnet thermobarometer (Ashchepkov 2006).

(1) The thermometer for peridotites uses the correlations of *KD* with estimates based on the Opx method of (Brey & Köhler 1990):

$$T(^\circ\mathrm{C}) = 5272.5[\ln(KD)/P]^3 + 10265[(\ln(KD)/P]^2 + 6472[\ln(KD)/P] + 2113$$

where $KD = \mathrm{MgO} \times [\mathrm{TiO_2}/(\mathrm{CaO} + \mathrm{MgO})^2] \times \mathrm{FeO} \times \mathrm{Al_2O_3}$.

The barometer is calibrated against pressures obtained with the Al–Opx method (McGregor 1974):

$$P_0 = [5.25\mathrm{Cr_2O_3}/(\mathrm{CaO} + \mathrm{MnO} + 2\mathrm{FeO})^{0.4} + 0.0T(^\circ\mathrm{C}) + 22.5\mathrm{Na_2O} + \mathrm{MgO}/20) + 0.5\mathrm{CaO} + (\mathrm{FeO}/7 - \mathrm{TiO_2} - 15)] \times 2.5$$

and the approximation

$$P = -0.0001P_0^3 + 0.0081P_0^2 + 0.8078P_0 + 0.8308.$$

(2) For pyroxenites and peridotites impregnated by melts, we use the approximation of temperatures obtained with the Gar–Cpx thermometer of Krogh (1988):

$$T(^\circ\mathrm{C}) = 1700 + 3607[\ln(KD)/P] + 3138[\ln(KD)/P^2]$$

where $KD = \mathrm{Na_2O} \times \mathrm{MnO} \times [\mathrm{TiO_2}/(\mathrm{CaO} + \mathrm{MgO})] \times \mathrm{FeO} \times \mathrm{Al_2O_3}$, with the additional correction

$$T(^\circ\mathrm{C}) = [(T - 800) \times 1.55] + 923.$$

The pressures are calculated with the following equation:

$$P(\mathrm{kbar}) = 4 + 4.975\mathrm{Cr_2O_3} + 0.0135T(^\circ\mathrm{C}).$$

Chromite

Dependence of the $Cr/(Cr + Al)$ in spinel (O'Neill 1981) on pressure in the garnet stability field determined using Al–En barometry (McGregor 1974) was calibrated using >300 associations ($R = 0.87$) (Ashchepkov & Vishnyakova 2006) $P = 0.065[Cr/(Cr + Al)] \times T(^{\circ}C)$ (formula units). For pressures greater then 32, the correction $P = P - 11$ is used.

A systematic difference from the results of the Opx method is correlated by applying second approximations for two variants:

(1) $P = -0.0053P_0^2 + 112.92P + 5.809 + 0.054[T(^{\circ}C)] \times Ti$ for the low-temperature branch (see Fig. 2);

(2) $P = -0.000006P_0^4 + 0.0011P_0^3 - 0.0623P_0^2 + 1.92P + 0.054[T(^{\circ}C)] \times Ti$ for the high-temperature branch of geothermal gradients beneath Udachnaya pipe.

The temperatures are determined using the monomineralic version of the Ol–Sp thermometer (O'Neill & Wall 1987), where the Fo content in olivine is calculated with the empirical equations $Fo = 1 - 0.0493[Fe_{chr}/Mg_{chr}] - 0.0582$ for the high-temperature branch and $Fo = 1 - 0.08 - 0.0005P$ for the low-temperature branch.

Ilmenite

Dependence of the geikielite component on pressure was used for the ilmenite barometer. The internal exchange $(TiO_2 \times MgO)$–$(Fe_2O_3 \times Fe_2O_3)$ has a large effect on the cell volume in picroilmenite. $KD = TiO_2/MgO$ is simplified to $KD = k \times TiO_2$ (*k c.* 5) by utilizing the linear correlation between TiO_2 and MgO in the compositional trend of megacrysts.

Additional correction to Cr_2O_3 is made for Cr-bearing (>1.0%) ilmenites:

$$P_0 = ((TiO_2 - 23) \times 2.15 - [T(^{\circ}C) - 700]/20MgO \times Cr_2O_3 - 1.5MnO)T(^{\circ}C)/1273$$

and further corrections $P_1 = 10[(60 - P_0)/60] + P_0$ reproduce the pressure estimates obtained with the clinopyroxene barometer (Ashchepkov 2003) for 120 ilmenite-bearing peridotites from the database of Alymova *et al.* (2005) ($R = 0.71$).

Ilmenite temperatures are calculating using the monomineralic version of the Ol–Il thermometer (Taylor *et al.* 1998) with estimation of the Fo content in olivine coexisting with the megacrysts as $Fo = 1 - 0.12 - 0.00025P$ for pressures lower than 30 kbar and $Fo = 1 - 0.11 - 0.00025P$ for greater pressures. For Cr-bearing picroilmenites ($Cr_2O_3 > 1\%$) the correlation $Fo = 1 - 0.033[Fe_{Ilm}/Mg_{Ilm}] - 0.0133 - 0.0008P - 0.00005(T_0 - 1000)$ (formula units) found in ilmenite peridotites (>150 associations) (Alymova *et al.* 2004) permits determination of the forsterite content of olivine using an iteration scheme. Data is available online at http://www.geolsoc.org.uk/SUP18300.

Application to the reconstruction of mantle columns beneath kimberlite pipes

Clinopyroxene Jd–Di thermobarometry (Ashchepkov 2002, 2003) gives very good agreement with the estimates based on the Al-enstatite barometer (McGregor 1974) for the pipes where the composition of the mantle peridotites is relatively depleted, but it also gives realistic P–T estimates and good agreement for the Mg-rich eclogites. They often produce clustering of data at 40 kbar. These pressures correspond to 4–5% Cr_2O_3 in pyropes. These values refer to inflections and deviations from the linear trend in the garnet Cr_2O_3–CaO diagram (Sobolev 1977; Kopylova *et al.* 2000; Carlson *et al.* 2004). This level in the mantle is commonly marked by relatively high-temperature associations and an abundance of pyroxene-rich associations. Most Cr-bearing pyroxenites in Udachnaya (Kuligin & Pokhilenko 1998; Pokhilenko *et al.* 2000; Ashchepkov *et al.* 2003*a*) and Mir pipes (Roden *et al.* 1999), as well as Obnazhennaya (Taylor *et al.* 2003), record P–T values close to this mantle layer.

For relatively depleted mantle columns the new garnet thermobarometer provides the only good possibility for reconstruction of mantle layering and P–T structure. Griffin and colleagues used Cr-barometry (Ryan *et al.* 1996) and Ni-thermometry (Griffin *et al.* 1989) for garnets with difference between pyroxenites and common peridotites (Griffin *et al.* 1999*a*, *b*). We show in our diagrams the most probable variants of P–T estimates for peridotites and pyroxenites separately.

The high P–T conditions near 40–42 mW m^{-2} correspond to Ti-rich associations that are probably related to intrusions of protokimberlite melt (Ehrenberg 1979). The coldest associations located near the 35 mW m^{-2} geotherm mark depleted peridotite horizons with subcalcic garnets, which should represent the dunite or harzburgite layers (Boyd *et al.* 1993). Temperature methods using Ti in garnet are restricted to $T < 1300\ ^{\circ}C$, the limit of calibration. Using the Ni approximation method (Ashchepkov 2006*a*, *b*) higher temperatures may be obtained, but the relatively low precision ($R = 0.65$) of this method often gives temperatures that are too low and located near the 35 mW m^{-2} geotherm.

The $P-T$ estimates obtained using the chromite thermobarometer (Ashchepkov & Vishnyakova 2006) yield geotherm positions and lithological layering very similar to those determined by pyroxenes. As a rule they reveal irregularly heated harzburgite and dunite horizons (Pokhilenko *et al.* 1991; Griffin *et al.* 1999*a*; Ashchepkov *et al.* 2003*b*) in lower regions of the lithosphere, which are not revealed by the pyroxenes and garnets. For diamond inclusions they define high temperatures to 1500 °C at the base of the lithospheric mantle columns. High temperature estimates are also found at 40 kbar for pyroxenite lenses and in the garnet–spinel facies. Cr-spinels indicate a sharply layered mantle with a low conductive geotherm for the Daldyn and Alakite regions. For the Udachnaya pipe mantle column they show seven different lithological horizons (Ashchepkov *et al.* 2003*a*).

In the detailed papers devoted to the calibration of the five single-mineral self-consistent methods (Ashchepkov 2002, 2003, 2006*a*, *b*; Ashchepkov & Vishnyakova 2006), most of these methods show correlations that allow their use in mantle thermobarometry (Ashchepkov *et al.* 2005*b*, *c*; Ashchepkov 2006*a*, *b*). The modified versions of the monomineral thermometers and barometers show better coincidence (Fig. 1).

Comparisons of the $P-T$ diagrams based on five minerals reveal very similar configuration of $P-T$ fields for each method using the database of the 2200 peridotite and pyroxenite associations from kimberlite deep-seated xenoliths. For a database of over 500 mantle xenoliths from Udachnaya (Schulze 1995; Boyd *et al.* 1997; Kuligin & Pokhilenko 1998; Smith 1999; Malygina 2000; Pokhilenko *et al.* 2000; Alymova *et al.* 2004; Pokhilenko 2006), each monomineralic method closely reproduces the $P-T$ plot for Udachnaya pipe derived from standard thermobarometric schemes such as those of Finerty & Boyd (1987), McGregor (1974) or Brey & Köhler (1990). The layering is emphasized by interchange of heated and cold horizons (Fig. 2). They are visible on diagrams using only the orthopyroxene method (Fig. 2e) as well as on diagrams obtained with polymineral thermobarometry (Fig. 2d and e). Each new monomineralic method gives $P-T$ values plotting on the orthopyroxene-derived points but also provides additional $P-T$ points corresponding to orthopyroxene-free associations.

Data set

In this paper we use >15 000 new analyses obtained from 2004 to 2006 in the course of three projects between ALROSA Stock Company and UIGGM SD RAS devoted to detailing of the mantle structure beneath the Yakutian diamond province. The EPMA was carried out according to standard methods using a CamebaxMicro system. The data include 300–900 analyses for each pipe for the 10 major oxide components. Additionally, the analyses of Udachnaya xenolith minerals from the dissertations of Kuligin (1997), Malygina (2000) and Pokhilenko (2006) were used to check the agreement between the methods of polymineral and monomineral thermobarometry.

Reconstruction of the mantle columns beneath the kimberlite fields of the Siberian Platform

Daldyn region

Four types of mantle section may be recognized here (Fig. 3). The first one is characteristic of the Udachnaya (Ashchepkov *et al.* 2003*a*) and Zarnitsa pipes (Ashchepkov *et al.* 2003*b*) and shows discrete intervals of lithological layering. This may be explained by the presence of pyroxenite horizons at the base of a series of stacked palaeo-slabs connected with the lithospheric keel (B-type eclogites) (Jacob *et al.* 1994; Beard *et al.* 1996; Snyder *et al.* 1997; Sobolev *et al.* 1998). In the middle part of the section (40–50 kbar) the anatectic and hybrid pyroxenites (Pokhilenko *et al.* 1999, 2000; Logvinova *et al.* 2001; Kuligin *et al.* 2003) form a pyroxenite lens. Pyroxenite bodies are also abundant in the spinel facies and near the Gar–Sp transition. Highly depleted dunites (Pokhilenko *et al.* 1991) are found within two intervals from 45 to 60 kbar (Ashchepkov *et al.* 2003*a*). Cr-spinel rocks are the more abundant representatives of the lowest-temperature conditions in the 32–58 kbar interval for the Udachnaya pipe. Garnet-bearing rocks record higher temperature values. Ortho- and clinopyroxenes give ranges of temperatures at the same pressures. For the mantle sequence beneath the Zarnitsa pipe, three discrete intervals of pressure were found using garnets and pyroxenes. Cr-spinels mark the layers above and below these three horizons. The ilmenites mark all the intervals, showing temperature branches close to those revealed by garnets with different degrees of heating. It is possible that not only did magma affect only selected intervals (as apparent) but also a contrast in lithology of the mantle sequence gave the different pressure intervals for Cr-spinels and garnet–pyroxenes (Fig. 3).

The pyroxenite layer definitely seen on the $P-T$ diagram for Udachnaya is not evident on the diagram for the Zarnitsa pipe. In these mantle lithosphere sections heating to $P-T$ conditions approximating the SE Australia geotherm (SEAG; O'Reilly *et al.* 2001) at the level of the Sp–Gar transition and above is indicated. The subvertical subadiabatic $P-T$ gradient determined from orthopyroxene for the Udachnaya pipe contrasts with mantle columns where nearly conductive $P-T$ gradients prevail.

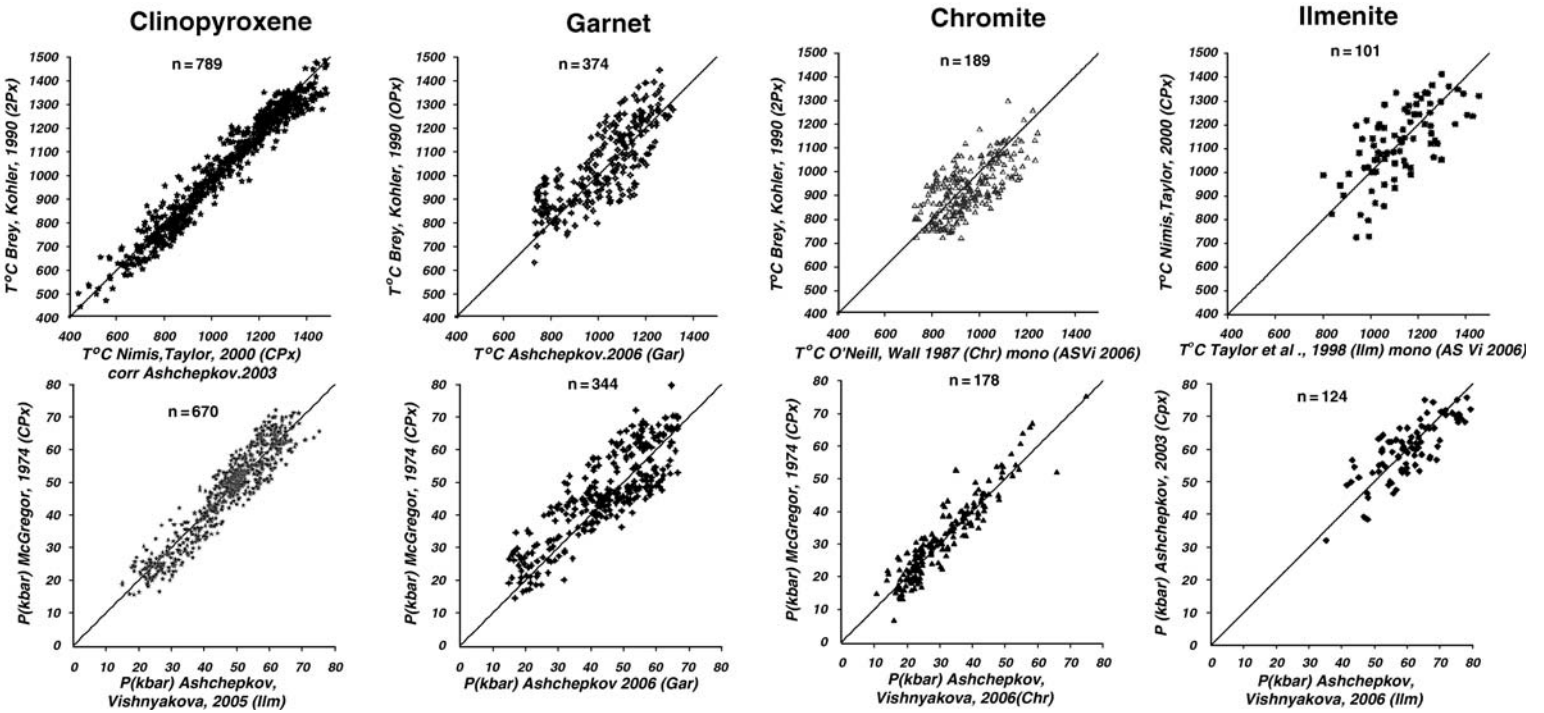

Fig. 1. Correlation diagrams between temperatures and pressures used in monomineral thermobarometers used in this paper for mantle reconstructions and other thermometers and barometers (references are given on the axes).

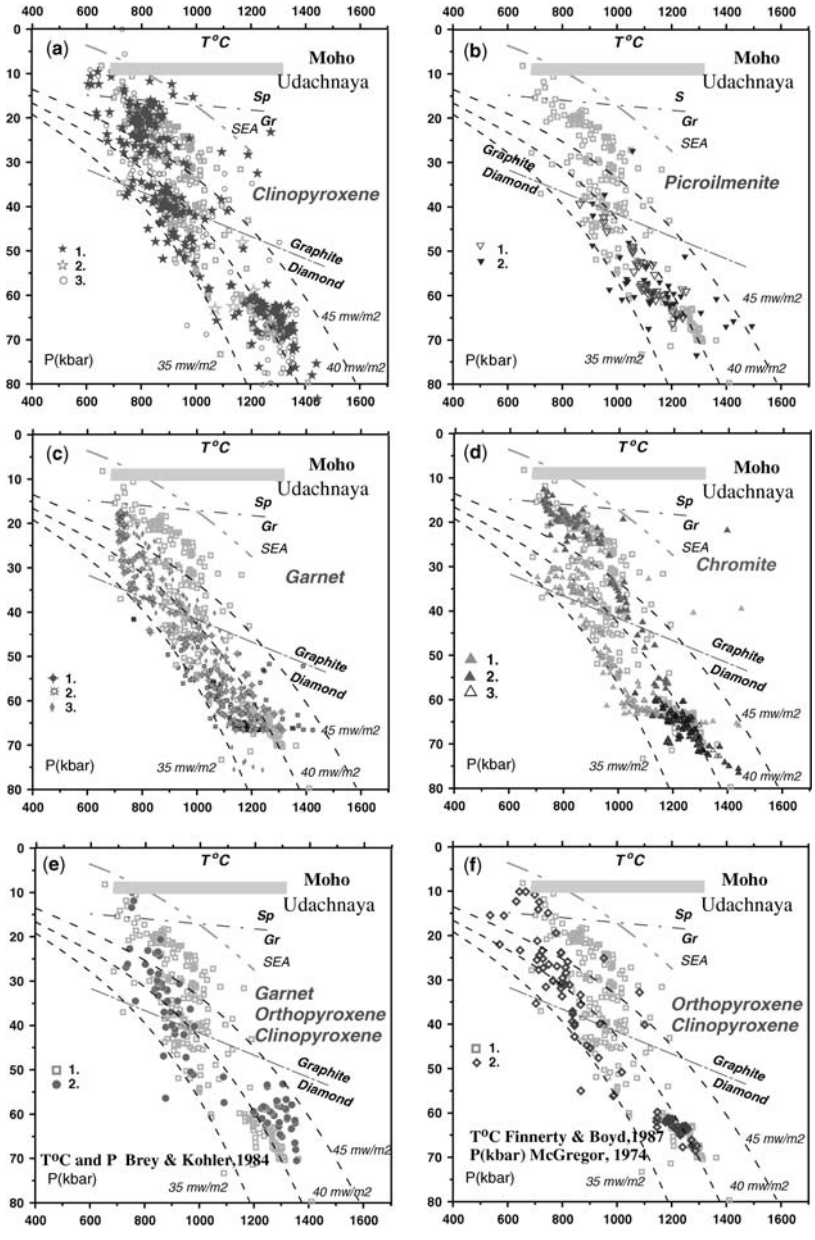

Fig. 2. *P*–*T* plots for xenoliths from the Udachnaya pipe (>480 associations) produced with the monomineral thermobarometers plotted together with the values determined by the orthopyroxene thermobarometer (grey squares) *T* (°C) (Brey & Köhler 1990) and *P* (kbar) (McGregor 1974). (**a**) Clinopyroxene *T* (°C) (Nimis & Taylor 2000) corrected 1, *P* (kbar) (Ashchepkov 2003); 2, the same for diamond inclusions (Sobolev *et al*. 2004); 3, *T* (°C) and *P* (kbar) (Nimis & Taylor 2000). (**b**) Picroilmenite *T* (°C) (Taylor *et al.* 1998)–*P* (kbar) (Ashchepkov & Vishnyakova 2006). 1, For megacrystals (Cr_2O_3 <1%); 2, for pyroxenites and metasomatites. (**c**) Garnet (Ashchepkov 2006). 1, Peridotites; 2, diamond inclusions (Sobolev *et al*. 2004); 3, pyroxenites. (**d**) Cr-spinel. 1, *T* (°C) (O'Neill & Wall 1987)–*P* (kbar) (Ashchepkov & Vishnyakova 2006), high-temperature branch; 2, the same, for low-emperature branch; 3, for diamond inclusions (Sobolev *et al*. 2004), high-temperature branch. For comparison, plots produced by common mantle thermobarometers are represented: (**e**) 1, *T* (°C) (Brey & Kohler 1990) (OPx)–P (kbar) (McGregor 1974); 2, *T* (°C) and *P* (kbar) (Brey & Köhler 1990); (**f**) 1, as in (e); 2, *T* (°C) (Finnerty & Boyd 1987)–*P* (kbar) (McGregor 1974). SEA, SE Australian geothem.

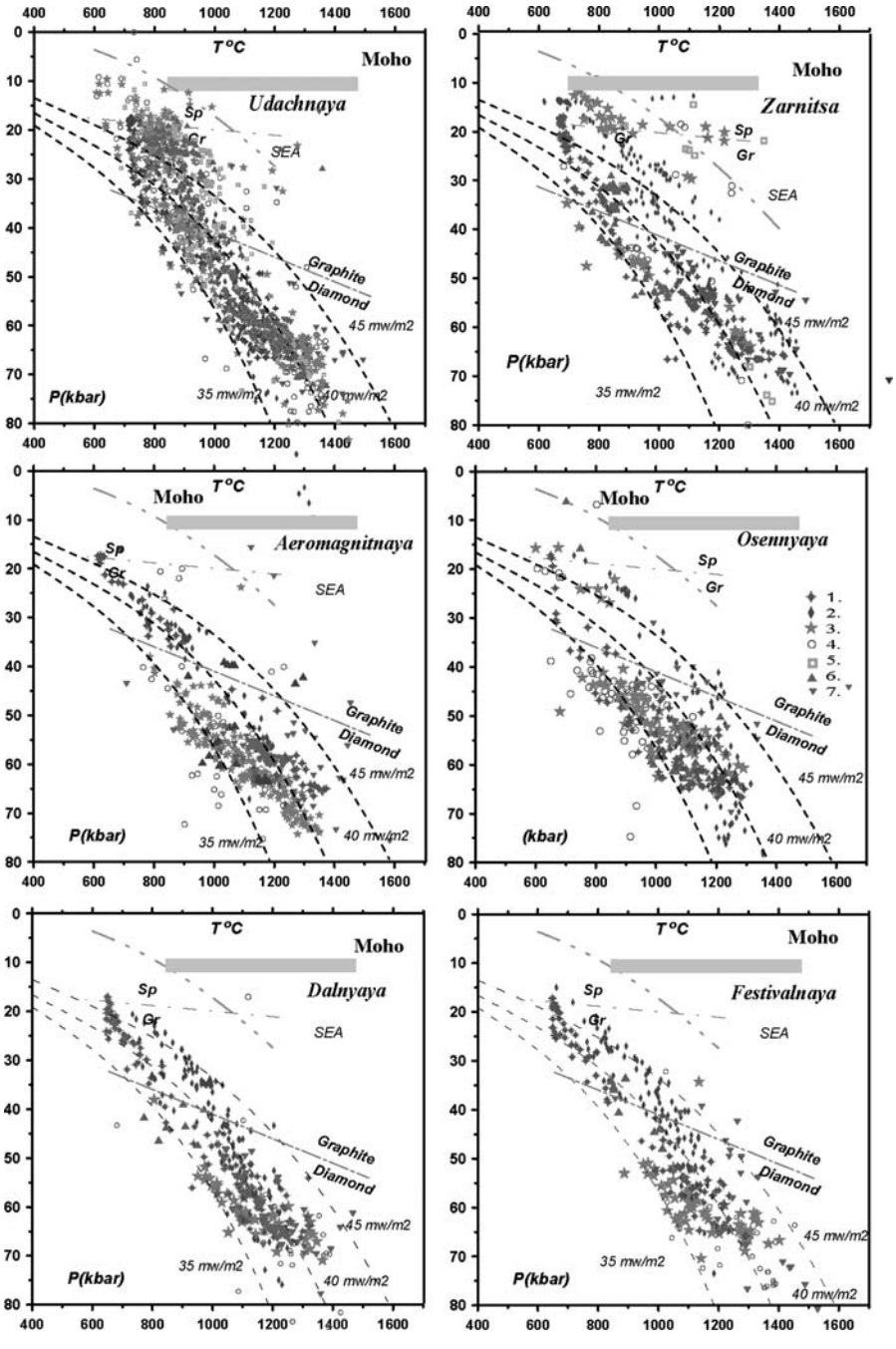

Fig. 3. *P–T* estimates for the mantle columns beneath the kimberlite fields of the Daldyn region. 1, Garnet thermobarometry for peridotites (Ashchepkov 2006*a*, *b*); 2, the same for pyroxenites; 3, clinopyroxene thermobarometry (Nimis & Taylor 2000); 4, *T* (°C) (Nimis & Taylor 2000); 4, *T* (°C) (Nimis & Taylor 2000) *P* (kbar) (Ashchepkov 2003); 5, orthopyroxene thermobarometry: *T* (°C) (Brey & Kohler 1990) *P* (kbar) (McGregor 1974); 6, Cr-spinel thermobarometry: *T* (°C) (Taylor *et al.* 1998) *P* (kbar) (Ashchepkov & Vishnyakova 2006); 7, Ilmenite thermobarometry: *T* (°C) (Taylor *et al.* 1998) *P* (kbar) (Ashchepkov & Vishnyakova 2006).

Ilmenite $P–T$ estimates for Udachnaya refer to the deepest (>40 kbar) parts of the mantle lithosphere, which are more heated, whereas for Zarnitsa (Ashchepkov *et al.* 2003*a*, *b*) they trace pressure intervals from 65 to 25 kbar.

The second type of mantle section is found for the Osennyaya (Osernayya) pipe and the nearby Zimnyaya, Letnyaya and Gornyatskaya pipes, where the more fertile clinopyroxene-rich rocks make up the interval from 40 to 55 kbar, close to the estimates from ilmenites. The maximal pressure (55 kbar) is similar to that obtained from the shift of the Raman peak for a coesite inclusion in diamond (Sobolev *et al.* 2000). Below 55 kbar the depleted dunite horizon is represented in concentrate by coarse chromite grains giving high-temperature conditions at 60 kbar. The garnet estimates are low temperature. Ilmenite $P–T$ points suggest a broad distribution of the high-temperature Ilm–Cpx metasomatites within a large pressure interval.

The third type of mantle section is found at the Aeromagnitnaya pipe. Cpx-based estimates are distributed in the lower part of the mantle column, with three dense clusters close to 70 kbar, 60–65 kbar and 50–55 kbar. Ilmenite $P–T$ estimates cluster within the range 65–45 kbar, suggesting a split into three branches with different degrees of heating. Garnet $P–T$ values preferentially populate the upper (30–20 kbar) and lower (50–65 kbar) parts of the mantle section. Cr-spinel estimates correspond to low-temperature conditions, but at the level of 40 kbar they mark three geotherms of 35, 40 and 45 mW m^{-2} in the pyroxenite layer.

The fourth type of mantle structure, which occurs beneath Dal'nyaya and Festival'nyaya, the Dolgozhdannaya and Irelyakhskaya pipes, shows only a Cpx-rich base to the mantle lithosphere and a transition from convective to conductive geotherms in a restricted interval from 50 to 70 kbar. Garnet, chromite, and ilmenite $P–T$ parameters are close to those determined with clinopyroxene analyses.

Judging from the example of the Daldyn region it is possible to say that in the same kimberlite field the structure of the mantle beneath closely spaced pipes may vary to a high degree. The pipes with in a single field may contain varying sets of mantle peridotite xenoliths as well as eclogites and metasomatites.

Alakite region

The most detailed reconstructions of the mantle were obtained for the kimberlite pipes of the Alakite field (Fig. 4) (Sobolev *et al.* 2003; Ashchepkov *et al.* 2004*a*, *b*, *d*). The $P–T$ diagram for the Aykhal pipe reveals a structure similar to that calculated for the South African pipes (Nixon 1973; Nixon & Boyd 1973; Smith 1999). Essential heating from 38 to 45 mW m^{-2} was found for the lower part from 80 to 50 kbar, including a garnet dunite horizon at 50–60 kbar. Eight to nine lithologically distinct pressure intervals are indicated by $P–T–X$ data from garnets and clinopyroxenes. A similar structure is revealed in the mantle column beneath the Yubileynaya pipe (Ashchepkov *et al.* 2004*a*, *d*), although that column is enriched in clinopyroxene compared with the others. Two horizons of depleted rocks are found at the base of the mantle column at 58–65 kbar. The high-temperature garnet branch (*c.* 45 mW m^{-2}) to 40 kbar most probably corresponds to pyroxenites or peridotites from the contact zones of deep seated magmatic feeder channels. The mantle column beneath the Ozernaya pipe, which is located very close to Yubileynaya, shows a low-temperature conductive geotherm splitting at 40 kbar to a subadiabatic trajectory from 40 to 25 kbar, and a polybaric ilmenite trend with deviations from a conductive geotherm to a high-temperature subadiabatic path approaching the SEAG.

The lower part of the mantle section beneath the Sytykan pipe is represented by garnet harzburgites and dunites at 60–50 kbar, with several lenses of eclogite-like rocks suggested above. A pyroxenite lens was found at 45–35 kbar, above the depleted layers (harzburgite is suggested). Cr-spinel $P–T$ estimates are located along the low-temperature conductive branch for the Sytykanskaya, Aykhal and Ozernaya mantle columns. However, in the lithosphere beneath Komsomolskaya and Yubileynaya they trace several (3–4) separate layers with extensive heating (Fig. 4). More high-temperature estimates usually are located near the pyroxenite layer. In the mantle beneath Sytykanskaya (Reimers *et al.* 1998) spinel peridotites form the lens between the heated depleted layer at 65–58 kbar and an essentially pyroxene-enriched horizon at 60–50 kbar. The mantle column under the Komsomolskaya pipe is more fertile compared with the mantle horizons beneath the southern kimberlite pipes (Aykhal and Yubileynaya). The layering is more similar to that of mantle beneath the Upper Muna field. The deviations for the clinopyroxene $T–P$ estimates to lower temperatures are typical for eclogites and similar rocks with high Na_2O content in pyroxenes.

The $P–T$ conditions for the ilmenites from Aykhal pipe overlap those determined with clinopyroxene, garnet and chromite in the interval from 40–60 kbar. These conditions range from 35 to 40 mW m^{-2}, the higher temperatures prevailing at deeper levels. For the Yubileynaya pipe, the deviations to the high-temperature field on the $P–T$ diagram are more pronounced in the upper part of the mantle column. The nearby Zarya pipe shows a

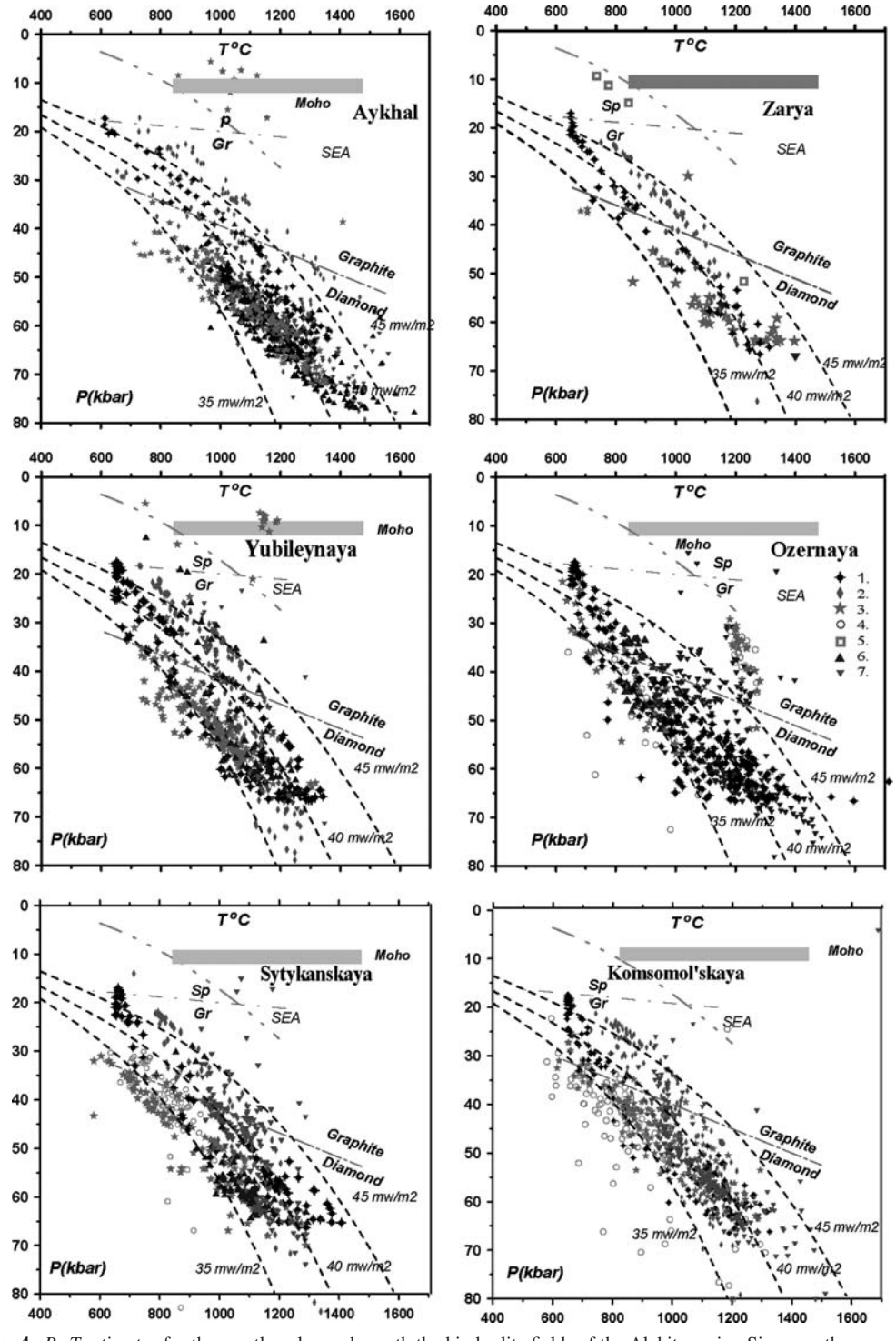

Fig. 4. *P–T* estimates for the mantle columns beneath the kimberlite fields of the Alakite region Signs are the same.

stepped mantle geotherm traced by clinopyroxene and garnet.

The $P-T$ estimates for ilmenites beneath the Sytykanskaya pipe reveal low-temperature gradients in the lower part of the mantle section and essentially coincide with garnet $P-T$ points, suggesting broad ilmenite–clinopyroxene metasomatism such as that occurring in xenoliths as hydrous Cpx–Ilm veinlets. However, in the upper part of the mantle section it gives more heated conditions than the $P-T$ gradients derived from the common mantle peridotites. The lower part of the mantle section beneath the Komsomolskaya pipe is also represented by metasomatites close in $P-T$ conditions to the common harzburgites. As in the Sytykanskaya case, heated metasomatites are located above. Protokimberlite melt intrusion in several stages and accompanying metasomatism is the most probable cause of these phenomena.

Malo–Botuobinsky field

The mantle sequence beneath the Mir pipe (Ashchepkov *et al.* 2004*b*, *c*) is based on 530 new analyses of minerals from concentrate and on data for about 30 xenoliths from the literature (Beard *et al.* 1996; Roden *et al.* 1999). Despite the difference in the chemical features of minerals from the Mir and Internationalnaya pipes, the structure of the lithosphere is generally similar (Fig. 5). Highly depleted rocks are distributed beneath the Mir pipe mainly in the 60–50 kbar interval. In the upper part, lherzolites including metasomatic minerals (phlogopite and amphibole) are more typical. Lenses of eclogite, pyroxenite and metasomatites occur in the middle part, and the pyroxenites are found at the base. In the mantle section under the Internationalnaya pipe heating to 1400 °C is found from the base of the lithosphere to 55 kbar. Three large peridotitic units are recognizable in the lower part of the mantle section of both pipes. For Internationalnaya the lower units contain essentially eclogitic or hybrid peridotite layers judging by the pyroxene compositions. The spinel $P-T$ trajectories trace the conductive geotherm in the lower regions, but above this horizon it splits, and branches to the highest-temperature trajectories appearing in our $P-T$ plots. The structure of the mantle beneath the Dachnaya pipe should be very close to that for the Mir pipe. Spinel horizons reside only at a conductive geotherm of 35 mW m^{-2} and at the 35 kbar level it shows heating. Pyroxenes give very low-temperature conductive estimates, in clusters that nearly coincide in pressure with those determined from ilmenites (Fig. 5).

The structure of the mantle lithosphere beneath Amakinskaya and Taezhnaya is probably similar although we have insufficient data. Chromite $P-T$ estimates refer to the middle part of the section and clinopyroxene to the base of the lithosphere beneath the Amakinskaya pipe. A stepped, high-temperature geotherm is traced by both garnets and ilmenites from 65 to 45 kbar.

The ilmenite trends for the Amakinskaya pipe refer to the lower part of the section, with a gradient close to conductive characterizing the metasomatites. For the Mir pipe ilmenites give $P-T$ conditions of high-temperature metasomatites at the base. For the Dachnaya pipe they extend also to the upper zones, forming subadiabatic gradients. Here they are probably tracing the fractures of a feeder system rising to the Moho. The clusters of pressure values for ilmenites correspond to those for garnet and pyroxenes. In the mantle column of the Internationalnaya pipe the ilmenites from the lowest zone show good correspondence to the conductive geotherms and from 50 kbar upwards the rising subadiabatic gradients.

Upper Muna field

Detailed $P-T$ diagrams were obtained for the Deimos, Zapolyarnaya, Novinka and Komsomolskaya–Magnitnaya pipes (Ashchepkov *et al.* 2005*d*), with fewer representatives for Poiskovaya, Inter-Kosmos, Mechta and Debyut. All these pipes reveal a rather different $P-T$ sequence from the other regions. They show the presence of clinopyroxene-enriched horizons at the base of the lithosphere. This feature is more typical for the Mesozoic kimberlites of South Africa and other parts of the post Gondwana continents (Nixon & Boyd 1973). They reveal gently inclined geotherms at the base of the lithosphere except for Deimos. The 4–5 repeated flattened arrays of $P-T$ estimates for clinopyroxenes are typical for the lower part of the mantle section (Fig. 6).

Three types of mantle section can be identified there. The mantle column beneath the Zapolyarnaya pipe contains a wide range of rocks with metasomatic and pyroxenitic signatures within the 65–30 kbar interval. The high-temperature Ti-rich garnet branch probably indicates contact associations developed near rising protokimberlite magma systems. The separate chains of $P-T$ points probably correspond to the $P-T$ paths of the mantle melts. The ilmenite $P-T$ estimates plot sometimes as for Deimos on the three $P-T$ trajectories. These together with clinopyroxene $P-T$ values form the inflections on the geotherms in the 55–50 kbar interval.

High-temperature clinopyroxene rocks are typical for the Novinka and Zapolyarnaya pipes in the lithosphere base, but are rather rare in Deimos. Inclined geotherms for the lithosphere beneath Poiskovaya and inter-Kosmos are shown by the

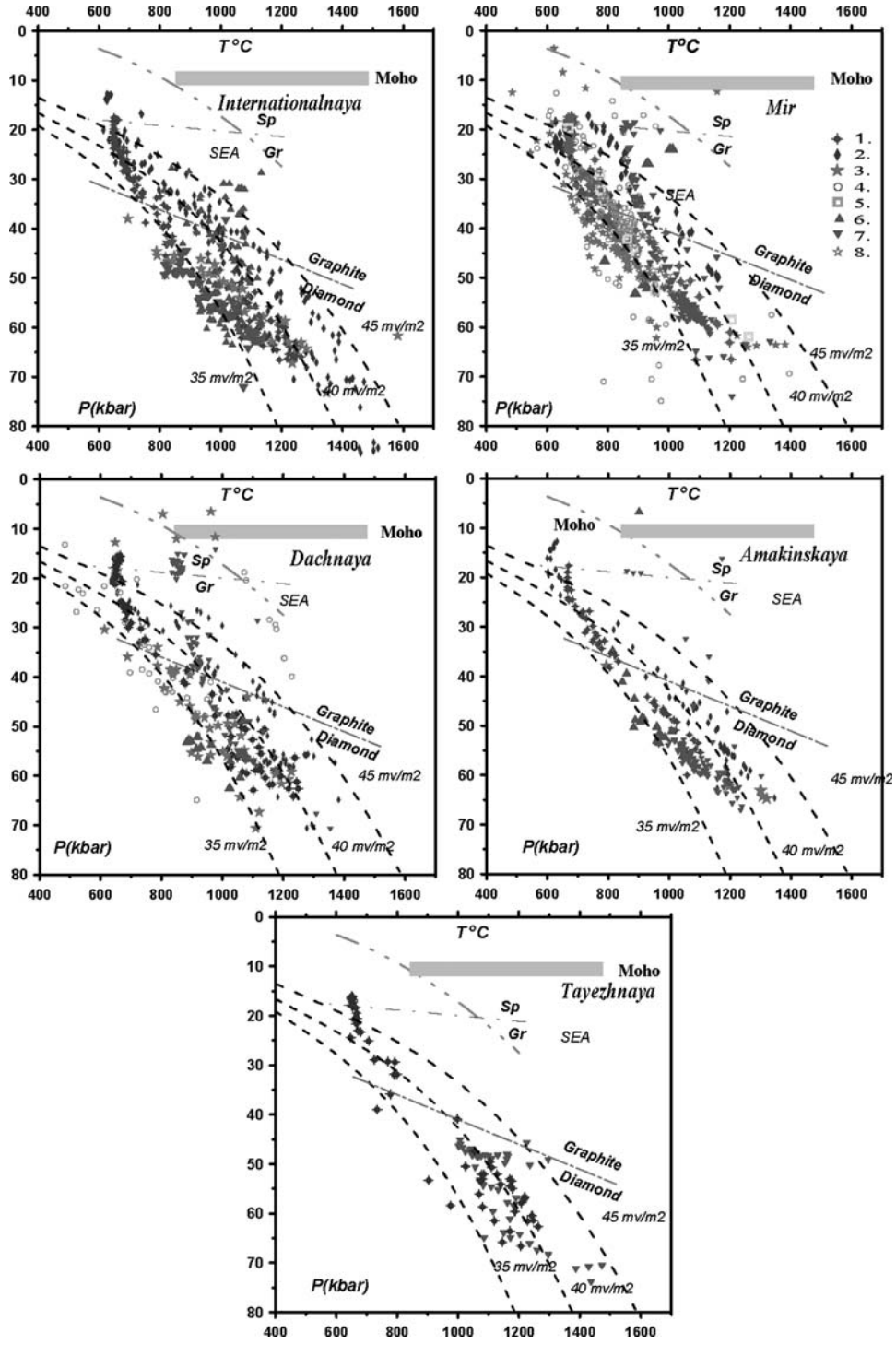

Fig. 5. *P–T* estimates for the mantle columns beneath the kimberlite fields of the Malo-Botuobinsky region. Signs are the same.

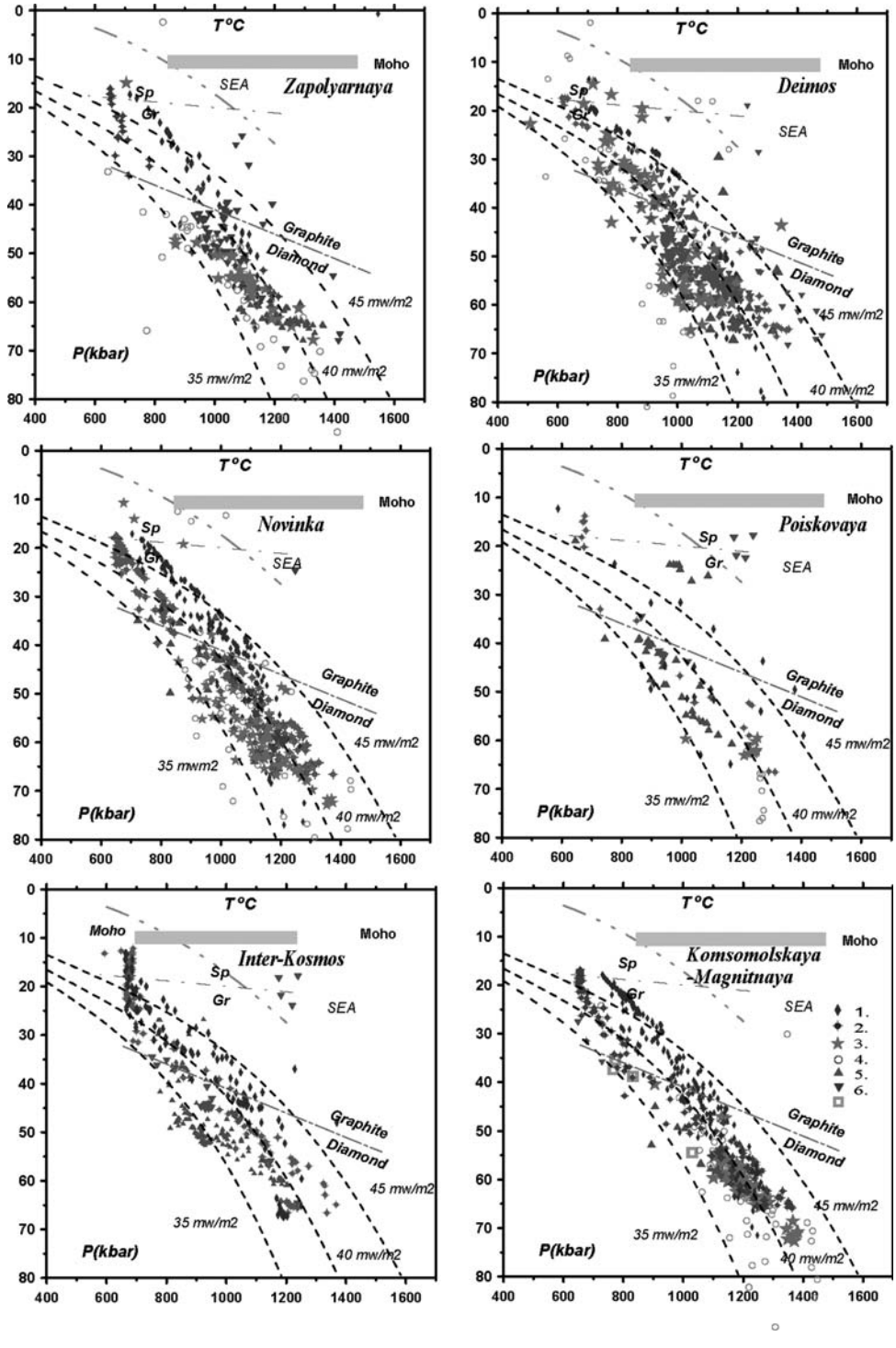

Fig. 6. *P–T* estimates for the mantle columns beneath the kimberlite fields of the Upper Muna region. Signs are the same.

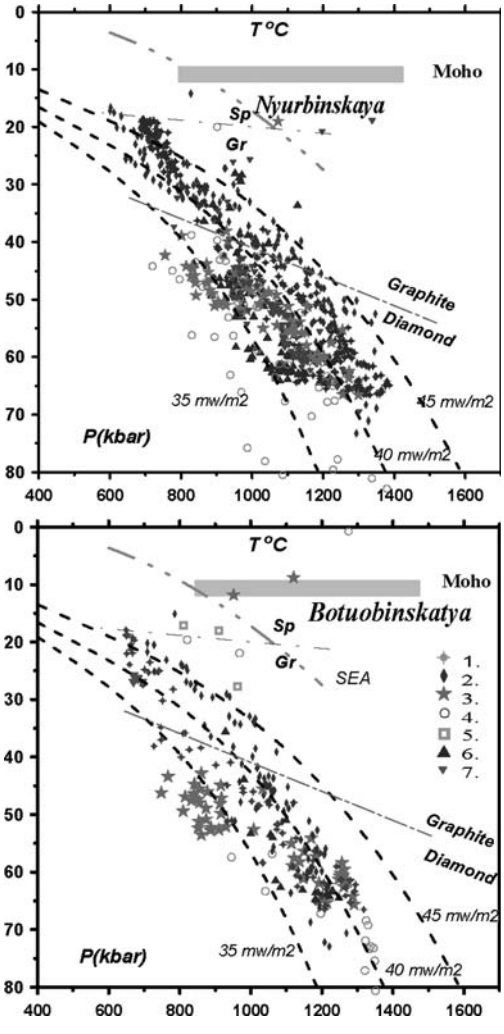

Fig. 7. *P–T* estimates for the mantle columns beneath the kimberlite fields of the Nakyn region. Signs are the same.

spinels; they are repeated three times in the lower mantle sequence. Ti-rich garnets widely developed there are more high-temperature in the lower part of the mantle columns. In the upper part of mantle column near 30 kbar the high-temperature branch approaching *P–T* of the SEAG or 60–65 mW m^{-2} is outlined by several points. Ilmenite rocks characterize separate discrete levels of probably mantle metasomatites at the base of the lithosphere near the pyroxenite lens (40 kbar) and Gar–Sp transition. They are related to the various *P–T* gradients of mantle diapirs and magmatic systems.

Nakyn field

Peridotite mantle beneath the Nakyn field (Spetsius *et al.* 2004) is heated, based on garnet *P–T* estimates of geotherms up to 40 mW m^{-2} (Fig. 7). Pyroxene geotherms in the lower part form an inflection from an inclined convective branch to a conductive branch, which reflects heating of the base to 43 from 35 mW m^{-2} or lower, and is more obvious for the Botuobinskaya mantle sequence.

In the mantle section beneath the Nyurbinskaya pipe the pyroxene estimates from 55 to 40 kbar trace heating conditions from 35 to 42 mW m^{-2}, practically coinciding with the ilmenite *P–T* path. Garnets mainly trace the stepped high-temperature branch near 40 mW m^{-2}. Some of *P–T* estimates are close to the conductive 35 mW m^{-2} geotherm and the convective branch in the base. *P–T* points of Cr-spinels occur in three pressure intervals in the mantle beneath the Nurbinskaya pipe. In the lowest part they coincide with the convective branch, as elsewhere in the world (Nixon & Boyd 1973; Boyd *et al.* 1997). In the middle part, from 52 to 45 kbar, they are close to the pyroxene estimates, and in the highest part, at 40 kbar, they reflect the high-temperature conditions of the pyroxenite layer.

The lower part is essentially heated. According to experimental data, temperatures of *c.* 1200 °C are favourable for growth of good quality diamonds (Fedortchouk *et al.* 2003), so these conditions suggest high diamond potential.

P–T diagrams for the Nyurbinskaya and Botuobinskaya pipes are similar in configuration, but the latter has a more depleted mantle column as revealed by the rarity of pyroxenes and their low-Al composition (Fig. 7).

Discussion

Models of the mantle column evolution

Major conclusions and simple evolutionary schemes were developed as a result of the study of monomineral thermobarometry and chemistry of the xenocrysts from 25 kimberlite pipes. Mantle domains in each region have specific features although the structure of the mantle column in the kimberlite field may be highly variable. Interaction of deep-seated melts and fluids with the lithospheric mantle results in peculiarities of composition of rocks and minerals, and variable distribution of metasomatites, pyroxenites and megacrystalline rocks in mantle sections. Metasomatites are mostly developed in the lower regions of the mantle lithosphere, as in South Africa (Grégoire *et al.* 2002), and reflect the influence of deep-seated magmatic systems.

For the Daldyn field the contrasting mineralogical layering of the peridotite and eclogite slices is typical for the majority of pipes (Ashchepkov *et al.*, 2003*a*, *b*, 2005*c*; Alymova *et al.* 2004;

Ashchepkov 2006*b*). Peridotites are moderately depleted, with low Na, Al and Cr contents (Boyd *et al.* 1997; Pokhilenko *et al.* 1991, 2000). The Alakite field is characterized by the wide distribution of metasomatism in the mantle column (Sobolev 1977; Sobolev *et al.* 1997, 2003; Reimers *et al.* 1998; Ashchepkov *et al.* 2004*a*, *d*; Logvinova *et al.* 2005). In the Malo–Botuobinsky region (Sobolev 1977; Beard *et al.* 1996; Roden *et al.* 1999) the middle part of the section is characterized by a peridotite composition moderately enriched in Al, Na, Ca, Si and Fe, which is typical for continental mantle. Similar features were recognized for the Nakyn region, which has abundant eclogites and metasedimentary rocks (Spetsius *et al.* 2004). Specific features in the Upper Muna field (Ashchepkov *et al.* 2005*d*) are abundant metasomatites and a moderately enriched character of the pyroxenes in the deeper part of the mantle section.

Broad variation of the mantle column structure may occur in the same kimberlite field, probably as a result of the inclined position of the mantle layers or variable compositions of palaeo subduction slabs residing in the lithospheric keel (Jacob *et al.* 1994), as well as the local distribution of the zones of metasomatism.

There is an impression that the composition of the mantle rocks at the lithospheric base influences the degree of metasomatic alteration and the diamond potential. The pipes highly enriched in diamonds have thick depleted dunite horizons at the base of the lithosphere, and original enrichment in diamonds probably occurred at the stage of lithospheric craton growth and is probably subduction-related. It is well known that dunites are effective melt conduits (Braun & Kelemen 2002), hence they should concentrate the subduction-related magmas as well as various plume melts, including the stage of kimberlitic magmatism. The melts flowing along the base of the lithosphere selectively infiltrate into the upper lithosphere along dunite horizons, creating pyroxenites at different levels and heating the mantle column. In favourable f_{O_2} conditions (Fedortchouk *et al.* 2003) and in the presence of carbon in the rocks, diamond grains should nucleate. Some diamonds derive from the P–T conditions of pyroxenite lenses. The composition of the basal lithologies determines also the type of interaction with metasomatic melts. Interaction of melt with dunites creates impregnated peridotites with porphyroblastic textures. Intrusion of the melt results in shearing (Moore & Lock 2001). Such structures and rocks were found in the zones of contact with megacrystalline ilmenite-bearing rocks (Pokhilenko *et al.* 1991). In the case of essentially pyroxenitic rocks or fertile peridotites, a high-temperature magmatic metasomatism occurs, such as that in the Thumb diatreme, Colorado Plateau (Smith *et al.* 1991; Ehrenberg 1982). This may result in the creation of hybrid low-Cr pyroxenites, which are typical for the Mir pipe, for South Africa (Nixon & Boyd, 1973) and for the Festival'naya, Dal'nyaya, Dolgozhdannaya, Irelyahskaya and other pipes in the Daldyn field.

The largest pipes (600–1000 m) in their respective fields, including Mir in the Malo–Botuobinsky region, Udachnaya and Zarnitsa in the Daldyn field, and Aykhal, Yubilenaya, Sytykanskaya and Komsomolskaya in the Alakite field, have large dunite lenses in the lithosphere base according to thermobarometry and a high frequency of deep-seated subcalcic garnets (Sobolev *et al.* 1973; Pokhilenko *et al.* 1991).

Large pipes also have steeper geothermal gradients, which are sometimes close to subadiabatic. This probably results from heating of the mantle columns by large quantities of rising melt. This heating is a favourable factor for diamond growth. The high development of the pyroxenite association and the signs of contact interaction (Kuligin *et al.* 2003) with the increase of Na, Ti, Al and Fe in minerals is another characteristic feature of large pipes.

The largest pipes were formed in the most permeable zones in the lithosphere, which usually are represented by dominantly dunite slices. The advective geothermal gradients result partially from the upwelling of large magmatic masses in the continental keel with associated heating. This is a possible set of favourable conditions for diamond growth.

Average-sized pipes (200–500 m) such as Dal'nyaya usually contain in the base a pyroxene-rich layer in which the low-Cr pyroxenes are associated with Ti-pyropes and ilmenites.

In some mantle columns in the Alakite region the metasomatism penetrates through the entire lower part of the mantle columns, resulting in the smoothing of contrasting layering. However, rising melts create additional layers of pyroxenite and metasomatic rocks at the boundaries of primary subduction slabs, which are marked by ilmenites and Fe-pyroxene P–T estimates. The pyroxenite lenses marked by inflection in the garnet CaO–Cr_2O_3 trend are found in practically all the regions of the world (Sobolev 1977; Griffin *et al.* 2002). The level near *c*. 40 kbar is the source region of the partial melting. The varying character of metasomatism from K-type in the lower regions to Na type above is probably due to the decomposition of primary subduction amphibole in this layer. For example, the mantle column beneath the Yubileynaya pipe demonstrates a high degree of development of K-metasomatites with richterite and phlogopite, including K-pyroxenes in the lower part of the mantle section and Na-pargasite in the upper part (Ashchepkov *et al.* 2004*a*).

Large magmatic systems that interact with the continental lithosphere are of several types.

Hydrous lamproite melts and basaltic melt pass easily through the continental lithosphere to the 30–20 kbar level where, at the minimum on the volatile-bearing peridotite solidus (Wyllie 1995), basaltic magmas sometimes accompanying kimberlite magmatism are generated. They are responsible for heating to conditions of the SEAG gradient, fertilization and Fe-metasomatism, such as occurs in mantle columns beneath the Udachnaya pipe and the diatremes of the Aldan shield (Ashchepkov *et al.* 2001). Protokimberlite and essentially carbonatite melts, which appear as a result of the long differentiation, cause Ti-metasomatism and heating to 40–45 mW m^{-2}, mainly in the lower part of the mantle section up to 40 kbar. They form series of megacrystalline essentially pyrope- and ilmenite-bearing rocks, which are very close in geochemistry to kimberlites (Nowell *et al.* 2004) and show signs of a high degree of differentiation (Griffin *et al.* 1997), probably in the feeder system developing before eruptions (Ashchepkov *et al.* 2005*a*). This interaction is possibly a favourable factor in diamond growth. Melts responsible for the creation of the high-temperature (to 1600 °C) branches of geotherms at the base of the lithosphere should have a high-pressure and probably lower mantle origin.

The major models arising from thermobarometric study are the following. Mantle domains in each region have specific features of lithological construction and of interaction with deep-seated magmatic systems. The primary structure of the lithosphere is inferred to have formed by subduction during ocean–continent convergence. The fragments of the mantle lithosphere in each geodynamic environment have characteristic compositions that result in major compositional features after the coupling to the continental cratonic lithosphere. The melts and fluids in subduction- and plume-related environments may change the geochemical features of the most permeable zones in the lithospheric keels of cratons. Usually mantle columns are separated into two parts at the level of 40 kbar by a pyroxenite layer formed as a result dehydration and melting of subducting slabs near 120–130 km (van Keken *et al.* 2002).

The common feature for the Palaeozoic kimberlites of Siberia is the layering consisting of 10–12 slices. The upper part consists of 4–5 horizons that are more fertile than the lower part as a result of ancient enrichment (Francis 2003), or as a result of transformation by basaltic melts and those derived from the pyroxenite lens. The lower 4–5 layers usually show progressive depletion. For the region subjected to the influence of the Permian–Triassic superplume in the Anabar and Aldan shield, the characteristic is deep depletion in pyroxenes (Ca, Al) but Fe-metasomatism of the mantle column below 40 kbar (Ashchepkov *et al.* 2001).

Protokimberlite melts (which should be essentially carbonatitic at the last stages of evolution) are responsible for the creation of the megacrystalline kimberlite associations at the stage of creation of the feeder system. This is accompanied by Ti-metasomatism, usually to the 40 kbar level, with elevation of the thermal gradient to 40–45 mW m^{-2}. This stage may be one factor in diamond growth.

Conclusions

(1) Methods of monomineral thermobarometry applied to five separate minerals show agreement of the P–T estimates, and the possibility of determining the general features of the lithological stratigraphy of the mantle columns from which they are derived.

(2) Ilmenite trends and associated Ti-metasomatites and contact associations are the result of formation of magmatic feeder systems preceding kimberlite eruptions. They are polybaric and were created in several pulses.

(3) Mantle sections containing large amount of eclogites have, as a rule, peridotites with hybrid features, and sometimes metasomatites and anatexic pyroxenites.

(4) A layered mantle structure is characteristic beneath most kimberlite pipes and is probably related to the periodicity of superplume activity (Dobretsov & Kirdyashkin 1994) in the Precambrian.

(5) The largest diamondiferous pipes exhibit specific structural features of their underlying mantle columns: the presence of dunite horizons, subadiabatic temperature gradients and large amounts of pyroxenites.

The work was supported by RBRF grant 05-05-64718. The work contains the result of the projects 77-2, 65-03, 02-05 of UIGGM SD RAS and ALROSA Stock Company. We are grateful to D. Bell, who kindly improved the manuscript, and are indebted to N. V. Sobolev for useful remarks.

References

ALYMOVA, N. A., KOSTROVITSKY, S. I., IVANOV, A. S. & SEROV, V. P. 2004. Picroilmenites from kimberlites of Daldyn field, Yakutia. *Doklady Earth Sciences*, **395a**, 444–447.

ASHCHEPKOV, I. V. 2002. Empirical clinopyroxene thermobarometer for mantle rocks on the base of Jd–Di exchange. *Doklady Earth Sciences*, **382**, 366–370.

ASHCHEPKOV, I. V. 2003. More precise equation of the Jd–Di barometer. *Herald of Earth Sciences Department Russian Academy of Sciences*, **N1**. World Wide Web address: http://www.scgis.ru/russian/cp1251/h_dgggms/1-2003/informbul-1_2003/term-7e.pdf.

ASHCHEPKOV, I. V. 2006*a*. Empirical garnet thermobarometry for mantle peridotite. *Russian Geology and Geophysics*, **47**, 1071–1085.

ASHCHEPKOV, I. V. 2006*b*. Empirical chromite and ilmenite thermobarometry for mantle peridotites of garnet facies. *Herald of the Earth Sciences Department Russian Academy of Sciences*, **1**. World Wide Web address: www.scgis.ru/russian/cp1251/h_dgggms/1-2006/informbul-1_2006/term-1e.pdf.

ASHCHEPKOV, I. V., VLADYKIN, N. V., SAPRYKIN, A. I. & KHMELNIKOVA, O. S. 2001. Composition of thermal structure of the mantle in peripheral parts of the ancient shields within Siberian craton, *Revista Brasileira de Geociências*, **31**, 527–536.

ASHCHEPKOV, I., VLADYKIN, N., POKHILENKO, N. *ET AL*. 2003*a*. Clinopyroxene geotherms for the mantle columns beneath kimberlite pipes from Siberian craton. *In*: *8th International Kimberlite Conference, Extended Abstracts*, abstract FLA_0355.

ASHCHEPKOV, I. V., VLADYKIN, N. V., AMSHINSKY, A. N. *ET AL*. 2003*b*. Minerals from Zarnitsa pipe kimberlite: the key to enigma of the mantle composition and constuction. *In*: VLADYKIN, N. V. (ed.) *Plume and Problems of Deep Sources of Alkaline Magmatism. Proceedings of International Workshop*. Irkutsk State University, Khabarovsk, 20–38.

ASHCHEPKOV, I. V., VLADYKIN, N. V., NIKOLAEVA, I. V. *ET AL*. 2004*a*. Mineralogy and geochemistry of mantle inclusions and mantle column structure of the Yubileinaya kimberlite pipe, Alakit field, Yakutia. *Doklady Earth Sciences*, **395**, 517–523.

ASHCHEPKOV, I. V., VLADYKIN, N. V., LOGVINOVA, A. M., ROTMAN, A. Y., ANOSHIN, G. N., SAPRYKIN, A. I. & KHMELNIKOVA, O. S. 2004*b*. *Abstracts and Program, Goldschmidt Conference, Copenhagen, Denmark 5–11 June 2004. Geochimica et Cosmochimica Acta, Conference Supplement*, 5.7.P08A724.

ASHCHEPKOV, I. V., VLADYKIN, N. V., ROTMAN, A. Y. *ET AL*. 2004*c*. Mir and International'naya kimberlite pipes—trace element geochemistry and thermobarometry of mantle minerals. *In*: VLADYKIN, N. V. (ed.) *Deep-seated Magmatism, its Sources and their Relation to Plume Processes*. Institute of Geography SB RAS, Irkutsk–Ulan-Ude, 194–208.

ASHCHEPKOV, I. V., VLADYKIN, N. V., ROTMAN, A. Y. *ET AL*. 2004*d*. Reconstructions of the mantle layering beneath the Alakite kimberlite field: comparative characteristics of the mineral geochemistry and *TP* sequences. *In*: VLADYKIN, N. V. (ed.) *Deep seated Magmatism. Its Sources and their Relation to Plume Processes*. Institute of Geography SB RAS, Irkutsk–Ulan-Ude, 160–178.

ASHCHEPKOV, I. V., VLADYKIN, N. V., POKHILENKO, N. P. *ET AL*. 2005*a*. Ilmenite trends from kimberlites of Siberia: Do they represent the mantle feeding vein system? *Geophysical Research Abstracts*, **7**, abstract 00593.

ASHCHEPKOV, I. V., VLADYKIN, N. V., POKHILENKO, N. P., ROTMAN, A. Y., AFANASIEV, V. P. & LOGVINOVA, A. M. 2005*b*. Use of the monomineral thermobarometry for the reconstruction of the mantle sections. *In*: VLADYKIN, N. V. (ed.) *Problems of Sources of Deep-seated Magmatism and Plumes*. Institute of Geography SB RAS, Petropavlovsk-Kamchatsky–Irkutsk, 210–228.

ASHCHEPKOV, I. V., POKHILENKO, N. P., SOBOLEV, N. V. *ET AL*. 2005*c*. Use of correlating monomineral thermobarometry for mantle peridotites (correlating methods). *In*: *AGU Fall Meeting, 5–9 December 2005, San Francisco, CA,* abstract V41E-1511.

ASHCHEPKOV, I. V., VLADYKIN, N. V., ROTMAN, A. Y. *ET AL*. 2005*d*. Variations of the mantle mineralogy and structure beneath Upper Muna kimberlite field. *In*: VLADYKIN, N. V. (ed.) *Problems of Sources of Deep-seated Magmatism and Plumes*. Institute of Geography SB RAS, Petropavlovsk-Kamchatsky–Irkutsk, 170–188.

ASHCHEPKOV, I. V. & VISHNYAKOVA, E. V. 2006. Monomineral ilmenite thermo- and oxybarometry and its application to reconstruction of magmatic systems and metasomatism within mantle Columns of siberian platform. *Geophysical Research Abstracts*, **8**, abstract 00921.

BEARD, B. L., FRARACCI, K. N., TAYLOR, L. A., SNYDER, G. A., CLAYTON, R. N., MAYEDA, T. K. & SOBOLEV, N. V. 1996. Petrography and geochemistry of eclogites from the Mir kimberlite, Yakutia, Russia. *Contributions to Mineralogy and Petrology*, **125**, 293–310.

BERTRAND, P. & MERCIER, J. C.-C. 1985. The mutual solubility of coexisting ortho- and clinopyroxene: toward the absolute geothermometer for the natural system? *Earth and Planetary Science Letters*, **76**, 122–152.

BOYD, F. R. & FINNERTY, A. A. 1980. Conditions of origin of natural diamonds of peridotite affinity. *Journal of Geophysical Research: Solid Earth*, **85**, 6911–6918.

BOYD, F. R., PEARSON, D. G., NIXON, P. H. & MERTZMAN, S. A. 1993. Low-calcium garnet harzburgites from southern Africa: their relations to craton structure and diamond crystallization. *Contributions to Mineralogy and Petrology*, **113**, 352–366.

BOYD, F. R., POKHILENKO, N. P., PEARSON, D. G., MERTZMAN, S. A., SOBOLEV, N. V. & FINGER, L. W. 1997. Composition of the Siberian cratonic mantle: evidence from Udachnaya peridotite xenoliths. *Contributions to Mineralogy and Petrology*, **128**, 228–246.

BRAUN, M. G. & KELEMEN, P. B. 2002. Dunite distribution in the Oman ophiolite: implications for melt flux through porous dunite conduits. *Geochemistry, Geophysics, Geosystems*, **3**, no. 11.

BREY, G. P. & KÖHLER, T. 1990. Geothermobarometry in four-phase lherzolites. II. New thermobarometers, and practical assessment of existing thermobarometers. *Journal of Petrology*, **31**, 1353–1378.

CARLSON, R. W., IRVING, A. J., SCHULZE, D. J. & HEARN, B. C. 2004. Timing of Precambrian melt depletion and Phanerozoic refertilization events in the lithospheric mantle of the Wyoming Craton and adjacent Central Plains Orogen. *Lithos*, **77**, 453–472.

DAWSON, J. B. 1980. *Kimberlites and their Xenoliths.* Springer, New York.

DOBRETSOV, N. L. & KIRDAYSHKIN, A. G. 1994. *Deep-Level Geodynamics.* UIGGM SD RAS, Novosibirsk.

EHRENBERG, S. N. 1979. Garnetiferous ultramafic inclusions in minette from the Navajo volcanic field. *In*: BOYD, F. R. & MEYER, H. O. A. (eds) *The Mantle Sample: Inclusions in Kimberlites and Other Volcanics*. American Geophysical Union, Washington, DC, 330–344.

EHRENBERG, S. N. 1982. Petrogenesis of garnet lherzolite and megacrystalline nodules from the Thumb, Navajo Volcanic Field. *Journal of Petrology*, **23**, 507–547.

FEDORTCHOUK, Y., CANIL, D. & CARLSON, J. A. 2003. Oxygen fugacity of kimberlite magmas and their relationship to the characteristics of diamond populations, Lac de Gras, N. W. T., Canada. *In*: *Extended Abstracts of the 8th International Kimberlite Conference*, abstract FLA_0098.

FINNERTY, A. A. & BOYD, F. R. 1987. Thermobarometry for garnet peridotite xenoliths: a basis for upper mantle stratigraphy. *In*: NIXON, P. H. (ed.) *Mantle Xenoliths*. Wiley, Chichester, 381–402.

FRANCIS, D. 2003. Cratonic mantle roots, remnants of a more chondritic Archean mantle? *Lithos*, **71**, 135–152.

GRÉGOIRE, M., BELL, D. R. & LE ROEX, A. P. 2002. Trace element geochemistry of phlogopite-rich mafic mantle xenoliths: their classification and their relationship to phlogopite-bearing peridotites and kimberlites revisited. *Contributions to Mineralogy and Petrology*, **142**, 603–625.

GRIFFIN, W. L., COUSENS, D. R., RYAN, C. G., SIE, S. H. & SUTER, G. F. 1989. Ni in chrome pyrope garnets: a new geothermometer. *Contributions to Mineralogy and Petrology*, **103**, 199–202.

GRIFFIN, W. L., MOORE, R. O., RYAN, C. G., GURNEY, J. J. & WIN, T. T. 1997. Geochemistry of magnesian ilmenite megacrysts from Southern African kimberlites. *Russian Geology and Geophysics*, **38**, 398–419.

GRIFFIN, W. L., RYAN, C. G., KAMINSKY, F. V. *ET AL*. 1999*a*. The Siberian lithosphere traverse: Mantle terranes and the assembly of the Siberian Craton. *Tectonophysics*, **310**, 1–35.

GRIFFIN, W. L., DOYLE, B. J., RYAN, C. G. *ET AL*. 1999*b*. Layered mantle lithosphere in the Lac de Gras area, Slave craton: Composition, structure and origin. *Journal of Petrology*, **40**, 705–725.

GRIFFIN, W. L., FISHER, N. I., FRIEDMAN, J. H., O'REILLY, S. Y. & RYAN, C. G. 2002. Cr-pyrope garnets in the lithospheric mantle. 2. Compositional populations and their distribution in time and space. *Geochemistry, Geophysics, Geosystems*, **3**, 35.

JACOB, D., JAGOUTZ, E., LOWRY, D., MATTEY, D. & KUDRJAVTSEVA, G. 1994. Diamondiferous eclogites from Siberia: Remnants of Archean oceanic crust. *Geochimica et Cosmochimica Acta*, **58**, 5195–5207.

KHARKIV, A. D., ZINCHUK, N. N. & KRYUCHKOV, A. I. 1968. *Diamonds of Yakutia*. Nedra, Moscow.

KOPYLOVA, M. G., RUSSELL, J. K., STANLEY, C. & COOKENBOO, H. 2000. Garnet from Cr- and Ca-saturated mantle: implications for diamond exploration. *Journal of Geochemical Exploration*, **68**, 183–199.

KROGH, E. J. 1988. The garnet–clinopyroxene Fe–Mg geothermometer—a reinterpretation of existing experimental data. *Contributions to Mineralogy and Petrology*, **99**, 44–48.

KULIGIN, S. S. 1997. *Complex of pyroxenite xenoliths in kimberlites from different regions of Siberian platform.* PhD thesis, United Institute of Geology, Geophysics & Mineralogy, Novosibirsk.

KULIGIN, S. S. & POKHILENKO, N. P. 1998. Mineralogy of xenoliths of garnet pyroxenites from kimberlite pipes of Siberian platform. *In*: *Extended Abstracts of the 7th Kimberlitic Conference*. Red Roof Design, Cape Town, 480–482.

KULIGIN, S. S., MALKOVETS, V. G., POKHILENKO, N. P., VAVILOV, M. A., GRIFFIN, W. L. & O'REILLY, S. Y. 2003. Mineralogical and geochemical characteristics of a unique mantle xenolith from the Udachnaya kimberlite pipe. *In*: *Extended Abstracts of the 8th International Kimberlite Conference*, *abstract* FLA_0114.

LOGVINOVA, A. M., ZEDGENIZOV, D. A. & SOBOLEV, N. V. 2001. Pyroxenite paragenesis of numerous mineral and probable fluid inclusions in microdiamonds from the MIR kimberlite pipe. *Doklady Earth Sciences*, **380**, 363–367.

LOGVINOVA, A. M., TAYLOR, L. A., FLOSS, C. & SOBOLEV, N. V. 2005. Geochemistry of multiple diamond inclusions of harzburgitic garnets as examined *in-situ*. *International Geology Review*, **47**, 1223–1233.

MALYGINA, E. V. 2000. *Xenoliths of granular mantle peridotites in Udachnaya pipe.* PhD thesis, United Institute of Geology, Geophysics & Mineralogy, Novosibirsk.

MCGREGOR, I. D. 1974. The system $MgO–SiO_2–Al_2O_3$: solubility of Al_2O_3 in enstatite for spinel and garnet peridotite compositions. *American Mineralogist*, **59**, 110–119.

MOORE, A. E. & LOCK, N. P. 2001. The origin of mantle-derived megacrysts and sheared peridotites—evidence from kimberlites in the northern Lesotho–Orange Free State (South Africa) and Botswana pipe clusters. *South African Journal of Geology*, **104**, 23–38.

NICKEL, K. G. & GREEN, D. H. 1985. Empirical geothermobarometry for garnet peridotites and implications for the nature of the lithosphere, kimberlites and diamonds. *Earth and Planetary Science Letters*, **73**, 158–170.

NIMIS, P. & TAYLOR, W. 2000. Single clinopyroxene thermobarometry for garnet peridotites. Part I. Calibration and testing of a Cr-in-Cpx barometer and an enstatite-in-Cpx thermometer. *Contributions to Mineralogy and Petrology*, **139**, 541–554.

NIXON, P. H. (ed.) 1973. *Lesotho Kimberlites*. Lesotho National Development Corporation, Maseru.

NIXON, P. H. & BOYD, F. R. 1973. Petrogenesis of the granular and sheared ultrabasic nodule suite in kimberlites. *In*: NIXON, P. H. (ed.) *Lesotho Kimberlites*. Lesotho National Development Corporation, Maseru, 48–56.

NOWELL, G. M., PEARSON, D. G., BELL, D. R., CARLSON, R. W., SMITH, C. B., KEMPTON, P. D. & NOBLE, S. R. 2004. Hf isotope systematics of kimberlites and their megacrysts: new constraints on their source regions. *Journal of Petrology*, **45**, 1583–1612.

O'NEILL, H. S. C. 1980. The transition between spinel lherzolite and garnet lherzolite and its use as a geobarometer. *Contributions to Mineralogy and Petrology*, **77**, 185–194.

O'NEILL, H. St. C. & WALL, V. J. 1987. The olivine orthopyroxene–spinel oxygen geobarometer, the nickel precipitation curve, and the oxygen fugacity of the Earth's upper mantle. *Journal of Petrology*, **28**, 1169–1191.

O'REILLY, S. Y., GRIFFIN, W. L., DIOMANY, P. & MORGAN, P. 2001. Are lithospheres forever? *GSA Today*, **11**, 4–9.

POKHILENKO, L. N. 2006. *Volatile composition and oxidation state of mantle xenoliths from Siberian kimberlites.* PhD thesis, United Institute of Geology, Geophysics & Mineralogy, Novosibirsk.

POKHILENKO, N. P., PEARSON, D. G., BOYD, F. R. & SOBOLEV, N. V. 1991. Megacrystalline dunites: sources of Siberian diamonds. *Carnegie Institution of Washington Yearbook*, **90**, 11–18.

POKHILENKO, N. P., SOBOLEV, N. V., KULIGIN, S. S. & SHIMIZU, N. 1999. Peculiarities of distribution of pyroxenite paragenesis garnets in Yakutian kimberlites and some aspects of the evolution of the Siberian craton lithospheric mantle. *In*: *Proceedings of the 7th International Kimberlite Conference. The P. H. Nixon Volume*. Red Roof Design, Cape Town, 690–707.

POKHILENKO, N. P., BOYD, F. R., ASHCHEPKOV, I. V., KULIGIN, S. S. & MALYGINA, E. V. 2000. Layered mantle beneath Udachnaya kimberlite pipe: OPX thermobarometry. *Geophysical Research Abstracts*, **2**, 154.

REIMERS, L. F., POKHILENKO, N. P., YEFIMOVA, E. S. & SOBOLEV, N. V. 1998. Ultramafic mantle assemblages from Sytykanskaya kimberlite pipe (Yakutia). *In*: *Seventh International Kimberlite Conference, Extended Abstracts*. Cape Town, 730–732.

RODEN, M. F., LAZKO, E. E. & JAGOUTZ, E. 1999. The role of garnet pyroxenites in the Siberian lithosphere: evidence from the Mir kimberlite. *In*: *Proceedings of the 7th International Kimberlite Conference. The P. H. Nixon Volume*. Red Roof Design, Cape Town, 714–720.

RYAN, C. G., GRIFFIN, W. L. & PEARSON, N. J. 1996. Garnet geotherms: pressure–temperature data from Cr-pyrope garnet xenocrysts in volcanic rocks. *Journal of Geophysical Research: Solid Earth*, **101**, 5611–5625.

SCHULZE, D. J., ANDERSON, P. F. N., HEARN, B. C. & HETMAN, C. M. 1995. Origin and significance of ilmenite megacrysts and macrocrysts from kimberlite. *International Geology Review*, **37**, 780–812.

SMITH, D. 1999. Temperatures and pressures of mineral equilibration in peridotite xenoliths: Review, discussion and implications. *In*: FEI, Y., BERTKA, C. M. & MYSEN, B. O. (eds) *Mantle Petrology: Field Observations and High Pressure Experimentation: A Tribute to Francis R. (Joe) Boyd*. Geochemical Society, Special Publications, **6**, 171–188.

SMITH, D., GRIFFIN, W. L., RYAN, C. G. & SIE, S. H. 1991. Trace element zonation in garnets from the Thumb: heating and melt infiltration below the Colorado Plateau. *Contributions to Mineralogy and Petrology*, **107**, 60–79.

SNYDER, G. A., TAYLOR, L. A., CROZAZ, G., HALLIDAY, A. N., BEARD, B. L. & SOBOLEV, V. N. 1997. The origins of Yakutian eclogite xenoliths. *Journal of Petrology*, **38**, 85–113.

SOBOLEV, N. V. 1977. *Deep-Seated Inclusions in Kimberlites and the Problem of the Composition of the Upper Mantle*. American Geophysical Union, Washington, DC.

SOBOLEV, N. V. & YEFIMOVA, E. S. 1998. The specific features of eclogitic paragenesis of diamonds from Mir and Udachnaya kimberlite pipes (Yakutia). *Geologia i Geofizika*, **39**, 1667–1678 [in Russian].

SOBOLEV, N. V., LAVRENT'EV, Y. G., POKHILENKO, N. P. & USOVA, L. V. 1973. Chrome-rich garnets from the kimberlites of Yakutia and their parageneses. *Contributions to Mineralogy and Petrology*, **40**, 39–52.

SOBOLEV, N. V., POKHILENKO, N. V. & EFIMOVA, E. S. 1984. Xenoliths of diamond bearing peridotites in kimberlites and problem of the diamond origin. *Geologiya i Geofizika*, **12**, 63–80.

SOBOLEV, N. V., KAMINSKY, F. V., GRIFFIN, W. L., YEFIMOVA, E. S., WIN, T. T., RYAN, C. G. & BOTKUNOV, A. I. 1997. Mineral inclusions in diamonds from the Sputnik kimberlite pipe, Yakutia. *Lithos*, **39**, 135–157.

SOBOLEV, N. V., SNYDER, G. A., TAYLOR, L. A., KELLER, R. A., YEFIMOVA, E. S., SOBOLEV, V. N. & SHIMIZU, N. 1998. Extreme chemical diversity in the Mantle during eclogitic diamond formation evidence from 35 garnet and 5 pyroxene inclusions in a single diamond. *International Geology Review*, **40**, 567–578.

SOBOLEV, N. V., FURSENKO, B. A., GORYAINOV, S. V., SHU, J., HEMLEY, R. J., MAO, H.-K. & BOYD, F. R. 2000. Fossilized high pressure from the Earth's deep interior: The coesite-in-diamond barometer. *Proceedings of National Academy of Sciences of the USA*, **97**, 11875–11879.

SOBOLEV, N. V., LOGVINOVA, A. M., ZEDGENIZOV, D. A. *ET AL.* 2003. Mineral inclusions in diamonds from Komsomolskaya and Krasnopresnenskaya pipes, Yakutia: evidence for deep lithospheric heterogeneities in Siberian craton. *In*: *8th International Kimberlite conference, Extended Abstracts*, abstract FLA_0141.

SOBOLEV, N. V., LOGVINOVA, A. M., ZEDGENIZOV, D. A., SERYOTKIN, Y. V., YEFIMOVA, E. S., FLOSS, C. & TAYLOR, L. A. 2004. Mineral inclusions in microdiamonds and macrodiamonds from kimberlites of Yakutia: a comparative study. *Lithos*, **77**, 225–242.

SPETSIUS, Z. V., MITYUKHIN, S. I. & IVANOV, A. S. 2004. First finding of diamond bearing xenolith in kimberlite of Botuobinskaya pipe (Nakyn field, Yakutia). *Doklady Earth Sciences*, **390**, 681–684.

TAYLOR, W. R., KAMMERMAN, M. & HAMILTON, R. 1998. New thermometer and oxygen fugacity sensor calibrations for ilmenite and chromian spinel-bearing peridotitic assemblages. *In*: *7th International Kimberlite Conference, Extended Abstracts*. Cape Town, 891–901.

TAYLOR, L. A., GREGORY, A., KELLER, S. R. *ET AL.* 2003. Petrogenesis of group A eclogites and websterites: evidence from the Obnazhennaya kimberlite, Yakutia. *Contributions to Mineralogy and Petrology*, **145**, 424–443.

VAN KEKEN, P. E., KIEFER, B. & PEACOCK, S. 2002. High-resolution models of subduction zones: Implications for mineral dehydration reactions and the transport of water into the deep mantle. *Geochemistry, Geophysics, Geosystems*, **3**, 20.

WYLLIE, P. J. 1995. Experimental petrology of upper mantle materials, process and products. *Journal of Geodynamics*, **20**, 429–468.

Index

Page numbers in *italic* denote figures. Page numbers in **bold** denote tables.

Twenty years have passed since Menzies & Hawkesworth extended the concept of metasomatism to mantle processes. The aim of this book is to gather together progress made on this topic since then. Most of the 14 papers reported in the volume rely on *in situ* major and trace element analyses of minerals and glasses in mantle xenoliths, and deal with different kinds of metasomatic agents at variable fluid / rock ratios in tectonic settings as different as intra-plate, mid-ocean ridge (ophiolites) and supra-subduction. The book contributes to the wide debate on the nature of the fluids migrating into the mantle wedge, as well as on the different residential times of the subduction signature. In addition papers on intra-plate settings deal with the problem of relating various metasomatic signatures to one single metasomatic event through an infiltration-reaction process.